

**MICROSTRUCTURAL EVOLUTION OF  
WELDED CREEP AGED 12% Cr  
MARTENSITIC STAINLESS STEEL**

**G. Marx**

**2019**

# **Microstructural Evolution of Welded Creep Aged 12% Cr Martensitic Stainless Steel**

by

**Genevève Marx**

Submitted in fulfilment of the requirements for the degree of

**Doctor of Philosophy (Physics)**

to be awarded at the Nelson Mandela University

April 2019

Supervisor: Dr. J.E. Westraadt

Co-Supervisor: Prof. J.H. Neethling

*Soli Deo gloria*


**This thesis is dedicated to my husband and parents.**

*For their endless love, support and encouragement*

# DECLARATION

---

I, **Genevève Marx** with student number **210059257**, hereby declare that this **thesis** for the **degree of Doctor of Philosophy (Physics)** is my own work and that it has not previously been submitted for assessment or completion of any postgraduate qualification to another University or for another qualification.

Signature:  \_\_\_\_\_  
Date: 19/3/2019

Official use:

In accordance with Rule G.5.6.3 of the General Prospectus,

5.6.3 A treatise/dissertation/thesis must be accompanied by a written declaration on the part of the candidate to the effect that it is his/her own original work and that it has not previously been submitted for assessment to another University or for another qualification. However, material from publications by the candidate may be embodied in a treatise/dissertation/thesis.

# ACKNOWLEDGEMENTS

First and foremost, I would like to praise and give thanks to my God Who enabled me, through the grace of my Lord and Saviour Jesus Christ, to complete this study. He is the rock on whom I confidently trusted.

I would then like to thank my supervisor Dr. J.E. Westraadt for his guidance throughout this project. This project has been a vision of his that I have been fortunate enough to be able to realise. I would not be the independent researcher I am today without his mentorship. A great thanks for steadfast support I give to my co-supervisor Prof. J.H. Neethling.

The financial assistance from the NRF, Nelson Mandela University and the Materials and Mechanics Specialisation Group (UCT) of the Eskom Power Plant Engineering Institute is gratefully acknowledged. Also thank you to Eskom R&D for supplying the samples for this study. I would like to thank Mr. W.E. Goosen, Mr. E.G. Minnaar and Dr. A. Janse van Vuuren for providing me with training on the electron microscopes at the Centre for HRTEM. A special thank you to Mr. N. Mfuma (Centre for HRTEM) for his assistance with sample preparation during the study. The assistance from Ms. L. Matthews, Mr. W. Pens and Mr. R. Brown with LM, Vickers MHT, EDM and PWHT, respectively, at eNtsa is gratefully acknowledged. For the Gleeble™ simulations and XRD measurements I would like to thank Ms. S. von Willingh from UCT and Dr. R. Forbes from Wits, respectively.

A special thank you to my friends and family for their prayers and support throughout this project. Specifically, thank you to Bianca, Lizanne and Lindsay for lending an ear and making me smile when I needed it the most. To my mom and dad – I cannot express my gratitude in words for providing me with the best opportunities in life no matter at what cost. Lastly, my amazing husband, Divan, thank you for sacrificing so much to ensure I reach my full God purposed potential. Your love, understanding and encouragement has meant more to me than you can ever imagine.

# SUMMARY

Tempered martensite ferritic (TMF) steels with 9-12% Cr additions are used extensively for high-pressure steam pipes in coal-fired power plants. They operate at temperatures above 500°C and are consequently susceptible to creep damage. Due to economic reasons, welding must be performed on service exposed materials when a component needs to be replaced. Fusion welding results in the formation of different microstructural regions within the weldment. The primary failure mechanism of TMF steel welded components is Type IV cracking that results from accelerated void formation in the fine-grained heat affected zone (FGHAZ) during creep. Short-term creep-tests performed across weldments made on new and service exposed steels have shown that the weldment consistently fails in the FGHAZ of the service exposed material. This observation has not yet been fully explained since not much is known about the microstructural evolution of creep aged material during welding. Thus, further investigation on the microstructure of welded creep aged material is warranted. The main aim of this thesis was to investigate the microstructural evolution when welding upon creep aged 9-12% Cr martensitic steels using advanced electron microscopy techniques.

X20CrMoV12-1 (12% Cr) in the virgin and long-term service-exposed state were investigated. Gleeble™ weld simulation of the FGHAZ was performed on the materials. Detailed microstructural investigations were conducted on the parent and simulated FGHAZ materials to analyse the voids, dislocation density, micro-grains, and precipitates ( $M_{23}C_6$ , MX, Laves, Z-phase) in the materials. Light Microscopy (LM) and Scanning Electron Microscopy (SEM) was used to examine the voids. Twin-jet electropolished specimens were prepared for precipitate, micro-grain and substructure analyses using Transmission Kikuchi Diffraction (TKD) combined with Energy Dispersive Spectrometry (EDS), Concentric Backscatter (CBS) imaging, Energy-Filtered Transmission Electron Microscopy (EFTEM), and Annular Dark-Field Scanning Transmission Electron Microscopy (ADF-STEM) combined with EDS. The precipitates were extracted from the iron matrix using Bulk Replication and further investigated using EFTEM and STEM-EDS.

Semi-automated image analysis was performed using MIPAR™ to quantify the various microstructural parameters.

The measured microstructural data was used in a microstructure-based creep model to determine the creep strength of each material. The model failed to explain the preference of Type IV failure on the creep aged material side instead of the new material side of the weldment - a higher creep strength was predicted for the creep aged simulated FGHAZ materials compared to the new simulated FGHAZ material. Subsequently, the distinct microstructural differences between the new and creep aged simulated FGHAZ materials were further considered to provide a possible explanation.

The creep aged simulated FGHAZ materials were found to have voids that are smaller but higher in both number density and area fractions compared to the new simulated FGHAZ material. These results are an indication that the creep aged simulated FGHAZ materials have considerably higher creep damage than the new simulated FGHAZ material. This creep damage was inherited from the corresponding parent materials. Considerably larger  $M_{23}C_6$  carbides ( $\varnothing > 300$  nm) were observed in the creep aged simulated FGHAZ materials and not in the new simulated FGHAZ material. Therefore, the pre-existing creep voids in the creep aged parent material and the large  $M_{23}C_6$  carbides in the FGHAZ after welding are proposed as the main microstructural contributions that could accelerate Type IV failure on the creep aged side of TMF steel weldments.

From the results of this study, recommendations were made towards the use of a microstructure-based assessment of TMF steels for determining their weldability limits.

*Keywords: TMF steels, FGHAZ, Gleeble™ Simulation, Type IV Cracking, Microstructure, Electron Microscopy, Weldability.*



# OPSOMMING

Verharde martensitiese ferritiese (VMF) staalsoorte met 9% tot 12% Cr-toevoegsels word ekstensief gebruik vir hoëdruk-stoompepe in steenkool-aangedrewe kragstasies. Die material opereer teen temperature bo 500 °C en is dus vatbaar vir kruipkade. Weens ekonomiese redes is dit nodig dat materiale wat reeds in diens is, gesweis word wanneer dit nodig is om 'n komponent te vervang. Smelt sweiswerk veroorsaak die vorming van verskeie mikrostrukturele streke binne die sweisement. Die vernaamste breukmeganisme van gesweide komponente van VMF-staal is Tipe IV-kraak wat die gevolg is van versnelde holteformasie in die fyngekorrelde hitte-aangetaste sone (FKHAS) tydens kruip. Korttermyn kruiptoetse wat op nuwe en diens-blootgestelde sweisemente uitgevoer is, het getoon dat die sweisement aanhoudend in die FKHAS van die diens-blootgestelde staalsoorte misluk. Aangesien nie veel van die mikrostrukturele ontwikkeling van kruipverouderde material tydens sweis bekend is nie, is hierdie verskynsel nog nie ten volle verklaar nie en word verdere ondersoek van die mikrostruktuur van gesweide kruipverouderde materiaal benodig. Dus is die hoofdoel van hierdie tesis 'n ondersoek van die mikrostrukturele ontwikkeling tydens sweiswerk op kruipverouderde 9% tot 12% Cr martensitiese stalle met gebruik van gevorderde elektron-mikroskopiese tegnieke. Die verskynsel van Tipe IV-kraak is hersien om sodoende die implikasies van die FKHAS-mikrostruktuur op die bevordering van hierdie soort mislukkings beter te verstaan.

In hierdie studie is X20CrMoV12-1 (12% Cr) in beide die onbeplekte en die langtermyn diens-blootgestelde toestand ondersoek. Gleeble™ sweissimulering van die FKHAS is op die materiaal uitgevoer om sodoende vir die ondersoek 'n groter proefvolume te skep met 'n homogene mikrostruktuur. Gedetailleerde mikrostrukturele ondersoeke is op die basismetale en die gesimuleerde FKHAS-materiale uitgevoer om sodoende die leemtes, ontwrigtingsdigtheid, mikro-greine en presipitate ( $M_{23}C_6$ , MX, Laves, Z-fase) in die materiale te kwantifiseer. LM en SEM was toegepas op die basismetale en gesimuleerde FKHAS-materiale om die leemtes te analiseer. Rietveld-verfyning van X-straal Diffraksie patrone is gebruik om die ontwrigtingsdigtheid uit die massamonsters te kwantifiseer. Dubbelstraal elektrogepoleerde monsters is voorberei vir analyses van presipitate,

mikrogrein en substruktuur met gebruik van TKD, gekombineer met EDS, CBS beeldvorming, EFTEM en ADF-STEM wat met EDS gekombineer is. Die presipitate is uit die ystermatriks uitgetrek met behulp van massareplikasie en verder ondersoek met gebruik van EFTEM en ADF-STEM. Half-outomatiese beeldanalise is met behulp van MIPAR™ uitgevoer om die verskeie mikrostrukturele parameters te kwantifiseer.

Uit die resultate is die mikrostrukturele staat van die kruipverouderde basis- en FKHAS materiale bepaal. Die mikrostrukture van die nuwe en kruipveroudeerde gestimuleerde FKHAS-materiale is vergelyk. Die kruipverouderde gestimuleerde FKHAS materiale het heelwat meer kruipskade as die nuwe gestimuleerde FKHAS materiale aangesien die leemtes kleiner is, maar het ook hoë getalsdensiteit en gebiedsbreuke. Hierdie kruipskade is van die ooreenkomstige basismateriale oorgeërf. Besonderse groot  $M_{23}C_6$  presipitate ( $\varnothing > 300$  nm) is in die kruipverouderde gesimuleerde FKHAS materiale opgelet, maar nie in die nuwe gesimuleerde FKHAS materiale nie. Na verdere kruip-blootstelling sal die groter  $M_{23}C_6$  presipitate aanmerklik groei en verkieslike liggings vir leemte-kernvorming word, en die bestaande leemtes sal vergroot en verenig. Dus word die voorafbestaande kruipleemtes in die kruipverouderde basismateriaal en die groot  $M_{23}C_6$  presipitate in die FKHAS na sweiswerk geïdentifiseer as die mikrostrukturele hoofbydrae wat Tipe IV-kraak aan die kruipverouderde kant van VMF-staal-sweisemente veroorsaak.

Mikrostruktuur-gebaseerde kruipmodelle kan gebruik word om die kruipsterkte te bepaal. 'n Beskouing van sulke kruipmodelle word in hierdie tesis weergee. Uit hierdie beskouing en die resultate van hierdie studie is aanbevelings gemaak in die rigting van die gebruik van 'n mikrostruktureel-gebaseerde skatting van 9% tot 12% Cr-staalsoorte vir die bepaling van hul sweisbaarheidsperke.

*Sleutelwoorde: VMF-staalsoorte, FKHAS, Gleeble™ simulering, Tipe IV-kraak, mikrostruktuur, electron-mikroskopies, sweisbaarheid.*

# LIST OF ABBREVIATIONS

---

---

Abbreviation	Meaning
--------------	---------

---

ADF	Annular Dark Field
BC	Band Contrast
bcc	body-centered cubic
BF	Bright Field
BM	Base Material
BRT	Bulk Replication Technique
BSE	Backscattered Electron
CBS	Concentric Backscatter
CCT	Continuous Cooling Transformation
CDM	Continuum Damage Model
CGHAZ	Coarse-Grained HAZ
CL	Camera Length
CM	Critical Misorientation
CSEF	Creep Strength Enhanced Ferritic
DF	Dark Field
DH	Dislocation Hardening
EBS	Electron-Backscatter Diffraction
ECD	Equivalent Circular Diameter
EDS	Energy Dispersive Spectrometry
EELS	Electron Energy-Loss Spectroscopy
EFTEM	Energy-Filtered TEM
EM	Electron Microscopy
fcc	face-centered cubic
FEG	Field Emission Gun
FGHAZ	Fine-Grained HAZ
FIB	Focused Ion Beam

---

---

---

GB	Grain Boundary
GBS	Grain Boundary Sliding
GIF	Gatan Imaging Filter
HAADF	High-Angle Annular Dark Field
HAGB	High-Angle Grain Boundary
HAZ	Heat Affected Zone
HTPP	High Temperature Pressure Pipework
ICHAZ	Inter-Critical HAZ
IPF	Inverse Pole Figure
KS	Kurdjumov-Sachs
LAGB	Low-Angle Grain Boundary
LB	Lath Boundary
LI	Linear Intercept
LM	Light Microscopy
MGB	Micro-grain Boundary
MHT	Microindentation Hardness Testing
MMA	Manual Metal Arc
MO	Misorientation
ND	Normal Direction
NND	Nearest Neighbour Distance
NW	Nishiyama–Wasserman
PAG	Prior Austenite Grain
PAGB	Prior Austenite Grain Boundary
PH	Precipitate Hardening
PWHT	Post-Weld Heat Treatment
RD	Rolling Direction
RGB	Red, Green and Blue
SBH	Sub-Boundary Hardening
SE	Secondary Electrons
SEM	Scanning Electron Microscope
SGB	Subgrain Boundary

---

---

SI	Spectrum Imaging
SRF	Strength Reduction Factor
SSH	Solid-Solution Hardening
STEM	Scanning TEM
TD	Transverse Direction
TEM	Transmission Electron Microscope
TKD	Transmission Kikuchi Diffraction
TMF	Tempered Martensite Ferritic
WM	Weld Metal
WSF	Weld Strength Factor
X20	X20CrMoV12-1
XRD	X-Ray Diffraction

---

# LIST OF FIGURES

**Figure 1.1:** Eskom’s mix of generating power plants (Constructed from (Eskom 2017)). ..... 1

**Figure 1.2:** Overview of the historical development and corresponding 100 000 h creep rupture strength at 600 °C of heat-resistant 9-12% Cr steels (Francis, Mazur and Bhadeshia 2006). ..... 2

**Figure 2.1:** Schematic illustration and images of boiler components of a coal-fired power plant and the typical component materials (Igarashi 2008). ..... 13

**Figure 2.2:** (a), (b) and (c) Examples of theoretical creep curves of steels under constant tensile load and temperature. (d), (e) and (f) Corresponding creep rate curves as a function of time (Abe 2008). ..... 18

**Figure 2.3:** Creep curve for X20 martensitic steel (EPRI 2006). ..... 18

**Figure 2.4:** Creep rupture strength for X20CrMoV12-1 Steel at 550 °C (EPRI 2006). ..... 19

**Figure 2.5:** CCT diagram for X20CrMoV12-1 steel (Aghajani 2009). ..... 21

**Figure 2.6:** Fe-Cr-C phase diagram and schematic illustration of microstructure resulting from heat treatment of 9-12% Cr martensitic steels, highlighting normalising N (blue) and tempering T (green) ranges (Pandey, Mahapatra, Kumar and Saini 2018). ..... 23

**Figure 2.7:** Schematic illustration of shear and surface tilt resulting from the formation of martensite plate (Krauss 2015). ..... 25

**Figure 2.8:** Hierarchical microstructure of lath martensite defined in four scales: parent austenite grains, packets, blocks and laths (Hatem and Zikry 2009). ..... 26

**Figure 2.9:** Bain Strain mechanism of lattice distortion and correspondence to obtain the martensite variant from the parent austenite. There is a compression along one of the  $\langle 100 \rangle_{\gamma}$  cube axes and a uniform expansion in the perpendicular planes until it becomes bcc (Bhadeshia and Wayman 2014). ..... 27

**Figure 2.10:** Schematic illustration of the ideal initial microstructure of tempered martensite microstructure in 9-12%Cr ferritic steels. Single micro-grain outlined in white. ..... 31

**Figure 2.11:** Micrograph of most common precipitates in 9-12% Cr martensitic steels (Danielsen and Hald 2006). ..... 37

<b>Figure 2.12:</b> TEM micrographs that provide evidence of the direct interaction of MGB carbides on dislocation processes at boundaries and on boundary migration: (a) Carbides interrupt knitting reactions between dislocations and SGB. (b) Carbides stabilise a small micro-grain by exerting Zener forces (Kostka, Tak, Hellmig, Estrin and Eggeler 2007). .....	41
<b>Figure 2.13:</b> Schematic illustrations of Laves phase nucleation. (a) Initial microstructure. (b) Mo and Si segregation to the micro-grain boundary. (c) Nucleation and rod-like growth along the boundary with the direction indicated by red arrow. (d) Growth into a bulky shape at later stages (Isik, Kostka and Eggeler 2014). .....	47
<b>Figure 2.14:</b> (a) and (b) TEM results of the growth mechanism of Laves phase precipitates by swallowing of adjacent $M_{23}C_6$ carbides in creep aged 10% Cr steel. (c) Schematic diagrams of swallowing growth mechanism (Xu, Nie, Wang, Li and Jin 2017). .....	48
<b>Figure 2.15:</b> Two proposed nucleation mechanisms of Z-phase precipitates (Yan, Wang, Shan and Yang 2013). .....	51
<b>Figure 2.16:</b> Schematic diagram of intergranular damage development ( $t_f$ corresponds to the time to failure) (Sklenička, Kuchařová, Svoboda, Kloc, Buršík et al. 2003). .....	63
<b>Figure 2.17:</b> Schematic creep curves for a uniaxial stress state and a multiaxial stress state if creep cavitation is the dominant mechanism. $\sigma_0$ , $t_u$ , LTC, $\sigma_v$ and $\epsilon_{ur}$ indicates nominal applied stress (MPa), rupture time (h), lifetime consumption, equivalent stress and uniform rupture strain (%), respectively (Schleyer, Speicher, Klenk and Seidenfuß 2017). .....	69
<b>Figure 2.18:</b> Schematic diagram of a cross-section through an MMA girth weld performed on a steam pipe. The weld axes are given as the rolling (weld) direction (RD), normal direction (ND) and transverse direction (TD) (Marx 2016). .....	71
<b>Figure 2.19:</b> Schematic illustration of the different microstructural regions in the HAZ correlated to the calculated equilibrium phase diagram of a P91 (X10CrMoVNb9-1) type steel (Cerjak and Mayr 2008). .....	73
<b>Figure 2.20:</b> Schematic illustration of the microstructural evolution of the FGHAZ in the as-welded and PWHT condition (Pandey, Mahapatra, Kumar and Saini 2018). .....	77
<b>Figure 2.21:</b> Schematic illustration of the ICHAZ microstructure (Wang, Kannan and Li 2016). .....	78
<b>Figure 2.22:</b> Schematic illustration of the various cracking modes in a creep resistant ferritic steel weldment (Cerjak and Mayr 2008). .....	88

<b>Figure 2.23:</b> Schematic diagram of different tube (pipe) welds. S, L and T refer to the short transverse, longitudinal and transverse directions, respectively (Bilat, Gourgues-Lorenzon, Besson and Pineau 2006).	91
<b>Figure 2.24:</b> Schematic illustration of creep rupture stress versus time to show the reduction in creep rupture strength after the onset of Type IV cracking for weldments at a fixed temperature. Expected fracture location is indicated. As can be seen, Type IV cracking occurs much earlier than for a parent or weld metal specimen under the same test conditions (Abson and Rothwell 2013).	92
<b>Figure 2.25:</b> Schematic illustration of the Type IV cracking mechanism (Constructed from Cerjak and Mayr (2008)).	94
<b>Figure 2.26:</b> Schematic illustration of the surface replication technique (Marder 1989).	100
<b>Figure 2.27:</b> Cavitation evolution at different stages of creep life as determined from surface replication (Gupta, Toda, Mayr and Sommitsch 2015).	103
<b>Figure 2.28:</b> Illustration of the main difference between phenomenological and physical creep models.	109
<b>Figure 2.29:</b> A proposed combination of thermodynamic, kinetic and creep modelling to predict creep strength (Adapted from Vanstone (2001)).	116
<b>Figure 2.30:</b> Schematic illustration of how a dislocation will pass precipitates by (a) the Orowan mechanism, (b) the general climb mechanism and (c) the local climb mechanism (Abe 2008).	119
<b>Figure 2.31:</b> Detailed illustration of the bypass of strong precipitates by a dislocation according to the Orowan mechanism, where the mean interparticle spacing is given by $\lambda$ (Holzer 2010).	121
<b>Figure 3.1:</b> Image of the X20 steel pipework used in this research (Molokwane 2014).	133
<b>Figure 3.2:</b> Schematic illustration of the position and direction of the $\varnothing 11\text{mm} \times 140\text{ mm}$ rods cut from the pipework (Adapted from Aghajani (2009)).	136
<b>Figure 3.3:</b> Images of (a) $\varnothing 11\text{mm} \times 140\text{ mm}$ rods cut from a bulk piece of pipework and (b) final $\varnothing 10\text{ mm} \times 140\text{ mm}$ samples used for Gleeble <sup>TM</sup> simulation.	137
<b>Figure 3.4:</b> Image of sample set-up in the Gleeble <sup>TM</sup> 3800 (Rasiawan 2017). The sample is held in place by copper grips and fixed into position by C-grips (indicated by red arrows).	139



**Figure 3.5:** Gleeble™ FGHAZ simulation temperature-time profiles for (a) new X20 base material, (b) creep aged 1 base material and (c) creep aged 2 base material. Thermocouple 1 and 2 refers to centre and 5 mm from centre thermocouples, respectively..... 140

**Figure 3.6:** Images of (a) thermocouples spot-welded onto Gleeble™ simulated rod samples and (b) furnace set-up for PWHT. .... 141

**Figure 3.7:** Measured temperature-time profile for PWHT performed on weld thermal cycle simulated samples. .... 143

**Figure 3.8:** Image of final simulated FGHAZ rods and subsequent sectioning using wire cutting. Sections A and D correspond to the parent bulk specimens and sections B and C correspond to the simulated FGHAZ bulk specimens. The “x” symbols mark the surface on which XRD was performed for the simulated FGHAZ samples and from which subsequent 1.2 mm discs was sectioned for thin foil specimens. .... 144

**Figure 3.9:** Schematic diagram of a twin-jet electropolished specimen. The circular grey area is the area available for analyses..... 147

**Figure 3.10:** Schematic illustration of the main steps of the Bulk Replication Technique. (a) Polish the bulk specimen surface. (b) Etch away the top layer of the iron matrix to expose the precipitates for extraction. (c) Deposit a carbon coat on top of specimen surface to cover the exposed precipitates. (d) Obtain carbon coat specimen containing only precipitates by chemically dissolving the rest of the iron matrix (Marx 2016). .... 148

**Figure 3.11:** Comparison of sampling areas in (a) FIB specimen ( $\pm 5 \times 5 \mu\text{m}^2$ ), (b) conventional (ion-mill, twin-jet electropolished) TEM specimen and (b) extraction replica ( $\pm 2.5 \times 2.5 \text{mm}^2$ ) (Marx 2016). The area available for analysis is indicated by the grey areas. .... 149

**Figure 3.12:** Selected specimen orientation in AZtechKL EBSD software. Refer to **Figure 2.18** for descriptions of abbreviations..... 155

**Figure 3.13:** Schematic illustration of a CBS detector layout and angular separation of the BSE signal (FEI 2013)..... 158

**Figure 3.14:** Screenshots from ARPGE software of parameters used for reconstruction of PAG in (a) parent and (b) simulated FGHAZ materials. .... 169

**Figure 3.15:** Illustration of fitted equivalent measurements (right) to thresholded micro-grains from CBS images (left) using MIPAR™. .... 177

<b>Figure 3.16:</b> Schematic illustration of the various dislocations in the tempered martensite microstructure of 9-12% Cr ferritic steels and the corresponding techniques that can analyse their densities (Yadav, Kalácska, Dománková, Yubero, Resel et al. 2016). .....	179
<b>Figure 4.1:</b> 1.1 x 0.8 mm <sup>2</sup> BF optical micrographs of the etched bulk specimen surfaces.....	185
<b>Figure 4.2:</b> Montage of 23 x 3 BF optical micrographs taken across etched surface of cross section of simulated FGHAZ Ø 10 mm rod specimen (sample area = 5 x 0.8 mm <sup>2</sup> ). .....	186
<b>Figure 4.3:</b> Mean measured Vickers hardness values of the parent (9 indents) and simulated FGHAZ X20 steel (36 indents). The error is reported as the 95% CI. ....	187
<b>Figure 4.4:</b> Measured Vickers hardness values for the new parent and simulated FGHAZ X20 steel from this study plotted on Vickers MHT profile along new X20 weldment measured in the study by Marx (2016). The range of values obtained along 3 lines of indents are indicated and the subsequent different weld regions identified by Marx (2016). ....	188
<b>Figure 4.5:</b> 204 x 153 µm <sup>2</sup> Colour maps of reconstructed PAG from EBSD maps. Random colour coding used. ....	191
<b>Figure 4.6:</b> 204 x 153 µm <sup>2</sup> EBSD IPF_Z <sub>0</sub> map with reconstructed PAGB outlined (204 x 153 µm <sup>2</sup> , 15 kV, 4 nA, 200 nm step-size). ....	192
<b>Figure 4.7:</b> Box-and-whisker plots of PAG size distributions measured using ARPGE software for (a) all samples, (b) new simulated FGHAZ and actual weldment regions from Marx (2016), (c) only parent and (d) simulated FGHAZ specimens. The “x” symbol indicates the mean. ....	193
<b>Figure 4.8:</b> (a) Micrograph of EBSD polished surface (296 x 296 µm <sup>2</sup> area) of creep aged 2 parent X20 bulk specimen. (b) Thresholded voids (1 to 3 µm ECD) of the same area as in (a). ....	195
<b>Figure 4.9:</b> 2D Measured ECD histogram plots of the voids observed from the LM micrographs of (a) parent and (b) simulated FGHAZ materials, (c) new, (d) creep aged 1 and (e) creep aged 2 materials (total area of 1.4 mm <sup>2</sup> analysed). ....	196
<b>Figure 4.10:</b> ECD KDE distribution plots (scalar factor = 0.30 – 0.42) of corrected void size measurements from the LM micrographs of (a) parent and (b) simulated FGHAZ materials, (c) new, (d) creep aged 1 and (e) creep aged 2 materials (total area of 1.4 mm <sup>2</sup> analysed). ....	197
<b>Figure 4.11:</b> Mean void ECD measured from corrected ECD distributions of parent and simulated FGHAZ specimens (1.4 mm <sup>2</sup> sampling area). The error is given as 95% CI.....	198

**Figure 4.12:** Mean void number densities  $N_A$  measured from parent and simulated FGHAZ bulk specimens (total sampling area of  $1.4 \text{ mm}^2$ ). The error is given by Equation (3.17). ..... 199

**Figure 4.13:** Box-and-whisker plots of the nearest neighbour distance (NND) distributions of voids measured from parent and simulated FGHAZ bulk specimens (total sampling area of  $1.4 \text{ mm}^2$ ). The “x” symbol indicates the mean..... 199

**Figure 4.14:** Colour maps of area fraction across 16 areas analysed (total area of  $1.4 \text{ mm}^2$  analysed) per parent and simulated FGHAZ specimen. Cooler colours correspond to lower area fractions of voids. ....200

**Figure 4.15:** 10 kV SE-SEM image of EBSD (colloidal) polished surface of new parent material. Some of the cavities and their ECD are indicated by the red arrows. ....201

**Figure 4.16:** 10 kV SE-SEM image of EBSD (colloidal) polished surface of new simulated FGHAZ material. The image on the right is an enlargement of the area bounded by the red rectangle in the image on the left. Some of the cavities and their ECD are indicated by the red arrows. ....202

**Figure 4.17:** 10 kV SE-SEM image of EBSD (colloidal) polished surface of creep aged 1 parent material. PAGB shown by the red line in the image on the left and the image on the right is the enlarged area of the same PAGB. Some of the cavities and their ECD are indicated by the red arrows. ....202

**Figure 4.18:** 10 kV SE-SEM image of EBSD (colloidal) polished surface of creep aged 2 parent material. The image on the right is an enlargement of the area bounded by the red rectangle in the image on the left. Some of the cavities and their ECD are indicated by the red arrows. ....203

**Figure 4.19:** 10 kV SE-SEM images of EBSD (colloidal) polished surface of creep aged 1 simulated FGHAZ material. Some of the cavities and their ECD are indicated by the red arrows. ....204

**Figure 4.20:** 10 kV SE-SEM images of EBSD (colloidal) polished surface of creep aged 2 simulated FGHAZ material. Some of the cavities and their ECD indicated by red arrows. ....205

**Figure 4.21:** (a) SE image, (b) BSE image, (c) BC map, (d) BC map with voids (blue) and cavities (red) isolated, (e) EBSD BC and GB map, and (f) EBSD IPF\_ $Z_0$  map of the same area on creep aged 2 parent bulk specimen. The white dotted line indicates some PAGB. ....206

**Figure 4.22:** (a) BSE image, (b) BC map with voids (blue) and cavities (red) isolated, (c) EBSD BC and GB map, and (d) EBSD IPF\_ $Z_0$  map of the same area on creep aged 2 simulated FGHAZ bulk specimen. The white dotted line indicates some prior PAGB. ....207

**Figure 4.23:** Relative frequency of misorientation angles measured from 204 x 153  $\mu\text{m}^2$  EBSD maps acquired from parent and simulated FGHAZ X20 steel. Boundaries with misorientations below  $15^\circ$  are defined as low-angle boundaries (LAGB) and those with misorientations above  $15^\circ$  as high-angle boundaries (HAGB). The dashed line represents the expected distribution for a randomly textured polycrystal cubic system as given by the Mackenzie distribution (Mackenzie 1958). .....215

**Figure 4.24:** Summary of MO distributions of parent and simulated FGHAZ X20 steel (204 x 153  $\mu\text{m}^2$  sampling area). Some of the peaks have been enlarged to enhance visibility. The dashed line represents the expected distribution for a randomly textured polycrystal cubic system as given by the Mackenzie distribution (Mackenzie 1958). The vertical black lines indicate the MO for the variant intersections from Payton, Aghajani, Otto, Eggeler and Yardley (2012), and Brust, Niezgodna, Yardley and Payton (2018).....216

**Figure 4.25:** Relative frequency and MO of estimated variant intersections for parent and simulated FGHAZ X20 materials (204 x 153  $\mu\text{m}^2$  sampling area).....218

**Figure 4.26:** 12 x 12  $\mu\text{m}^2$  TKD GB maps of parent and simulated FGHAZ X20 twin-jet electropolished specimens (30 nm step-size).....219

**Figure 4.27:** Boundary (green) and interior (pink) Cr-enriched  $\text{M}_{23}\text{C}_6$  carbides isolated from 12 x 12  $\mu\text{m}^2$  Cr TKD-EDS map and superimposed onto corresponding TKD GB ( $\text{MO} > 2^\circ$ ) map obtained from parent and simulated FGHAZ twin-jet electropolished specimens. The same areas as in Figure 4.26 is shown.....223

**Figure 4.28:** 18.6 x 12.3  $\mu\text{m}^2$  5 kV CBS images of 18.6 x 12.3  $\mu\text{m}^2$  area scanned across parent and simulated FGHAZ twin-jet electropolished specimens. ....226

**Figure 4.29:** Thresholded boundary (green) and interior (pink)  $\text{M}_{23}\text{C}_6$  carbides overlaid onto corresponding 18.6 x 12.3  $\mu\text{m}^2$  CBS image obtained from parent and simulated FGHAZ twin-jet electropolished specimens. Black boundaries outline MGB given by CBS image. The same areas as in Figure 4.28 is shown.....227

**Figure 4.30:** 6 x 6  $\mu\text{m}^2$  RGB composite maps of EFTEM Cr (green) and V (red) elemental maps acquired from an area in the parent and simulated FGHAZ twin-jet electropolished specimens. ....229

**Figure 4.31:** 6 x 6  $\mu\text{m}^2$  RGB composite maps of EFTEM Cr (green) and V (red) elemental maps acquired from an area in the parent and simulated FGHAZ extraction replica specimens. ....230

**Figure 4.32:** Outlines of thresholded VX precipitates from 6 x 6  $\mu\text{m}^2$  EFTEM V maps acquired from parent and simulated FGHAZ extraction replica specimens. The yellow arrow indicates an area that is an O enriched area that has been inaccurately determined as V due to overlapping energy windows. The O signal is from the underlying carbon coat. ....232

**Figure 4.33:** STEM-EELS spectrum acquired from the edge of an  $M_{23}C_6$  carbide (area indicated by the tiny green square) in new parent material extraction replica specimen. ....233

**Figure 4.34:** Corrected  $M_{23}C_6$  carbide (boundary and interior combined) ECD KDE distribution plots (scalar factor = 0.014 – 0.027) measured from CBS images of (a) parent and (b) simulated FGHAZ materials, (c) new, (d) creep aged 1 and (e) creep aged 2 materials (total area of 915  $\mu\text{m}^2$  analysed). ....235

**Figure 4.35:** Corrected boundary (green) and interior (pink)  $M_{23}C_6$  carbide ECD KDE distribution plots (scalar factor = 0.014 – 0.027) measured from CBS images of (a) new, (b) creep aged 1 and (c) creep aged 2 parent materials, and (d) new, (e) creep aged 1 and (f) creep aged 2 simulated FGHAZ materials (total area of 915  $\mu\text{m}^2$  analysed).....236

**Figure 4.36:** Mean corrected diameter ( $d_s$ ) calculated for the boundary and interior  $M_{23}C_6$  carbides obtained from CBS images of parent and simulated FGHAZ twin-jet electropolished specimens (total area of 915  $\mu\text{m}^2$  analysed). The error is given by Equation (3.15).....237

**Figure 4.37:** Mean corrected diameter ( $d_s$ ) for both boundary and interior  $M_{23}C_6$  carbides combined and obtained from CBS images of parent and simulated FGHAZ twin-jet electropolished specimens (total area of 915  $\mu\text{m}^2$  analysed). The error is given by Equation (3.15).....238

**Figure 4.38:** Box-and-whisker plots of distributions of (a) distances of interior  $M_{23}C_6$  carbides from MGB in CBS images and (b)  $M_{23}C_6$  carbide 2D NND (interparticle spacing) measured from CBS images of parent and simulated FGHAZ twin-jet electropolished specimens (total area of 915  $\mu\text{m}^2$  analysed). The “x” symbol indicates the mean. ....239

**Figure 4.39:** Mean number density  $N_v$  of boundary and interior  $M_{23}C_6$  carbides measured from CBS images of parent and simulated FGHAZ twin-jet electropolished specimens (total area of 915  $\mu\text{m}^2$  analysed). The error is given by Equation (3.17). ....240

**Figure 4.40:** Mean overall number density  $N_v$  of both boundary and interior  $M_{23}C_6$  carbides measured from CBS images of parent and simulated FGHAZ twin-jet electropolished specimens (total area of 915  $\mu\text{m}^2$  analysed). The error is given by Equation (3.17).....241

**Figure 4.41:** Mean 2D interparticle spacing  $\lambda$  of  $M_{23}C_6$  carbides measured from CBS images of parent and simulated FGHAZ twin-jet electropolished specimens (total area of  $915 \mu\text{m}^2$  analysed). The error is given by Equation (3.17). .....242

**Figure 4.42:** Mean volume fraction  $f_v$  of  $M_{23}C_6$  carbides measured from CBS images of parent and simulated FGHAZ twin-jet electropolished specimens (total area of  $915 \mu\text{m}^2$  analysed). The error is given by Equation (3.17). .....242

**Figure 4.43:** Relative % Cr measured in 50  $M_{23}C_6$  carbides from parent and simulated FGHAZ extraction replica specimens. The error is indicated as the 95% CI. ....243

**Figure 4.44:** Relative % Fe measured in 50  $M_{23}C_6$  carbides from parent and simulated FGHAZ extraction replica specimens. The error is indicated as the 95% CI. ....244

**Figure 4.45:** Relative % Mo measured in 50  $M_{23}C_6$  carbides from parent and simulated FGHAZ extraction replica specimens. The error is indicated as the 95% CI. ....244

**Figure 4.46:** Mean ECD of VX precipitates measured from EFTEM V elemental maps acquired from parent and simulated FGHAZ extraction replica specimens. The error is given as 95% CI (sampling area =  $360 \mu\text{m}^2$ ). .....245

**Figure 4.47:** Box-and-whisker plots of ECD size distribution of VX precipitates measured from EFTEM V elemental maps acquired from parent and simulated FGHAZ extraction replica specimens (sampling area =  $360 \mu\text{m}^2$ ). The “x” symbol indicates the mean. ....246

**Figure 4.48:** Box-and-whisker plots of 2D NND distributions of VX precipitates measured from EFTEM V elemental maps of parent and simulated FGHAZ twin-jet electropolished specimens (sampling area =  $576 \mu\text{m}^2$ ). The “x” symbol indicates the mean. ....247

**Figure 4.49:** Mean number density of MX precipitates measured from EFTEM V elemental maps of parent and simulated FGHAZ twin-jet electropolished specimens. The error is given by Equation (3.17) (sampling area =  $576 \mu\text{m}^2$ ). .....248

**Figure 4.50:** Mean volume fraction of VX precipitates measured from EFTEM V elemental maps of parent and simulated FGHAZ twin-jet electropolished specimens. The error is given by Equation (3.17) (sampling area =  $576 \mu\text{m}^2$ ). .....248

**Figure 4.51:** Mean 2D surface-to-surface interparticle spacing  $\lambda$  of VX precipitates obtained from EFTEM V elemental maps acquired from parent and simulated FGHAZ twin-jet electropolished specimens. The error is determined by combining the errors of the mean ECD and mean  $N_v$  using standard error propagation. ....249

<b>Figure 4.52:</b> STEM-EDS spectrum acquired from VX precipitate in extraction replica specimen of new simulated FGHAZ material.....	250
<b>Figure 4.53:</b> (a) HAADF-STEM image of an area on new parent extraction replica specimen with STEM-EELS SI analysis area outlined. STEM-EELS RGB maps of (b) V (red) and N (blue), and (c) V (red) and Cr (green). STEM-EELS elemental maps of (d) V (515.0 - 543.5 eV), (e) N (397.0 - 435.5 eV) and (f) Cr (576.5 - 605.0 eV).....	251
<b>Figure 4.54:</b> Mean approximate Zener pinning pressure exerted by boundary $M_{23}C_6$ carbides calculated from CBS images of parent and simulated FGHAZ twin-jet electropolished specimens. The error is given by Equation (3.17). .....	262
<b>Figure 4.55:</b> CBS images of Mo-enriched Laves phase precipitates observed in the various materials. Arrows highlight the Laves phase precipitates (bright) in: (a), (b) creep aged 1 parent and (c) simulated FGHAZ, (d) and (e) creep aged 2 parent and (f) simulated FGHAZ twin-jet electropolished specimens. ....	265
<b>Figure 4.56:</b> CBS image (left) and EFTEM RGB composite (right) of Cr (green) and V (red) elemental maps of the same area in creep aged 1 simulated FGHAZ twin-jet electropolished specimen. ....	266
<b>Figure 4.57:</b> $6 \times 6 \mu\text{m}^2$ EFTEM RGB composite of Cr (green) and V (red) maps of areas from the (a), (b), (c) creep aged 1 and (d), (e), (f) creep aged 2 parent twin-jet electropolished specimens. The white dotted outlines indicate possible Z-phase precipitates and/or regions favourable for Z-phase formation. ....	267
<b>Figure 4.58:</b> $6 \times 6 \mu\text{m}^2$ EFTEM RGB composite of Cr (green) and V (red) maps of areas from the creep aged 2 parent extraction replica specimen. Areas of overlapping Cr and V signals indicate possible Z-phase precipitates.....	268
<b>Figure 4.59:</b> STEM-EDS image of adjacent precipitates in the creep aged 2 parent extraction replica specimen, and their corresponding spectrum and chemical composition. The % V and Cr are highlighted in yellow. The spectrum on the left corresponds to that of a Z-phase particle and on the right is the spectrum of the adjacent $M_{23}C_6$ carbide. ....	269
<b>Figure 4.60:</b> $6 \times 6 \mu\text{m}^2$ ADF-STEM image (left) and TKD GB map (right) of the same area on new parent twin-jet electropolished specimen. Arrows indicate different boundary types identified from the TKD GB map, “x” labels a single micro-grain and a subgrain within in this micro-grain is outlined. The colour coding in the TKD GB map is the same as that used in Figure 4.26. ....	270

<b>Figure 4.61:</b> 576 $\mu\text{m}^2$ montage of ADF-STEM images acquired from parent and simulated FGHAZ twin-jet electropolished specimens.....	272
<b>Figure 4.62:</b> ADF-STEM images of equiaxed micro-grains (marked “x”) observed in the creep aged 1 simulated FGHAZ material. ....	273
<b>Figure 4.63:</b> (a) ADF-STEM image, (b) TKD GB map overlaid onto thresholded TKD-EDS Cr (green) and V (red) elemental maps, (c) CBS image and (d) EFTEM RGB composite of Cr (green) and V (red) elemental maps of same micro-grain (marked by “x”) in creep aged 1 simulated FGHAZ twin-jet electropolished specimen.....	274
<b>Figure 4.64:</b> Thresholded substructure from 6 x 6 $\mu\text{m}^2$ ADF-STEM image (top row), micro-grains drawn from 12 x 12 $\mu\text{m}^2$ TKD GB MO > 2° map (middle row) and 12 x 12 $\mu\text{m}^2$ TKD GB MO > 5° map (bottom row) for an area on the parent and simulated FGHAZ twin-jet electropolished specimens. The same area is illustrated for the TKD maps.....	277
<b>Figure 4.65:</b> XRD spectra acquired from parent and simulated FGHAZ bulk specimens. The peaks labelled (a), (b) and (c) are enlarged.....	278
<b>Figure 4.66:</b> Summary of mean subgrain size measurements for parent and simulated FGHAZ X20 materials from CBS (916 $\mu\text{m}^2$ ), TKD (576 $\mu\text{m}^2$ ), DF-STEM (576 $\mu\text{m}^2$ ) and XRD (40-80 mm <sup>2</sup> ). Subgrain size is measured as minor axis length of micro-grains in CBS and TKD data, minor axis length of substructure in the DF-STEM images, and crystallite size from the XRD data. For visual purposes, all simulated FGHAZ data is pattern filled. ....	279
<b>Figure 4.67:</b> Linear fit plots of cumulative % (30 to 70%) vs log(area) for each measured micro-grain in TKD GB MO > 5° maps acquired from parent and simulated FGHAZ twin-jet electropolished specimens. ....	280
<b>Figure 4.68:</b> ADF-STEM images of the creep aged 1 (a) parent and (b) simulated FGHAZ X20 materials indicating the different dislocations visible. (c) and (d) are the enlarged areas outlined by the yellow squares in (a) and (b), respectively.....	287
<b>Figure 4.69:</b> Internal dislocations (red) isolated from 6 x 6 $\mu\text{m}^2$ ADF-STEM images acquired from the parent and simulated FGHAZ twin-jet electropolished specimens. ....	288
<b>Figure 4.70:</b> Internal dislocation densities $\rho_{int}$ determined from ADF-STEM images of the parent and simulated FGHAZ twin-jet electropolished specimens (total area of 576 $\mu\text{m}^2$ analysed). The error is given by Equation (3.17). ....	289



**Figure 4.71:** Dislocation densities  $\rho$  determined from peak broadening in XRD spectra (Equations (3.12) and (3.13)) acquired from the parent and simulated FGHAZ bulk specimens (total area of  $915 \mu\text{m}^2$  analysed). The error was calculated using systematic error calculated in TOPAS™ and standard error propagation.....290

**Figure 5.1:** Summary of measured microstructural parameters for all materials. Values are plotted relative to the new parent material. Pattern filled columns correspond to simulated FGHAZ results.....296

**Figure 5.2:** Back-stress as a linear combination of precipitate (PH), dislocation (DH) and sub-boundary (SBH) strengthening for each material determined using mean values and Equations (2.16), (2.19) and (2.21). The back-stress value in MPa is indicated in the data table. An asterisk indicates that the difference in back-stress value compared to the new parent material is statistically significant.....297

**Figure 5.3:** Difference in strengthening mechanisms (Equations (2.16), (2.19), (2.21), (2.26) and (2.27) of new and creep aged simulated FGHAZ X20 materials plotted relative to new simulated FGHAZ values. The asterisk indicates statistically significant differences in the mean values between the creep aged simulated FGHAZ material and the new simulated FGHAZ material.299

**Figure 6.1:** Difference in microstructural parameters of new and creep aged simulated FGHAZ X20 materials plotted relative to new simulated FGHAZ values. The asterisk indicates statistically significant differences in the mean values between the creep aged simulated FGHAZ material and the new simulated FGHAZ material. ....310

**Figure 6.2:** Difference in microstructural parameters of parent and corresponding simulated FGHAZ for new (blue), creep aged 1 (green) and creep aged 2 (red) X20 materials plotted relative to new simulated FGHAZ values. The asterisk indicates statistically significant differences in the mean values between the parent and corresponding simulated FGHAZ material.....311

# LIST OF TABLES

<b>Table 2.1:</b> Chemical compositions of different standards of X20 steel grade (EPRI 2006). .....	15
<b>Table 2.2:</b> Chemical compositions (mass%, bal.Fe) and typical heat treatment parameters of main 9-12% Cr steam pipe steels (Hald 2017). .....	22
<b>Table 2.3:</b> Typical transformation temperatures of 9-12% Cr martensitic steels (Constructed from Abe, Kern and Viswanathan (2008), and Pandey, Mahapatra, Kumar and Saini (2018)). .....	23
<b>Table 2.4:</b> Summary of basic characteristics of common precipitates in 9-12% Cr steels (Constructed from Aghajani, Richter, Somsen et al. 2009, Aghajani, Somsen and Eggeler 2009, and Zhang, Wu, Liu, Liu and Yao 2017). .....	38
<b>Table 2.5:</b> Misorientations of different boundary types found in the microstructure of 9-12% Cr martensitic steels. ....	53
<b>Table 2.6:</b> Regions in the HAZ of a weldment, the peak temperature experienced and the corresponding transformation reaction, microstructure characteristics and mechanical properties (Constructed from Bhadeshia and Honeycombe (2006), and Pandey, Mahapatra, Kumar and Saini (2018)). .....	74
<b>Table 2.7:</b> Comparison of different HAZ simulation techniques (Buchmayr 2005). .....	84
<b>Table 2.8:</b> Critical areas for high-temperature failure in coal-fired power plants (Adapted from Wilson (1990)). .....	98
<b>Table 2.9:</b> Power plant component life philosophy (Molokwane 2014). .....	104
<b>Table 2.10:</b> Potential input parameters to be included in a creep model (Krenmayr and Sonderegger 2016). .....	106
<b>Table 2.11:</b> Summary of creep strength parameters for an X20CrMoV12-1 (DIN 17175) steel operating at 550 °C (Constructed from Aghajani, Somsen and Eggeler (2009)). .....	118
<b>Table 2.12:</b> Summary of some semi-physical creep models that have been applied to 9-12% Cr martensitic steels. ....	129
<b>Table 2.13:</b> Key microstructural features and the available techniques for their analysis (Hansen and Barlow 2014). .....	131
<b>Table 3.1:</b> Operating conditions for X20 steel pipework analysed in this study. ....	133
<b>Table 3.2:</b> Chemical composition of DIN 17175 Grade X20CrMoV12-1 and X20 steel pipework analysed in this study. ....	134

<b>Table 3.3:</b> Creep damage classification of X20 pipework according to surface replication results. .....	135
<b>Table 3.4:</b> Weld thermal cycle steps and parameters used for Gleeble™ simulation. ....	138
<b>Table 3.5:</b> Peak temperatures $T_p$ measured by thermocouples during Gleeble™ simulation...	139
<b>Table 3.6:</b> PWHT steps and parameters applied to weld thermal cycle simulated samples. ...	142
<b>Table 3.7:</b> Measured holding and final temperatures measured by thermocouples during PWHT of weld thermal cycle simulated samples. ....	142
<b>Table 3.8:</b> Summary of samples analysed in the study. ....	144
<b>Table 3.9:</b> Final matrix of specimens analysed in the study. ....	151
<b>Table 3.10:</b> Conditions and AZtechHKL software parameters used for EBSD map acquisition.	154
<b>Table 3.11:</b> Conditions and AZtechHKL software parameters used for TKD-EDS analyses.....	157
<b>Table 3.12:</b> Window energies and acquisition parameters for different EFTEM maps acquired. .....	160
<b>Table 3.13:</b> Mean thickness of areas analysed on twin-jet electropolished specimens with TKD- EDS and STEM.....	161
<b>Table 3.14:</b> Conditions and AZtec software parameters used for STEM-EDS analyses.....	163
<b>Table 3.15:</b> Conditions used for ADF-STEM analysis. ....	166
<b>Table 3.16:</b> Instrument specifications used for XRD analysis.....	168
<b>Table 3.17:</b> Formulae used to calculate $M_{23}C_6$ carbide parameters from CBS images.....	173
<b>Table 3.18:</b> Formulae used to calculate precipitate parameters from TKD-EDS and EFTEM maps acquired from twin-jet electropolished specimens. ....	174
<b>Table 3.19:</b> Experimental techniques and corresponding microstructural feature (property) analysed. ....	183
<b>Table 4.1:</b> Number of voids and cavities measured on total sampling area of 1.4 mm <sup>2</sup> .....	194
<b>Table 4.2:</b> Summary of void measurements.....	208
<b>Table 4.3:</b> Estimated variant information determined from Payton, Aghajani, Otto et al. (2012) and relative frequency measured from EBSD MO profiles of parent and simulated FGHAZ X20 materials. ....	217
<b>Table 4.4:</b> Number of Cr-enriched $M_{23}C_6$ precipitates measured from Cr TKD-EDS maps covering a total area of 576 μm <sup>2</sup> . ....	222

<b>Table 4.5:</b> Number of Cr-enriched $M_{23}C_6$ precipitates measured from CBS maps covering a total area of $915 \mu\text{m}^2$ . .....	222
<b>Table 4.6:</b> Number of V-enriched MX (VX) precipitates measured from EFTEM V elemental maps. ....	231
<b>Table 4.7:</b> Summary of mean $M_{23}C_6$ carbide parameters and chemical composition (O = overall, B = boundary and I = interior).....	252
<b>Table 4.8:</b> Summary of mean measured MX precipitate parameters.....	257
<b>Table 4.9:</b> Number of subgrains and micro-grains analysed. ....	275
<b>Table 4.10:</b> Crystallite size and strain parameters measured from XRD peak broadening using TOPAS™ (sampling area = $40\text{-}80 \text{ nm}^2$ ).....	276
<b>Table 4.11:</b> Substructure and crystallite sizes measured from ADF-STEM and XRD results. .	281
<b>Table 4.12:</b> Summary of mean subgrain sizes measured using CBS imaging and TKD. ....	283
<b>Table 4.13:</b> Mean dislocation densities determined using ADF-STEM and XRD.....	290

# LIST OF EQUATIONS

Equation (2.1) .....	16
Equation (2.2) .....	16
Equation (2.3) .....	16
Equation (2.4) .....	40
Equation (2.5) .....	41
Equation (2.6) .....	42
Equation (2.7) .....	43
Equation (2.8) .....	66
Equation (2.9) .....	92
Equation (2.10) .....	92
Equation (2.11) .....	99
Equation (2.12) .....	102
Equation (2.13) .....	117
Equation (2.14) .....	117
Equation (2.15) .....	120
Equation (2.16) .....	120
Equation (2.17) .....	120
Equation (2.18) .....	121
Equation (2.19) .....	122
Equation (2.20) .....	122
Equation (2.21) .....	122
Equation (2.22) .....	123
Equation (2.23) .....	124
Equation (2.24) .....	124
Equation (2.25) .....	124
Equation (2.26) .....	125
Equation (2.27) .....	125

<i>Equation (2.28)</i> .....	127
<i>Equation (2.29)</i> .....	128
<i>Equation (3.1)</i> .....	173
<i>Equation (3.2)</i> .....	173
<i>Equation (3.3)</i> .....	173
<i>Equation (3.4)</i> .....	173
<i>Equation (3.5)</i> .....	173
<i>Equation (3.6)</i> .....	173
<i>Equation (3.7)</i> .....	174
<i>Equation (3.8)</i> .....	174
<i>Equation (3.9)</i> .....	174
<i>Equation (3.10)</i> .....	174
<i>Equation (3.11)</i> .....	179
<i>Equation (3.12)</i> .....	180
<i>Equation (3.13)</i> .....	180
<i>Equation (3.14)</i> .....	181
<i>Equation (3.15)</i> .....	181
<i>Equation (3.16)</i> .....	181
<i>Equation (3.17)</i> .....	182

# TABLE OF CONTENTS

DECLARATION.....	i
ACKNOWLEDGEMENTS .....	ii
SUMMARY .....	iii
OPSOMMING .....	v
LIST OF ABBREVIATIONS.....	vii
LIST OF FIGURES.....	x
LIST OF TABLES.....	xxii
LIST OF EQUATIONS.....	xxv
TABLE OF CONTENTS .....	xxvii
CHAPTER 1: INTRODUCTION.....	1
1.1 Background.....	1
1.2 Problem Statement .....	6
1.3 Research Question .....	7
1.4 Research Aim.....	8
1.5 Research Objectives.....	8
1.6 Significance of the Study.....	8
1.7 Scope of the Study.....	9
1.8 Outline of Thesis .....	9
CHAPTER 2: LITERATURE REVIEW.....	12
2.1 Overview of Power Plant Application of 9-12% Cr Martensitic Creep Resistant Steels.....	12
2.1.1 General Overview.....	12
2.1.2 X20 (12% Cr) Martensitic Stainless Steel.....	14
2.1.3 Creep Properties .....	15
2.2 Metallurgy and Microstructure.....	20
2.2.1 Chemical Composition.....	21
2.2.2 Heat Treatment.....	22
2.2.3 Initial Tempered Martensite Microstructure.....	29
2.3 Microstructural Evolution of Martensitic Creep-Resistant 9-12% Cr Steels During Creep Exposure.....	31

2.3.1	Creep Deformation Mechanisms .....	33
2.3.2	Creep Strengthening and Behaviour of Precipitates .....	36
2.3.3	Creep Strengthening and Behaviour of Grains and Subgrains .....	52
2.3.4	Creep Strengthening and Behaviour of Dislocations .....	58
2.3.5	Strengthening and Effect of Creep on Solid Solution.....	61
2.3.6	Creep Damage and Fracture .....	61
2.3.7	Summary of Microstructural Evolution and Effect on Creep Curve .....	66
2.4	Microstructure and Creep Strength Implications of Welding on Creep-Resistant 9 – 12% Cr Steels .....	69
2.4.1	Evolution of Microstructure during Welding .....	72
2.4.2	Creep Behaviour of the FGHAZ.....	79
2.4.3	Simulation of the FGHAZ.....	82
2.5	Type IV Cracking Mechanism .....	87
2.5.1	Role of Constraint and Welding Direction .....	89
2.5.2	Weld Strength Factor.....	91
2.5.3	Microstructural Degradation and Failure Mechanism.....	93
2.6	Conventional Remaining Life Assessment and Weldability Limits .....	96
2.6.1	Current Remaining Life Assessment Procedures .....	98
2.7	Creep Modelling .....	105
2.7.1	Phenomenological Creep Models .....	109
2.7.2	Semi-Physical Creep Models.....	113
2.8	Characterisation of Microstructure .....	130
CHAPTER 3: MATERIALS AND EXPERIMENTAL METHODS .....		132
3.1	Introduction .....	132
3.2	Sampling .....	132
3.2.1	Steel Sections.....	132
3.2.2	Surface Replication .....	135
3.3	FGHAZ Simulation .....	136
3.3.1	Sample Preparation.....	136
3.3.2	Weld Thermal Cycle Simulation.....	137
3.3.3	Post-Weld Heat Treatment .....	140
3.4	Sample Preparation .....	143
3.4.1	Cutting and Polishing.....	143



3.4.2	Twin-Jet Electropolishing.....	145
3.4.3	Bulk Replication.....	147
3.4.4	Final Sample Matrix.....	151
3.5	Vickers Microindentation Hardness Testing .....	152
3.6	Experimental Techniques.....	152
3.6.1	LM Analysis .....	152
3.6.2	EBSD Analysis .....	153
3.6.3	TKD-EDS Analysis.....	155
3.6.4	CBS Analysis.....	158
3.6.5	EFTEM Analysis.....	159
3.6.6	STEM-EDS Analysis.....	162
3.6.7	STEM Analysis .....	163
3.6.8	XRD Analysis.....	166
3.7	Microstructural Evaluation Methodologies.....	168
3.7.1	Prior Austenite Grains.....	168
3.7.2	Creep Cavities .....	170
3.7.3	M <sub>23</sub> C <sub>6</sub> Precipitates .....	171
3.7.4	MX Precipitates .....	175
3.7.5	Chemical Composition of Precipitates .....	176
3.7.6	Micro-grains and Substructure.....	177
3.7.7	Dislocations .....	178
3.8	Statistical Analysis of Measurements.....	181
3.9	Summary of Techniques and Analyses.....	183
CHAPTER 4: RESULTS AND DISCUSSION .....		184
4.1	Introduction .....	184
4.2	Qualitative Comparison of Microstructures.....	184
4.3	Hardness.....	187
4.3.1	Results.....	187
4.3.2	Discussion .....	187
4.4	Prior Austenite Grain Analysis.....	190
4.4.1	Results.....	190
4.4.2	Discussion .....	193

4.5	Creep Voids .....	194
4.5.1	Results.....	194
4.5.2	Discussion .....	208
4.6	Boundary Character .....	213
4.6.1	Results.....	213
4.6.2	Discussion .....	220
4.7	M <sub>23</sub> C <sub>6</sub> and MX Precipitates.....	221
4.7.1	Qualitative Results: M <sub>23</sub> C <sub>6</sub> Precipitates.....	221
4.7.2	Qualitative Results: MX Precipitates.....	231
4.7.3	Quantitative Results: M <sub>23</sub> C <sub>6</sub> Precipitates .....	234
4.7.4	Quantitative Results: MX Precipitates.....	245
4.7.5	Discussion .....	252
4.8	Other Secondary Phases .....	264
4.8.1	Laves Phase Analysis.....	264
4.8.2	Z-phase Analysis .....	266
4.9	Micro-Grain and Substructure .....	270
4.9.1	Results.....	270
4.9.2	Discussion .....	281
4.10	Dislocation Density.....	286
4.10.1	Results.....	286
4.10.2	Discussion .....	290
CHAPTER 5: RECOMMENDATIONS FOR A MICROSTRUCTURE-BASED MODEL FOR REMAINING LIFE ASSESSMENT .....		295
5.1	Introduction .....	295
5.2	Microstructural Input Parameters .....	295
5.3	Back-Stress Model Application.....	297
5.4	Recommendations for a Microstructure-Based Model for Remaining Life Assessment .....	299
CHAPTER 6: CONCLUSIONS.....		302
CHAPTER 7: LIMITATIONS AND CALL FOR FUTURE RESEARCH .....		313
REFERENCES.....		315
RESEARCH OUTPUTS .....		354

# CHAPTER 1

## INTRODUCTION

### 1.1 BACKGROUND

Fossil fuels remain an essential energy source for electricity generation in the world and IEA (International Energy Agency) scenarios predict that in 2040 about 30 to 60 % of electricity worldwide will still be generated by fossil fuels (Powertech 2018). Coal-fired power plants produce 41% of the global electricity (World Coal Association 2017). The South African public electricity utility, Eskom produces approximately 96% of South Africa's electricity and in addition more than 45% of Africa's electricity (Eskom 2017). A total of 84.53% of the electricity generated by Eskom is from 14 coal-fired power plants since the country is the fifth largest coal producing country in the world (Eskom 2016). There are 2 new plants currently in the process of being commissioned (Eskom 2017). A breakdown of the generation plant mix of Eskom is given in **Figure 1.1**. Consequently, the operation management and effective maintenance of coal-fired power plants are still of great importance today and power plant companies strive to develop strategies for optimal life assessment of their power plant components.

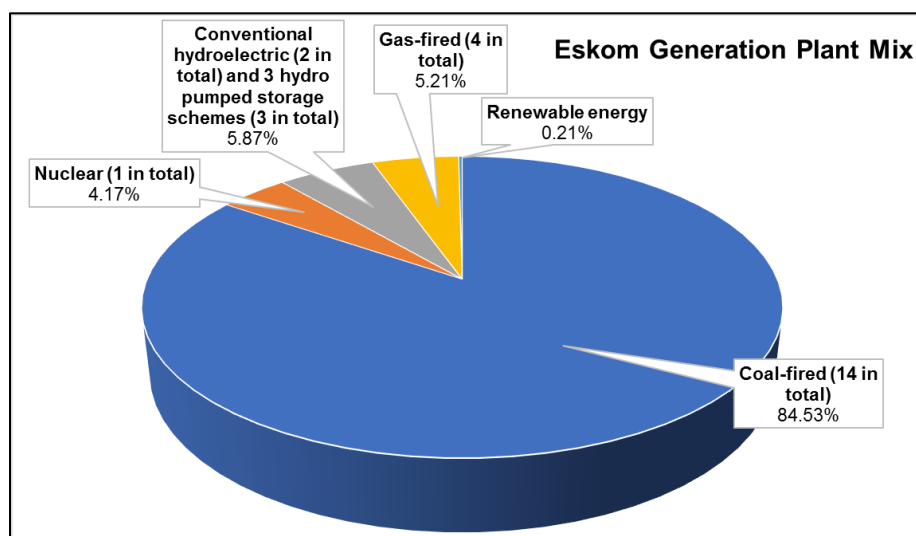


**Figure 1.1:** Eskom's mix of generating power plants (Constructed from (Eskom 2017)).

High-pressure steam pipes and turbine blades in the turbine generator are the two critical components of coal-fired power plants. These components operate under high temperature and stress. To withstand these severe service conditions, the component materials used are creep-resistant steels with different chromium contents (9 - 12%) to provide corrosion resistance (Abe, Kern and Viswanathan 2008). **Figure 1.2** summarises the historical development of these steels. One of the first martensitic steels to be used for the high-pressure steam pipes and boiler components of coal-fired power plants is the DIN designation X20CrMoV12-1 (X20) with 12% Cr content (EPRI 2006, Hald 2017). This alloy has been proven to be very successful for long-term service operation at 565°C, but not for higher temperatures. To improve the efficiency of coal-fired power plants, new steel grades were required that can operate at higher temperatures. Therefore, the last 30 years materials research focused on the development of improved creep-resistant martensitic 9-12% Cr steels for use in advanced highly efficient coal-fired power plants. The new martensitic steel grades are P91 (X10CrMoVNb9-1) and the state-of-the-art today P92 (X10CrWMoVNb9-2) and COST FB2, which allowed the steam parameters to be increased to 300 bar and 600 to 620 °C (Hald 2016).

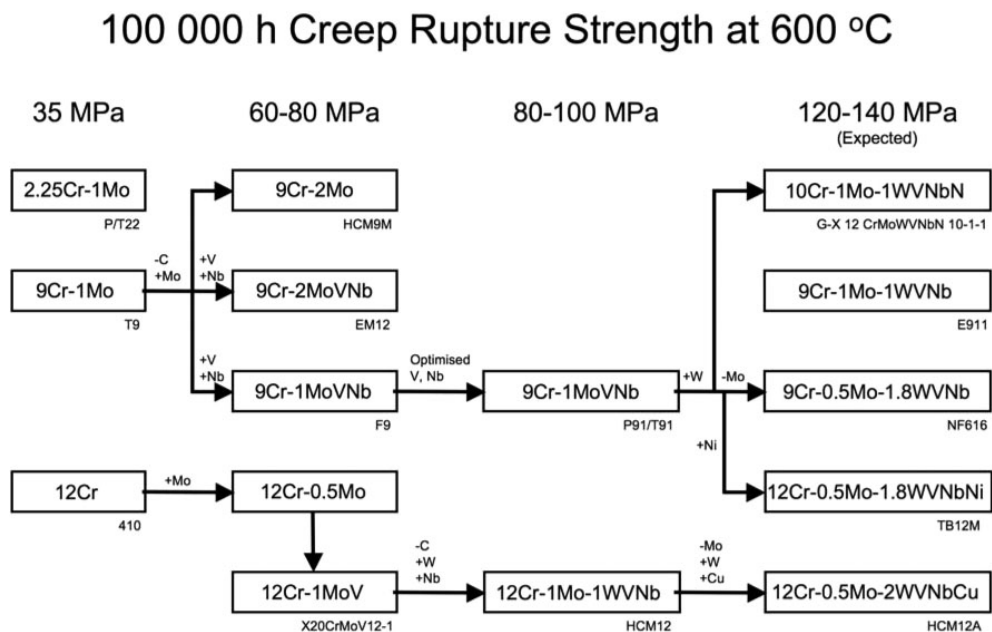


**Figure 1.2:** Overview of the historical development and corresponding 100 000 h creep rupture strength at 600 °C of heat-resistant 9-12% Cr steels (Francis, Mazur and Bhadeshia 2006).

Presently (2019), X20 steel is still used in old coal-fired power plants and most of South Africa's coal-fired plants. Therefore, it is still of great importance to understand the long-term stability of X20 steel to manage existing X20 steel components optimally. Most of the microstructural data on X20 steel has been acquired with older techniques due to the strong focus on the new steel grades.

Extensive studies have been performed on the microstructure of the new steel grades using the latest microscopy techniques (Ennis 2002, EPRI 2006, Panait, Bendick, Fuchsmann, Gourgues-Lorenzon and Besson 2010, Panait, Zielinska-Lipiec and Koziel 2010, Gu, West, Thomson and Parker 2014, Pandey, Giri and Mahapatra 2016, Pandey, Mahapatra, Kumar and Saini 2018). It is only in the last decade that X20 has been studied with new advanced microscopy techniques (Aghajani, Richter, Somsen, Fries, Steinbach *et al.* 2009, Aghajani, Somsen and Eggeler 2009, Aghajani 2009, Kinoshita, Yardley and Tsurekawa 2011, Isik, Kostka, Yardley, Pradeep, Duarte *et al.* 2015, Marx 2016). Currently, there is the development of new stable 12Cr martensitic steels that has the potential to enable coal-fired power plants to run at even higher efficiency with steam temperatures of up to 650 °C (Hald 2016). Therefore, since X20 shares the same basic microstructural features with the new steel grades, any information gained from X20 has possible significance for understanding the stability of the other martensitic steels.

The service conditions cause the microstructure to continually evolve which implies that the mechanical properties will change accordingly and may reach a stage when the material is no longer fit for purpose. This time-dependent deformation of the steel at high-temperatures and stress well below the yield strength is known as creep (Abe, Kern and Viswanathan 2008). Also, component replacement is performed using welding, which significantly alters the microstructure and hence the mechanical properties of the joined materials. This high-temperature welding process results in the formation of different microstructural regions within the weldment (Abe, Kern and Viswanathan 2008). Consequently, the understanding of creep behaviour in weldments has become important over the last few decades (Middleton, Timmins and Townsend 1996). Previous studies have shown that the lowered creep strength of the weld region, known as the fine-grained

heat-affected zone (FGHAZ), caused it to be the weakest link in 9-12% Cr steel weldments (Smith, Walker and Kimmins 2003, Francis, Mazur and Bhadeshia 2006).

Voids form within the material during service and in the FGHAZ there is an enhanced rate of creep void formation. Mainly, these creep voids coalesce to form cracks and the weldments fail prematurely in the FGHAZ. This damage mechanism is known as Type IV cracking. Even though many great efforts have been put into the characterisation of weld metals and weldments to determine the creep properties as with base metals, the Type IV failure mechanism is not fully understood yet (Cerjak and Mayr 2008). Most studies on the Type IV cracking mechanism have focused on the microstructural evolution during short-term creep exposure of weldments performed on virgin material. The study by Rasiawan (2017) investigated the creep properties of cross-welds of virgin onto prior long-term creep exposed X20 steel. Short-term creep tests were performed on two such cross-welds and for both samples failed in the FGHAZ of the creep aged material on the existing creep side. The only possible explanation they could provide is that it is the voids that existed in this FGHAZ prior to damage.

A creep aged component does not only reach a stage where it is no longer fit for operation solely due to creep, but it also reaches a point where welding will degrade the material to such a degree that further safe operation is not possible. This point is defined as the weldability limit of the material and it is set by the life management strategies. The weldability limits of the material are determined from the results of non-destructive tests and metallographic replication (Marder 1989) that considers only the surface of the material and not the microstructure. These techniques quantify creep damage as the number of voids that are visible on the component or test piece surface. The major problem is that the tiny creep voids form at prolonged rates and usually only become detectable by these techniques when up to approximately 70% of the component life is reached (Shibli 2017). These voids then link up at a much faster rate and failure can result without much warning. Also, Type IV cracking starts sub-surface, which cannot be detected with the conventional techniques.

Previous research has shown that it is possible to use a microstructure-based approach for determining the extent of creep damage (Eggeler, Nilsvang and Ilschner 1987, Aghajani 2009, Holzer 2010, Sonderegger 2012, Molokwane 2014, Marx 2016, Yadav, Sonderegger, Stracey and Poletti 2016). These studies are based on the fact that there are four main microstructural contributions to creep strength: precipitates, dislocations, subgrains, and solid solution. This approach involves the calculation of the creep strength of the material by quantitatively measuring the parameters of these contributions. However, all these studies fall short in illustrating the use of a microstructure-based approach to predict remaining life and define more accurate weldability limits for 9-12% Cr steels. This shortfall is mainly a direct result of the assumptions made in the development of these models to account for the mechanism in which each microstructural feature contributes to the creep strength. Since the solid solution strengthening is superimposed onto the other strengthening mechanisms, its contribution usually is not considered. Understanding processing-microstructure-property relationships of power plant steels form the foundation of life assessment using a microstructure-based approach. However, to establish these relationships a statistically reliable number of physical measurements of the microstructure using experimental techniques is necessary.

An approach that does not require mechanical testing to determine remaining life is the use of creep models, i.e., to model the creep behaviour of the material. They are used to either predict the ultimate lifetime of a material or the deformation rate or total deformation at a well-defined point of time. Numerous attempts at modelling the creep behaviour of tempered martensitic steels have been made (Yadav, Sonderegger, Stracey and Poletti 2016). Krenmayr and Sonderegger (2016) have done an extensive literature review on the development of a creep strength estimation method based on microstructural simulation in the modified 9Cr-1Mo steels. There are two main types of creep models: phenomenological and semi-physical creep models. Semi-physical creep models can predict and describe the microstructure, the microstructural evolution and the link between microstructure and macroscopic properties (Yadav, Sonderegger, Stracey and Poletti 2016). The prediction ability of these models extends much further than phenomenological models. However, the use of semi-physical models requires

quantitative microstructural data from the precipitates, subgrains, dislocations and creep voids, as input. These models provide more realistic results, but they remain an approximation. These models have been developed from short-term creep data of parent material and their use for long-term creep data and applicability to weldments are yet to be verified.

## **1.2 PROBLEM STATEMENT**

Limitations of conventional non-destructive testing and metallographic replication for quality control and plant life management of the complex creep-resistant steel components are a significant driver for power plant companies to develop complementary state of the art techniques. The weldability limits of 9 – 12 % Cr steel components as set out in the current life assessment strategies of coal-fired power plants are not based on microstructural data of the weak FGHAZ region. To determine the weldability of the component material, large pieces are sectioned that are subjected to mechanical property tests and the material's response to welding cycles and heat treatment (Doubell, Scheepers, Downes, Pottas, Stangroom *et al.* 2012). This approach is not ideal since the sectioning of the test pieces renders the component unfit for service or requires a costly repair (Marder 1989). The material is deemed weldable if the minimum requirements of no linear defect introduction by the welding cycle, and in the heat-treated condition, have mechanical properties that meet at least the minimum properties demanded from the base material near the area of the repair weld (Doubell, Scheepers, Downes *et al.* 2012). The determination of the linear defects is achieved by surface replication (Marder 1989). After the material is welded upon, surface replicas are also prepared across the welded region to ensure no damage has been caused (Eskom 2017). Since the microstructure is not considered with surface replication and creep cavitation starts sub-surface, the weldability limit of the material is not accurately determined.

In addition, there is a knowledge gap in the understanding of the creep behaviour of 9-12% Cr weldments and Type IV cracking to prevent premature failures. Specifically, a significant investigation is still required to understand the impact of welding on prior creep exposed 9-12% Cr material to explain the consistent failure of weldments in the FGHAZ



of the creep aged material side. This information is especially important since most of the South African coal-fired power plants have X20 steel components that need to be welded upon when replacement is due. Even the cross-welds of P92, the strongest 9-12% Cr martensitic steel to date, has shown to have similar low creep rupture strength as the cross-welds of the other 9-12% Cr steel grades (Abson and Rothwell 2013).

The desired knowledge of the FGHAZ can only be gained by first performing a full microstructural study on welded creep aged 9-12% Cr material. To obtain reliable and representative results from such study is difficult since the microstructural gradient within the weldment region results in a narrow FGHAZ. However, physical weld thermal cycle simulation can be used to simulate the FGHAZ, resulting in much larger sample volumes available to study.

The focus of this study is to investigate the microstructural evolution of a 12% Cr martensitic steel during long-term creep ageing and during welding on the long-term creep aged material. Microstructural measuring techniques used in the previous study by Marx (2016) will be optimised and complementary techniques developed in order to fully characterise the microstructure of long-term creep aged 9-12% Cr weldments by evaluating the precipitates, subgrains, dislocations and creep voids. These techniques employ advanced electron microscopy. Representative microstructural measurements of the FGHAZ of 9-12% Cr weldments are difficult to obtain since this weldment region is narrow. Therefore, in this study, the weldment microstructure will be evaluated from the weld thermal cycle simulated FGHAZ creep aged material.

### **1.3 RESEARCH QUESTION**

The main research question of this study is:

*How does the microstructure of a creep aged 9-12% Cr martensitic steel evolve when welded on in comparison to a virgin 9-12% Cr martensitic steel?*

## 1.4 RESEARCH AIM

The main aim of this study is to investigate the microstructural evolution when welding on creep aged 9-12% Cr martensitic steels using advanced electron microscopy techniques.

## 1.5 RESEARCH OBJECTIVES

1. To review the literature of Type IV cracking in 9-12% Cr martensitic steels to gain a better understanding of this mechanism.
2. To review existing microstructure-based creep models.
3. To determine the microstructural state of creep aged parent and FGHAZ material by the quantitative measurement of the microstructure.
4. To make recommendations towards the use of a microstructure-based assessment of 9-12%Cr steels for determining their weldability limits.

## 1.6 SIGNIFICANCE OF THE STUDY

The novelty aspect of this project originates from narrowing the research gap of the FGHAZ formed due to welding on prior creep exposed material and the implication it has on the strength of the material. This is achieved by gaining a better understanding of the microstructural evolution of the FGHAZ of creep aged 9-12% Cr martensitic steel weldments and hence their main failure mechanism, Type IV cracking.

The main limitation of existing microstructure-based creep models is that they make non-physical assumptions that mostly assume a single microstructural feature to be the rate-determining step. For example, the model from Oruganti, Karadge and Swaminathan (2013) assumes the MX precipitate evolution to be the rate-determining step during creep, but Kostka, Tak, Hellmig *et al.* (2007) has experimentally shown that both the  $M_{23}C_6$  carbides and micro-grain boundaries contribute significantly to the creep strength. The existing microstructure-based models are mainly constructed from microstructural measurements from short-term creep tests since accurately measured long-term microstructural data has limited availability. Also, the models have not been developed to provide weldability limits. Thus, since the results of this study are long-term creep

microstructural data, as well as FGHAZ data of both virgin and long-term creep aged material, the results may be used in future studies to verify and improve the existing models or develop entirely new models. In turn, these models can be implemented to determine remaining life and weldability limits of 9-12% Cr martensitic steels.

Even though the steel analysed in this study (X20) has been phased out in certain countries, most of the high-pressure steam pipes at South Africa's coal-fired power plants are still made of X20 steel grade. Due to the same basic microstructure of 9-12% Cr martensitic steels, any coal-fired power plant company stands to gain from the results of this study.

## **1.7 SCOPE OF THE STUDY**

As-received and long-term service exposed (creep aged) X20 (12% Cr) steel pipework has been provided by an industrial sponsor. The FGHAZ microstructures are simulated on samples prepared from the as-received and creep aged pipework using a heat treatment performed by a Gleeble™ simulator. The level of creep damage of each material is determined using standard power plant procedures (Eskom 2017).

The microstructural state of the parent material and simulated FGHAZ for as-received and creep aged X20 material is determined using advanced electron microscopy. To characterise the microstructure, quantitative microstructural measurement techniques that evaluate the precipitates, subgrains, dislocations and creep voids are implemented.

No small-scale mechanical testing (such as small punch creep testing) or uni-axial testing to determine the creep properties is performed in this experiment. The results of previous studies are used where needed. Hardness is the only mechanical property determined in this study. In this project, no attempt is made to implement, develop or improve existing microstructure-based creep models.

## **1.8 OUTLINE OF THESIS**

The outline of this thesis is as follows. In Chapter 2 a full literature review on the microstructure of 9-12% Cr martensitic power plant steel weldments and the different

strengthening mechanisms is provided. The evolution of the microstructure of these steels with creep ageing and welding is also provided, with the focus on the microstructure of the FGHAZ. An extensive literature study of the Type IV cracking mechanism is also provided. In addition, a review of creep modelling with a focus on semi-physical creep models is given. Research objectives 1 and 2 are addressed in this chapter.

All the relevant experimental methods followed in this study are discussed in Chapter 3. The sampling and sample preparation methods used to prepare the various specimens from the X20 steel pipework for analysis are given. Included is the physical simulation of the FGHAZ specimens, sectioning, polishing and etching of the samples, TEM thin foil preparation with twin-jet electropolishing and extraction replica preparation using bulk replication. Brief summaries of the analyses using Vickers Microindentation Hardness Testing (MHT), Light Microscopy (LM), Scanning Electron Microscopy (SEM), X-ray Diffraction (XRD) Transmission Kikuchi Diffraction (TKD) combined with Energy Dispersive Spectrometry (EDS), Concentric Backscatter (CBS) imaging, Energy-Filtered Transmission Electron Microscopy (EFTEM), and Annular Dark-Field Scanning Transmission Electron Microscopy (ADF-STEM) combined with EDS are also provided. This section is followed by the methodologies that explain the use of the results of the analyses to investigate the different microstructural features and hence characterise the microstructural state. In addition, background is given regarding previous studies that have quantified the microstructure to measure the voids, precipitates, subgrains and dislocations. This chapter partially addresses research objective 3.

Chapter 4 entails the evaluation of the microstructural evolution of the creep aged parent and simulated FGHAZ X20 steel specimens. The results from the qualitative and quantitative analysis of the hardness, prior austenite grains, boundary character, creep voids, precipitates, subgrains and dislocations are presented and discussed. Consequently, the microstructural state of each material is determined. Research objective 3 is further addressed in this chapter.

Lastly, conclusions derived from the findings of the study, future work and recommendations regarding the use of microstructure-based life assessment methods are given in Chapter 5. This chapter will address research objective 4.

# CHAPTER 2

## LITERATURE REVIEW

---

### 2.1 OVERVIEW OF POWER PLANT APPLICATION OF 9-12% Cr MARTENSITIC CREEP RESISTANT STEELS

#### 2.1.1 General Overview

Martensitic creep-resistant 9-12% Cr steels, also known as tempered martensite 9-12% Cr ferritic steels (*TMF steels*), have been used extensively in thick-section components of steam power plants, with 12CrMoV steel being the first one introduced in power plants in the mid-60s (Hald 2008). Good oxidation and corrosion resistance, high tensile strength, fabricability, high thermal conductivity, low thermal expansion, relatively low cost, weldability and the most important, high creep strength, make 9-12% Cr martensitic steels of great importance in their application (Maruyama, Sawada and Koike 2001, Masuyama 2001, Muruganath and Bhadeshia 2002, Yan, Wang, Shan and Yang 2013).

As mentioned in Chapter 1, fossil fuel power plants are one of the major electricity generating technologies in the world, and it is predicted that in 2040 they will still produce 30 to 60% of the global electricity (Powertech 2018). Consequently, since energy conservation and environmental protection are critical worldwide issues, fossil fuel companies are designing plants that operate with higher efficiency and lowered CO<sub>2</sub> emissions. Di Gianfrancesco (2017) provides an extensive overview of fossil plants and their newest technologies. For coal-fired power plants, ultra-supercritical (USC) power plants have been implemented and are state-of-the-art today. An efficiency increase from 30-35% to 42-47% and CO<sub>2</sub> emission reduction of about 30% are attained by increasing the steam parameters from 180 bar/ 530-540 °C to 250-300 bar/600-620 °C. These plants could only be realised by the development of new 9-12% Cr martensitic steels, such as T/P91, T/P92 and E911, for the high-temperature components to meet these extreme operating conditions. Consequently, the creep rupture strength of these steels

has doubled over the last three decades (Maruyama, Sawada and Koike 2001, Masuyama 2001, Hald 2005, Hald 2008, Di Gianfrancesco, Vipraio and Venditti 2013, Hald 2016).

Martensitic 9-12% Cr steels are mainly used for two critical components of the boiler system of coal-fired power plants, namely the header and main steam lines such as the High Temperature Pressure Pipework (HTPP). These components operate in the creep range of 500 to 650 °C and are critical since the header pipe collects the superheated steam and the main steam pipe then transfers the high-pressure steam to a turbine system (Igarashi 2008, Di Gianfrancesco 2017). **Figure 2.1** gives the layout and images of the different components of the boiler system in a coal-fired power plant. A detailed summary of the history of martensitic creep-resistant 9-12% Cr steel grades is given by Hald (2017). To simplify, martensitic creep-resistant 9-12% Cr steels (TMF steels) will be further referred to in the text as *9-12% Cr martensitic steels*.

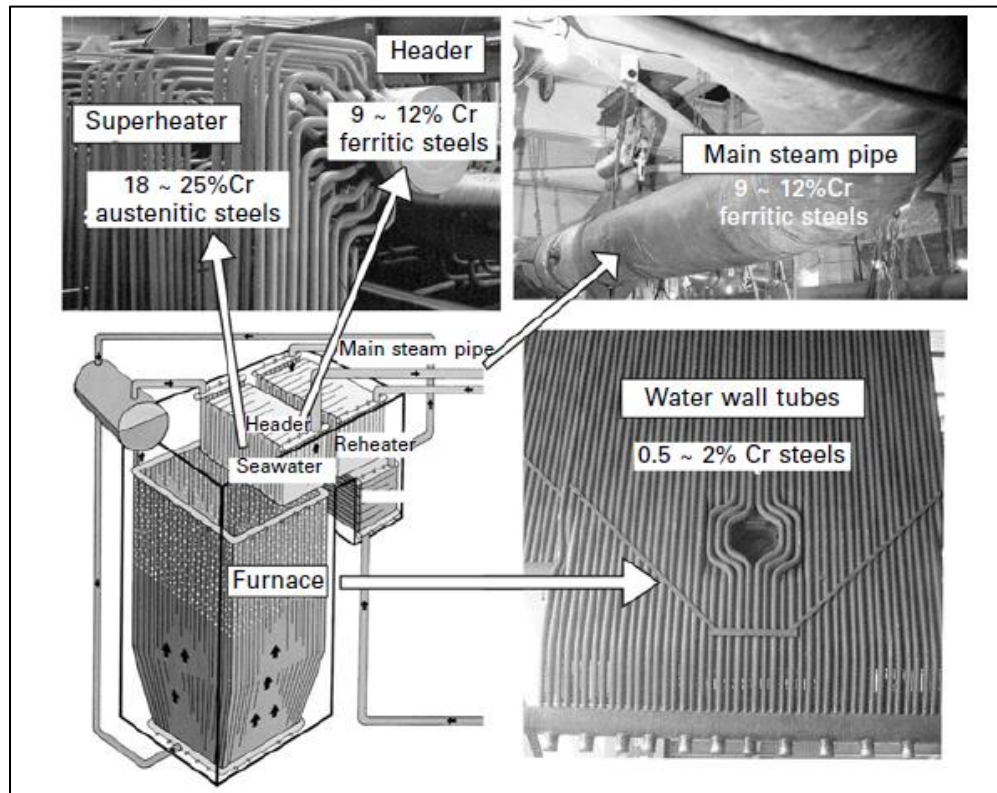


**Figure 2.1:** Schematic illustration and images of boiler components of a coal-fired power plant and the typical component materials (Igarashi 2008).

### 2.1.2 X20 (12% Cr) Martensitic Stainless Steel

Martensitic stainless-steel grade with DIN designation X20CrMoV12-1 (X20) was first developed in Germany around 1950 and is to date still extensively used in South African coal-fired power plants. It was the first 12% CrMoV steel used for boiler and steam pipe applications and was implemented in coal-fired power plants in 1963. The delay in development and application was that it could not be welded on without cracking since the martensitic transformation occurred during welding (Section 2.2.2). In the 1950s improved welding procedures that include preheating were developed to ensure the martensitic transformation only takes place during cooling after welding. Consequently, this led to the successful application of this steel. Since then this alloy has been very successful for long-term service operation at 565°C. The X20 steel grade has been developed based on the corrosion-resistant 13% Cr high-temperature steels that contain up to 0.25% carbon in the tempered condition (EPRI 2006, Hald 2017). The motivation for the development of X20 was that pipework wall thickness could be reduced by 30% compared to previous low-alloy steel pipework (Nebhnani, Bhakta, Gowrisankar and Biswas 2002). This results in weight decrease and faster temperature changes during boiler startup and load changes. Its enhanced creep strength (Section 2.3) made it possible to construct larger power plants that operate with more efficient steam parameters (EPRI 2006).

There are several standards of X20 steel due to slight chemical composition variations. **Table 2.1** provides the chemical compositions for the different standards. X20 steel can be used for any component in both power generation and chemical plants that require high creep strength, corrosion and oxidation resistance under high-temperature service. Superheater and reheater tubes, main steam pipes, and turbine cases and blades are some of these components (**Figure 2.1**) (EPRI 2006, Hald 2017).



**Table 2.1:** Chemical compositions of different standards of X20 steel grade (EPRI 2006).

Standard (Designation)	Chemical composition (wt%)								
	C	Si	Mn	P	S	Cr	Mo	Ni	V
DIN 17175 (X20CrMoV12-1)	0.17-0.23	≤0.50	≤1.00	≤0.030	≤0.030	10-12.50	0.80-1.20	0.30-0.80	0.25-0.35
ISO 9327 (X20CrMoV11-1)	0.17-0.23	≤0.04	0.30-1.00	≤0.035	≤0.030	10-12.50	0.80-1.20	0.30-0.80	0.25-0.35
EN10222-2 (X20CrMoV11-1)	0.17-0.23	≤0.04	0.30-1.00	≤0.025	≤0.015	10-12.50	0.80-1.20	0.30-0.80	0.25-0.35

Even though X20 steel has been in use for decades, risk-based inspection methods have only recently been implemented to assess X20 steel component replacement. Also, it is only in the last decade that advanced techniques could be developed to investigate its microstructure fully. There have been numerous investigations on X20CrMoV12-1 steam pipes that have been exposed to long-term service (Storesund, Borggreen and Zang 2006, Hu, Yang, He and Chen 2008, Aghajani, Richter, Somsen *et al.* 2009, Aghajani, Somsen and Eggeler 2009, Aghajani 2009, Kinoshita, Yardley and Tsurekawa 2011, Auerkari, Salonen, Holmström, Laukkanen, Rantala *et al.* 2013, Isik, Kostka, Yardley *et al.* 2015, Marx 2016).

### 2.1.3 Creep Properties

Plastic deformation of a material is an irreversible process. Creep can be defined as a slow time-dependent component of plastic deformation at absolute temperatures greater than one half the absolute melting temperature  $T_m$ . This follows from the fact that creep is strongly dependent on the service environment (temperature, stress and time) and not an intrinsic material response, but rather a performance-based behaviour of the material (Labossiere 2007). Similarly, creep deformation is also defined as time-dependent

straining under constant applied stress or a given load (Abe 2008). Creep is differentiated from conventional plastic deformation since it occurs due to long-term exposure and is usually considered at elevated temperatures of higher than  $0.4T_m$  and stresses below the material's yield stress.

The traditional approach to creep life estimation has been based on a power law relationship between temperature  $T$  and stress  $\sigma$ . The assumption is that the minimum creep rate  $\dot{\epsilon}_{min}$  is governed by a thermodynamically activated creep mechanism within the material. Consequently, the Arrhenius relationship follows from this assumption and leads to the characteristic "Boltzmann temperature dependence" (Abe 2008, Abdallah, Gray, Whittaker and Perkins 2014):

$$\dot{\epsilon}_{min} \propto e^{-Q_C/RT} \quad (2.1)$$

and Norton's law:

$$\dot{\epsilon}_{min} \propto \sigma^n \quad (2.2)$$

where  $\dot{\epsilon}_{min}$  is the secondary (steady-state) or minimum creep rate;  $Q_C$  is the activation energy for creep;  $n$  is the stress exponent; and  $R$  is the universal gas constant. The basic power law for creep is yielded by combining Equations (2.1) and (2.2):

$$\dot{\epsilon}_{min} = A \cdot \sigma^n \cdot e^{-Q_C/RT} \quad (2.3)$$

where  $A$  is the proportionality constant and includes microstructural parameters such as grain size. Initially, it was assumed that  $Q_C$  and  $n$  are constants, but after further research it has been found that they varied according to the imposed creep conditions and mechanisms involved in different stress and temperature ranges (Brown, Evans and Wilshire 1986).

Creep tests are performed to observe the material's response to creep in an experimental setting. They are either carried out at constant rate or constant force of which the latter is the most common creep test. During such a creep test, the specimen is kept at constant temperature while a static load is applied. A creep curve is the primary result from a creep test and represents graphically the evolution of strain with time measured over a reference or gauge length. **Figure 2.2** illustrates creep curves and corresponding creep rate curves for application of constant tensile load and temperature. The ideal creep curve consists of three main stages of creep (**Figure 2.2** (a)): primary or transient creep; secondary or steady-state creep; and tertiary or acceleration creep (Labossiere 2007, Abe 2008). These stages are affected by the microstructural response to creep and will be further elaborated on in Section 2.3. A real creep curve for X20 steel creep tested at 165 MPa and 550 °C is given in **Figure 2.3**.

Relatively low stresses are used for creep tests to mimic actual service conditions. Testing conditions are usually determined by considering the limits of the testing equipment and the available time. The duration of a creep test ranges typically from 2 000 h to 10 000 h and the total strain is usually less than 0.5%. The creep test data may be extrapolated to foresee long-term behaviours. It is important to note that since creep tests take a long time to perform, data generation is expensive and hence scarce (EPRI 2006).

Creep strength is defined as the stress that produces a  $\dot{\epsilon}_{min}$  of 0.0001%/h or 0.001%/h at a given temperature. The  $\dot{\epsilon}_{min}$  is the most important design parameter that can be obtained from the creep curve. As a requirement for steam turbine alloys such as X20 steel, it is the stress to produce a creep rate of 0.00001%/h or 1% in 100 000 h. The creep properties of the material are dependent on the chemical composition, microstructure and heat treatment. In the case of X20 steel, the optimal creep strength is achieved at C contents higher than 0.17% (EPRI 2006).

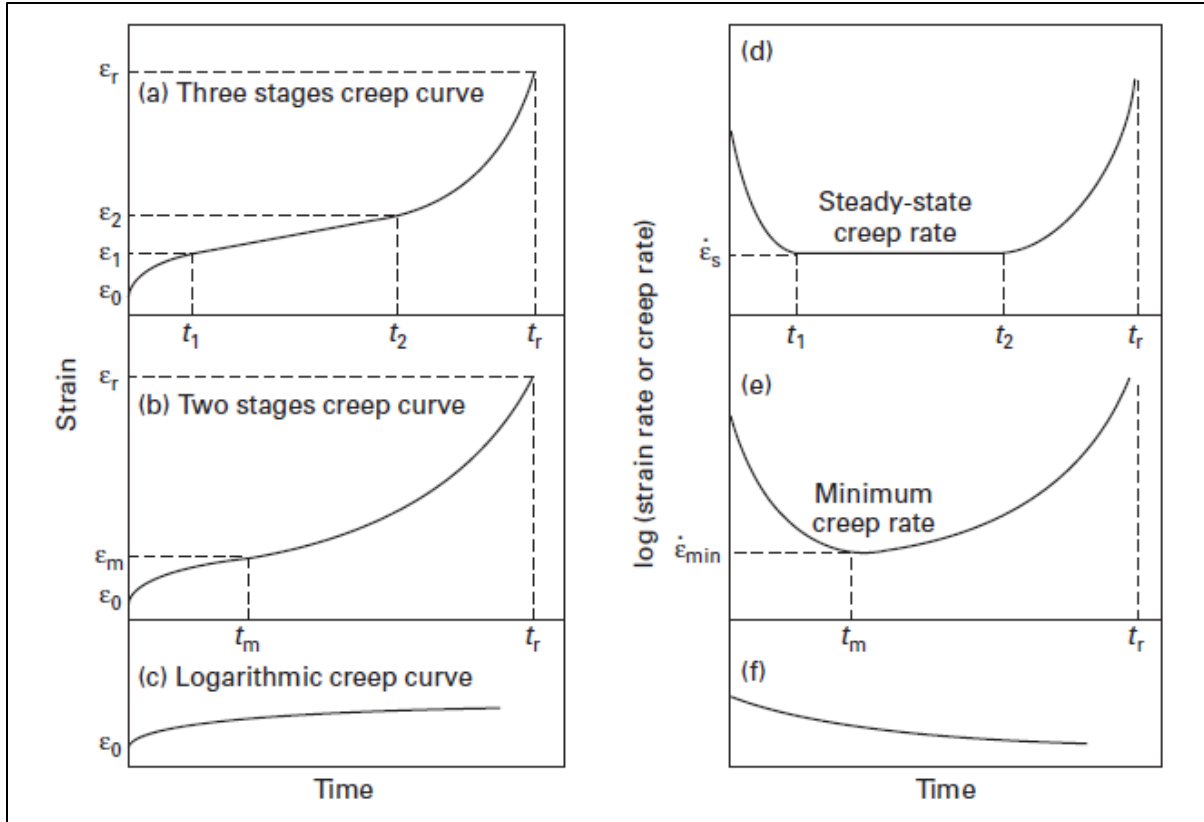


**Figure 2.2:** (a), (b) and (c) Examples of theoretical creep curves of steels under constant tensile load and temperature. (d), (e) and (f) Corresponding creep rate curves as a function of time (Abe 2008).

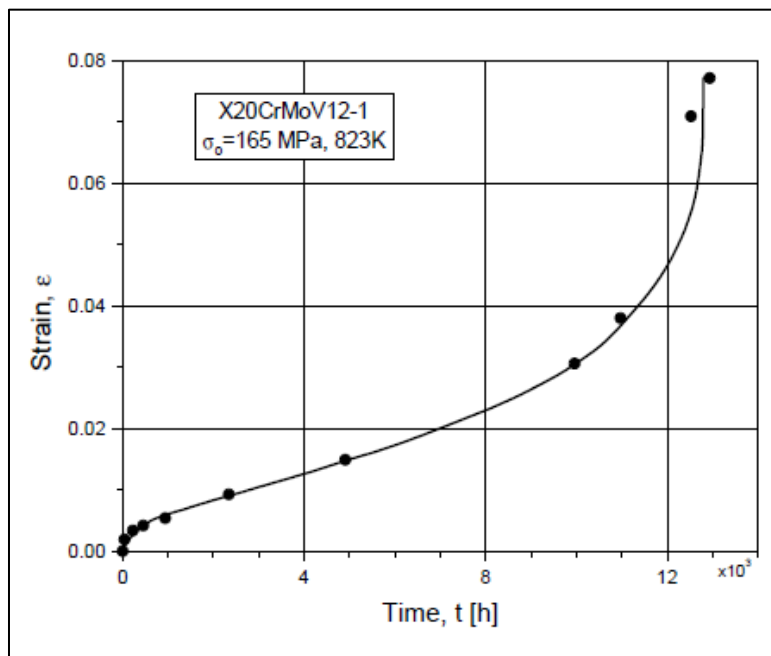


**Figure 2.3:** Creep curve for X20 martensitic steel (EPRI 2006).

The creep strength of boiler and steam pipe 9-12% Cr martensitic steel components can be defined as the material property that sets the maximum steam pressure and temperature at which these highly stressed pressurised components can be designed with a wall thickness thin enough to allow rapid temperature changes during load changes and boiler startup (Hald 2017).

Consequently, high-temperature power plant components that are used under creep conditions are designed using an allowable stress. This allowable stress is generally determined based on 100 000 h creep rupture strength at the operating temperature. The 100 000 h creep rupture strength at a given temperature is defined as the stress at which creep rupture, which is the last point in the creep curve (**Figure 2.2(a)** and (b)), occurs at 100 000 h (Abe 2008). This value is determined from the creep rupture curve for a given temperature as shown in **Figure 2.4** for X20 steel at 550 °C. The critical allowable stress is then determined from the lower bound and using a safety factor of 1/0.8 (EPRI 2006). Therefore, a highly conservative design stress is used. The scatter in the values may be improved and the lower bound increased by performing microstructural screening of the samples before creep rupture tests. Consequently, an increased allowable stress can then be attained.

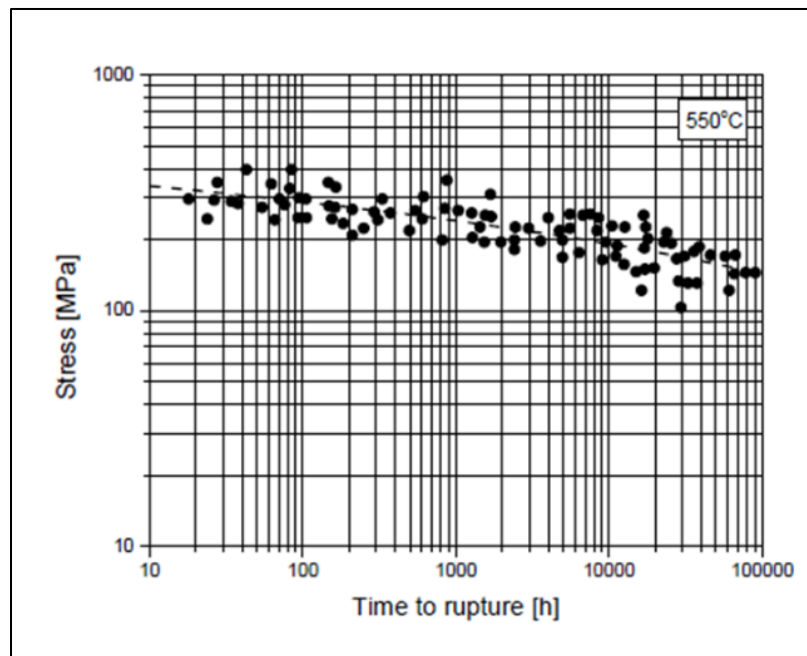


**Figure 2.4:** Creep rupture strength for X20CrMoV12-1 Steel at 550 °C (EPRI 2006).

## 2.2 METALLURGY AND MICROSTRUCTURE

Mechanical, creep and fracture properties of 9-12% Cr martensitic steels are highly dependent on the microstructure. The meaning of the term *microstructure* stems from the fact the characteristic features of internal steel structures range in size from resolvable by the naked eye to only resolvable by light and electron microscopy (Krauss 2015). The initial or as-received microstructure is determined by the chemical composition and heat treatment steps of the material. The 9-12% Cr martensitic steels are also referred to as tempered martensite ferritic (TMF) steels since they are manufactured by the tempered martensite heat treatment regime and they have a ferrite matrix after heat treatment (Kostka, Tak, Hellmig *et al.* 2007, Holzer 2010, Yan, Wang, Shan and Yang 2013). Therefore, these steels all share the common feature of a single phase as-received tempered martensite microstructure in the parent material.

Standard testing methods are used to determine the material engineering properties to obtain information about the component design and service behaviour. Continuous Cooling Transformation (CCT) diagrams are used to describe the evolution of the microstructure as a function of time at temperature. They are usually experimentally determined, and the diffusion coefficients and transformation temperatures are also determined from the experiments. The CCT diagram for X20CrMoV12-1 steel is given in **Figure 2.5**. As can be seen, ferrite forms upon slower cooling rates, corresponding to near equilibrium conditions. Under more rapid cooling conditions, bainite or martensite forms. Consequently, CCT diagrams are of great importance since they can be used for various manufacturing processes to develop and identify the thermal cycle that needs to be applied to obtain the desired microstructure (EPRI 2006). The chemical composition, standard heat treatment and as-received tempered martensite microstructure of 9-12% Cr martensitic steels are discussed in this section.

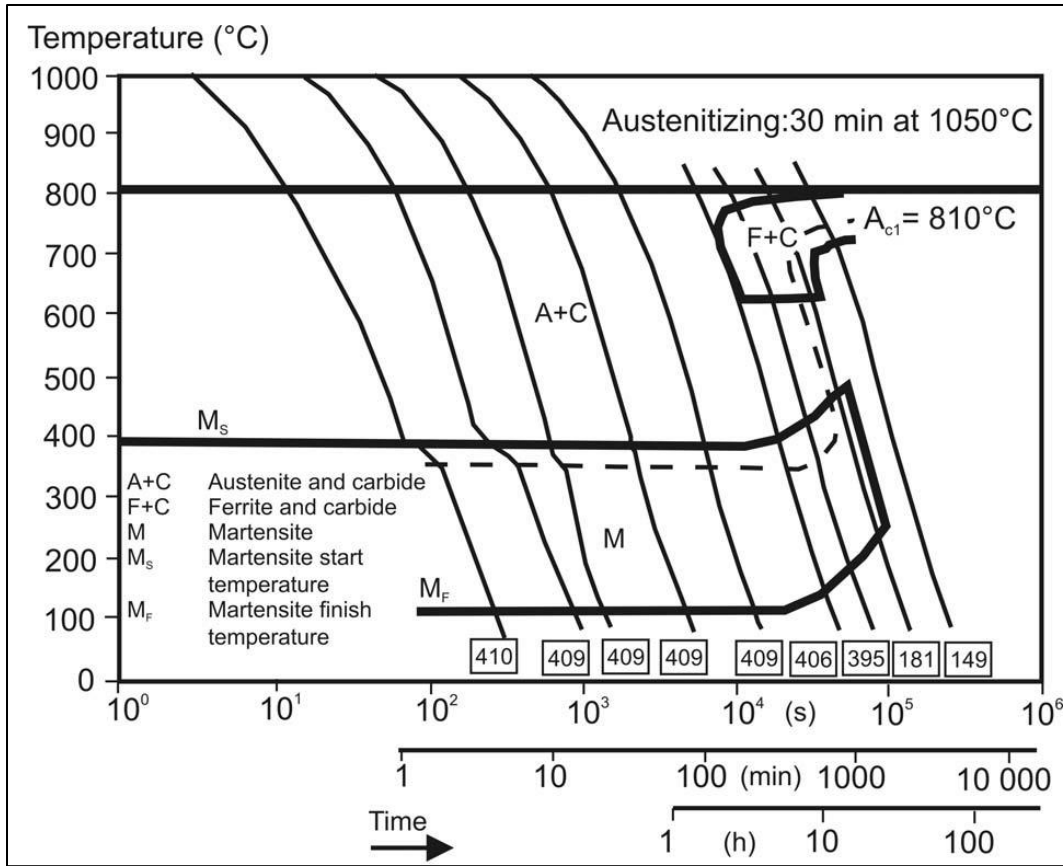


**Figure 2.5:** CCT diagram for X20CrMoV12-1 steel (Aghajani 2009).

### 2.2.1 Chemical Composition

The  $M_s$  and  $M_f$  temperatures in **Figure 2.5** is controlled by the chemical composition of the steel (Aghajani 2009). The chemical composition of X20 steel has been given in **Table 2.1**. For comparison, the alloying elements and typical heat treatment parameters of other martensitic creep-resistant 9-12% Cr steels used in steam pipes (pressure vessels) are provided in **Table 2.2**. As can be seen, these steels are mainly characterised by a relatively low quantity of C ( $\leq 0.2\%$ ) and 9 to 12 wt% Cr content. It is also evident that these steels have been developed with an increase in the number of alloying elements. Also, the improvements in the strength of these steels have been mainly attained by minor alloy additions. For example, the microalloying of Nb and N resulted in the first strength increase from X20 to P91 steel and the second increase to P92 was attained by partial replacement of Mo by W and adding B (Hald 2008). Hofer (1999), Schaffernak (2000),

Yan, Wang, Shan and Yang (2013) and Pandey, Mahapatra, Kumar and Saini (2018) give detailed explanations on the exact effect of the alloying elements on the properties of these steels.

**Table 2.2:** Chemical compositions (mass%, bal.Fe) and typical heat treatment parameters of main 9-12% Cr steam pipe steels (Hald 2017).

Element (wt%)	X20	P91	P92
C	0.2	0.1	0.1
Si	0.3	0.3	0.3
Mn	0.5	0.45	0.45
Cr	11	9	9
Mo	1	1	0.45
W			1.75
Ni	0.5	<0.2	<0.4
V	0.3	0.2	0.2
Nb		0.08	0.06
N		0.05	0.05
B			0.003
Normalising	1050 °C	1050 °C	1065 °C
Tempering	750 °C	750 °C	770 °C

### 2.2.2 Heat Treatment

Austenitising and then air cooling, followed by tempering and air cooling again, make up the standard heat treatment of these steels. This heat treatment of these steels optimises the material properties of these steels. For example, the high creep strength of these steels, even at elevated temperatures is obtained by the delicate balance between high strength and high toughness of these steels, which is achieved by relatively high austenitising and tempering temperatures (Yoshizawa and Igarashi 2007, Hald 2017). Typical austenitising, tempering, critical and martensite formation temperatures for 9-12% Cr martensitic steels are given in **Table 2.2** and **Table 2.3**, respectively. In **Figure 2.6** the portion of the Fe-Cr-C phase diagram applicable to the carbon wt.% ranges of these



steels is given, as well as simple schematic illustrations of the microstructure resulting from each heat treatment step.

**Table 2.3:** Typical transformation temperatures of 9-12% Cr martensitic steels (Constructed from Abe, Kern and Viswanathan (2008), and Pandey, Mahapatra, Kumar and Saini (2018)).

Phase Transformation	Temperature
Lower critical temperature $A_{C1}$	810 – 825 °C
Upper critical temperature $A_{C3}$	912 – 930 °C
Martensite formation start temperature $M_s$	390 – 400 °C
Martensite formation finish temperature $M_F$	100 – 150 °C

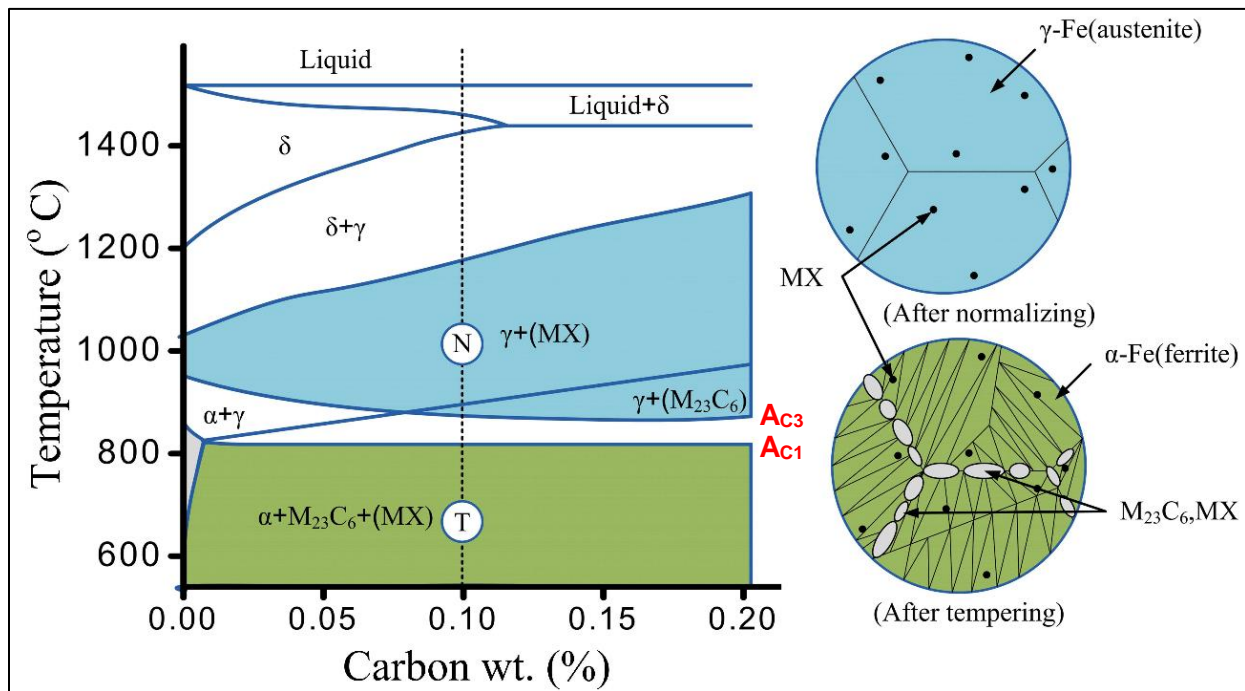


**Figure 2.6:** Fe-Cr-C phase diagram and schematic illustration of microstructure resulting from heat treatment of 9-12% Cr martensitic steels, highlighting normalising N (blue) and tempering T (green) ranges (Pandey, Mahapatra, Kumar and Saini 2018).

### **(i) Austenitising**

During austenitising of X20 steel, the steel is heated above the  $Ac_1$  temperature (between 1020°C and 1070°C) for about 30 min and ferrite or  $\alpha$ -Fe (body-centered cubic (bcc)) transforms into austenite or  $\gamma$ -Fe (face-centered cubic (fcc)) (Maruyama, Sawada and Koike 2001, EPRI 2006, Aghajani 2009). The primary carbides and nitrides are dissolved as a prerequisite for the subsequent precipitation of fine secondary phase particles during tempering. However, some undissolved primary carbides are necessary to pin the austenite grain boundaries to restrict growth, as can be seen in **Figure 2.6** (Hald 1996). Pinning of grain boundaries by precipitates will be discussed more in Section 2.3.2. Low austenitising temperatures may lead to an insufficient degree of dissolution of the primary carbides, whereas from too high austenitising temperatures undesired  $\delta$  – ferrite formation results that cause embrittlement (Chilukuru 2007). For further discussion of the effect of normalising and tempering temperatures on the microstructure stability and mechanical properties of the 9-12% Cr martensitic steels the extensive discussions by Pandey et al. (Pandey, Giri and Mahapatra 2016, Pandey, Giri and Mahapatra 2016, Pandey, Mahapatra, Kumar and Saini 2017, Pandey, Mahapatra, Kumar and Saini 2018) can be consulted.

### **(ii) Martensitic Transformation**

Upon air cooling to room temperature after austenitising, the material completely transforms into a martensitic structure. Martensite is a highly strained body-centered tetragonal (bct) form of ferrite that is supersaturated with carbon (Bhadeshia 2002). The martensitic transformation results in high shear strains due to the supersaturated carbon content in the matrix. Some curvature is introduced to minimise the strain energy and therefore thin laths form (Morito, Nishikawa and Maki 2003, Bhadeshia and Honeycombe 2006). The martensitic transformation is diffusionless since the atoms are displaced in a coordinated manner less than one atomic spacing and without a change in composition (Bhadeshia 2002). Also, since the martensitic transformation is a shear or displacive transformation, there exists a crystallographic relationship between the parent and product phases. **Figure 2.7** provides a comprehensive schematic illustration of the shear

and surface tilt resulting in the formation of a martensite plate. The habit plane shown in this diagram refers to the preferred crystal plane of austenite on which the martensite crystals form (Krauss 2015). Plate types of ferrous martensite usually have variants of habit planes, whereas lath martensite only has one. For 9-12% martensitic steels with less than 0.4 wt% C, a lath structure forms with a habit plane is approximately the  $\{111\}_\gamma$  plane (Porter, Easterling and Sherif 2009). The shape of the martensite crystals is dependent on the transformation temperature and carbon concentration (Bhadeshia and Wayman 2014).

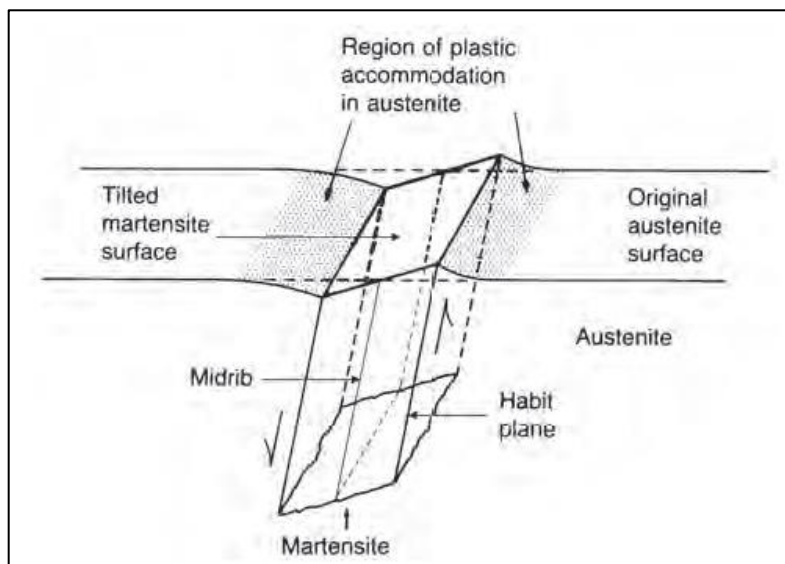


**Figure 2.7:** Schematic illustration of shear and surface tilt resulting from the formation of martensite plate (Krauss 2015).

Due to the single habit plane, martensite laths tend to cluster together hierarchically organised into blocks and packets within a specific prior-austenite grain (**Figure 2.8**). Laths of similar orientation in space form a block and a packet is a group of blocks that share the same  $\{111\}_\gamma$  close-packed plane of the parent austenite to which the corresponding  $\{011\}_\alpha$  plane is nearly parallel. This relation of martensite to the parent austenite is referred to as the Kurdjumov-Sachs (KS) crystallographic relation. There are other relations such as the Nishiyama–Wasserman (NW) that can also be used to describe this crystallographic relationship. Therefore, the habit planes of laths within a packet make small angles with respect to each other but have different crystallographic

orientations. In contrast, those within blocks have similar crystallographic orientations. For the planar match  $(111)_\gamma \parallel (011)_\alpha$  there are a total of six KS relations (Morris Jr, Kinney, Pytlewski and Adachi 2013). Consequently, since there are four independent  $\{111\}_\gamma$  reference planes, there are only four distinguishable packets possible and a possibility of a total of 24 independent KS orientations (variants) for the martensite laths produced by the transformation of a single austenite grain. Misorientations of near  $60^\circ$  can be produced by the four KS variant intersections, i.e., a combination of two variants (Payton, Aghajani, Otto *et al.* 2012). Two of the variant intersections produce packet boundaries and the other two block boundaries. If the prior austenite grains are small, then not all four of the different packets will be visible within a single grain (Bhadeshia 2002, Bhadeshia and Honeycombe 2006, Bhadeshia and Wayman 2014, Krauss 2015). The KS and NW orientation relationships are only ideal and Brust, Niezgod, Yardley and Payton (2018) and Payton, Aghajani, Otto *et al.* (2012) has found that the misorientations of the experimental variant intersections deviate from those given by these relationships.

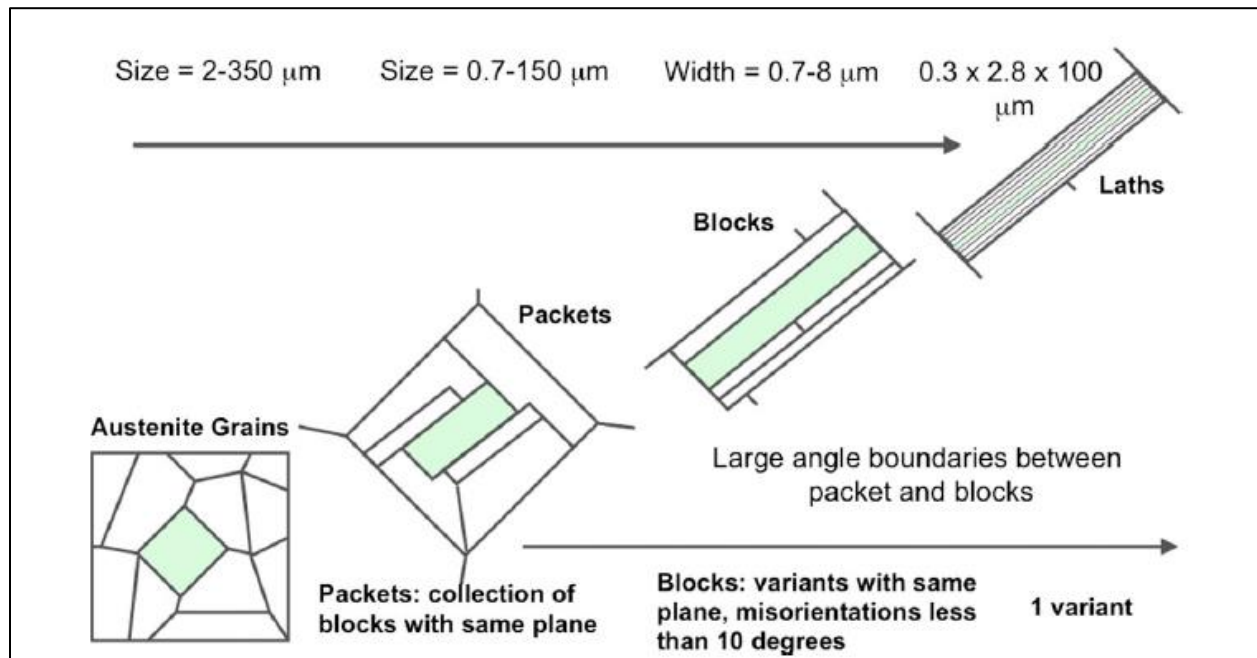


**Figure 2.8:** Hierarchical microstructure of lath martensite defined in four scales: parent austenite grains, packets, blocks and laths (Hatem and Zikry 2009).

During the martensitic transformation, there is not only a small relative rotation of the corresponding unit cells in the parent and product phases but also a homogeneous lattice

distortion that precedes to account for the known structural change of the fcc lattice to bcc (or bct) lattice. There are many proposed mechanisms for such a homogeneous lattice distortion, but the most favoured is the Bain deformation (also known as Bain Strain) proposed by Edgar C Bain (1924). **Figure 2.9** illustrates this proposed mechanism. The cube compression axis ( $z$ -axis in the case of **Figure 2.9**) is called the Bain axis and is the most important feature of martensite. This axis determines the transformation strain and the relative orientation of its  $\{100\}$  planes. Thus, the six KS variants for the planar match  $(111)_\gamma \parallel (011)_\alpha$  correspond to the two representatives of each of the three Bain variants, i.e., compression along the  $x$ ,  $y$  or  $z$  directions. From this, a block can also be defined as a group of laths consisting of two variants with small misorientation or of the same Bain variant (Bhadeshia 2002, Bhadeshia and Honeycombe 2006, Porter, Easterling and Sherif 2009, Morris Jr, Kinney, Pytlewski and Adachi 2013, Bhadeshia and Wayman 2014, Krauss 2015).

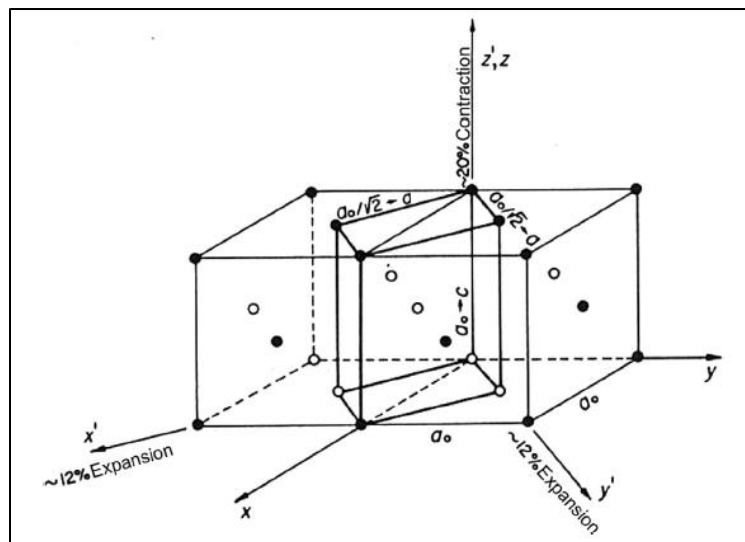


**Figure 2.9:** Bain Strain mechanism of lattice distortion and correspondence to obtain the martensite variant from the parent austenite. There is a compression along one of the  $\langle 100 \rangle_\gamma$  cube axes and a uniform expansion in the perpendicular planes until it becomes bcc (Bhadeshia and Wayman 2014).

Plastic accommodation occurs with the shape deformation, leading to a higher dislocation density in the austenite into which the martensite grows (Bhadeshia and Wayman 2014).

Consequently, a high-density cellular dislocation structure is induced by the martensitic transformation which is one of the main contributors to the strength of martensite (Abe 2008, Christien, Telling and Knight 2013, Krauss 2015).

### **(iii) Tempering**

Martensite is highly unstable for reasons such as the supersaturation of carbon atoms in the bcc martensite lattice, strain energy connected to the fine cellular dislocation substructure within the laths, and the interfacial energy related to the high density of lath boundaries. Therefore, tempering is required to stabilise the microstructure.

Several tempering cycles in the range of 650°C to 780°C (below the  $A_{e1}$  temperature) are applied to the steel after austenitising (Holzer 2010, Yan, Wang, Shan and Yang 2013). During tempering (Krauss 2015):

- there is a driving force for carbide formation and coarsening from the supersaturation of martensite with carbon atoms;
- a driving force for recovery due to the high strain energy associated with the fine dislocations in the laths;
- and a driving force for grain growth or coarsening of the ferrite matrix from the high interfacial energy associated with the high density of LB.

Subsequently, several phenomena occur during tempering (Maruyama, Sawada and Koike 2001, Abe 2008, Aghajani 2009, Holzer and Kozeschnik 2010):

- (i) precipitation of secondary phase particles (precipitates) on boundaries;
- (ii) packet boundaries transform into new high angle ferrite grain boundaries, and hence the martensitic lath structure changes into a fine elongated ferritic subgrain structure;

(iii) the dislocation density decreases; a subgrain structure is introduced by the formation of small-angle grain boundaries, referred to as subgrain boundaries (SGBs), due to the recovery of the dislocation cell structures;

(iv) and dislocations are found inside the subgrain structure.

Thus, the result of tempering is to transform the martensitic microstructure into a ferritic structure with a high dislocation density and elongated  $\mu\text{m}$ -sized ferritic subgrains (Kostka, Tak, Hellmig *et al.* 2007).

### 2.2.3 Initial Tempered Martensite Microstructure

From the previous section it follows that the complex lath martensitic microstructures of 9-12% Cr martensitic steels before tempering has many levels of hierarchy within a single prior austenite grain (**Figure 2.8**) (Kalwa, Schnabel and Schwaab 1986, Morito, Tanaka, Konishi, Furuhashi and Maki 2003, Kitahara, Ueji, Tsuji and Minamino 2006, Payton, Aghajani, Otto *et al.* 2012):

1. Individual approximately parallel laths all with same habit plane and virtually identical orientation in space;
2. Sub-blocks grouping laths of same K-S variant;
3. Blocks consisting of laths of two specific K-S variant groups (sub-blocks) with small misorientation (about  $10^\circ$ );
4. Packets consisting of well-developed parallel blocks with slightly different orientations, but approximately the same  $(111)_\gamma \parallel (011)_\alpha$  orientations (habit plane);
5. Interpenetrating packets outlining a prior austenite grain.

Point number 3 explains why blocks and sub-blocks are observed to have different contrast when viewing the etched surface of the steel under a light microscope. For low carbon alloys, Morito, Tanaka, Konishi *et al.* (2003) has found that within a single packet

there are three blocks of different orientations. During tempering, the SGB within the subgrain structure is then another type of internal interface added to the hierarchy.

The ideal tempered martensite microstructure of martensitic creep-resistant 9-12% Cr steels with its characteristic features is schematically illustrated in **Figure 2.10**. The most prominent feature of this complex microstructure is ultra-fine grains that are elongated  $\mu\text{m}$ -sized ferritic subgrains and are bounded by both high angle grain boundaries (HAGB) and low angle grain boundaries (LAGB). The type of precipitates that form during tempering is determined by the chemical composition. Each microstructural feature will be elaborated on in Section 2.2.3.

The terminology used in literature for referring to these elongated ferritic subgrains is not consistent. Therefore, the terminology from Pešička and co-authors (Dronhofer, Pešička, Dlouhý and Eggeler 2003, Pešička, Kužel, Dronhofer and Eggeler 2003, Pešička, Dronhofer and Eggeler 2004, Pešička, Aghajani, Somsen, Hartmaierc and Eggeler 2010) is adopted in this study to refer to *micro-grains*. They are the elongated ferritic subgrains that are adjacent with the same variant (orientation) and are bounded by both low-angle boundaries and high-angle boundaries (Kostka, Tak, Hellmig *et al.* 2007). It is more accurate to refer to micro-grains rather than subgrains or laths. By referring to subgrains, one excludes the ferritic subgrains that have high angle boundaries, and the term laths will only be appropriate in the fully martensitic state. In addition, these grains fit the general description of micro-grains as tiny grains with sub-micrometre dimensions. These micro-grains are approximately 2  $\mu\text{m}$  long and 0.5  $\mu\text{m}$  wide. Thus, the term micro-grain separates the smallest features in the ferrite microstructure from martensite laths (Payton, Aghajani, Otto *et al.* 2012). As an illustration, a single micro-grain is outlined in **Figure 2.10**.

From Bhadeshia and Wayman (2014) it follows then that the micro-grain size defines a *crystallographic grain size* which is the scale of connected regions that have a similar orientation in space. However, these regions may still exhibit a substructure when observed with a Scanning Electron Microscope (SEM), which is the case for the tempered martensite microstructure. Precipitates are decorated on or near the boundaries of these



micro-grains and a very high dislocation density within the micro-grains (Eggeler, Nilsvang and Ilschner 1987, Eggeler 1989, Eggeler, Earthman, Nilsvang and Ilschner 1989, Pešička, Kužel, Dronhofer and Eggeler 2003, Isik, Kostka, Yardley *et al.* 2015). A group of micro-grains that are elongated in the same direction forms a packet.

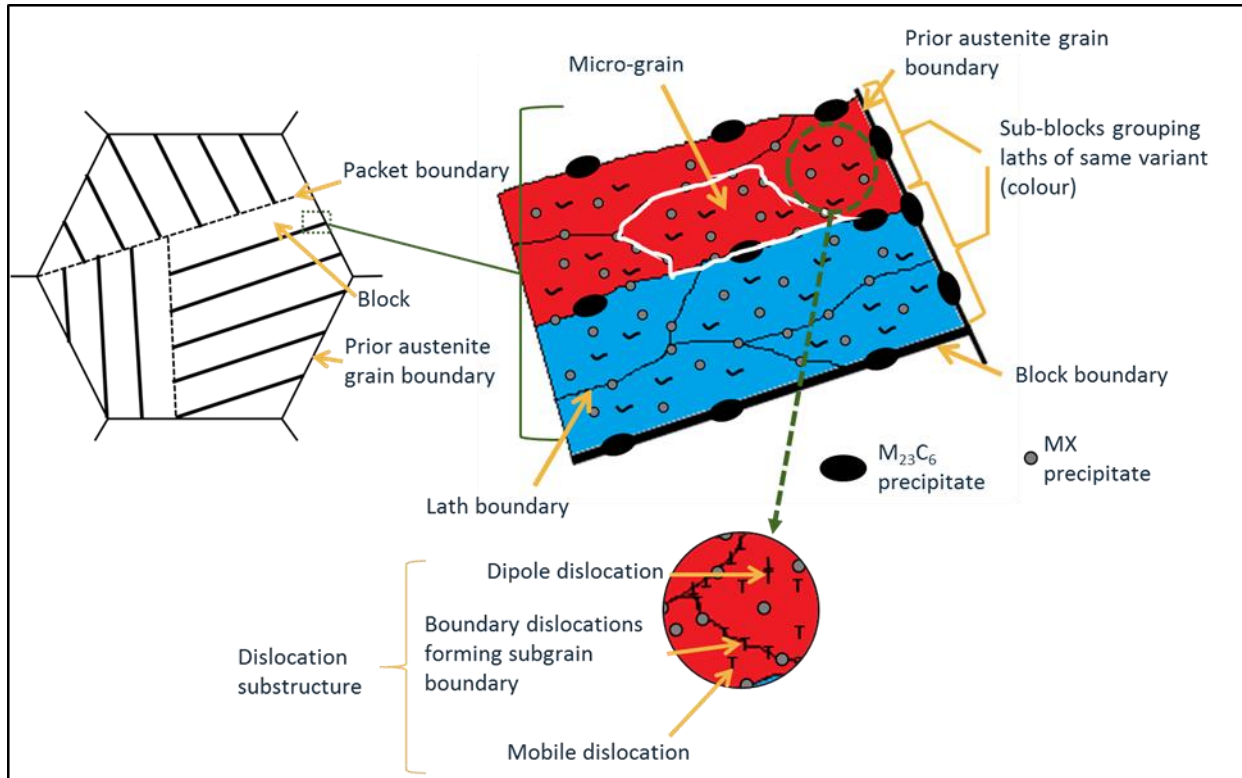


**Figure 2.10:** Schematic illustration of the ideal initial microstructure of tempered martensite microstructure in 9-12%Cr ferritic steels. Single micro-grain outlined in white.

### 2.3 MICROSTRUCTURAL EVOLUTION OF MARTENSITIC CREEP-RESISTANT 9-12% CR STEELS DURING CREEP EXPOSURE

Martensitic creep-resistant 9-12% Cr steels have a complex non-equilibrium initial microstructure since the tempered martensite phase is not a thermodynamic equilibrium phase. Therefore, the microstructure will tend to continually evolve and degrade to attain equilibrium when exposed to service conditions of high stress and elevated temperature, which has an impact on the long-term performance of the power plant component (Di

Gianfrancesco, Vipraio and Venditti 2013). Blum, Straub and Vogler (1991), Blum (1993) and Kostka, Tak, Hellmig *et al.* (2007) have explained the creep of X20 steel to be a case where a material with tiny initial subgrain size and very high dislocation density adjust to a new low-stress equilibrium state. Nevertheless, martensitic creep-resistant 9-12% Cr steels have been designed to inherit a high creep strength (creep resistance) from strengthening mechanisms at work from the various microstructural features (Maruyama, Sawada and Koike 2001).

Due to the component material degradation effect of creep during service, extensive effort has been made to explain and predict this deformation mechanism (Section 2.7). To attain a better understanding and description of creep and its effect on material properties, it is important to fully consider the relationship between the creep process and the microstructure of the material.

During dislocation creep, which occurs at low stresses, the movement of free dislocations and micro-grain boundary (MGB) migration are considered to be the cause deformation of the material (Blum 1993, Hald 2008). Each of the microstructural features acts as obstacles to hinder the movements of these free dislocations and SGB, which are low energy arrangements of dislocations (Eggeler, Nilsvang and Ilschner 1987). These microstructural features are the MGB, free dislocations within the micro-grains, and the precipitates.

The evolution of the microstructure with creep is normally characterised by micro-grain coarsening, prior austenite GB disappearance, the emergence of subgrains, coarsening of precipitates and the precipitation of new phases (Yan, Wang, Shan and Yang 2013).

Firstly, an introduction is provided to the various creep deformation mechanisms. The contribution to creep strength of the microstructural features and their evolution during creep is discussed in the sections to follow.

### 2.3.1 Creep Deformation Mechanisms

The creep mechanism that is operating in a material depends on the stress and temperature. A total of six different deformation mechanisms are responsible for creep, namely (Abe 2008):

1. defect-less flow;
2. glide motion of dislocations;
3. dislocation creep;
4. volume diffusion flow (Nabarro-Herring creep);
5. grain boundary diffusion flow (Coble creep);
6. and twinning.

It is assumed that all six of these mechanisms are mutually independent and operate in parallel. Based on this assumption and considering only steady-state flow with no fracture, Ashby (1972) proposed the concept of a deformation mechanism map. This map is useful to predict a dominant deformation mechanism at the beginning of creep under specific stress and temperature conditions.

Due to the mechanisms operating independently, each one will contribute additively to the total strain rate. Consequently, creep deformation will be dominated by the mechanism with the highest strain rate. This dominance corresponds to a field in the deformation mechanism map. At stresses lower than this ideal strength such as in short-time tensile tests, deformation is caused by dislocation glide. Dislocation creep can take place with the aid of diffusion at stresses lower than the yield stress, specifically volume diffusion at high homologous temperatures and dislocation core diffusion at low homologous temperatures (Abe 2008).

At further lower stresses, dislocation movement is prolonged and therefore can generally be ignored so that deformation is caused mainly by the transport of material through diffusion instead of dislocation motion (Rastogi 2005). Therefore, the diffusional creep mechanisms come into play at low stresses and elevated temperatures. The mobility of atoms and the equilibrium concentration of vacancies both increase with increasing temperature. Nabarro-Herring creep, or volume diffusion flow, is the flow of vacancies

through the lattice of the grain, while Coble creep or grain boundary flow is the flow of vacancies along the grain boundary (Nabarro and De Villiers 1995).

### **(i) Diffusional creep**

Oikawa and Iijima (2008) state that diffusion is one of the fundamental processes that govern creep deformation. Diffusional creep is defined as the process where the material is transferred from one section of the lattice to another by the movement of atoms along the tracks of moving vacancies (Kozeschnik 2013). It is well established that the temperature dependence, or activation energy, of diffusional creep, is the same as the rate of vacancy diffusion. In other words, at temperatures higher than half the material's melting temperature, the creep strain rate and diffusion rate is similar. Nabarro-Herring creep mainly governs the creep rate at low stresses and these high temperatures (Oikawa and Iijima 2008).

Diffusion can be described on the different scales: macroscopic (engineering); mesoscopic (microstructure); and microscopic (atoms and vacancies). The theory of diffusion at the macroscopic level is defined by Fick's laws of diffusion (Crank 1975).

Several of the microstructure heterogeneities are considered as perfect vacancy sources and vacancy sinks. Examples of these vacancy generation and annihilation sites are (Kozeschnik 2013):

1. free surfaces;
2. grain boundaries;
3. incoherent or semi-coherent phase boundaries;
4. subgrain boundaries;
5. dislocation jogs.

Vacancy diffusion occurs by three different mechanisms: migration of vacancies over the surface of the grain that has a small activation energy; vacancies flowing along the grain boundaries that has intermediate activation energy; and diffusion of vacancies through the bulk of the material that has much larger activation energy. As mentioned previously, Nabarro-Herring creep, which is bulk diffusion, is the effective creep mechanism at

elevated temperatures and low stresses. The considerable activation energy is compensated for by the high temperature (Nabarro and De Villiers 1995).

Grain boundary sliding (GBS) is another deformation mechanism and is closely related to diffusional creep. The flux of vacancies and atoms during diffusion results in the grain changing shape. These changes need to be accommodated with a further process of mass transfer at the grain boundaries. If there is no accommodation, then the formation of voids and cracks (Section 2.3.6) occurs and hence the coherency of the material is lost. GBS is the necessary and generally accepted accommodating process for diffusional creep to maintain the material's structural integrity (Yamakov, Wolf, Phillpot and Gleiter 2002). At low strain rates, GBS becomes an important deformation mode (Maruyama, Nakamura, Sekido and Yoshimi 2017).

Precipitates significantly reduce the rate of diffusional creep. Firstly, they pin the boundaries (Section 2.3.2), inhibiting GBS. Secondly, the precipitate-matrix boundary has low vacancy mobility and is much less effective than the grain boundaries as a source and sink of vacancies (Nabarro 2002). Weyer (2016), Kozeschnik (2013), Oikawa and Iijima (2008), Krauss (2015), and Porter, Easterling and Sherif (2009) provides further detailed descriptions of diffusion in steels and the role of diffusion in creep deformation.

## **(ii) Dislocation creep**

Intrinsically, creep at elevated temperatures results from complex dislocation behaviour. Therefore, dislocation creep is the time-dependent plastic deformation or creep of a material due to dislocation motion. The key to understanding the elementary mechanics of material plasticity is the dependence of dislocation mobility on stress and temperature. The flow stress of a metal is influenced by two major components: the long-range interaction of mobile dislocations with the crystal microstructure and the stress necessary to move the mobile dislocations over local energy barriers that are hindering their movement. When considering dislocation creep in precipitate hardened steels under creep deformation, the latter is of great consequence. The dislocations are assisted by thermal activation to overcome the energy barriers (Caillard and Martin 2003). Equations used to describe dislocation creep are further discussed in Section 2.7.2.

The stress and temperature ranges of technical interest for creep testing and service exposure of martensitic creep-resistant 9-12% Cr steels are 250 - 20 MPa at 500 - 700 °C (Danielsen and Hald 2009). For relevant loading conditions in this range, rupture times of between 100 and 300 000 h with  $\dot{\epsilon}_s$  between  $3 \times 10^{-6}$  and  $3 \times 10^{-12} \text{ s}^{-1}$  are found. Hald (2017) is of the view that the main creep mechanism in these ranges are dislocation creep. Consequently, the important microstructural changes are those who result in greater mobile dislocation movement and hence greater creep rates. This entails the glide of mobile dislocations and migration of MGB during creep that results in decreased mobile dislocation density and coarsening of micro-grains. Hence, dislocation creep can be further elaborated on by considering the microstructural changes that occur during creep exposure (Sections 2.3.2 to 2.3.7).

### **2.3.2 Creep Strengthening and Behaviour of Precipitates**

Martensitic creep-resistant 9-12% Cr steels have been developed with the aim of forming precipitates since the creep strength is increased by precipitate hardening (PH). Precipitates introduce additional barriers and strain fields. Thus, they inhibit the climb and glide of mobile dislocations by acting as obstacles and decreases the coarsening rate of the microstructure by pinning the SGB (Murugananth and Bhadeshia 2002). It is essential to have a fine distribution of highly thermally stable precipitates to obtain a high creep strength in 9-12%Cr steels.

The initial tempered microstructure is characterised by dislocations boundary (SGB) and tangles of dislocations around the precipitates (Section 2.2.3). In the areas of low density of precipitates, the SGB have already formed, whereas in high particle density areas the precipitates are the centre of dislocation activity. Hence, the high number density of precipitates reduces the tendency of dislocations to arrange in low-energy boundary structure (SGB) (Hansen and Barlow 2014).

It is the heat treatment and chemical composition that determine the nature of precipitates that form. The main strength determining precipitates that form during tempering is the  $M_{23}C_6$  (M = Cr, Fe, Mo) carbides and MX (M = V, Nb and X = C, N) carbonitrides (Holzer

2010, Yan, Wang, Shan and Yang 2013). Thus, the creep strength of these steels is dependent strongly on their phase fraction, size distribution and spatial dispersion.

Other intermetallic compounds such as Laves phase and Z-phase may also form during tempering and creep. These precipitates have been studied extensively for 9-12% Cr martensitic steels (Cerjak, Hofer and Schaffernak 1999, Aghajani, Richter, Somsen *et al.* 2009, Aghajani, Somsen and Eggeler 2009, Isik, Kostka, Yardley *et al.* 2015, Xu, Zhang, Tian, Chen, Nan *et al.* 2016, Xu, Nie, Wang *et al.* 2017). **Table 2.4** summarises the various precipitates and their characteristics and a micrograph displaying these precipitates are given in **Figure 2.11**. It has been shown that X20 (12% Cr) steel grade usually contains  $M_{23}C_6$ , MX, Laves and Z-phase after tempering and creep aging (Eggeler, Nilsvang and Ilschner 1987, Eggeler 1989, Eggeler, Earthman, Nilsvang and Ilschner 1989, Aghajani, Richter, Somsen *et al.* 2009, Aghajani, Somsen and Eggeler 2009, Aghajani 2009, Di Gianfrancesco, Vipraio and Venditti 2013, Xu, Zhang, Tian *et al.* 2016). Therefore, only these precipitates are now discussed in more detail for martensitic creep-resistant 9-12% Cr steel.

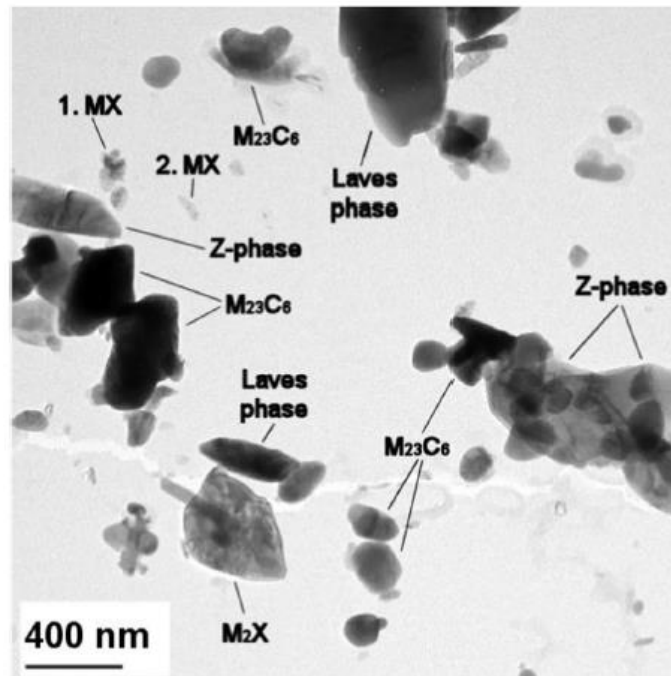


**Figure 2.11:** Micrograph of most common precipitates in 9-12% Cr martensitic steels (Danielsen and Hald 2006).

**Table 2.4:** Summary of basic characteristics of common precipitates in 9-12% Cr steels (Constructed from Aghajani, Richter, Somsen et al. 2009, Aghajani, Somsen and Eggeler 2009, and Zhang, Wu, Liu, Liu and Yao 2017).

Precipitate Type	Composition	Crystal Structure	Nucleation Period	Size and Shape	Characteristics	Main Contribution
<b>M<sub>23</sub>C<sub>6</sub></b>	Cr <sub>23</sub> C <sub>6</sub> Minor = Fe, Mo, W, B	cubic	tempering	Elongated, rounded shapes with lengths 200 – 500 nm and widths 20-50 nm	<ul style="list-style-type: none"> <li>• Forms on PAGB and LB</li> <li>• Medium growth rate during creep</li> </ul>	PH Stabilise micro-grain structure
<b>MX</b>	NbC, VN, (Nb,V)(C,N) Minor = Cr,C	cubic	tempering above 700 °C creep exposure	Elongated sharp rods or spheres with lengths up to 100 nm and thickness up to 30 nm	<ul style="list-style-type: none"> <li>• Forms Inside substructure, micro-grains and /or dislocations</li> <li>• High dimensional stability during creep</li> </ul>	PH
<b>M<sub>2</sub>X</b>	Cr <sub>2</sub> N Minor = V	hexagonal	tempering below 700 °C	morphologically like Z-phase	<ul style="list-style-type: none"> <li>• Few in low N steels</li> <li>• Forms inside micro-grains and substructure</li> <li>• Dissolves during creep at high temperatures</li> </ul>	PH
<b>Laves phase</b>	Fe <sub>2</sub> (Mo,W) Minor = Cr, Si	hexagonal	long-term creep exposure	various size and shape – can be larger (> 200 nm)	<ul style="list-style-type: none"> <li>• Forms on PAGB and MGB on M<sub>23</sub>C<sub>6</sub></li> <li>• Dissolution above 650 °C</li> <li>• Fast coarsening at 600 °C</li> </ul>	Decrease SSH Lower PH Poor plasticity
<b>Z-phase</b>	Cr(V,Nb)N Minor = Fe, Mo, W	tetragonal	long-term creep exposure	faceted particles that absorb MX - may be larger than 1 µm	<ul style="list-style-type: none"> <li>• Forms on M<sub>23</sub>C<sub>6</sub> and Nb(C,N) precipitates</li> <li>• Dissolution of Nb(C,N), M<sub>2</sub>X and VN</li> <li>• High coarsening rate</li> </ul>	Lower PH



### (i) $M_{23}C_6$ Carbides

These precipitates are commonly referred to as Cr-enriched  $M_{23}C_6$  carbides since their main composition is  $Cr_{23}C_6$  with Cr atoms replaced by minor amounts of Fe, Mo, W and B (**Table 2.4**). They have an fcc structure (lattice parameter of 1.057 to 1.068 nm) and usually are 50 to 285 nm in size (Aghajani, Somsen and Eggeler 2009, Holzer 2010, Pandey, Mahapatra, Kumar and Saini 2018).

Coarser  $M_{23}C_6$  precipitates are normally nucleated along the PAGB and prior martensite lath boundaries, and finer  $M_{23}C_6$  precipitates along or near the SGB with elongated shapes that follow the boundary (**Figure 2.10**) (Isik, Kostka, Yardley *et al.* 2015, Wang, Kannan and Li 2016, Zhang, Wu, Liu *et al.* 2017, Pandey, Mahapatra, Kumar and Saini 2018). Eggeler, Nilsvang and Ilschner (1987) made the important observation that in as-received (new) X20 steel a large portion of the new MGBs formed from the martensite interfaces during tempering were not pinned by  $M_{23}C_6$  precipitates.

It is well-known that the creep strength of 9-12% Cr martensitic steels over extended periods at elevated temperatures rely mainly on micro-grain stability (Abe and Nakazawa 1992, Abe 2003, Kostka, Tak, Hellmig *et al.* 2007). Armaki, Chen, Maruyama and Igarashi (2011) have found that during short-term creep micro-grain coarsening is controlled by strain and proceeds more gradually with higher % Cr, but during long-term creep it is controlled by the stability of precipitates rather than creep plastic deformation itself. Specifically, they have found that  $M_{23}C_6$  precipitates play a more significant role than MX precipitates in controlling micro-grain growth. The reason for this is that the  $M_{23}C_6$  precipitates and thickness of SGB have similar sizes during long-term static aging or creep.

The exact mechanism of PH is not yet fully understood. For the direct precipitate and dislocation interaction, it is proposed that at high temperatures and low stresses the dislocation can overcome the precipitate only by general or local climb, or by the Orowan (1948) mechanism which has little temperature dependence and only operates under high loads. The Orowan mechanism will be expanded on more in Section 2.7.2 and a detailed description of the climb mechanisms has been given by Holzer (2010).

### ***Precipitate- Micro-grain interaction***

Micro-grain and substructure growth occur during creep deformation as will be discussed in Section 2.3.3. The driving force for the growth is the reduction of the stored energy in the MGB and SGB as the grains grow. Assuming that the stored energy is uniform, the driving force evenly distributed, and the boundary energy  $\gamma$  is constant during growth, the driving pressure  $P$  can be given as (Humphreys and Hatherly 2004):

$$P = \frac{\alpha\gamma}{R} \quad (2.4)$$

where  $R$  is the radius of the micro-grain or subgrain. It should be noted that  $\gamma$  is a function of the misorientation of the adjacent micro-grain/ subgrain and therefore the driving pressure  $P$  may not remain constant during micro-grain and substructure growth.

Kostka, Tak, Hellmig *et al.* (2007) concluded that other proposed mechanisms such as detachment processes or strengthening effects obtained from intermetallic lattices do not account for PH. Instead, they show that fine MGB  $M_{23}C_6$  carbides stabilise the microstructure and hence contribute to the creep strength by “carbide stabilised substructure hardening”. These carbides impede knitting reactions between free dislocations and SGB, and stabilise the micro-grain structure by exerting a back-driving particle-pinning force (Zener force (Smith 1948)) on the MGB. **Figure 2.12** shows TEM images of these mechanisms. They conclude that the creep rates are decreased by many orders of magnitude due to the presence of the MGB carbides. The most important aspect is that this mechanism governs many of the other microstructural processes. In addition, they conclude that these carbides prevent the tempered martensite ferritic microstructure from recrystallising.

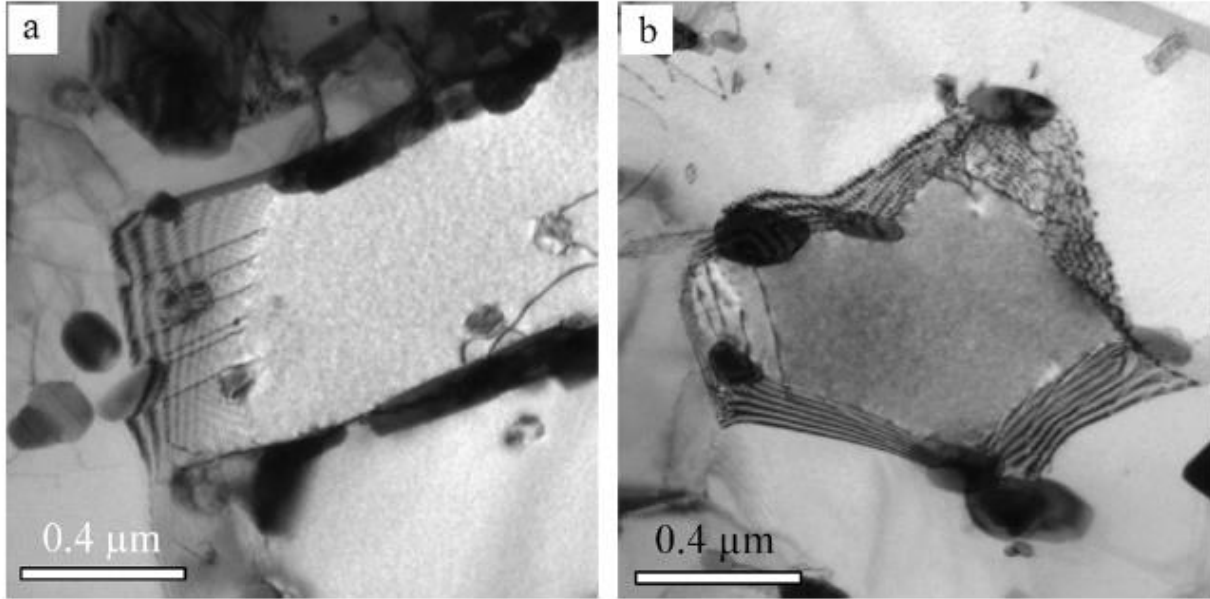


**Figure 2.12:** TEM micrographs that provide evidence of the direct interaction of MGB carbides on dislocation processes at boundaries and on boundary migration: (a) Carbides interrupt knitting reactions between dislocations and SGB. (b) Carbides stabilise a small micro-grain by exerting Zener forces (Kostka, Tak, Hellmig, Estrin and Eggeler 2007).

The Zener pinning pressure  $P_Z$  exerted by a random distribution of spherical particles with radius  $r$  on a unit area of the boundary is given by (Humphreys and Hatherly 2004):

$$P_Z = N_{interact}(\pi r \gamma) = \frac{3 f_V \gamma}{2r} \quad (2.5)$$

where  $N_{interact}$  is the number density of those particles that are within one particle radius of the boundary that can interact with it,  $\gamma$  is the energy of the boundary per unit area, and  $f_V$  is the total volume fraction of the particles. The boundary energy increases with an increase in misorientation of the boundary and decreases with increasing temperature (Porter, Easterling and Sherif 2009). For coherent/semi-coherent precipitate-matrix interface  $\gamma$  is of the order of  $10^{-1}$  J/m<sup>2</sup> and  $10^0$  J/m<sup>2</sup> for an incoherent precipitate-matrix interface (NPTEL 2013). However, a precipitate on a boundary is a special situation since it entails the formation of interfaces with two differently oriented grains. There are three possibilities for the precipitate-matrix interface (Porter, Easterling and Sherif 2009):

1. The precipitate can have incoherent interfaces with both grains;
2. The precipitate can have a coherent/semi-coherent interface with one grain and an incoherent interface with the other;
3. The precipitate can have a coherent/semi-coherent interface with both grains.

The third possibility is highly unlikely due to the restrictive crystallographic conditions imposed by the differently oriented grains.

For further discussion on the knitting interaction mechanism and Zenner pinning the literature can be consulted (Smith 1948, Eggeler, Nilsvang and Ilschner 1991, Kuchařová, Němec and Dlouhý 1996, Raabe 2014). It should be noted these carbides need only be close to and not necessarily on the MGB to stabilise the micro-grain. Aghajani, Somsen and Eggeler (2009) have shown that carbide stabilised substructure hardening is both the primary short term and long-term creep strengthening mechanism for 9-12% Cr martensitic steels, specifically X20 steel.

### ***Coarsening of $M_{23}C_6$ precipitates***

The large coarsening rate of the  $M_{23}C_6$  precipitates in martensitic creep-resistant 9-12% Cr steels during long-term creep exposure is their main disadvantage. Their tendency to coarsen is due to high solubility of their major constituents, namely Cr and Fe, in the ferrite matrix at elevated temperature (Taneike, Sawada and Abe 2004). Ostwald ripening has been found to describe the way  $M_{23}C_6$  and MX precipitates coarsen (Yamasaki 2004, Aghajani, Somsen and Eggeler 2009, Prat, Garcia, Rojas, Carrasco and Kaysser-Pyzalla 2010, Liu, Fors, Golpayegani, Andrén and Wahnström 2012). The reduction of the interface free-energy of the material is the driving force for this process – smaller particles in solution have a higher surface-to-volume ratio than larger particles and therefore an increase in the mean particle size reduces the total free-energy of the system. This phenomenon is described by the famous Lifshitz and Slyozov and Wagner (LSW) theory (Lifshitz and Slyozov 1961, Wagner 1961):

$$d^3 - d_0^3 = kt \quad (2.6)$$

$$\rho_n = \frac{k'}{t} \quad (2.7)$$

where  $d_0$  and  $d$  are the particle sizes at the start and after time  $t$ ,  $k$  and  $k'$  are constants,  $\rho_n$  is the particle area number density. Therefore, the larger precipitates grow at the expense of small particles that dissolve into the matrix, while the volume fraction remains constant. Voorhees (1985) provides an extensive overview of the theory of Ostwald ripening. This coarsening is the most critical degradation process of PH since both the dissolution of the fine micro-grain stabilising carbides and coarsening of the larger carbides lead to a decrease in pinning of the MGB. There is an inverse relationship between the Zener force a particle applies and its radius (Raabe 2014). Hence, the effectiveness of the  $M_{23}C_6$  precipitates in pinning the MGB decreases upon coarsening. Therefore, quantitatively it is expected that the radius increases, and number density decreases with creep aging for  $M_{23}C_6$  precipitates.

Therefore, to ensure micro-grain and hence microstructure stability it is essential to inhibit the growth of these precipitates. It has been shown that this can be achieved by minor additions of Co, B and W (Abe 1999, Hättestrand and Andrén 1999, Gustafson and Ågren 2001).

It has been observed by Aghajani, Somsen and Eggeler (2009) that the mean particle diameter of  $M_{23}C_6$  precipitates in an X20 steel increase from 160 nm in as-received condition to 230 nm after 140 000 hours of creep exposure at 550 °C (120 MPa). An even larger size increase of approximately 120 nm after 100 000 h of creep exposure at 600°C has been observed by Panait, Zielinska-Lipiec and Koziel (2010) in a P91.

The chemical composition of the  $M_{23}C_6$  precipitates also changes during long-term creep according to their temperature dependent local thermal equilibrium. In X20 steel, these precipitates have a volume fraction of close to 10% and take about 50 000 h creep exposure to reach their new equilibrium chemical composition (Aghajani, Somsen and Eggeler 2009). It was found that the Cr and Mo content of the  $M_{23}C_6$  precipitates increases at the expense of their Fe content with an increase in creep exposure time.

Section 2.3.3 described how micro-grains grow by MGB migration and recombination during creep aging, which results in some  $M_{23}C_6$  precipitates losing their contact with the MGB. It has been found that  $M_{23}C_6$  precipitates that remain in contact with the MGB coarsen faster than those which lose contact during long-term creep aging (Kostka, Tak, Hellmig *et al.* 2007, Aghajani, Somsen and Eggeler 2009). This is evidence that short-circuit diffusion occurs along the MGB.

### **(iii) MX carbonitrides**

In martensitic creep-resistant steels, the MX carbonitrides have much smaller volume fraction than  $M_{23}C_6$  precipitate phase and are formed with minor alloying additions of strong carbide/nitride formers, such as Ti, Nb, V, Zr, Ta. After austenitising, nitrogen remains in solid solution and therefore it is available during tempering to nucleate fine MX (X = N,C) carbonitrides with an fcc structure. The main carbonitrides are VN and NbC, but other compositions include NbN, TiN, TiC, VC. In the case of X20 steel, the main carbonitrides is of type VX (V-enriched MX) since Nb and Ti concentrations are too low (Aghajani 2009, Pandey, Mahapatra, Kumar and Saini 2018). The other types are found in P91 steel and have been extensively studied by Maruyama, Sawada and Koike (2001).

The MX carbo-nitrides range from 25 to 50nm in size in the “as-received” condition of the various martensitic creep-resistant 9-12% Cr steels (Pandey, Mahapatra, Kumar and Saini 2018). They are uniformly distributed within the micro-grains and along SGB (**Figure 2.10**), often referred to as the intra-lath region. Due to their small size, high uniform density, and location, MX precipitates are effective in inhibiting the movement of free dislocations within micro-grains. However, due their small size they are easily overcome by the movement of the SGBs and are therefore do not exert effective Zener forces on the boundaries (Taneike, Sawada and Abe 2004, Aghajani, Somsen and Eggeler 2009, Xu, Nie, Wang *et al.* 2017, Pandey, Mahapatra, Kumar and Saini 2018). MX precipitates may continue to nucleate during creep (Maruyama, Sawada and Koike 2001).

### ***Dissolution of MX precipitates***

Unlike the  $M_{23}C_6$  precipitates, the V- and Nb-enriched MX precipitates are extremely stable against coarsening during long-term creep exposure at 600 °C and lower (Panait, Zielinska-Lipiec and Koziel 2010, Kipelova, Belyakov and Kaibyshev 2012, Srinivas-Prasad, Rajkumar and Hari Kumar 2012, Vanaja, Laha, Mythili, Chandravathi, Saroja *et al.* 2012, Yan, Wang, Shan and Yang 2013, Pandey, Mahapatra, Kumar and Saini 2018). For X20 steel, Aghajani *et al.* (Aghajani, Somsen and Eggeler 2009) observed that the VX precipitate size remains constant at approximately 70 nm even after 140 000 hours of creep exposure at 550 °C. They also concluded that these precipitates are stable regarding projected area fraction, number density and chemical composition.

However, fine VN carbonitrides may be dissolved by the precipitation of the complex nitride known as the modified Z-phase (**Table 2.4**). This phenomenon is discussed later in this section. Sawada, Kubo and Abe (2001) have concluded that the MX growth is accelerated by stress or strain.

#### **(iv) Laves phase**

Laves phase is an intermetallic compound that precipitates in martensitic creep-resistant 9-12% Cr steels only after long-term thermal aging and creep (Aghajani, Richter, Somsen *et al.* 2009, Prat, Garcia, Rojas, Carrasco and Inden 2010, Xu, Wang, Wang, Gu, Chen *et al.* 2015). They are typically enriched with W and Mo and have the chemical composition designations such as  $Fe_2W$ ,  $Fe_2Mo$ ,  $(Fe, Cr)_2(W, Mo)$ ,  $Fe_2Nb$ ,  $Fe_2Ti$  etc. (Eggeler 1989, Yamamoto, Kimura and Mishima 2003, Maile 2007, Aghajani, Somsen and Eggeler 2009, Panait, Bendick, Fuchsmann *et al.* 2010, Kipelova, Belyakov and Kaibyshev 2012). Prat, Garcia, Rojas *et al.* (2010) have reported of Laves phase nucleation after heat treatment.

The Laves phase particles in X20 steel have been determined by Aghajani, Richter, Somsen *et al.* (2009) to be Mo-enriched with a chemical composition close to  $(Fe, Cr)_2Mo$ . The first particles were detected after 12 456 h and all precipitates had a specific average composition of approximately 32 at.% Mo, 45 at.% Fe, 12 at.% Cr, 7 at.% Si and 1 at.%

P. They also found that these precipitates can only nucleate and grow once this chemical equilibrium is reached. This chemical composition is not affected by stress and remains constant during long-term creep. However, the Laves phase precipitates number densities (0.04 to 0.12 particles/ $\mu\text{m}^2$ ), projected area fractions (0.2 to 1.3%) and mean diameters (340 nm to 440 nm) gradually increase during long-term creep. They showed that the presence or absence of mechanical stress does not affect the formation of the Laves phase precipitates. However, the creep strain resulting from load could enhance the growth rate. A final observation from this study was that even after 139 971 h of long-term creep exposure at 550 °C and 120 MPa, the Laves phase precipitates do not reach thermodynamic equilibrium. In a later study, Aghajani, Richter, Somsen *et al.* (2009) show that this is due to the slow diffusion of Si in the ferrite matrix.

This importance of Si was first shown by Hosoi, Wade, Kunimitsu and Urita (1986) that found lower Si concentrations resulted in longer elevated temperature exposure times before Laves phase formation. In martensitic creep-resistant 9-12% Cr steels with negligible Si content, Laves phase particles could not be detected.

The nucleation mechanism of Laves phase particles is difficult to investigate since it is difficult to find small Laves phase precipitates (Aghajani, Somsen and Eggeler 2009). Isik, Kostka and Eggeler (2014) studied the nucleation mechanism of Mo-enriched Laves phase precipitates in creep aged (550 °C; 120 MPa) X20 steel and found that:

1. Segregation of Mo and Si to MGB must occur before the nucleation of Laves phase precipitates at MGB.
2. They tend to preferentially nucleate at the boundary where a Si-enriched MGB is in contact with an  $\text{M}_{23}\text{C}_6$  precipitate.

Upon further experimental investigation by Isik, Kostka, Yardley *et al.* (2015), they found that  $\text{M}_{23}\text{C}_6$  precipitates nucleate and grow, they continually reject Si atoms into the surrounding ferrite matrix until they are Si-free at equilibrium, resulting in a Si-rich environment close to the ferrite/carbide interface. In addition, Laves phase precipitates contain P, which has no solubility in the  $\text{M}_{23}\text{C}_6$  precipitates and segregates at internal



surfaces. Consequently, there is a strong segregation Si- and P-rich regions surround the MGB  $M_{23}C_6$  precipitate, which thermodynamically promotes the formation of the Laves phase particle where the MGB is in contact with the carbide. All these stages of Laves formation are schematically illustrated in **Figure 2.13**. Both the studies by Aghajani, Somsen and Eggeler (2009) and Isik, Kostka and Eggeler (2014) found that the Laves phase in X20 steel has a characteristic 7 at.% Si. Other previously proposed mechanisms include the direct transformation of a carbide to a Laves phase precipitate (Tsuchida, Okamoto and Tokunaga 1995); Mo transfer from carbides to the Laves phase precipitates (Tsuchida, Okamoto and Tokunaga 1995); promotion of Laves phase formation by Cr-depleted regions around the  $M_{23}C_6$  precipitates (Senior 1989).

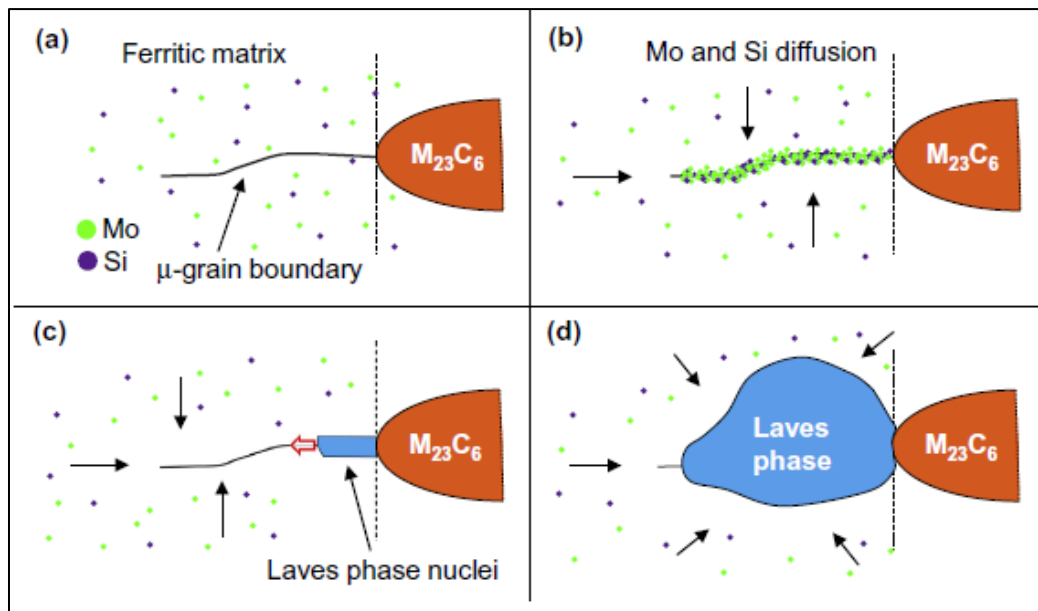


**Figure 2.13:** Schematic illustrations of Laves phase nucleation. (a) Initial microstructure. (b) Mo and Si segregation to the micro-grain boundary. (c) Nucleation and rod-like growth along the boundary with the direction indicated by red arrow. (d) Growth into a bulky shape at later stages (Isik, Kostka and Eggeler 2014).

Investigations on a 10% Cr steel exposed to long-term thermal aging at 650 °C revealed that the minority of Laves phase precipitates nucleated close to  $M_{23}C_6$  precipitates, whereas the majority Laves phase precipitates nucleated independently along the PAGB and prior martensite lath boundaries (Xu, Wang, Wang *et al.* 2015, Xu, Nie, Wang *et al.*

2017). This is due to the point (1) mentioned above. Most of the Laves phase precipitates nucleated on boundaries with a misorientation of  $40^\circ$  to  $60^\circ$  and these precipitates were larger than those on the low-angle boundaries. It was also observed that the Laves phase precipitates that formed near the  $M_{23}C_6$  precipitates grew by swallowing the carbide, resulting in a cluster. This swallowing growth mechanism is illustrated in **Figure 2.14**.

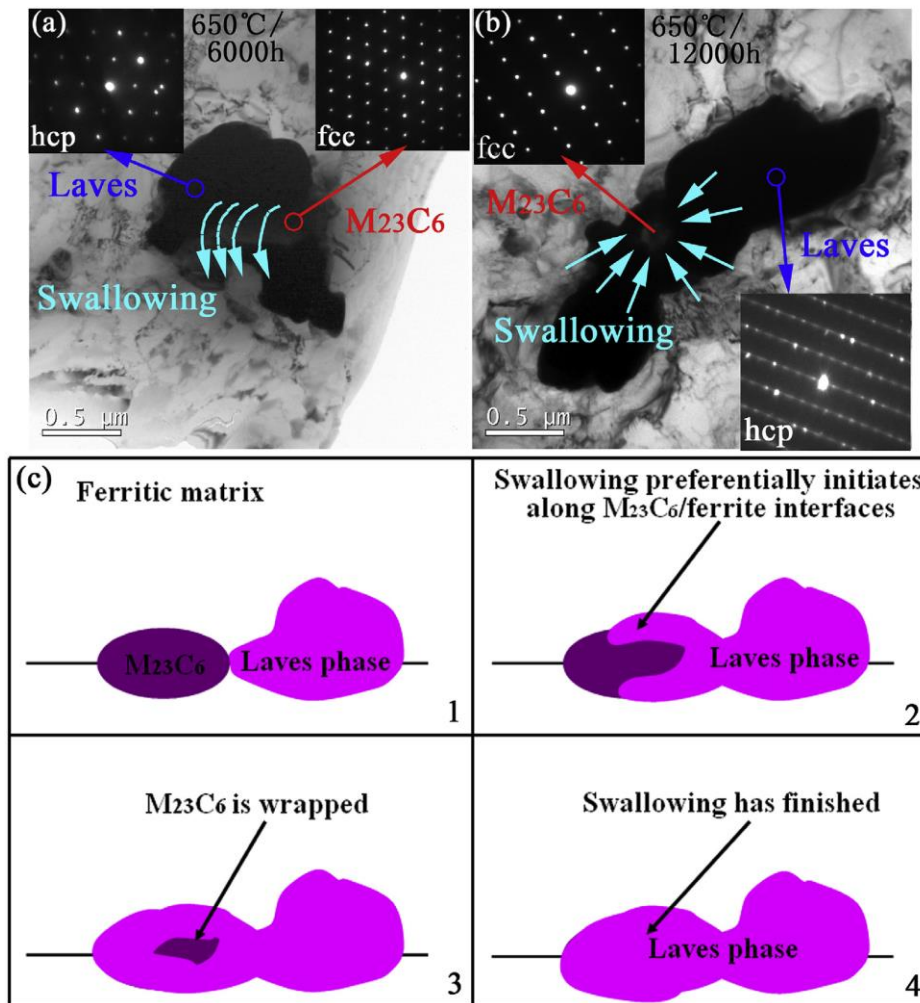


**Figure 2.14:** (a) and (b) TEM results of the growth mechanism of Laves phase precipitates by swallowing of adjacent  $M_{23}C_6$  carbides in creep aged 10% Cr steel. (c) Schematic diagrams of swallowing growth mechanism (Xu, Nie, Wang, Li and Jin 2017).

Zhang, Wu, Liu *et al.* (2017) investigated Laves phase precipitates in modified 9Cr-1Mo (grade F91) steel exposed to 600 °C thermal aging and crept at 550 °C and 600 °C,

respectively, under different stress levels. They found that Mo-enriched Laves phase precipitates formed after thermal exposure at 1000 h and creep exposure at 600 °C. No Laves phase formation was observed at creep aging at 550 °C. The nucleation of the Laves phase precipitates showed to be both stress and temperature dependent.

Upon initial precipitation, Laves phase precipitates have a short bar-like shape that lies in the direction of the boundary (**Figure 2.13(c)**) that grows into a large square shape or irregular shape, in the case of swallowing (**Figure 2.14**). Laves-phase precipitates have a high growth rate that is increased with an increase in Mo, W and Co content. They are also inhomogeneously distributed along the various boundaries (Yan, Wang, Shan and Yang 2013).

The contribution to creep strength by the precipitation of the Laves phase on the MGB and hence greater pinning of MGB is short-lived due to the high coarsening rate of the Laves phase during creep exposure. Large Laves phase particles act as preferred nucleation sites for creep cavities (Panait, Bendick, Fuchsmann *et al.* 2010). Hence, cavity formation is triggered when the size of the Laves phase reaches a critical value due to its high coarsening rate. Brittle intergranular fracture then results (Yan, Wang, Shan and Yang 2013). Lee, Armaki, Maruyama, Muraki and Asahi (2006) found that this critical size is approximately 130 nm in P92 steel. Thus, Laves phase precipitates have an inevitable and detrimental effect on creep strength.

Further creep strength degradation is caused by the Laves phase that nucleates at the expense of the solute W and Mo in the ferrite matrix, resulting in a reduction of solid solution strengthening (Section 2.3.5). However, the loss of Mo and W from solid solution by Laves phase nucleation decreases the coarsening rate of  $M_{23}C_6$  precipitate making them more stable (Hald 2008).

Nucleation of the Laves phase is strenuous when the creep temperature is close to the solution temperature. Subsequently, only a few particles can form, and the growth phase is extended, leading to the formation of large precipitates. This accounts for the P91 steel having much larger Laves phase precipitates than the P92 steel. The Mo-enriched Laves phase has a lower solubility than the W Laves phase. Therefore, W allows that formation

of fine stable W-enriched Laves phase precipitates in P92 steel when the creep temperature is adequately below the solution temperature. It is this consideration that accounts for the enhanced creep strength of P92 steel compared to the other 9-12% Cr steels grades. Therefore, significant PH can be obtained by the Laves phase provided that a large number of precipitates nucleate (Hald 2008).

#### **(v) Z-phase**

In addition to the Laves phase, Z-phase, a type of Cr-enriched nitride compound is another intermetallic compound that forms in martensitic creep-resistant 9-12% Cr steels during long-term service exposure. This complex nitride has been fascinating researchers since its first discovery in 1987 in a martensitic 11% Cr steel (Schnabel, Schwaab and Weber 1987). Therefore, extensive studies and reviews have been performed on the Z-phase in martensitic creep-resistant 9-12% Cr steels and their main findings are further discussed below (Danielsen and Hald 2006, Danielsen 2007, Danielsen and Hald 2009, Cipolla, Danielsen, Venditti, Di Nunzio, Hald *et al.* 2010, Liu and Andrén 2010, Panait, Bendick, Fuchsmann *et al.* 2010, Yan, Wang, Shan and Yang 2013, Danielsen 2016, Pandey, Mahapatra, Kumar and Saini 2018).

For the various martensitic creep-resistant 9-12% Cr steels, the composition of Z-phase has been observed as CrNbN and Cr(V,Nb)N. The latter is referred to as the modified Z-phase where half the Nb atoms are replaced by V. In the case of X20, that is Nb-free, the Z-phase precipitates as CrVN. The Z-phase (CrNbN) is the most thermodynamically stable nitride in 9-12% Cr steels with solution temperatures as high as 1250 °C. In 11-12% Cr steels, the modified Z-phase and Nb-free Z-phase have a solubility temperature close to 800 °C (Danielsen 2007). They are believed to be metastable.

Nucleation of Z-phase precipitates is a slow and continuous process with the fastest observation of nucleation after 1000 h exposure at 650 °C. The nucleation mechanism is a transformation of thermodynamically unstable MX precipitates into cubic Z-phase and then tetragonal Z-phase, which is controlled by the diffusion of Cr atoms. Consequently, Z-phase nucleation is driven by Cr content and contents higher than 10.5% cause accelerated precipitation of Z-phase. In the case of X20 steel, a low number of Z-phase

precipitates have been observed after 150 000 h exposure at 650 °C even though it has a 12% Cr concentration. Therefore, it follows that the nucleation process is much slower without the presence of Nb. Two proposed nucleation mechanisms are given in **Figure 2.15**. A similar mechanism has been proposed by Cipolla, Danielsen, Venditti *et al.* (2010). The prior martensite lath boundaries and PAGB are the preferred nucleation sites for the Z-phase precipitates.

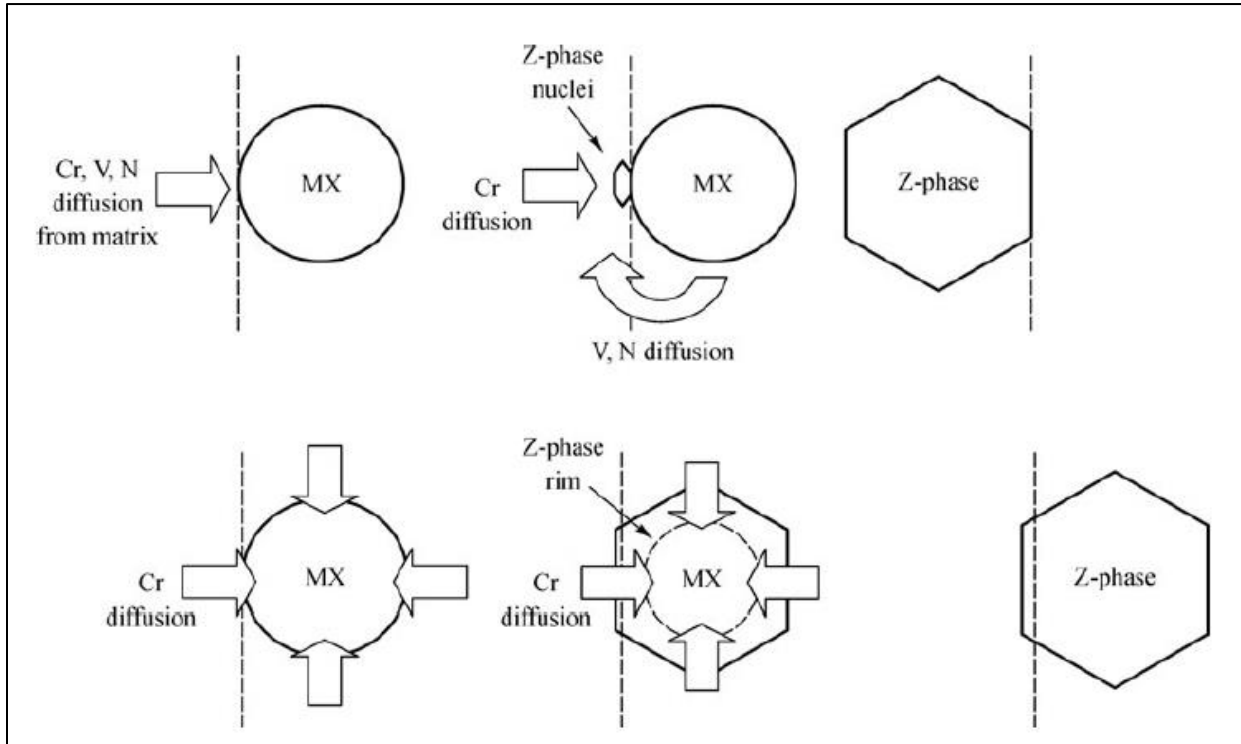


**Figure 2.15:** Two proposed nucleation mechanisms of Z-phase precipitates (Yan, Wang, Shan and Yang 2013).

The Z-phase precipitates have high coarsening rates and therefore grow rapidly. The modified Z-phase and Nb-free Z-phase grows at the expense of the MN (M= V,Nb) precipitate that have not transformed. As discussed previously, these MN precipitates are crucial for PH and by their dissolution, there is a detrimental loss in creep strength. There is no cause for concern regarding creep stability if a few large Z-phase precipitates are observed in the microstructure. It is alarming when a high rate of dissolution of the MN precipitates is also observed. This has been the case in premature failure of T122 (12CrWMoCuVNbN) steel tubes where extensive precipitation of Z-phase precipitates

has occurred and almost all MX precipitates were dissolved (Hald 2008). Danielson and Hald (2009) proposed a novel alloy design concept called Z-phase strengthening. These alloys entail a new family of 12% Cr steels where Ta and Nb replace V to enhance creep strength by the formation of a dense distribution of Z-phase instead of VN precipitates. Rashidi (2017) performed an extensive study of the microstructure of these steels.

Panait, Bendick, Fuchsmann *et al.* (2010) found a small number of Z-phase precipitates in P91 steel creep tested for 113 431 h (600 °C; 80 MPa), while Aghajani (2009) could not observe Z-phase in X20 steel even after long-term creep exposure of 139 971 h (550 °C; 120 MPa). Another excellent study on Z-phase particles observed in 9-12% Cr steels has been done by Di Gianfrancesco, Vipraio and Venditti (2013).

### 2.3.3 Creep Strengthening and Behaviour of Grains and Subgrains

There are many different types of boundaries in the tempered martensite microstructure (Section 2.2.3). **Table 2.5** summarises the misorientations across the different boundaries. It is widely agreed that there exists no single microstructural unit for a lath-type structure that determines both the yield strength and toughness properties like a grain in a pure ferrite structure (Kalwa, Schnabel and Schwaab 1986). In the case of martensitic creep-resistant 9-12% Cr steels, the prior packet and block structures control deformation (Krauss 1999). Due to larger misorientations across packet boundaries than between blocks within a packet, the packet size is the main toughness determining factor (Wang, Wang, Shi, Hui and Dong 2008).

High-angle grain boundaries (HAGB) have misorientations across them that are greater than 10 to 15° (Faulkner 2008). They contribute to creep strength since they are overall impenetrable by mobile dislocations and therefore act as major obstacles against dislocation motion during creep (Abe 2008). From **Table 2.5** it follows that the HAGB in the tempered martensite microstructure are the PAGB, prior martensite packet and block grain boundaries. These boundaries are the MGB and therefore the critical structural parameter when considering strength-structure relationships is the shortest (short) width size of the micro-grains (Morito, Huang, Furuhashi, Maki and Hansen 2006, Morito,

Yoshida, Maki and Huang 2006). The creep strengthening effect of the MGB is known as Sub-Boundary Hardening (SBH).

**Table 2.5:** Misorientations of different boundary types found in the microstructure of 9-12% Cr martensitic steels.

Boundary	Misorientation
PAGB	10 – 48° (Gyhlesten Back and Engberg 2017)
Prior Packet boundary	> 15°
Prior Block boundary	49.5° to 60°; 70.5° around (110) <sub>α</sub> (Kalwa, Schnabel and Schwaab 1986, Morito, Tanaka, Konishi <i>et al.</i> 2003)
Prior Sub-block boundary	±10° (Morito, Tanaka, Konishi <i>et al.</i> 2003)
Prior lath boundary	2-5° (Gyhlesten Back and Engberg 2017)
SGB	± 1° (Pešička, Dronhofer and Eggeler 2004)

The behaviour in which a boundary and dislocation will interact depends on the misorientation across the boundary. Dislocations may be able to pass through the boundary of low-angle grain boundaries (LAGB). The stress required is inversely proportional to the dislocation spacing in the boundary (Kuhlmann-Wilsdorf 1989). In essence, it is the equivalent of the dislocations passing through a network of dislocations. The dislocations can effectively travel through by bowing between the pinning points, which are jogs. This is not possible with HAGB (misorientation > 15°) since the dislocation spacing is too small. Even though high-angle boundaries commonly act as dislocation

sources, the stresses required for this is too high and therefore these boundaries overall are a polycrystal strengthening mechanism. The high-angle grain boundaries (HAGB) usually act as barriers to slip, resulting in a pileup of dislocations. Slip can be initiated in a neighbouring grain and glide continue by the stress concentration caused when a slip plane and high-angle boundary meet. This barrier effect usually is related as a proportionality between the yield stress and the inverse square root of grain size (Section 2.7.2). In general, as a boundary traps more dislocations, its misorientation increases (Hansen and Barlow 2014).

The SGB and prior martensite lath boundaries have lower misorientations. Sonderegger, Mitsche and Cerjak (2008) have shown that the SGB have random small misorientations, whereas martensite lath boundaries show preferential axes-angle combinations.

Previous experimental evidence has shown that prior austenite grain (PAG) size has a significant effect on the packets and blocks sizes, whereas the effect on lath substructure development is negligible (Morito, Yoshida, Maki and Huang 2006, Hoseiny, Caballero, San Martin and Capdevila 2012, Zhang, Wang, Ren, Li, Wang *et al.* 2012, Zhang, Wang, Ren, Li, Wang *et al.* 2012).

Maruyama, Sawada *et al.* (2001) concluded that SBH is the predominant strengthening mechanism in martensitic creep-resistant 9-12% Cr steels since the SBH mechanism can provide higher creep strength by more effectively obstructing dislocations than the Orowan mechanism of precipitates. However, subgrain stability is of great importance to ensure the full exploitation of SBH during creep. This can only be achieved by carbide stabilised substructure hardening (Section 2.3.2). Subsequently, it is suggested that SBH is dependent on this hardening and hence precipitates are of the highest importance to SBH.

The typical creep deformation behaviour of the elongated micro-grains related to the martensitic transformation is to become equiaxed subgrains (Maruyama, Sawada and Koike 2001). This is discussed later in this section. Thus, it can be concluded that SBH



is martensitic lath structure hardening that upon exhausted during creep is surpassed by subgrain hardening (Yan, Wang, Shan and Yang 2013).

### **(i) Evolution of misorientation**

Overall for martensitic creep-resistant 9-12% Cr steels, there is a significant increase in the frequency of low angle boundaries (misorientation less than 15°) during creep exposure, whereas there is no change in the frequency of the high-angle boundaries with 60° misorientation (Sanchez-Hanton and Thomson 2007, Aghajani, Somsen and Eggeler 2009, Aghajani 2009, Tak, Schulz and Eggeler 2009). For X20 steel specifically, it has been determined by Peřička, Dronhofer and Eggeler (2004) that during short-term laboratory creep testing the frequency of SGB (1° misorientation) sharply increases, and the frequency of prior lath boundaries (2-5° misorientation) decreases. However, these values have been determined using EBSD data and the technique has an angular resolution of 0.5 to 1.5° (Humphreys 2001).

### **(ii) Micro-grain growth**

Micro-grain coarsening has been observed during long-term creep testing. The coarsening results in the elongated micro-grains expanding and finally evolving into an equiaxed substructure. Aghajani, Somsen and Eggeler (2009) have observed for X20 steel a steady increase in the short-width of the micro-grains (subgrain size) from 0.70  $\mu\text{m}$  in the as-received condition to 1.07  $\mu\text{m}$  after 140 000 h of creep exposure (550 ° C; 120 MPa). No significant changes in the subgrain size were observed during thermal aging which is expected due to the high thermal stability of the as-received microstructure. Studies on other 9-12% Cr steel grades made similar observations (Maruyama, Sawada and Koike 2001, Endo, Masuyama and Park 2003, Abe 2004, Szabó 2004, Tak, Schulz and Eggeler 2009, Hu, Yan and Sha 2011). Therefore, it is concluded that micro-grain coarsening is stress and strain dependent.

Micro-grain coarsening can be attributed to the following occurrences during creep (Payton, Aghajani, Otto *et al.* 2012):

1. A decrease in prior martensite lath boundaries (Section (i) above).
2. A decrease in prior martensite packet, block and sub-block boundaries.

During creep, there is an accumulation of strain that results in local parts of the boundaries of the micro-grains to bulge out and migrate. This is called strain-induced grain-boundary migration (Raabe 2014). The entire boundary then migrates by the reoccurrence of this local part bulging and migrating (Sawada, Taneike and Kimura 2003). Consequently, micro-grains coarsen by MGB migration and recombination during creep aging. Carbide stabilised substructure hardening (Section 2.3.2) is not completely effective in prohibiting this degradation mechanism since carbides along the PAGB, prior martensite block, sub-block and lath boundaries are larger. Even though, the MGB moves into the interior of the adjacent micro-grain where there are the fine MX precipitates and SGB with fine  $M_{23}C_6$  precipitates (Section 2.3.2), the boundary easily overcomes these small precipitates. In addition, the MGB effortlessly overcomes the SGB too since they are planar dislocation networks. Subsequently, MGB migration does not stop until it reaches another MGB. Strain also accelerates the coarsening of the precipitates, resulting in loss of their pinning effect (Section 2.3.2). In addition, Laves and Z-phase precipitates also contribute to the loss of pinning effect as discussed in Section 2.3.2. Thus, strain only has a noticeable effect on micro-grain growth during short-term creep, whereas during long-term creep exposure precipitate stability has the most pronounced effect. It has also been observed that relatively small micro-grains will shrink and disappear (Yan, Wang, Shan and Yang 2013). It has been proposed by Abe, Araki and Noda (1991), Abe and Nakazawa (1992), and Abe (2003) that the onset of accelerated creep is marked by a substantial migration of MGB and hence micro-grain coarsening.

### **(iii) Substructure evolution**

As discussed in Section 2.2, a dislocation substructure of SGB and dislocations within micro-grains forms during tempering due to the recovery of the dislocation cell structures. This substructure is not fully developed and creep deformation promotes dynamic recovery, which is a softening mechanism (Cerjak, Hofer and Schaffernak 1999, Maruyama, Sawada and Koike 2001, Panait, Bendick, Fuchsmann *et al.* 2010, Panait,

Zielinska-Lipiec and Koziel 2010, Pešička, Aghajani, Somsen *et al.* 2010, Armaki, Chen and Maruyama 2011, Yan, Wang, Shan and Yang 2013). Recovery is the materials attempt to restore the properties and microstructure to their values before deformation. During dynamic recovery the following phenomena occur (Doherty, Hughes, Humphreys, Jonas, Jensen *et al.* 1997):

1. Micro-grains reduce their stored energy by removing dislocations, including SGB, from their crystal structure through an annihilation process (Section 2.3.4). After annihilation, there is an excess of one type of dislocation.
2. Further reduction in stored energy is achieved by the rearrangement of remaining dislocations to form low-angle boundaries, i.e., SGB (polygonization).

Upon further creep exposure, the subgrain structure formed by the SGB coarsens, i.e., the mean size increases, but the number of subgrains decreases. This occurs to reduce the stored energy further by decreasing the total area of the grain boundary. It should be noted that LAGB are very immobile and the rate of subgrain growth is controlled by the migration of LAGB (Doherty 1997, Humphreys and Hatherly 2004). The second point supports the observations of a substantial increase in low-angle boundaries during early creep exposure as discussed in Section (i) above. Subsequently, it seems that the formation of new SGB occurs during the early stages of creep. The coarsening of the substructure is expected to start later than micro-grain coarsening since the SGB are decorated with finer precipitates in the as-received condition. The polygonization of the subgrains leads to an equiaxed substructure to evolve during creep. It seems then as if recrystallisation is taking place. The final result is that equiaxed subgrains replace the prior micro-grains, i.e., there is no distinction possible between micro-grains and subgrains. For more extensive discussions on these topics of recovery, the works of Humphreys and Hatherley (2004) can be consulted.

Grain boundary diffusion can assist in microstructural changes around PAGB. Sawada, Sekido, Kushima and Kimura (2017) confirmed preferential recovery of the substructure around PAGBs in T91, P91, T92 and 12Cr steels.

#### **(iv) Prior austenite grain boundary disappearance**

The PAGB gradually disappear after long-term creep exposure until the trace of their previous existence is left behind by the precipitates that normally nucleate along them. These boundaries are unique HAGB that consist of walls of dislocations that can catch and release dislocations. These boundaries are well stabilised by the  $M_{23}C_6$  precipitates on them and the stabilisation is lost during creep exposure due to their coarsening and preference of Laves phase precipitates to nucleate on them (Section 2.3.2). Consequently, the PAGB are gradually freed during creep aging from the  $M_{23}C_6$  precipitate pinning effect and finally disappear through dislocation movement (Yan, Wang, Shan and Yang 2013). Similar reasoning could be used for the decrease in prior martensite packet, block and sub-block boundaries mentioned in (ii).

#### **2.3.4 Creep Strengthening and Behaviour of Dislocations**

Dislocations are introduced into the microstructure through the martensitic transformation during cooling after austenitising to accommodate the lattice misfit (Section 2.2.2). During tempering, the dislocation density decreases and the extent of decrease in dislocation density is determined by the tempering temperature. A strain field is associated with each dislocation that contributes minutely to the materials stored energy. At elevated temperature, dislocations become mobile and can climb, glide or cross-slip (Doherty, Hughes, Humphreys *et al.* 1997).

A dislocation substructure within the micro-grains is obtained after heat treatment and it is composed of boundary dislocations that form low-angle boundaries (SGB) and free dislocations (Maruyama, Sawada and Koike 2001, Holzer 2010). Therefore, the total dislocation density can be subdivided into two types of dislocations: dislocations that are free (mobile dislocations) and those that are in the SGB (boundary dislocations) (Pešička, Kužel, Dronhofer and Eggeler 2003, Pešička, Dronhofer and Eggeler 2004). The dislocations are linear defects.

Even after tempering, the martensitic creep-resistant 9-12% Cr steels have very high densities of mobile dislocations within the micro-grains ( $0.1 - 10 \times 10^{14} m^{-2}$ ) (Pešička,

Kužel, Dronhofer and Eggeler 2003, Abe 2008)). Due to the high density of mobile dislocations and their mobility at elevated temperatures, it is inevitable that dislocations will pass one another in parallel slip planes, re-orientate into a parallel section and form a stable configuration. Consequently, a third type of dislocation known as a dipole dislocation results that is a static pair of parallel dislocations with opposite Burgers vectors, or otherwise stated two antiparallel segments with the same Burgers vector (Kroupa 1966, Ghoniem, Matthews and Amodeo 1989). The total dislocation density of these steels is made up of three different types of dislocations.

Since the boundary dislocations have short range stress fields associated with them, they are easily overcome by other boundaries and dislocations. The dipole dislocations have exceedingly small stress fields compared to mobile dislocations (Yadav, Kalácska, Dománková *et al.* 2016). Hence, boundary and dipole dislocations are not effective obstacles to dislocation motion. The mobile dislocations have long-range stress fields, which makes them significant obstacles to other dislocations. Therefore, they are the main dislocation contribution to creep strength by Dislocation Hardening (DH). However, they are also carriers of plastic deformation under creep conditions due to their high densities promoting recovery of the dislocation substructure at elevated temperature (Pešička, Dronhofer and Eggeler 2004).

### **(i) Evolution of dislocation densities**

Dislocations can interact in many ways during creep exposure (Ghoniem, Matthews and Amodeo 1989):

1. Mobile dislocations within the substructure interact and multiply by the Frank-Read Source (Frank and Read Jr 1950) mechanism.
2. Static dislocations can form dipoles with boundary dislocations.
3. When two dislocations of opposite sign meet while gliding they effectively cancel each other out and annihilate.
4. Annihilation, absorption or emission of the dislocations in the SGB.

5. Nucleation of new SGBs from the boundary dislocations.
6. Subgrain growth by the rearranging and interaction of the dislocations.

Pešička, Aghajani, Somsen *et al.* (2010) determined that X20 steel has a very high initial mobile dislocation density of  $1.02 \times 10^{14} \text{ m}^{-2}$  that rapidly decreases by a factor of 10 to  $1.16 \times 10^{13} \text{ m}^{-2}$  after  $\pm 12\,000$  h (550 °C; 120 MPa) creep exposure. After long-term creep exposure of  $\pm 140\,000$  h the mobile dislocation density then steadily decreases down to  $0.68 \times 10^{13} \text{ m}^{-2}$ . They also found that the dislocations are heterogeneously distributed across the micro-grains, which can be due to the orientation dependence of dynamic recovery (Section 2.3.3) in micro-grains oriented differently. Maruyama, Sawada and Koike (2001) discusses the mobile dislocation densities of three other steel grades.

The results from Pešička, Dronhofer and Eggeler (2004) show that the decrease in mobile dislocation density of 9-12% Cr martensitic steels during tempering and long-term creep aging is due to most of the dislocations annihilating due to static and dynamic recovery processes. They also concluded that the total boundary dislocation density remains constant during later stages of long-term creep aging due to a balance between increasing relative frequency of SGB (Section 2.3.3) and a decrease in the overall boundary area per volume from micro-grain coarsening. The initial rapid decrease in dislocation density results in a significant loss of DH that can rationalise primary creep. Since the dislocation density does not change significantly during long-term creep exposure, it is assumed that the loss in creep strength cannot be associated with DH loss. Consequently, at elevated temperature, DH is only useful for short-term creep strength and not for long-term creep strength (Abe 2008).

Yadav, Kalácska, Dománková *et al.* (2016) investigated all three dislocation types in martensitic creep-resistant 9-12% Cr steels. They performed their study on a novel 12% Cr steel martensitic steel that has been short-term creep tested (5 793 h; 650 °C). They found that the total dislocation density decreased by 4.5 times and the micro-grain size increased from 0.52  $\mu\text{m}$  to 1.5  $\mu\text{m}$ . During primary creep, the annihilation of all dislocations dominates their production. The annihilation of the dipole dislocations are greater than that of the mobile dislocations. As expected, the decrease of the boundary

dislocation density is attributed to the growth of the micro-grains by the recombination and migration of SGB. They also observed that the dislocations are heterogeneously distributed in the microstructure.

### **2.3.5 Strengthening and Effect of Creep on Solid Solution**

As can be seen from **Table 2.2**, there are a wide variety of solute atoms in the ferrite matrix of martensitic creep-resistant 9-12% Cr steels. The differing sizes of these solute atoms result in local strain fields surrounding them. These local strain fields increase the resistance of the lattice to deformation by inhibiting the movement of the dislocations near solute atoms. Accordingly, the creep strength of the steel is enhanced by Solid Solution Hardening (SSH) (Holzer 2010).

When considering the effect of the substitutional atoms in the matrix, the main solid solution strengtheners are Mo and W atoms since their radii are much larger than that of the solvent Fe atoms. Unfortunately, the extent of SSH from Mo and W contributing to the creep strength is superimposed on the other strengthening mechanisms, mainly PH (Abe 2008). During creep exposure, the solute content of Mo and W in the matrix decreases due to the formation of Laves-phase precipitates (Section 2.3.2), resulting in the loss of SSH. Hald (2008) concluded that long-term microstructural stability of martensitic creep-resistant 9-12% Cr steels is controlled by PH and SSH from Mo and W has no significant effect.

In the case of interstitial atoms, N is the recognised strengthener that benefits the long-term creep strength through SSH, as well as PH (Section 2) (Abe 2008). However, it has been shown by Maruyama, Sawada and Koike (2001) that SSH can only be useful in the absence of PH and DH.

### **2.3.6 Creep Damage and Fracture**

Creep cavities have been observed in martensitic creep-resistant 9-12% Cr steels (Eggeler, Earthman, Nilsvang and Ilchner 1989, Hald 2008, Aghajani, Somsen and Eggeler 2009). The cavitation state of the steel determines the life-time strongly during

service (Ragab 2002). All the creep degradation mechanisms discussed in Sections 2.3.2 to 2.3.5 leads to a decrease in the density of obstacles to dislocation motion inside the matrix. Hence, the material is weakened, and creep cavitation is promoted by these degradation mechanisms. In general, cavity nucleation, growth and coalescence is the well-known failure mechanism of martensitic creep-resistant 9-12% Cr steels during service exposure (Yao, Xuan, Wang and Tu 2007). Many studies have reported that the microcavities nucleate in polycrystalline metals and alloys during the primary and secondary creep stages, and that their growth and agglomeration leads to tertiary creep, which culminates to creep rupture occurs (Hull and Rimmer 1959, Perry 1974, Kassner and Hayes 2003, Sklenička, Kuchařová, Svoboda *et al.* 2003, Yao, Xuan, Wang and Tu 2007). They describe the following mechanisms of cavity nucleation as a function of temperature and stress:

1. impurity particles that lack cohesion with the matrix result in vacancy accumulation;
2. when incompatibility caused by grain boundary sliding cannot be accommodated by elastic accommodation, diffusion flow or plastic flow;
3. dislocation pile-ups that break through the boundary.

Mechanism number 2 has been shown to be a critical cause for cavity nucleation at grain boundaries (Edward and Ashby 1979). The nucleation and growth mechanisms vary under different loading conditions and temperatures. Also, there is no single mechanism at work, but several mechanisms may work and each one may become dominant at different stages of the creep life (Perry 1974).



It is proposed that cavities tend to grow and transform into macro cavities by either diffusion, plasticity or by coupled diffusion and plasticity (constrained cavity growth) (Perry 1974, Kassner and Hayes 2003, Yadav, Rosc, Sartory, Brunner, Sonderegger *et al.* 2014, Yadav, Sonderegger, Sartory, Sommitsch and Poletti 2015). When the cavities grow to a size of half the mean cavity spacing, then coalescence occurs (Yao, Xuan, Wang and Tu 2007). Finally, this linking of these macro cavities then leads to microcrack formation and eventual crack propagation to final rupture. This is known as intergranular creep fracture under long-term creep conditions (Sklenička, Kuchařová, Svoboda *et al.* 2003). Thus, cavity coalescence is not a rupture criterion, but the formation and growth of microcracks from closely spaced cavitating grain boundary interfaces are (Eggeler, Earthman, Nilsvang and Ilschner 1989). The damage development during intergranular creep fracture is schematically illustrated in **Figure 2.16**. Edward and Ashby (1979), and Cocks and Ashby (1980) provide detailed information on intergranular fracture and power-law creep under multi-axial stresses. They also state that this mechanism of intergranular fracture needs to be understood to develop accurate multi-axial creep models.

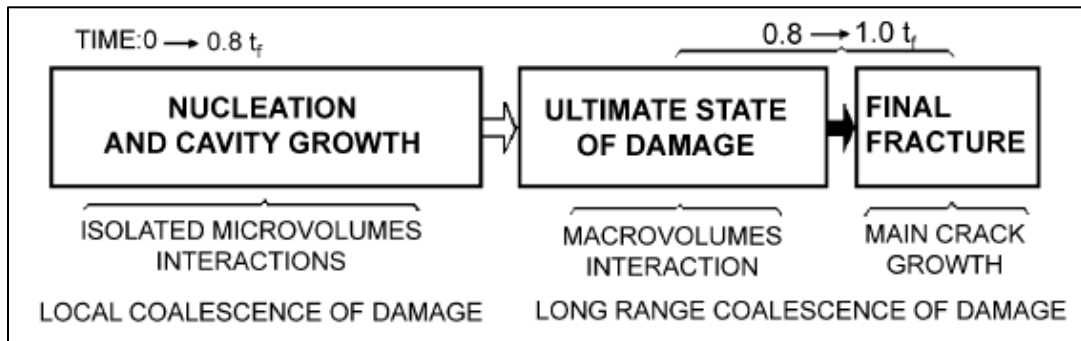


**Figure 2.16:** Schematic diagram of intergranular damage development ( $t_f$  corresponds to the time to failure) (Sklenička, Kuchařová, Svoboda, Kloc, Buršík *et al.* 2003).

Cavity growth mechanisms are better understood than cavity nucleation mechanisms. Nucleation along lath boundaries has been observed in E911 steel by Sket, Dzieciol, Borbély, Kaysser-Pyzalla, Maile *et al.* (2010) and they further deduced that the cavities growth mechanism is constrained cavity growth. This conclusion was confirmed by Eggeler, Earthman, Nilsvang and Ilschner (1989) and Wu and Sandström (1995) who applied a constrained cavity growth model on the results obtained from X20 steel.

Constrained cavity growth occurs if closely spaced cavities are present only on isolated grain boundaries. Yao, Xuan, Wang and Tu (2007) also provides a detailed review of the constrained growth mechanism and modelling of it. Eggeler, Earthman, Nilsvang and Ilschner (1989) also found that the cavities lying on transverse PAGB play the dominant role in the creep rupture process since these cavities are larger and more densely spaced than those on the MGB within PAG.

Under constrained cavity growth, the cavities grow by different combinations of processes such as grain boundary diffusion, surface diffusion and power-law creep. Though, for 9-12% Cr martensitic steels under service conditions, pure diffusional growth is less probable since constraints are applied by the less compliant material that surrounds cavitated regions (Sklenička, Kuchařová, Svoboda *et al.* 2003).

There may be rare cases where there are pre-existing cavities in the material after the manufacturing process. Yadav and co-workers (Yadav, Rosc, Sartory *et al.* 2014, Yadav, Sonderegger, Sartory *et al.* 2015) investigated cavities in P91 steel both 2D and 3D. They found pre-existing macro cavities with mean diameters of 2.56  $\mu\text{m}$  in the as-received material that grew and coalesced to mean diameters of 5.42  $\mu\text{m}$  after 9000 h of creep loading (650 °C; 60 MPa). Microcavities nucleated during creep with diameters smaller than 0.6  $\mu\text{m}$ . The volume fraction of the pre-existing macro cavities was nearly twelve times larger than that of the micro creep cavities. They conclude that if there are pre-existing macro cavities in the material, they will be responsible for final rupture. A cavity growth model based on local stress levels has also been developed by this group. Another study of the creep cavities in creep aged X20 steel was performed by Rasiawan (2017). Creep cavities were found in the creep exposed parent material and it was suggested that this is the leading cause of failure of cross-weld samples on the creep exposed parent material side.

Creep cavities of sizes of 3 to 7  $\mu\text{m}$  have been found by Panait, Bendick, Fuchsmann *et al.* (2010) in P91 steel specimen crept at 600 °C (80 MPa) and ruptured after 113 431 h. The cavities have found to be nucleated close to coarse precipitates, presumably  $\text{M}_{23}\text{C}_6$  precipitates, along grain boundaries. The same has been found by other studies on 9-

12% Cr martensitic steels (Gooch 1982, Sklenicka 1996, Lee, Armaki, Maruyama *et al.* 2006). It is widely believed that cavities nucleate due to grain boundary sliding at geometrical irregularities, such as non-coherent inclusion particles, on grain boundaries, where there are high local stress concentrations that can develop (Sklenička, Kuchařová, Svoboda *et al.* 2003).

Cavities have also been found inside the ferrite matrix at carbide precipitates (Wu and Sandström 1995). Consequently, this indicates that the interface between the carbides and the matrix are the preferred nucleation sites. Hence, decohesion between carbides and the matrix most probably controls cavity formation. Gooch (1982) provided experimental evidence of this decohesion mechanism in X20 steel and that it is caused by stress concentrations that result from grain boundary sliding or deformation, inter-lath boundary deformation, or intergranular dislocation movement. All of this is observed during creep exposure (Sections 2.3.2 to 2.3.4). As soon as decohesion occurs, preferred nucleation sites become available. Gooch (1982) therefore concludes that creep failure of X20 steel occurs at 565 °C due to mixed intergranular and transgranular cavitation. In addition, Gooch found that growth at long-term testing is controlled by vacancy diffusion, while it is controlled by local flow tensions at short-term testing. Eggeler, Earthman, Nilsvang and Ilschner (1989) also suggests vacancy diffusion during long-term creep since segregation occurs on the boundaries (see Section 2.3.2) that facilitates diffusion. Sulphides, silicate, and oxide inclusions are also preferred cavity nucleation sites.

Aghajani (2009) found that in X20 steel creep specimens that creep ruptured after 139 397 h, the number of cavities on the PAGB perpendicular to the stress direction is substantially higher than those on the PAGB parallel to the stress direction. A similar conclusion was made by Wiesner, Earthman, Eggeler and Ilschner (1989) who studied creep cavitation and cracks in X20 steel. These conclusions illustrate the dependence of cavity growth on the stress direction.

### 2.3.7 Summary of Microstructural Evolution and Effect on Creep Curve

The creep curve (Section 2.1.3) in essence portrays the response of the microstructure to creep. Therefore, the three stages of creep on the creep curve can be explained by the microstructural evolution as discussed in this section.

#### (i) Primary Creep

Consider the creep curves drawn in **Figure 2.2**. In **Figure 2.2(a)** Primary creep (until  $t_1$ ) or transient creep initially increases rapidly and then slows down with time, resulting in a decreasing creep rate. A power law, similar to Norton's law in Equation (2.2), is one of the classic equations used to represent the creep strain  $\varepsilon$  in the primary stage (Graham and Walles 1955):

$$\varepsilon = A\sigma^n t^p \quad (2.8)$$

where  $p$  is a time exponent. The primary creep deformation has been ascribed to strain hardening caused by a decrease in the mobile dislocations. During this stage, restructuring of dislocations start and hence microstructural evolution in the form of micro-grain growth and recovery commences. However, precipitate coarsening and coalescence does not occur during the primary creep stage. In terms of diffusional creep, this stage would be attributed to the initial rapid flow of vacancies into the grain body where the rate of vacancy generation exceeds vacancy absorption (Ohtani 2007, Abe 2008). In a two-stage creep curve (**Figure 2.2(b)**) the primary stage immediately progresses to the tertiary creep stage. The logarithmic creep curve (**Figure 2.2(c)**) consists only of the primary creep stage and only arises at low homologous temperatures of approximately  $0.2T_m$ .

#### (ii) Secondary Creep

In the ideal creep curve (**Figure 2.2(a)**), a uniform creep rate (between  $t_1$  and  $t_2$ ) is observed during secondary creep. Therefore, it is described as a steady-state creep. Equation (2.3) is usually used to describe the creep rate of this stage. The prevailing

notion is to attribute this steady-state as a state of balance between competing mechanisms of the annihilation of dislocations by the recovery of them to form subgrains, which contributes to softening, and generation of dislocations, which contribute to strain hardening. Precipitate coarsening and coalescence start in this stage. The end of this stage is marked by the substructure slowly coarsening, boundary dislocations increasing and internal (dipole and mobile) dislocation density decreases (Ohtani 2007).

The secondary stage is described in diffusional creep by the formation of steady-state gradient of vacancy concentration throughout the grain. This represents equilibrium in the generation and absorption of the vacancies at the grain boundaries. Since creep mainly involves diffusion at high temperatures, the recovery rate is high enough to balance work hardening (Abe 2008).

There is no real steady-state creep stage in creep resistant alloys and steels since there is a point where the softening process immediately dominates the hardening process. This point is shown as an inflection point on the two-stage creep curve as illustrated in **Figure 2.2(b)**. Subsequently, this illustrates that true dynamic equilibrium of the microstructure is impossible. Norton's law (Equation (2.2)) is mostly used to find the minimum or steady-state creep resulting from an applied stress (Abe 2008). The main problem, however, is that this law fails at high stresses and low stresses (Langdon 2000).

### **(iii) Tertiary Creep**

Referring to **Figure 2.2**, during the tertiary creep stage (between  $t_2$  and  $t_r$ ) there is an accelerated creep rate until rupture at time  $t_r$ . It is important to note that under the constant tensile load, the stress continuously increases as creep progresses. It is only during the tertiary creep stage that the most prominent effect of the stress increase on the creep rate is observed. Therefore, the accelerated creep rate during this stage can either be due to increased stress or microstructural evolution, which includes the evolution of damage due to creep. During this stage, microstructural evolution consists of various phenomena such as dynamic recrystallisation, dynamic recovery, and significant coarsening and coalescence of precipitates. These phenomena lead to softening and ultimately a decrease in creep resistance of the material since the distance between pinning points

becomes large enough for dislocation movement to occur. Subsequently, the micrograins and substructure coarsen, resulting in further material softening. Creep damage evolution also includes the formation of creep voids and crack development mainly along the grain boundaries (Section 2.3.6). A higher strain results since a higher vacancy concentration is created by the stress increase in the material due to the nucleated cavities (Abe 2008). The sudden transition to the tertiary creep stage in the two-stage creep curve (**Figure 2.2(b)**) results from the hardening processes being overcome by the microstructural evolution caused softening processes.

#### **(iv) Temperature and Stress**

Over extended periods and low stresses, a more complex creep curve is measured than depicted in **Figure 2.2**. There are definite variations in these curves with a change in testing stress or temperature. An increase in stress or temperature results in the total elongation increasing but the time to rupture decreasing. The interatomic spacing and shear modulus will vary with a temperature change. Faster creep rates result from a temperature increase since the rate of microstructural evolution also increases and therefore the material strength decreases (Nabarro and De Villiers 1995).

The rate of vacancy or dislocation generation is enhanced with increased applied stress, resulting in increased microstructural evolution and strength loss rates. Systems typically respond linearly to low applied stresses, in a similar way to that for diffusional creep, where the creep rate is proportional to stress. At intermediate applied stresses, falling within the practical interest range, power-law creep is observed and is described by Norton's law. Higher applied stresses result in power-law breakdown since the creep rate increases more rapidly than any power of the stress (Nabarro and De Villiers 1995). In addition to stress and temperature, both microstructural and external variables also have a marked influence of creep and creep rupture properties. External variables include pre-straining (cold-working), oxidation and corrosion, additional heat treatments, stress mode such as uniaxial (one-direction) or multiaxial (more than one direction) loading, and superimposition of cyclic loading (creep-fatigue mode) (Abe 2008). When pressure vessels retain steam, the pressure from the steam exerts biaxial (longitudinal and

circumferential) stresses on the pipe (Esposito, Bonora and Dichiaro 2013). Hence, the material is under a multiaxial stress state and the effect of this state on the creep curve is illustrated in **Figure 2.17**.

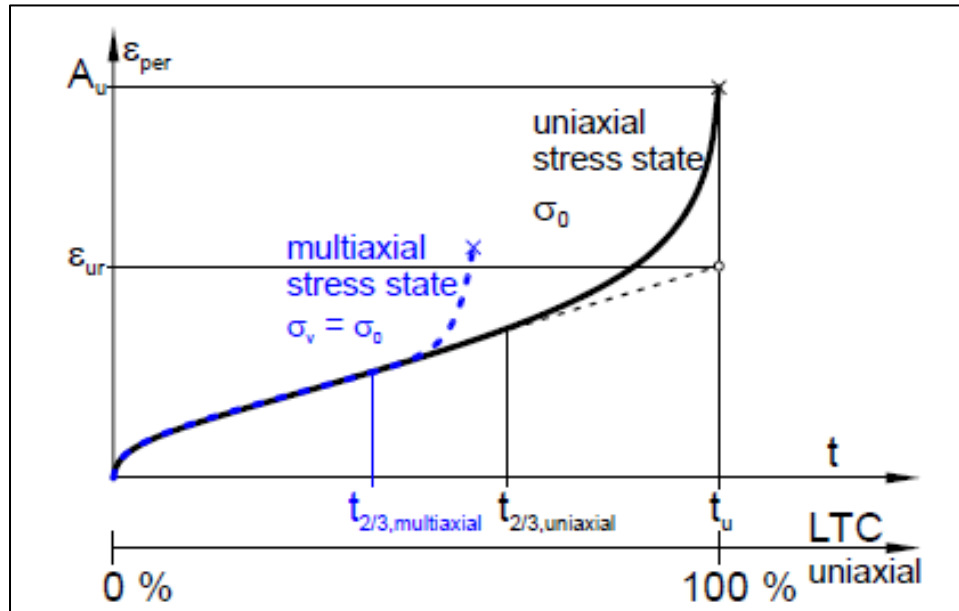


**Figure 2.17:** Schematic creep curves for a uniaxial stress state and a multiaxial stress state if creep cavitation is the dominant mechanism.  $\sigma_0$ ,  $t_u$ , LTC,  $\sigma_v$  and  $\varepsilon_{ur}$  indicates nominal applied stress (MPa), rupture time (h), lifetime consumption, equivalent stress and uniform rupture strain (%), respectively (Schleyer, Speicher, Klenk and Seidenfuß 2017).

## 2.4 MICROSTRUCTURE AND CREEP STRENGTH IMPLICATIONS OF WELDING ON CREEP-RESISTANT 9 – 12% CR STEELS

Welding is still the key fabrication process used to join and repair martensitic creep-resistant 9-12% Cr steel power plant components (Cerjak and Mayr 2008). Thus, these steels have been developed to have good weldability. Welding is a high-temperature process and therefore significantly alters the microstructure and mechanical properties of the material. All components exposed to high temperatures during services have the primary design criterion of the 100 000-h creep rupture strength of not just the bulk material (BM), but also the weld metal (WM) and cross-welds (Cerjak and Mayr 2008).

Welding involves practically every metallurgical phenomenon: solidification, solid-state phase transformations, heat treatment, residual stress development and subtle chemical composition effects (Bhadeshia 2001). Di Gianfrancesco (2017) provides thermal vision images as evidence that the critical points in steam lines are the outer surface of bends (extrados) and the weld joints.

Fusion welding is the most widely used welding process in power plants. It entails the use of a very intense heat source to dilute and melt back of the weld metal (WM). The weld thermal cycle consists of extreme heating and cooling, which results in high stresses and strains. Manual Metal Arc (MMA) welding is the most commonly applied type of fusion welding. The literature by Easterling (1992) and Kou (2003) is proposed for further reading on fusion welding.

*Steel weldability* is a metallurgical term that is used to define the state of a steel so that it can be welded upon without defects and the weld joint can still perform satisfactorily during service exposure (Yurioka 2001). Another definition of weldability is the susceptibility of the steel when welded upon to the various types of cracking mechanisms that are associated with steel weldments (Easterling 1992). These cracking mechanisms will be discussed in Section 2.5.

The 9-12% Cr martensitic steels air-harden to martensite, which leads to cracking of constrained welds in thick-section components upon cooling to room temperature after welding or post-weld heat treatment (PWHT). Therefore, the martensitic transformation must be prevented during welding. In the case of X20 steels, the martensitic transformation takes place in the range of 270 °C ( $M_s$ ) to 50 °C ( $M_f$ ) upon air cooling of components with wall thicknesses of up to  $\pm 100$  mm. Subsequently, it is crucial to preheat to 250 °C and keep the interpass temperature above this value to ensure the martensitic transformation will only occur during cooling after welding. In order to temper the brittle martensitic structure and relieve some of the stresses induced by welding, PWHT needs to be applied. Therefore, it is also important to cool below 150 °C to transform more than 90% of the weld to martensite. This is done to prevent untransformed martensite (austenite) from remaining after PWHT. Otherwise, the martensitic transformation occurs



during cooling after the PWHT leading to increased risk of crack formation. All these precautions contribute to the martensitic creep-resistant 9-12% Cr steels good weldability (Hald 2017). In the case of P91 steels, post-weld heating is applied before PWHT to remove the diffusible hydrogen (Pandey, Mahapatra, Kumar and Saini 2018).

For comprehensiveness and later use in Chapter 3, the weldment orientation axes need to be defined. **Figure 2.18** indicates the weldment orientation axes on a cross-section of an MMA girth (circumferential) weld performed on a steam pipe. These axes are defined according to the weld processing geometry: The rolling direction (RD), the normal direction (ND) which is in the direction of the through-thickness of the weld, and the transverse direction (TD) (Engler and Randle 2010).

In the sections to follow, the transformation of the microstructure during welding will be reviewed, followed by a more extensive discussion on the microstructure and creep behaviour of the problematic weld region known as the fine-grained heat affected zone (FGHAZ).

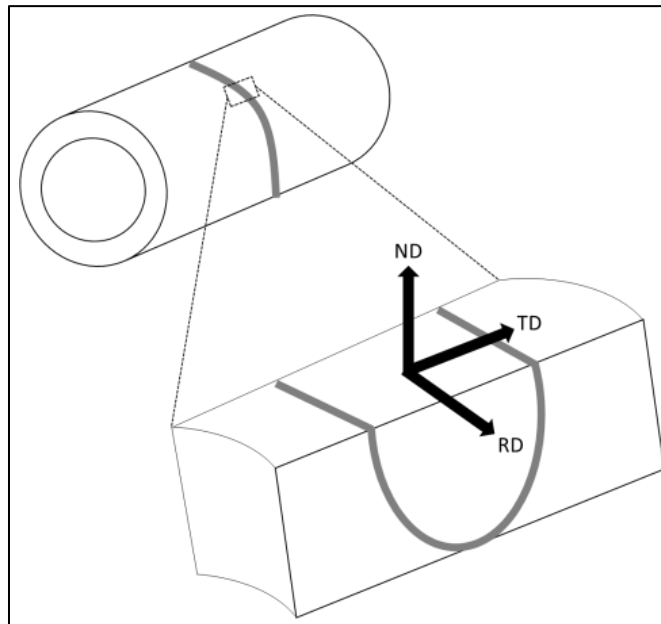


**Figure 2.18:** Schematic diagram of a cross-section through an MMA girth weld performed on a steam pipe. The weld axes are given as the rolling (weld) direction (RD), normal direction (ND) and transverse direction (TD) (Marx 2016).

### 2.4.1 Evolution of Microstructure during Welding

Mainly, the weld thermal cycle applies a local and highly inhomogeneous heat treatment to the BM (Cerjak and Mayr 2008). The result is a weld joint that has two main regions: the fusion zone and adjacent to it the Heat-Affected Zone (HAZ). The deposited WM and melted parts have a solidification microstructure. As the name suggests, the HAZ includes any non-melted areas whose microstructures are altered due to the heat flow during welding (Bhadeshia and Honeycombe 2006). This HAZ is a narrow non-equilibrium region. The temperature experienced in the HAZ is in the range of just above  $A_{c1}$  to melting temperature  $T_m$  (Pandey, Mahapatra, Kumar and Saini 2018). Hence, due to the temperature gradient experienced in the HAZ, the resulting microstructure is heterogeneous and there is a continuous change in microstructure moving from the fusion line into the base metal. Each microstructure corresponds to a sub-zone in the HAZ. These regions have no borderlines and are classified based on the peak temperature experienced  $T_p$  and prior austenite grain size.

The sub-zones in the HAZ are: grain growth coarse-grained HAZ (CGHAZ); grain refined fine-grained HAZ (FGHAZ); partially transformed inter-critical HAZ (ICHAZ) and over-tempered BM (Cerjak and Mayr 2008). **Figure 2.19** provides a schematic illustration of the various weldment regions and the peak temperatures they experience during welding alongside the calculated equilibrium phase diagram of P91 (X10CrMoVNb9-1) steel. The specific  $T_p$  range values characteristic of each sub-zone in the HAZ is given in **Table 2.6**. Since each region has its unique microstructure, each region has its corresponding properties which are also summarised in **Table 2.6**.

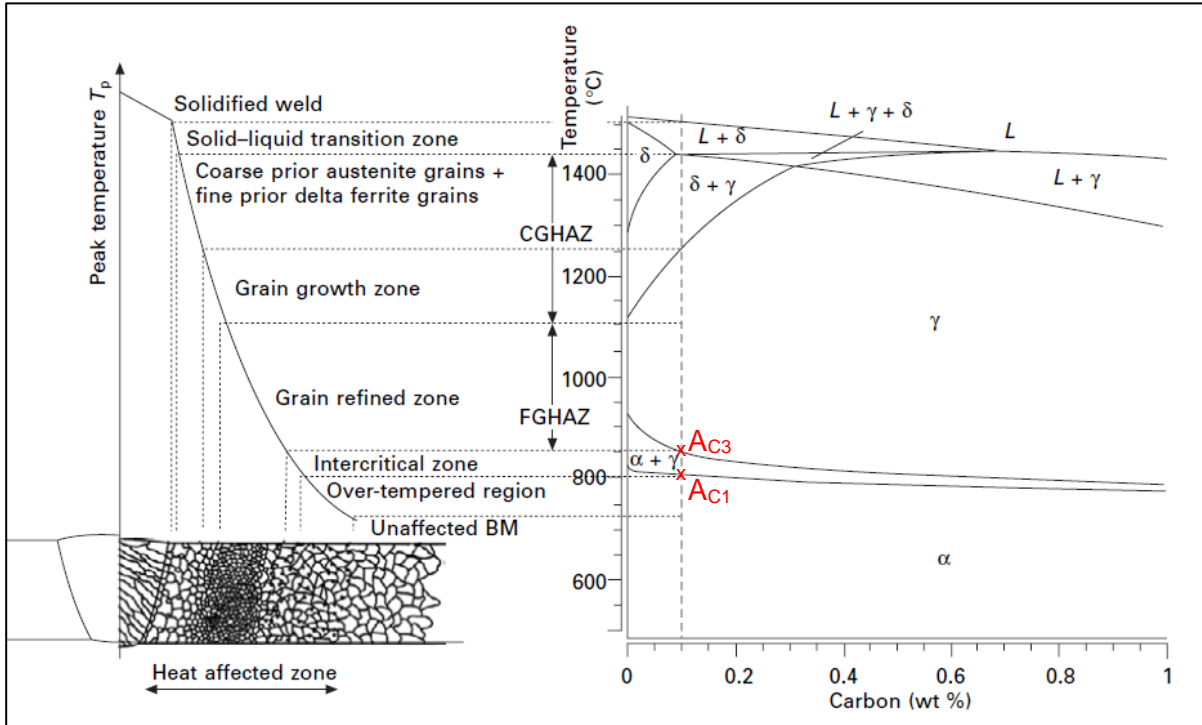


**Figure 2.19:** Schematic illustration of the different microstructural regions in the HAZ correlated to the calculated equilibrium phase diagram of a P91 (X10CrMoVNb9-1) type steel (Cerjak and Mayr 2008).

**Table 2.6:** Regions in the HAZ of a weldment, the peak temperature experienced and the corresponding transformation reaction, microstructure characteristics and mechanical properties (Constructed from Bhadeshia and Honeycombe (2006), and Pandey, Mahapatra, Kumar and Saini (2018)).

HAZ region	Peak temperature experienced	Transformation reactions	Microstructure characteristics	Mechanical properties
Coarse-grained austenite (CGHAZ)	$T_m > T_p > T_{\gamma\delta}$	$\gamma + \delta \rightarrow M + \delta$	Untempered martensite, undissolved NbX, dissolved $M_{23}C_6$	Poor toughness and high strength
	$T_{\gamma\delta} > T_p > A_{C3}$ ( $1500^\circ\text{C} > T_p > 1200^\circ\text{C}$ )	Coarse.. $\gamma \rightarrow M$	Untempered martensite, undissolved NbX, dissolved $M_{23}C_6$	Poor toughness and high strength
Fine-grained austenite (FGHAZ)	$T_{\gamma\delta} > T_p > A_{C3}$ ( $1200^\circ\text{C} > T_p > A_{C3}$ )	Fine.. $\gamma \rightarrow M$	Untempered martensite, undissolved MX, dissolved fine $M_{23}C_6$ , coarse $M_{23}C_6$	Adequate toughness and strength
Partially austenitised zone (ICHAZ)	$A_{C3} > T_p > A_{C1}$	$\gamma \rightarrow M + OM$	Untempered martensite, tempered martensite, undissolved MX, dissolved very fine $M_{23}C_6$ , coarse $M_{23}C_6$	High toughness and poor strength
Tempered regions (Over-tempered)	$A_{C1} > T_p$	OM	Tempered martensite, undissolved MX, coarse $M_{23}C_6$	High toughness and poor strength

Where,  $\gamma$  = austenite;  $\delta$  = ferrite;  $M$  = martensite;  $OM$  = over-tempered martensite;  $T_p$  = temperature experienced during welding;  $T_m$  = melting point of steel;  $T_{\gamma\delta}$  = temperature at which  $\gamma$  to  $\delta$  transformation completed during heating;  $A_{C3}$  upper critical temperature at which  $\alpha$  to  $\gamma$  transformation completed on heating;  $A_{C1}$  lower critical temperature at which  $\alpha$  to  $\gamma$  transformation started on heating.

Fusion welding has maximum heating rates of few hundreds  $K \cdot s^{-1}$ . As a result, there is a shift of the transformation and temperatures to considerably higher temperatures than predicted by the equilibrium phase diagram of the steel. Also, the solution temperature of the precipitates is increased. In addition, the heating rate affects the recrystallisation temperature, coarsening rate and solution temperature of carbides and nitrides, and the main proportion of grain growth (Cerjak and Mayr 2008).

Section 2.3 explains that microstructural stability ultimately depends on precipitate stability and the most crucial strengthening mechanism is PH. Therefore, precipitate stability is also an important factor in the HAZ of the weldment. Cerjak and Mayr (2008) suggest that there are three scenarios to be considered when welding on martensitic creep-resistant 9-12% Cr steels that are precipitate strengthened:

1.  $T_p$  is so high that it completely dissolves all the precipitates, leading to enhanced grain growth since boundary pinning is lost;
2.  $T_p$  is high enough to only cause coarsening of some precipitates and partial dissolution of others, and hence some boundary pinning is lost, and grain growth occurs;
3.  $T_p$  is too low to have a visible effect on the precipitates.

These three scenarios play an essential role in the final microstructure of each of the HAZ regions (**Table 2.6**). Since the IC/FGHAZ is of interest for this study, these microstructures are now discussed further and have been compiled from the literature by Bhadeshia and Honeycombe (2006), Cerjak and Mayr (2008), Pandey, Mahapatra, Kumar and Saini (2018), Abd El-Azim, Nasreldin, Zies and Klenk (2005), Wang, Kannan and Li (2016), and Mayr and Cerjak (2010).

#### **(i) FGHAZ Microstructure ( $T_p > A_{c3}$ )**

The FGHAZ is the grain refined zone and it experiences lower peak temperatures than the adjacent CGHAZ of just above  $A_{c3}$  in **Figure 2.19** ( $\pm 1100^\circ\text{C}$ ). Due to the relatively low affinity of  $M_{23}C_6$  precipitates to carbon at the peak temperature, these particles

dissolve in the austenite matrix during welding. However, the peak temperature is not sufficiently high enough to completely dissolve the precipitates, specifically the Cr-rich  $M_{23}C_6$ , and in the case of creep aged material, Laves phase boundary precipitates. The FGHAZ does not have a normal martensitic microstructure. Fine equiaxed austenite grains form since the undissolved precipitates pin the boundaries and limit grain growth. A local strain distribution results in the FGHAZ due to the martensitic transformation from the fine prior austenite grains. The small sized grains also result in martensite laths with lower aspect ratios to form within them.

The microstructure after welding, before PWHT, consists of elongated martensite laths within fine prior austenite grains. Upon cooling, new precipitates nucleate and the existing  $M_{23}C_6$  and Laves phase precipitates coarsen, leading to a bi-modal distribution of precipitate sizes. The VN and (V,Nb)CN precipitates remain fine and stable during welding and they do not dissolve.

Due to the fine-grained structure, there is a higher boundary density and enhanced diffusion along GB occurs. Consequently, all diffusional governed processes proceed to a much faster extent. This leads to a significant decrease in the creep strength of this region in the HAZ by the accelerated coarsening of precipitates and partial dissolution of a fraction of precipitates. This region and the ICHAZ is considered the weakest regions in weldments during service due to Type IV cracking that occurs, which will be further discussed in Section 2.5. The FGHAZ is characterised by lower hardness than the CGHAZ and moderate toughness.

During PWHT (tempering at 760 °C for 2h), two main processes have been observed to occur in the FGHAZ for P91 steel:

1. Partial annihilation of the martensite lath structure by the formation of coarse polygonal subgrains from the existing elongated martensite laths (micro-grains) and recovery of dislocations within these polygonal subgrains.
2. Significant coarsening of  $M_{23}C_6$  and Laves phase (if any) precipitates along MGB and nucleation of fine VN and Nb(CN) precipitates.

These processes are similar to those observed after tempering and creep exposure of BM during manufacturing (Section 2.2). The result is a fine tempered martensite microstructure. **Figure 2.20** schematically illustrates the FGHAZ microstructure after welding and PWHT, respectively. The undissolved precipitates outline the previous PAGB of the BM. In P91 steel weldment of new material, the FGHAZ has an average PAG size of 15  $\mu\text{m}$ . Other studies on the effect of PWHT on the HAZ of 9-12% Cr martensitic steels have also been performed by Mayr, Holzer and Cerjak (2011), and Milović, Vuherer, Blačić, Vrhovac and Stanković (2013).

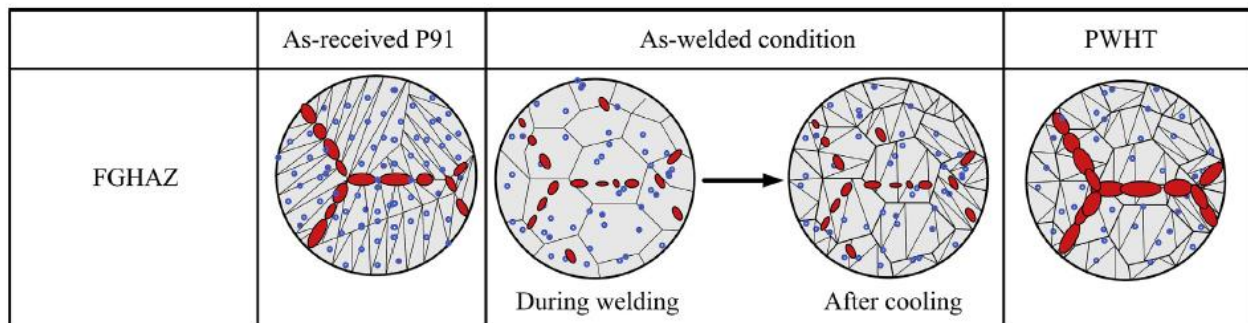


**Figure 2.20:** Schematic illustration of the microstructural evolution of the FGHAZ in the as-welded and PWHT condition (Pandey, Mahapatra, Kumar and Saini 2018).

### (ii) ICHAZ Microstructure ( $A_{c1} < T_p < A_{c3}$ )

The ICHAZ is the narrowest region in the HAZ. It is known as the partially transformed region since a partial transformation of ferrite into austenite takes place upon heating due to the peak temperature between  $A_{c1}$  and  $A_{c3}$ . New austenite grains form at preferred sites, such as PAGBs or martensite lath boundaries. The welding thermal cycle only tempers the remaining tempered martensite microstructure. Since carbon has a higher solubility in  $\gamma$ -Fe, the newly formed austenite grains have a higher carbon concentration. This leads to these newly formed grains having higher strain levels. As with the FGHAZ, there is only partial dissolution of the  $M_{23}C_6$  and Laves phase (if any) precipitates and coarsening of these undissolved precipitates during welding. Both these processes occur simultaneously. Subsequent PWHT causes this coarsening to be more pronounced.

The ICHAZ has a complex structure after cooling: untempered lath martensite, retained over-tempered martensite; newly formed prior austenite grains; coarse tempered prior austenite grains with newly formed fine and coarse undissolved  $M_{23}C_6$  precipitates along the new PAGB. A higher density of precipitates is present along the newly formed PAGB. The ICHAZ has the largest fraction and size of Cr-enriched  $M_{23}C_6$  precipitates compared to the other HAZ regions. A schematic illustration of the final microstructure of ICHAZ from weldment of as-received material is provided in **Figure 2.21**.

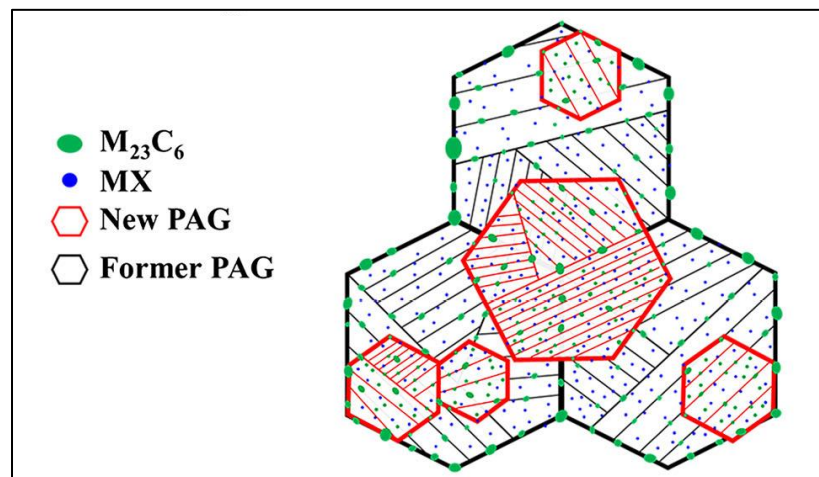


**Figure 2.21:** Schematic illustration of the ICHAZ microstructure (Wang, Kannan and Li 2016).

This region has typically the lowest measured hardness values in a weldment and therefore is characterised as the softest zone. Accordingly, the hardness values of the FGHAZ is in between the CGHAZ maximum value and ICHAZ minimum value. The ICHAZ has the highest toughness among the HAZ regions due to the lower solubility of carbon in solid solution. The hardness of the ICHAZ follows from two competing effects:

1. Increase in hardness due to the formation of the untempered laths with high dislocation density.
2. Decrease in hardness due to the over-tempering of the initial tempered martensite, resulting in annealing of the mobile dislocations.



## 2.4.2 Creep Behaviour of the FGHAZ

As discussed in the previous section all diffusion-governed processes proceed to a much faster extent in the FGHAZ due to the higher number of GB from the fine-grained structure. Therefore, the creep degradation mechanisms discussed in Sections 2.3.2 to 2.3.6 is expected to occur at an enhanced rate.

Abd El-Azim, Nasreldin, Zies and Klenk (2005) have made the following observations in the FGHAZ of a P91 weldment during long-term creep testing (600 °C; 70 MPa) interrupted after 26 035h:

1. The recovery of the subgrains is continued by the formation of coarser, more equiaxed subgrains with decreased dislocation densities in the interior (similar to Section 2.3.3). This recovery process seems to be heterogeneous.
2. The martensite lath subgrains (micro-grains) grow by the migration of the high angle boundaries that are strongly pinned by the fine  $M_{23}C_6$  precipitates and the annihilation of the other MGB by the recovery of the dislocations (Section 2.3.3).
3. There is coarsening and clustering of the  $M_{23}C_6$  precipitates (Section 2.3.2). Coarse carbide particles were observed along the MGB, while fewer finer carbides were observed within the subgrains.
4. Fine VN and (Nb)CN precipitates remain stable (Section 2.3.2) and there is additional fine nucleation of these precipitates on the  $M_{23}C_6$  precipitates.
5. Formation of coarse Laves phase precipitates on PAGB and MGB (Section 2.3.2).
6. Z-phase precipitation at the vicinity of  $M_{23}C_6$  precipitates (Section 2.3.2).
7. Creep cavitation occurred by the formation of cracks on the PAGB and the tempered martensite lath interfaces that were normal to the tensile stress (Section 2.3.6). This was only observed in the FGHAZ and not in the other weldment regions.

They found that the lower creep resistance of the welded joint compared to the BM is due to the FGHAZ that has the lowest creep resistance in comparison to the BM and welded joint. They conclude the low creep resistance of the FGHAZ during creep exposure is due to:

1. Softening that occurs during creep is mainly due to the growth of the micro-grains and recovery of their dislocations in their interior. Sawada, Maruyama, Hasegawa and Muraki (2000) found that for 9% Cr steels the creep strength is inversely proportional to subgrain size and dislocation density within the micro-grains.
2. The loss of PH due to coarsening and agglomeration of the  $M_{23}C_6$  carbides at the MGB and loss of their pinning effect. Subsequently, the rate of micro-grain growth and hence softening is increased.
3. The contribution of the newly nucleated fine VN and (Nb)CN precipitates to PH is inhibited since they form on the coarse  $M_{23}C_6$  precipitates.
4. Formation of Laves phase and Z-phase particles resulting in a decrease of both PH and SSH (Sections 2.3.2 and 2.3.5).

These four factors play the same role in creep strength reduction in the various weldment regions during creep exposure but at different rates.

### **(i) Influence of prior austenite grain size on creep behaviour**

Most of the mechanical properties of martensitic steels are affected by the PAG and packet size. Smaller PAG and hence packet size result in an increase of the hardness, yield strength, tensile strength, fatigue strength, toughness and impact strength at room temperature (Białobrzaska, Konat and Jasiński 2017). Subsequently, larger PAG sizes cause embrittlement of the material.

As mentioned previously, the recovery of the martensite lath subgrains occurs heterogeneously in both the BM and FGHAZ, specifically during lower stress and long-term creep exposure, significantly recovered regions was observed near the PAGB,

although the microstructure within the grains remained fine (Kimura, Kushima and Booker 2000, Abd El-Azim, Nasreldin, Zies and Klenk 2005). This preferential recovery in the vicinity of PAGB during long-term creep deformation is due to the higher internal stresses introduced near the grain boundaries compared to within the grains during the martensitic transformation. The higher stress promotes recovery of the tempered martensitic structure, i.e., lath widening and subgrain coarsening (Section 2.3.3). The onset of tertiary creep is accelerated by the preferential recovery near PAGBs since creep deformation is mainly dependent on the deformation in this region.

The fine PAG result in a large boundary area of PAGB per unit volume. To decrease the stored energy during creep exposure, coarsening of the micro-grains is accelerated, and hence the rate of recovery of the dislocations within the micro-grains is enhanced (Section 2.3.3). Consequently, the rate of softening increases and the creep resistance decreases.

Similarly, the ICHAZ also has poor creep strength due to a large number of HAGB with higher mobility and energy resulting in the higher potential to undergo recovery (Wang, Kannan, Zhang and Li 2017).

As mentioned in Section 2.3.6, it has been found that creep cavities that lie on transverse PAGB play the dominant role in the creep rupture process. The reason is that these cavities are larger and more closely spaced than those on the MGB within the grains. Thus, due to the fine prior austenite grain size and coarse precipitates on the PAGB in the FGHAZ, there are a significant number of preferred nucleation sites for large and closely spaced cavities during creep. Hence, creep cavitation and the creep rupture process are accelerated. It has also been mentioned in Section 2.3.3 that HAGB such as PAGB results in dislocation pile-ups in their vicinity. If the strain is high, as is the case in the FGHAZ, the dislocation pile-ups can break through the boundary. This is a mechanism of cavity nucleation (Section 2.3.6).

## **(ii) Influence of peak temperature during welding on creep behaviour**

High densities of dislocations are introduced in lath martensite by the plastic accommodation of the transformation strain in martensite (Section 2.2.2). Since the

austenite grains are small in the FGHAZ (Section 2.4.1), the shape strain and volume change after the martensitic transformation is decreased, resulting in smaller plastic accommodation and hence a smaller number of dislocations stored after the transformation (Morito, Nishikawa and Maki 2003). This decrease in dislocation density may explain a measured softer martensite matrix (lower hardness) in the IC/FGHAZ of martensite creep-resistant 9-12% Cr steel weldments compared to the WM, CGHAZ and BM regions (Abd El-Azim, Nasreldin, Zies and Klenk 2005, Molokwane 2014, Marx 2016, Rasiawan 2017). Consequently, the FGHAZ has the highest rate of recovery of the martensitic structure during creep exposure and the lowest creep strength.

### **2.4.3 Simulation of the FGHAZ**

To perform representative investigations on the HAZ of actual welds is difficult since the microstructural regions in the HAZ are extremely narrow. To overcome this problem, it is possible to simulate the weld thermal cycle under laboratory conditions and hence a large sampling volume with a homogenous microstructure of each region is available for analysis (Easterling 1992). Each microstructural region can be simulated and hence representatively produced, separately by the controlled application of the thermal or thermo-mechanical cycles according to a specific weldment geometry and welding parameters. The input data for physical weld HAZ simulation is the time-temperature profile for the specific microstructural region. This data is obtained either by physical measurement using a thermocouple during actual welding, derivation by analytical solutions of the heat conduction equation or by using refined numerical thermal heat source models (Easterling 1992). Simulation of the weld thermal cycle usually is performed using the following methods (Mayr 2007):

- Heating by induction and then hold at peak temperature followed by cooling in an oil bath.
- Heating in a hot salt bath until the peak temperature is reached followed by immediate cooling in a salt bath at a moderate temperature.
- Heating in a furnace to peak temperature followed by cooling in air or an oil bath.

- Resistance heating using a thermo-mechanical weld simulator such as a Gleeble™ or Smitweld™.
- Controlled induction heating and cooling using a quenching dilatometer.

**Table 2.7** provides a comparison of the differences between the HAZ simulation techniques that can be applied to samples large enough for subsequent sample preparation. The main advantages that Gleeble™ simulation has over the other techniques are much faster heating rates, a high degree of reproducibility and agreement with actual HAZ structure. Therefore, it was chosen for the FGHAZ simulation in this study (Section 3.3). Previous studies by Sulaiman, Li, Drew and Dunne (2009), and Rasiawan (2017) have shown the success in FGHAZ simulation on virgin 9-12% Cr martensitic steels using the Gleeble™.

**Table 2.7:** Comparison of different HAZ simulation techniques (Buchmayr 2005).

Feature	Gleeble™ simulation	Induction heating + oil quenching	Salt bath heating + salt bath cooling	Furnace heating + cooling
Heating rate	Fast like HAZ	Slower than in HAZ	Slower than in HAZ	Slower than in HAZ
Peak temperature $T_p$	Exactly programmable	Exactly controllable	Exact when using thermocouples	Exact when using thermocouples
Holding time at $T_p$	Rounded T-t curve as numerically predicted	Some seconds	None	None
Cooling rate	Programmable	Limited by oil temperature and sample size	Determined by salt bath temperature and sample size	
Homogeneity of microstructure	Limited length of approx. 10 mm	Whole sample length	Whole sample length	Whole sample length
Gauge length	Reduced ( $\pm 10$ mm)	User-defined	User-defined	User-defined
Degree of reproducibility	High	Moderate	Moderate	Moderate
Extent of agreement with actual HAZ structure	Excellent	Good	Good	Good
Consideration of constraint effects	Possible by applying mechanical loading	Not done	Not possible	No possible
Additional data measurable	Dilatation	None	None	Dilatation
Simulation costs and duration	High	Low	Low	Low cost, but time-consuming

### (i) Gleeble™ Simulation

The Gleeble™ is fully interfaced to allow for programming the reference signal for closed-loop control of both thermal and mechanical operations. Resistance heating is achieved by the flow of low-frequency AC in the specimen with rates of up to 1 000K/s (Rasiawan 2017). For closed loop signal, a feedback signal is required and is obtained from a fine wire thermocouple welded onto the specimen surface. The weld thermal cycle is entered in the control computer and a cylindrical sample is heated up rapidly to the set peak temperature  $T_p$  with a direct current flow of up to 6 000 A. Cooling is achieved by the flowing of heat through the copper/stainless steel jaws that hold the sample in position. Slow cooling rates result in controlled temperature-time curves. However, the distance between the jaws can be reduced, air quenching or external gas cooling used to attain faster cooling rates. From **Table 2.7** the advantages of Gleeble™ can be summarised as follows (Rasiawan 2017):

- For a predefined region in the HAZ, the application and measurement of the thermal cycle can be accurately applied.
- A large sampling volume is available after simulation for subsequent mechanical tests and microstructural characterisation.
- The scatter of the HAZ properties is reduced by the high homogenous microstructure for a large volume.
- Any phase transformation during welding can be measured by thermal analysis (Van Rooyen 2016) or dilatometric measurement.
- Mechanical stresses during cooling can be imposed to simulate any constraint from surrounding material.
- Mechanical properties during cooling from high temperature can be directly measured and then used as input into finite element simulations.

- Other combined thermo-mechanical tests can be performed such as reheat relation test, hot ductility test, partial melting and then cooling afterward.

The disadvantages of the simulation technique can be summarised as (Rasiawan 2017):

- Experimental problems may be experienced in the temperature profile in the longitudinal direction.
- Local gradients in the microstructure, properties and residual stress effects are not taken into account.

## **(ii) Determining the Weld Thermal Cycle**

The HAZ simulation is mainly based upon the transformation temperatures of the material. For the prediction of the weld thermal cycle, the most widely adopted procedure is based on the analytical solution of the heat conduction equation derived by Rosenthal (1941). The procedure is the standardised cooling time concept according to the German standard SWE 088 (Buchmayr 2005). Two-dimensional heat flow (thin sheet) and three-dimensional heat flow (thick plate) are the main focus of this principle and the cooling time is predicted. Various sets of information can be used to predict the cooling time such as:

- plate thickness,
- preheating temperature;
- arc voltage;
- welding current and welding speeds;
- electrode diameter and runout time; and
- electrode diameter and fused area.

An overview on applying this information to predict the cooling time is given by Molokwane (2014). One specific subzone in the HAZ can be simulated by application of a single temperature-time cycle under given welding conditions. The welding conditions include heat input, cooling time and peak temperature.

Molokwane (2014) performed FGHAZ simulation on X20 steel using three thermal cycles to mimic the conditions of a multi-pass weld HAZ. However, there were concerns with



using three weld thermal cycles for the simulation. Rasiawan (2017) then built upon the research of Molokwane (2014) and adopted the same model used to simulate the FGHAZ on X20 steel for a single pass weld. The time-temperature profile for the simulation requires the  $A_{C3}$  and  $A_{C1}$  transformation temperatures (Section 2.4.1). Subsequently, the  $A_{C1}$  and  $A_{C3}$  temperatures were determined in 2 ways:

- (i) MatCalc software (MatCalc® Engineering 2018) to predict the equilibrium transformation temperatures of X20
- (ii) Dilatometry testing using the Gleeble™3800 to determine the  $A_{C1}$ ,  $A_{C2}$ ,  $A_{C3}$ ,  $M_s$  and  $M_f$  temperatures of X20

Finally, Rasiawan (2017) chose to simulate the FGHAZ as a simulated welding profile of a single pass weld with peak temperature  $T_p$  of 980 °C. Subsequent analysis of the mechanical properties and microstructure with LM and SEM of the simulated FGHAZ samples proved that the simulation was a success. However, detailed microstructural evaluation was not performed.

## **2.5 TYPE IV CRACKING MECHANISM**

This section addresses explicitly Research Objective 1 “*to review the literature of Type IV cracking in 9-12% Cr martensitic steels and compare with experimental results to gain a better understanding of this mechanism*”.

Cracking in service exposed martensite creep-resistant 9-12 % Cr steel weldments is the primary mechanism whereby failure occurs in a power plant component (Cerjak and Mayr 2008). The study from Rasiawan (2017) discussed in the previous section also performed creep tests on cross-welds of virgin onto creep aged X20 steel and found that all the samples failed in the FGHAZ of the creep aged material on the existing creep side.

For the first time in 1974, the cracks were classified into different modes according to their location and orientation within the weldments by Schüller, Hagn and Woitscheck (1974). This classification of the possible crack modes within a weldment is schematically

illustrated in **Figure 2.22**. Each one corresponds to a different failure or deformation mechanism.

Cracks that form within the deposited WM and develop in either the longitudinal or transversal direction are labelled as Type I and Type II cracks. The difference between Type I and Type II cracks is that Type I cracks remain in the WM, whereas Type II cracks can propagate into the HAZ or even into the BM. The other types of cracks develop within the HAZ. Type III cracks initiate within the CGHAZ close to the fusion boundary and can extend further in this region as well as into the BM. A further classification of Type IIIa was assigned by Brett (2004) to cracks that form very close to the fusion boundary in a fully refined HAZ structure with higher fracture ductility. Type IV cracks form and are restricted to within the FGHAZ or ICHAZ.

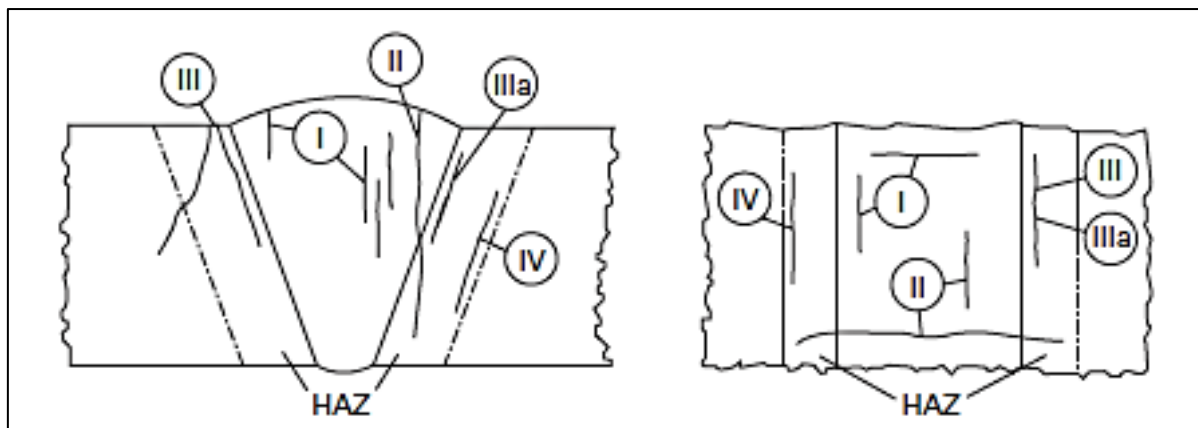


**Figure 2.22:** Schematic illustration of the various cracking modes in a creep resistant ferritic steel weldment (Cerjak and Mayr 2008).

At present, Type IV cracking is considered the leading cause for the “end of life” of martensite creep-resistant 9-12% Cr steel welded components in the power plant industry. Therefore, the Type IV mechanism is further discussed in detail. For overviews on the other failure mechanisms, Cerjak and Mayr (2008) can be consulted.

Type IV cracking is formally defined as the formation and propagation of cracks or failures in the FGHAZ and ICHAZ weldment regions. Due to the similar microstructural features of these two regions, it is generally difficult to separate these regions precisely. Type IV cracking has been observed in P91, X20, P92, P122 and E911, and also low alloy

ferritic/bainitic steels by Gooch and Kimmins (1987), Middleton and Metcalfe (1990), Brühl, Weber, Cerjak and Schwaab (1991), Brett 1994, Parker and Stratford (1996), Brear, Fairman, Middleton and Polding (2000), Fujibayashi and Endo (2001), Shibli and Le Mat Hamata (2001), Ennis 2002, Smith, Walker and Kimmins (2003), Takemasa, Nonaka, Ito, Saitou, Miyachi *et al.* (2004), Tezuka and Sakurai (2005), Laha, Chandravathi, Parameswaran, Rao and Mannan (2007), Tabuchi, Hongo, Watanabe, Sawada and Takahashi (2009), Abe, Tabuchi, Tsukamoto and Shirane (2010), Abd El-Azim, El-Desoky, Ruoff, Kauffmann and Roos (2013), and Sakthivel, Laha, Vasudevan, Koteswara Rao and Panneer Selvi (2016). These studies confirmed the poor creep strength of weld joints compared to the BM is attributed to premature Type IV cracking. They found that most of the martensitic creep-resistant 9-12% Cr steel weldments under long-term service and relatively low stresses fail within the FGHAZ or ICHAZ by Type IV cracking. It is also concluded that the ICHAZ and FGHAZ both show similar proneness to Type IV cracking.

Extensive review papers on Type IV cracking in martensitic creep-resistant 9-12% Cr steels has been written by Middleton and Metcalfe (1990), Ellis and Viswanathan (1998), Francis, Mazur and Bhadeshia (2006), Abson and Rothwell (2013), and Pandey, Mahapatra, Kumar and Saini (2018). Further discussion is drawn from these papers.

Martensitic 9-12% Cr steel weldment failures during creep exposure take place randomly in either the BM, WM or the HAZ at high stress levels. However, under lower stresses (creep tests with stresses below 100 MPa) the fracture location shifts into only the narrow FGHAZ or ICHAZ. Hence, Type IV cracking originates from the weakest zone present in weldments. Even though there is no specific data on the residual stresses in martensitic creep-resistant 9-12% Cr steel weldments, it is well-known that there exist residual stresses due to welding.

### **2.5.1 Role of Constraint and Welding Direction**

The time to rupture for failures in the Type IV region (IC/FGHAZ) is sensitive to the stress state and the applied loading direction (Cerjak and Mayr 2008). The high carbide coarsening rate and partial dissolution of precipitates in the FGHAZ and ICHAZ causes

them to be soft relative to the other weldment regions during creep exposure (Section 2.4). Therefore, Type IV cracking can be viewed as the result of a microstructural zone of material weak in creep strength surrounded by a material with a microstructure resulting in a stronger creep strength. It is this mismatch in creep properties that lead to strain being concentrated in the weaker IC/FGHAZ during early stages of creep. Therefore, a critical factor in the clarification of the type IV cracking mechanism is the role of constraint in the creep weak IC/FGHAZ region from the adjacent stronger CGHAZ and BM (Cerjak and Mayr 2008).

To simplify, the load condition is seen as plain tensile loading of the different regions of the HAZ in series. Therefore, the weakest part attempts to deform transversely under high strains. The region will be constrained to deform by the adjacent stronger material if it is sufficiently thin. Consequently, a triaxial stress state predominates and prevents the weaker region from deforming. This multiaxial constraint situation becomes more complicated during creep exposure and is expected to increase with specimen size and therefore improve creep rupture times. Extensive discussion exists in literature for example that by Kimmins, Coleman and Smith (1993).

Type IV cracking has been observed in both seam welds as well as girth welds (Cerjak and Mayr 2008). The different welds are illustrated in **Figure 2.23**. Girth welds are loaded with system stresses and tend to fail by a “leak before break” mechanism. Hoop stresses load seam welds and failures can be catastrophic (Ellis and Viswanathan 1998). Under general pure pressure, the principal stress for the seam welds is twice that to which the girth weld is subjected (Abson and Rothwell 2013). However, system stresses superimpose and do allow type IV failure to occur in the HAZ of girth welds, for example, those welds attaching header end caps.

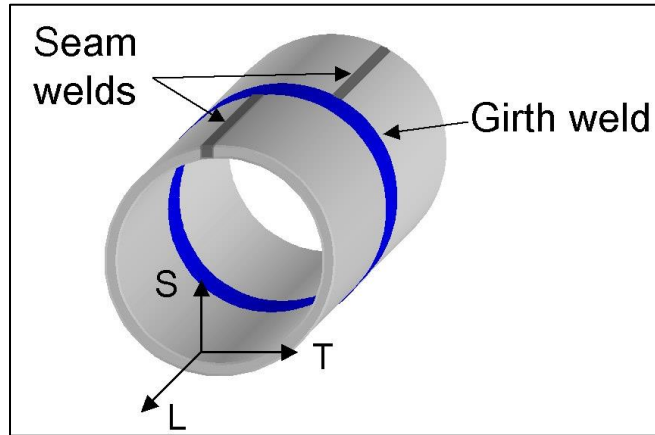


**Figure 2.23:** Schematic diagram of different tube (pipe) welds. S, L and T refer to the short transverse, longitudinal and transverse directions, respectively (Bilat, Gourgues-Lorenzon, Besson and Pineau 2006).

### 2.5.2 Weld Strength Factor

The lower creep strength of 9-12% Cr martensitic steels is a significant concern for longitudinal (seam) welds since in these welds the weaker material will be subjected to the same stress as the parent (Abson and Rothwell 2013). In short-term creep tests, the parent and cross-weld creep strengths remain similar until the onset of Type IV cracking. There is an immediate reduction in creep performance of the cross-weld when Type IV cracking has set in. This “Type IV” shortfall is schematically illustrated in **Figure 2.24** and the onset of Type IV cracking causes an inflection point in the creep rupture strength. There is a threshold stress level associated with the inflection point for a given temperature and material. Below this threshold stress, the difference in creep strength between the parent and cross-weld becomes larger with increased time and lower stress.

One approach to quantify the “Type IV” shortfall is by defining a weld strength factor (WSF) or a weld strength reduction factor (SRF) during the design stage of new components as well as remaining life assessment of existing structures. The two values are opposites and the WSF is defined as the ratio of creep rupture stress at a certain time and temperature between weldments and base material (Cerjak and Mayr 2008).

Consequently, the European Creep Collaborative Committee (ECCC) defined these factors in their ECCC Recommendations as follows (Morris 2001):

$$WSF(t, T) = \frac{R_{u(w)/t/T}}{R_{u/t/T}} \quad (2.9)$$

$$SRF(t, T) = \frac{R_{u/t/T} - R_{u(w)/t/T}}{R_{u/t/T}} \quad (2.10)$$

where  $R_{u/t/T}$  is the creep rupture strength of the base material samples at time  $t$  and temperature  $T$  and  $R_{u(w)/t/T}$  is the creep rupture strength of the cross-weld samples at time  $t$  and temperature  $T$ . It is desired to have a high WSF and low SRF. Abson and Rothwell (2013) provide a good illustration of the determination of these factors for 9-12% Cr martensitic steels. It is these factors that will help determine the weldability (Section 2.4.1) of the creep aged material.

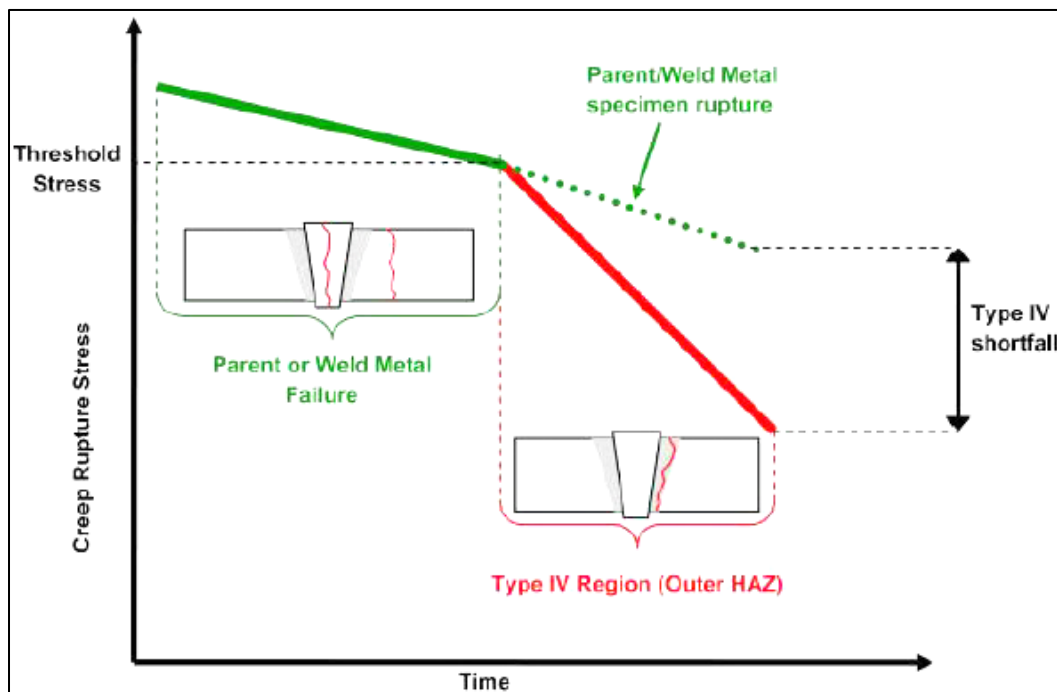


**Figure 2.24:** Schematic illustration of creep rupture stress versus time to show the reduction in creep rupture strength after the onset of Type IV cracking for weldments at a fixed temperature. Expected fracture location is indicated. As can be seen, Type IV cracking occurs much earlier than for a parent or weld metal specimen under the same test conditions (Abson and Rothwell 2013).

### 2.5.3 Microstructural Degradation and Failure Mechanism

The triaxial stress state causes localised strain in the IC/FGHAZ, which results in accelerated coarsening of the microstructure compared to the other weldment regions during creep exposure (Section 2.4.2). Subsequently, since the IC/FGHAZ regions have the largest precipitates already before creep exposure and coarse precipitates are preferred nucleation sites for cavities (2.3.6), it follows that creep cavity formation is accelerated in these regions during creep exposure. The cavities nucleate mainly on the PAGB, grow and coalesce to form a crack. **Figure 2.25** summarises the Type IV mechanism that is governed by creep cavitation.

The triaxial stress state has been recognised to accelerate creep cavity growth. A three-dimensional FE model that takes the diffusive growth of creep cavities into account has been used by Abe and Tabuchi (2004) to simulate creep crack growth behaviour in P122 weldments. They found creep cracks grow faster in the centre of the specimen thickness than in the perimeter. This observation illustrated that the higher multiaxiality in the centre of the specimen thickness leads to higher vacancy concentration, which is consistent with the experimental observation of creep cavities initiating in the centre.

Since the IC/FGHAZ have the largest precipitates, the boundaries are pinned insufficiently, and grain boundary sliding will occur preferably within these regions during creep exposure. In turn, grain boundary sliding results in stress concentrations and finally decohesion between precipitates and the matrix, resulting in preferred nucleation sites for cavities to become available. Consequently, microstructural changes, such as precipitate coarsening and Laves and Z-phase formation, that takes place in the HAZ during welding, subsequent PWHT and high-temperature service promote Type IV cracking. Since SBH is dependent on precipitate stability, it can be used to determine the susceptibility of a steel to Type IV cracking and the life of Type IV fracture can be increased if anything is carried out to enhance SBH.

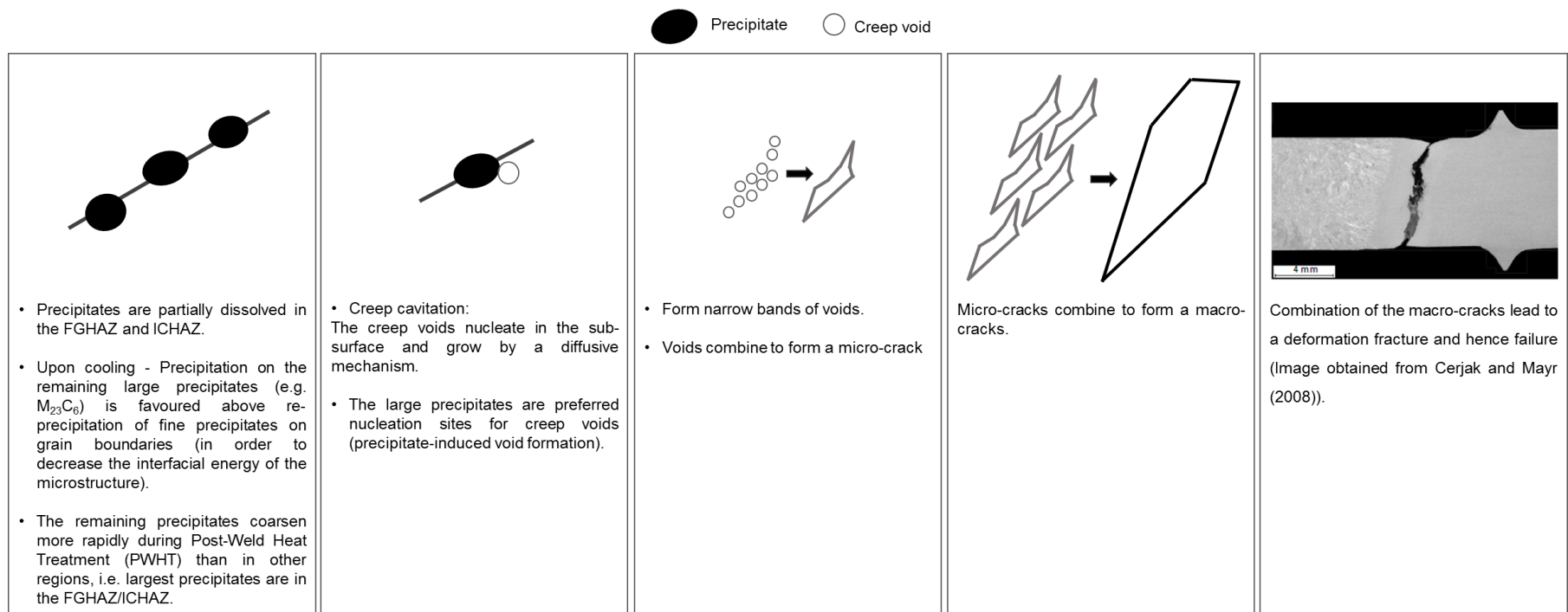


**Figure 2.25:** Schematic illustration of the Type IV cracking mechanism (Constructed from Cerjak and Mayr (2008)).



From high stress creep tests on simulated samples with homogeneous microstructures it has been found that the minimum creep strength microstructure coincides with the minimum hardness or softest microstructure, i.e., the ICHAZ. Though, at low stresses comparable to service conditions, the FGHAZ, which does not have the minimum hardness, corresponds to the minimum creep strength microstructure. Thus, hardness along weldments in the transverse direction is not a feasible parameter to use as an indicator of Type IV susceptibility or the location of where Type IV failure may occur. Recent EPRI research has established that the IC/FGHAZ should be more correctly defined as partially transformed (Gu, West, Thomson and Parker 2014).

It has been discussed in Section 2.4.3 that the FGHAZ can be simulated. Simulated samples are mechanically homogeneous and do not contain triaxial stresses. It has been found that the creep lives of cross-welds that failed by Type IV cracking are longer than those for the simulated FGHAZ specimens and hence FGHAZ simulated samples have poor creep properties (Francis, Mazur and Bhadeshia 2006). Consequently, this indicates that even though the triaxial stress state accelerates creep cavity growth, it does not lead to a reduction in creep life of the weldment. There is mechanical constraint that results from the property gradients in the HAZ of cross-weld samples (Section 2.5.1), which delays failure in the FGHAZ. At lower service stresses the grain boundaries are less resistant to sliding. Continuum models model Type IV cracking as damage accumulation that is accelerated by multiaxial stresses.

In contrast, the finite models of Kimmins and Smith (1998) for cross-welds proposed that constraint from the heterogeneous microstructure is relaxed by grain boundary sliding during creep exposure. Subsequently, easier Type IV failure results. They also found that grain boundary sliding in cross-weld specimens results in a more significant number of cavities than in simulated HAZ specimens. It is important to note that these conclusions have been drawn from short-term creep tests. It is only once sliding has been accommodated and constraint relaxed, that similar rupture times are obtained for both cross-weld and simulated Type IV specimens.

In conclusion, it can be considered that the formation of Type-IV creep damages are influenced by both the concentration of creep strain and the high multiaxial stress condition in the IC/FGHAZ (Tabuchi, Hongo, Watanabe *et al.* 2009). Thus, stress triaxiality must be taken into account for accurate life prediction and damage evolution in martensitic 9-12% Cr steel welds.

## **2.6 CONVENTIONAL REMAINING LIFE ASSESSMENT AND WELDABILITY LIMITS**

To determine a safe operating life of high-temperature power plant components, creep life assessment is essential.

Wilson (1990) suggests that there are the following considerations when determining the remaining life of components:

- The lack of accurate predictive models results in the use of large safety factors.
- High-temperature components are designed based on uniaxial creep rupture data.
- The base material is assumed to be chemically homogeneous, resulting in a further source of inaccuracies.
- It has become evident from examinations of in-service components that the safe creep design life of creep resistant low-alloy steels has been underestimated significantly, which leads to unnecessary replacements.
- This problem is assumed to arise as a result of the inaccuracies of remaining life prediction techniques, specifically modelling of creep is complicated due to the complexity of the power plant systems and the harsh operating environment.
- A significant inaccuracy results from the use of standard creep data in prediction models that have been derived from small test samples. The behaviour of these small samples under a specific set of environmental conditions may differ from the bulk components.

- Service conditions can be highly variable and even at times exceed the design specifications.
- A further source of error in remaining life predictions is due to welds and weldments, whose complex microstructure and chemical inhomogeneity leads to non-uniform stress distributions and sites of stress concentrations. These sites are susceptible to cavitation in the initial creep stage.
- However, although these stress concentration sites are critical for creep damage, they are not necessarily so concerning life exhaustion since in many cases non-destructive monitoring and repair are relatively easy for weldments.
- As a consequence, most remaining life prediction models focus primarily on the parent material.
- Accurate assessment of problems in high-risk areas, i.e., the areas of harsh creep environment, should be an essential part to any remaining life prediction procedures.
- Several components have been identified as being especially susceptible to high-temperature failure. They are listed in **Table 2.8**. Subsequently, remaining life assessment is concentrated on these components.

**Table 2.8:** Critical areas for high-temperature failure in coal-fired power plants (Adapted from Wilson (1990)).

	<b>Area</b>	<b>Life-limiting factor</b>
<b>Boilers</b>	Drums	Creep and thermal fatigue
	Headers	Creep and thermal fatigue
	Furnace wall, superheater, reheater tubing	Fireside and waterside corrosion
<b>Pipework</b>	Main and reheater pipes	Creep and thermal fatigue, weld and HAZ cracking
<b>Turbines</b>	All rotors	Creep and thermal fatigue
	Low pressure rotors and turbine blades	Fretting fatigue, corrosion fatigue, stress corrosion and pitting etc., temper embrittlement
	Steam chests and casings	Creep and thermal fatigue
	Elevated temperature boltings	Creep and thermal fatigue, stress corrosion

### 2.6.1 Current Remaining Life Assessment Procedures

The methods available for assessing remaining life of power plant components can usually be divided into two broad categories (Wilson 1990):

1. Monitoring of operational parameters (temperature, pressure, steam data, etc.) and the use of collected data in combination with standard materials data and the

life fraction rule (Section (ii) below) to determine an estimate of the available life of the component.

2. Examination of the component material either during service in the form of external inspection, plant outage using non-destructive testing (NDT) or other more detailed investigations. In the latter case, crack detection, on plant strain measurement and non-destructive removal of small test specimens can be carried out. These small test specimens are then used for microstructural, bulk physical (e.g., crack examination) or mechanical (e.g, accelerated creep rupture tests) analyses.

An actual power plant life-management strategy will include procedures of both types.

### **(i) Method based on operational data monitoring (Category 1)**

During a planned plant outage, the first life estimate calculations performed by a power plant company are carried out using master curves since only the operating parameters are available at that stage (category 1 above) (Molokwane 2014). The standard PD 6525 (1990) used for these curves defines the master curve for a steel as a representation of the average rupture stress values over the range of time, temperature and stress values used in the assessment as a function of stress. This is given in the form of a time and temperature parameter, as follows:

$$P(\sigma) = a + b(\log \sigma) + c(\log \sigma)^2 + d(\log \sigma)^3 + e(\log \sigma)^4 \quad (2.11)$$

$$P(\sigma) = \frac{\log t_r - \log t_a}{(T - T_a)^r}$$

where  $P(\sigma)$  is the stress rupture parameter,  $\sigma$  the stress (in N/mm<sup>2</sup>),  $a$  to  $e$  are constants,  $r$  is the temperature exponent, normally with values of -1 or 1,  $T$  is the temperature (in K),  $t_a$  and  $T_a$  are material constants, and  $t$  is the time to rupture (in h), and. The life estimates determined using master curves is strongly operating conditions (temperature and stress) dependent. This phenomenological model (see Section 2.7.1) is more sensitive to the time-temperature relationship than for example the Larson-Miller (Larson and Miller 1952)

approach since the parameter is composed of two constants that relate time to temperature. However, the physical meaning of  $t_a$  and  $T_a$  is unknown and their representation unclear (Abdallah, Gray, Whittaker and Perkins 2014, Abdallah, Perkins and Arnold 2018).

## (ii) Method using post-service material (Category 2)

The second stage of life management usually involves replica lifting from component and weldment surface (Molokwane 2014). Metallographic surface replication is used extensively by Eskom as a quantitative non-destructive assessment of creep damage and any other damage to determine the remaining life of their high-temperature components (Van Zyl, von dem Bongart, Bezuidenhout, Doubell, Havinga *et al.* 2005). This technique also allows for in-situ measurements of the microstructure of both etched and polished specimens. A schematic illustration of the technique is shown in **Figure 2.26** and a full description of the technique is provided.

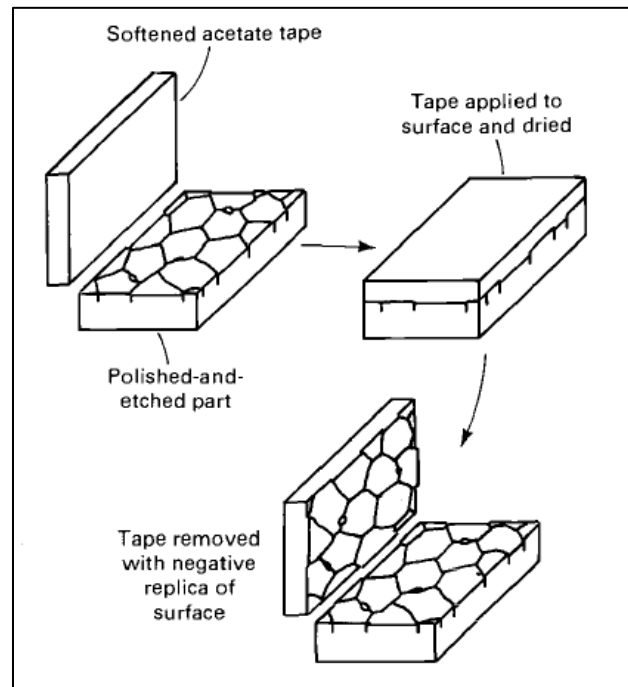


**Figure 2.26:** Schematic illustration of the surface replication technique (Marder 1989).

Before replication, the surface is cleaned from any corrosion or oxidation product, or decarburized layer that may have developed during service. This step is usually

performed with coarse grinding equipment while ensuring proper precautions are taken to not introduce any artefacts into the structure due to overheating or plastic deformation. After this initial preparation steps, standard mechanical polishing techniques are applied. Finally, the microstructure is revealed by applying the appropriate etchant for the specific material (Marder 1989, Molokwane 2014).

Both plastic and oxide material can be used for the technique. Plastic (acetate film) methods are the least destructive and do not require any further preparation to make additional replicas. The replicas provide an image of the surface topography of the specimen and are examined under an optical microscope. The microvoid damage is quantified at a magnification of 400x. However, qualification of the voids may be done at higher magnifications. The voids are counted and expressed as the number of voids per  $\text{mm}^2$ . Any other information related to the microstructure such as inclusions, shape, density and associated voids is also recorded. It is also possible with further sample preparations to examine the replicas in an electron microscope (Van Zyl, von dem Bongart, Bezuidenhout *et al.* 2005, Molokwane 2014).

Section 2.3.6 explains that micro (sub-microscopic) cavities with diameters less than  $0.1 \mu\text{m}$  initiate as early as 10 percent of the creep rupture life of the material. Some of these voids will grow during further creep exposure and become visible under an optical microscope at a magnification of 400x when they have reached a size of  $1 \mu\text{m}$  ( $\pm 0.5 \mu\text{m}$ ) (Van Zyl, von dem Bongart, Bezuidenhout *et al.* 2005). This is typically observed for low alloy and 12CrMoV steels where at life fractions consumed of between 0.2 and 0.5, the strain rate is less than  $10^{-6} \text{h}^{-1}$ .

During the secondary creep stage, the microcavities have an insignificant contribution to the strain rate due to their small volumes. In contrast, the creep voids visible at 400x increases slowly both in number and size (until  $\pm 0.7$  of life). In the tertiary creep stage (after 0.8 of life), the number of voids visible at 400x increases negligibly, but there is a rapid size increase due to their coalescence to form a macrocrack. These observations follow from metallographic replica data from more than 30 years ago (Van Zyl, von dem Bongart, Bezuidenhout *et al.* 2005, Tabuchi, Hongo, Watanabe *et al.* 2009).

A damage model that includes constrained cavity growth (Section 2.3.6) is used to determine the remaining life fraction (Van Zyl, von dem Bongart, Bezuidenhout *et al.* 2005):

$$\frac{t}{t_r} = \left[ 1 - \left( 1 - \frac{N}{N_f} \right)^\lambda \right] \quad (2.12)$$

where  $t$  is the exposure time (in h),  $\lambda$  is the creep ductility parameter,  $N$  is the number of voids/mm<sup>2</sup> and  $N_f$  is the number of voids/mm<sup>2</sup> at fracture. In this model,  $N_f$  is generally limited to 1000 voids/mm<sup>2</sup> and  $\lambda$  is 3.4 (Molokwane 2014), but in practice it could develop to a few thousand voids/mm<sup>2</sup> before crack formation and development occurs in the component.

If the life fraction and corresponding void fraction are known,  $\lambda$  can be calculated. This parameter will be different for a weldment compared to the parent material since they have different material properties. The value of  $\lambda$  is conventionally determined from the knowledge gained from years of metallographic work and post exposure tests. For examples, it is well documented that for low alloy steels and 12CrMoV, creep voids become visible ( $N \approx 50 - 100$  voids/mm<sup>2</sup>) when a life fraction of between 0.3 and 0.55 has been expended, provided the exposure time has been more than 100 000 h (Van Zyl, von dem Bongart, Bezuidenhout *et al.* 2005). The reason is that creep voids appear later for shorter exposure times. For life assessment of X20 steel components,  $\lambda$  is assumed to be 3.4 for the parent material (Molokwane 2014).

The evolution of creep cavitation at the different creep stages is illustrated in **Figure 2.27**. As can be seen, the creep cavitation evolution can be classified into four stages (Gupta, Toda, Mayr and Sommitsch 2015):

- (A) isolated cavities
- (B) oriented cavities
- (C) linked cavities
- (D) macro cracks



The interpretation of the remaining life estimates or outage philosophy of a power plant company is summarised in **Table 2.9**.

The limitations of the damage model (Equation (2.12)) are (Van Zyl, von dem Bongart, Bezuidenhout *et al.* 2005):

- (i) Poor fitting over the entire creep curve, as well as between curves of different creep rupture lives.
- (ii) Inaccurate accounting for voids in a non-constraint cavity growth situation.

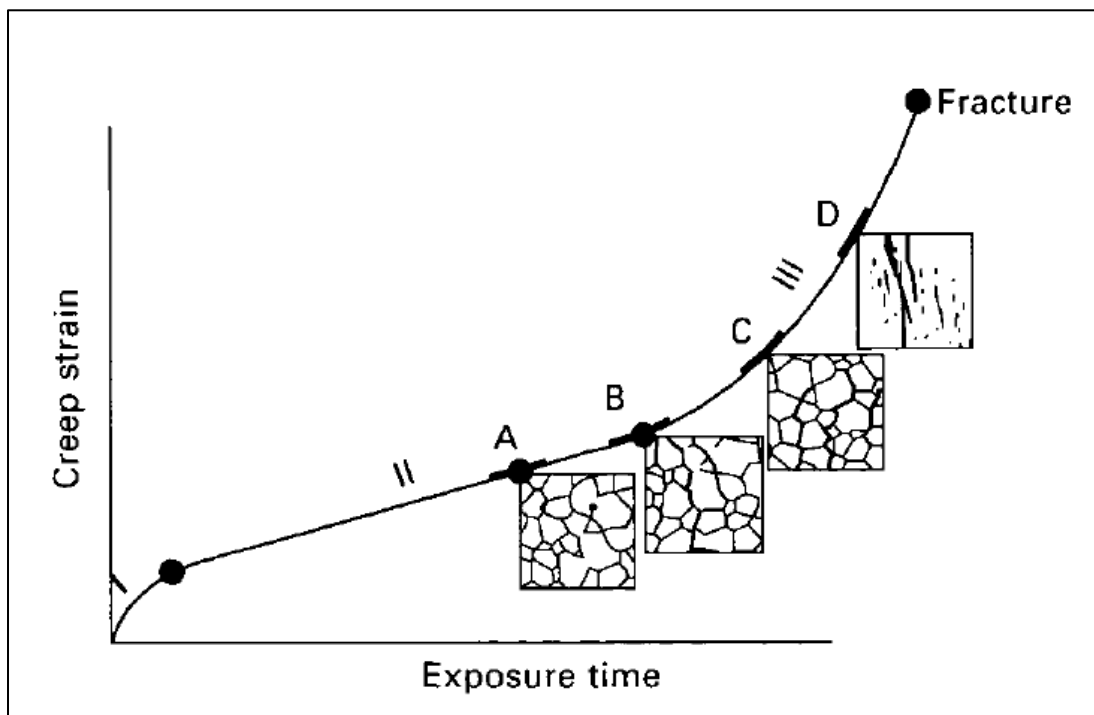


**Figure 2.27:** Cavitation evolution at different stages of creep life as determined from surface replication (Gupta, Toda, Mayr and Sommitsch 2015).

**Table 2.9: Power plant component life philosophy (Molokwane 2014).**

Damage Classes	Remaining years calculated	Default Recommendations
<p style="text-align: center;"><b>CLASS 1</b></p> <ul style="list-style-type: none"> <li>• Component at the end of its useful life.</li> <li>• Not manageable inside the outage philosophy.</li> <li>• High risk of failure with continued operation.</li> </ul>	<p style="text-align: center;">Less than 3 years</p>	<ol style="list-style-type: none"> <li>1. Replace immediately. Do not operate further.</li> <li>2. Maybe limit operation with full risk assessment and special mitigation measures.</li> </ol>
<p style="text-align: center;"><b>CLASS 2</b></p> <ul style="list-style-type: none"> <li>• Component approaching end of its useful life.</li> <li>• Still manageable inside outage philosophy.</li> <li>• Plan replacement and operate within design.</li> </ul>	<p style="text-align: center;">3 – 9 years</p>	<ol style="list-style-type: none"> <li>1. Replace within 3 years.</li> <li>2. Investigate all excursions and dynamic events.</li> </ol>
<p style="text-align: center;"><b>CLASS 3</b></p> <ul style="list-style-type: none"> <li>• Damaged component with significant remnant life.</li> <li>• Safely manageable by inspections.</li> </ul>	<p style="text-align: center;">10 – 18 years</p>	<ol style="list-style-type: none"> <li>1. Inspect within 3 years.</li> <li>2. Operate within design and maintain within Eskom philosophy.</li> </ol>
<p style="text-align: center;"><b>CLASS 4</b></p> <ul style="list-style-type: none"> <li>• Component without damage.</li> <li>• Manageable within outage intervals.</li> </ul>	<p style="text-align: center;">More than 18 years</p>	<ol style="list-style-type: none"> <li>1. Inspect mostly within 6 years if past design life.</li> <li>2. In exceptional cases, inspection intervals could be extended to 9 years.</li> </ol>

The main advantage of surface replication is that it can give warnings of severe creep damage at critical areas inexpensively and quickly, and without requiring knowledge of the thermal history of the component. However, it has been observed that microstructural damage rather than creep void cavity formation is the predominant damage mechanism found in practice in steam headers and therefore surface replication is not a representative creep life prediction technique (Wilson 1990).

Also, Tabuchi, Hongo, Watanabe *et al.* (2009) have shown that for a 9% Cr steel welded component, creep voids mostly formed at an area 20% below the surface, within the plate thickness. Subsequently, this highlights the main problem with surface replication that only examines the surface for creep damage. As mentioned in Section 2.5.1, it is crucial that stress triaxiality is considered for accurate life prediction and damage evaluation in martensitic creep-resistant 9-12% Cr steels. Equation (2.12) does address this factor to some extent since this equation considers constrained cavity growth.

## 2.7 CREEP MODELLING

Most creep models are based on the fundamental power-law for creep (Equation (2.3)). This section aims to provide a literature review on creep models applicable to martensitic creep-resistant 9-12% Cr steels. Existing creep models, both physical and Continuum Damage Mechanics (CDM) based for BM and FGHAZ, are reviewed for evaluating:

- Dislocation density evolution during creep
- Micro-grain evolution during creep
- Creep strain
- Backstress from microstructural contributions
- Creep rupture life estimation using the conventional methods

Creep models have a two-fold purpose to either predict

- (i) the ultimate or remaining life of a material or
- (ii) the (creep) deformation rate or total deformation at a well-defined point in time (Krenmayr and Sonderegger 2016).

Due to the demanding nature of experimental creep tests, the development and application of creep models are motivated strongly by the desire to minimise experimental effort. Regrettably, creep modelling has been found to be a complex task since creep deformation strongly depends on the type of material, the material history and the applied loads. **Table 2.10** summarises the potential input parameters to be included in a creep model.

**Table 2.10:** Potential input parameters to be included in a creep model (Krenmayr and Sonderegger 2016).

<b>External Parameters</b>	<b>Internal Parameters: Material Constants</b>	<b>Internal Parameters: Microstructural Contributions</b>
<p>Temperature (may be time-dependent)</p> <p>Stress (may be time-dependent, as well as uniaxial or multiaxial)</p>	<p>Young's modulus</p> <p>Yield strength (temperature dependent)</p> <p>Lattice constants and structure (temperature dependent)</p> <p>Chemical composition</p>	<p>Grain boundary types</p> <p>Grain size or distribution</p> <p>Dislocation density (mobile, boundary or dipole)</p> <p>Precipitate type, size, number density, volume fraction</p> <p>The relation between individual microstructural contributions</p> <p>Inhomogeneities</p> <p>Texture effects</p>

Specific material conditions such as “as-cast”, “as-received”, “as-welded”, “post-weld heat treated” or FGHAZ can be automatically included by adapting the existing creep models:

- In the case of extrapolation methods and phenomenological models, selecting appropriate material constants or fit parameters or
- In the case of physically-based or semi-physical models, selecting suitable material constants and microstructural parameters.

Most existing creep models model only the behaviour of either the primary, secondary or tertiary creep stage. Spatially resolved simulation of the deformation of a component is not in general included in a basic creep model, but such a model instead describes the behaviour of a macroscopically uniform piece of material and assumes the external parameters to be homogenous. Nonetheless, creep modelling can be potentially implemented in a finite element simulation in order to simulate component performance (Krenmayr and Sonderegger 2016). This literature review aims to describe creep models and not the implementation of these models in simulations.

From literature, creep models can be divided into two main categories (Krenmayr and Sonderegger 2017):

### **1. Phenomenological creep models**

Specific creep mechanisms are not usually considered in these models. They are preferably based on analytical functions that describe the creep rate or ultimate lifetime of a material. These functions are convenient to implement and supported by macroscopic creep test results. The problem, however, is that they rely strongly on experimentally determined fit-parameters. These parameters may be dependent on conditions such as temperature, stress, material type and material history and therefore they may not be constant. Consequently, the predictivity of phenomenological models are limited. Still, these models have shown to be useful if the conditions remain close to those of the initial experimental conditions.

## 2. Physically-based or semi-physical creep models

These models have the potential to take into account physical parameters such as material type, material history, temperature, stress and initial microstructure in order to describe the microstructure, the microstructural evolution and the link between microstructure and macroscopic properties. Subsequently, the prediction capability of physically-based models reaches further than phenomenological models. There are, however, two main drawbacks to these models. Firstly, the microstructure cannot be fully accounted for due to its vast complexity and therefore a physically-based model still gives only an approximation. This also means that a few fit-parameters are incorporated into these models. Therefore, it is more accurate to refer to these models as “semi-physical creep models”. The second disadvantage is that the computing time required to implement these models are much higher than that required for the phenomenological models. “Microstructure-based creep models” can also be used to refer to the semi-physical creep models that require microstructural data as input.

For understanding the effect of initial microstructure on creep properties, it follows that semi-physical models are the only option. If these models are implemented correctly and reasonably complete regarding creep phenomena, they have the potential to consider effects that alter the initial microstructure such as chemical composition, heat treatment, welding and PWHT.

There are some cases where a specific creep model may have characteristics of both categories and therefore cannot be clearly classified into a single group. **Figure 2.28** provides a schematic diagram to illustrate the main difference between phenomenological and physical creep models when considering the processing-microstructure-property relationship of a material. Phenomenological models use processing parameters as input to predict the creep life of the material, while physical models use processing parameters to obtain the microstructure to use as input to provide the same output.

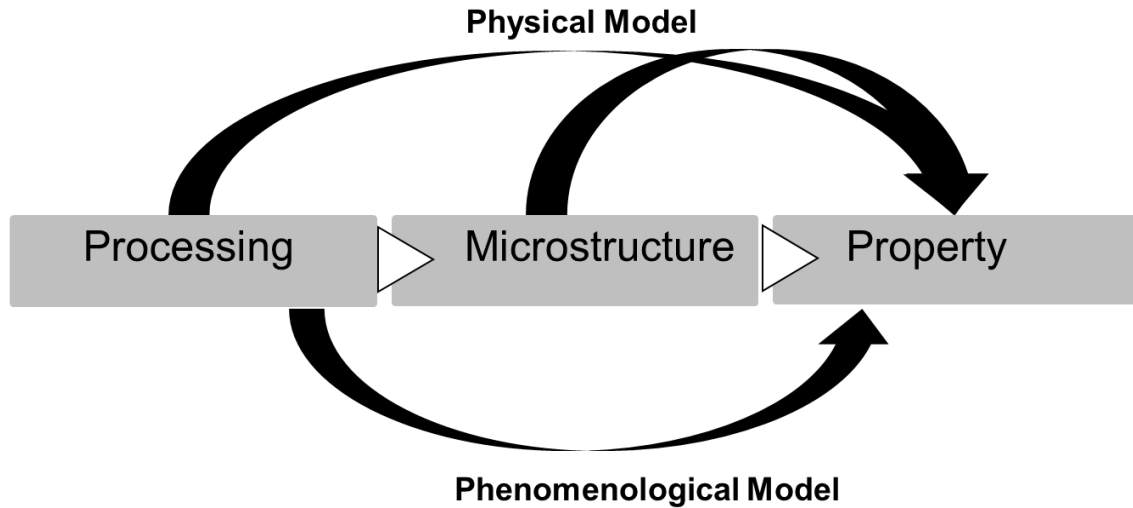


**Figure 2.28:** Illustration of the main difference between phenomenological and physical creep models.

The succeeding sections are split between conventional phenomenological creep models (extrapolation methods), other phenomenological creep models and semi-physical (microstructure-based) creep models. Since there is a vast amount of literature on the different creep models developed to date, this review will only include models mostly used in literature. It is important to be aware of the limitations and inherent assumptions of a creep model. These limitations and assumptions are included in the discussions to follow.

## 2.7.1 Phenomenological Creep Models

### (i) Extrapolation Methods

Extrapolation methods are the most widely used conventional phenomenological creep models for creep life prediction of power plant components. Specifically, the Monkman-Grant (1956) and Larson-Miller (Larson and Miller 1952) methods are the most recognised extrapolation methods. The application of these methods is straightforward as soon as the correct fit-parameters have been determined. Since they are phenomenological models, their applications are limited to cases with similar conditions for which the assessment has been completed. The assessment is usually performed with short-term (uniaxial) creep test results (up to about 1 000 h) and then the extrapolation is then applied to long-term (up to about 100 000 h) to predict long-term

creep strength. The main assumption of the Monkman-Grant relationship is that the fracture of creep-deforming materials in uniaxial tension under constant stress is controlled by the steady-state creep rate.

The Monkman-Grant approach does not include temperature. Extrapolation methods that introduce temperature dependence are known as time-temperature parameter (TTP) methods and the Larson-Miller relation is the most widely used TTP method (Viswanathan 1989).

Heinemann, Linn, Scwienheer, Kontermann and Oechsner (2017) quantified the extrapolation quality of the various extrapolation methods and found that the Monkman-Grant generates consistently higher quality factors than any other methods.

Extrapolation always has the risk of under- or over-estimation due to change of microstructure or creep mechanisms. Thus, systematic errors will be introduced by the extrapolation method in both cases. It has become clear that extrapolation methods tend to over-predict the long-term creep strength of the material because of microstructural degradation phenomena. Dimmler, Weinert and Cerjak (2008) identified a change in creep mechanism with applied stress in the creep rupture curves of 9-12% Cr steels. Therefore, they conclude that there is a considerable potential for over-estimation of creep strength from extrapolated short-term creep rupture data. This finding is reasonable since the extrapolation methods usually assume only a single creep mechanism to be operating during the material lifetime.

The newest developed extrapolation model to date is the Parametric Numerical Isothermal Datum (P-NID) method. Bolton (2017) describes and applies this model to different datasets and found that it provides a very reliable basis for analysis and extrapolation of creep rupture data. This method is even shown to be more reliable than the ECCC recommended extrapolation procedures.

Neural network analysis, a form of regression or classification modelling, is suggested as a better method to extrapolate short-term creep data. An extensive review is provided by (Bhadeshia 1999).



## (ii) Other Phenomenological Creep Models

The Monkman-Grant and Larson-Miller extrapolation methods and their combination predict the ultimate lifetime of the material. Other phenomenological models determine either the strain or strain rate at a specific point of time. These models are preferably suitable for fitting already quantified creep curves and not for extrapolating creep behaviour to long-term creep life. Therefore, these models are mostly used as simple models for implementation in finite element (FE) simulation of components.

Some of these phenomenological models are creep regime specific. Holdsworth, Askins, Baker, Gariboldi, Holmström *et al.* (2008) performed an extensive literature study on phenomenological creep models and summarised the most widely used models according to their creep regime application. However, all these models are mostly empirical and provide minimal microstructural or micromechanical information. Each one of these creep models depends on material parameters that must be experimentally determined. These models can include temperature dependence by simply adding Equation (2.1) to the creep model equation.

It also followed from the Holdsworth, Askins, Baker *et al.* (2008) study that the most suitable phenomenological creep models for application on P91 steel are:

1. Modified Graham-Walles Model (McHenry 1943)
2. Bolton Characteristic Strain Model (Bolton 1995)
3. MHG Model (Manson and Haferd 1953, Grounes 1969, Holmstrom and Auerkari 2004)

They also calculate and compare Z-parameter values for the different models, which is an indication of the model-fitting effectiveness.

Another critical review on conventional phenomenological creep models has been done by Abdallah, Gray, Whittaker and Perkins 2014, Abdallah, Perkins and Arnold (2018) and can be consulted in addition to Holdsworth, Askins, Baker *et al.* (2008) for descriptions on the various models. Ito, Yajima and Arai (2018) developed a method to use high-

temperature indentation creep testing to determine the creep coefficient and creep exponent in Norton's Law. They found that the creep life could be predicted with high accuracy.

### **(iii) Multiaxial Models**

As can be seen from the previous sections, many years of research has been on understanding damage and quantifying it to predict creep rupture and crack initiation and growth. The previously discussed phenomenological creep models are all uniaxial damage models that use constituent components of the stress/strain measured data which have inherent scatter. Multiaxial creep damage models are computationally intensive and can be classified into two groups:

1. Multiaxial ductility-based models that relate the stress state by a constraint parameter to multiaxial ductility (Rice and Tracey 1969, Cocks and Ashby 1980, Spindler 2004, Yatomi and Nikbin 2014, Biglari and Nikbin 2015, Wen, Tu, Xuan, Zhang and Gao 2016)
2. Numerically intensive Continuum Damage Models (CDM) that use different types of constraint factors to predict multiaxial failure, e.g. Type IV cracking (Perrin and Hayhurst 1999, Hayhurst 2001, Wen, Tu, Xuan *et al.* 2016).

An extensive review of the multi-axial creep damage constitutive equations and their applications are given in the study of Yao, Xuan, Wang and Tu (2007). Also included is an extensive review of the CDM-based methods. They identified two advantages of multi-axial damage models:

1. Multi-variables are introduced to distinguish different creep mechanisms and effects on damage evolution.
2. A sinh-function is included to replace the conventional power law and to describe the stress sensitivity of creep rates over a wide range of stresses.

From their results, it is concluded that an inverse relation exists between multiaxial constraint and failure strain. Although CDM models are scientifically relevant and fundamental in their approach, they usually are analytically complex or numerically intensive in order to make them universally applicable. Alang and Nikbin (2017) proposed a unifying multi-scale, remaining strain based empirical model that is simple in its implementation and can predict creep damage and rupture over a wide range of stress states and constraint levels. This proposed model simplifies to a linear inverse relationship that relates the microstructurally based remaining multiaxial strains to the local constraint which develops at grain boundaries due to diffusional void growth under hydrostatic pressure and other complex time-dependent creep damage mechanisms. Hence, an appropriate stress to rupture based on the local sub-grain constraint level can be derived. This model has shown to successfully predict uniaxial rupture over 100 000 hours and in notched bars.

### **2.7.2 Semi-Physical Creep Models**

The discussions of the preceding sections give some background on creep modelling. In this section Research Objective 2 “*to review existing microstructure-based creep-models*”, is addressed. The expected lifetime of power plant components is in reality based on the ability of the material to retain its high-temperature creep strength for a time period of at least twice the projected design life (Sklenička, Kuchařová, Svoboda *et al.* 2003). Consequently, creep property assessment methods that are based on the physical changes that are likely to occur in the material during service exposure is required rather than a simple parametric extrapolation of the short-term data.

Semi-physical or microstructure-based creep models all have the main aim of modelling the microstructural changes during creep exposure. They are developed to go some way to explain and predict the observed microstructural changes during creep and their effect on creep strength. Only the ones applicable to this study is further discussed in this section.

As mentioned in 2.3, the steel evolves towards a thermodynamically more stable condition during creep exposure. There has been the development of computer models

that use to available thermodynamic data as input to predict this thermodynamically stable combination of phases in the steel, which is the equilibrium condition where free energy is at a minimum. This is often referred to as *computational thermodynamics*. The result of such models is equilibrium phase diagrams that forecast the phases present and their fraction as a function of temperature. In addition, the chemical composition can also be predicted (Sklenička, Kuchařová, Svoboda *et al.* 2003).

The microstructure evolves slowly towards a state of equilibrium due to the slow kinetics governing many of the evolutionary processes. Therefore, models that describe the microstructural kinetics are required in order to fully understand and predict the rate of evolution (Sklenička, Kuchařová, Svoboda *et al.* 2003). When computer codes for general kinetic simulation are combined with computational thermodynamics, then *computational thermokinetics* can be introduced in all alloying systems where the necessary thermodynamic and mobility information is available (Kozeschnik 2013).

Thermo-Calc is a software package that has been used over the past 30 years for thermodynamic calculations. Significant attempts have been made to model the nucleation and growth precipitation kinetics (Sklenička, Kuchařová, Svoboda *et al.* 2003). To date, the following software packages (computer codes) are available for general precipitation kinetics and phase transformation simulations:

- Released 1994: DICTRA (Thermo-Calc Software Inc. 2018) – a Thermo-Calc diffusion module used for multicomponent phase transformation modelling by simulation of the diffusion-controlled reactions in a multicomponent alloy system.
- Released 2004: PrecipiCalc® (PRECIPitation CALCulation for Materials/Process Design and Optimization) (QuesTek Innovations LLC 2013) – calculates the 3D multiparticle diffusive precipitation kinetics of multi-phase systems.
- Released 2004: *MatCalc*® (Materials Calculator) (MatCalc® Engineering 2018) - computer simulation of phase transformations and microstructural evolution in metallic systems.

- Released 2010: PanPrecipitation (CompuTherm: For Materials Design 2018) – module from Pandat™ computation tool for simulation of precipitation kinetics during the heat treatment process.
- Released 2011: TC-PRISMA (Thermo-Calc Software Inc. 2018) - a Thermo-Calc precipitation module used for simultaneous nucleation, growth or dissolution, and coarsening of precipitates under arbitrary heat treatment conditions in both multi-component and multi-phase systems.

In most of these simulations, the CALPHAD (Computer Coupling of Phase Diagrams and Thermochemistry) (Spencer 2008) approach and databases are used which are available for many types of alloying systems and forms the basis for developing of models using computational thermodynamics or thermokinetics. These databases store reliable thermodynamic data in the form of Gibbs free energies of individual phases as a function of chemical composition, temperature, and sometimes pressure. An overview of each simulation package is provided by Kozeschnik (2013).

The goal itself is not understanding and predicting microstructural evolution, but instead to model the link between microstructure and creep strength (**Figure 2.28**). Subsequently, these models can then be implemented to predict creep strength. Modelling of the accumulation of creep strain as a function of microstructural parameters has been done. These models are not entirely accurate yet and still require further validation or development. Thus, the platform is open for a combined model which will be able to predict the creep strength from knowledge of the chemical composition and heat treatment (Sklenička, Kuchařová, Svoboda *et al.* 2003). This has been the main focus in recent years for microstructure-based creep modelling developments. In order to validate existing microstructure-based models, a more quantitative description of the microstructure is necessary.

For a complete description of the microstructure, quantitative measurements of many parameters are required. These parameters include:

- The chemical composition of the matrix;

- dislocation density (mobile and/or dipole and/or boundary);
- subgrain size;
- size, shape and chemical composition of each precipitate type at each of the characteristic locations within the microstructure (PAGB, MGB and SGB).

These parameters need to be known at the start of service life, as well as their evolution during operation until the point of rupture. Models that link the microstructure to creep behaviour also require further development to take into account the influence of SSH (Sklenička, Kuchařová, Svoboda *et al.* 2003).

Microstructure-based (physical) models, in general, have a great potential to provide powerful necessary tools for material development and use. Nonetheless, to provide the reliable thermochemical, thermodynamical and diffusion data required and to develop a microstructural database for validation, further research is necessary to extend and combine current semi-physical creep models. Vanstone (2001) has proposed an approach to combine thermodynamical, kinetic and creep modelling to predict the creep strength. The approach is illustrated in **Figure 2.29**.

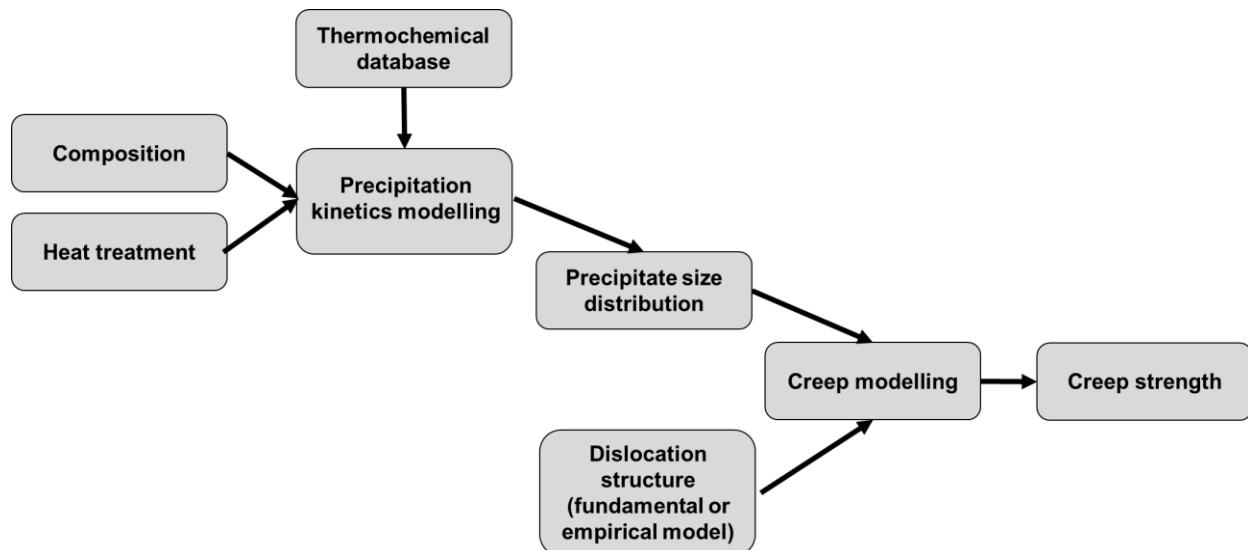


**Figure 2.29:** A proposed combination of thermodynamic, kinetic and creep modelling to predict creep strength (Adapted from Vanstone (2001)).

Some semi-physical creep models that have been used to predict microstructure-creep property relationships in martensitic creep-resistant 9-12% Cr steels are now reviewed.

### (i) Back-Stress Model

The *back-stress concept* is motivated by previous microstructure models on the yield strength such as that of Norström (1976). These models share the general idea that the yield strength is associated with plastic deformation, which can only occur if an external force exceeds the yield strength. In turn, the yield strength can be seen as the sum of “backholding stresses” originating from the different counteracting constituents such as precipitates and interfaces (boundaries) of the internal microstructure. Thus, only the part of the external stress  $\sigma_{ex}$  that exceeds the back-stress (long-range inner stress)  $\sigma_i$  from the counteracting microstructural constituents, contributes effectively to the creep process. Therefore, it follows that the actual creep stress  $\sigma_{eff}$  can be given by (Kozeschnik and Holzer 2008):

$$\sigma_{eff} = \sigma_{ex} - \sigma_i \quad (2.13)$$

Consequently, this effective stress is defined as the remaining amount of applied stress that is available for creep deformation and responsible for the movement of mobile dislocations over thermal barriers (Barkar and Ågren 2005).

Dimmler (2003) expresses the back-stress  $\sigma_i$  as a superposition of individual microstructural contributions from the dislocations and the precipitates. If the contribution from the MGBs, i.e., SBH, are also taken into account, then the following equation can be derived for the back-stress  $\sigma_i$  :

$$\sigma_i = M \cdot \sum \tau_i = M \cdot (\tau_{DH} + \tau_{Or} + \tau_{SBH}) = \sigma_{DH} + \sigma_{Or} + \sigma_{SBH} \quad (2.14)$$

where  $M$  is the Taylor factor, usually between 2 and 3 (Holzer 2010),  $\sigma$  are the individual back-stress contributions, and  $\tau$  is the shear stress.

By including the Taylor factor  $M$  to determine the back-stress  $\sigma_i$ , the derived structure-property models are extended to polycrystalline behaviour. The Taylor factor relates the macroscopically imposed strain to the total slip on all active glide planes in the grains and therefore the macroscopic flow stress  $\sigma$  to the acting shear stress  $\tau$  in all the slip systems (Roters, Raabe and Gottstein 2000). Hence, these models can be classified as macro-mechanical models. The individual back-stress contributions can be obtained by quantifying the strengthening mechanisms discussed in Sections 2.3.2 to 2.3.5. This is illustrated in the next sections. It should be noted that the back-stress concept is based on dislocation creep mechanisms. **Table 2.11** contains the values of the Taylor factor, shear modulus and Burgers vector for X20CrMoV12-1 stainless steel operating at 550°C.

**Table 2.11:** Summary of creep strength parameters for an X20CrMoV12-1 (DIN 17175) steel operating at 550 °C (Constructed from Aghajani, Somsen and Eggeler (2009)).

<b>Parameter</b>	<b>Symbol</b>	<b>Value</b>
<b>Taylor factor</b>	$M$	3
<b>Shear modulus</b>	$G$	65 GPa
<b>Burgers vector</b>	$b$	$2.5 \times 10^{-10}$ m

### ***Precipitate Hardening***

As discussed in Section 2.3.2, PH is one of the most critical and effective strengthening mechanisms in 9-12% Cr martensitic steels. The direct interaction between a precipitate and dislocation needs to be considered to determine the back-stress contribution from the precipitates. Due to the character of the precipitates in these steels, it is assumed that the precipitates are not cut by the mobile dislocations (Holzer 2010).

In the case of incoherent or semi-coherent precipitates, there are two main governing interactions for the dislocation to bypass the precipitate: general or local climb, and



Orowan mechanism or dislocation looping (Abe 2008). It is these mechanisms that have the most significant contribution to creep deformation. Diagrams illustrating these mechanisms are given in **Figure 2.30**. The difference between these mechanisms is that the Orowan mechanism has little temperature dependence and becomes operative only under higher loads, while the climb mechanisms determine the strain rate at higher temperatures and lower stresses. A concise description of these mechanisms is given by Holzer (2010).

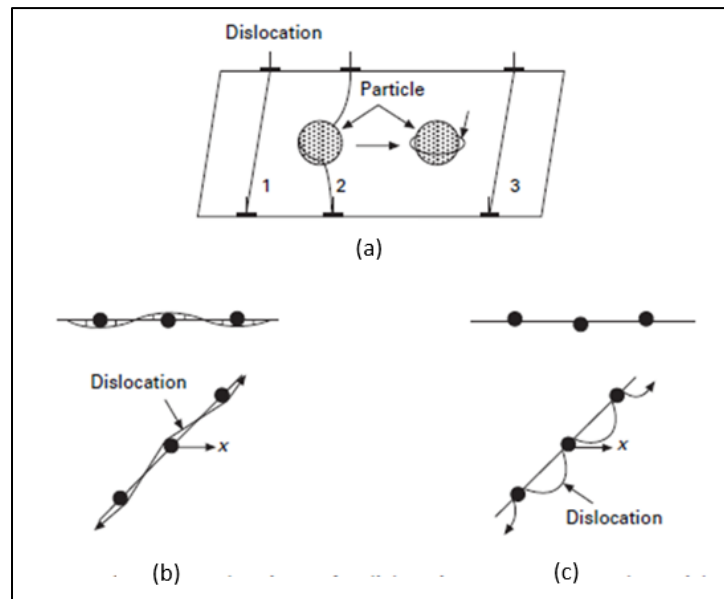


**Figure 2.30:** Schematic illustration of how a dislocation will pass precipitates by (a) the Orowan mechanism, (b) the general climb mechanism and (c) the local climb mechanism (Abe 2008).

When a dispersion of particles intercepts the glide plane of a dislocation, a threshold stress for dislocation glide is introduced. In the case of both mechanisms, the crucial parameter governing the level of this back-stress is the interparticle spacing  $\lambda$ . This parameter indicates the surface-to-surface distance between two particles in the slip plane of a dislocation and is not a constant according to Ashby (1968), but rather provides a probability distribution. Nevertheless, Kocks (1966) has shown that plastic deformation can only effectively take place when at least one third of the mobile dislocations can overcome the threshold stress. The combination of these two criteria and assuming

equally sized particles results in the following formula to determine the mean 2D surface-to-surface interparticle spacing (effective 2D particle distance)  $\lambda$  (Holzer 2010):

$$\lambda = \sqrt{\frac{\ln 3}{2\pi N_V \bar{r}} + 4\bar{r}^2} - 1.63\bar{r} \quad (2.15)$$

where  $\bar{r}$  is the mean particle radius and  $N_V$  is the number density (number of particles per unit volume). Even though the 3D surface-to-surface distance is an important microstructural parameter, it is this 2D distance that is the one necessary for strength contribution of the precipitates since it gives the mean particle distance in the slip plane of the dislocation. Equation (2.15) is derived on the assumption that the particles are spherical and randomly distributed.

In the case of Orowan looping (Figure 2(a)), the back-stress is defined as the Orowan stress  $\sigma_{Or}$  (Holzer 2010). This Orowan stress  $\sigma_{Or}$  is described as (Abe 2008, Aghajani, Somsen and Eggeler 2009):

$$\sigma_{Or} = \frac{0.8MGb}{\lambda} \quad (2.16)$$

where  $M$  is the Taylor factor,  $G$  is the shear modulus and  $b$  is the Burgers vector (**Table 2.11**). A more detailed illustration of the Orowan mechanism is provided in **Figure 2.31**. The effect of precipitate coarsening due to creep exposure to reduce dislocation pinning and loop formation is also shown. It should be noted that dislocation climb reduces the Orowan back-stress since the number of non-climbed particles decreases.

Ahmadi, Povoden-Karadeniz, Öksüz, Falahati and Kozeschnik (2014) revised the standard precipitation strengthening models and combines them into a new model that accounts for shearable particles and coherency effects, which are not relevant to 9-12% Cr steels. They conclude on the final formulation for the Orowan threshold stress:

$$\tau_{Or} = \frac{JGb}{2\pi\lambda(1-\nu)} \cdot \ln \frac{2r_s}{r_i} \quad (2.17)$$

where  $\tau_{Or}$  is the shear stress related to Orowan looping,  $J$  is a correction factor for specific arrangements of precipitates (random versus ordered, 0.8 – 1.0),  $\nu$  is the Poisson ratio of the matrix,  $r_s$  is the equivalent radius of the precipitates and  $r_i$  is the inner-cut-off distance of dislocations. This model has been implemented in the MatCalc software (Section 2.4.3).

Since more than one precipitate types are contributing to PH, the mean interparticle spacing  $\lambda$  can be defined as follows using the approach of Magnusson and Sandström (2007):

$$\frac{1}{\lambda^2} = \sum \frac{1}{\lambda_k^2} \quad (2.18)$$

where  $\lambda_k$  is the mean interparticle spacing determined by Equation (2.15) for each precipitate type  $k$ .

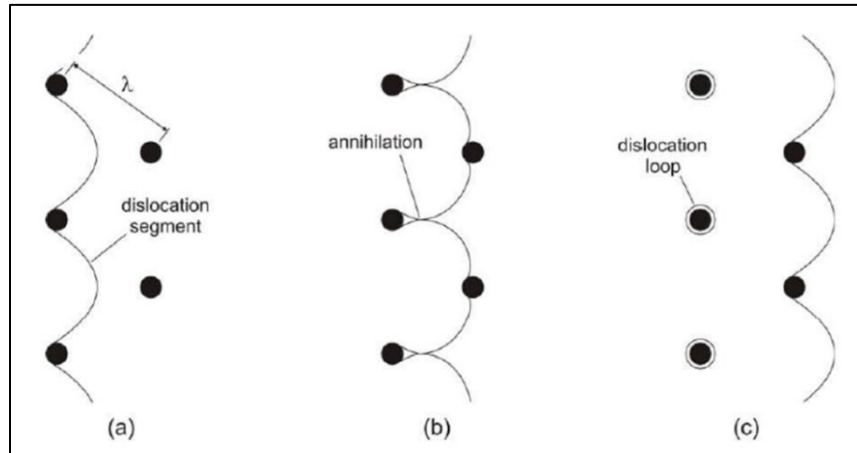


**Figure 2.31:** Detailed illustration of the bypass of strong precipitates by a dislocation according to the Orowan mechanism, where the mean interparticle spacing is given by  $\lambda$  (Holzer 2010).

### ***Dislocation Hardening***

DH is associated with the mobile dislocations (Section 2.3.4). The contribution of these dislocations to the creep strength by DH can be quantified as follows:

$$\sigma_{DH} = 0.5 M G b \sqrt{\rho_m} \quad (2.19)$$

where  $\rho_m$  is the mobile dislocation density, and  $M, G$  and  $b$  are the same as in Equation (2.16). As motivated in Section 2.3.4, at elevated temperature, DH is only useful for short-term creep strength and not for long-term creep strength.

### ***Sub-Boundary Hardening***

The HAGB are overall impenetrable by mobile dislocations and therefore act as major obstacles against dislocation motion during creep, therefore, contributing to creep strength (Section 2.3.3). The smaller the grains and sub-grains, the higher the obstacle density and thus the more substantial the strength contribution. This strength contribution by grain refinement can be depicted by the classic Hall-Petch equation and is given by (Holzer 2010):

$$\tau_{gr} = k_{gr} \cdot d_{gr}^{-\frac{1}{2}} \quad (2.20)$$

where  $k_{gr}$  is the strengthening coefficient and  $d_{gr}$  is the grain diameter. However, in the case of martensitic creep-resistant 9-12% Cr steels, the prior austenite grain strength contribution is insignificant since their large size results in the fraction of GBs being very small compared to the fraction of SGB.

It is concluded in Section 2.3.3, that the critical structural parameter when considering SBH is the short width of the micro-grains. Subsequently, a similar equation to Equation (2.20) can be written that provides the SBH back-stress as follows (Abe 2008):

$$\sigma_{SBH} = \frac{10Gb}{\lambda_{sg}} \quad (2.21)$$

where  $\lambda_{sg}$  is the subgrain width or, in this case, the micro-grain short width. The constant 10 is derived from the Hall-Petch slope and is the Taylor factor  $M$  (Morito, Yoshida, Maki and Huang 2006).

### ***Solid Solution Hardening***

The increase in creep strength due to SSH follows from the lattice resistance to deformation from the differing sizes of solute atoms (Section 2.3.5). This increase in creep strength due to SSH can be quantified using the following equation (Holzer 2010):

$$\Delta\tau_{ssh} = k \cdot c^n \quad (2.22)$$

where  $k$  is a constant strengthening coefficient,  $c$  is the concentration of the solute atom in the matrix and  $n$  is a concentration exponent, usually between  $\frac{1}{2}$  and 1 depending on solute concentration and temperature. For a detailed derivation and summary of  $k$  values reported in the literature for both substitutional and interstitial solute atoms in bcc Fe, the reader is referred to the discussion by Holzer (2010).

### ***Proposed Combined Approach***

From the above, it follows that the primary obstacles for dislocation motion in martensitic creep-resistant 9-12% Cr steels are:

1.  $M_{23}C_6$  and MX precipitates
2. MGB
3. mobile dislocations

There is no unique concept to treat the superposition of more than one obstacle type or strengthening mechanism. The back-stress concept (Equation (2.14)) is one such approach. Another approach is to define a mean obstacle spacing  $\lambda_{ob}$  and assume that with increasing obstacle density, the slip length must decrease. This can be accounted for by the following equation (Roters, Raabe and Gottstein 2000):

$$\frac{1}{\lambda_{ob}} = \sum_i \frac{w_i}{\lambda_i} \quad (2.23)$$

where  $\lambda_i$  is the specific spacing of each obstacle and  $w_i$  is a weight factor which will adjust the obstacle spacing to be dominated by the shortest spacing among the various obstacles. However, this relation does not account for different obstacle strengths or the dislocation arrangement due to the dislocation-obstacle interaction, but rather indicates an effective influence of the obstacles collectively.

The combined spacing  $\lambda$  of the  $M_{23}C_6$  ( $\lambda_C$ ) and MX ( $\lambda_{CN}$ ) precipitates follows from Equation (2.18):

$$\lambda = \sqrt{\frac{\lambda_C^2 \lambda_{CN}^2}{\lambda_C^2 + \lambda_{CN}^2}} \quad (2.24)$$

The spacing of the mobile dislocations can be approximated as the inverse of the square root of the mobile dislocation density  $\rho_m$  (Murchú, Leen, O'Donoghue and Barrett 2017) and the obstacle spacing of the MGBs can be assumed to be the short width of the micrograins  $\lambda_{sg}$ .

Subsequently, substituting into Equation (2.23) and assuming equal weighted effect of each obstacle, the mean obstacle spacing can be approximated as:

$$\frac{1}{\lambda_{ob}} = \sqrt{\frac{\lambda_C^2 + \lambda_{CN}^2}{\lambda_C^2 \lambda_{CN}^2}} + \frac{1}{\lambda_{sg}} + \sqrt{\rho_m} \quad (2.25)$$

By comparing Equation (2.25) with Equations (2.16), (2.19), and (2.21), it can be deduced that a back-stress value could also be derived by multiplying  $\frac{1}{\lambda_{ob}}$  with the factor  $MGb$ :

$$\sigma_i = \frac{Mgb}{\lambda_{ob}} \quad (2.26)$$

Similarly, Murchú, Leen, O'Donoghue and Barrett (2017) defines a creep constant  $\sigma_o$  that is a stress quantity related to the key microstructural strengthening mechanisms by the obstacle spacing  $\lambda_{ob}$ :

$$\sigma_o = \frac{Mk_B T}{b^2 \lambda_{ob}} \quad (2.27)$$

where  $k_B$  is the Boltzmann constant and  $T$  the absolute temperature.

## **(ii) Other Semi-Physical Creep Models**

In general, semi-physical creep models assume a specific initial microstructure and then link the microstructural evolution to the creep deformation rate. This criterion separates the back-stress model from other semi-physical creep models.

The model developed by Ghoniem, Matthews and Amodeo (1989) is still presently the basis of advanced semi-physical creep models. It is a physically based approach that includes microstructural parameters such as precipitation state, dislocation densities and subgrain size to model the creep behaviour of HT-9 martensitic steel. This model has been used in the studies of Krumphals, Wlanis, Sommitsch, Holzer, Sonderegger *et al.* (2009), Krumphals, Reggiani, Donati, Wlanis and Sommitsch (2012), and Krumphals (2014) to predict the microstructure evolution of tool steel during service.

Dyson (2009) derived a physically based model that provides a creep equation for precipitation strengthened alloys, which includes 9-12% Cr steels, using a climb and glide particle bypass micro-mechanism. However, the Ghoniem, Matthews and Amodeo (1989) model includes more microstructural elements (the SGB and their interaction with dislocations) than the Dyson (2009) model and therefore is assumed to be more complete than the Dyson (2009) model. Barker and Ågren (2005) developed a composite model to

describe the creep behaviour of 9-12% Cr steels by defining hard and soft regions within the microstructure. Two different approaches have also been used by Magnusson and Sandström (2007) to predict the primary and tertiary creep stages of creep in 9-12% Cr steels to model the entire creep curve.

A parallel development is physically based CDM models. Dyson (2000) provides an excellent overview of CDM modelling and shows how physically based CDM is a unifying framework for some seemingly diverse methods of predicting design and remnant creep lifetimes. Such models can describe the evolution of strain and several other coupled microstructural features that includes (Ghosh 2013):

- redistribution of stresses between the matrix and precipitates;
- kinetics of precipitate coarsening;
- solute elements depletion from the matrix;
- nucleation, growth and coalescence of grain boundary cavities;
- and environmental interaction.

Even though all the semi-physical creep models have made significant contributions to modelling the creep curve, there still exists a lack of focus on the exact influence of the internal variables involved in creep behaviour modelling. Subsequently, Yadav, Sonderegger, Stracey and Poletti (2016) developed a hybrid approach to describe the creep behaviour using microstructural parameters and analysing their evolution in conjunction with the creep curves. This model couples the physically based model from Ghoniem, Matthews and Amodeo (1989) with the physically based CDM model proposed by Basirat, Shrestha, Potirniche, Charit and Rink (2012). The Ghoniem, Matthews and Amodeo 1989 model is based on two assumptions:

1. Creep can be portrayed by dislocation creep and mobile dislocations are the only carriers of creep deformation.



2. The creep rate is proportional to the mobile dislocation density  $\rho_m$  multiplied by their mean glide velocity  $v_g$ .

When the evolution of the mobile dislocations and their glide velocity is known, then the creep rate can be determined from these parameters using the classical Orowan equation that expresses the macroscopic creep strain rates  $\dot{\epsilon}$  as the cumulative strain rate produced by mobile dislocation glide (Ghoniem, Matthews and Amodeo 1989):

$$\dot{\epsilon} = b\rho_m v_g \quad (2.28)$$

It is assumed that it is a smooth glide process and that any climb driven by the applied stress does not contribute to the macroscopic strain.

The Basirat, Shrestha, Potirniche *et al.* (2012) model was developed for specific application in martensitic creep-resistant 9-12% Cr steels and has been applied to P91 steel.

As discussed before, when materials are loaded at high temperature with an applied stress  $\sigma_{app}$ , the microstructure will evolve due to diffusional and relaxation processes. During the dislocation creep, the glide and climb of dislocations play important roles in these relaxation processes (Yadav, Sonderegger, Stracey and Poletti 2016). The main interactions during the microstructural evolution can be described as:

- (i) Multiplication of dislocations (Frank-Read sources) (Section 2.3.4)
- (ii) Immobilisation of dislocations at SGB
- (iii) Annihilation of dislocations
- (iv) Subgrain growth

The mobile dislocations start to move as soon as an external load is applied to the material at high temperatures. The average glide velocity is expressed according to Ghoniem, Matthews and Amodeo (1989) as:

$$v_g = a_1 e^{-Q/kT} \cdot \frac{\Omega}{kT} \cdot \sigma_{eff} \quad (2.29)$$

where  $Q$  is the activation energy for dislocation glide, which replaces the fitting parameter  $W_g$  of the Ghoniem et al. model,  $\Omega$  is the atomic volume,  $a_1$  is a fitting parameter and  $\sigma_{eff}$  is the effective stress as defined by Equation (2.13).

There are many considerations for describing the internal stress  $\sigma_i$ . In addition to Equations (2.14) and (2.26), the internal stress has been described as:

- the contribution from dipoles and precipitates (Ghoniem, Matthews and Amodeo 1989, Salazar, Politano and Walgraef 1997);
- the contribution from mobile dislocations and precipitates (Barkar and Ågren 2005);
- the contribution from both dipole and mobile dislocations (Basirat, Shrestha, Potirniche *et al.* 2012).

Many physically based CDM approaches have been applied to predict the creep life of 9-12% Cr steels such as in the studies of McLean and Dyson (2000), Yin and Faulkner (2006), Semba, Dyson and McLean (2008), Basirat, Shrestha, Potirniche *et al.* (2012), Christopher, Sainath, Srinivasan, Samuel, Choudhary *et al.* (2013), Nandi, Vikrant, Ahv, Singh and Ghosh (2013), Oruganti, Karadge and Swaminathan (2013), and Stracey (2016). Some of the semi-physical creep models that have been applied to 9-12% Cr martensitic steels are summarised in **Table 2.12**. Included in the table is a comparison of the main microstructural features considered in the models. The main disadvantages of CDM models are that they are analytically complex or numerically intensive in order to make them universally applicable, and reliable estimation of model parameters is difficult due to the limited availability of creep strain data in the open literature (Ghosh 2013).

**Table 2.12:** Summary of some semi-physical creep models that have been applied to 9-12% Cr martensitic steels.

Model	Microstructural features on which damage parameters are based	Dominant creep mechanism
<b>Ghoniem, Matthews and Amodeo (1989)</b>	<ul style="list-style-type: none"> <li>• Mobile dislocations - primary cause of damage</li> <li>• Dipole dislocations</li> <li>• Boundary dislocations</li> <li>• Subgrains and SGB</li> <li>• Precipitates</li> </ul>	Dislocation Creep
<b>Basirat, Shrestha, Potirniche <i>et al.</i> (2012)</b>	<ul style="list-style-type: none"> <li>• Mobile dislocations</li> <li>• <math>M_{23}C_6</math> coarsening</li> <li>• Solid solution depletion due to Laves phase formation</li> <li>• Formation of creep cavities</li> </ul>	Dislocation Creep
<b>Yadav, Sonderegger, Stracey and Poletti (2016)</b>	<ul style="list-style-type: none"> <li>• Mobile dislocations - primary cause of damage</li> <li>• Dipole dislocations</li> <li>• Boundary dislocations</li> <li>• Growth of subgrains</li> <li>• <math>M_{23}C_6</math> coarsening</li> <li>• Formation of creep cavities</li> </ul>	Dislocation Creep
<b>Dyson-McClean (Dyson and McLean 1998)</b>	<ul style="list-style-type: none"> <li>• Mobile dislocation density decrease</li> <li>• Particle coarsening</li> </ul>	Dislocation Creep
<b>Oruganti, Karadge and Swaminathan (2013)</b>	<ul style="list-style-type: none"> <li>• Subgrain evolution</li> <li>• MX coarsening evolution</li> </ul>	Dislocation Creep
<b>Christopher, Sainath, Srinivasan <i>et al.</i> (2013)</b>	<ul style="list-style-type: none"> <li>• Mobile dislocation density decrease due to dislocation network coarsening</li> <li>• <math>M_{23}C_6</math> coarsening evolution (from Ostwald ripening)</li> </ul>	Dislocation Creep
<b>Yin and Faulkner (2006)</b>	<ul style="list-style-type: none"> <li>• Mobile dislocations</li> <li>• Cavity growth damage</li> <li>• <math>M_{23}C_6</math> and MX nucleation, growth and coarsening evolution</li> <li>• Solid solution evolution</li> </ul>	Dislocation Creep

<b>Stracey (2016)</b>	<ul style="list-style-type: none"> <li>• <math>M_{23}C_6</math> and MX coarsening (considering Orowan stress)</li> <li>• Subgrain coarsening and growth</li> </ul>	Dislocation Creep
<b>Weyer (2016)</b>	<ul style="list-style-type: none"> <li>• Grains</li> <li>• Grain boundaries</li> <li>• Vacancies</li> <li>• Precipitates</li> <li>• Voids</li> </ul> <p>Each element has the same set of properties that they are controlled by:</p> <ul style="list-style-type: none"> <li>• Young's modulus</li> <li>• Poisson's ratio</li> <li>• Diffusion coefficient</li> <li>• Vacancy concentration</li> <li>• Stress state</li> </ul>	Diffusional creep by vacancy migration

**2.8 CHARACTERISATION OF MICROSTRUCTURE**

As can be seen from the previous sections, the measurement of the microstructural parameters forms the basis for the investigation of microstructural evolution, analysis of strengthening mechanisms and implementation of existing semi-physical creep models. To measure the microstructural features, a range of techniques are necessary to analyse them first. Hansen and Barlow (2014) provide a summary of the key microstructural features and the techniques required to analyse them. This summary is provided in **Table 2.13**. The typical size of the feature is also given. The specific techniques and procedures applied to evaluate the microstructural evolution of welded long-term creep aged 9-12 % Cr martensitic steels in this study is further discussed in the next chapter (Chapter 3).

**Table 2.13:** Key microstructural features and the available techniques for their analysis (Hansen and Barlow 2014).

<i>Microstructural feature</i>	<i>Principal techniques available</i>	<i>Typical size of feature</i>
Grain, subgrain and cell sizes and aspect ratios	LM, SEM, TEM (light, scanning electron, transmission electron microscopy) X-ray	Grain sizes: Typically 10 $\mu\text{m}$ up to mm Subgrain and cell sizes: 0.1–10 $\mu\text{m}$
Nature and distribution of second-phase particles	LM SEM TEM	Sizes 0.5–10 $\mu\text{m}$ Sizes 0.1–10 $\mu\text{m}$ Sizes 0.01–3 $\mu\text{m}$
Macrotexture	Neutron, X-ray,	Whole specimen
Microtexture (local)	SEM, TEM, X-ray	Subgrain size 0.1–5 $\mu\text{m}$
Macroscopic grain and subgrain orientation (with respect to external stress)	SEM, TEM X-ray	Grain sizes: Typically 10 $\mu\text{m}$ up to mm Subgrain sizes: 0.1–10 $\mu\text{m}$
Orientation across grain and subgrain boundaries	SEM, TEM	Spatial resolution required to be at least that of grain or subgrain size.
Dislocations	TEM, X-ray	5–20 nm
Structure of dislocation boundaries (width; tilt or twist misorientation)	TEM	2–100 nm
Macroscopic stress fields	Neutron, X-ray	Up to sample dimensions: 10 mm or more
Local stress fields	TEM, SEM, X-ray	2–20 nm

# CHAPTER 3

## MATERIALS AND EXPERIMENTAL METHODS

---

### 3.1 INTRODUCTION

This chapter describes the microstructural characterisation techniques applied to evaluate the microstructural evolution of virgin and long-term creep aged parent and simulated FGHAZ X20 steel. Firstly, information is provided on the materials studied and the weld thermal cycle simulation used to obtain FGHAZ samples. Further sample preparation techniques, such as twin-jet electropolishing and bulk replication are discussed. The experimental techniques performed on these prepared specimens are then described, followed by the methodologies developed to investigate the microstructural evolution from the results acquired using these techniques. A brief discussion on the statistical analysis used to report measured values is also provided.

### 3.2 SAMPLING

#### 3.2.1 Steel Sections

In this study, the stainless steel analysed is the German grade X20 that is used in the High Temperature Pressure Pipework (HTPP) at Eskom's coal-fired power plants. A detailed discussion on this steel and its use in coal-fired power plants was given in Section 2.1.2. Eskom's Sustainability Division provided virgin/new X20 steel pipework and long-term creep aged (damaged) /Ex-service X20 steel for this research. The pipework had the following dimensions (**Figure 3.1**): 255 mm  $\pm$  5 mm internal diameter and 35 mm  $\pm$  1 mm wall thickness. **Table 3.1** summarises the operating and design conditions for the X20 steel pipework received from Eskom. The assigned designation to the different pipework (base material) that is used throughout this study is also included in this table.

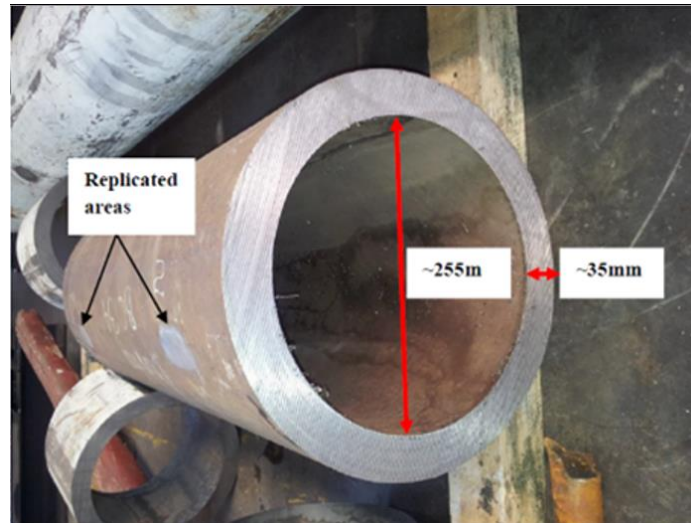


**Figure 3.1:** Image of the X20 steel pipework used in this research (Molokwane 2014).

**Table 3.1:** Operating conditions for X20 steel pipework analysed in this study.

	<b>Material Designation</b>	<b>Operating Temperature (°C)</b>	<b>Operating Pressure (MPa)</b>	<b>Operating Hours</b>
<b>New material</b>	<b>New</b>	N/A	N/A	0
<b>Power Station 1</b>	<b>Creep aged 1 or D1</b>	532	16.1	156 000
<b>Power Station 2</b>	<b>Creep aged 2 or D2</b>	555	17.0	129 801

As can be seen, both X20 pipework has been long-term creep exposed for more than 120 000 h. The pipework from Power Station 1 has operated at a lower temperature and pressure, but for a longer time than the pipework from Power Station 2. Both sets of pipework have operated below the design conditions, except for the pipework from Power Station 2 which has operated at a 10°C higher temperature than the design temperature.

A sample from each pipework was sectioned and the chemical composition determined with spectrographic analysis (SLS SPC) based on the ASTM A751-01 standard (ASTM 2014). **Table 3.2** summarises the determined chemical compositions of the pipework. For comparison, the standard chemical composition for DIN 17175 Grade X20CrMoV12-1 from **Table 2.1** is also included.

**Table 3.2:** Chemical composition of DIN 17175 Grade X20CrMoV12-1 and X20 steel pipework analysed in this study.

Element (wt%)	DIN 17175 (X20CrMoV12-1)	New X20	Creep aged 1 X20	Creep aged 2 X20
<b>C</b>	0.17-0.23	0.19	0.17	0.19
<b>Si</b>	≤0.50	0.14	0.20	0.36
<b>Mn</b>	≤1.00	0.47	0.59	0.63
<b>P</b>	≤0.030	0.007	0.015	0.013
<b>S</b>	≤0.030	≤0.005	≤0.005	≤0.005
<b>Cr</b>	10-12.50	11.5	11.6	11.7
<b>Mo</b>	0.80-1.20	0.89	0.94	0.91
<b>Ni</b>	0.30-0.80	0.64	0.71	0.67
<b>V</b>	0.25-0.35	0.30	0.34	0.32
<b>Cu</b>		0.12	0.11	0.10
<b>Al</b>		0.011	0.021	0.020
<b>Nb</b>		≤0.005	≤0.005	0.006
<b>Ti</b>		≤0.005	≤0.005	≤0.005
<b>Co</b>		0.008	0.013	0.012
<b>Fe</b>	Matrix	Matrix	Matrix	Matrix

The X20 steel used for this study is of the DIN 17175 X20CrMoV12-1 grade since the chemical composition of each sample falls within its specification range. The other standards require the wt. % of Si to be lower than 0.04 (**Table 2.1**). Creep aged 2 base material has a higher Si and Nb content than the other base materials. There is also a much higher Al content in the creep aged base materials compared to the new base material. The other elemental contents are similar for all the base materials.



### 3.2.2 Surface Replication

As discussed in Section 2.6.1, the second and main stage of component life management involves replica lifting from the component surface. Examples of these areas where the surface of the pipework has been replicated is shown in **Figure 3.1**. Eskom prepared replica specimens of the surface of the X20 steel pipework according to their standard procedure (Eskom 2017). They then analysed these surface replica specimens at 500x magnification with a Leica light microscope to determine the level of creep damage. The measured creep void densities and the corresponding damage classification (Section 2.6.1) is given in **Table 3.3**.

**Table 3.3:** Creep damage classification of X20 pipework according to surface replication results.

<b>Material Designation</b>	<b>Creep Damage (voids/mm<sup>2</sup>)</b>	<b>Power Plant Damage Class</b>
<b>New</b>	No damage	CLASS 4 - No damage
<b>Creep aged 1 (D1)</b>	200 - 300	CLASS 3 - Medium damage
<b>Creep aged 2 (D2)</b>	300 - 800	CLASS 1 -Very high damage

Surface replication according to the same standard procedure was performed to obtain similar results for the simulated FGHAZ samples. However, the replication was unsuccessful due to the small sample size. Nevertheless, the creep voids were analysed for each sample by Light Microscopy (LM) and Scanning Electron Microscopy (SEM) as discussed in Section 3.7.2.

### 3.3 FGHAZ SIMULATION

#### 3.3.1 Sample Preparation

For larger sampling areas of homogeneous FGHAZ microstructure, weld thermal cycle simulation (Section 2.4.3) on a Gleeble™3800 was performed on  $\text{Ø}10 \text{ mm} \times 140 \text{ mm}$  rod samples of the base materials (**Table 3.1**). This size was chosen to maximize the size of the hot zone and hence have as large as possible sampling volume (Walsh, Cieslak and Savage 1986). Firstly,  $\text{Ø}11 \text{ mm} \times 140 \text{ mm}$  rods were cut from the pipework using Wire Cut EDM (Electrical Discharge Machining). This sectioning technique was chosen to minimise material loss. **Figure 3.2** provides a schematic to illustrate the position and direction the rod samples were cut from the pipework.

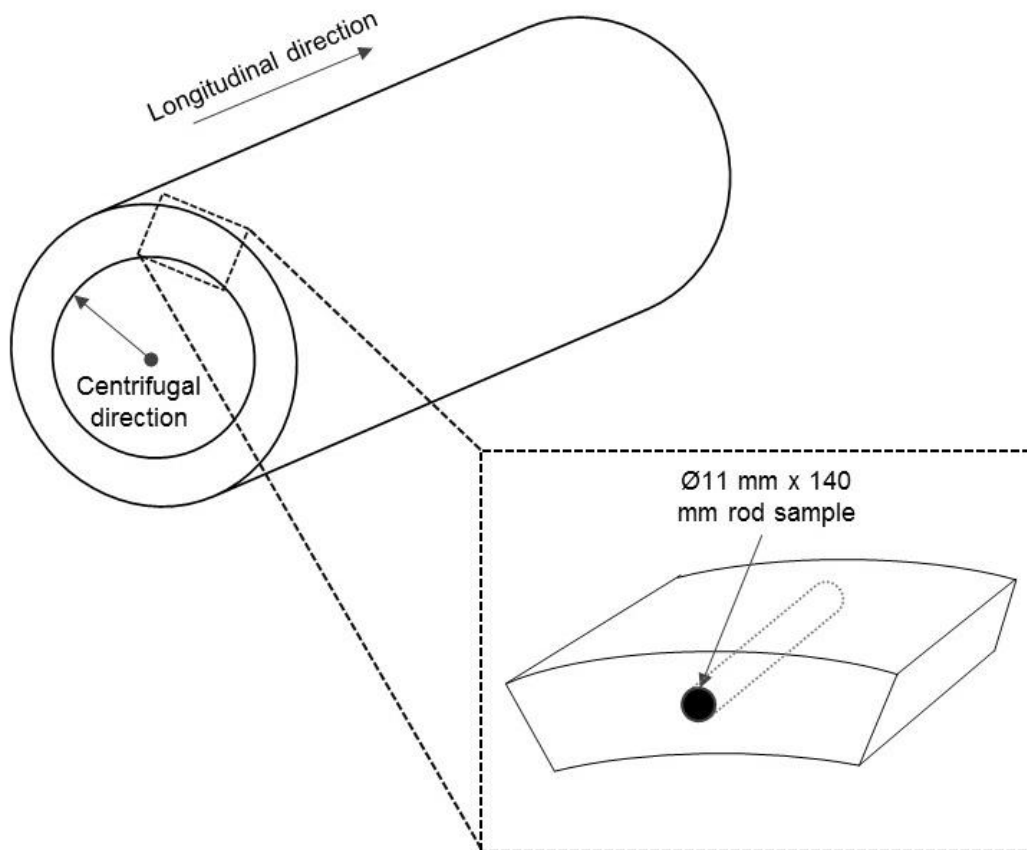


**Figure 3.2:** Schematic illustration of the position and direction of the  $\text{Ø}11 \text{ mm} \times 140 \text{ mm}$  rods cut from the pipework (Adapted from Aghajani (2009)).

With a CNC machine, the rods were then machined to a final size of  $\text{Ø}10\text{mm} \times 140\text{ mm}$  with 1.5 mm M10 threads on the sides to mount the sample in the clamping mechanisms of the Gleeble<sup>TM</sup>. Images of the rod samples after each sectioning step is shown in **Figure 3.3**. Two rods were prepared for each material type to ensure there is a back-up in case simulation is unsuccessful on the first attempt.

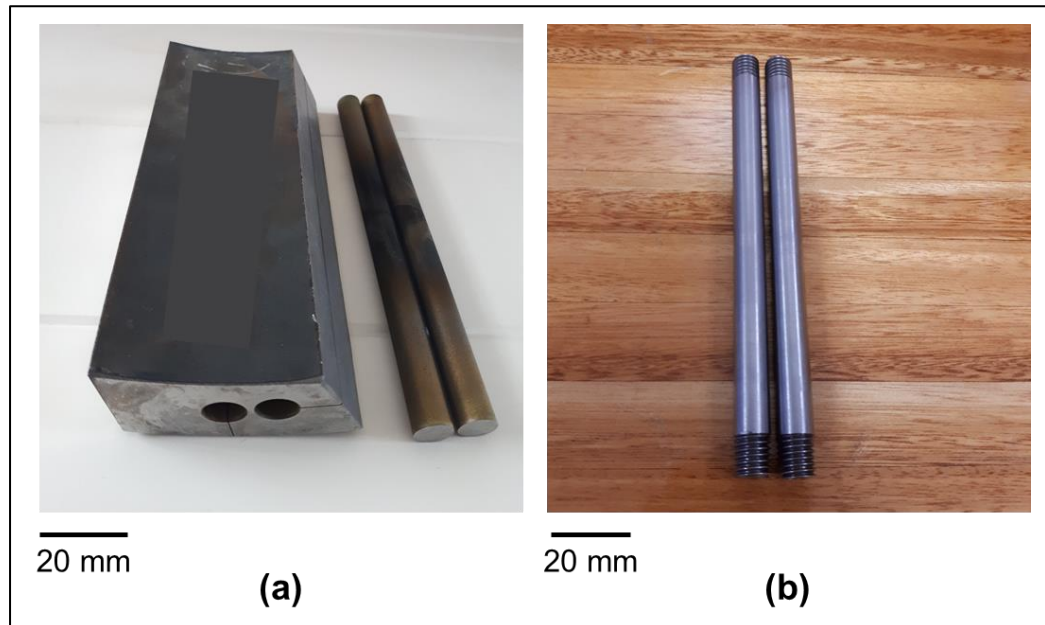


**Figure 3.3:** Images of (a)  $\text{Ø}11\text{mm} \times 140\text{ mm}$  rods cut from a bulk piece of pipework and (b) final  $\text{Ø}10\text{ mm} \times 140\text{ mm}$  samples used for Gleeble<sup>TM</sup> simulation.

### 3.3.2 Weld Thermal Cycle Simulation

As discussed in Section 2.4.3, the  $A_{C1}$  and  $A_{C3}$  transformation temperatures of the material are critical for the parameters of the weld thermal cycle simulation. The model used for the FGHAZ simulation in the Gleeble<sup>TM</sup> was directly replicated from the one developed by Rasiawan (2017). This model was chosen since it was successfully applied to the same virgin and creep aged 2 Eskom X20 pipework as is analysed in this study. The weld thermal cycle steps and all parameters used for the Gleeble<sup>TM</sup> is summarised in **Table 3.4**.

**Table 3.4:** Weld thermal cycle steps and parameters used for Gleeble™ simulation.

Weld Cycle Step	Description	Parameter
1	Heat from ambient temperature to 250 °C	Heating rate = 45 °C/s
2	Hold at 250 °C	Time = 20 s
3	Heat further to $T_p = 980$ °C	Heating rate = 200 °C/s
4	Hold at $T_p = 980$ °C	Time = 4 s
5	Air quenched to 100 °C	Cooling rate = 26.4 °C/s

The samples for this study were simulated with the same Gleeble™3800 system used by Rasiawan (2017) at the Centre for Materials Engineering, University of Cape Town (UCT). **Figure 3.4** shows the sample geometry inside the Gleeble™. To measure the exact temperature and if a temperature gradient is experienced, two thermocouples connected to the Gleeble™ system were spot-welded onto the sample with a model 35200 Gleeble™ Thermocouple Welder. The thermocouples were of Ni-base K-type consisting of Nickel-Chromium / Nickel-Alumel junction. A Gleeble™ thermocouple amplifier was used to measure the voltage from the thermocouples.

The first thermocouple (Thermocouple 1) was the temperature control thermocouple and it was placed at the centre of the sample. A second thermocouple (Thermocouple 2) was placed 5 mm from the first one. This position was chosen assuming strictly one-dimensional heat conduction along the specimen axis and a symmetric temperature gradient around the first thermocouple.

**Table 3.5** provides the actual peak temperatures measured for each thermocouple for the three base materials and the temperature-time profiles of the Gleeble™ simulation are given in **Figure 3.5**.

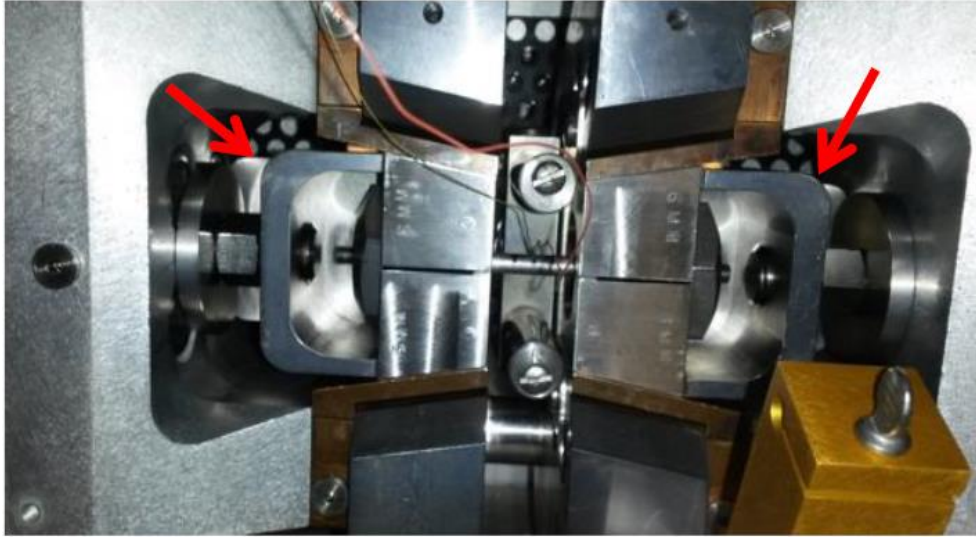


**Figure 3.4:** Image of sample set-up in the Gleeble™3800 (Rasiawan 2017). The sample is held in place by copper grips and fixed into position by C-grips (indicated by red arrows).

**Table 3.5:** Peak temperatures  $T_p$  measured by thermocouples during Gleeble™ simulation.

Base Material	Thermocouple 1 $T_p$ (°C)	Thermocouple 2 $T_p$ (°C)	Average Temperature Gradient (°C/mm)
New	984.37	978.53	-1.17
Creep aged 1	984.44	979.22	-1.04
Creep aged 2	984.23	998.91	+2.94

It is seen from **Table 3.5** that the magnitude of the temperature gradient measured to 5 mm from the centre of the rod is less than 3 °C/mm, which is within the error range of a Nickel-Chromium / Nickel-Alumel K-type thermocouple of 0.75% (REOTEMP Inc. 2018). Even though, the creep aged 2 material experienced the highest temperature above  $A_{c3}$ . As the results will show in Chapter 4, the temperature was still too low for the CGHAZ microstructure to form and therefore the FGHAZ simulation of this material is classified as successful despite these anomalies.

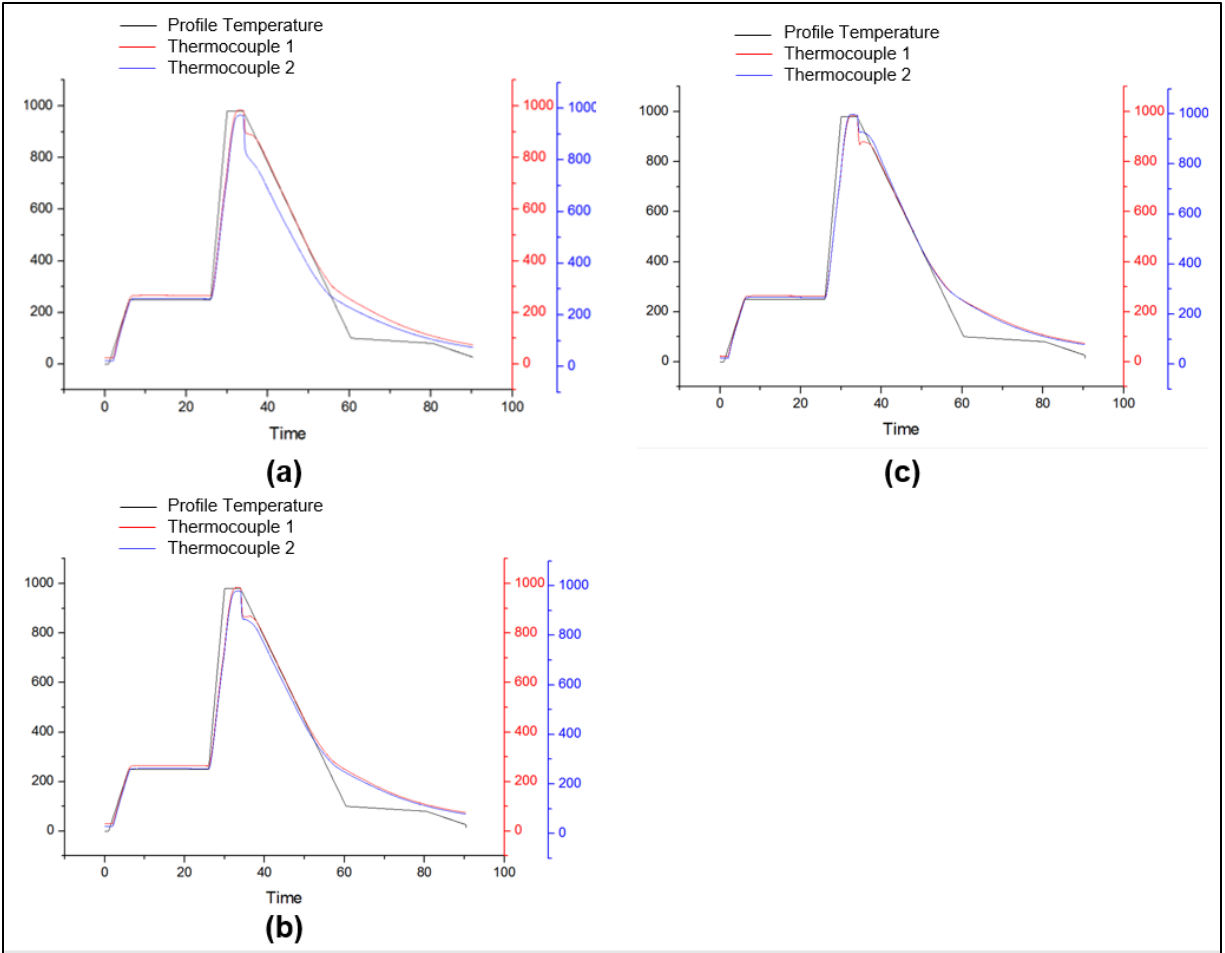


**Figure 3.5:** Gleeble™ FGHAZ simulation temperature-time profiles for (a) new X20 base material, (b) creep aged 1 base material and (c) creep aged 2 base material. Thermocouple 1 and 2 refers to centre and 5 mm from centre thermocouples, respectively.

### 3.3.3 Post-Weld Heat Treatment

To finish the FGHAZ simulation, subsequent post-weld heat treatment (PWHT) was performed on all the weld thermal cycle (Gleeble™) simulation samples. The PWHT was performed as described in the X20 Steel Handbook (EPRI 2006). There was no need to coat the samples to prevent oxidation during PWHT since all subsequent sampling was done through the cross-section of the rod, far enough away from the outer edge. As with the Gleeble™ simulation, thermocouples were spot-welded as indicated in **Figure 3.6(a)**

onto a rod of each base material to ensure accurate measurement of temperature. The samples were then placed in a furnace as shown in **Figure 3.6(b)**.

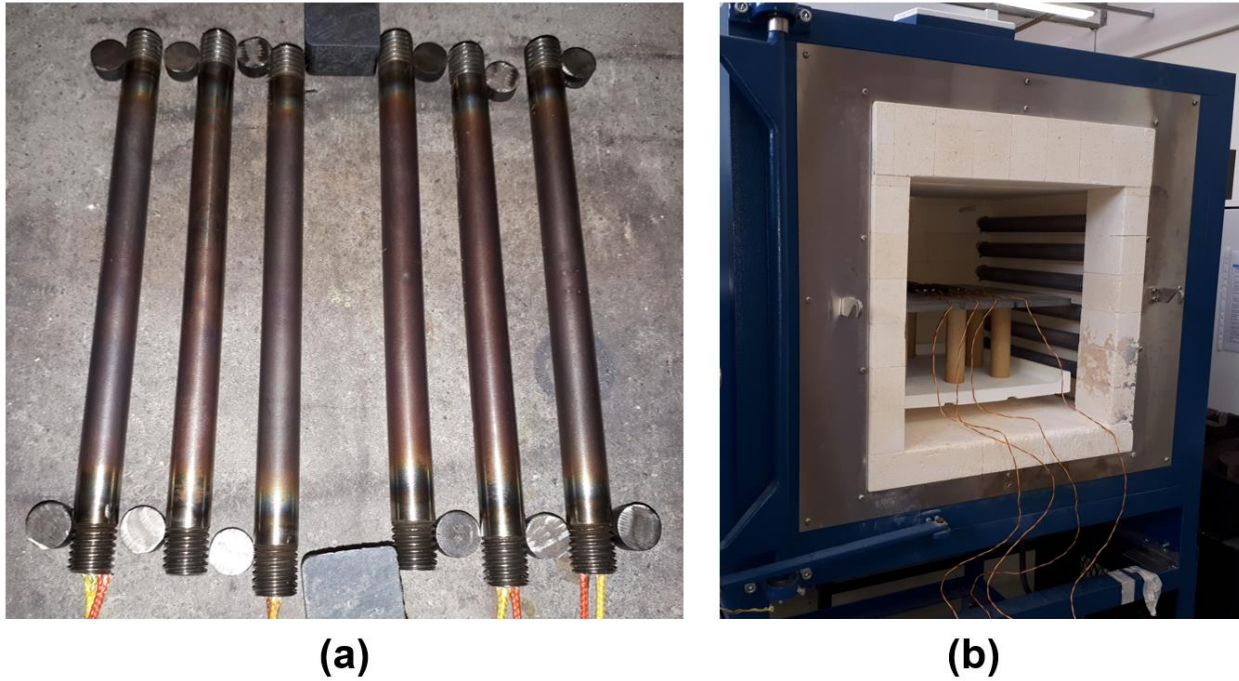


**Figure 3.6:** Images of (a) thermocouples spot-welded onto Gleeble<sup>TM</sup> simulated rod samples and (b) furnace set-up for PWHT.

The steps followed, and parameters used for the PWHT is summarised in **Table 3.6**. Due to the large volume of the furnace, steps 1 and 2 were added, and a 15 min longer holding time was applied to ensure the furnace is heated thoroughly through its volume. The actual holding and final temperatures measured for the different base materials is given in **Table 3.7**. In **Figure 3.7** the measured temperature-time profile is given for all the base materials. As can be seen, the temperature variation between the base materials during PWHT is negligible.

**Table 3.6:** PWHT steps and parameters applied to weld thermal cycle simulated samples.

<b>PWHT Cycle Step</b>	<b>Description</b>	<b>Parameter</b>
<b>1</b>	Heat from 62 °C to 80 °C	Heating rate = 32.7 °C/hr
<b>2</b>	Heat from 80 °C to 90 °C	Heating rate = 1.5 °C/hr
<b>3</b>	Heat from 90 °C to 740 °C	Heating rate = 100.0 °C/hr
<b>4</b>	Hold at 740 °C	Time = 45 min
<b>5</b>	Cool from 740 °C to 190 °C	Cooling rate = 100.0 °C/hr
<b>6</b>	Cool from 190 °C to ambient temperature by opening the furnace door	Uncontrolled

**Table 3.7:** Measured holding and final temperatures measured by thermocouples during PWHT of weld thermal cycle simulated samples.

<b>Base Material</b>	<b>Measured Holding Temperature (°C)</b>	<b>Final temperature (°C)</b>
<b>New</b>	738.20	33.40
<b>Creep aged 1</b>	737.90	33.60
<b>Creep aged 2</b>	737.50	35.10



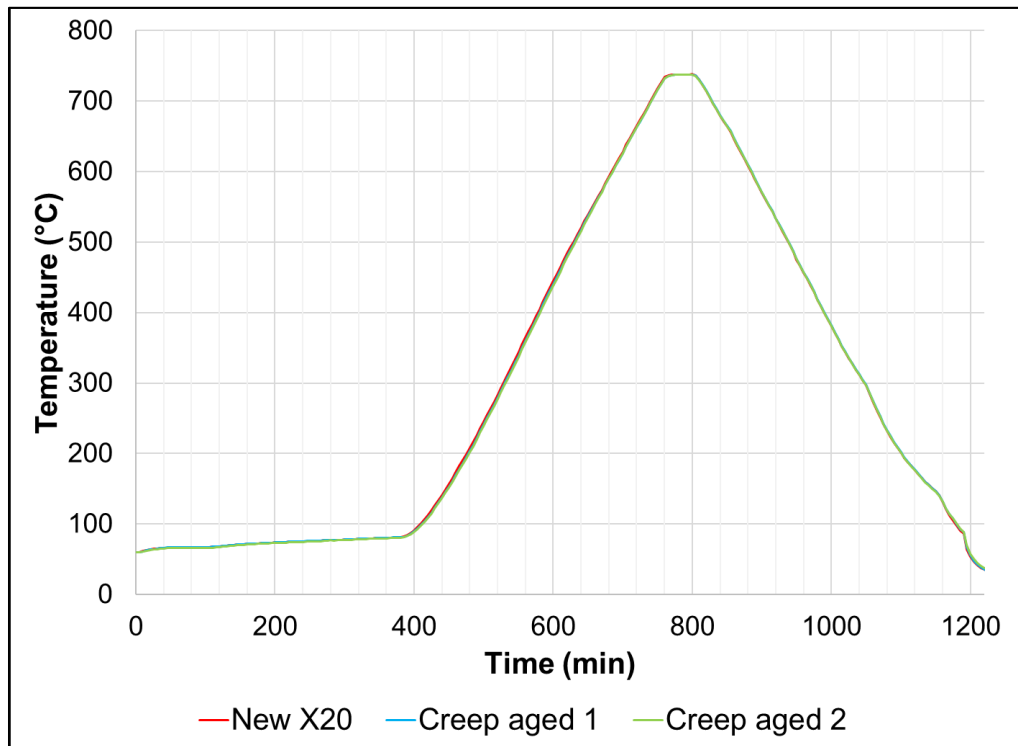


**Figure 3.7:** Measured temperature-time profile for PWHT performed on weld thermal cycle simulated samples.

## 3.4 SAMPLE PREPARATION

### 3.4.1 Cutting and Polishing

A summary of the samples analysed in this study and from which subsequent specimens were prepared is summarised in **Table 3.8**. Therefore, there is a total of 6 samples analysed: for each base material, there is a parent sample and the corresponding sample obtained by performing FGHAZ simulation on the parent material. Since in an actual weldment the parent material will also experience PWHT, the parent samples were sectioned from the ends ( $\pm 1$  cm from the side) of the FGHAZ simulated rod samples. From the study of Walsh, Cieslak and Savage (1986), which investigates the size of the central constant temperature region from physical weld simulation, it was estimated that the FGHAZ section is approximately 1.5 cm about the centre, i.e., a total simulated FGHAZ section of 3 cm. Therefore, it was a reasonable assumption that the sides of the

rod will not be simulated with the FGHAZ and will have the microstructure of PWHT parent material. The acquired results from these samples further confirm this point.

**Table 3.8:** Summary of samples analysed in the study.

New X20 material	Creep aged 1 (D1) X20 material	Creep aged 2 (D2) X20 material
Parent	Parent	Parent
Simulated FGHAZ	Simulated FGHAZ	Simulated FGHAZ

**Figure 3.8** illustrates the sectioning of the samples in **Table 3.8** from the simulated FGHAZ rod sample of each base material using wire cutting as before. Sections A and D corresponds to the parent bulk specimens and sections B and C correspond to the simulated FGHAZ bulk specimens.

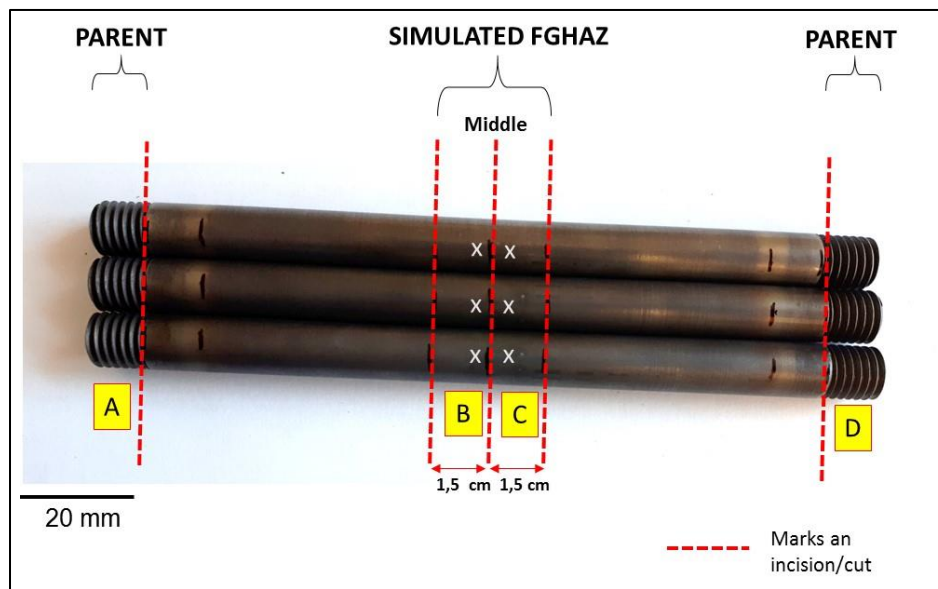


**Figure 3.8:** Image of final simulated FGHAZ rods and subsequent sectioning using wire cutting. Sections A and D correspond to the parent bulk specimens and sections B and C correspond to the simulated FGHAZ bulk specimens. The “x” symbols mark the surface on which XRD was performed for the simulated FGHAZ samples and from which subsequent 1.2 mm discs was sectioned for thin foil specimens.

For X-Ray Diffraction (XRD), Electron-Backscatter Diffraction (EBSD) and void LM and Scanning Electron Microscopy (SEM) analysis, the bulk specimens (Sections A and B) of each material type (new, creep aged 1 and creep aged 2) were mounted in a bakelite resin and polished to a colloidal surface finish using grit paper (P400, P800 and P1200) followed by successively finer diamond suspensions (6 $\mu$ m, 3 $\mu$ m, 1 $\mu$ m and 0.25 $\mu$ m) to remove any prior surface damage. Final polishing was with a 0.05  $\mu$ m colloidal silica suspension and an acid base. The polished surface, and hence surface analysed, was the side precisely in the centre of each rod (marked “x” in **Figure 3.8**).

### **3.4.2 Twin-Jet Electropolishing**

Electron-transparent thin foils specimens were prepared for Scanning Transmission Electron Microscopy (STEM) and Transmission Kikuchi Diffraction (TKD) using the technique known as twin-jet electropolishing or twin-jet electrolytic thinning (Ayache, Beaunier, Boumendil, Ehret and Laub 2010). This technique is not as site-specific as Focused Ion Beam (FIB) microscopy and is performed on  $\varnothing$ 3 mm discs of 50 to 100  $\mu$ m thickness prepared from the bulk material.

To prepare the specimens for the electropolisher, the bulk specimens (Sections C and D in **Figure 3.8**) of each material type was sectioned into smaller specimens. The aim of this study was to sample as much as possible from the region where the exact simulation temperature was known (**Table 3.5**)

Therefore, discs of 1.2 mm thickness were wire cut from the simulated FGHAZ bulk specimens. Each disc was labelled, starting with number 1 as the one closet to centre (side marked “x” in **Figure 3.8**). In the case of the parent material precision was not necessary and the bulk specimens were cut into three smaller sections using a diamond blade saw.

To ensure representativity of the actual microstructure, two of the smaller sectioned specimens of each parent and simulated FGHAZ materials was further prepared for twin-jet electropolishing. Specifically, for the simulated FGHAZ specimens, the two 1.2 mm discs closest to the centre (number 1 and 2) was further prepared, i.e., sampled from 2.4

mm of centre. Consequently, analyses are performed on two different sections of material. The specimens were then ground and polished down on both sides to 0.05  $\mu\text{m}$  colloidal silica as described in Section 3.4.1 to a final thickness of 50 to 100  $\mu\text{m}$ . Using a disc punch system,  $\text{\O}3$  mm discs were cut from these specimens. The discs were then twin-jet electropolished using a Struers TenuPol-5 Automatic Twin-Jet Electropolisher with 5% perchloric acid ( $\text{HClO}_4$ ) solution at  $-20$   $^\circ\text{C}$  and an applied voltage of 21 to 30 V. The measured current values was 35mA, although this value changes depending on the contact between the sample and the sample holder.

Twin-jet electropolishing was chosen as the technique for thin foil specimen preparation for the following reasons:

- (i) Specimens are prepared without any mechanical damage or generation of strain hardening or surface deformation.
- (ii) A larger area is available for analysis compared to conventional FIB specimens.
- (iii) Correlative microscopy can be performed on the prepared specimens. Due to the high quality of the polished surface, SEM and EBSD can also be performed on the specimen in addition to TEM/STEM and TKD.

The main limitation of this sample preparation technique, in general, is that it is not site specific and it is difficult to find the correct electropolishing solution, temperature, potential and current conditions, especially with samples containing precipitates or segregations. However, the extent of site-specific sample preparation as with FIB was not desired in this study and good quality specimens were prepared using the conditions given above. A schematic diagram of a twin-jet electropolished specimen is given in **Figure 3.9**. As can be seen, twin-jet electropolished specimens have a varying thickness with the circular grey area usually having thicknesses of 20 to 200 nm. This non-uniform thickness was a limitation of the technique in this study causing variations in the calculations of thickness-dependent parameters. However, the main limitation of this technique specific to this study was the presence of the iron matrix that magnetically interferes with the objective lens in the TEM.

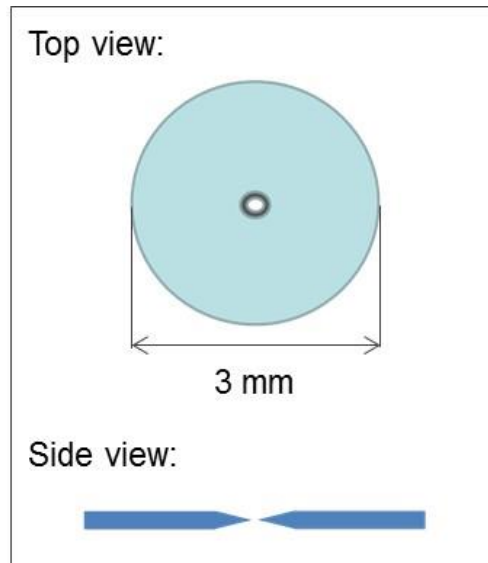


**Figure 3.9:** Schematic diagram of a twin-jet electropolished specimen. The circular grey area is the area available for analyses.

### 3.4.3 Bulk Replication

For improved particle analysis, the Bulk Replication Technique (BRT) for specific application to X20 steel has been used by Marx (2016) from the works of Mitchell and Sulaiman (2006) who developed the technique for P91 steel. The BRT is based on the basic principle of extracting only particles from the surface of a specimen to view them directly in the TEM (Ayache, Beaunier, Boumendil *et al.* 2010). For stainless steels, it entails embedding the precipitates on a carbon film and then separating them from the metallic matrix by chemically dissolving the iron matrix. Subsequently, the BRT overcomes the sampling, stereological projection, magnetic interference and shape distortion problems associated with thin-foil specimens. As with twin-jet electropolishing, the BRT is applied to bulk materials. A summary of the main steps of the BRT is given in **Figure 3.10**.

Extraction replica specimens of the surface of one of the remaining bulk samples (**Table 3.8**) sectioned for twin-jet electropolishing (Section 3.4.2) was prepared. In the case of the FGHAZ samples, the 5<sup>th</sup> Ø10 mm disc, sampled 6 mm away from the centre of the rod, was used. Firstly, the specimen was polished down to 0.25 µm surface finish as

described in Section 3.4.1 (**Figure 3.10(a)**). To expose the precipitates for extraction, the top layer of the iron matrix was etched away using Vilella's reagent (1 g picric acid, 5 ml hydrochloric acid and 100 ml ethanol) for 2 minutes (**Figure 3.10(b)**). This step was performed in an ultrasonic bath to attempt to discard any sectioned precipitates by the vibration. A  $\pm 20$  nm carbon coat was then deposited (4 pulses of evaporation at  $1 \times 10^{-2}$  mbar) onto the etched specimen surface to cover the exposed precipitates (**Figure 3.10(c)**). A carbon deposition system consisting of Quorum Emitech K950X Turbo Evaporator was used. The specimen surface was then scored into  $\pm 2.5$  mm blocks and immersed in Vilella's reagent until the iron matrix was sufficiently dissolved so that the foils floated off. After capturing the films, they were washed in 10% methanol water and floated onto a copper TEM grid. The final product is a carbon coat specimen that only contains the precipitates (**Figure 3.10(d)**).

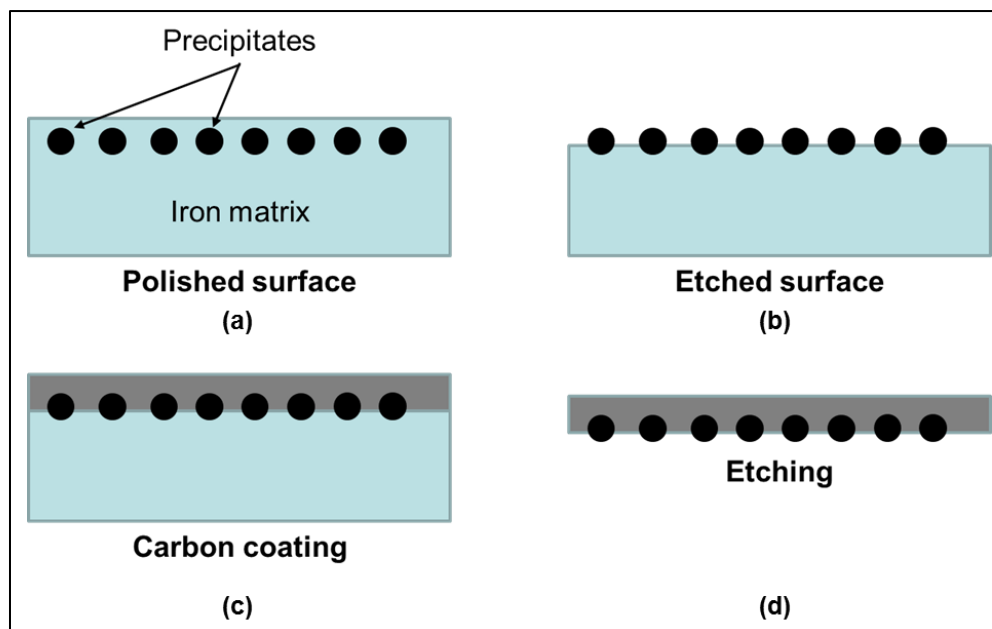


**Figure 3.10:** Schematic illustration of the main steps of the Bulk Replication Technique. (a) Polish the bulk specimen surface. (b) Etch away the top layer of the iron matrix to expose the precipitates for extraction. (c) Deposit a carbon coat on top of specimen surface to cover the exposed precipitates. (d) Obtain carbon coat specimen containing only precipitates by chemically dissolving the rest of the iron matrix (Marx 2016).

In addition to overcoming the thin foil problems mentioned above, the other advantage of the BRT is that it produces TEM specimens with a much larger sampling area and many specimens can be simultaneously prepared from a single specimen. For comparison, the extraction replica sampling area ( $\pm 2.5 \times 2.5 \text{ mm}^2$  divided into  $\pm 50 \times 50 \mu\text{m}^2$  squares on the copper grid) is shown relative to that of a FIB specimen ( $\pm 5 \times 5 \mu\text{m}^2$ ) and conventional (ion-mill or twin-jet electropolished) TEM specimen in **Figure 3.11**. Therefore, good statistical and representative results can be obtained from extraction replica specimens about true precipitate size, shape, structure and chemical composition (Mitchell and Sulaiman 2006, Ayache, Beaunier, Boumendil *et al.* 2010, Marx 2016). Di Gianfrancesco, Vipraio and Venditti (2013) also performed a study on the precipitates in 9-12% Cr steel grades from extraction replicas.

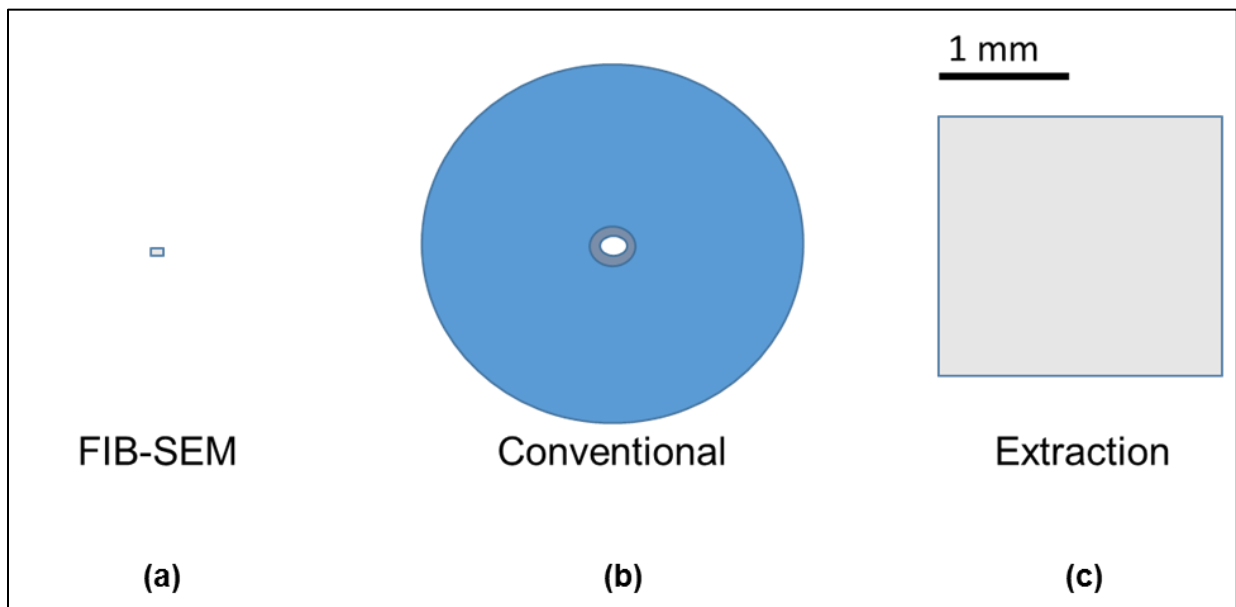


**Figure 3.11:** Comparison of sampling areas in (a) FIB specimen ( $\pm 5 \times 5 \mu\text{m}^2$ ), (b) conventional (ion-mill, twin-jet electropolished) TEM specimen and (c) extraction replica ( $\pm 2.5 \times 2.5 \text{ mm}^2$ ) (Marx 2016). The area available for analysis is indicated by the grey areas.

Marx (2016) discussed the limitations of the BRT and proposed solutions. The main limitations can be summarised as follows:

- (i) The sampling volume is uncertain since the thickness of the initial etching of the surface is not known.
- (ii) There is possible low extraction efficiency of small precipitates that are smaller than the thickness of the etched layer.
- (iii) The accuracy of reproducibility of the microstructure in the x, y and z directions is unknown.

Consequently, the effect of these limitations was avoided in this study by only investigating precipitate size, shape and chemical composition from the extraction replica specimens. The advantages of twin-jet electropolishing and bulk replication techniques as discussed above demonstrate the need for simulated FGHAZ materials from which the microstructure of the narrow FGHAZ weldment region can be accurately characterised by preparing specimens with these techniques.



### 3.4.4 Final Sample Matrix

A summary of the final specimens used in subsequent analyses is given in **Table 3.9**.

**Table 3.9:** Final matrix of specimens analysed in the study.

Base material	Sample	Sample name	Type of specimen		
			Bulk	Twin-jet electropolished (2 specimens from different sections)	Extraction replica
New X20	Parent	<b>New parent</b>	X	X	X
	Simulated FGHAZ	<b>New sim FGHAZ</b>	X	X	X
Creep aged 1 X20	Parent	<b>Creep aged 1 parent</b> / D1 parent	X	X	X
	Simulated FGHAZ	<b>Creep aged 1 sim FGHAZ</b> / D1 sim FGHAZ	X	X	X
Creep aged 2 X20	Parent	<b>Creep aged 2 parent</b> / D2 parent	X	X	X
	Simulated FGHAZ	<b>Creep aged 2 sim FGHAZ</b> / D2 sim FGHAZ	X	X	X

### **3.5 VICKERS MICROINDENTATION HARDNESS TESTING**

Hardness measurements of the parent and simulated FGHAZ materials were performed using standard Vickers Microindention Hardness Testing (MHT) (Kamm and Vander Voort 1997, ASTM 2011). A damage free surface is necessary to ensure accurate Vickers MHT results. Therefore, the specimens analysed were mounted and polished as described in Section 3.4.1. The Vickers MHT results were acquired from the Ø10 mm discs cut during twin-jet electropolishing sample preparations (Section 3.4.2). To ensure representativity and investigate homogeneity, hardness measurements were recorded from the 4 simulated FGHAZ specimens, which are the discs labelled 1 to 4 (sampled within 4.8 mm from the centre). After performing hardness measurements on one of the discs of each parent material it was seen that there is minimal variation in hardness and therefore it was deemed not necessary to analyse more than one of the parent material specimens.

For each specimen, a 3 x 3 matrix of  $\pm 2.5$  mm spaced indents were made with a standard load of 300 gf for stainless steels, and the corresponding Vickers hardness measured using an Automatic Micro Vickers Hardness Tester that is a combination of a Future-Tech FM-700 Microhardness Tester and a Future-Tech FM-ARS9000 Full-Automatic Hardness Testing System. All measurements were calibrated with a Cu block standard and indentation performed sufficiently away from the specimen edge to avoid any edge effects.

### **3.6 EXPERIMENTAL TECHNIQUES**

#### **3.6.1 LM Analysis**

Light Microscopy (LM) is the most widely used method of observing the microstructure of 9-12% Cr martensitic steels as shown by Hald (2005), Maile (2007), Di Gianfrancesco, Vipraio and Venditti (2013), and Milović, Vuherer, Blačić *et al.* (2013). To make an initial observation of the microstructure and verify successful simulation of the FGHAZ, the surface of the specimens used for Vickers MHT was etched with Villela's reagent and

Bright Field (BF) optical micrographs of  $1.1 \times 0.8 \text{ mm}^2$  areas acquired with an Olympus DSX510 Digital Microscope.

Creep cavities in creep aged 9-12% Cr martensitic steels have been studied with LM, and Backscattered Electron (BSE) and Secondary Electron (SE) SEM imaging by Eggeler, Earthman, Nilsvang and Ilschner (1989), Wu and Sandström (1995), Auerkari, Holmström, Veivo and Salonen (2007), Aghajani, Somsen and Eggeler (2009), Panait, Gourgues-Lorenzon, Besson, Fuchsmann, Bendick *et al.* (2010), Panait, Bendick, Fuchsmann *et al.* (2010), Zhao, Jing, Xu, Han and Xiu (2012), Nie, Zhang, Huang, Liu, Zhu *et al.* (2014), Yadav, Rosc, Sartory *et al.* (2014), Yadav, Sonderegger, Sartory *et al.* (2015), and Rasiawan (2017).

The cavities were quantitatively analysed using LM. Micrographs of a 4x4 matrix of 16 ( $296 \times 296 \mu\text{m}^2$ ) areas were taken from the surface of the polished bulk specimens (**Table 3.9**) using the same microscope as above. The micrographs were acquired with a “mix” imaging mode, which is a mixture between BF and Dark Field (DF) imaging. The total sampling area per specimen was  $1.4 \text{ mm}^2$ .

### 3.6.2 EBSD Analysis

As discussed in Section 2.3.3 each type of boundary has its unique misorientation (MO). Consequently, it has been shown that grains, subgrains and boundary character can be characterised using EBSD (Humphreys 1998, Humphreys, Huang, Brough and Harris 1999, Humphreys 2001, Goldstein, Newbury, Joy, Lyman, Echlin *et al.* 2003, Humphreys 2004, Humphreys 2004, Maitland and Sitzman 2007, Engler and Randle 2010, Panait, Bendick and Fuchsmann 2010, Josefsson 2012, Hino, He, Li, Chang and Shin 2013). Presently, the angular resolution of EBSD is approximately limited to  $0.5^\circ$  to  $1.5^\circ$  due to orientation noise (Humphreys 2001). This orientation noise refers to the limitations in the transformation of the Kikuchi pattern to Hough space for the identification of orientation. The main advantage of EBSD is that large areas of even few  $\text{mm}^2$  order of magnitude can be sampled within a few datasets and representative results acquired. However, the technique is limited by maximum spatial resolutions of up to 100 nm in deformed materials

and long acquisition times (Humphreys, Huang, Brough and Harris 1999). Aghajani (2009) has studied the MO of boundaries in long-term creep aged (140 000 h) X20 steel.

To analyse the PAG and boundaries, a large field of view EBSD orientation map covering an area of 204 x 153  $\mu\text{m}^2$  (500x magnification) was acquired from each polished bulk specimen (**Table 3.9**) using a Nordlys HKL system fitted to a JEOL JSM 7001F FEG-SEM. The Oxford AZtechHKL EBSD software (version 3.3) was used for the acquisition and analysis of the EBSD (Kikuchi) patterns. **Table 3.10** summarises the experimental conditions and software parameters used. In the AZtechHKL software, the specimen orientation was chosen as shown in **Figure 3.12** before exporting each data set. The acquired maps were of good quality since indexing rates of between 85% and 99% were measured.

The EBSD maps were further analysed with HKL CHANNEL5 EBSD post-processing software. Before the commencement of any MO measurements, a clean-up of non-indexed and misindexed points in each EBSD map was performed using the wild spike and zero solution extrapolation methods in the software. No more than 10% of the points were modified as prescribed by the ASTM:E2627 (ASTM 2010) standard.

**Table 3.10:** Conditions and AZtechHKL software parameters used for EBSD map acquisition.

<b>Accelerating Voltage</b>	15 kV	<b>Probe Current</b>	4 nA
<b>Specimen Tilt</b>	70°	<b>Step size</b>	200 nm
<b>Working Distance</b>	± 22 mm	<b>Static and Auto Background Correction</b>	On

<b>Detector Insertion Distance</b>	187.4 mm	<b>Hough Resolution</b>	75
<b>EBSD Camera Binning Mode</b>	4x4	<b>Band Detection Mode</b>	Centers
<b>EBSD Camera Gain</b>	1	<b>Number of Bands Detected</b>	12
<b>Frame Averaging</b>	1 frame	<b>Indexing Mode</b>	Refined Accuracy

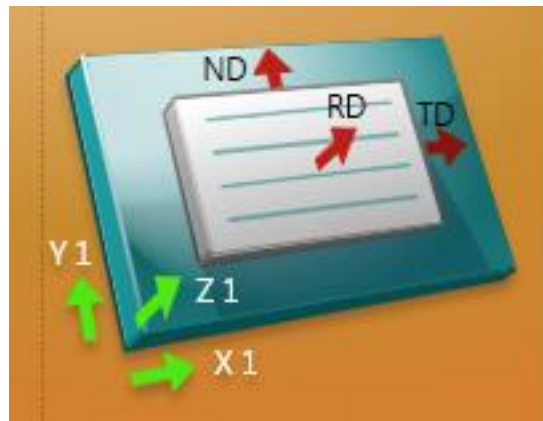


**Figure 3.12:** Selected specimen orientation in AZtechHKL EBSD software. Refer to **Figure 2.18** for descriptions of abbreviations.

### 3.6.3 TKD-EDS Analysis

Transmission Kikuchi Diffraction (TKD) or transmission EBSD (t-EBSD) is also an SEM-based diffraction technique that overcomes the spatial resolution limit of EBSD with resolutions better than 10 nm (Keller, Geiss and Rice 2013, Trimby 2013, Aracil 2014). As with EBSD, the technique is limited by the same angular resolution of 0.5° to 1.5° due

to orientation noise (Humphreys 2001). Even though EBSD has been used to measure subgrain sizes in 9-12% Cr martensitic steels for example the studies of Fujiyama, Mori, Matsunaga, Kimachi, Saito *et al.* (2009), Panait, Zielinska-Lipiec and Koziel (2010), Marx (2016), TKD is a technique that provides much higher spatial resolution and therefore more accurately resolves the micro-grains. Not many studies have performed TKD on 9-12% Cr martensitic steels.

Localised chemical analysis can be performed with Energy Dispersive X-ray Spectrometry (EDS or EDX) that evaluates the X-ray spectrum emitted by a solid sample bombarded with a focused beam of electrons (Tiedt 2002, Friel 2003, Ducati 2013, CFAMM 2018). An EDS system can be implemented in both an SEM and TEM/STEM. Elemental maps are obtained by scanning the beam in a raster pattern and displaying the intensity of the X-ray line of the selected element. The main two limitations of EDS are:

- (i) The EDS signal is impaired by beam broadening and therefore high spatial resolution X-ray mapping is not possible.
- (ii) EDS is inaccurate for light elemental analysis since it is not sensitive to elements with  $Z < 10$ .

However, the main advantage of EDS over other microanalysis techniques such as EELS is a more accurate analysis of heavier elements.

The SEM system used for EBSD analysis can perform TKD and EDS simultaneously. Therefore,  $12 \times 12 \mu\text{m}^2$  ( $400 \times 400$  pixels<sup>2</sup>) TKD and EDS maps were acquired from the twin-jet electropolished specimens (**Table 3.9**) using a Nordlys HKL system and Oxford X-Max EDS SDD detector fitted to a JEOL JSM 7001F FEG-SEM. The same Oxford AZtechHKL EBSD software was used for the acquisition and analysis. Since the interaction volume need not be limited as with EBSD, a higher accelerating voltage of 30 kV was used. A step size of 30 nm was found to provide sufficient spatial resolution with reasonable acquisition time. The acquisition conditions and parameters for the TKD-EDS analyses are summarised in **Table 3.11**. Two areas from each twin-jet electropolished specimen were analysed with TKD-EDS, resulting in a total of 4 areas per material type.

The TKD maps were post-processed similarly to the EBSD maps using the HKL CHANNEL 5 software.

**Table 3.11:** Conditions and AZtechHKL software parameters used for TKD-EDS analyses.

<b>Accelerating Voltage</b>	30 kV	<b>Probe Current</b>	4 nA
<b>Specimen Tilt</b>	-20°	<b>Step size</b>	30 nm
<b>Working Distance</b>	± 10 mm	<b>Static and Auto Background Correction</b>	On
<b>Detector Insertion Distance</b>	186 mm	<b>Hough Resolution</b>	75
<b>EBSD Camera Binning Mode</b>	4x4 (336x256 pixels)	<b>Band Detection Mode</b>	Centers
<b>EBSD Camera Gain</b>	1 (1s exposure)	<b>Number of Bands Detected</b>	12
<b>Frame Averaging</b>	1 frame	<b>Indexing Mode</b>	Refined Accuracy
<b>Energy Range</b>	10 keV	<b>Number of Channels/ Process Time</b>	2048/3

### 3.6.4 CBS Analysis

Compositional (Z) contrast can be obtained by imaging with BSE in the SEM (Goldstein, Newbury, Joy *et al.* 2003). Therefore, it is possible to distinguish between different phases and previous studies by Panait, Bendick, Fuchsmann *et al.* (2010), Hino, He, Li *et al.* (2013), and Yadav, Sonderegger, Sartory *et al.* (2015) have investigated the precipitates in 9-12% Cr martensitic steels using BSE-SEM. Due to Laves-phase precipitates being enriched with Mo with a high atomic number, they appear brightest in a BSE-SEM image, while MX precipitates that are enriched with V that has a lower atomic number will appear the darkest. In addition, BSE images can also provide information on topography and crystallography (grain orientation).

Traditionally, BSE imaging is performed with a 4-quadrant-type BSE detector where the angle of BSE detected is controlled by altering the working distance. This method suffers many unwanted side effects such as surface contamination, the build-up of charge on non-conductive samples and electron beam sensitivity destroying the sample structure. These side effects are avoided by using a Directional BSE (DBS) detector, also known as a Concentric Backscatter (CBS) detector, that has a concentric ring design. The emittance angle separates the BSE signal and multiple signals are simultaneously detected by four separate rings (FEI 2013). A schematic illustration of a CBS detector is given in **Figure 3.13**.

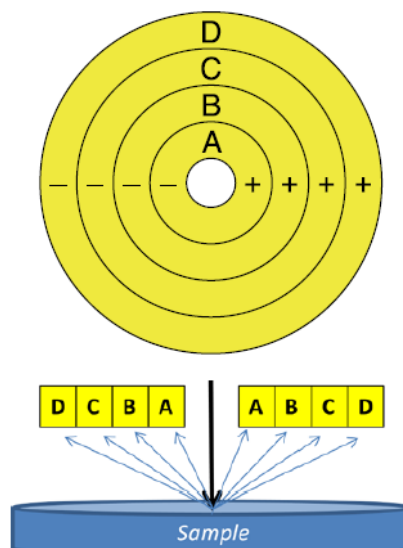


**Figure 3.13:** Schematic illustration of a CBS detector layout and angular separation of the BSE signal (FEI 2013).



CBS images of  $18.6 \times 12.3 \mu\text{m}^2$  areas on the twin-jet electropolished specimens were acquired using an FEI DBS (CBS) detector on an FEI Helios NanoLab DualBeam 650 FIB-SEM. Since both compositional and grain orientation information was of interest, the conditions used is 5 kV, 0.20 nA, 4 mm WD and the CBS detector set to detect BSE signal from all the rings. High-resolution images with good signal-to-noise ratio were obtained with 100  $\mu\text{s}$  pixel dwell time and  $3075 \times 2048 \text{ pixel}^2$  scan size. For cross-correlation, the same 4 areas as TKD-EDS was analysed.

### 3.6.5 EFTEM Analysis

Energy- Filtered TEM (EFTEM) has been shown by Maile (2007), Mayr, Holzer and Cerjak (2011), Marx (2016) to be a useful technique to analyse  $\text{M}_{23}\text{C}_6$  and MX precipitates in X20 steel by acquiring Cr and V elemental maps.

EFTEM investigations were performed using a Gatan Quantum GIF fitted to a JEM JEOL2100 (LaB<sub>6</sub>) TEM operated at 200 kV. A 150  $\mu\text{m}$  condenser aperture was used to provide the highest signal and an objective aperture inserted to restrict the collection angle to 10 mrad. The  $\text{M}_{23}\text{C}_6$  and MX precipitates were imaged by acquiring  $6 \times 6 \mu\text{m}^2$  Cr and V elemental maps, respectively, using the three-window method. Acquisition and display of the 2D EFTEM maps were performed using Gatan's Digital Micrograph (DM) software.

To make use of the advantage of each sample preparation technique, EFTEM was performed on both twin-jet electropolished specimens and extraction replica's prepared from the different materials (**Table 3.9**). For the twin-jet electropolished specimens, a total of 16 EFTEM elemental maps ( $6 \times 6 \mu\text{m}^2$ ) was acquired across the same areas on the twin-jet electropolished specimens as in the TKD and CBS analysis. Due to the larger sampling volume of the extraction replicas, 10 EFTEM V elemental maps ( $6 \times 6 \mu\text{m}^2$ ) provided a statistically sufficient number of VX precipitates for analysis.

Since the thickness is required for microstructural measurements from thin foils, the corresponding thickness ( $t/\lambda$ ) map was acquired with the EFTEM elemental maps for the

twin-jet electropolished specimens. They were generated by obtaining the zero loss and unfiltered BF images.

**Table 3.12** summarises the window energies and other experimental parameters used to acquire the EFTEM elemental maps using the three-window method and thickness map.

**Table 3.12:** Window energies and acquisition parameters for different EFTEM maps acquired.

Element	V	Cr	Thickness
Z	23	24	
Edge type	L	L	
Edge Energy (eV)	513	575	
Pre-edge 1 (eV)	465	527	
Pre-edge 2 (eV)	495	557	
Post-edge Energy (eV)	528	590	
Filter Slit Width (eV)	30	30	15
Exposure Time (s)	Auto ( $\pm 2-4$ )	Auto ( $\pm 3-5$ )	Auto ( $\pm 0.1$ )
Resolution (pixels <sup>2</sup> )	512x512	512x512	
Pixel Binning	4	4	1

To determine the thickness of each area a 2D parametric surface fit was performed on the acquired thickness map in ImageJ (Schindelin, Arganda-Carreras, Frise, Kaynig, Longair *et al.* 2012) to smooth out the contrast variations due to dynamical electron diffraction. The mean free path  $\lambda'$  of 200 keV electrons in 12% Cr stainless steels was

taken to be 100 nm and was based upon the calculation found in Egerton (1996), and Williams and Carter (2009). A conversion error of the order of 20% is estimated for this calculation. The accuracy of the 2D parametric surface fit still needs to be further investigated.

For parameters measured from the EFTEM maps, the thickness was determined from the corresponding smoothed map. However, in the case of parameters measured from TKD-EDS maps and STEM images, a single area is equivalent to 4 EFTEM thickness maps as discussed above. For these calculations, the thickness values of the 4 maps were combined and the corresponding mean thickness determined. These values are given in **Table 3.13**.

**Table 3.13:** Mean thickness of areas analysed on twin-jet electropolished specimens with TKD-EDS and STEM.

Sample	Mean thickness (nm)			
	Area 1	Area 2	Area 3	Area 4
New parent	33 ± 7	33 ± 5	22 ± 7	33 ± 12
New sim FGHAZ	16 ± 6	27 ± 13	35 ± 4	44 ± 7
Creep aged 1 parent	13 ± 3	37 ± 10	39 ± 7	51 ± 14
Creep aged 1 sim FGHAZ	27 ± 4	30 ± 7	29 ± 4	25 ± 10
Creep aged 2 parent	66 ± 7	55 ± 10	33 ± 9	32 ± 12
Creep aged 2 sim FGHAZ	66 ± 6	45 ± 7	44 ± 7	52 ± 7

For technical explanations on EFTEM the extensive literature reviews from Thomas and Midgley (2002), and Williams and Carter (2009) can be consulted.

### 3.6.6 STEM-EDS Analysis

Scanning Transmission Electron Microscopy (STEM) combined with EDS has been used by Aghajani 2009, Xu, Nie, Wang *et al.* (2017) to determine the chemical composition of the precipitates in 9-12% Cr martensitic steels. These studies were performed on thin foil specimens. Since there is no iron matrix like with the thin foil specimens, the chemical composition of the precipitates in the extraction replica specimens (**Table 3.9**) could be accurately analysed using STEM-EDS. The analysis was performed using a JEOL JEM 2100 LaB<sub>6</sub> TEM fitted with an Oxford X-Max 80 EDS SDD detector in STEM mode. Acquisition and post-processing of the spectra were done in the Oxford AZtec analysis software (version 3.3). In the software, the pre-defined elements were set as Cr, V, Fe, Mo, Si, Ni, C and N and the Ratio Standard setting was set to Silicon K-series. The exact STEM conditions and Aztec software parameters are provided in **Table 3.14**. The k-ratio method (Williams and Carter 2009) built into the software was used to perform the quantitative analysis. Accurate elemental quantification from EDS in TEM/STEM is complex and previous studies have attempted to use various standards to calibrate the EDS measurements for a particular elemental system (Mitchell and Sulaiman 2006). Spot analysis of precipitates chosen at random in 4 different areas of the extraction replica specimens was performed. For the literature on STEM-EDS the literature by Tiedt (2002), Watanabe (2011), and Carter and Williams (2016) can be consulted.

**Table 3.14:** Conditions and AZtec software parameters used for STEM-EDS analyses.

STEM Parameters		EDS Parameters	
Accelerating Voltage	200 kV	Number of Channels	2048
Convergence Angle	27 mrad	Energy Range	20 eV
Mode	AMAG	Process Time	3-5
Inner Detector Collection Angle (Inner)	158 ± 5 mrad	Count limit	30 000
Outer Detector Collection Angle	418 ± 5 mrad	Pulse Pile-Up Correction	On
		Energy per Channel	10.0 eV

### 3.6.7 STEM Analysis

Transmission Electron Microscopy (TEM) has been shown to be a well-established technique to determine dislocation density, especially in the study of large numbers of dislocations (Baker 2001). The free dislocation density in 9-12% Cr martensitic steels has been mainly studied using TEM (Eggeler, Nilsvang and Ilschner 1987, Ennis, Zielinska-Lipiec and Czyska-Filemonowicz 2001, Pešička, Kužel, Dronhofer and Eggeler 2003). Pešička, Aghajani, Somsen *et al.* (2010) and Aghajani (2009) has found that the dislocation substructure in X20 steel can be imaged with much higher quality using High-Angle Annular DF (HAADF) Scanning TEM (STEM) instead of conventional TEM. Enhanced dislocation contrast with large fields of view is provided by STEM. Marx (2016) has shown that dislocations are imaged with the highest quality by applying Annular DF

(ADF) STEM to twin-jet electropolished specimens that have damage free surfaces (Section 3.4.2).

The thickness of the TEM thin foil specimen has been shown by Pešička, Kužel, Dronhofer and Eggeler (2003), Aghajani (2009), and Pešička, Aghajani, Somsen *et al.* (2010) to be crucial for accurate dislocation studies. High-quality results are obtained for foil thicknesses of  $200 \pm 30$  nm. However, for sufficient contrast in BF and DF images, a thickness of 100 nm or less is desired. The problem with thinner foils is that they are often bent and there are associated high internal stresses. There is also a potential loss of dislocations to the free surface of the foil. In thicker foils, several diffraction contrast mechanisms operate in conventional TEM that result in insufficient contrast between the dislocations and surrounding matrix. Conversely, STEM can be applied to thicker specimens since bend contours and auxiliary contrast effects can be suppressed while retaining defect contrast (Phillips, Brandes, M.J.Mills and M.DeGraef 2011).

All the aforementioned TEM and STEM studies on dislocations in 9-12% Cr martensitic steels have used the approach of tilting the specimen to two-beam conditions (Williams and Carter 2009) to invoke the invisibility criterion and alleviate the difficulty with measuring high dislocation densities. However, from these studies it has been found that several factors limit this method:

- (i) Due to the magnetic iron matrix, the astigmatism of the objective lens needs to be re-adjusted for each tilt position.
- (ii) Diffraction patterns with diffuse Kikuchi lines are obtained because high dislocation densities are associated with internal stresses. Subsequently, this further encumbers tilting the specimen to two beam conditions.
- (iii) For each micro-grain, the two-beam condition must be adjusted and hence dislocation density can only be evaluated from small regions in a single TEM/STEM image.
- (iv) The sample preparation can influence the measured dislocation density. Ion-beam damage due to ion-milling or FIB sectioning may introduce artefacts.

The dislocation substructure was analysed in this study by performing ADF-STEM on the twin-jet electropolished specimens (**Table 3.9**) using a JEOL JEM 2100 LaB<sub>6</sub> TEM in STEM mode. The problem (iv) above is overcome by performing analysis on the twin-jet electropolished specimens. The FGHAZ microstructure have smaller grains, which makes tilting to two-beam conditions even more difficult according to the points above. Subsequently, to overcome the tilting problems (points (i) to (iii)) and obtain more statistically reliable results, the specimen was analysed with ADF-STEM in an un-tilted position. The limitations of this approach are discussed in Chapter 4. The advantage STEM has over TEM for dislocation analysis is that the STEM probe is convergent and will interact with the sample at multiple angles all at once, whereas with the TEM there is only parallel illumination of the sample. Consequently, a range of Bragg angles are satisfied simultaneously and the dislocations become more visible.

Areas of 6 x 6 μm<sup>2</sup> in size were imaged. For cross-correlation, the same areas as CBS and TKD analysis were analysed and a total of 16 images were acquired to cover the same sampling size as that of the TKD analysis (576 μm<sup>2</sup>). Subsequently, 4 DF-STEM images covered the same area as 1 TKD map. The ADF-STEM conditions are summarised in **Table 3.15**. The conditions were chosen such that STEM-EDS can be performed simultaneously with sufficient signal while retaining adequate dislocation contrast in the ADF-STEM image. However, the STEM-EDS results from the extraction replica specimens proved to be more accurate and therefore the results from STEM-EDS on the thin foils were not included in the final results. To obtain high-resolution images with high signal-to-noise ratios, a pixel scan size of 2048 x 2048 with a dwell time 50 μs was used.

The precipitate parameters and subgrain sizes in 9-12% Cr martensitic steels have also been studied with DF-STEM by Aghajani, Somsen and Eggeler (2009), and BF-TEM by Eggeler, Nilsvang and Ilschner (1987), Sklenička, Kuchařová, Svoboda *et al.* (2003), Maile (2007), Hino, He, Li *et al.* (2013), Milović, Vuherer, Blačić *et al.* (2013), and Xu, Zhang, Tian *et al.* (2016). In this study, the other techniques discussed in the previous sections have been found to be more efficient in measuring these parameters. For a

review on the literature of STEM the reader is referred to the detailed discussions given by Carter and Williams (2016).

**Table 3.15:** Conditions used for ADF-STEM analysis.

<b>Accelerating Voltage</b>	200 kV
<b>Convergence Angle</b>	27 mrad
<b>Mode</b>	AMAG
<b>Inner Detector Collection Angle (Inner)</b>	18 ± 5 mrad
<b>Outer Detector Collection Angle</b>	47 ± 5 mrad

### 3.6.8 XRD Analysis

X-ray Diffraction (XRD) is used for obtaining diffraction information such as the crystallographic phase, orientation and lattice parameters (Suryanarayana and Norton 1998, Pešička, Kužel, Dronhofer and Eggeler 2003, Tang, Lynch, Cheary and Clark 2006, Sardela 2008, Hammond 2009). Broadening of the peak profiles in the XRD spectrum is observed due to softening of Bragg's Law caused by instrumental effects and the sample itself (Girgsdies 2015). The sample-related contribution to broadening is from crystallite size, micro-strain, stacking faults and other defects in the sample.

It is assumed that broadening caused by 9-12% Cr martensitic steel samples is only from dislocations and crystallite size. Specifically, the strain broadening is caused by the extended displacement fields in the crystals due to the dislocations. The crystallite size is the size of the coherently diffracting domains. It can either be the crystallites or the domains within the crystallites that diffract coherently. Small crystallite sizes and high dislocation densities usually result in broader XRD peaks. To extract the crystallite size and micro-strain components, deconvolution of the broadened peak profiles is necessary. One such deconvolution method is Rietveld refinement where least-squares fitting of the



experimental pattern is done with a specific instrumental model (Ungár 2001). A good overview of the different deconvolution methods and their limitations is given by Balzar, Audebrand, Daymond, Fitch, Hewat *et al.* (2004).

The bulk specimens (**Table 3.9**) were prepared for XRD analysis as described in Section 3.4.1. XRD diffraction patterns were collected on a laboratory Bruker D2 Phaser (Bragg-Brentano geometry) diffractometer using the instrument specifications given in **Table 3.16** and from  $2\theta$   $20^\circ$  to  $120^\circ$  in  $0.02^\circ$  steps. A cobalt instead of copper radiation source was used in preference to a copper source to limit the low signal-to-noise ratio due to fluorescence when iron-based materials are analysed using copper radiation. The instrumental line broadening was determined experimentally with a calibration standard made from polycrystalline Si. The XRD pattern from the calibration standard was fitted using Rietveld refinement to model the angular dependence of the instrumental line broadening using the TOPAS<sup>TM</sup> software (Perl, Shin, Schümann, Faddegon and Paganetti 2012). These instrumental line broadening coefficients were then fixed during subsequent refinements of the sample parameters. The experimental XRD patterns were then scanned for the bulk specimen of each material type.

Evidence of line broadening for the different samples was determined by visual inspection of the (110), (200) and (211) peaks. The experimental XRD spectra were imported into the software known as TOPAS<sup>TM</sup> to quantitatively extract the contributions of crystallite size and strain, and to deconvolute the effects of the instrument. The refinement was performed using the alpha-iron crystal structure (Ferrite:  $Im\text{-}3m$ ,  $a_0 = 2.87 \text{ \AA}$ ). It was assumed that the line broadening due to crystallite size is Lorentzian, while the line broadening due to strain is Gaussian. Refinement was allowed on the (i) sample height, (ii) lattice parameter, (iii) background, (iv) crystallite size  $L$  and (v) strain  $G$ , while all the other parameters were kept constant. The peaks were fitted using the Fundamental Parameters Line Profile Fitting (FPPF) in conjunction with the Rietveld Refinement method. The background was fitted using a Chebyshev polynomial of order 3. The “Crystallite size Lorentzian” parameter was recorded as the crystallite size measurement, the “Strain  $G$ ” was recorded as the micro-strain and “ $\epsilon_0$ ” from strain was reported as the total micro-

strain in the sample. TOPAS™ calculates this  $\epsilon_0$  value assuming the strain is both Gaussian and Lorentzian.

**Table 3.16:** Instrument specifications used for XRD analysis.

Component	Parameter	Value
<b>Goniometer Radii</b>	Primary Radius (mm)	70.7
	Secondary Radius (mm)	70.7
<b>Detector</b>	Linear PSD 2theta angular range (°)	3.242
<b>Slits</b>	Secondary Söller (°)	2.5
<b>X-ray Source</b>	Co $K\alpha_1$ (Å)	1.789
	Co $K\alpha_2$ (Å)	1.793
<b>Operational Setting</b>		30 kV; 10 mA

### 3.7 MICROSTRUCTURAL EVALUATION METHODOLOGIES

In the following sections the microstructural measurement procedures developed to investigate the microstructural evolution of new and long-term creep aged parent and simulated FGHAZ X20 steel from the results acquired using the techniques in Section 3.6, is explained.

#### 3.7.1 Prior Austenite Grains

The grains were reconstructed using the software known as ARPGE (Automatic Reconstruction of Parent Grains from EBSD) (Cayron 2007) to better analyse the PAG. As the name suggests, the software reconstructs PAG from the acquired EBSD maps (Section 3.6.2) using a selected phase transition. The software preset "KS fcc => bcc (Fe)" phase transition was selected. A screenshot from the software of the parameters

used for the reconstructions is provided in **Figure 3.14**. The only difference between the parameters used for the parent and simulated FGHAZ materials is the minimum number of daughter grains in a parent grain. A value of 3 instead of 5 was chosen for the simulated FGHAZ materials since the PAG are smaller and therefore there are fewer daughter grains in a single grain. Inaccurate reconstructions were obtained for the simulated FGHAZ materials using a value of 5. The size of the PAG was also measured using the software.

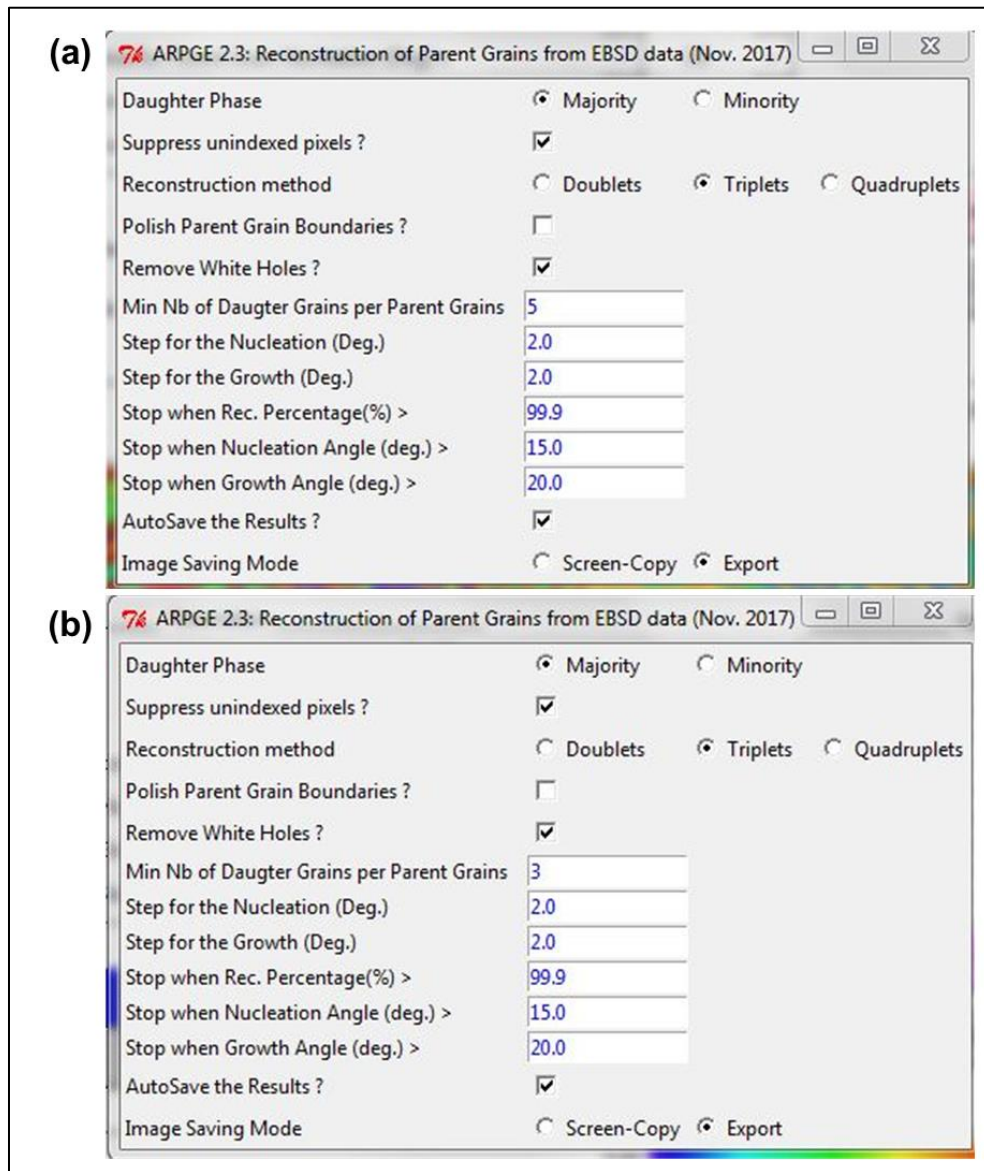


**Figure 3.14:** Screenshots from ARPGE software of parameters used for reconstruction of PAG in (a) parent and (b) simulated FGHAZ materials.

### 3.7.2 Creep Cavities

Semi-automated image analysis using the software MIPAR™ (Sosa, Huber, Welk and Fraser 2014) was used to threshold the cavities from the acquired LM micrographs (Section 3.6.1). The Equivalent Circular Diameter (ECD) was directly measured from the thresholded images using MIPAR™. Inclusions were measured as features with ECD larger than 3  $\mu\text{m}$  and excluded from the analyses. It is assumed that voids with minimum size of 1  $\mu\text{m}$  can be analysed with conventional surface replication techniques (Section 3.2.2). Therefore, for comparison to the surface replication results measured by Eskom (**Table 3.3**), the voids data was separated into features with ECD smaller than 3  $\mu\text{m}$  and those with ECD between 1 and 3  $\mu\text{m}$ . Even though the spatial resolution limit of LM at the working magnification is  $\pm 1 \mu\text{m}$ , features (or artefacts) were detected from the micrographs with ECD smaller than 1  $\mu\text{m}$  and therefore the separation of the data was necessary. *For simplification, the voids with ECD smaller than 3  $\mu\text{m}$  will be referred to further as “cavities” and those with 1 to 3  $\mu\text{m}$  ECD as “voids”.*

Since the voids are comparable to the surface replication results, they are further quantitatively analysed. The number density  $N_A$  and nearest neighbour distance (NND) of the voids were also measured directly from the thresholded images in MIPAR™. It should be noted that the NND measured in MIPAR™ is the centre-to-centre distance between the nearest features.

To stereologically correct for sectioning of the 3D voids, the measured 2D ECD distributions were unfolded into 3D ECD distributions in MIPAR™. The software implements the unfolding model for planar sections developed by Payton (2012). The accuracy of this unfolding is strongly dependent on the bin size is chosen for the distribution. Since the 3D ECD distribution must be larger than the 2D distribution by logical reasoning, the number of bins was determined as the first value from 5 that resulted in this criterion being met. Further work is still needed to determine the accuracy of this unfolding approach. Nonetheless, the corrected distributions do not show any anomalies compared to the 2D distributions. To illustrate the variation in the number

density of the voids across the different areas and materials, a montage was created of the 16 micrographs and the area fraction of the voids plotted as a colour map in MIPAR™.

A higher spatial resolution than LM is required to investigate the location and shape of the cavities. Therefore, SE-SEM images were obtained from the same bulk specimens using a JEOL JSM 7001F FEG-SEM with conditions of 10 kV, 0.27 nA and approximately 8 mm WD. To further analyse the location of the cavities, a 120 x 92  $\mu\text{m}^2$  EBSD map was acquired from the creep aged 2 parent and simulated FGHAZ bulk specimens. Except for a step size of 100 nm, the same conditions and parameters as in **Table 3.10** were used.

### 3.7.3 $\text{M}_{23}\text{C}_6$ Precipitates

Since there is no significant amount of Nb in the X20 steel (**Table 3.2**), only  $\text{M}_{23}\text{C}_6$  (M = Cr, Fe, Mo) carbides and VX (X = C, N) carbonitrides are present in the microstructure of X20 steel (Section 2.3.2). The  $\text{M}_{23}\text{C}_6$  carbides were analysed from the TKD-EDS Cr elemental maps and the CBS images. Even though the same areas on the twin-jet electropolished specimens have been analysed for both techniques, the CBS images cover a larger surface area of 915  $\mu\text{m}^2$  (4 x (18.6x12.3  $\mu\text{m}^2$ )) than the TKD-EDS maps that cover 576  $\mu\text{m}^2$  (4 x (12x12  $\mu\text{m}^2$ )).

The carbides were identified in the CBS images as those whose contrast is not a minimum or a maximum since they are enriched with Cr. Using semi-automatic image analysis in MIPAR™ the  $\text{M}_{23}\text{C}_6$  carbides were thresholded from the TKD-EDS Cr elemental maps and CBS images.

The TKD grain boundary (GB) maps of  $\text{MO} > 2^\circ$  was plotted using the HKL CHANNEL 5 software and superimposed onto the corresponding EDS Cr elemental map. Consequently, it was possible to separate the thresholded carbides into boundary carbides and interior carbides using a simple image arithmetic in MIPAR™. Boundaries with  $\text{MO} > 1^\circ$  (SGB) could not be used since these maps include the orientation noise. Grain orientation contrast from the micro-grains was visible from the CBS images and therefore using semi-automatic image analysis in MIPAR™ the MGB were isolated. The boundary and interior carbides could then be separated similarly to the TKD-EDS data.

The ECD of the thresholded carbides were measured in MIPAR™. Due to sectioning of the  $M_{23}C_6$  carbides in the twin-jet electropolished specimens, stereological correction is required to correct for smaller measured diameters. In the case of the CBS images, the carbides are measured from a 2D planar section and standard Stereology formulae apply. The usual Stereology criterion of ensuring no sampling bias was satisfied by sampling from more than one area and sample. The measured 2D ECD distributions were unfolded into 3D ECD distributions using the same procedure as for the cavities (Section 3.9.2) with a number of 100 bins. The Stereology equations used to calculate the precipitate parameters per area is summarised in **Table 3.17**. In MIPAR™, 1000 randomly oriented lines were drawn on the area and the total number of intersections and total test line length recorded. The area fraction  $A_A$  was also measured with MIPAR™.

The  $M_{23}C_6$  carbides in the TKD-EDS maps are projections from a thin foil and therefore specimen thickness must be considered. Sonderegger (2006) developed correction factors for arbitrary precipitate distributions to obtain the true precipitate size distribution. This approach assumes the precipitates to be spherical and homogeneously distributed throughout the specimen. **Table 3.18** summarises these developed formulae used to calculate the precipitate parameters from the TKD-EDS Cr elemental maps. These formulae were applied to the measured ECD data over all areas.

**Table 3.17:** Formulae used to calculate  $M_{23}C_6$  carbide parameters from CBS images.

Parameter Name and Reference	Formula	
The number of intersections between test lines $I_L$ (Gokhale 2004)	$I_L = \frac{\text{Total number of test line intersections}}{\text{Total test line length}}$	(3.1)
Total surface area per unit volume $S_V$ (Gokhale 2004)	$S_V = 2 I_L$ <i>Must be determined from more than one area. Applicable to microstructural features of any arbitrary geometry.</i>	(3.2)
Volume fraction $V_V$ (Underwood 1973)	$V_V = A_A$ <i>Applicable to microstructural features of any arbitrary geometry.</i>	(3.3)
Surface area averaged particle size (caliper diameter) $d_s$ (Gokhale 2004)	$d_s = \frac{6V_V}{S_V}$ <i>Applicable to any collection of convex particles of different shapes and sizes. Microstructure need not be isotropic.</i>	(3.4)
Average volume per precipitate $\bar{V}_P$	$\bar{V}_P = \frac{4}{3} \pi \left(\frac{d_s}{2}\right)^3$	(3.5)
Number density $N_V$	$N_V = \frac{f_V}{\bar{V}_P}$	(3.6)
Mean 2D surface- to-surface particle distance $\lambda$ (Holzer 2010)	$\lambda = \sqrt{\frac{\ln 3}{2\pi N_V \bar{r}} + 4\bar{r}^2} - 1.63\bar{r}$ Where: $\bar{r} = \frac{d_s}{2} \equiv \text{mean particle radius of precipitates}$	(2.15)

**Table 3.18:** Formulae used to calculate precipitate parameters from TKD-EDS and EFTEM maps acquired from twin-jet electropolished specimens.

Parameter Name and Reference	Formula	
Corrected diameter of $i^{\text{th}}$ precipitate (Sonderegger 2006)	$d_i = \frac{2}{\pi}(d_{m,i} - t_i) + \sqrt{\frac{2}{\pi}(d_{m,i} - t_i)^2 + \frac{4d_{m,i}t_i}{\pi}}$ <p>Where:  <math>d_{m,i} \equiv</math> measured diameter of precipitate <math>i</math>  <math>t_i \equiv</math> sample thickness of area where precipitate <math>i</math> is located</p>	(3.7)
Phase fraction $f_V$ (Sonderegger 2006)	$f_V = \frac{V_V}{V_{\text{Sample}}} = \frac{1}{A_{\text{Sample}}} \sum_i A_i \left( \frac{2d_{m,i}/t_i}{2d_{m,i}/t_i + 3} \right)$ <p>Where:  <math>V_V \equiv</math> Total volume of precipitates  <math>A_{\text{Sample}}/V_{\text{Sample}} \equiv</math> examined sample area/volume  <math>A_i \equiv</math> projected area of precipitate <math>i</math></p>	(3.8)
Number density $N_V$ (Sonderegger 2006)	$N_V = \frac{N_A}{V_{\text{Sample}}} = \frac{1}{A_{\text{Sample}}} \sum_{i=1 \dots N_A} \frac{1}{t_i + d_{m,i}}$ <p>Where:  <math>N_A \equiv</math> measured number of precipitates per sample area</p>	(3.9)
Weighted mean precipitate diameter $\bar{d}$ (Sonderegger 2006)	$\bar{d} = \frac{\sum_i d_i [t_i / (t_i + d_i)]}{\sum_i [t_i / (t_i + d_i)]}$	(3.10)
Mean 2D surface- to- surface particle distance $\lambda$ (Holzer 2010)	$\lambda = \sqrt{\frac{\ln 3}{2\pi N_V \bar{r}} + 4\bar{r}^2 - 1.63\bar{r}}$ <p>Where:  <math>\bar{r} = \frac{\bar{d}}{2} \equiv</math> mean particle radius of precipitates</p>	(2.15)



### 3.7.4 MX Precipitates

EFTEM has been chosen as the primary analysis technique for the V-enriched MX (VX) precipitates for the following main reasons:

- (i) TKD-EDS does not provide sufficient spatial resolution to resolve the small VX precipitates
- (ii) and it is not possible to distinguish in a CBS image between voids and VX precipitates since both features appear black.

The main limitation with the analysis of VX precipitates in a TEM thin-foil using EFTEM or EDS is that due to their small size the iron matrix interferes with getting a sufficient signal-to-noise ratio from small VX precipitates, especially in thicker areas, and these precipitates are either not measured or their boundaries poorly resolved. As mentioned in Section 3.4.3, a proposed solution is analysing an extraction replica where no iron matrix can interfere, and the true precipitate size and shape can be analysed. However, as BRT has its limitations as discussed in Section 3.4.3. Therefore, EFTEM results from the extraction replicas was used only to look at the exact VX precipitate shape and size, while all the other precipitate parameters such as volume fraction and number density were determined from the results acquired from the twin-jet electropolished specimens.

The VX precipitates were thresholded from the EFTEM V elemental maps acquired from the twin-jet electropolished and extraction replica specimens, using semi-automatic image analysis in MIPAR™. From the thresholded maps, the ECD was measured in MIPAR™. Since it is assumed that the VX precipitates are too small to be sectioned, no stereological corrections were necessary for the ECD. Equations (3.8), (3.9) and (2.15) in **Table 3.18** was used to calculate the other parameters.

### 3.7.5 Chemical Composition of Precipitates

The chemical composition of the  $M_{23}C_6$  carbides was determined by performing STEM-EDS point analysis on the extraction replica specimens (Section 3.6.6). As discussed in Section 2.3.2, the M in the  $M_{23}C_6$  carbides is mainly Cr and Fe with a minor content of Mo. Therefore, these carbides were identified as those with high Cr content of larger than 50 at% and lower Fe content of approximately 20 at%. A total number of 50  $M_{23}C_6$  carbides was chosen at random across 4 areas per material type and analysed. Only the relative amounts of Cr, Fe and Mo in the carbides was calculated from the at% to prevent significant error by quantifying light elements such as carbon and nitrogen using EDS.

As mentioned in Section 2.3.2, only V-enriched MX precipitates form in X20 steel with X being either carbon or nitrogen. The chemical composition measured using STEM-EDS point analysis is not accurate due to the discrepancies of EDS with light elemental analysis. Also, erroneous copper amounts are detected due to the copper grid used for the extraction replica. This problem can also not be overcome by measuring relative amounts as for the  $M_{23}C_6$  carbides since V is the only heavy element of interest. Nonetheless, STEM-EDS point analysis was performed on some VX precipitates in the extraction replica specimens. These precipitates were identified with only V in significant content. However, due to the small size and overlapping of the VX precipitates with the  $M_{23}C_6$  carbides in the extraction replicas, a statistically significant amount of VX precipitates could not be analysed.

Since EDS cannot quantify light elements such as C and N accurately, it is not possible to determine if the VX precipitates in X20 steel are of the type VC or VN. Electron Energy Loss Spectroscopy (EELS) is a complementary technique to EDS since it has a detection sensitivity in the range of 0.1 to 1 wt% for light elements ( $Z < 11$ ) (Brydson 2001). Therefore, the type of VX precipitate was determined using STEM Spectrum Imaging (SI) with the same TEM and STEM conditions as the STEM-EDS (**Table 3.14**) and an acceptance angle of 24 mrad. A single area in the extraction replica of the new parent material was analysed. This was only a proof of concept and future work will include mapping more areas and the rest of the samples with STEM-EELS.

### 3.7.6 Micro-grains and Substructure

As discussed in Section 3.7.3, the MGB could be isolated from the CBS images and hence the micro-grain size measured. For comparison, the MGB was completed from the TKD GB maps (Sections 3.6.2 and 3.7.3) with  $MO > 2^\circ$  and  $MO > 5^\circ$  using semi-automatic image analysis in MIPAR™. Analyses could then be performed on the outlined micro-grains. Similarly, the substructure was analysed by thresholding the boundaries in the ADF-STEM (Section 3.6.7) images using semi-automatic image analysis in MIPAR™.

Section 2.6.2 explains that it is the short width of the micro-grains that plays a vital role in creep strengthening. To obtain the short width value, the minor axis length of a fitted equivalent ellipse was measured from each thresholded image. This is illustrated in **Figure 3.15**. The advantage is that the edge micro-grains or substructure features need not be excluded since by fitting an ellipse across them their minor axis is still accurately measured. Also, regardless of the projection of the feature, the shortest width is measured. The substructure was also quantified as the size of the coherently diffracting domains (crystallite size) measured from the XRD spectrum using the TOPAS™ software (Section 3.6.8).

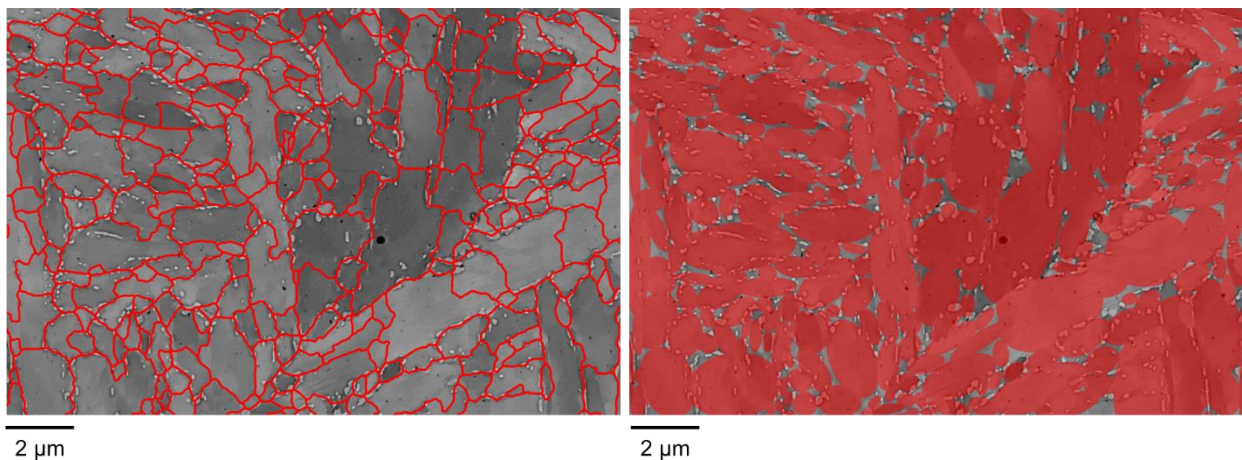


**Figure 3.15:** Illustration of fitted equivalent measurements (right) to thresholded micro-grains from CBS images (left) using MIPAR™.

### 3.7.7 Dislocations

Yadav, Kalácska, Dománková *et al.* (2016) and Pešička, Kužel, Dronhofer and Eggeler (2003) have studied the evolution of dislocation density in X20 and P91 steels during heat treatment and creep using TEM/STEM and XRD as complementary methods. Yadav, Kalácska, Dománková *et al.* (2016) studied mobile, dipole and boundary dislocation densities in X20 steel. **Figure 3.16** summarises the techniques they used to analyse the different dislocation types. Since it is not possible to distinguish between the dipole ( $\rho_{\text{dip}}$ ) and mobile dislocation ( $\rho_{\text{m}}$ ) densities inside the substructure in the TEM/STEM images, it is the combined internal dislocation density ( $\rho_{\text{int}}$ ) that is measured from these images.

The strain broadening of the XRD diffraction peaks (Section 3.6.8) is associated with long-range stress fields from the dislocations inside the substructure. Boundary dislocations are configured in low energy positions and therefore they have short range stress fields (Section 2.3.4). The dipoles have relatively low range stress fields compared to the mobile dislocations. Consequently, only mobile dislocations are considered to contribute to the XRD peak broadening due to strain.

Yadav, Kalácska, Dománková *et al.* (2016) applied the approach developed by Pešička, Dronhofer and Eggeler (2004) that estimates the boundary dislocation density ( $\rho_{\text{b}}$ ) from the fraction of SGB and their MO from EBSD maps. This is currently the only approach for determining boundary dislocation density for 9-12% Cr martensitic steels. Due to the limited angular resolution of EBSD and TKD (Sections 3.6.2 and 3.6.3), it is not possible to accurately analyse purely the SGB whose MO is between  $1^\circ$  to  $2^\circ$ . Thus, the accuracy of this approach is questionable and boundary dislocation density was not analysed in this study.

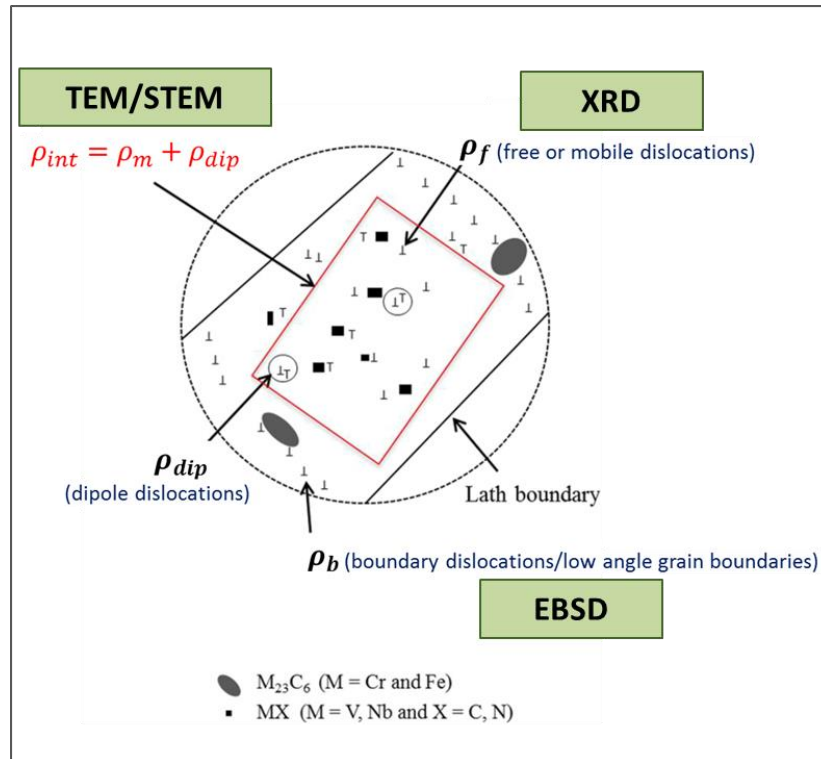


**Figure 3.16:** Schematic illustration of the various dislocations in the tempered martensite microstructure of 9-12% Cr ferritic steels and the corresponding techniques that can analyse their densities (Yadav, Kalácska, Dománková, Yubero, Resel et al. 2016).

The internal dislocations were thresholded from the acquired ADF-STEM images using semi-automatic image analysis in MIPAR™. The mean linear intercept method (Pešička, Aghajani, Somsen et al. 2010) was then applied by drawing 1000 randomly oriented lines on the area and measuring the total number of intersections and total test line length. MIPAR™ was also used for this measurement. The internal dislocation density  $\rho_{int}$  was then calculated using the following formula:

$$\rho_{int} = \frac{1}{t} \left( \frac{\text{total number of intersections with test lines per area}}{\text{total test line length}} \right) \quad (3.11)$$

where  $t$  is the thin foil thickness as determined using EFTEM (Section 3.6.5). It is noted that the areas analysed are thin (**Table 3.13**). As stated these areas were chosen for cross-correlation to TKD and EFTEM which require thinner areas. Thus, the results are

carefully interpreted keeping the thickness limitations as discussed in Section 3.6.7 in mind.

Yadav, Kalácska, Dománková *et al.* (2016) extracted the mobile dislocation density from the micro-strain value determined from the XRD peak broadening for 9-12% Cr martensitic steels. The formula they used is developed from the work of Williamson and Smallman (1956) and determines the mobile dislocation density  $\rho_m$  from the root-mean-square of the lattice micro-strain as follows:

$$\rho_m = \frac{k(\langle \varepsilon^2 \rangle^{\frac{1}{2}})^2}{Fb} \quad (3.12)$$

where  $b$  is the Burgers vector (**Table 2.11**),  $\langle \varepsilon^2 \rangle^{\frac{1}{2}}$  is the micro-strain (Gaussian or Lorentzian) measured from Rietveld refinement (also known as root-mean-square (RMS) lattice strain),  $k = 14.4$  and  $F = 1$  for a bcc crystal structure. It is not explicitly stated by Yadav, Kalácska, Dománková *et al.* (2016) if they assumed a purely Gaussian or Lorentzian profile for strain broadening.

Another formula developed by Williamson and Smallman (1956) has been proposed by Soleimanian and Mojtahedi (2015) to determine the dislocation density from both the micro-strain and crystallite size determined using Rietveld refinement:

$$\rho = (\rho_D \rho_s)^{\frac{1}{2}} = \frac{2\sqrt{3} \langle \varepsilon^2 \rangle^{\frac{1}{2}}}{b \langle D \rangle} \quad (3.13)$$

where  $\rho_D$  is the dislocation densities due to the crystallite size,  $\rho_s$  is the dislocation densities due to the micro-strain, and  $\langle D \rangle$  is the crystallite size determined from Rietveld refinement.

The dislocation densities were calculated from both Equation (3.12) and (3.13), and compared. The value for the micro-strain  $\langle \varepsilon^2 \rangle^{\frac{1}{2}}$  was used as the  $\varepsilon_0$  value from strain determined from TOPAS™ (Section 3.6.8) instead of the micro-strain from strain\_G since a more realistic assumption is that the peak profile of strain broadening is a mixture of

Gaussian and Lorentzian. This micro-strain value is in units of  $2\theta$  degrees and therefore first needed to be converted to a strain ratio value by multiplying with  $\frac{\pi}{360}$ .

### 3.8 STATISTICAL ANALYSIS OF MEASUREMENTS

It is assumed that the thickness variation of the twin-jet electropolished specimen contributes to the most significant error in the measured parameters (**Table 3.13**). Hence, each parameter that is dependent on thickness was determined with the minimum and maximum thickness value instead of with only the mean value (Section 3.6.5). To incorporate the range of values calculated, the following relations were used to report the mean and error values:

$$\text{mean} = \frac{\text{maximum value} + \text{minimum value}}{2} \quad (3.14)$$

$$\text{error} = \frac{\text{maximum value} - \text{minimum value}}{2} \quad (3.15)$$

In the case where the parameters were determined per area, Equations (3.14) and (3.15) was used to report the mean and error values. Where a parameter was determined from a single dataset, standard Gaussian statistics of mean and 95% Confidence Interval (CI) as the error, was reported. Some parameters varied per area and MIPAR™ was able to determine the mean and standard deviation per area. To obtain a combined mean and 95 % CI across all areas the “One-Way Normal or Gaussian Model” was used (Vardeman and Jobe 2016). This approach is very basic and it is assumed that the dataset from each area is normally (Gaussian) distributed. The single mean value for the parameter was then determined as the mean of the means. The combined standard deviation is then estimated by a “pooled estimator”  $s_p$  calculated as follows (Vardeman and Jobe 2016):

$$s_p = \sqrt{\frac{(n_1 - 1)s_1^2 + (n_2 - 1)s_2^2 + \dots + (n_r - 1)s_r^2}{n - r}} \quad (3.16)$$

where  $n_1, n_2, \dots, n_r$  is the sample size for each area,  $s_1, s_2, \dots, s_r$  is the sample standard deviation of each area and  $r$  is the number of samples (areas). The 95% CI can then be determined as the error from this pooled estimator as (Vardeman and Jobe 2016):

$$error = 95\% CI = 1.96 s_p \sqrt{\left(\frac{1}{r}\right)^2 \left[\frac{1}{n_1} + \frac{1}{n_2} + \dots + \frac{1}{n_r}\right]} \quad (3.17)$$

In this study, this approach is used as an estimation and further work is still required to determine the accuracy of using this approach to report the overall mean and error. Other means of error reporting in the study will be explicitly stated in the results (Chapter 4).



### 3.9 SUMMARY OF TECHNIQUES AND ANALYSES

**Table 3.19** provides a summary of the experimental techniques employed and the corresponding microstructural feature measured with the technique.

**Table 3.19:** *Experimental techniques and corresponding microstructural feature (property) analysed.*

Technique	Specimen Type	Microstructural Feature /Property
Vickers MHT	Bulk	Hardness
Light Microscopy	Bulk	Cavities
EBSD	Bulk	PAG Boundary character
SE-SEM	Bulk	Cavities
TKD-EDS	Twin-jet electropolished	M <sub>23</sub> C <sub>6</sub> carbides Micro-grains
CBS	Twin-jet electropolished	M <sub>23</sub> C <sub>6</sub> carbides Micro-grains
EFTEM	Twin-jet electropolished Extraction replica	MX precipitates
ADF-STEM	Twin-jet electropolished	Substructure Internal dislocations
XRD	Bulk	Substructure Mobile dislocations
STEM-EDS	Extraction replica	Chemical composition of M <sub>23</sub> C <sub>6</sub> carbides and MX precipitates

# CHAPTER 4

## RESULTS AND DISCUSSION

---

### 4.1 INTRODUCTION

This chapter focuses on describing the microstructural evolution of the virgin and long-term creep aged parent and simulated FGHAZ X20 steel. To achieve this, the results from the hardness, prior austenite grain, boundary character, creep void, precipitate, subgrains and dislocation analyses discussed in Chapter 3, are presented and discussed.

### 4.2 QUALITATIVE COMPARISON OF MICROSTRUCTURES

Initially, the microstructure of each sample was qualitatively compared using optical microscopy. **Figure 4.1** shows BF-mode low magnification optical micrographs taken from the etched surface of each bulk specimen. The parent material has PAG that are visible from these micrographs, while the PAG are too small to observe from the simulated FGHAZ specimens. This was the first indication that simulation of the FGHAZ has been successful. The homogeneity of the simulated microstructure through the diameter of the rod sample was evaluated by obtaining a stitched montage of the 1.1 x 0.8 mm<sup>2</sup> BF optical micrographs acquired as described in Section 3.6.1, across the cross-section of the simulated FGHAZ bulk specimens, which is a cross-section of the rod sample (Section 3.3). These stitched montages are given in **Figure 4.2**. As can be seen, the microstructure seems to be homogeneously simulated along the cross-section of the specimen.

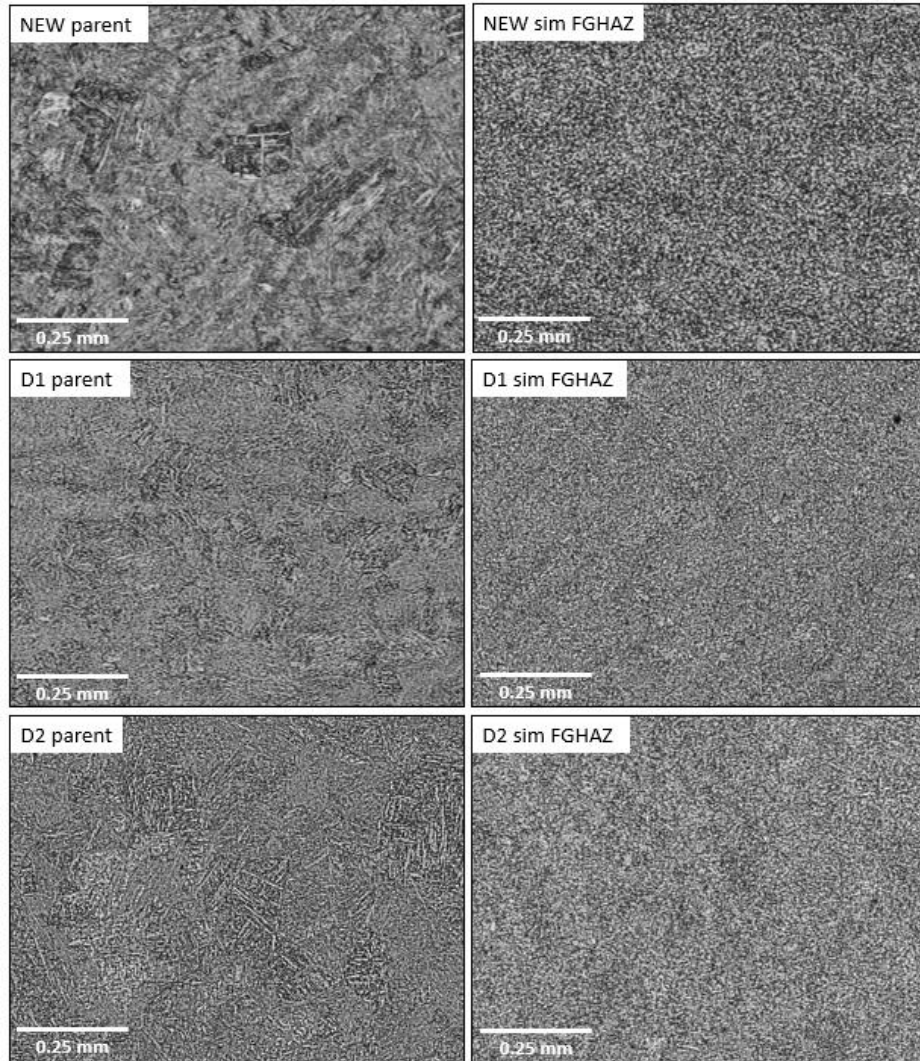


**Figure 4.1:**  $1.1 \times 0.8 \text{ mm}^2$  BF optical micrographs of the etched bulk specimen surfaces.

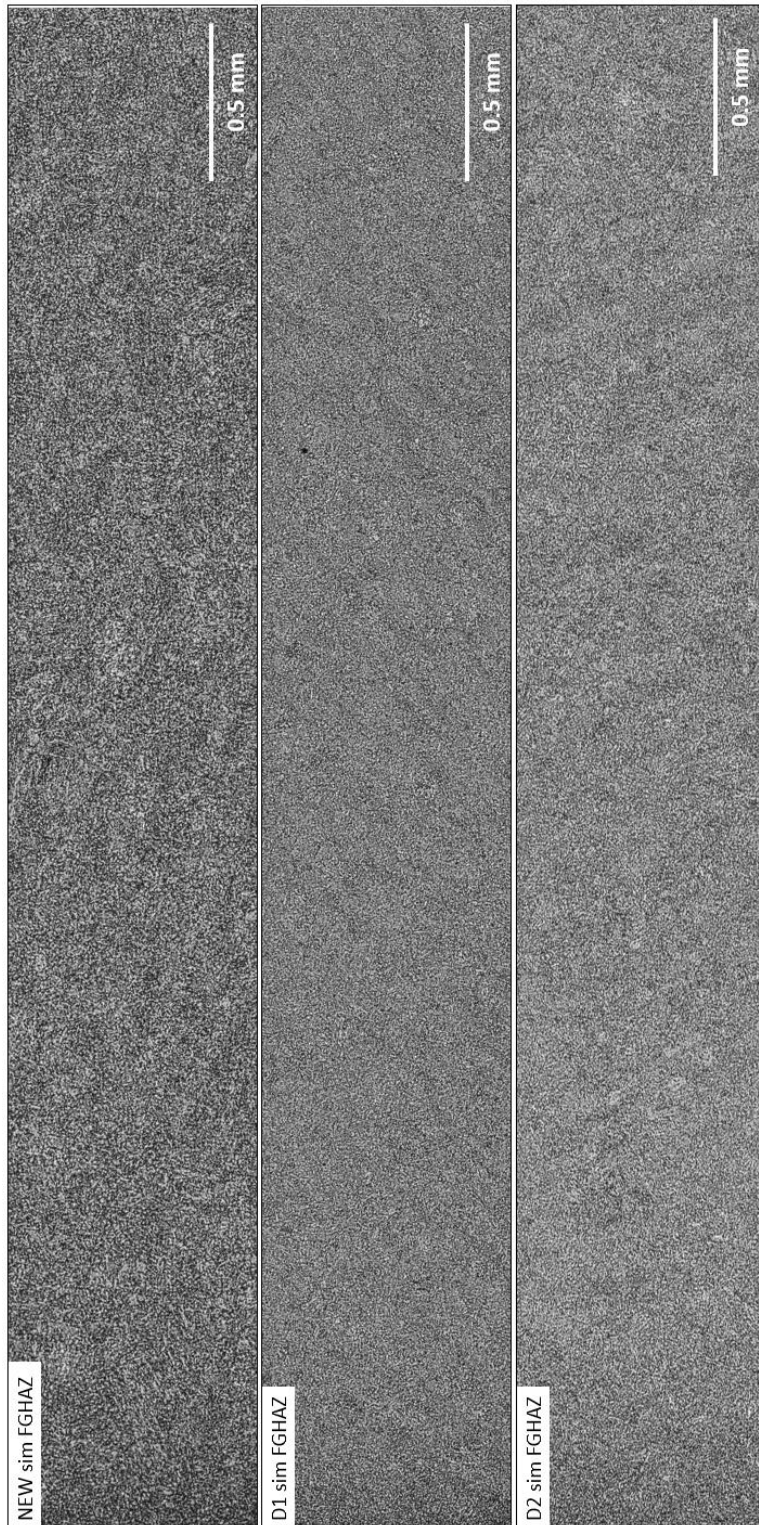


**Figure 4.2:** Montage of 23 x 3 BF optical micrographs taken across etched surface of cross section of simulated FGHAZ  $\varnothing 10$  mm rod specimen (sample area =  $5 \times 0.8 \text{ mm}^2$ ).

## 4.3 HARDNESS

### 4.3.1 Results

The results from the Vickers MHT are plotted in **Figure 4.3** as the mean Vickers hardness (HV 0.3) measured across the parent and simulated FGHAZ bulk specimens as described in Section 3.5.

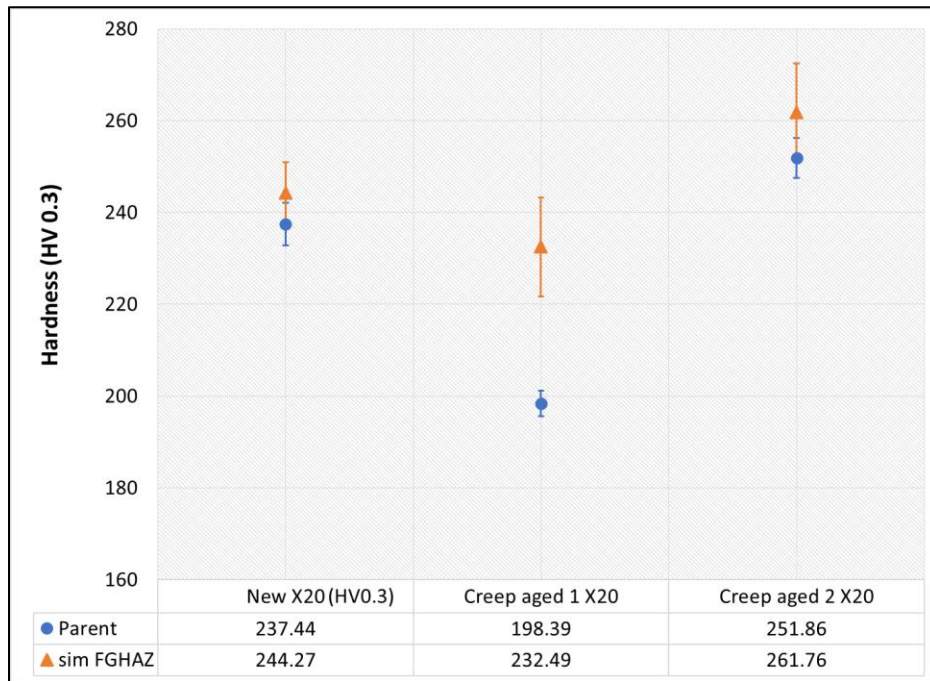


**Figure 4.3:** Mean measured Vickers hardness values of the parent (9 indents) and simulated FGHAZ X20 steel (36 indents). The error is reported as the 95% CI.

### 4.3.2 Discussion

To further verify the success of the FGHAZ simulation, the measured hardness values of the new parent ( $237.44 \pm 4.61$  HV0.3) and simulated FGHAZ ( $244.27 \pm 6.74$  HV0.3) was plotted on the hardness profile measured by Marx (2016) for an actual weld made upon new X20 steel, as shown in **Figure 4.4**.

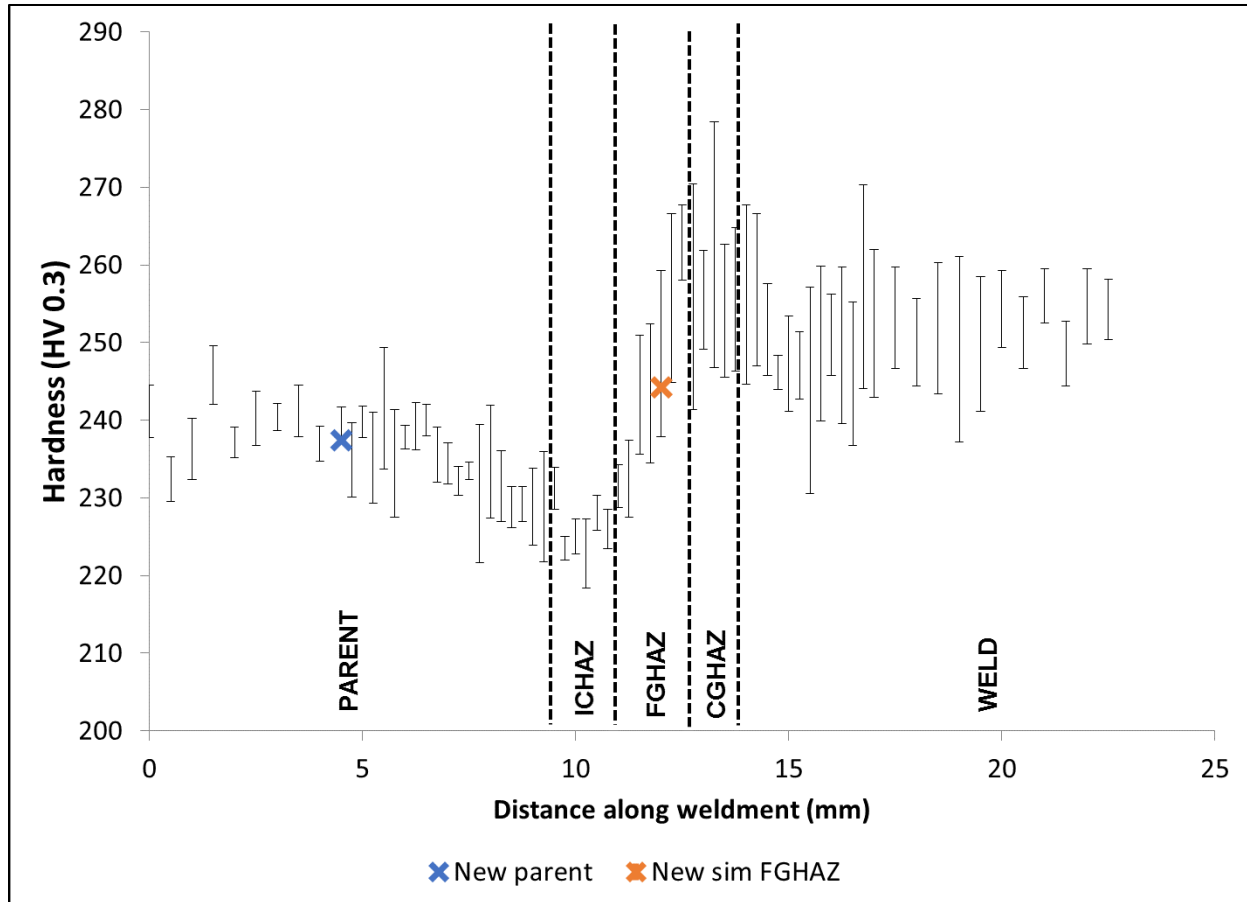


**Figure 4.4:** Measured Vickers hardness values for the new parent and simulated FGHAZ X20 steel from this study plotted on Vickers MHT profile along new X20 weldment measured in the study by Marx (2016). The range of values obtained along 3 lines of indents are indicated and the subsequent different weld regions identified by Marx (2016).

As can be seen, the hardness value measured for both the new parent and simulated FGHAZ fall within the parent and FGHAZ regions of the actual weldment, respectively. Thus, the success of simulating the FGHAZ from the parent material was further verified by this correspondence.

By comparing the measured hardness values of the parent materials in **Figure 4.3**, creep aged 1 parent material ( $198.39 \pm 2.83$  HV0.3) is the softest and creep aged 2 parent material ( $251.86 \pm 4.33$  HV0.3) is slightly harder than the new parent material. It has been shown by Molokwane (2014), Marx (2016) and Rasiawan (2017) that the hardness of service exposed X20 steel is usually lower than new X20 steel. The discrepancy of the

higher hardness of the creep aged 2 parent material compared to the new material can be accounted for by the fact that the initial X20 materials had undergone different processing during manufacturing. The measurements performed by other researchers corroborate this, for example, Aghajani (2009) has measured a hardness value of 262 HV0.3 for new X20 steel. Slight differences in design codes and compositions may explain the slight increase in hardness.

Similar trends as for the parent materials are observed among the simulated FGHAZ materials: the creep aged 1 simulated FGHAZ material ( $232.49 \pm 10.76$  HV0.3) has the lowest hardness, creep aged 2 simulated FGHAZ material ( $261.76 \pm 10.65$  HV0.3) the largest and the new simulated FGHAZ has a hardness in between these values.

There is an increase in hardness between the simulated FGHAZ and their corresponding parent material. This trend is also observed from the hardness profile of the actual weldment in **Figure 4.4** and other studies by Molokwane (2014) and Rasiawan (2017) of actual X20 weldments. Consequently, the lower creep strength of the FGHAZ (Section 2.4) is not related to the hardness. The most significant increase in hardness is observed when the FGHAZ is simulated upon then creep aged 1 material.

The decrease in hardness of creep aged specimens has been found to be due to the increase in average spacing of dislocations (decrease in dislocation density) within the laths, precipitates (precipitate coarsening) and high angle boundaries (block and packet boundaries) (Sawada, Miyahara, Kushima, Kimura and Matsuoka 2005). Subsequently, a decrease in these spacings should result in increased hardness. Since the dislocation density and precipitate spacing are determined in this study and further discussed in the subsequent sections, a final discussion on the observed hardness trends for the simulated FGHAZ materials will be given Chapter 5.

## 4.4 PRIOR AUSTENITE GRAIN ANALYSIS

### 4.4.1 Results

From the literature presented in Section 2, it follows that the PAG size has no contribution to the creep strength. However, to further verify the accuracy of the simulation of the FGHAZ, analysis of the prior austenite grains (PAG) was performed as described in Section 3.7.1. The results of the ARPGE software reconstruction of the PAG from the EBSD maps are shown in **Figure 4.5**. By superimposing the reconstructed PAGB with the EBSD inverse pole figure (IPF<sub>Z<sub>0</sub></sub>) map, the accuracy of each reconstruction is shown. These overlays are given in **Figure 4.6**. In the EBSD IPF<sub>Z<sub>0</sub></sub> maps the different colours correspond to different orientations as given in the standard triangle.

The size distributions of the reconstructed PAG were measured using the ARPGE software and these values are summarised in **Figure 4.7** as box-and-whisker plots. Also using ARPGE, the PAG was reconstructed from the EBSD maps acquired by Marx (2016) of the FGHAZ, ICHAZ and CGHAZ weldment regions of an actual weldment made upon new X20 steel. The new simulated FGHAZ PAG size distribution was then compared to these distributions as shown in **Figure 4.7(b)**.



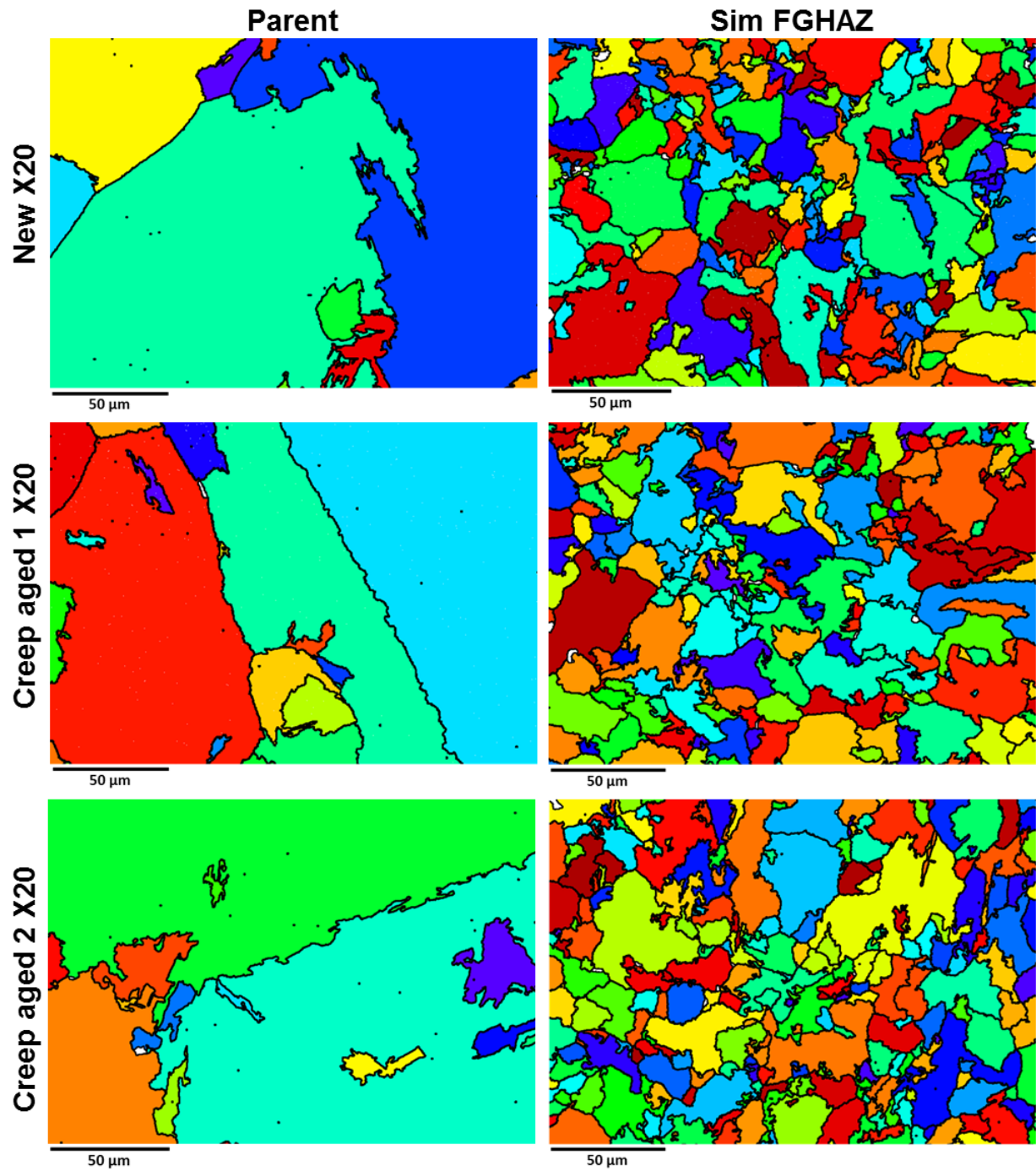


**Figure 4.5:**  $204 \times 153 \mu\text{m}^2$  Colour maps of reconstructed PAG from EBSD maps. Random colour coding used.

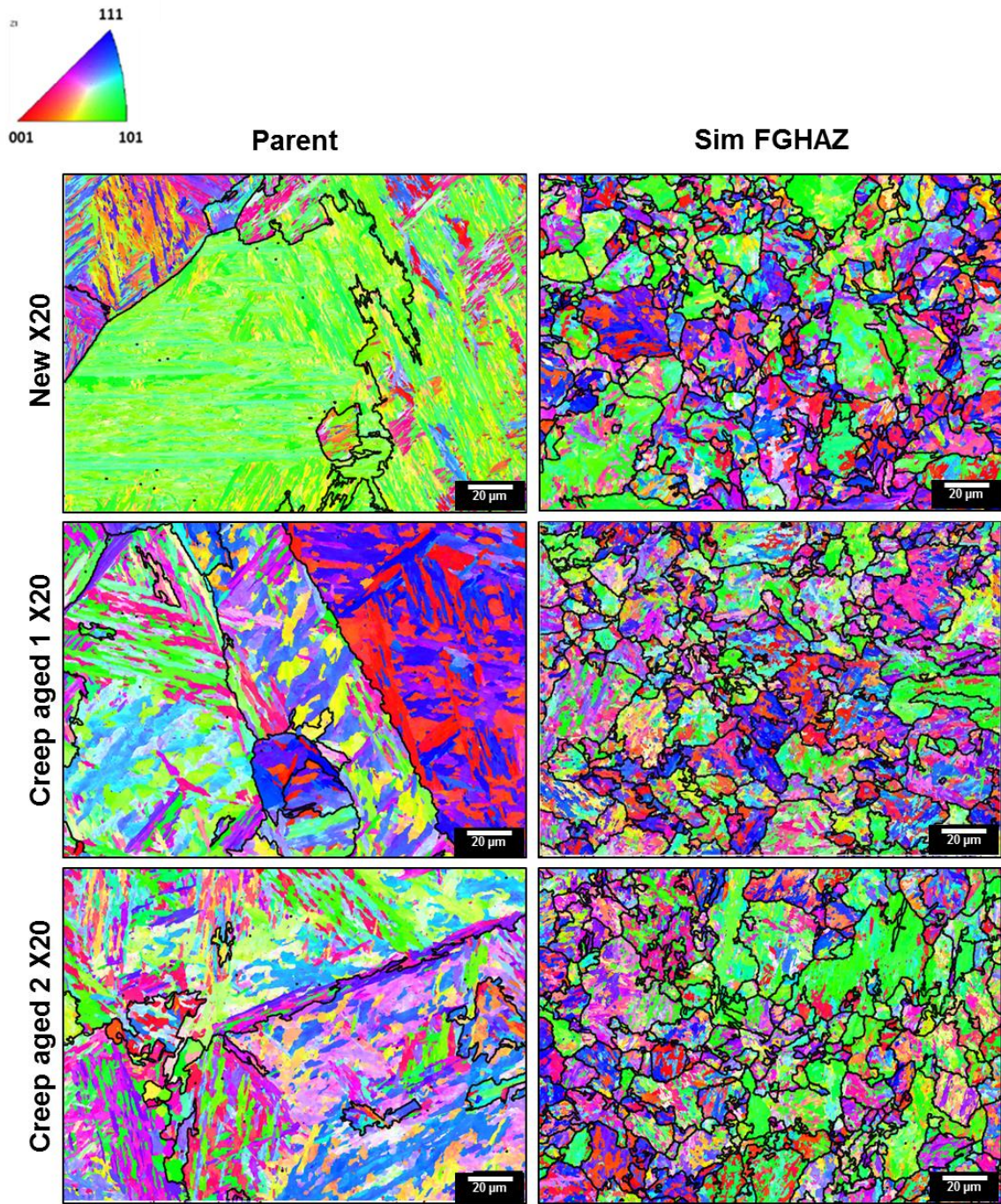


**Figure 4.6:**  $204 \times 153 \mu\text{m}^2$  EBSD IPF<sub>Z0</sub> map with reconstructed PAGB outlined ( $204 \times 153 \mu\text{m}^2$ , 15 kV, 4 nA, 200 nm step-size).

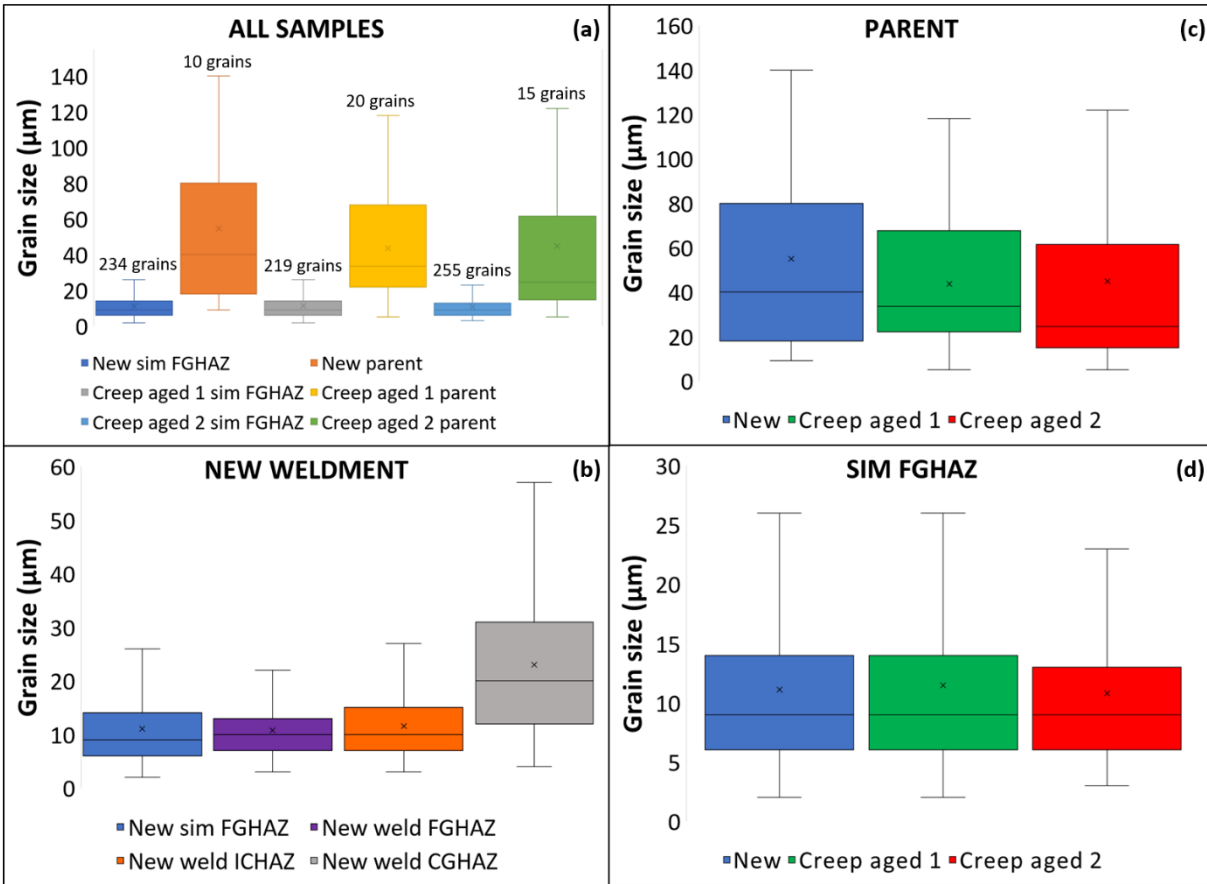


**Figure 4.7:** Box-and-whisker plots of PAG size distributions measured using ARPGE software for (a) all samples, (b) new simulated FGHAZ and actual weldment regions from Marx (2016), (c) only parent and (d) simulated FGHAZ specimens. The “x” symbol indicates the mean.

#### 4.4.2 Discussion

As can be seen from **Figure 4.6** the reconstructed PAGB do not include all the PAGB that are visible from the EBSD IPF<sub>Z0</sub> maps. However, the reconstructions are satisfactory for the sole purpose of successful verification of the FGHAZ simulation. Each of the simulated FGHAZ specimens has a fine PAG microstructure as expected (**Figure 4.5**). In **Figure 4.7(b)**, the new simulated FGHAZ material PAG distribution corresponds the most with that of the FGHAZ of the actual weldment. Thus, the success of the simulation of the FGHAZ, and not the ICHAZ or CGHAZ, is further confirmed.

As with the qualitative analysis, the parent materials have much larger PAG than the simulated FGHAZ materials. The small equiaxed ferrite grains correspond to previous studies by Mayr and Cerjak (2010), and Marx (2016), that observed the same for the FGHAZ of an actual weldment from EBSD. Due to the low number of PAG in the EBSD maps, no inference can be made from the measured sizes for the parent materials. However, a sufficient number of PAG are measured in the simulated FGHAZ materials and conclusions can be drawn. All three of the simulated FGHAZ materials have the same median and mean PAG sizes (**Figure 4.7(d)**), confirming the literature (Section 2.4.1) that all the PAG dissolve during the FGHAZ weld thermal cycle and new PAG nucleate.

Since there are many variables involved in reconstructing PAG with the ARPGE software (**Figure 3.14**). The main limitation is that the variants in the sample do not obey the simple KS or NW relationships and therefore the reconstruction is very sensitive to these reconstruction parameters.

## 4.5 CREEP VOIDS

### 4.5.1 Results

#### (i) Size and distribution

Quantitative analysis of the voids in each material type was performed using LM as described in Section 3.7.2. The total number of voids (ECD 1 to 3  $\mu\text{m}$ ) and cavities (ECD < 3  $\mu\text{m}$ ) measured across all the areas is summarised in **Table 4.1**. An example of the thresholded image of the voids is shown in **Figure 4.8**.

**Table 4.1:** Number of voids and cavities measured on total sampling area of 1.4 mm<sup>2</sup>.

	New		Creep aged 1		Creep aged 2	
	Parent	Sim FGHAZ	Parent	Sim FGHAZ	Parent	Sim FGHAZ
<b>Cavities</b>	1365	211	1855	1723	3791	738
<b>Void</b> s	277	107	558	441	1147	297

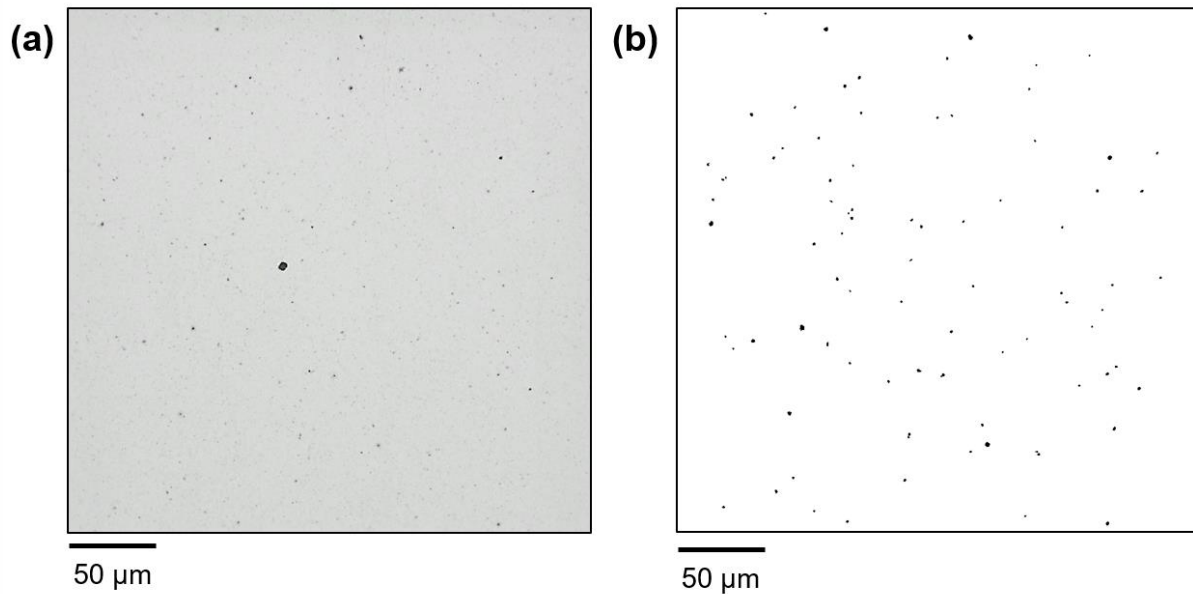


**Figure 4.8:** (a) Micrograph of EBSD polished surface ( $296 \times 296 \mu\text{m}^2$  area) of creep aged 2 parent X20 bulk specimen. (b) Thresholded voids (1 to 3  $\mu\text{m}$  ECD) of the same area as in (a).

Histograms of the 2D measured ECD are plotted in **Figure 4.9** to compare the differences in both area fraction and ECD. The total area analysed for each material was the same and therefore no normalization was necessary. The bin width was chosen using Doane's rule (Doane 1976). Since the voids are 3D objects, the measured 2D ECD distributions were stereologically corrected for sectioning and unfolded into 3D ECD distributions as explained in Section 3.7.2. In **Figure 4.10** comparisons of the corrected ECD distributions of the voids are illustrated as the Kernel Density Estimation (KDE) (VanderPlas 2016) plots for both parent and simulated FGHAZ materials. This type of density plot is a continuous version of a histogram that has been estimated from the data and the y-axis is a probability density and the only requirement is that the total area under the curve integrates to one. Overall, the effect of the stereological correction is to shift the distribution to larger values slightly.

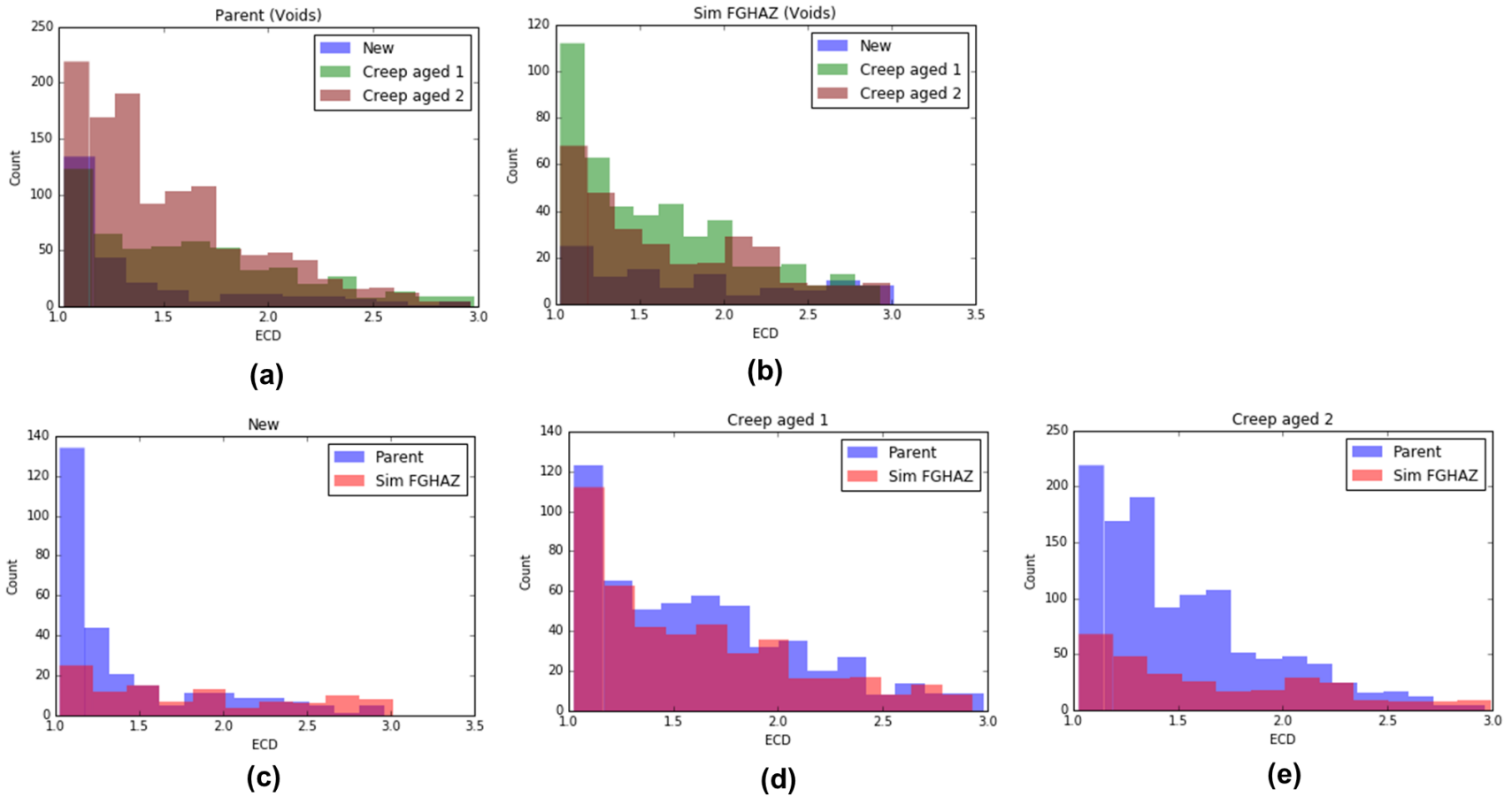


**Figure 4.9:** 2D Measured ECD histogram plots of the voids observed from the LM micrographs of (a) parent and (b) simulated FGHAZ materials, (c) new, (d) creep aged 1 and (e) creep aged 2 materials (total area of 1.4 mm<sup>2</sup> analysed).

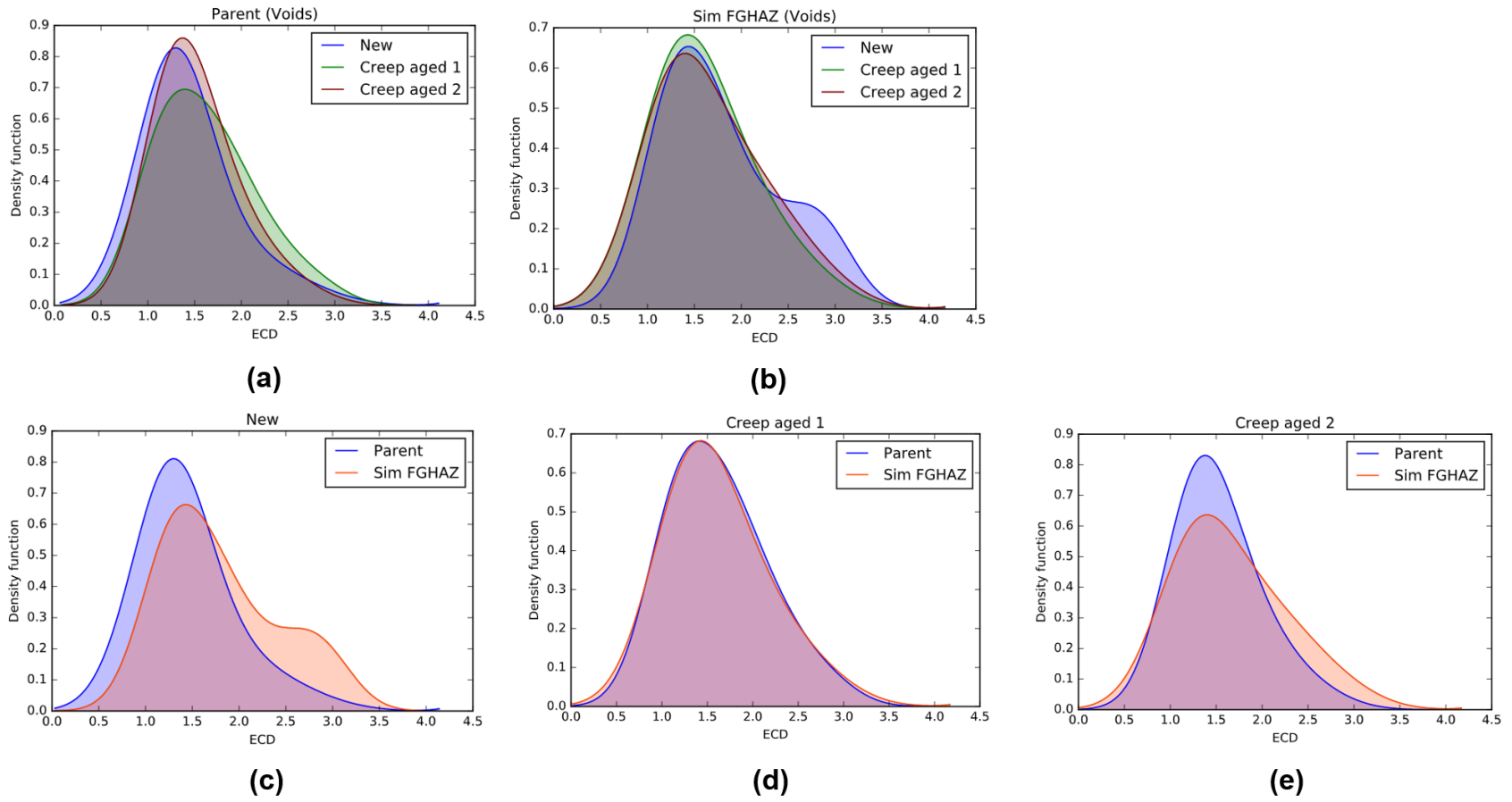


**Figure 4.10:** ECD KDE distribution plots (scalar factor = 0.30 – 0.42) of corrected void size measurements from the LM micrographs of (a) parent and (b) simulated FGHAZ materials, (c) new, (d) creep aged 1 and (e) creep aged 2 materials (total area of 1.4 mm<sup>2</sup> analysed).

The mean ECD was determined from the corrected distributions and the values plotted in **Figure 4.11**. Since the number density  $N_A$  was measured per area, the mean and error values were calculated using Equation (3.17). **Figure 4.12** summarises these calculated densities. The NND distributions for the voids is illustrated in **Figure 4.13**. This colour map of the area fraction across the total analysed area is shown in **Figure 4.14** to illustrate the variation in the number density of the voids across the different areas and materials.

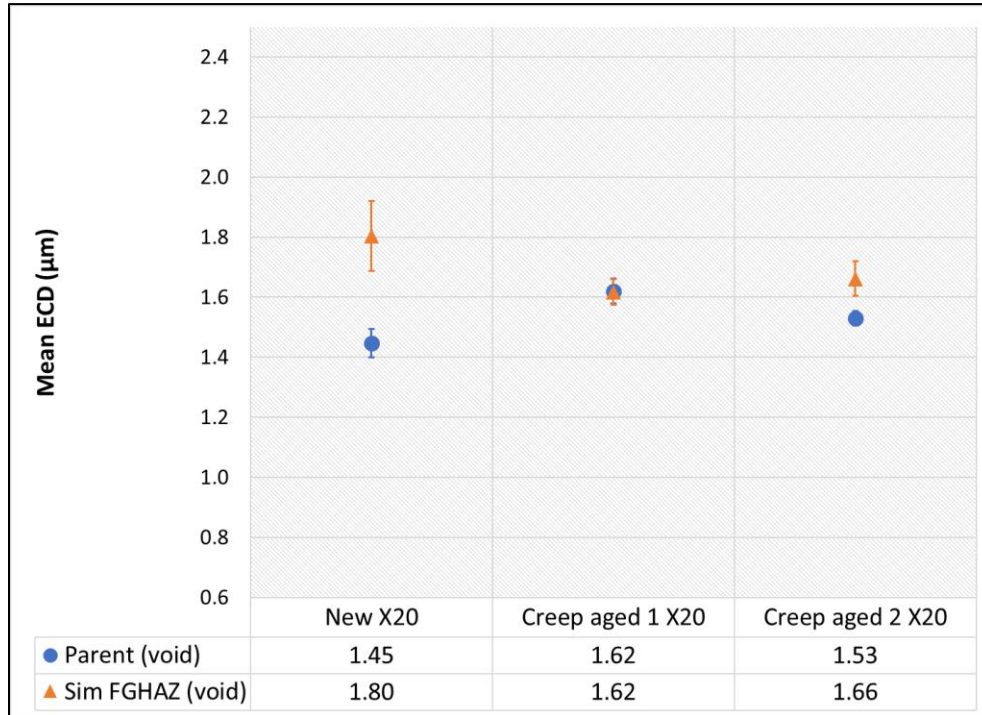


**Figure 4.11:** Mean void ECD measured from corrected ECD distributions of parent and simulated FGHAZ specimens ( $1.4 \text{ mm}^2$  sampling area). The error is given as 95% CI.



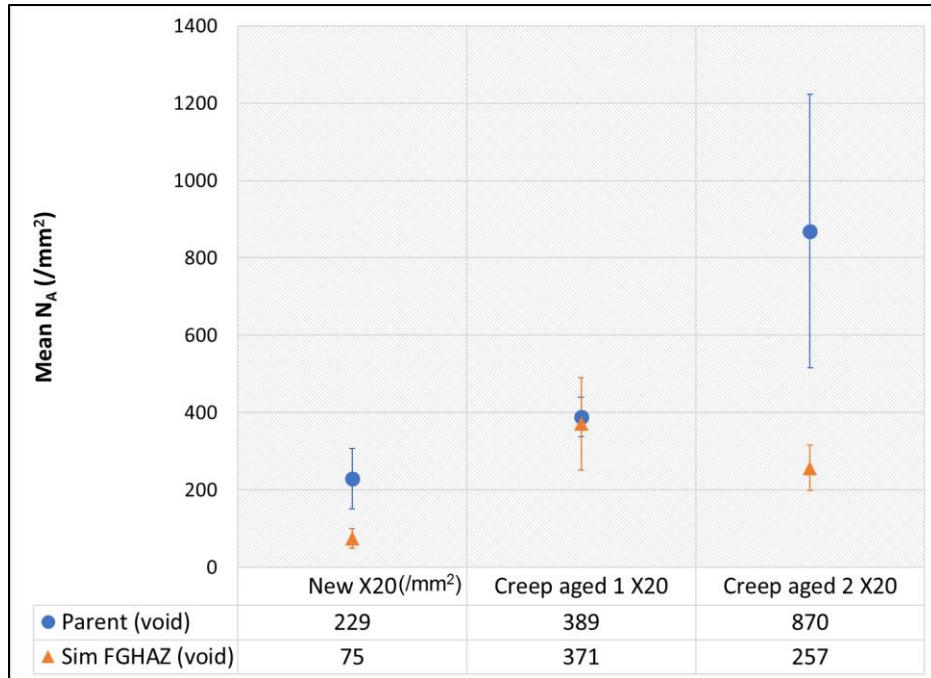


**Figure 4.12:** Mean void number densities  $N_A$  measured from parent and simulated FGHAZ bulk specimens (total sampling area of  $1.4 \text{ mm}^2$ ). The error is given by Equation (3.17).

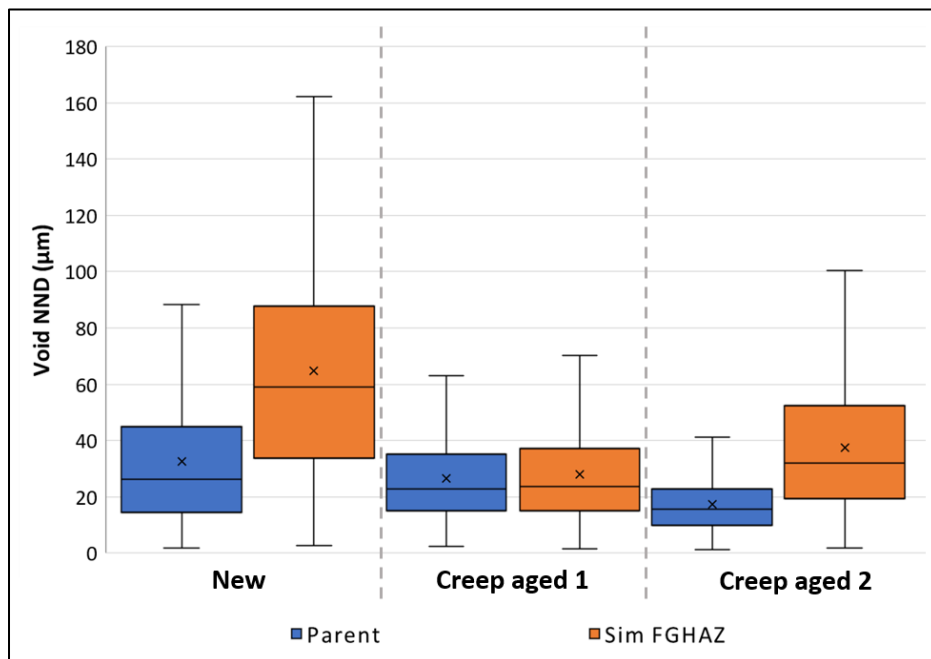


**Figure 4.13:** Box-and-whisker plots of the nearest neighbour distance (NND) distributions of voids measured from parent and simulated FGHAZ bulk specimens (total sampling area of  $1.4 \text{ mm}^2$ ). The “x” symbol indicates the mean.

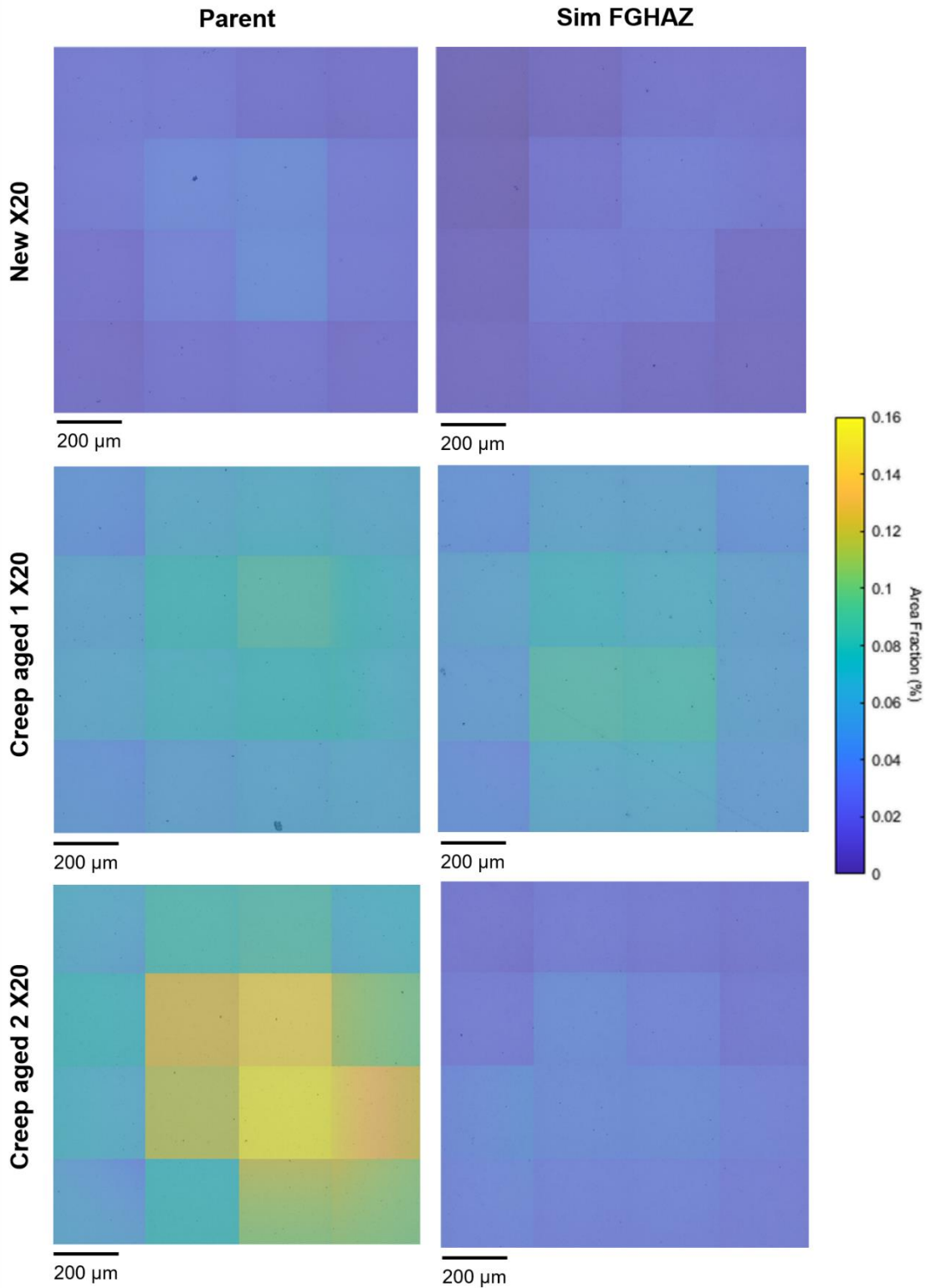


**Figure 4.14:** Colour maps of area fraction across 16 areas analysed (total area of 1.4 mm<sup>2</sup> analysed) per parent and simulated FGHAZ specimen. Cooler colours correspond to lower area fractions of voids.

## (ii) Location

Due to the limited spatial resolution of LM, the location and shape of the cavities were instead analysed with SE imaging (Section 3.7.2). Some of the SE images taken from the colloidal polished bulk specimens and qualitatively analysed is provided from **Figure 4.15** to **Figure 4.20**. To further analyse the location of the cavities, an EBSD map was acquired from the creep aged 2 parent and simulated FGHAZ materials as described in Section 3.7.2. These results are summarised in **Figure 4.21** and **Figure 4.22**.

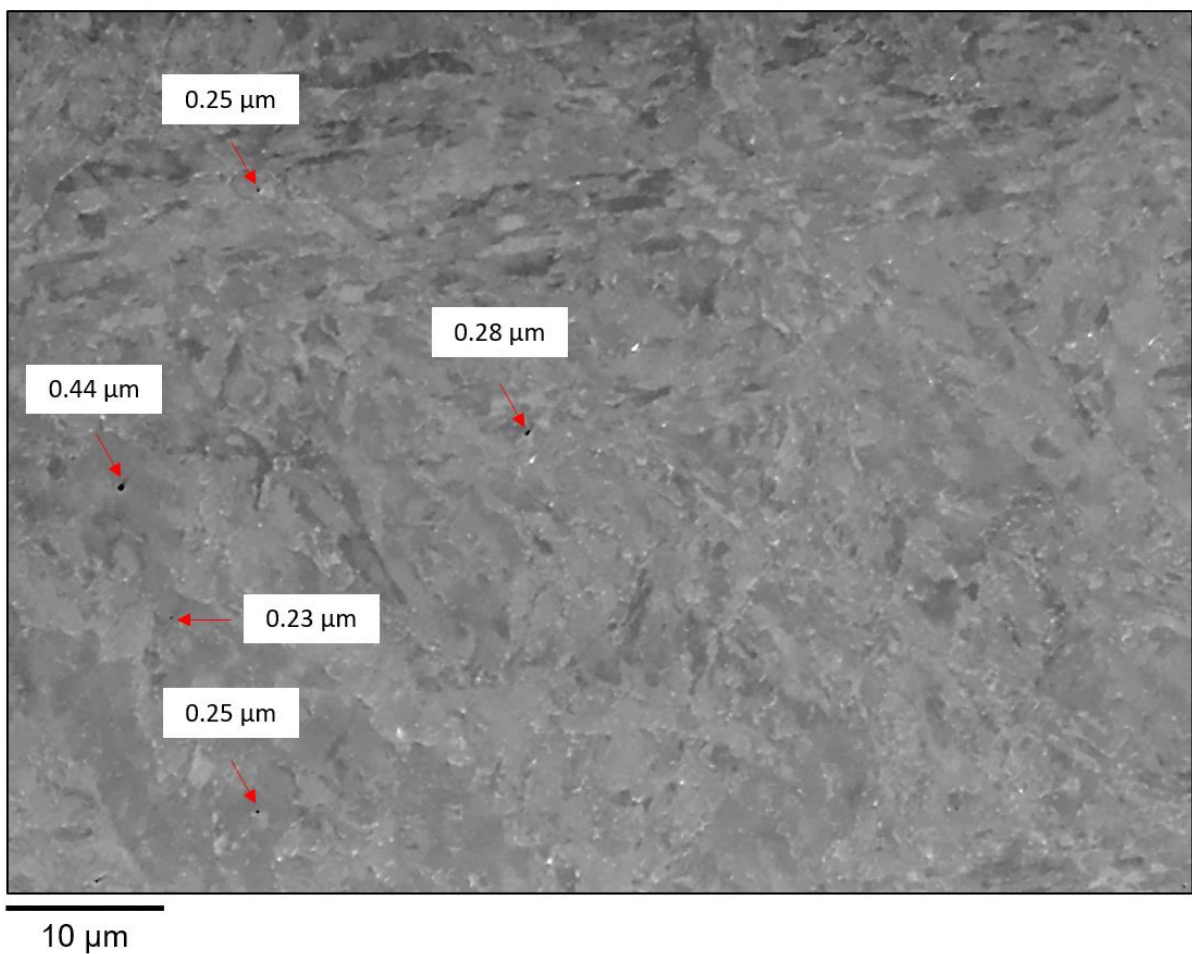


**Figure 4.15:** 10 kV SE-SEM image of EBSD (colloidal) polished surface of new parent material. Some of the cavities and their ECD are indicated by the red arrows.

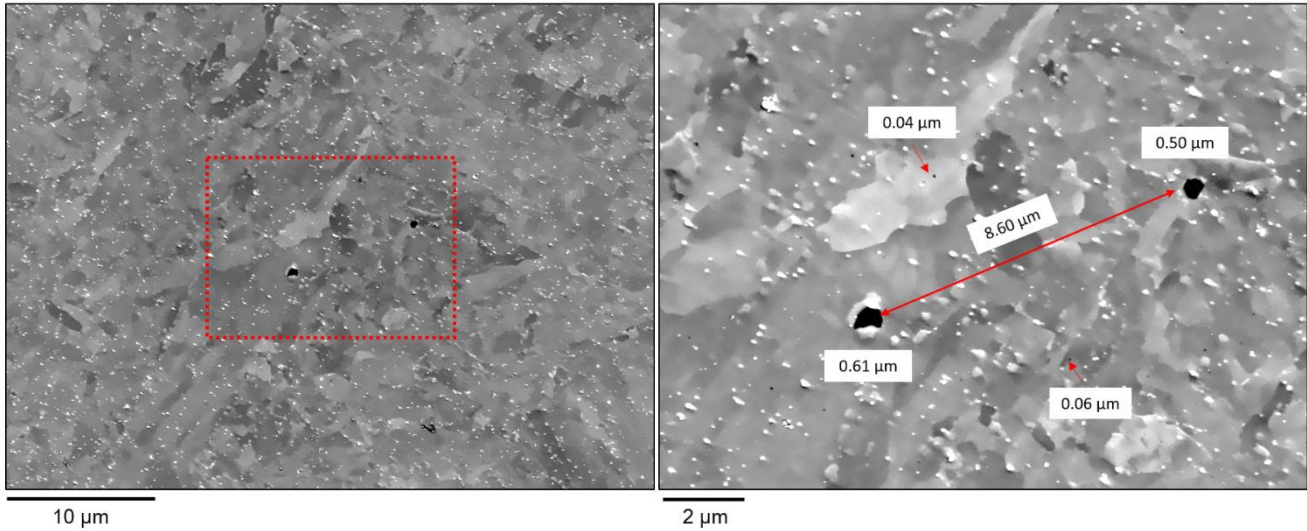


**Figure 4.16:** 10 kV SE-SEM image of EBSD (colloidal) polished surface of new simulated FGHAZ material. The image on the right is an enlargement of the area bounded by the red rectangle in the image on the left. Some of the cavities and their ECD are indicated by the red arrows.

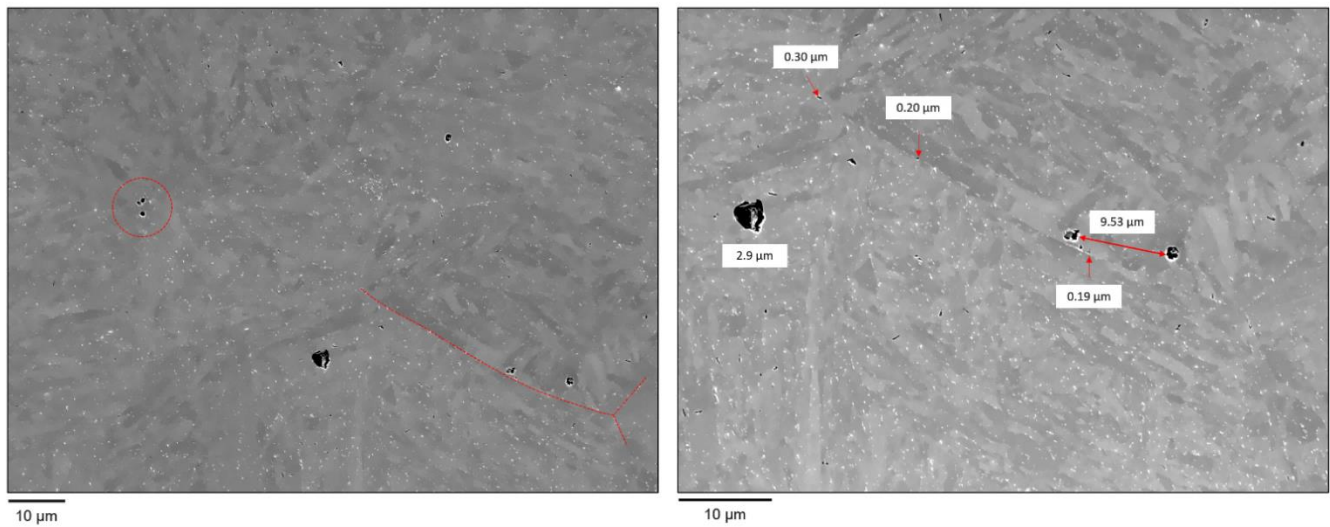


**Figure 4.17:** 10 kV SE-SEM image of EBSD (colloidal) polished surface of creep aged 1 parent material. PAGB shown by the red line in the image on the left and the image on the right is the enlarged area of the same PAGB. Some of the cavities and their ECD are indicated by the red arrows.

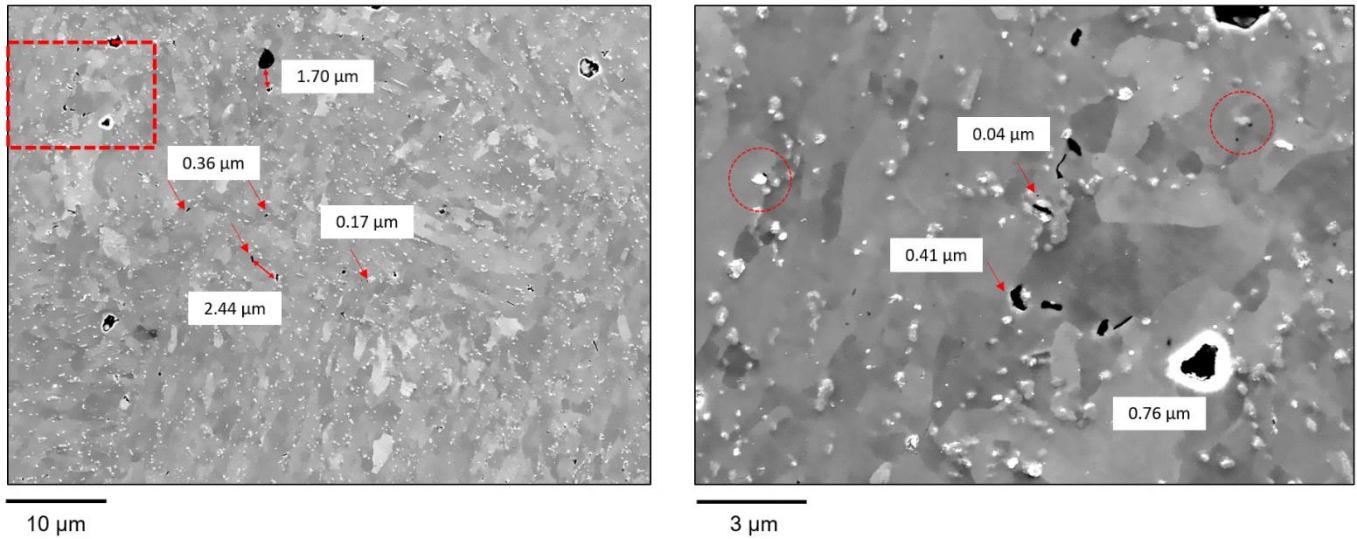


**Figure 4.18:** 10 kV SE-SEM image of EBSD (colloidal) polished surface of creep aged 2 parent material. The image on the right is an enlargement of the area bounded by the red rectangle in the image on the left. Some of the cavities and their ECD are indicated by the red arrows.

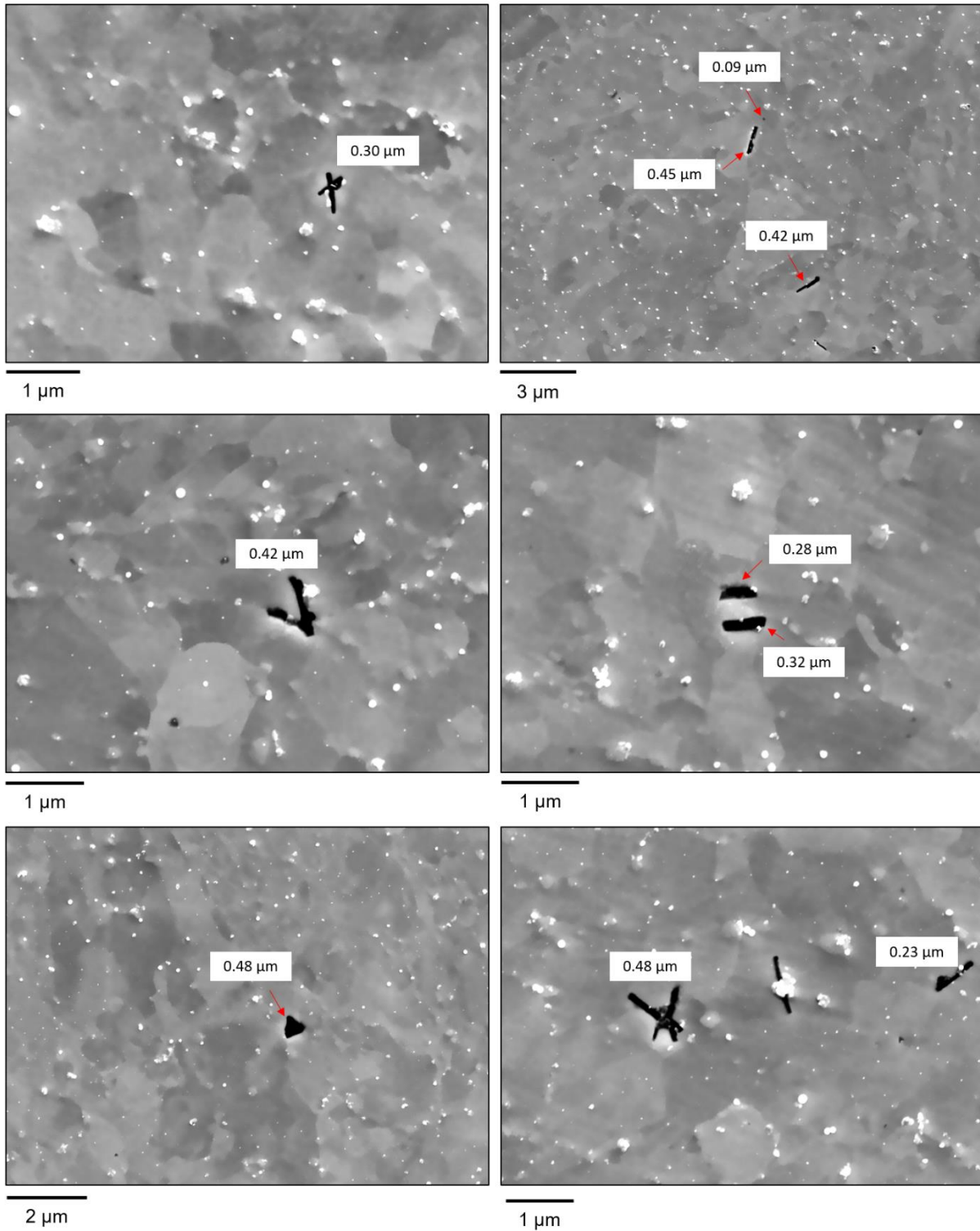


**Figure 4.19:** 10 kV SE-SEM images of EBSD (colloidal) polished surface of creep aged 1 simulated FGHAZ material. Some of the cavities and their ECD are indicated by the red arrows.

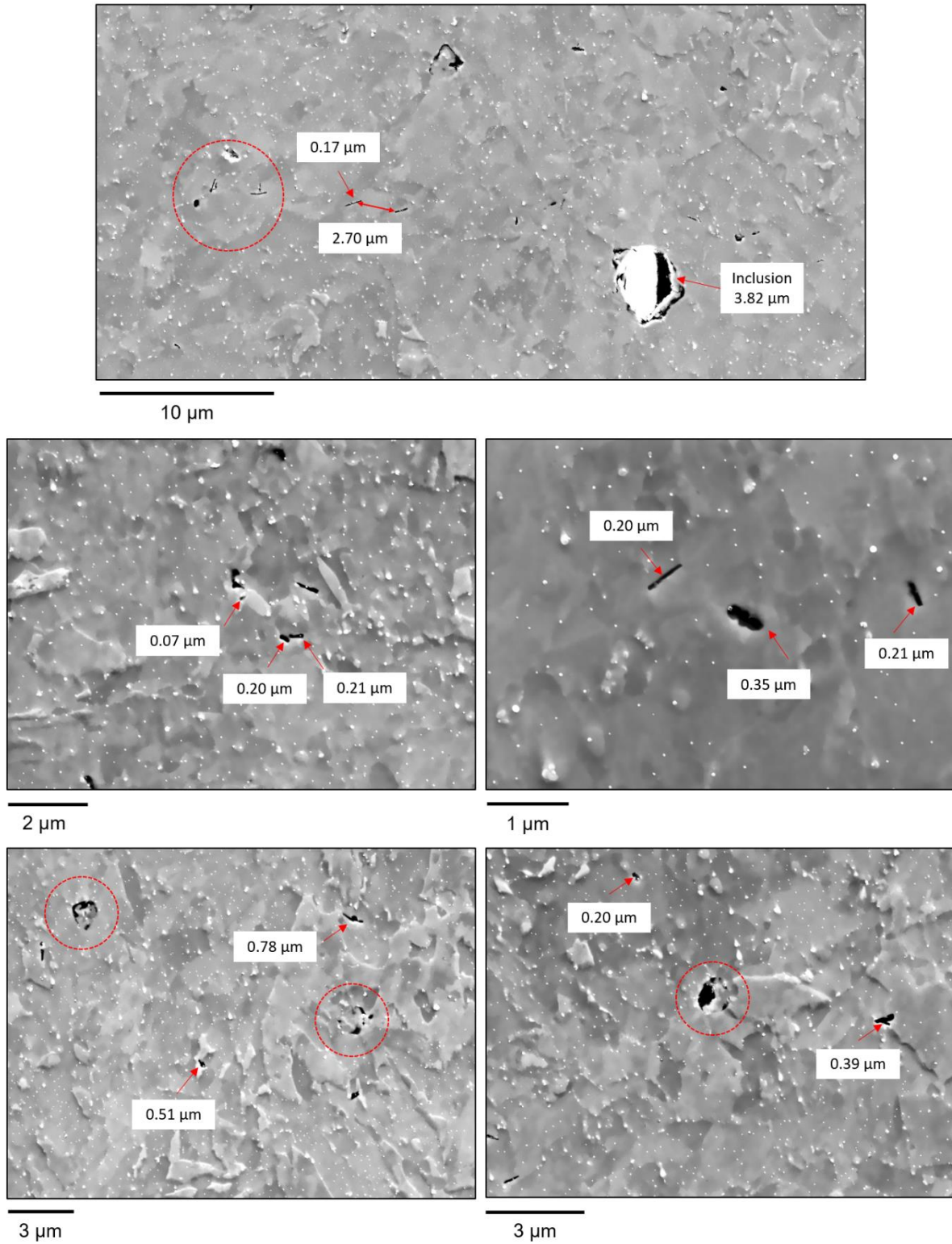


**Figure 4.20:** 10 kV SE-SEM images of EBSD (colloidal) polished surface of creep aged 2 simulated FGHAZ material. Some of the cavities and their ECD indicated by red arrows.

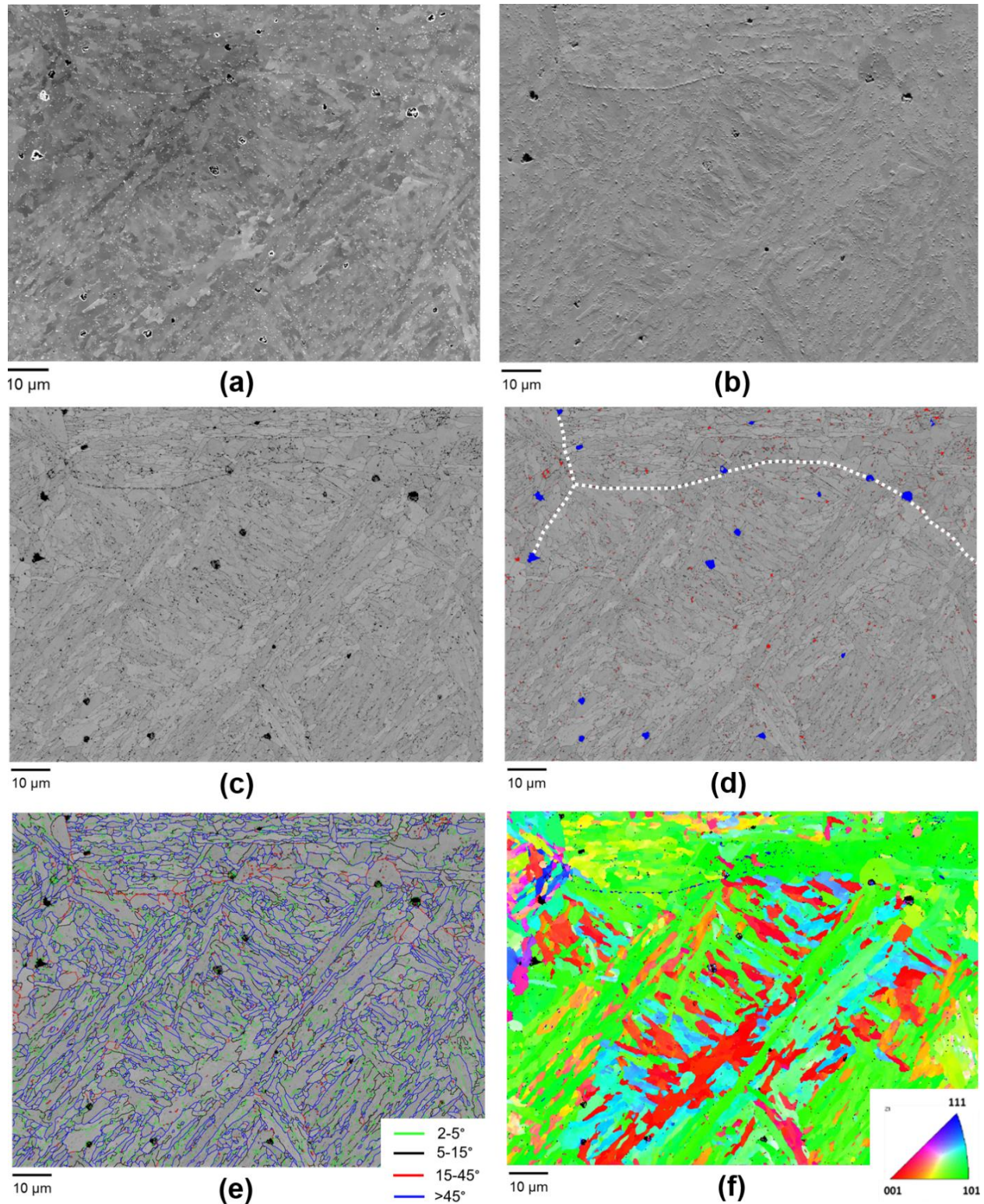


**Figure 4.21:** (a) SE image, (b) BSE image, (c) BC map, (d) BC map with voids (blue) and cavities (red) isolated, (e) EBSD BC and GB map, and (f) EBSD IPF<sub>Z0</sub> map of the same area on creep aged 2 parent bulk specimen. The white dotted line indicates some PAGB.



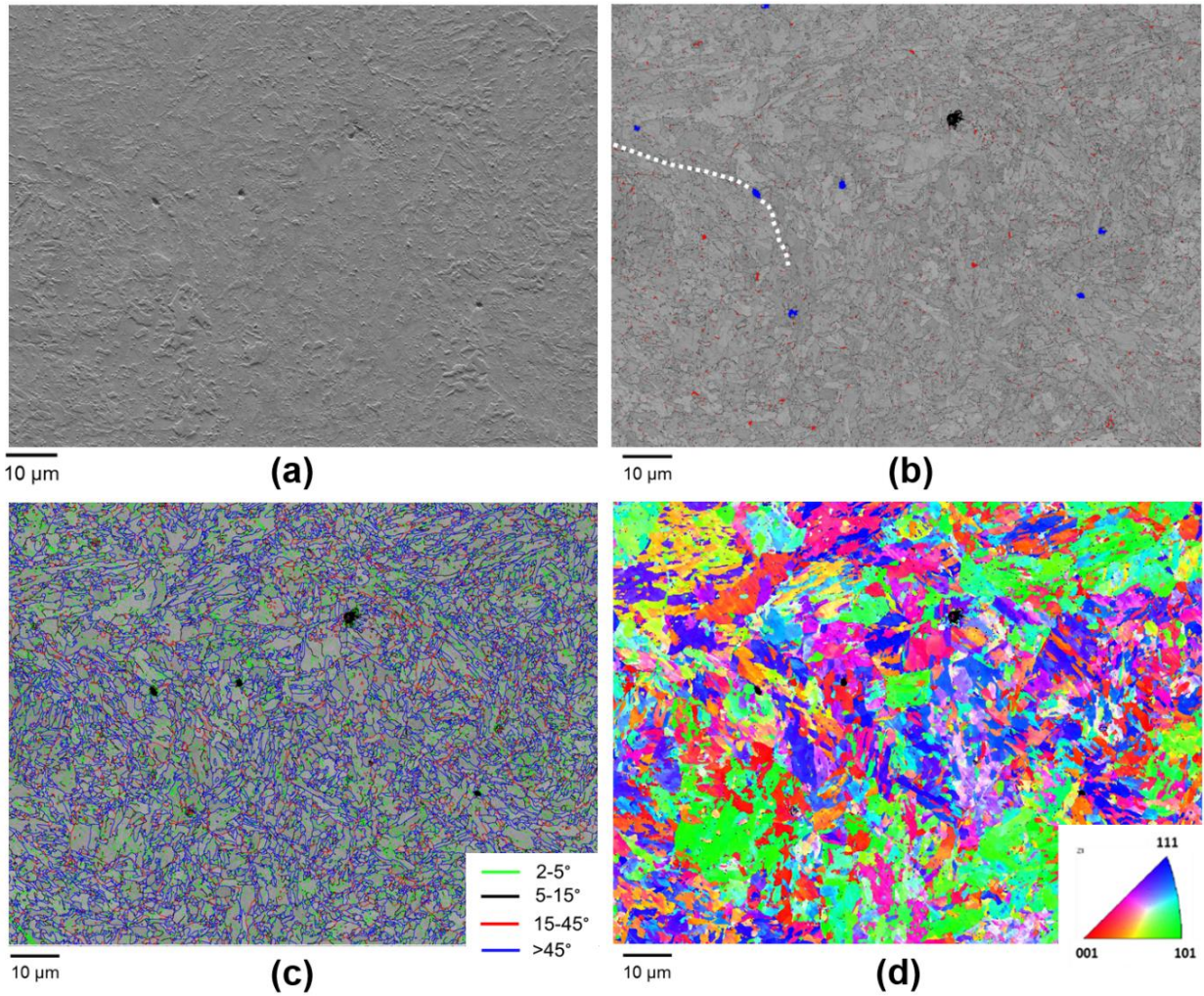


**Figure 4.22:** (a) BSE image, (b) BC map with voids (blue) and cavities (red) isolated, (c) EBSD BC and GB map, and (d) EBSD IPF<sub>Z0</sub> map of the same area on creep aged 2 simulated FGHAZ bulk specimen. The white dotted line indicates some prior PAGB.

## 4.5.2 Discussion

Since the new parent material has not been creep exposed, it is expected that no creep voids exist. This is the assumption that is made in conventional life management strategies (Section 2.6 and **Table 3.3**). However, previous studies discussed in Section 2.3.6 have reported pre-existing voids of mean diameters of more than 2  $\mu\text{m}$  in as-received 9 -12 % Cr martensitic steels and it was concluded that they are responsible for final rupture of the material. As can be seen from the LM results there are pre-existing cavities (ECD smaller than 3  $\mu\text{m}$ ) in the new parent material. The fact that small cavities with ECD less than 3  $\mu\text{m}$  were observed in the SEM (**Figure 4.15**) confirms that the LM results are correct. Explanations for the cause of these pre-existing voids are still required. For further discussion, the void measurements are summarised in **Table 4.2**.

**Table 4.2:** Summary of void measurements.

Base material	Sample	Mean ECD ( $\mu\text{m}$ )	Mean area fraction (%)	Mean $N_A$ (voids/ $\text{mm}^2$ )
New X20	Parent	$1.45 \pm 0.05$	$3.64 \pm 2.40$	$229 \pm 78$
	Sim FGHAZ	$1.80 \pm 0.12$	$2.42 \pm 2.09$	$75 \pm 25$
Creep aged 1 X20	Parent	$1.62 \pm 0.04$	$9.18 \pm 2.80$	$389 \pm 50$
	Sim FGHAZ	$1.62 \pm 0.04$	$8.65 \pm 4.97$	$371 \pm 120$
Creep aged 2 X20	Parent	$1.53 \pm 0.02$	$17.22 \pm 14.16$	$870 \pm 353$
	Sim FGHAZ	$1.66 \pm 0.06$	$6.06 \pm 3.61$	$257 \pm 59$

By comparing the ECD distributions of the voids in the parent materials (**Figure 4.9(a)**, **Figure 4.10(a)**, and **Figure 4.11**), it is seen that the new parent material had the distribution of smallest sizes (mean =  $1.45 \pm 0.05 \mu\text{m}$ ) and area fraction (mean =  $3.64 \pm 2.40 \%$ ), creep aged 2 parent materials had a slightly larger size distribution (mean =  $1.53 \pm 0.02 \mu\text{m}$ ) with the largest area fraction (mean =  $17.22 \pm 14.16 \%$ ) and creep aged 1 parent material had the largest size distribution (mean =  $1.62 \pm 0.04 \mu\text{m}$ ) with area fraction (mean =  $9.18 \pm 2.80 \%$ ) in between that of the other materials. Therefore, there was an increase in void size and area fraction with creep exposure.

For both the new and creep aged 2 materials (**Figure 4.9(c)** and (e), **Figure 4.10(c)** and (e), and **Figure 4.11**), a higher frequency of large voids was measured in the simulated FGHAZ materials, resulting in the mean void ECD to be shifted to larger values than the corresponding parent material (**Table 4.2**). The frequency of smaller voids was also much lower for these two simulated FGHAZ materials, with the most significant effect observed for the new material. The area fraction of voids in the creep aged 2 parent material significantly decreased after FGHAZ simulation. For the new and creep aged 1 materials the area fraction was slightly lower than that in the parent, but the difference was not statistically significant. Also, the FGHAZ simulation had no statistically significant effect on the ECD distribution of the creep aged 1 parent material (**Figure 4.9(d)**, **Figure 4.10(d)** and **Figure 4.11**).

The void ECD distributions and mean ECD values of the creep aged 1 and creep aged 2 simulated FGHAZ materials (**Figure 4.9(b)**, **Figure 4.10(b)** and **Figure 4.11**) were similar with respective mean sizes of  $1.62 \pm 0.04 \mu\text{m}$  (mean area fraction =  $8.65 \pm 4.97 \%$ ) and  $1.66 \pm 0.06 \mu\text{m}$  (mean area fraction =  $6.06 \pm 3.61 \%$ ). From the histogram, it is seen that the new simulated FGHAZ material had the lowest frequencies and the sizes of the voids are more evenly spread, whereas in the case of the creep aged materials there is a higher frequency of smaller voids. Consequently, the new simulated FGHAZ materials have the largest mean void size of  $1.80 \pm 0.12 \mu\text{m}$  and lowest mean area fraction of  $2.42 \pm 2.09 \%$ . Creep aged 1 simulated had the highest area fraction of voids, but it is only slightly higher than that of the creep aged 1 simulated FGHAZ material.

Care should be taken to interpret the sizes of the new simulated FGHAZ since the least number of voids could be analysed for this material (**Table 4.1**). It should also be noted that bimodality cannot be interpreted from the KDE plots since this plot normalises the distribution. Thus, these plots are only useful to see the distribution of the sizes and not the area fraction as with the histograms.

Similar conclusions as above regarding area fraction can be concluded from **Figure 4.14**. Also, the variation in colour per sample and the large 95% CI for the number density  $N_A$  (**Figure 4.12**) indicates the inhomogeneous distribution of voids. The mean  $N_A$  values of each material fall within the range of values measured with surface replication (**Table 3.3**), thereby verifying the correctness of the assumption that voids with approximately 1 to 3  $\mu\text{m}$  ECD is measured from surface replicas.

For the parent materials, the mean  $N_A$  increased from the new parent material ( $229 \pm 78$  voids/ $\text{mm}^2$ ) to  $389 \pm 50$  voids/ $\text{mm}^2$  and  $870 \pm 353$  voids/ $\text{mm}^2$  in the creep aged 1 and creep aged 2 parent materials, respectively. For the new and creep aged 2 materials, there were a significant decrease in the void  $N_A$  after FGHAZ simulation with the most significant decrease occurring in the creep aged 2 material. As with the ECD, there was no statistically significant difference in the  $N_A$  values of the creep aged 1 parent and simulated FGHAZ materials.

For the simulated FGHAZ materials, the creep aged 1 material had the largest  $N_A$  of voids ( $371 \pm 120$  voids/ $\text{mm}^2$ ) and the new material had the lowest  $N_A$  ( $75 \pm 25$  voids/ $\text{mm}^2$ ). However, the  $N_A$  of  $257 \pm 59$  voids/ $\text{mm}^2$  measured for the creep aged 2 simulated FGHAZ did not statically differ from that of the creep aged 1 simulated FGHAZ material.

By comparing the NND distributions (**Figure 4.13**) to the mean  $N_A$  values, it is found that the higher the number density, the smaller the NND, which is expected. The NND decreases with creep aging, which can be ascribed to the increased  $N_A$ . Creep aged 1 simulated FGHAZ had the largest NND and creep aged 2 parent material the smallest, which corresponds to them having the lowest and highest mean  $N_A$  values, respectively. The NND between the voids in the creep aged 1 parent and simulated FGHAZ material were similar.

Upon qualitative analysis of the SEM images (**Figure 4.15**), the cavities in the new parent material were much rounder and further spaced, whereas the cavities in the creep aged parent materials seem to be much further developed (**Figure 4.17** and **Figure 4.18**). From the results it follows that creep cavitation has extensively taken place during in-service exposure, specifically:

- (i) The high  $N_A$  and small NND of the voids in the creep aged parent materials indicate that nucleation has occurred. Since the mean ECD of these materials is larger than the new material, growth of the voids has taken place to some extent. This corresponds with the literature that cavities nucleate and grow during creep exposure (Section 2.3.6).
- (ii) Creep cavitation has taken place extensively in the creep aged 2 parent material since it has the highest void  $N_A$  and area fraction. However, it is possible that coalescence of the cavities has not significantly taken effect due to the very high  $N_A$  and small NND of voids. The SEM results (**Figure 4.18**) also shows that the cavities are closely spaced. Upon further creep aging local coalescence of the closely spaced cavities will occur (Section 2.3.6).
- (iii) The lower void  $N_A$  and area fraction measured for the creep aged 1 parent material does not necessarily indicate that the material is less damaged than the creep aged 2 parent material. Coalesced and large cavities surrounded by much smaller cavities were seen in the SEM results (**Figure 4.17**).

The LM results show that the evolution of the voids during FGHAZ simulation seems to be growth and coalescence of voids. This follows from the void NND and ECD increase, and number density decrease. Evolved cavities were also observed in the SEM images in **Figure 4.16**, **Figure 4.19** and **Figure 4.20**. In addition, during SEM analysis, it was observed, especially in the new material, that the cavities become more localised in the simulated FGHAZ material, which further suggests progression to coalescence. Cavity coalescence is not the main creep rupture criterion, but rather the formation and growth of microcracks from closely spaced cavitating grain boundary interfaces (Section 2.3.6).

Based on this criterion, it seems that cavitation damage has progressed the furthest in the creep aged 2 simulated FGHAZ material.

In addition, since both the area fraction and  $N_A$  significantly decreased from the parent to simulated FGHAZ of the creep aged 2 material, it can be concluded that a disappearance of voids has occurred, whether entirely or to a smaller size of less than 1  $\mu\text{m}$ . Repeating the analysis for larger areas will determine if this is a characteristic phenomenon and if it is found to be, then further research will be performed to formulate an explanation. A possible explanation is the voids disappear due to volume changes that occur during the phase transformations during FGHAZ simulation.

Even though there was not a significant difference in the void measurements of the creep aged 1 parent and simulated FGHAZ material, the cavities with ECD less than 1  $\mu\text{m}$  were observed to be elongated in the simulated FGHAZ material (**Figure 4.19**) and not in the parent material (**Figure 4.17**). This suggests that there was an evolution in the cavities with ECD less than 1  $\mu\text{m}$  during FGHAZ simulation and not the voids.

From the literature (Section 2.3.6) it follows that cavity formation in X20 steel is mainly controlled by the decohesion between carbides and the matrix that is caused by stress concentrations resulting from:

- (i) grain boundary sliding (GBS) or deformation,
- (ii) inter-lath boundary deformation
- (iii) or intergranular dislocation movement (dislocation pile-ups that break through the boundary).

The site of decohesion is then a preferred nucleation site for cavities. Consequently, rupture of the material occurs due to a mixture of intergranular and transgranular cavitation. In addition, impurity particles such as sulphides, silicate, and oxide inclusions are also preferred cavity nucleation sites since they result in vacancy accumulation. As can be seen from **Figure 4.15** to **Figure 4.22**, the larger cavities are mainly located on MGB and the smaller cavities also form inside micro-grains. Thus, this literature is

confirmed by the results. The strong decohesion caused by an inclusion is observed in **Figure 4.20**. To completely understand these effects, the microstructure needs to be further analysed, which is done in the subsequent sections.

Previous studies have shown that cavities preferentially form on the PAGB, with those perpendicular to the stress direction having much higher cavitation damage than those parallel to the stress direction (Section 2.3.6). All samples in this study have been analysed parallel to the RD and perpendicular to the TD (**Figure 2.18**), which is parallel to the circumferential stress in the steam pipe. As shown in **Figure 4.21** and **Figure 4.22**, there seems to be little to no cavitation along the PAGB. Also, the cavities lie on both LAGB and HAGB (**Figure 4.21(e)** **Figure 4.22(c)**).

The main limitation with the quantitative analysis is that the data was sorted only for voids with ECD between 1 to 3  $\mu\text{m}$ . However, the desired outcome was only to analyse voids that are of interest when it comes to plant life management. Analysis of small cavities is also limited by the sample preparation since these cavities may be smeared close and not visible due to the colloidal silica used for polishing. To overcome this problem, the surface can be polished with vibration polishing. Another concern is that if the sample surface is not clean, dirt may be detected with LM as voids. However, in this study freshly prepared samples were analysed with LM to avoid surface contamination.

## 4.6 BOUNDARY CHARACTER

### 4.6.1 Results

For boundary misorientation analysis, the same EBSD data from the PAG analysis is used (Section 4.3). The misorientations (MO) across all the boundaries of each map was measured using the Oxford Instruments HKL CHANNEL 5 software (Section 3.6.2). **Figure 4.23** provides the result from these measurements as MO distributions. The expected distribution for a randomly textured polycrystal cubic system as given by Mackenzie (Mackenzie 1958) is also included. Also, the MO distribution can be divided into low angle boundaries ( $\text{MO} < 15^\circ$ ) (LAGB) and high angle boundaries ( $\text{MO} > 15^\circ$ ) (HAGB).

**Figure 4.24** provides a comparison of the MO distributions of the parent and simulated materials. In addition to the maxima at the lowest MO, other distinct peaks originate in the distributions. Previous studies by Payton, Aghajani, Otto *et al.* (2012) and Brust, Niezgodá, Yardley and Payton (2018) on the orientation relationships between ferrite micro-grains in X20 steel has shown that the orientations inherited from the martensitic microstructure deviate from the well-known orientation relationships such as the Kurdjumov–Sachs (KS) (Kurdjumov and Sachs 1930). Upon comparison of the corresponding misorientations of the peaks in **Figure 4.24** with those determined in these studies for the variant intersections, it was possible to label each of the peaks with the approximate low-angle index. In addition, Payton, Aghajani, Otto *et al.* (2012) assigns a boundary type to each variant. It should be noted that the experimental MO values differ slightly from those determined in the studies due to binning of 0.5°. The estimated variant information and relative frequency determined from **Figure 4.24** and Payton, Aghajani, Otto *et al.* (2012) is summarised in **Table 4.3** and plotted in **Figure 4.25** for the parent and simulated FGHAZ X20 materials.



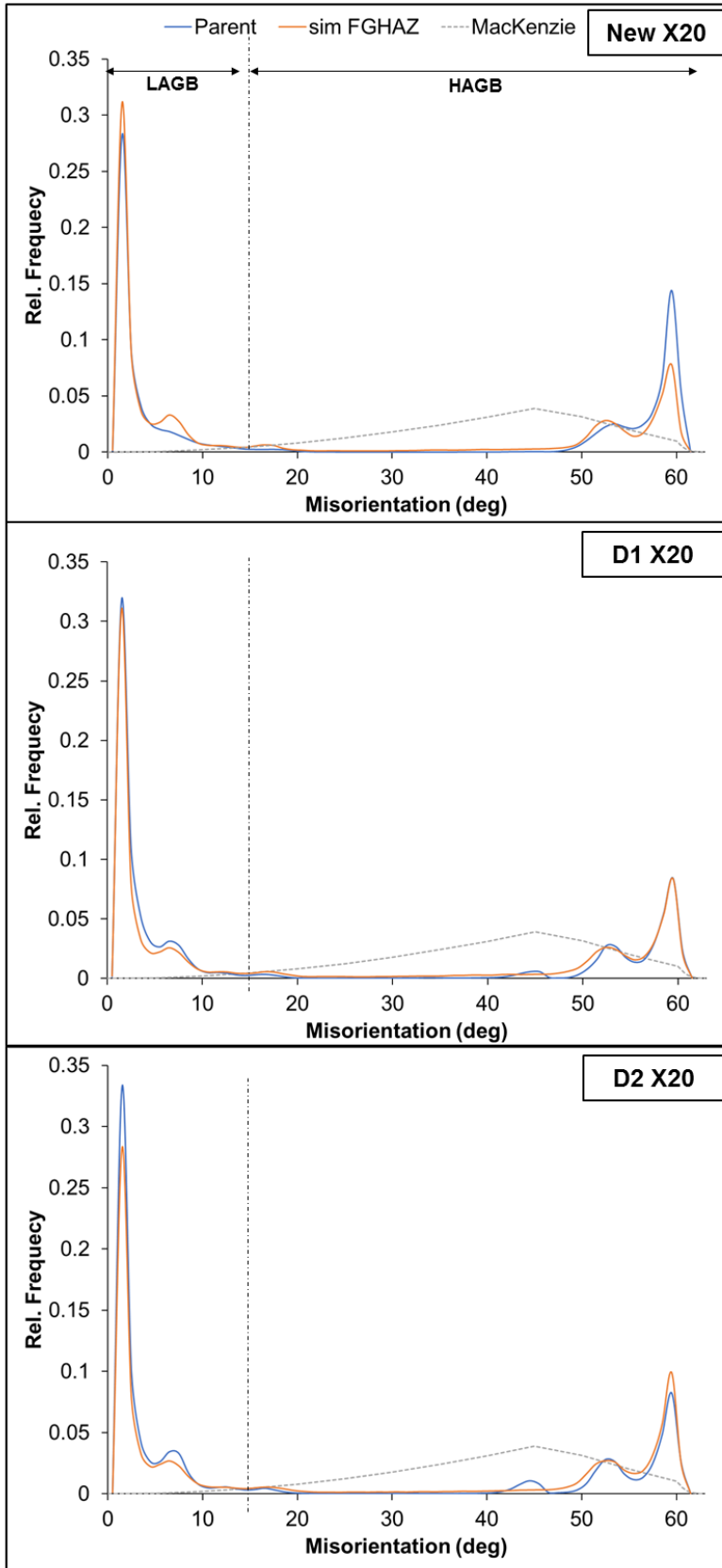


**Figure 4.23:** Relative frequency of misorientation angles measured from 204 x 153  $\mu\text{m}^2$  EBSD maps acquired from parent and simulated FGHAZ X20 steel. Boundaries with misorientations below  $15^\circ$  are defined as low-angle boundaries (LAGB) and those with misorientations above  $15^\circ$  as high-angle boundaries (HAGB). The dashed line represents the expected distribution for a randomly textured polycrystal cubic system as given by the Mackenzie distribution

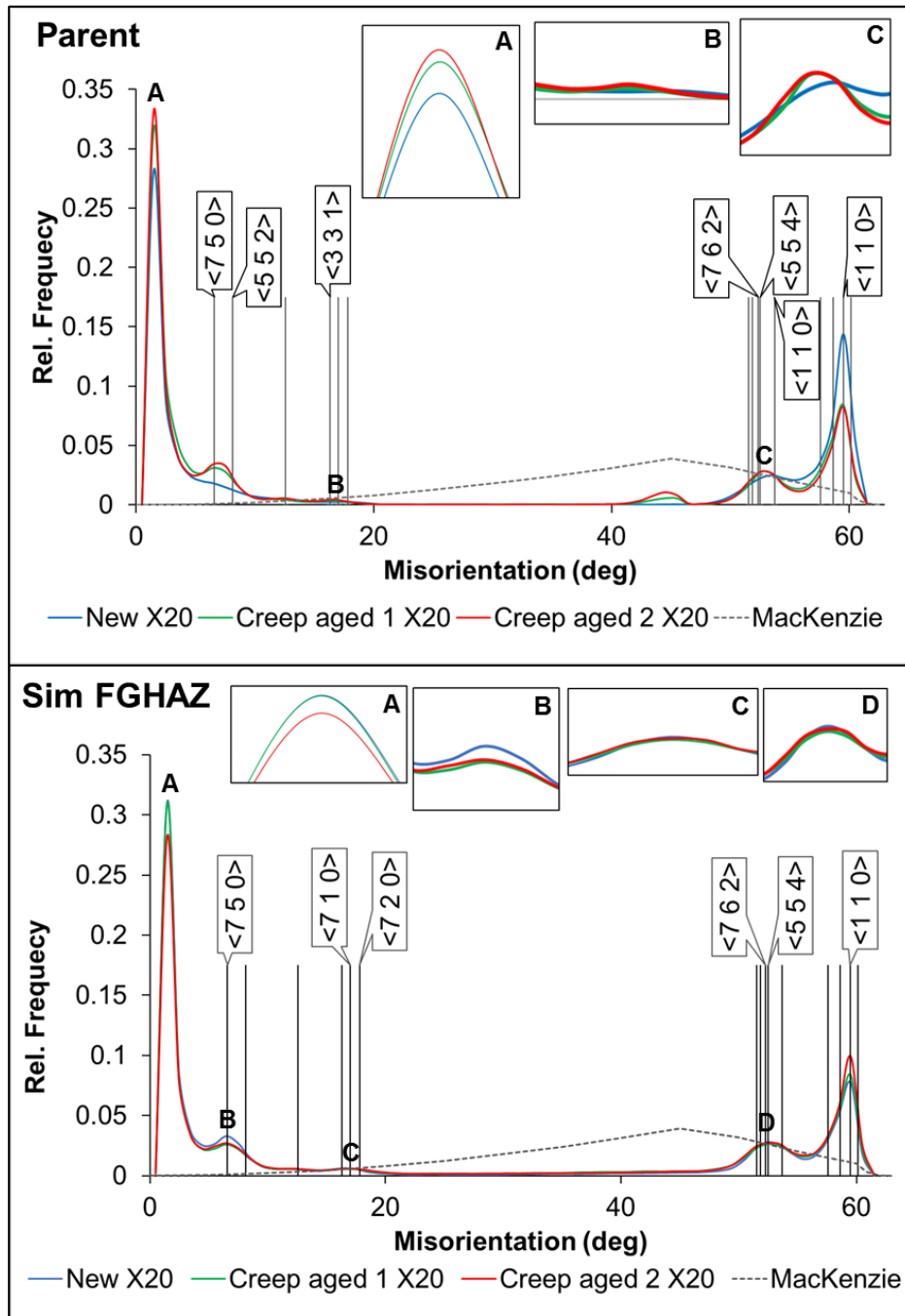


**Figure 4.24:** Summary of MO distributions of parent and simulated FGHAZ X20 steel (204 x 153  $\mu\text{m}^2$  sampling area). Some of the peaks have been enlarged to enhance visibility. The dashed line represents the expected distribution for a randomly textured polycrystal cubic system as given by the Mackenzie distribution (Mackenzie 1958). The vertical black lines indicate the MO for the variant intersections from Payton, Aghajani, Otto, Eggeler and Yardley (2012), and Brust, Niezgod, Yardley and Payton (2018).

**Table 4.3:** Estimated variant information determined from Payton, Aghajani, Otto et al. (2012) and relative frequency measured from EBSD MO profiles of parent and simulated FGHAZ X20 materials.

Approx. low-index axis	MO (deg)	Boundary type	Rel. frequency					
			Parent			Sim FGHAZ		
			New	Creep aged 1	Creep aged 2	New	Creep aged 1	Creep aged 2
<7 5 0>	± 6.5	Sub-block	0.0163	0.027	0.0159	0.0331	0.0258	0.0269
<5 5 2>	± 7.5	Packet	0.0117	0.0246	0.0121	0	0	0
<3 3 1>	± 16.5	Packet	0.0023	0.0029	0.0027	0	0	0
<7 1 0>; <7 2 0>	± 18.5	Packet	0	0	0	0.0034	0.0039	0.0043
<5 5 4>; <7 6 2>	± 52.5	Packet	0.0166	0.0211	0.0193	0.0282	0.0262	0.0271
<1 1 0>	± 53.5	Block	0.0186	0.0218	0.0201	0	0	0
<1 1 0>	± 59.5	Block	0.1038	0.0736	0.1018	0.0779	0.0837	0.0992

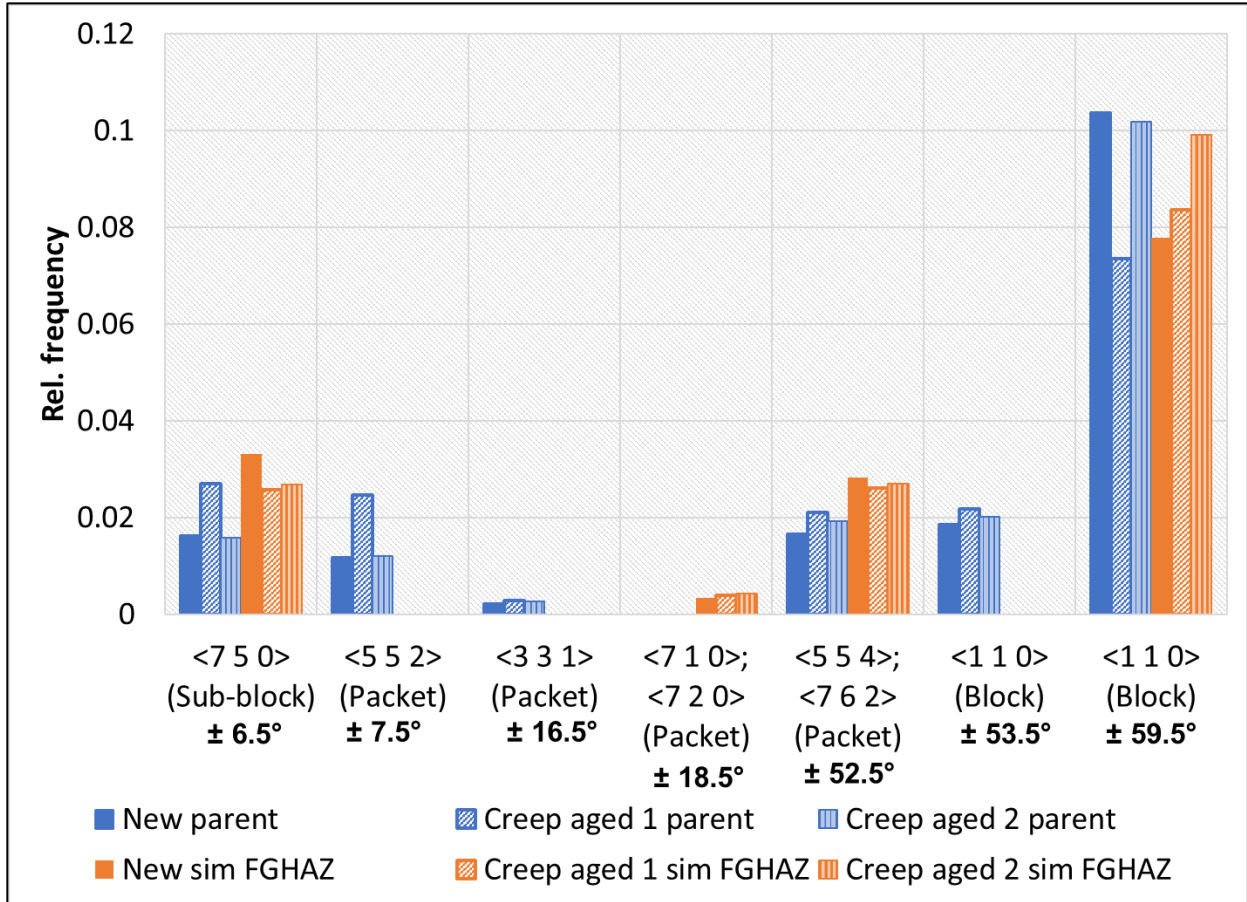


**Figure 4.25:** Relative frequency and MO of estimated variant intersections for parent and simulated FGHAZ X20 materials ( $204 \times 153 \mu\text{m}^2$  sampling area).

The boundary character was further investigated by analysis of the  $12 \times 12 \mu\text{m}^2$  area TKD maps acquired from 4 different areas of the twin-jet electropolished specimens of each material type (Section 3.6.3). These maps provide a higher spatial resolution of the boundaries (step size = 30 nm). As with the EBSD data, the misorientations (MO) across all the boundaries of each map was measured using the Oxford Instruments HKL CHANNEL 5 software. From these results, a GB map illustrating different boundaries with colours was obtained. Such a map of a single area from each material is provided in **Figure 4.26**. As can be seen not all the SGB boundaries ( $1 - 2^\circ$  MO) are completed due to the limited angular resolution.

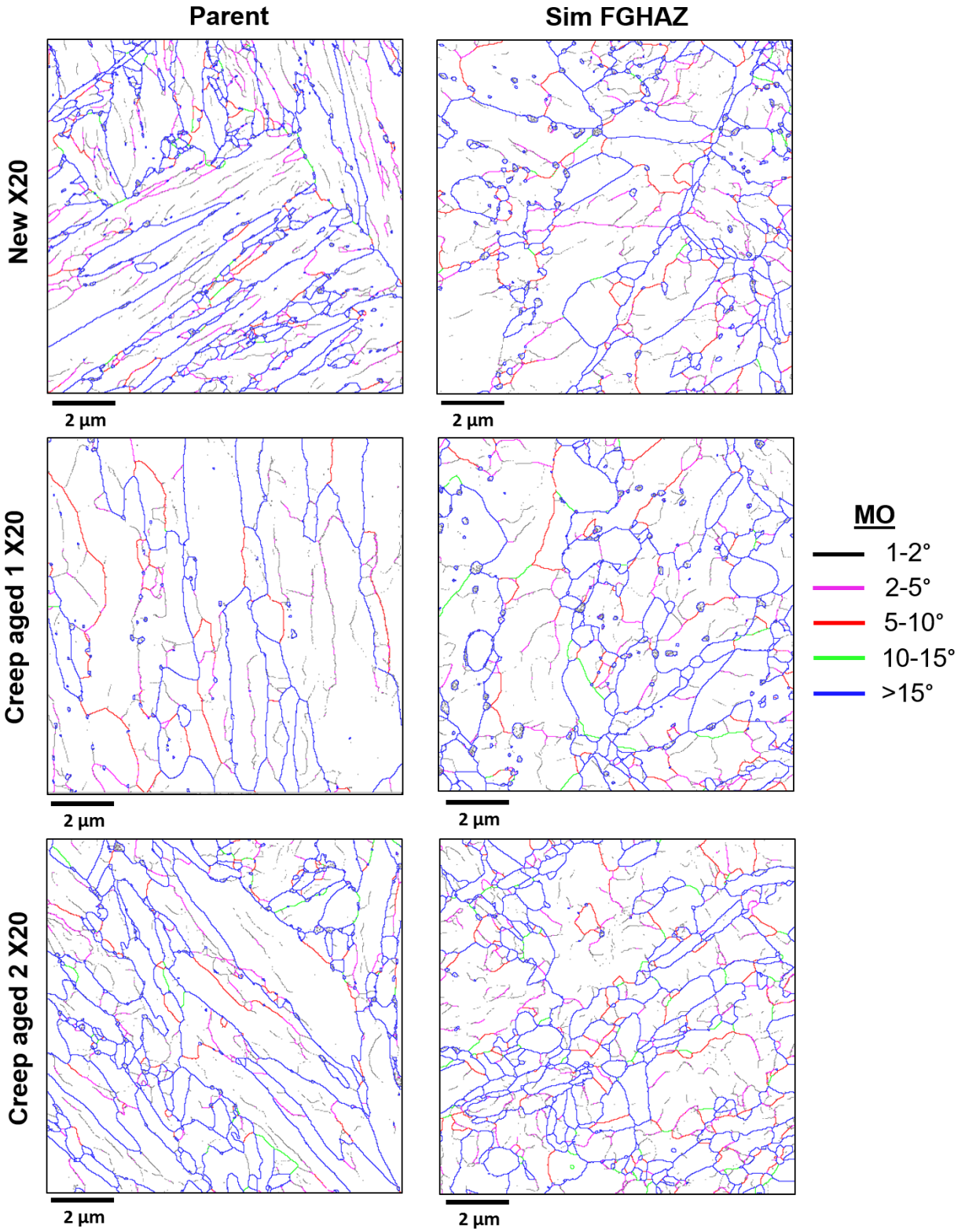


**Figure 4.26:**  $12 \times 12 \mu\text{m}^2$  TKD GB maps of parent and simulated FGHAZ X20 twin-jet electropolished specimens (30 nm step-size).

## 4.6.2 Discussion

In each distribution in **Figure 4.23**, the maximum occurs at the minimum MO ( $\sim 0.5^\circ - 1^\circ$ ). The following can be given as explanation for this maximum:

- 1) The angular resolution is limited to approximately  $0.5^\circ$  to  $1^\circ$  (Humphreys 2001) and the orientation noise is typically about  $1^\circ$ .
- 2) Since the misorientation of SGBs (Section 2.3.3) are  $\pm 1^\circ$ , most boundaries are SGBs (small angle boundaries).

It has been noted by Payton, Aghajani, Otto *et al.* (2012) that prior block and packet boundaries cannot be distinguished by MO alone since their MO all lie within  $58^\circ \pm 3^\circ$ . Consequently, the assigned variant intersections in **Table 4.3** are only an estimation and used for comparison.

In **Figure 4.25**, the observed variant relationships persist both throughout creep and in the simulated FGHAZ. Both the parent and simulated FGHAZ materials have  $\langle 7\ 5\ 0 \rangle$  ( $6.5^\circ$  MO) sub-block boundaries, with the simulated FGHAZ having a higher frequency than the corresponding parent material. In each of the simulated FGHAZ materials, the  $\langle 5\ 5\ 2 \rangle$  ( $7.5^\circ$  MO) and  $\langle 3\ 3\ 1 \rangle$  ( $16.5^\circ$  MO) packet, and  $\langle 1\ 1\ 0 \rangle$  ( $53.5^\circ$  MO) block boundaries have disappeared, while new  $\langle 7\ 1\ 0 \rangle / \langle 7\ 2\ 0 \rangle$  ( $18.5^\circ$ ) packet boundaries formed. Between the parent materials, creep aged 1 parent has the highest frequency of all the boundary types, except the  $\langle 1\ 1\ 0 \rangle$  ( $59.5^\circ$  MO) block boundary for which it has the lowest frequency. No such specific trend is observed among the simulated FGHAZ materials. Since the number of variant intersections decreases from 6 types to only 4 types during FGHAZ simulation, it follows that stronger texture is developed during welding in the FGHAZ, with texturing increasing when welding upon creep aged materials.

The fine scale of the microstructure posed as a challenge in this study and due to long acquisition times of EBSD and TKD, a trade-off had to be made to observe the details in the micro-grain structure at the expense of making observations in a sufficient number of PAG. Consequently, care should be taken when concluding the parent material results

since sampling occurred only from within a couple of PAG (**Figure 4.6**). Strong texturing of variants within a PAG occurs and sampling of only a few PAG may skew the results. Consequently, large sampling areas that contain many PAG are required to verify the observed variant information.

In the case of the simulated FGHAZ materials, the analysis is performed across many PAG due to their smaller size. Therefore, reasonably accurate conclusions can be drawn from the simulated FGHAZ variant results that are more statistically reliable. Future work includes to analyse a sampling area large enough to include a statistically significant number of PAG.

Due to the sampling issue as mentioned earlier, not much can be concluded from the TKD GB maps except that there are a much higher number of HAGB than LAGB for each material type (**Figure 4.26**). Quantitative analysis is required to make feasible comparisons.

## **4.7 M<sub>23</sub>C<sub>6</sub> AND MX PRECIPITATES**

### **4.7.1 Qualitative Results: M<sub>23</sub>C<sub>6</sub> Precipitates**

The methodology of measuring the M<sub>23</sub>C<sub>6</sub> precipitate parameters is discussed in Section 3.7.3. These parameters were measured from both the Cr TKD-EDS maps acquired simultaneously with the TKD maps, and the CBS images obtained from the same areas. Even though the same areas on the twin-jet electropolished specimens have been analysed for both techniques, the CBS images cover a larger surface area of 915 μm<sup>2</sup> (4 x (18.6x12.3 μm<sup>2</sup>)) than the TKD-EDS maps that cover 576 μm<sup>2</sup> (4 x (12x12 μm<sup>2</sup>)). The analysis was performed on all the M<sub>23</sub>C<sub>6</sub> carbides in an area, as well as the boundary carbides and carbides in the interior of the micro-grains. The total number of Cr-enriched M<sub>23</sub>C<sub>6</sub> precipitates thresholded from the TKD-EDS maps and CBS images are given in **Table 4.4** and **Table 4.5**, respectively.

**Table 4.4:** Number of Cr-enriched  $M_{23}C_6$  precipitates measured from Cr TKD-EDS maps covering a total area of  $576 \mu m^2$ .

	New		Creep aged 1		Creep aged 2	
	Parent	Sim FGHAZ	Parent	Sim FGHAZ	Parent	Sim FGHAZ
<b>Total</b>	1411	1167	954	1151	1327	1177
<b>On boundary</b>	1180	771	517	912	1118	1002
<b>Interior</b>	231	396	437	239	209	175

**Table 4.5:** Number of Cr-enriched  $M_{23}C_6$  precipitates measured from CBS maps covering a total area of  $915 \mu m^2$ .

	New		Creep aged 1		Creep aged 2	
	Parent	Sim FGHAZ	Parent	Sim FGHAZ	Parent	Sim FGHAZ
<b>Total</b>	4041	2730	1610	3400	3119	4678
<b>On boundary</b>	2912	2087	1287	2519	2407	3045
<b>Interior</b>	1129	643	323	881	712	1633

### (i) TKD-EDS Results

**Figure 4.27** provides the thresholded Cr-enriched  $M_{23}C_6$  boundary and interior carbides for a single Cr TKD-EDS map in the parent and simulated FGHAZ twin-jet electropolished specimens. For comparison, the same areas as in **Figure 4.26** are shown.



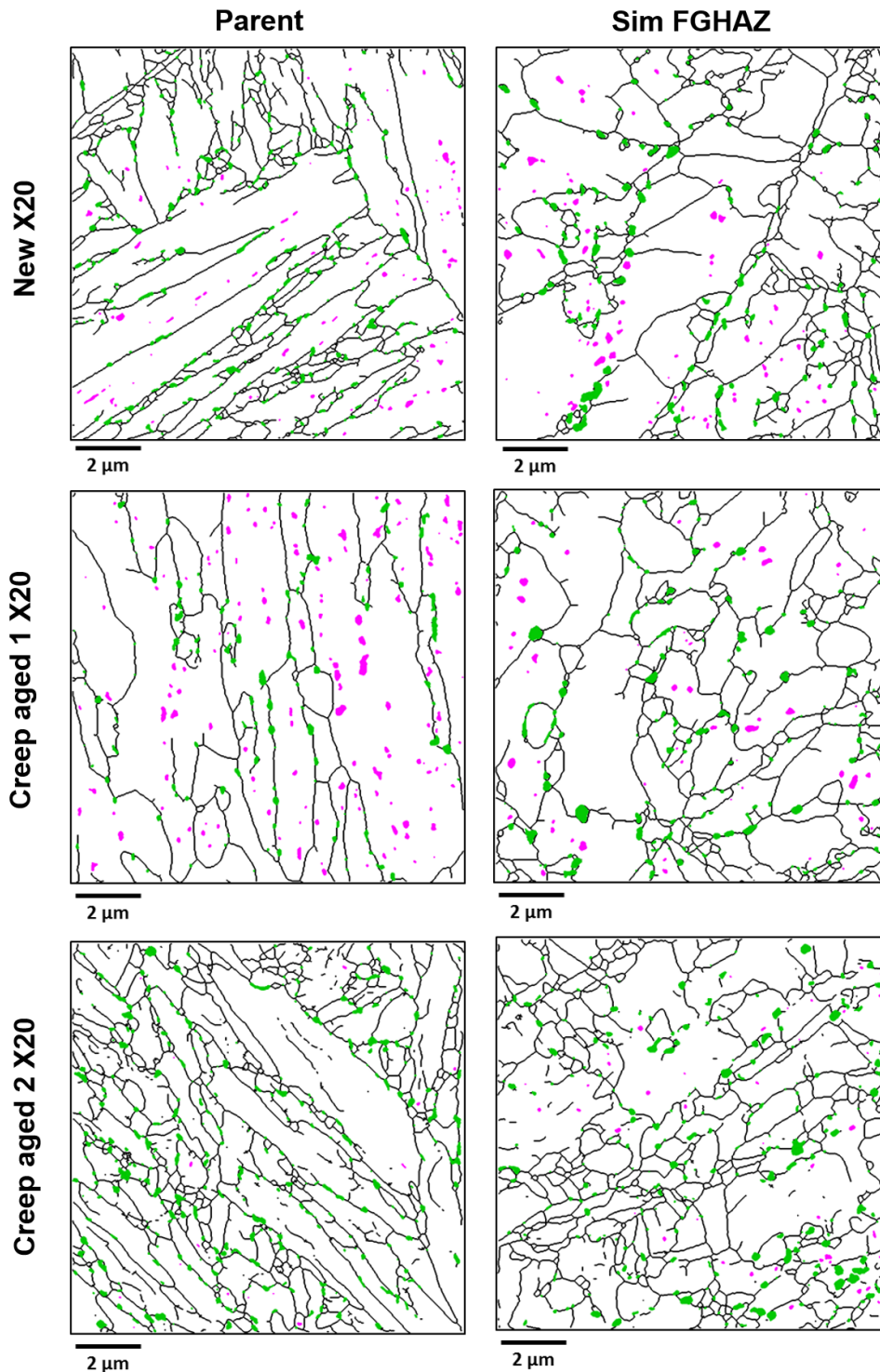


**Figure 4.27:** Boundary (green) and interior (pink) Cr-enriched  $M_{23}C_6$  carbides isolated from  $12 \times 12 \mu\text{m}^2$  Cr TKD-EDS map and superimposed onto corresponding TKD GB ( $MO > 2^\circ$ ) map obtained from parent and simulated FGHAZ twin-jet electropolished specimens. The same areas as in Figure 4.26 is shown.

## (ii) CBS Results

**Figure 4.28** provides the high-resolution CBS images obtained from an  $18.6 \times 12.3 \mu\text{m}^2$  area of each material (Section 3.6.4). In Section 3.7.3 the identification, thresholding and measurement of the  $\text{M}_{23}\text{C}_6$  carbides from the CBS images is explained. The  $\text{M}_{23}\text{C}_6$  carbides isolated from the CBS images for the same areas as in **Figure 4.28** is given in **Figure 4.29**. Also shown in these images is the MGB isolated from the CBS images. Even though the MO of the isolated boundaries is not known, by comparison to STEM data (Section 4.8) it is observed that micro-grains are outlined in the CBS images. Hence, it is correct to refer to MGB being isolated in the CBS images. For clarity, the key differences between the TKD-EDS and CBS  $\text{M}_{23}\text{C}_6$  precipitate data is:

- (i) The spatial resolution of the CBS images is approximately 30 nm, which is much higher than that of TKD-EDS maps. Consequently, the precipitate boundaries in the TKD-EDS Cr elemental maps are not clearly resolved as in the CBS images and the precipitate sizes can be underestimated, as well as small carbides may be excluded.
- (ii) The criterion for a boundary  $\text{M}_{23}\text{C}_6$  carbide in the TKD-EDS analysis is a carbide on an  $\text{MO} > 2^\circ$  boundary and in CBS analysis a carbide on an actual visible MGB.
- (iii) In TKD-EDS a projected area of the precipitates is analysed, while in CBS a planar section of the precipitates is analysed. Therefore, different stereological corrections are applied as discussed in Section 3.7.3.
- (iv) From point (iii) it follows that the TKD-EDS data is thickness dependent.
- (v) Even though the same location of areas is analysed in both techniques, the CBS data covers more than one and a half the area that the TKD-EDS data covers ( $916$  versus  $576 \mu\text{m}^2$ ). Hence, many more precipitates are analysed as seen in **Table 4.4** and **Table 4.5**.
- (vi) The stereological correction of the carbides measured from the TKD-EDS data assumes the precipitates to be spherical and homogeneously distributed and as

the results will show these assumptions are not valid for the carbides. For the stereological corrections of the carbide measurements from the CBS images, it is only assumed that the precipitates be convex (**Table 3.17**), which is a more realistic assumption.

Points (i), (iv), (v) and (vi) highlight the main limitations of the TKD-EDS  $M_{23}C_6$  precipitate measurements.

Possible limitations of the CBS data can be summarised as:

- (i) Due to the similar atomic contrast of the  $M_{23}C_6$  carbides and Z-phase precipitates in CBS images, Z-phase precipitates can be speciously included in the measurements.
- (ii) Due to the varying contrast of the micro-grains in the CBS images, it is difficult to accurately threshold the MGB compared to the direct thresholding from TKD GB maps where only the boundaries are visible.

If it is assumed that the Z-phase fraction is low, then their possible inclusion in the  $M_{23}C_6$  carbide results will not significantly affect the measurements of the carbides whose phase fraction is much higher.

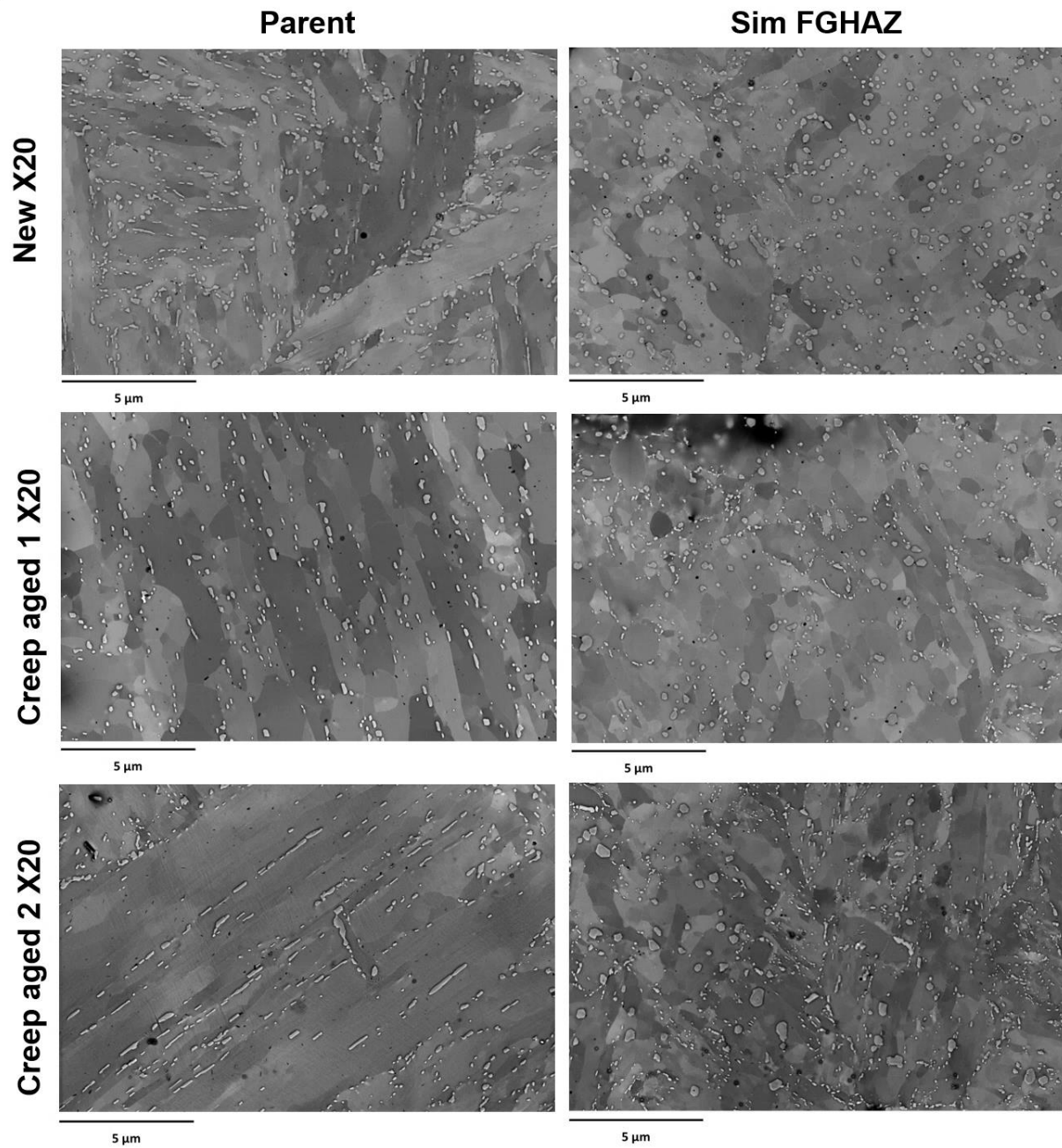


**Figure 4.28:**  $18.6 \times 12.3 \mu\text{m}^2$  5 kV CBS images of  $18.6 \times 12.3 \mu\text{m}^2$  area scanned across parent and simulated FGHAZ twin-jet electropolished specimens.

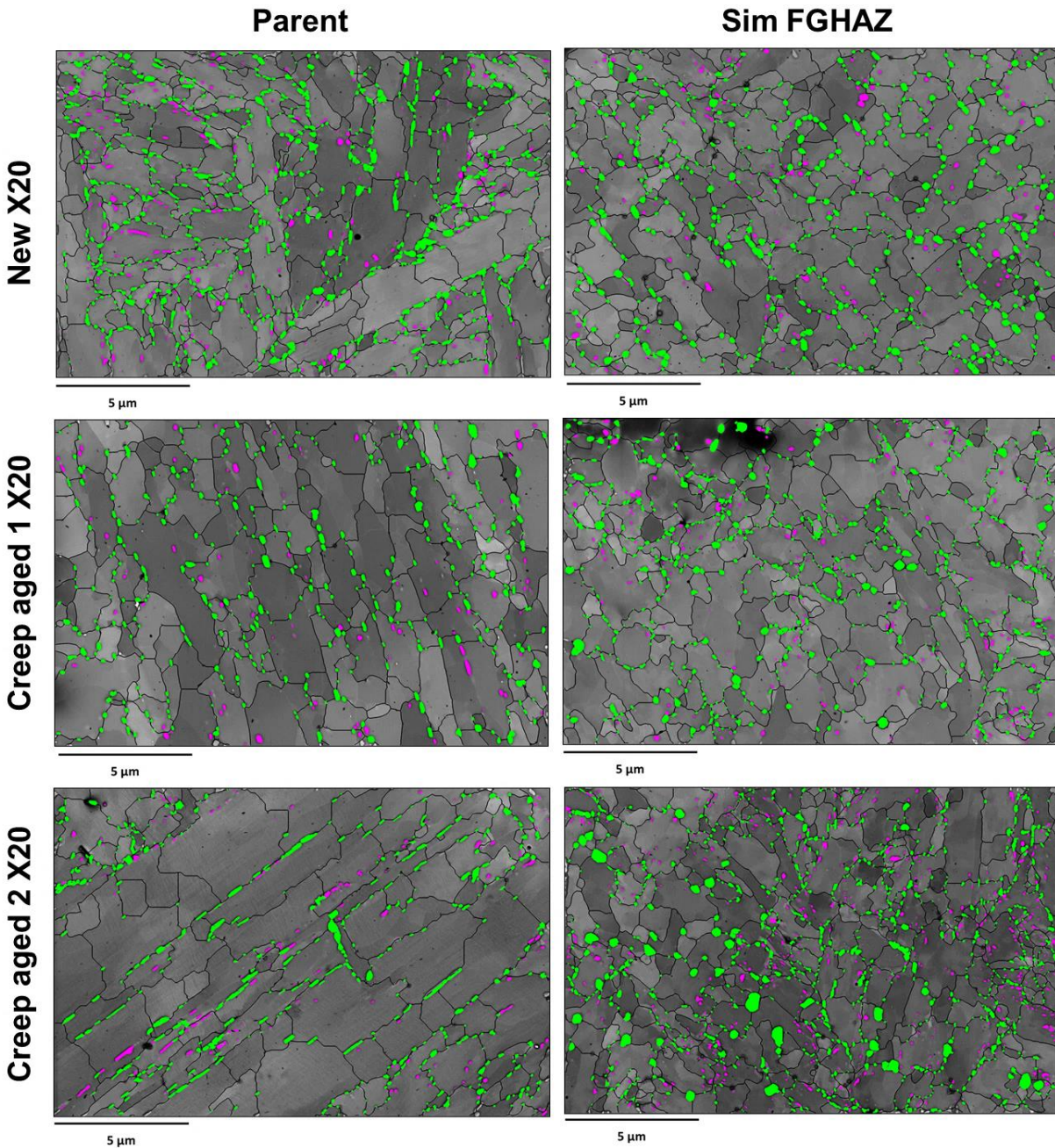


**Figure 4.29:** Thresholded boundary (green) and interior (pink)  $M_{23}C_6$  carbides overlaid onto corresponding  $18.6 \times 12.3 \mu\text{m}^2$  CBS image obtained from parent and simulated FGHAZ twin-jet electropolished specimens. Black boundaries outline MGB given by CBS image. The same areas as in Figure 4.28 is shown.

### (iii) EFTEM Results

EFTEM was performed on both the twin-jet electropolished and extraction replica specimens (Section 3.6.5). Even though EFTEM has a higher spatial resolution ( $\pm 5$  nm) than CBS, similar limitations argued in the preceding section for TKD-EDS can be argued for EFTEM performed on twin-jet electropolished (thin foil) specimens. In addition, EFTEM maps do not contain orientation information and therefore boundary and interior carbides cannot be separated as with CBS and TKD-EDS analyses. As discussed in Section 3.4.3, the true precipitate size and shape can be analysed from extraction replica specimens since no iron matrix can degrade the signal and hence the spatial resolution. However, the main limitation of this approach is that the sampling volume is not known and therefore volume fraction and number densities cannot be accurately determined.

The RGB composite maps of the acquired EFTEM Cr and V elemental maps from a single area of each twin-jet electropolished and extraction replica specimen is illustrated in **Figure 4.30** and **Figure 4.31**. The distinct difference between the sample preparation techniques is visible. More well-defined precipitates are visible in the maps of the extraction replicas. However, since the  $M_{23}C_6$  carbides are not sectioned as those in the thin foil, they are thicker in the centre and the signal is insufficient. Also, there is substantial overlap of the carbides due to the larger sampling volume of the replicas. These factors make thresholding of the carbides challenging and therefore quantitative analysis of the  $M_{23}C_6$  carbides was not performed on the EFTEM results from the extraction replicas.

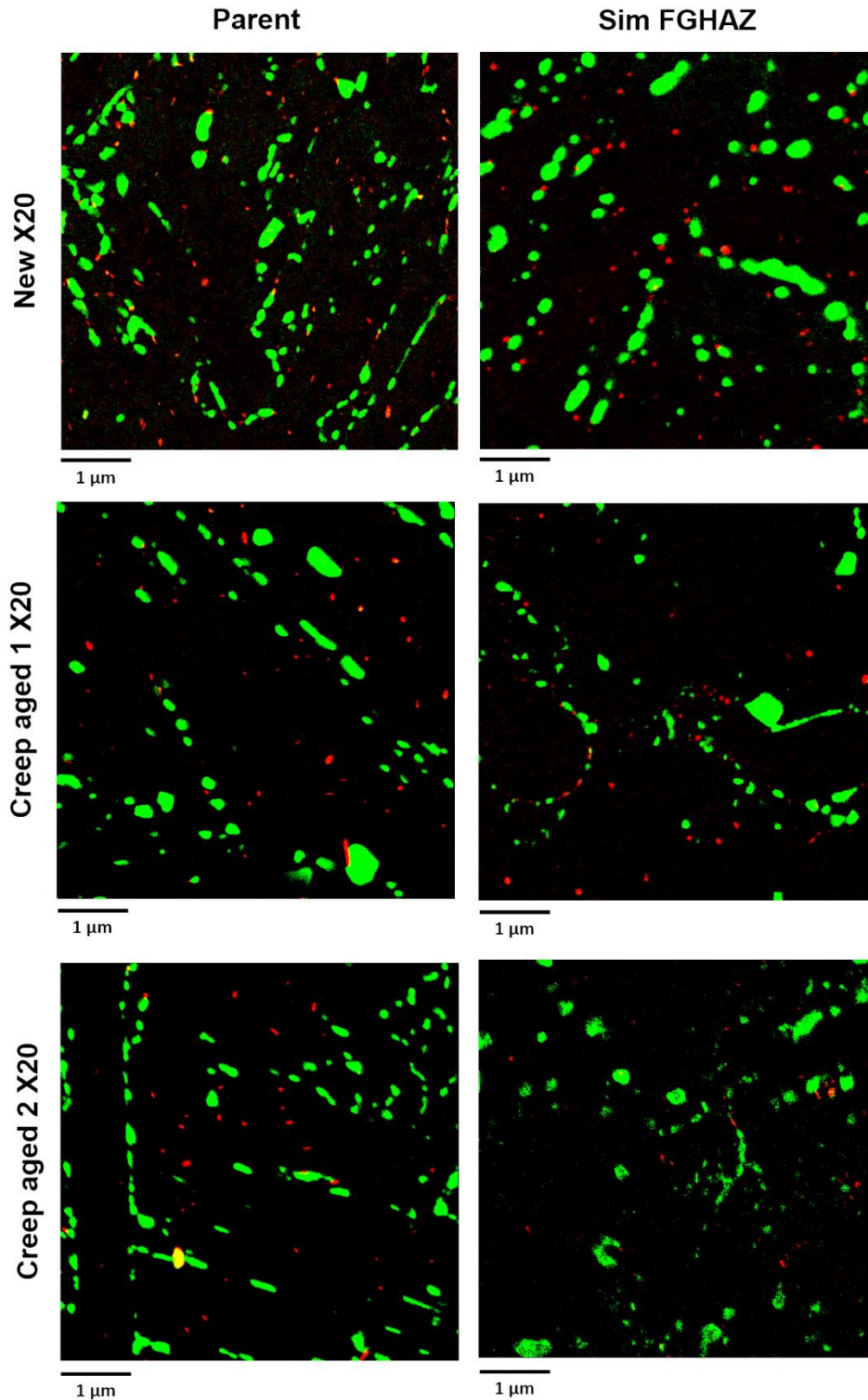


**Figure 4.30:**  $6 \times 6 \mu\text{m}^2$  RGB composite maps of EFTEM Cr (green) and V (red) elemental maps acquired from an area in the parent and simulated FGHAZ twin-jet electropolished specimens.

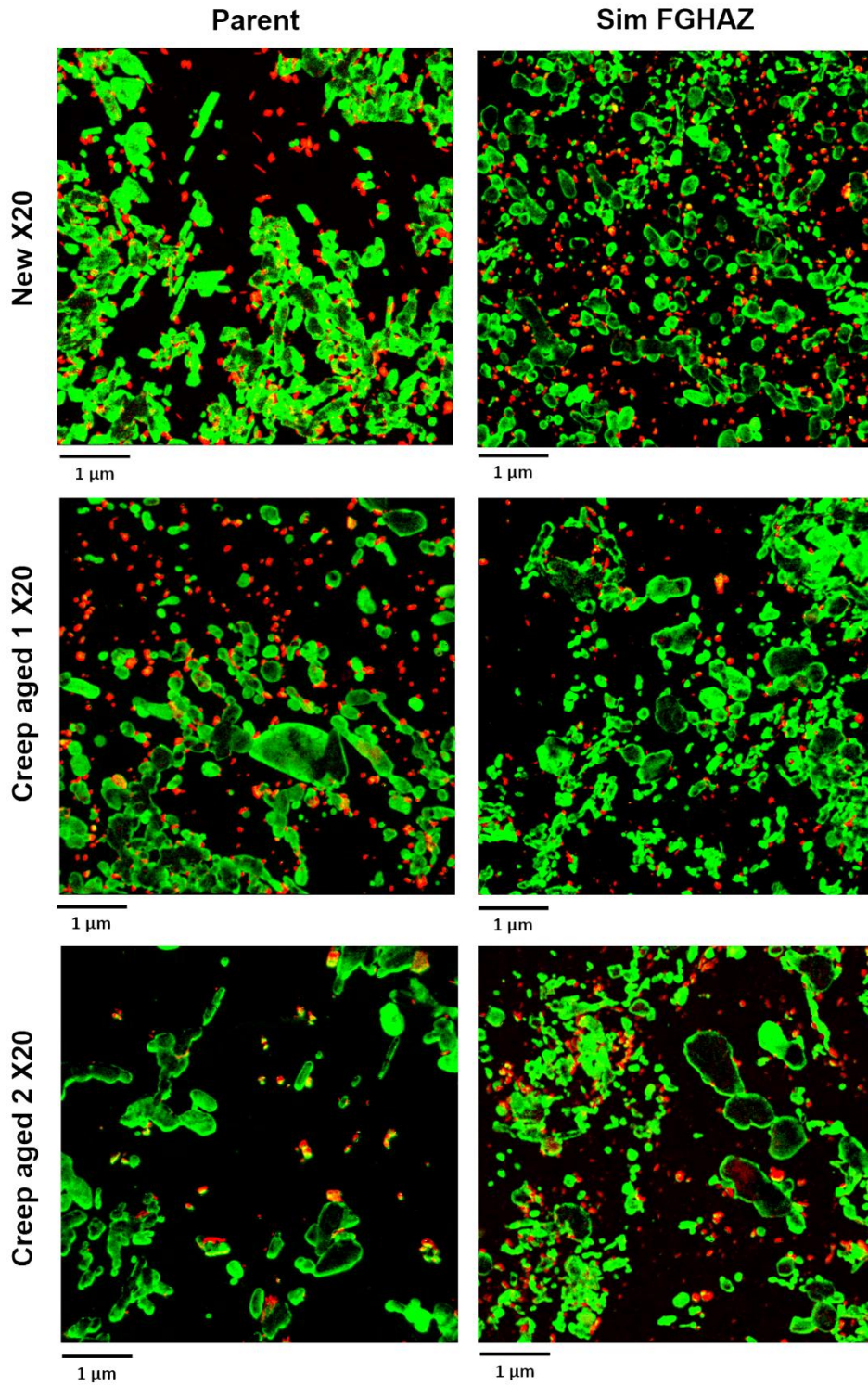


**Figure 4.31:**  $6 \times 6 \mu\text{m}^2$  RGB composite maps of EFTEM Cr (green) and V (red) elemental maps acquired from an area in the parent and simulated FGHAZ extraction replica specimens.



#### 4.7.2 Qualitative Results: MX Precipitates

As discussed in Section 3.7.4, EFTEM has been chosen as the primary analysis technique for the V-enriched MX (VX) precipitates. A total of 16 elemental maps (6 x 6  $\mu\text{m}^2$ ) was acquired across the same areas on the twin-jet electropolished specimens as in the TKD and CBS analysis. Due to the larger sampling volume of the extraction replicas, 10 EFTEM V elemental maps (6 x 6  $\mu\text{m}^2$ ) provided a statistically sufficient number of VX precipitates for analysis.

Section 3.7.4 explains how the VX precipitates were isolated for measurements from the EFTEM V elemental maps. **Figure 4.32** contains such a thresholded image of an area of each analysed extraction replica specimen. Similar thresholded images were obtained for the VX precipitates in the twin-jet electropolished specimens. **Table 4.6** summarises the number of VX precipitates analysed using EFTEM.

**Table 4.6:** Number of V-enriched MX (VX) precipitates measured from EFTEM V elemental maps.

	New		Creep aged 1		Creep aged 2	
	Parent	Sim FGHAZ	Parent	Sim FGHAZ	Parent	Sim FGHAZ
<b>Twin-jet electropolished</b> (sampling area = 576 $\mu\text{m}^2$ )	1274	911	445	728	408	461
<b>Extraction replica</b> (sampling area = 360 $\mu\text{m}^2$ )	5267	6393	3641	3133	955	4215

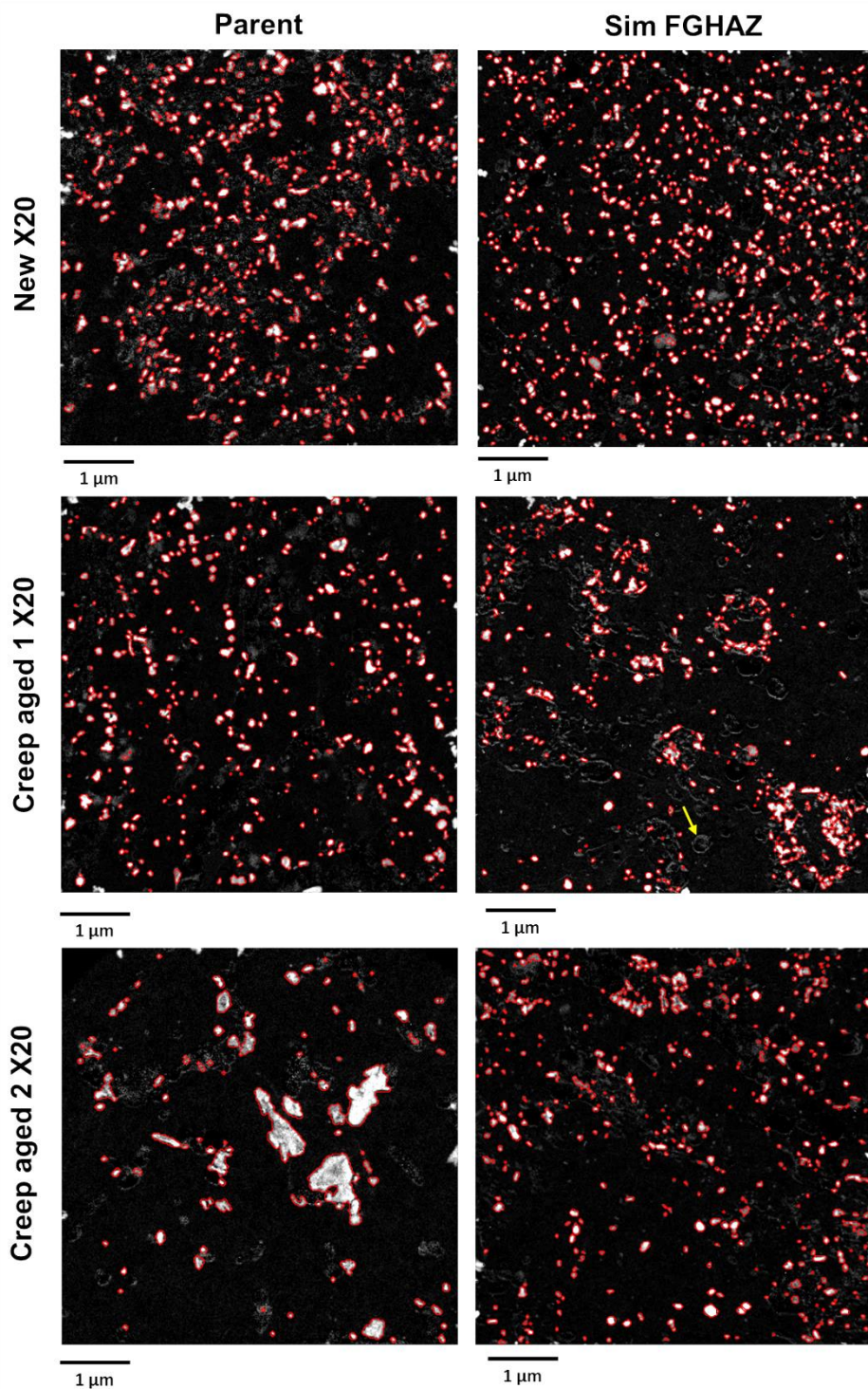


**Figure 4.32:** Outlines of thresholded VX precipitates from  $6 \times 6 \mu\text{m}^2$  EFTEM V maps acquired from parent and simulated FGHAZ extraction replica specimens. The yellow arrow indicates an area that is an O enriched area that has been inaccurately determined as V due to overlapping energy windows. The O signal is from the underlying carbon coat.

As can be seen in **Figure 4.32** there are some areas of V signal that were not included in the VX measurements. One such an area is indicated by the yellow arrow. The reason is that upon comparison with the EFTEM Cr elemental maps it was found that these areas outline the Cr-enriched  $M_{23}C_6$  carbides. The acquired STEM-EELS SI results were then also used to analyse the chemical composition of the edge of the Cr-enriched  $M_{23}C_6$  carbides. The STEM-EELS spectrum from such a carbide is shown in **Figure 4.33**. From the edge spectrum (green) it is seen that the signal is in fact from O whose energy window overlaps that of V. It is assumed that the O signal originates from the underlying carbon coat. Consequently, these areas were excluded from the EFTEM VX analyses.

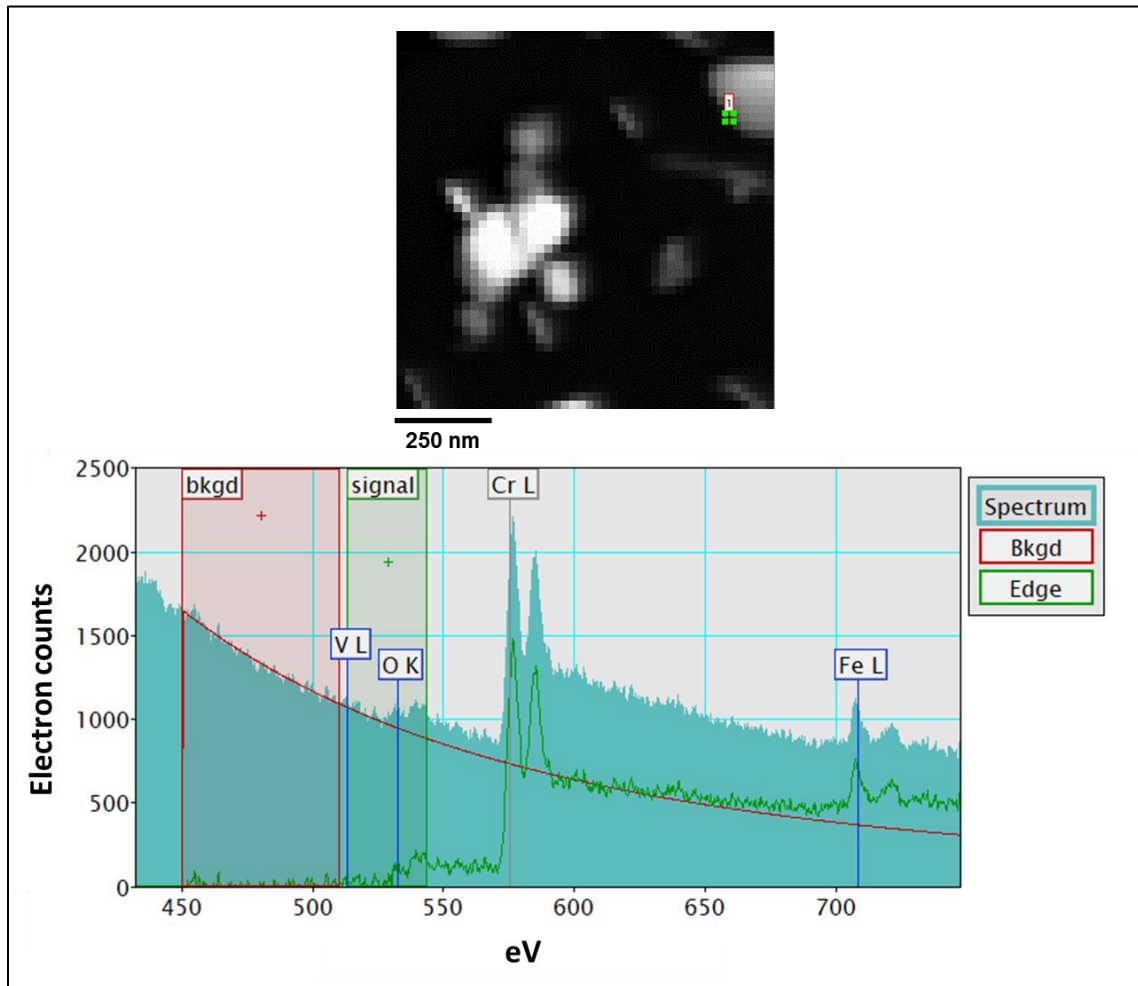


**Figure 4.33:** STEM-EELS spectrum acquired from the edge of an  $M_{23}C_6$  carbide (area indicated by the tiny green square) in new parent material extraction replica specimen.

### 4.7.3 Quantitative Results: $M_{23}C_6$ Precipitates

#### (i) Size and distribution

Upon comparison of the precipitate parameters obtained from the TKD-EDS and CBS data, inconsistencies have been found. These discrepancies are ascribed to the limitations discussed in Section 4.6.1. Since the CBS data has fewer limitations than TKD-EDS and EFTEM, it is decided to use the CBS data for final analysis of the  $M_{23}C_6$  precipitate parameters.

The procedure for measuring the  $M_{23}C_6$  carbides parameters is set out in Section 3.7.3. The ECD of the boundary and interior  $M_{23}C_6$  carbides were measured directly from the thresholded images (**Figure 4.29**). Since the carbides are 3D objects, the measured 2D ECD distributions were stereologically corrected for sectioning and unfolded into 3D ECD distributions (Section 3.7.2) As for the void measurements, the ECD distributions are plotted as KDE plots. For each distribution, the stereological correction shifts the distribution to larger ECD values, as expected. Comparisons of the corrected ECD KDE plots for all measured  $M_{23}C_6$  carbides (boundary and interior) from both parent and simulated FGHAZ materials is given in **Figure 4.34**. The corrected boundary and interior  $M_{23}C_6$  carbide ECD KDE distribution plots for the new, creep aged 1 and creep aged 2 materials is given in **Figure 4.35**.

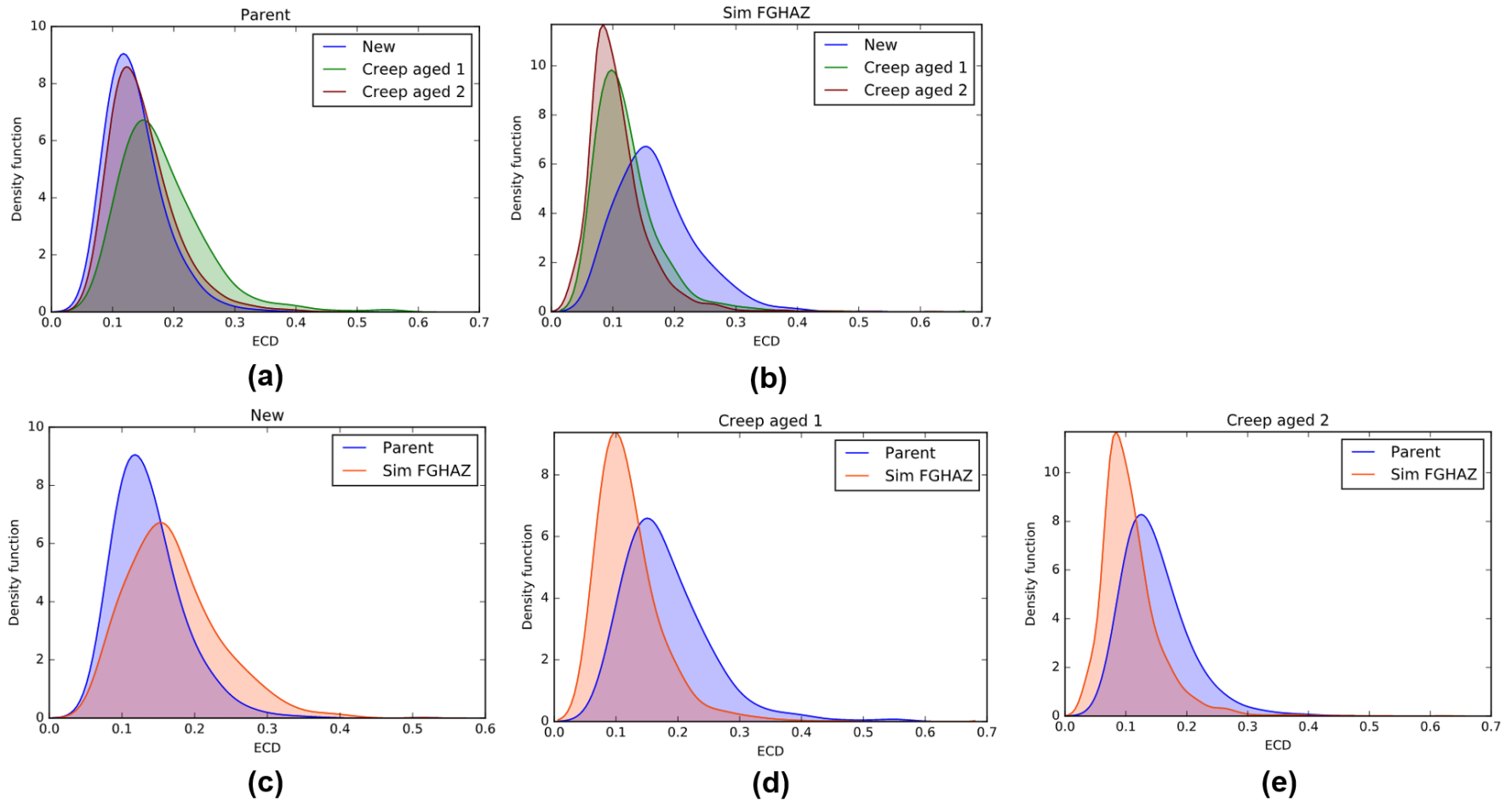


**Figure 4.34:** Corrected  $M_{23}C_6$  carbide (boundary and interior combined) ECD KDE distribution plots (scalar factor = 0.014 – 0.027) measured from CBS images of (a) parent and (b) simulated FGHAZ materials, (c) new, (d) creep aged 1 and (e) creep aged 2 materials (total area of 915  $\mu\text{m}^2$  analysed).

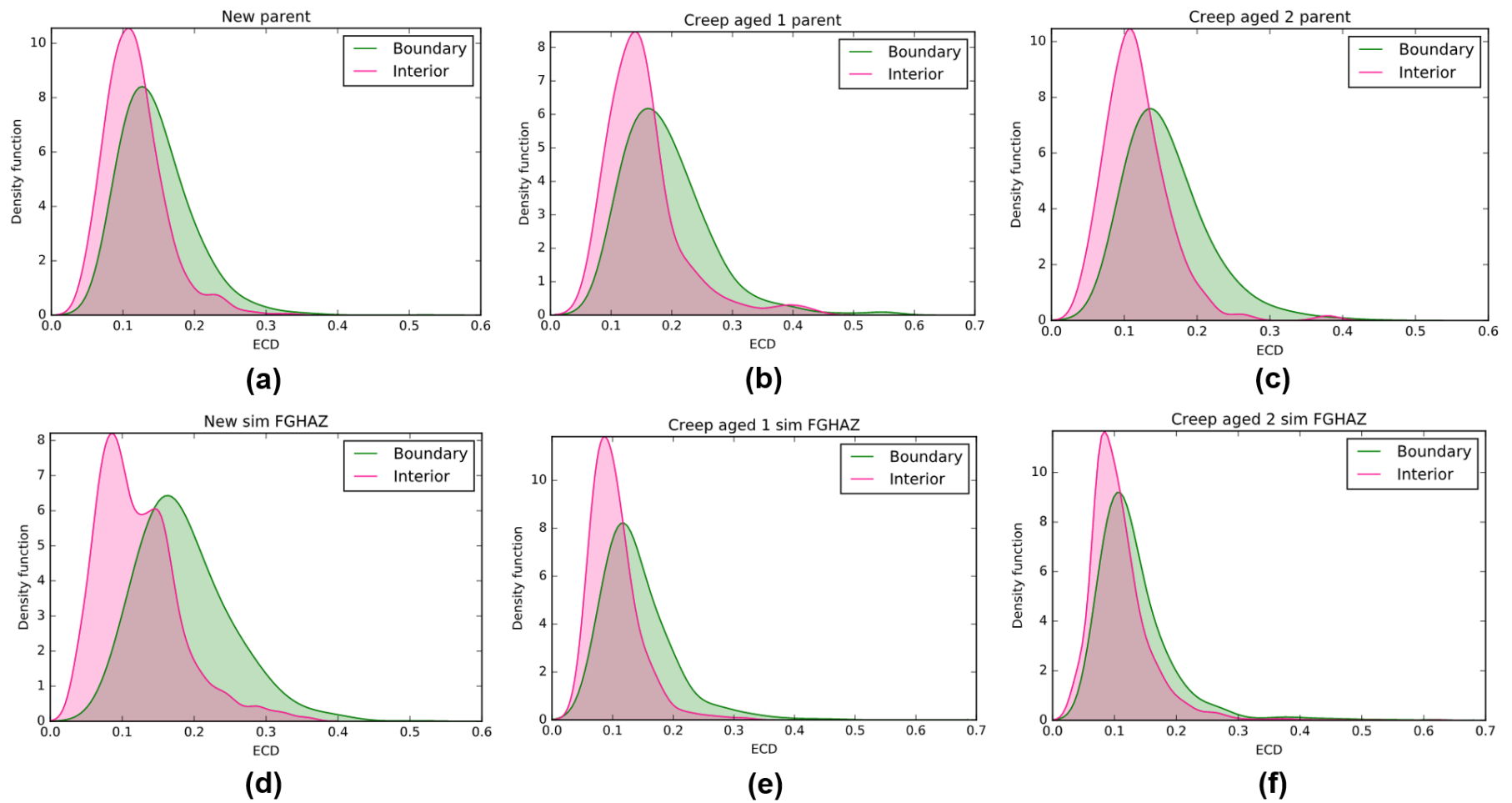


**Figure 4.35:** Corrected boundary (green) and interior (pink)  $M_{23}C_6$  carbide ECD KDE distribution plots (scalar factor = 0.014 – 0.027) measured from CBS images of (a) new, (b) creep aged 1 and (c) creep aged 2 parent materials, and (d) new, (e) creep aged 1 and (f) creep aged 2 simulated FGHAZ materials (total area of  $915 \mu\text{m}^2$  analysed).

The corrected diameter can be calculated as the stereological surface area averaged caliper diameter  $d_s$  (Equation (3.1)). This value is a good representation of the carbide size since this value is applicable even if all the particles are not the same shape and size. The mean surface area averaged caliper diameter  $d_s$  calculated for the boundary and interior carbides across the 4 CBS images of the parent and simulated FGHAZ X20 materials are plotted in **Figure 4.36**. The mean diameter  $d_s$  for both carbide types combined is given in **Figure 4.37**.

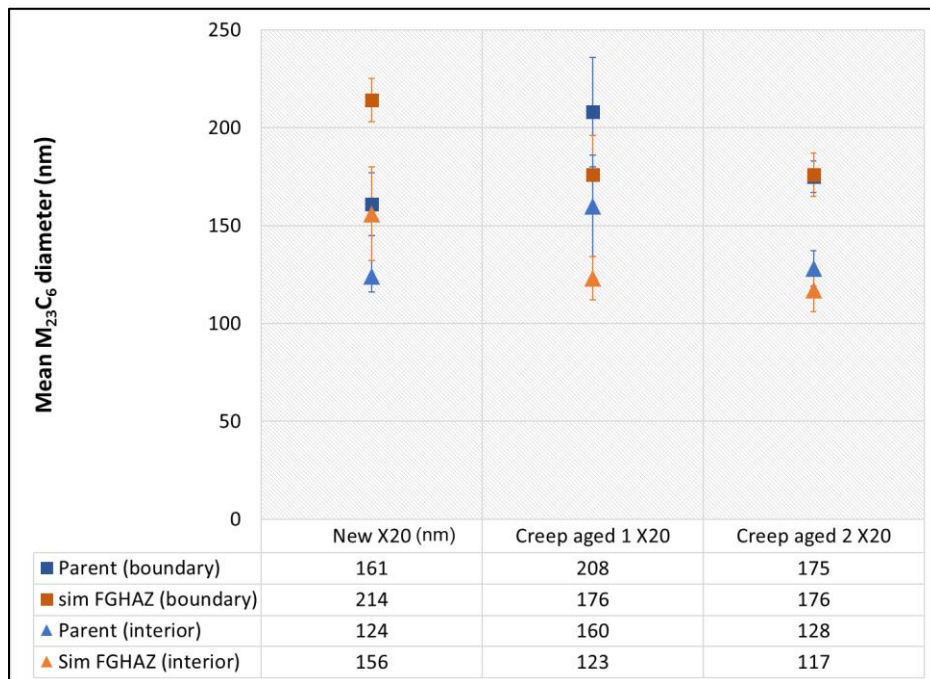


**Figure 4.36:** Mean corrected diameter ( $d_s$ ) calculated for the boundary and interior  $M_{23}C_6$  carbides obtained from CBS images of parent and simulated FGHAZ twin-jet electropolished specimens (total area of  $915 \mu\text{m}^2$  analysed). The error is given by Equation (3.15).

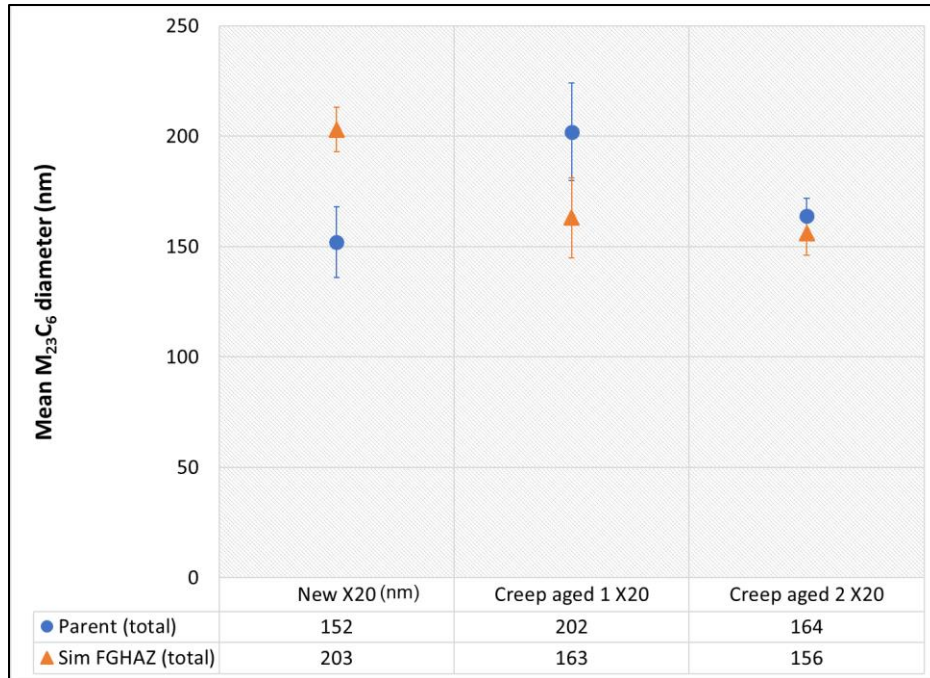


**Figure 4.37:** Mean corrected diameter ( $d_s$ ) for both boundary and interior  $M_{23}C_6$  carbides combined and obtained from CBS images of parent and simulated FGHAZ twin-jet electropolished specimens (total area of  $915 \mu\text{m}^2$  analysed). The error is given by Equation (3.15).

Using the Local Measurements function in MIPAR™, it was possible to measure the distance of the interior carbides from the MGB isolated from the CBS images (**Figure 4.29**). The distributions of these distances are plotted as box-and-whisker plots in **Figure 4.38(a)**. **Figure 4.38(b)** provides the measured NND distributions as box-and-whisker plots also.



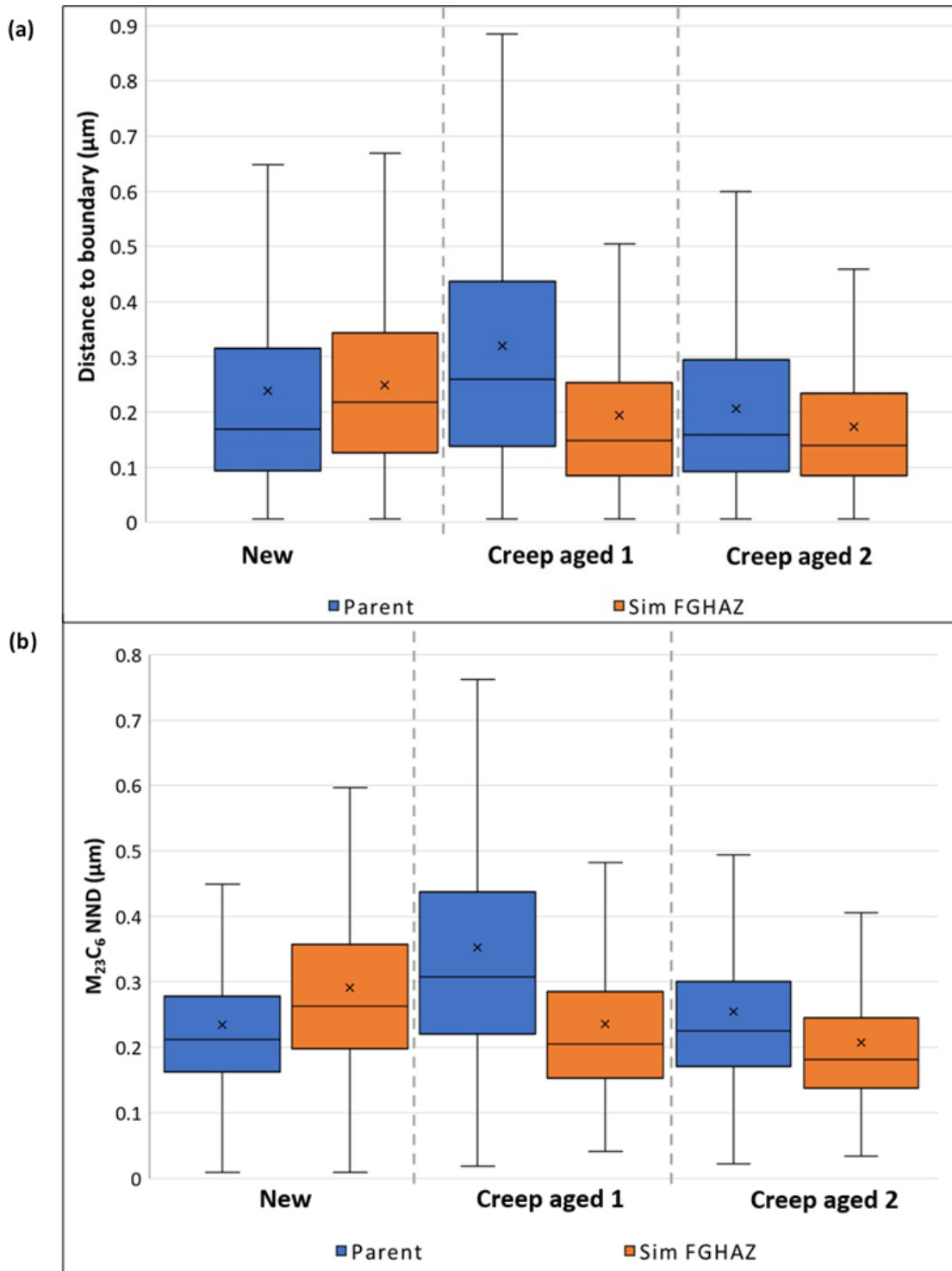


**Figure 4.38:** Box-and-whisker plots of distributions of (a) distances of interior  $M_{23}C_6$  carbides from MGB in CBS images and (b)  $M_{23}C_6$  carbide 2D NND (interparticle spacing) measured from CBS images of parent and simulated FGHAZ twin-jet electropolished specimens (total area of  $915 \mu\text{m}^2$  analysed). The “x” symbol indicates the mean.

**(ii) Number density and volume fraction**

The number density  $N_V$  of the boundary and interior  $M_{23}C_6$  carbides and their combination was calculated using Equation (3.6) and the results plotted in **Figure 4.39** and **Figure 4.40**.

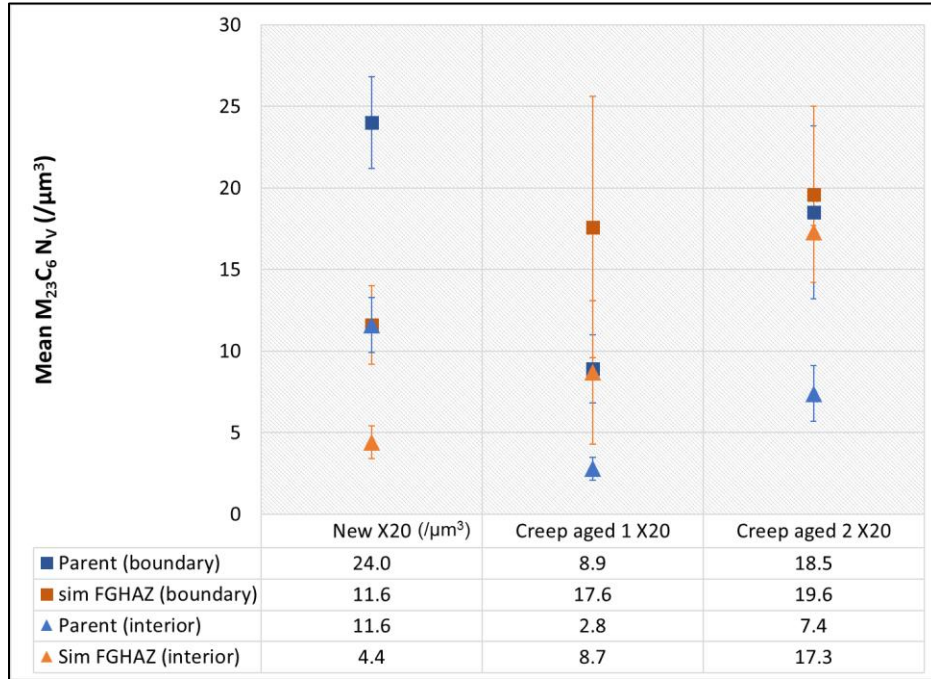


**Figure 4.39:** Mean number density  $N_V$  of boundary and interior  $M_{23}C_6$  carbides measured from CBS images of parent and simulated FGHAZ twin-jet electropolished specimens (total area of  $915 \mu\text{m}^2$  analysed). The error is given by Equation (3.17).

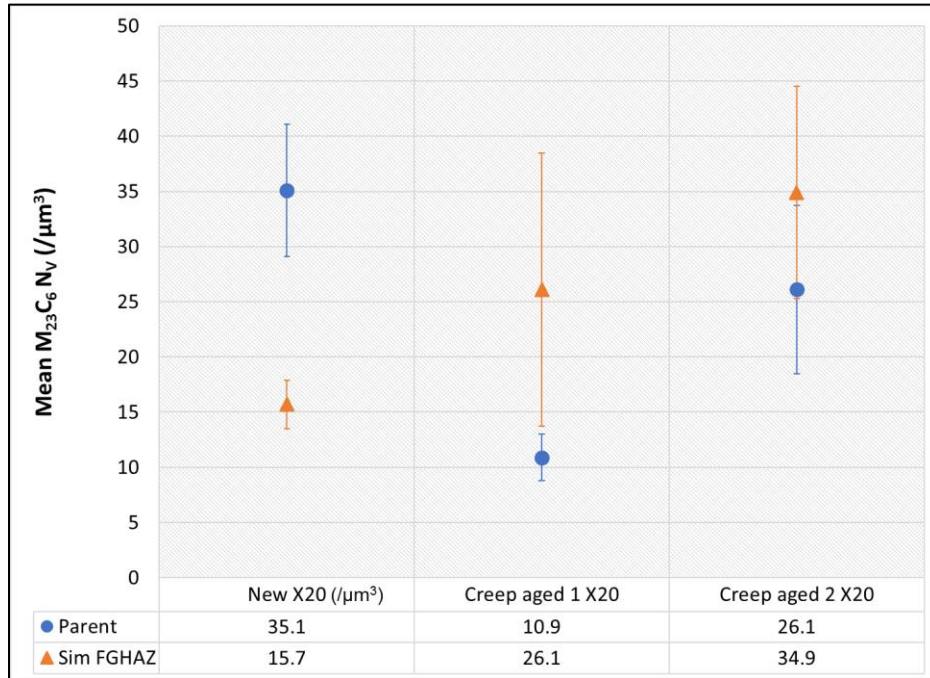


**Figure 4.40:** Mean overall number density  $N_V$  of both boundary and interior  $M_{23}C_6$  carbides measured from CBS images of parent and simulated FGHAZ twin-jet electropolished specimens (total area of  $915 \mu\text{m}^2$  analysed). The error is given by Equation (3.17).

From Chandrasekhar (1943), Underwood (1973), and Hull and Bacon (2001) it follows that for strong obstacles, such as the  $M_{23}C_6$  carbides, and flexible entities, such as dislocations, the interparticle spacing is best given by the NND. Holzer (2010) stated that it is the planar (2D) interparticle spacing  $\lambda$  (Equation (2.15)) that is important for PH. The interparticle spacing  $\lambda$  was calculated using the number density  $N_V$  and diameter  $d_s$  for each area and the mean value is plotted in **Figure 4.41**. **Figure 4.42** summarises the calculated mean volume fractions  $f_V$  of the  $M_{23}C_6$  carbides.

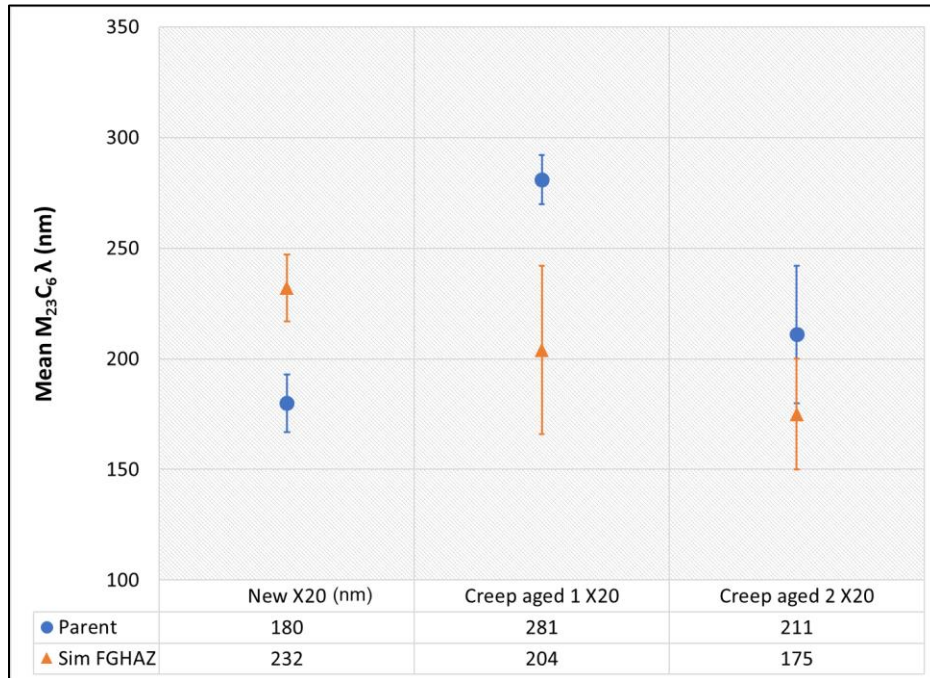


**Figure 4.41:** Mean 2D interparticle spacing  $\lambda$  of  $M_{23}C_6$  carbides measured from CBS images of parent and simulated FGHAZ twin-jet electropolished specimens (total area of  $915 \mu\text{m}^2$  analysed). The error is given by Equation (3.17).

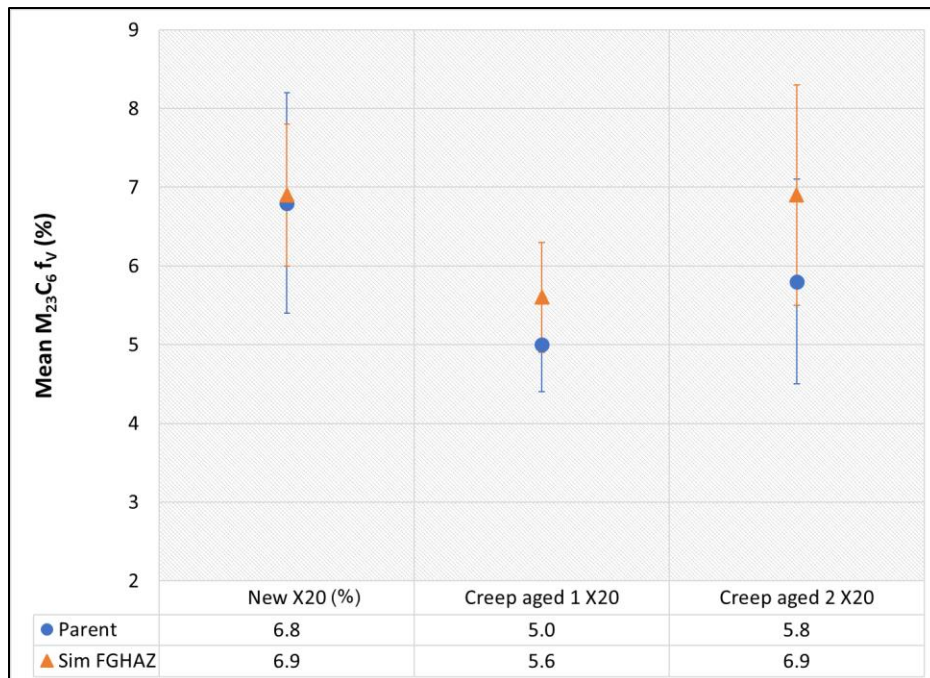


**Figure 4.42:** Mean volume fraction  $f_v$  of  $M_{23}C_6$  carbides measured from CBS images of parent and simulated FGHAZ twin-jet electropolished specimens (total area of  $915 \mu\text{m}^2$  analysed). The error is given by Equation (3.17).

### (iii) Chemical composition

The chemical composition of 50  $M_{23}C_6$  carbides was determined by performing STEM-EDS point analysis on the extraction replica specimens as described in Section 3.7.5. **Figure 4.43**, **Figure 4.44** and **Figure 4.45** summarise the mean relative amounts of Cr, Fe and Mo measured in the carbides for each material type.

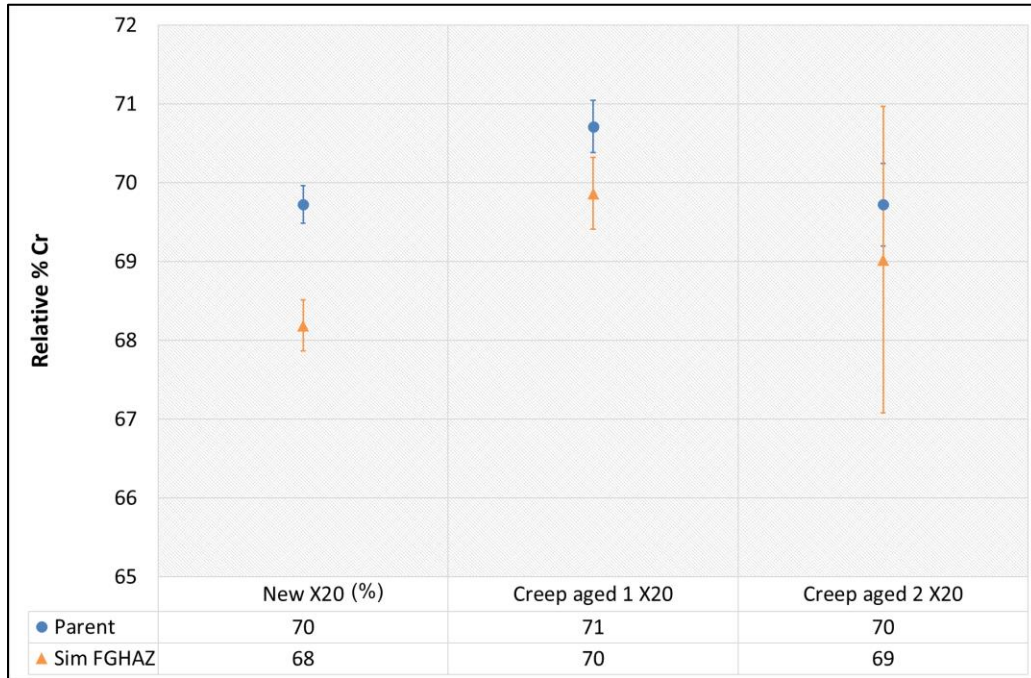


**Figure 4.43:** Relative % Cr measured in 50  $M_{23}C_6$  carbides from parent and simulated FGHAZ extraction replica specimens. The error is indicated as the 95% CI.

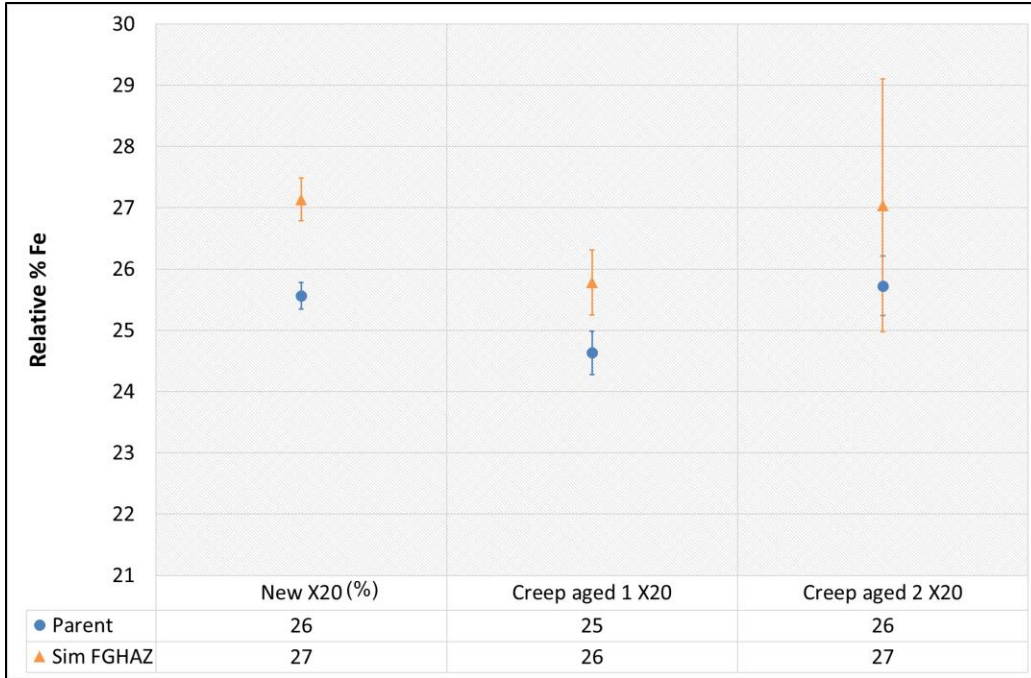


**Figure 4.44:** Relative % Fe measured in 50  $M_{23}C_6$  carbides from parent and simulated FGHAZ extraction replica specimens. The error is indicated as the 95% CI.

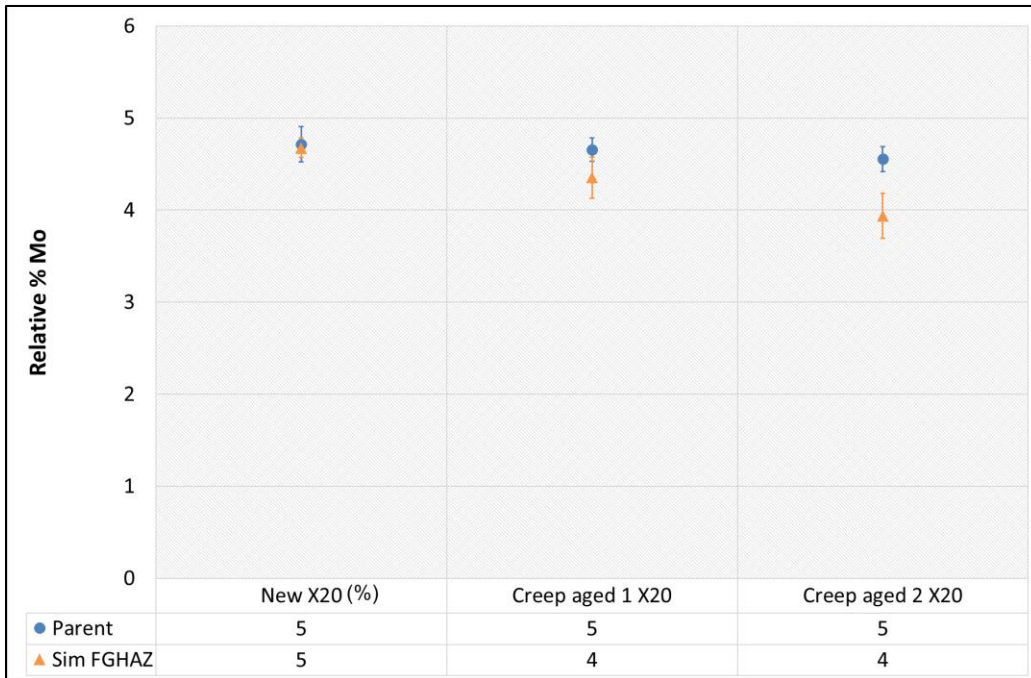


**Figure 4.45:** Relative % Mo measured in 50  $M_{23}C_6$  carbides from parent and simulated FGHAZ extraction replica specimens. The error is indicated as the 95% CI.

## 4.7.4 Quantitative Results: MX Precipitates

### (i) Size and Distribution

The measuring of the VX precipitate parameters is explained in Section 3.7.4. It is assumed that the VX precipitates are too small to be sectioned and therefore their actual size and shape are observed from the projected area in the EFTEM V elemental maps, whether the samples are thin foils or extraction replicas. Subsequently, no stereological corrections of their diameters were performed. The size distributions and mean ECD of the VX precipitates measured from the EFTEM V elemental maps is given in **Figure 4.46** and **Figure 4.47**, respectively. The distributions of the NND is plotted in **Figure 4.48** as box-and-whisker plots.

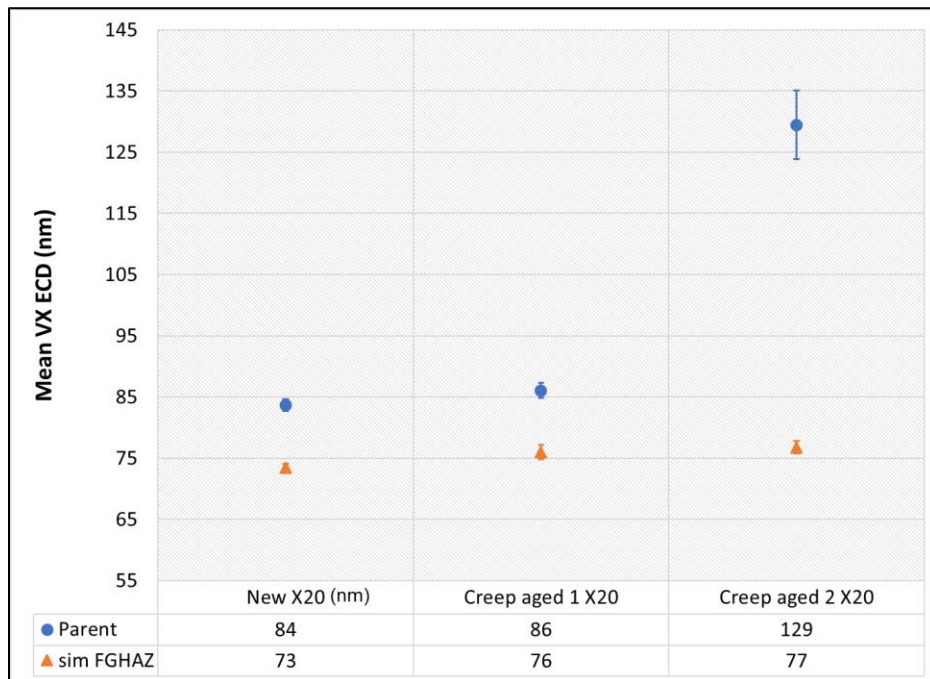


**Figure 4.46:** Mean ECD of VX precipitates measured from EFTEM V elemental maps acquired from parent and simulated FGHAZ extraction replica specimens. The error is given as 95% CI (sampling area =  $360 \mu\text{m}^2$ ).

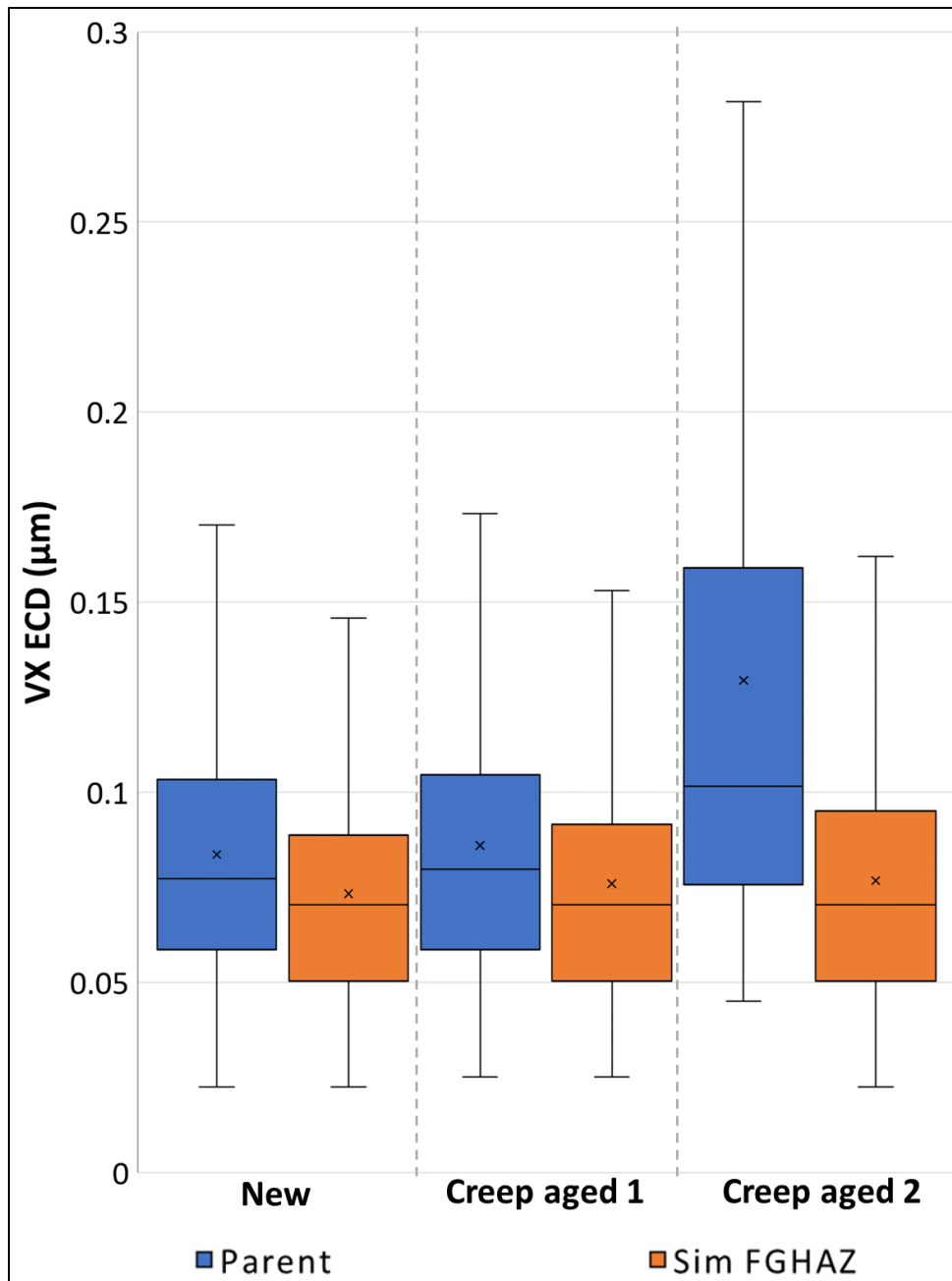


**Figure 4.47:** Box-and-whisker plots of ECD size distribution of VX precipitates measured from EFTEM V elemental maps acquired from parent and simulated FGHAZ extraction replica specimens (sampling area = 360  $\mu\text{m}^2$ ). The “x” symbol indicates the mean.



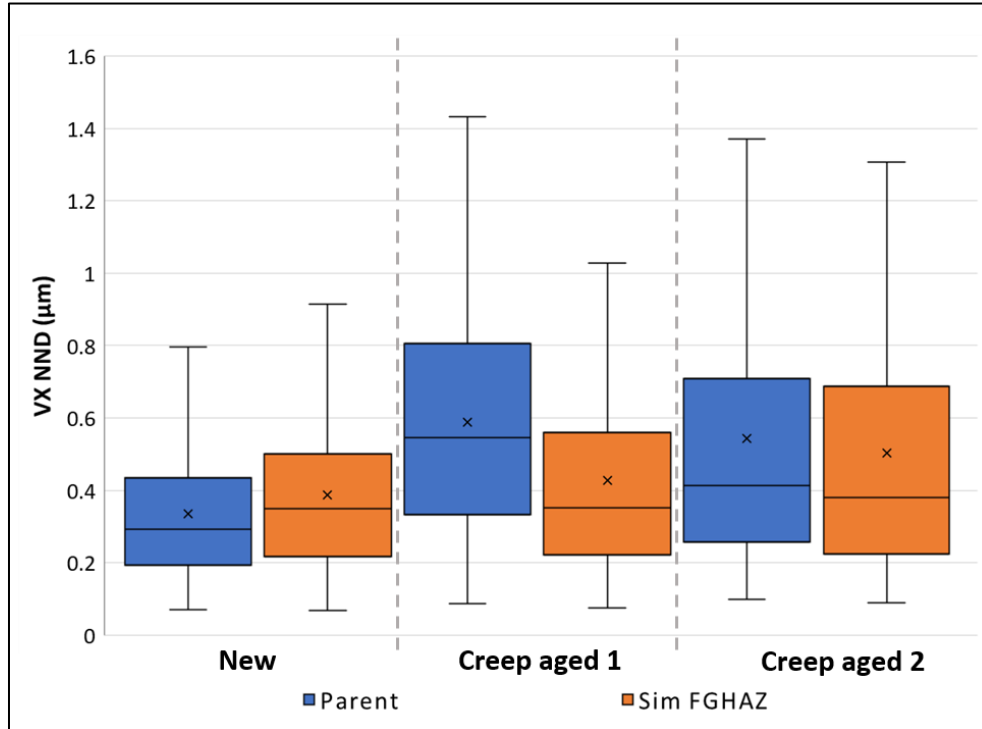


**Figure 4.48:** Box-and-whisker plots of 2D NND distributions of VX precipitates measured from EFTEM V elemental maps of parent and simulated FGHAZ twin-jet electropolished specimens (sampling area =  $576 \mu\text{m}^2$ ). The “x” symbol indicates the mean.

**(ii) Number density and volume fraction**

The mean calculated number density  $N_V$  and volume fraction  $f_V$  of the VX precipitates are plotted in **Figure 4.49** and **Figure 4.50**, respectively.

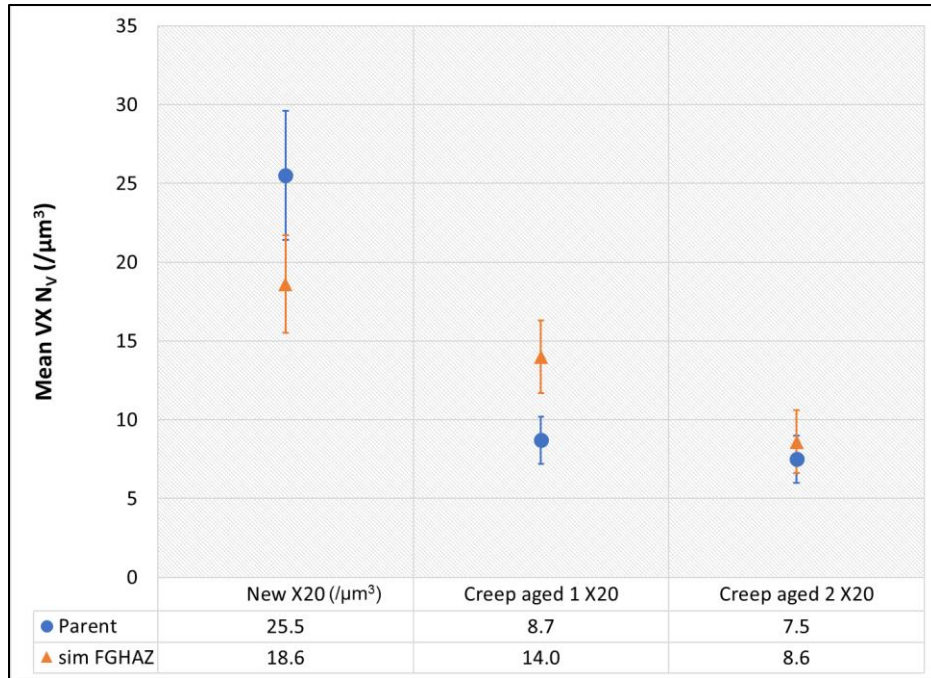


**Figure 4.49:** Mean number density of MX precipitates measured from EFTEM V elemental maps of parent and simulated FGHAZ twin-jet electropolished specimens. The error is given by Equation (3.17) (sampling area =  $576 \mu\text{m}^2$ ).

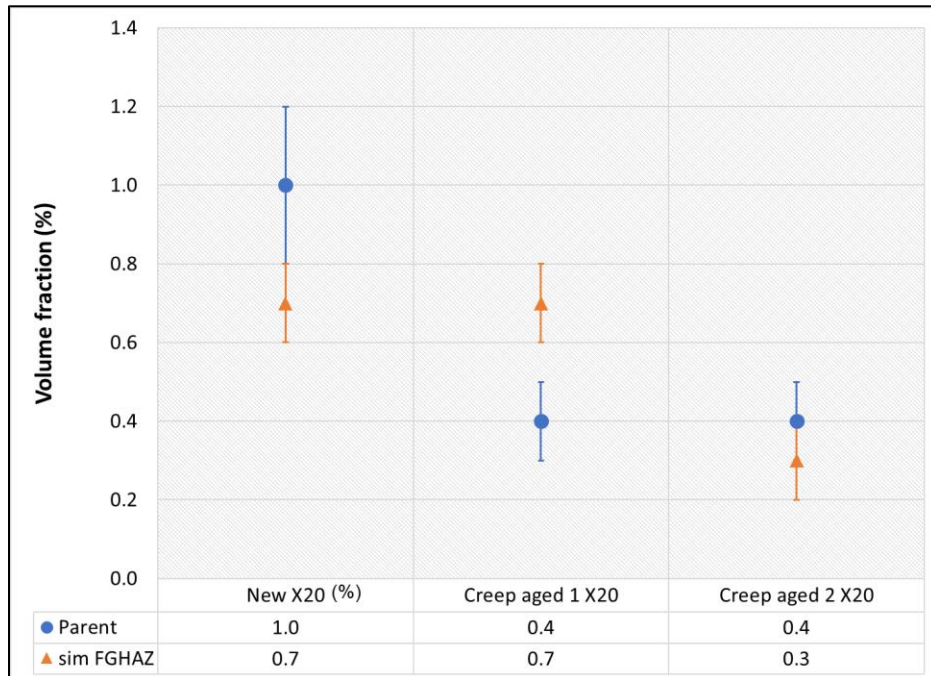


**Figure 4.50:** Mean volume fraction of VX precipitates measured from EFTEM V elemental maps of parent and simulated FGHAZ twin-jet electropolished specimens. The error is given by Equation (3.17) (sampling area =  $576 \mu\text{m}^2$ ).

The mean 2D surface-to-surface interparticle spacing  $\lambda$  was calculated using Equation (2.15) with the mean radius  $r$  taken as the extraction replica  $\frac{\text{mean ECD}}{2}$  and the number density  $N_V$  as that determined from the twin-jet electropolished specimens. **Figure 4.51** summarises these calculated  $\lambda$  values for the VX precipitates measured from the EFTEM V elemental maps.

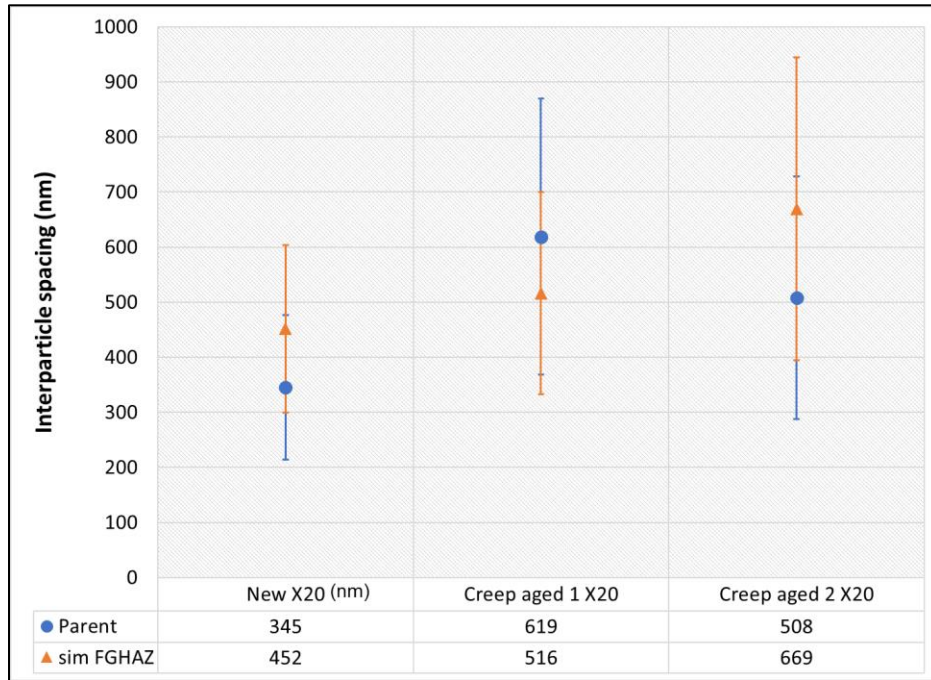


**Figure 4.51:** Mean 2D surface-to-surface interparticle spacing  $\lambda$  of VX precipitates obtained from EFTEM V elemental maps acquired from parent and simulated FGHAZ twin-jet electropolished specimens. The error is determined by combining the errors of the mean ECD and mean  $N_V$  using standard error propagation.

### (iii) Chemical composition

To investigate the chemical composition of the MX precipitates, STEM-EDS point analysis was performed on the VX precipitates in the extraction replica specimens (Section 3.7.5). A single spectrum acquired from a VX precipitate in the new simulated FGHAZ extraction replica specimen is shown in **Figure 4.52**.

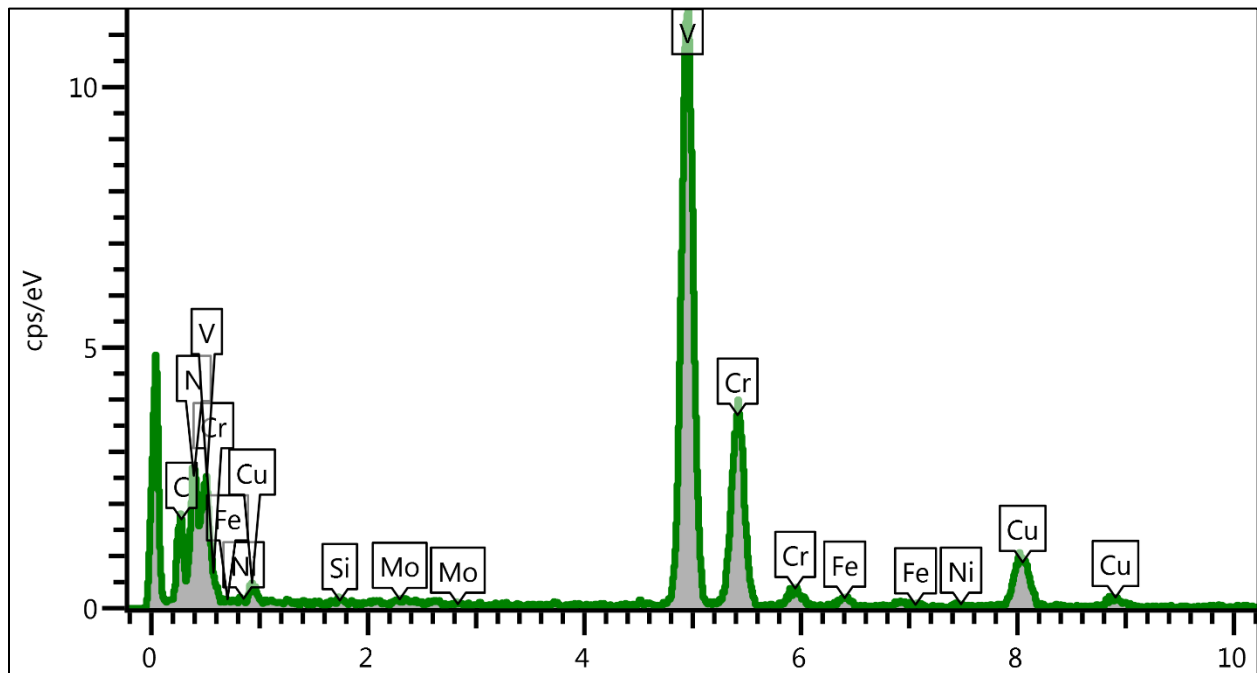


**Figure 4.52:** STEM-EDS spectrum acquired from VX precipitate in extraction replica specimen of new simulated FGHAZ material.

The copper signal detected should be ignored since it is from the copper grid used for the extraction replica specimens. As can be seen, a significant amount of Cr is found in these precipitates. This corresponds with **Table 2.4** that indicates minor content of Cr may be found in the MX precipitates. However, due to the small size and overlapping of the VX precipitates with the  $M_{23}C_6$  carbides in the extraction replica specimens, further analysis of the V:Cr ratio in the MX precipitates was not performed.

The results from the STEM-EELS SI analysis on a single area of the new parent extraction replica specimen are summarised in **Figure 4.53**. Since the STEM-EELS V and N maps overlap, it can be concluded that the VX precipitates are of the type VN.

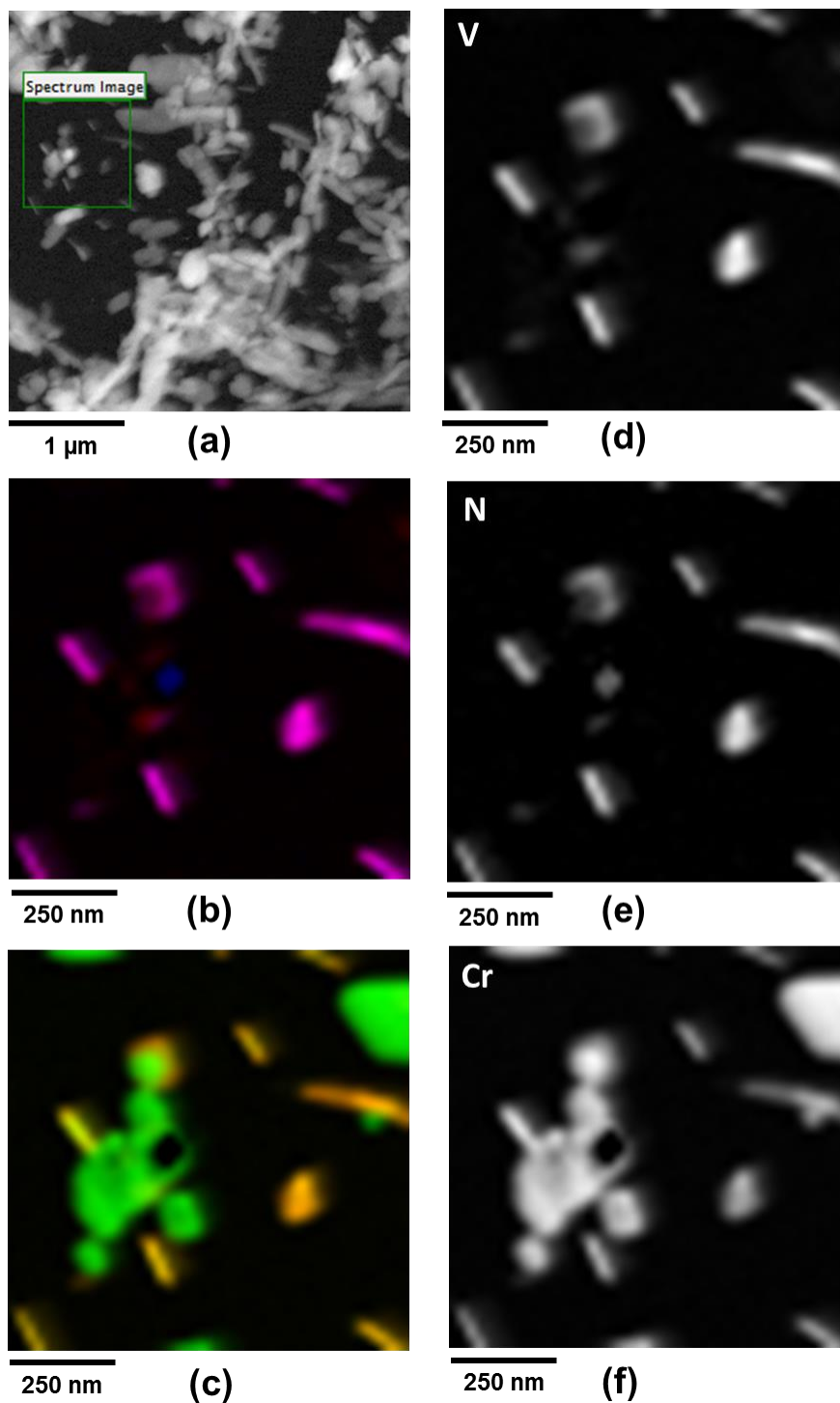


**Figure 4.53:** (a) HAADF-STEM image of an area on new parent extraction replica specimen with STEM-EELS SI analysis area outlined. STEM-EELS RGB maps of (b) V (red) and N (blue), and (c) V (red) and Cr (green). STEM-EELS elemental maps of (d) V (515.0 - 543.5 eV), (e) N (397.0 - 435.5 eV) and (f) Cr (576.5 - 605.0 eV).

## 4.7.5 Discussion

### (i) Evolution of $M_{23}C_6$ Carbide Parameters

A summary of the mean  $M_{23}C_6$  carbide parameters and their chemical composition is given in **Table 4.7**.

**Table 4.7:** Summary of mean  $M_{23}C_6$  carbide parameters and chemical composition (O = overall, B = boundary and I = interior).

		New		Creep aged 1		Creep aged 2	
		Parent	Sim FGHAZ	Parent	Sim FGHAZ	Parent	Sim FGHAZ
$d_s$ (nm)	O	152 ± 16	203 ± 10	202 ± 22	163 ± 18	164 ± 8	156 ± 10
	B	161 ± 16	214 ± 11	208 ± 28	176 ± 20	175 ± 8	176 ± 11
	I	124 ± 8	156 ± 24	160 ± 26	123 ± 11	128 ± 9	117 ± 11
$N_v$ ( $\mu\text{m}^3$ )	O	35.1 ± 6.0	15.7 ± 2.2	10.9 ± 2.1	26.1 ± 12.4	26.1 ± 7.6	34.9 ± 9.6
	B	24.0 ± 2.8	11.6 ± 2.4	8.9 ± 2.1	17.6 ± 8.0	18.5 ± 5.3	19.6 ± 5.4
	I	11.6 ± 1.7	4.4 ± 1.1	2.8 ± 0.7	8.7 ± 4.4	7.4 ± 1.7	17.3 ± 9.1
$\lambda$ (nm)	O	180 ± 13	232 ± 15	281 ± 11	204 ± 38	211 ± 31	175 ± 25
$f_v$ (%)	O	6.8 ± 1.4	6.9 ± 0.9	5.0 ± 0.6	5.6 ± 0.7	5.8 ± 1.3	6.9 ± 1.4
Cr %	O	69.72 ± 0.24	68.19 ± 0.32	70.71 ± 0.33	69.86 ± 0.46	69.72 ± 0.52	69.02 ± 1.94
Fe %	O	25.56 ± 0.22	27.14 ± 0.35	24.63 ± 0.35	25.78 ± 0.53	25.73 ± 0.49	27.04 ± 2.06
Mo %	O	4.71 ± 0.19	4.67 ± 0.11	4.66 ± 0.13	4.35 ± 0.22	4.55 ± 0.14	3.94 ± 0.25

There is coarsening of the  $M_{23}C_6$  carbides, both on the boundaries and in the interior of the micro-grains during creep (**Figure 4.34(a)**, **Figure 4.36** and **Figure 4.37**). The ECD distributions of the new and creep aged 2 parent materials are similar with mean diameters 152 ± 16 nm and 164 ± 8 nm, respectively. Creep aged 1 parent material shows the most significant coarsening with a mean diameter of 202 ± 22 nm. These mean values are within the range of carbide diameters measured by Aghajani (2009) for new and long-term creep aged X20 steel. These variations in size can also be seen qualitatively from extraction replica EFTEM RGB maps, and the thresholded TKD-EDS and CBS maps

(**Figure 4.27**, **Figure 4.29** and **Figure 4.31**). The more significant variation in the creep aged 1 parent material indicates that the size per area is not homogeneous and hence coarsening is not homogeneous. In turn, this could indicate that the chemical composition, especially the C content, is not homogeneous throughout the matrix.

Upon comparing the ECD distributions and mean diameters sizes of the simulated FGHAZ materials in **Figure 4.34(b)**, **Figure 4.36** and **Figure 4.37**, the new simulated FGHAZ has the distribution with the largest carbides with a mean of  $203 \pm 10$  nm. This size range corresponds with that of the creep aged 1 parent material. The distributions of creep aged 1 and 2 simulated FGHAZ materials have similar mean diameter values of  $163 \pm 18$  nm and  $156 \pm 10$  nm, respectively. However, upon closer examination of the creep aged 2 simulated FGHAZ distribution, there is a slight bimodality, which indicates that very large carbides are present. This bimodality is observed from the extraction replica EFTEM RGB maps, and TKD-EDS and CBS maps (**Figure 4.27**, **Figure 4.29** and **Figure 4.31**). Subsequently, the importance of drawing conclusions from the distribution of carbide sizes rather than just the mean value is highlighted.

From **Figure 4.35** it is observed that the sizes of the boundary carbides are much larger than that of the interior carbides for each material type, which is also seen in **Figure 4.27** and **Figure 4.29**. This result substantiates the conclusions from previous studies (Section 2.3.2) that short-circuit diffusion occurs along the GB. The boundary carbide diameter range overlaps with that of the combined diameter, which indicates that it is the boundary carbide size that dominates the overall carbide size measurements. Some variation is observed in the shape of the interior carbide distribution which is ascribed to artefacts from the low number of interior carbides (**Table 4.5**).

The effect of simulating the FGHAZ on the  $M_{23}C_6$  sizes is opposite for the new material compared to the creep aged materials (**Figure 4.34(c) to (e)**). The carbides coarsen from the new parent to simulated FGHAZ, while they decrease in size for the creep aged 1 and creep aged 2 materials. A more pronounced decrease in size is found for the creep 1 simulated FGHAZ material (**Figure 4.37**). The new material phenomenon corresponds to

the discussion in Section 2.4.1 which explains that accelerated coarsening of the undissolved precipitates occurs in the FGHAZ.

The differences in the shape of the carbides are observed from the extraction replica EFTEM RGB maps (**Figure 4.31**). Qualitatively, the carbides in the simulated FGHAZ materials are more equiaxed than the corresponding parent materials. Similar shapes are observed for the carbides in the new and creep aged 2 parent materials, while more equiaxed and irregular shaped carbides are observed in the creep aged 1 parent material.

As can be seen from **Figure 4.38**, the mean is larger than the median for each distribution, indicating that the distribution of the interior carbide-boundary distance and the carbide NND distributions are lognormal as expected. The same main trends of the diameter are followed for the distance between the interior carbides and the MGB (**Figure 4.38(b)**). During creep exposure, the distance between the interior carbides and MGB increase. This could suggest boundary migration and hence micro-grain coarsening (Section 2.3.3). Interior carbides within the creep aged 1 parent material are the furthest from the boundaries. For the new material, the interior carbide-boundary distance increases from parent to simulated FGHAZ, while it slightly decreases to similar distributions in the simulated FGHAZ creep aged materials. Of all the simulated FGHAZ materials, the interior carbides are the furthest away from the boundary in the new material. Due to the formation of new boundaries in the FGHAZ of a weldment (Section 2.4.1), it is expected that the interior carbide-boundary distance will decrease in the simulated FGHAZ materials.

The new parent material has a carbide number density  $N_V$  of  $35.1 \pm 6.0 \mu\text{m}^{-3}$  (**Figure 4.40**). For each material type except the creep aged 2 simulated FGHAZ, the boundary carbides have a number density of more than double of that of the interior carbides (**Figure 4.39**). In the case of the creep aged 2 simulated FGHAZ material, a high fraction of fine carbides has been observed to have nucleated in the interior of the micro-grains as can be seen from **Figure 4.29**.

There is a decrease in the number of carbides per unit volume during creep. Creep aged 1 parent material has the lowest number density of  $10.9 \pm 2.1 \mu\text{m}^{-3}$ , which is 3.5 times



smaller than that of the new material, and a mean number density of  $26.1 \pm 7.6 \mu\text{m}^{-3}$  was measured for the creep aged 2 parent material. For the simulated FGHAZ materials, the lowest number density of carbides is found in the new material ( $15.7 \pm 2.2 \mu\text{m}^{-3}$ ). The creep aged 1 and 2 simulated FGHAZ materials have number densities of  $26.1 \pm 12.4 \mu\text{m}^{-3}$  and  $34.9 \pm 9.6 \mu\text{m}^{-3}$ , respectively. These materials have the most substantial variation in the number density, which indicates the heterogeneous distribution of the carbides. Upon simulation of the FGHAZ, there is a large decrease in the number density in the new simulated FGHAZ material, and an increase in both creep aged simulated FGHAZ materials. The most significant increase is seen in the creep aged 1 material. There is a significant variance in the simulated FGHAZ damaged material number densities, which indicates the inhomogeneous distribution of the carbides in these materials. The same number densities are measured for the creep aged 1 simulated FGHAZ and creep aged 2 parent material.

The  $\text{M}_{23}\text{C}_6$  carbide NND distributions (**Figure 4.38(b)**) and the mean calculated interparticle spacing  $\lambda$  (**Figure 4.41**) follow the same trends. An increase in the interparticle spacing is observed during creep aging, which is explained by the increased diameter and decreased number density of the carbides. Creep aged 1 parent material has the largest increase in interparticle spacing from  $180 \pm 13$  nm in the new parent material to  $281 \pm 11$  nm. The interparticle spacing of the creep aged 2 parent material is only increased to  $211 \pm 31$  nm. Interparticle spacings of  $232 \pm 15$  nm,  $204 \pm 38$  nm and  $175 \pm 25$  nm is calculated for the new, creep aged 1 and creep aged 2 simulated FGHAZ materials. It is only the spacing of the creep aged 2 simulated FGHAZ materials that statistically significantly differ from the new simulated FGHAZ material. Since the interparticle spacing is dependent on the carbide size and number density, the same opposing trends for the parent compared to the simulated FGHAZ materials are observed. The interparticle carbide spacing is increased in the new material and decreased in creep aged materials after simulation of the FGHAZ. In the case of the creep aged 2 simulated FGHAZ material, the decrease is insignificant.

The mean measured  $\text{M}_{23}\text{C}_6$  carbide volume fractions  $f_v$  range from 5.0% to 6.9% across the different materials (**Figure 4.42**). Only the mean value of the creep aged 1 parent

material was statistically significantly lower than the mean of the new parent material. The mean volume fraction of the other materials did not significantly differ from that of the new parent material. Thus, there is no significant change in the volume fractions of the carbides during FGHAZ simulation. Aghajani (2009) found that for X20 steel the  $M_{23}C_6$  carbide projected area fraction measured from STEM images remains constant close to 9% during long-term creep. This contradicts the result from the creep aged 1 parent material whose volume fraction decreased slightly from the new parent material. The discrepancy is either due to the fact that the value reported by Aghajani (2009) was not stereologically corrected or the initial X20 materials have slightly different chemical compositions.

These contrasting effects of FGHAZ simulation on the parent materials can be explained by Ostwald ripening (Voorhees 1985). Consider **Figure 4.31**. There is no substantial variation in the carbide size in the new parent material. Heating to just above  $A_{C3}$  as in the FGHAZ during welding, all these carbides will dissolve to a similar extent. Upon cooling and subsequent PWHT new carbides nucleate, but they shrink, and some disappear due to the presence of the undissolved carbides that coarsen by Ostwald ripening. Also, the coarsening of the carbides is accelerated in the FGHAZ (Section 2.4.1) and therefore they have large final sizes. The decreased number density suggests that some of the pre-existing carbides dissolved completely.

In the case of the creep aged parent materials, short-circuit diffusion during creep exposure resulted in the boundary carbides to be much larger than those in the interior. Now during welding, these heterogeneously sized carbides, which is larger than that in the new parent material, dissolve and the undissolved carbides are also heterogeneous in size. Upon cooling and subsequent PWHT, again new carbides will nucleate, but now both the new carbides and small undissolved carbides will shrink since the larger undissolved carbides will coarsen by Ostwald ripening. Since there are much more smaller carbides that can shrink than in the new material, less of them will disappear than in the new material, and the result is large carbides and a larger number of smaller carbides. This explains the increase in number density. Subsequently, the large fraction of smaller carbides shifts the overall distribution of sizes to smaller values in the simulated

FGHAZ material compared to that of the parent material. The large carbides are then accounted for by the right-skewed distribution.

The boundary and interior carbide data are mainly limited by the quality of the thresholding of the MGB from the CBS image.

## (ii) Evolution of MX (VX) Precipitate Parameters

A summary of the mean  $M_{23}C_6$  carbide parameters and their chemical composition is given in **Table 4.8**.

**Table 4.8:** Summary of mean measured MX precipitate parameters.

	New		Creep aged 1		Creep aged 2	
	Parent	Sim FGHAZ	Parent	Sim FGHAZ	Parent	Sim FGHAZ
<b>d (nm)</b>	84 ± 1	73 ± 1	86 ± 1	76 ± 1	129 ± 6	77 ± 1
<b>N<sub>v</sub> (/μm<sup>3</sup>)</b>	25.5 ± 4.1	18.6 ± 3.1	8.7 ± 1.5	14.0 ± 2.3	7.5 ± 1.5	8.6 ± 2.0
<b>λ (nm)</b>	345 ± 132	452 ± 152	619 ± 251	516 ± 184	508 ± 220	669 ± 275
<b>f<sub>v</sub> (%)</b>	1.0 ± 0.2	0.7 ± 0.1	0.4 ± 0.1	0.7 ± 0.1	0.4 ± 0.1	0.3 ± 0.1

As expected, the VX precipitates are much smaller than the  $M_{23}C_6$  carbides. The VX precipitate ECD distributions (**Figure 4.47**) in the new and creep aged 1 material have mean values of 84 ± 1 nm and 86 ± 1 nm that statistically significantly differ (**Figure 4.46**). This corresponds to the previous studies discussed in Section 2.3.2 that show the VX precipitates do not significantly coarsen during creep aging in 9-12% Cr martensitic steels. The measured VX sizes fall within the range of 70 ± 30 nm measured by Aghajani (2009) for both new and long-term creep aged X20 steel. A distribution of much larger ECD values with a mean of 129 ± 6 nm is measured for the creep aged 2 parent material. From Section 4.7.2 it follows that Z-phase particles may have extensively formed in the creep aged 2 parent material. Since it is not possible to distinguish between them and VX in the EFTEM V elemental maps, they have been included in the VX measurements for the creep aged 2 parent material. This accounts for the much larger size measured for

the VX in this material. It should be noted that in the case of the creep aged simulated FGHAZ materials, any nucleated Z-phase precipitates would dissolve during welding since the dissolution temperature of Z-phase precipitates in X20 are approximately 800 °C (Danielsen 2007). Therefore, the measured VX parameters of the simulated FGHAZ materials are not affected by the inclusion of Z-phase precipitates.

The VX precipitate ECD distributions are measured for the simulated FGHAZ materials with mean values of  $73 \pm 1$  nm,  $76 \pm 1$  nm and  $77 \pm 1$  nm for the new, creep aged 1 and creep aged 2 materials, respectively. The mean sizes of the creep aged simulated FGHAZ are statistically significantly larger than the mean sizes measured for the new simulated FGHAZ material. The effect of the FGHAZ simulation is decreasing the VX precipitate size of the corresponding parent material.

From the extraction replica EFTEM RGB maps (**Figure 4.31**), a distinct difference in the shape of the VX precipitates is observed. In the new parent material, they have elongated plate-like shapes that become more equiaxed during creep ageing and FGHAZ simulation.

The mean measured VX precipitate volume fractions  $f_v$  range from 0.3% to 1.0% across the different materials (**Figure 4.50**). Both the creep aged parent materials and the simulated FGHAZ materials have mean  $f_v$  values that are significantly lower than the mean value of the parent material. Therefore, the volume fraction decreases during creep exposure and FGHAZ simulation.

The number density of the VX precipitates is lower than that of the  $M_{23}C_6$  carbides, which has also been shown by Aghajani (2009) for X20 steel. The number density  $N_v$  decreases significantly from  $25.5 \pm 4.1 \mu\text{m}^{-3}$  in the new parent material to values of  $8.7 \pm 1.5 \mu\text{m}^{-3}$  and  $7.5 \pm 1.5 \mu\text{m}^{-3}$  for the creep aged 1 and creep aged 2 parent materials, individually (**Figure 4.49**). If the Z-phase particles were to be excluded from the creep aged 2 parent material VX analysis, the number density would be even lower. The decrease in both  $N_v$  and  $f_v$  indicate dissolution of the VX precipitates during creep exposure.

The  $N_V$  and  $f_V$  trends do not correspond to the study of Aghajani (2009) that showed there is no significant change in number density  $N_V$  of VX precipitates during long-term creep exposure of X20 steel and the VX precipitate projected area fraction measured from STEM images remains constant close to 0.5%. Possible explanations for the differences are:

- (i) Aghajani (Aghajani 2009) did not identify any Z-phase precipitates in the creep aged X20 materials and therefore there was no dissolution of the VX precipitates due to Z-phase precipitation (Section 2.3.2).
- (ii) The number density was measured from EFTEM maps acquired from twin-jet electropolished specimens and as mentioned in Section 4.6.2 smaller VX precipitates embedded in the iron matrix may not give rise to sufficient signal-to-noise ratios. Therefore, these small precipitates can go undetected, especially if the sample area is thicker. This will cause a decrease in the measured number density.

Among the simulated FGHAZ materials, the new material has the highest VX precipitate number density of  $18.6 \pm 3.1 \mu\text{m}^{-3}$ , the creep aged 1 material has a lower density of  $14.0 \pm 2.3 \mu\text{m}^{-3}$  and the creep aged 2 material has the lowest density of  $8.6 \pm 2.0 \mu\text{m}^{-3}$ . The effect of FGHAZ simulation is to decrease the number density of VX precipitates in the new simulated FGHAZ material and increase the number density in the creep aged simulated FGHAZ materials.

Even though there are significant variations in the interparticle spacing  $\lambda$  of the VX precipitates, the means of the creep aged simulated FGHAZ materials are statistically significantly larger than the mean of the new simulated FGHAZ material (**Figure 4.51**). Also, the spacing increases from the new and creep aged 2 parent materials to the corresponding simulated FGHAZ materials but decreases from the creep aged 1 parent to the simulated FGHAZ material. It can also be concluded that the VX precipitates are much further spaced than the  $M_{23}C_6$  carbides with mean interparticle spacings ranging from 345 to 669 nm. Trends can be observed by considering the NND distributions in **Figure 4.48**. Since the mean is larger than the median for each distribution, it can be

concluded that the VX precipitates are not homogeneously distributed. The VX precipitates in both the creep aged parent materials are more sparsely spaced than in the new parent material. New and creep aged 1 simulated FGHAZ material have similar NND distributions, and the VX precipitates are the most widely spaced in the creep aged 2 simulated FGHAZ material. The VX precipitates are more spread out by FGHAZ simulation on the new parent material, and they are more closely spaced by FGHAZ simulation on the creep aged 1 parent material. There seems to be no effect of FGHAZ simulation on the NND spacing of the VX precipitates in the creep aged 2 material.

The evolution of the VX precipitates during FGHAZ simulation can be similarly explained with Ostwald ripening as for the  $M_{23}C_6$  carbides evolution observed for the new material FGHAZ simulation. The VX precipitates in the parent material have no considerable variation in their sizes. The MX precipitates in 9-12% Cr martensitic steels have been reported by Kozeschnik, Sonderegger, Holzer, Rajek and Cerjak (2007), Shrestha, Alsagabi, Charit, Potirniche and Glazoff (2015), and Yan, Liu, Wang, Liu, Si *et al.* (2017) to start dissolving at temperatures above 850 °C and completely dissolve at approximately 1200 °C. Due to their small sizes, it is assumed that they will completely dissolve during welding. Therefore, upon cooling and subsequent PWHT entirely new precipitates nucleate and grow by Ostwald ripening. The smaller sizes in VX precipitates after welding and PWHT was also observed by Mayr, Holzer and Cerjak (2011).

### (iii) Evolution of chemical composition

The evolution of the Cr, Fe and Mo content in the  $M_{23}C_6$  carbides is seen in **Figure 4.43**, **Figure 4.44** and **Figure 4.45**, respectively. The mean measured Cr, Fe and Mo content for the  $M_{23}C_6$  carbides in each material is summarised in **Table 4.7**. A Cr content of  $70 \pm 1$  % and Fe content of  $26 \pm 1$  % is measured for the carbides in the new and creep aged 2 parent materials. In the case of the creep aged 1 parent material, the Cr content significantly increases to  $71 \pm 1$  % and the Fe content significantly decreases to  $25 \pm 1$ %. No distinct variation is observed in the Mo content of the  $M_{23}C_6$  carbides of the new and creep aged parent materials.

Aghajani (2009) also found the same trend of Cr content increasing and the Fe content correspondingly decreasing in the  $M_{23}C_6$  carbides during long-term creep exposure of X20 steel. They found the relative Cr and Fe content to range from 55 - 59% and 36 - 40% in the new parent material to 69 - 73% and 22 - 25% after 140 000 h creep exposure. Their measured Mo content increased during creep exposure from 3.6% to 4.4%. Even though the content measured in this study corresponds with these values, the trends observed in this study is not as strong. The results of Aghajani (2009) were acquired from TEM thin foil specimens and not extraction replicas as in this study. Consequently, their contents measured may be overestimated due to the presence of the iron matrix. The main difference also follows from the starting X20 steels may have different chemical compositions.

The relative Cr, Fe and Mo content of the  $M_{23}C_6$  carbides in the simulated FGHAZ materials were measured as: [68 ± 1 %; 27 ± 1 %; 5 ± 1 %] for the new material, [70 ± 1 %; 26 ± 1 %; 4 ± 1 %] for the creep aged 1 material, and [69 ± 2 %; 27 ± 2 %; 4 ± 1 %] for the creep aged 2 material. Both the creep aged simulated FGHAZ materials have statistically significant higher Cr and lower Mo content than the new simulated FGHAZ material. A significantly lower Fe content is only measured for the carbides in the creep aged 1 simulated FGHAZ material. The carbides in the creep aged 1 simulated FGHAZ material has the highest Cr and lowest Fe content of the simulated FGHAZ materials.

After FGHAZ simulation, the Cr content significantly decreases, and the Fe content significantly increases in the  $M_{23}C_6$  carbides of all three the simulated FGHAZ materials. The increase in Fe content is expected since it is kinetically favourable for the newly formed carbides after FGHAZ simulation to have similar chemistry as the matrix. In the case of the Mo content, the FGHAZ simulation results in a decrease of Mo content in the creep aged simulated materials and has no significant effect on the Mo content of the carbides in the new simulated FGHAZ material.

#### **(iv) Zener pressure**

It is possible to approximate the Zener pinning pressure  $P_Z$  exerted by the boundary  $M_{23}C_6$  carbides on the GB using Equation (2.5). The advantage is that there is no need

to approximate the interacting carbide number density  $N_{interact}$  since the value of the boundary carbide density in **Figure 4.39** can be used. Also, the diameter of the boundary carbides (**Figure 4.36**) can be directly used instead of the overall mean diameter. As mentioned in Section 2.3.2 the precipitate-boundary interface can be both coherent/ semi-coherent or incoherent and that the boundary energy  $\gamma$  is also dependent on the MO of the boundary. It is assumed that most of the precipitate-boundary interfaces are incoherent. Hence, the Zener pinning pressure of the  $M_{23}C_6$  carbides was estimated for each CBS image with  $\gamma = 10^0 \text{ J/m}^2$  and the mean boundary carbide number density and diameter. For coherent/semi-coherent interfaces, this value would only be an order of magnitude smaller. The mean Zener pinning pressure across all areas of each material type is plotted in **Figure 4.54** with the error determined from Equation (3.17).

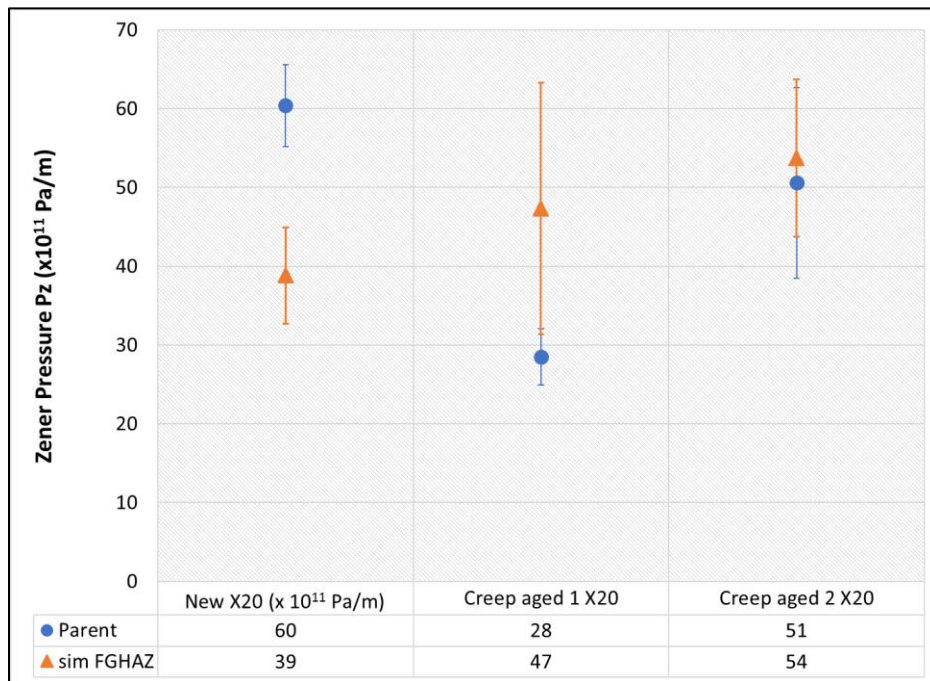


**Figure 4.54:** Mean approximate Zener pinning pressure exerted by boundary  $M_{23}C_6$  carbides calculated from CBS images of parent and simulated FGHAZ twin-jet electropolished specimens. The error is given by Equation (3.17).

The new parent material has a Zener pinning pressure of  $(60 \pm 5) \times 10^{11} \text{ Pa/m}$ . As expected, the Zener pinning pressure decreases significantly during creep. The creep aged 1 parent material boundary carbides exerts less than half the pinning pressure of



the new material with a pressure of  $(28 \pm 4) \times 10^{11}$  Pa/m, while those in the creep aged 2 material still exert a substantial pinning pressure of  $(51 \pm 12) \times 10^{11}$  Pa/m. This is due to coarsening and decrease in the number density of these carbides leading to them being less effective to pin the boundaries and the boundaries can cut or bypass the carbides.

For the simulated FGHAZ materials the approximate Zener pinning pressure was calculated as  $(39 \pm 6) \times 10^{11}$  Pa/m for the new material,  $(47 \pm 16) \times 10^{11}$  Pa/m for the creep aged 1 material and  $(54 \pm 10) \times 10^{11}$  Pa/m for the creep aged 2 material. Only the mean Zener pinning pressure of the creep aged 2 simulated FGHAZ is statistically significantly higher than the new simulated FGHAZ material.

After FGHAZ simulation, the Zener pinning pressure of the carbides in the new simulated FGHAZ material has almost halved. This follows from the fact that the mean size of the carbides is the largest and the number density the lowest in this material compared to the creep aged simulated FGHAZ materials. The increase in Zener pinning pressure of the carbides in the creep aged simulated FGHAZ materials after the FGHAZ simulation is statistically insignificant.

The approximated Zenner pinning pressure values are overall unrealistically high. This could be due to the following assumptions initially made by Smith (1948):

- (i) The particles are spherical.
- (ii) The particle-boundary interaction does not alter the passage of the boundary.
- (iii) Regardless of the contact position, each particle exerts the maximum pinning force on the boundary.
- (iv) Completely random contacts exist between the particles and boundaries.
- (v) The number density of the boundary particles is that expected for a random distribution of particles.

From **Figure 4.31** it is seen that the  $M_{23}C_6$  carbides are not spherical, and they are not distributed randomly, as discussed in Section (ii). Subsequently, an accurate assessment of the pinning force of precipitates is difficult and is dependent on the arrangement of the particles and grains/ subgrains.

## 4.8 OTHER SECONDARY PHASES

### 4.8.1 Laves Phase Analysis

Laves phase precipitates ((Fe,Cr)<sub>2</sub>Mo type) are easily visible as bright features in CBS images due to the higher atomic contrast of Mo compared to V, Cr or Fe (Section 3.6.4). However, upon inspection of the CBS images acquired, covering a total area of 3 664 μm<sup>2</sup> (4 x 916 μm<sup>2</sup>), for the M<sub>23</sub>C<sub>6</sub> carbide analyses no Laves phase precipitates could be found in the new parent material areas, which is expected as discussed in Section 2.3.2, and in the new simulated FGHAZ areas. **Figure 4.55** shows the only Mo-enriched Laves phase precipitates observed in the creep aged parent and simulated FGHAZ material CBS datasets. Most of these precipitates are observed adjacent to M<sub>23</sub>C<sub>6</sub> boundary carbides, which corresponds to the proposed Laves formation mechanism of previous studies (Section 2.3.2).

The number density and area fraction of Laves phase precipitates increase with increasing creep aging (Section 2.3.2). The Mo-enriched Laves phase precipitates seen in **Figure 4.55**(b) and (d) are not completely formed since no well-defined boundaries are visible between them and the adjacent carbides. A large fully formed Mo-enriched Laves phase precipitate is observed on the MGB in the creep aged 1 parent material (**Figure 4.55**(a)), while a small round Mo-enriched Laves phase precipitate is observed within a micro-grain on an SGB in the creep aged 2 parent material (**Figure 4.55**(e)). The latter is rarely observed as stated by Aghajani (2009).

For the creep aged simulated FGHAZ materials (**Figure 4.55**(c) and (e)) very small Laves phase precipitates or nuclei are observed as Mo-enriched regions on top of M<sub>23</sub>C<sub>6</sub> carbides. This could be due to the dissolution of previously formed Laves phase precipitates in the parent material or indicate the formation of new Laves phase nuclei.

The Laves phase precipitate composition consists of mainly Fe and Mo with a minor content of Cr and Si (**Table 2.4**). As discussed in Section 2.3.2, for their nucleation and growth, there must be Mo, Si and P segregation and hence enrichment around the involved carbide. Consequently, the TKD-EDS data acquired was also used for Laves phase analysis by overlapping the Mo, Cr, Si and P elemental maps. It was not possible to identify any Laves phase precipitates using this approach.

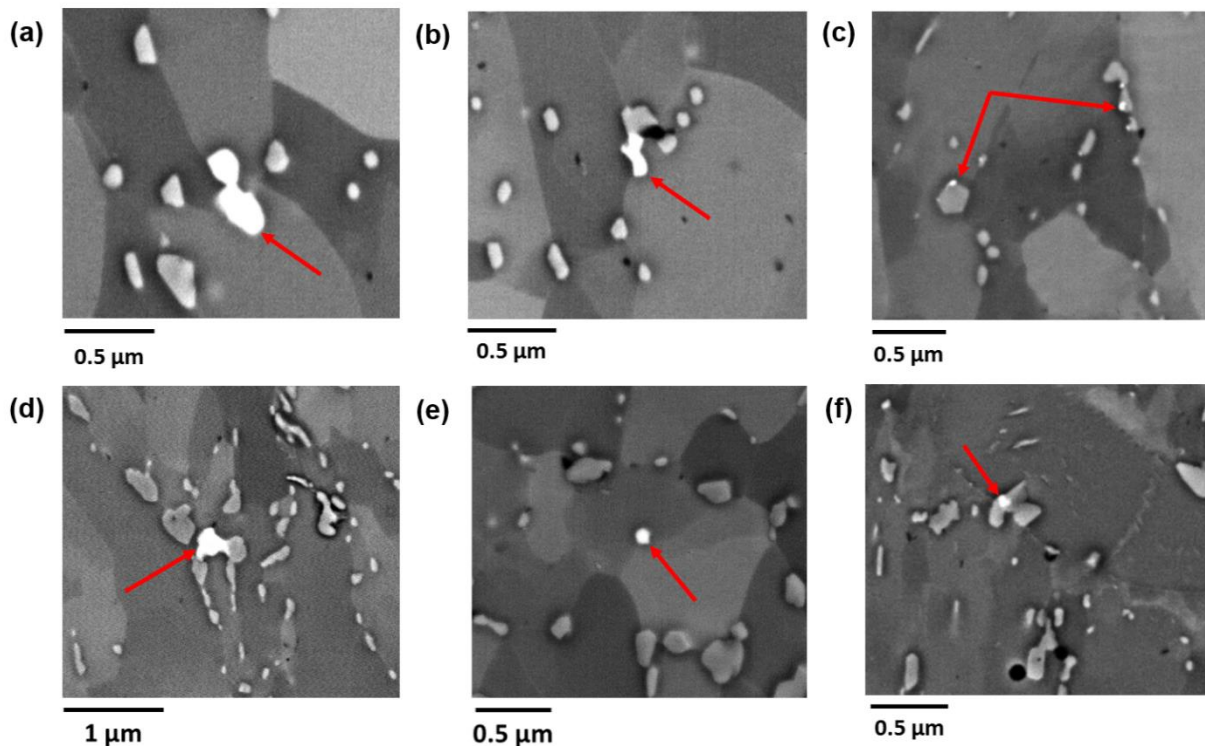


**Figure 4.55:** CBS images of Mo-enriched Laves phase precipitates observed in the various materials. Arrows highlight the Laves phase precipitates (bright) in: (a), (b) creep aged 1 parent and (c) simulated FGHAZ, (d) and (e) creep aged 2 parent and (f) simulated FGHAZ twin-jet electropolished specimens.

Due to the low numbers of observed Mo-enriched Laves phase precipitates, no valuable quantitative analysis could be performed. Two main reasons can be given for the little to no microscopic evidence of Laves phase precipitates in the analysed X20 materials:

- (i) It is difficult to distinguish small Laves phase precipitates from small boundary carbides using conventional CBS atomic contrast and as with the small MX

precipitates, these small Laves phase precipitates are too small to resolve with TKD-EDS.

- (ii) The concentrations of Si and P may be too low in the bulk material and therefore local Si and P enrichment is limited.

#### 4.8.2 Z-phase Analysis

Upon initial analysis of the CBS images, the large square (tetragonal) shaped precipitates in the creep aged materials (**Figure 4.28** and **Figure 4.29**) were thought to be Z-phase (CrVN) precipitates. These findings were further investigated by analysis of the EFTEM RGB composite maps of Cr and V (**Figure 4.30**) of the corresponding areas. No evidence for the presence of V was found in these large tetragonal shaped precipitates, indicating that these precipitates are  $M_{23}C_6$  carbides. To illustrate this conclusion the CBS image and EFTEM RGB composite map of the same area in the creep aged 1 simulated FGHAZ specimen are shown in **Figure 4.56**.

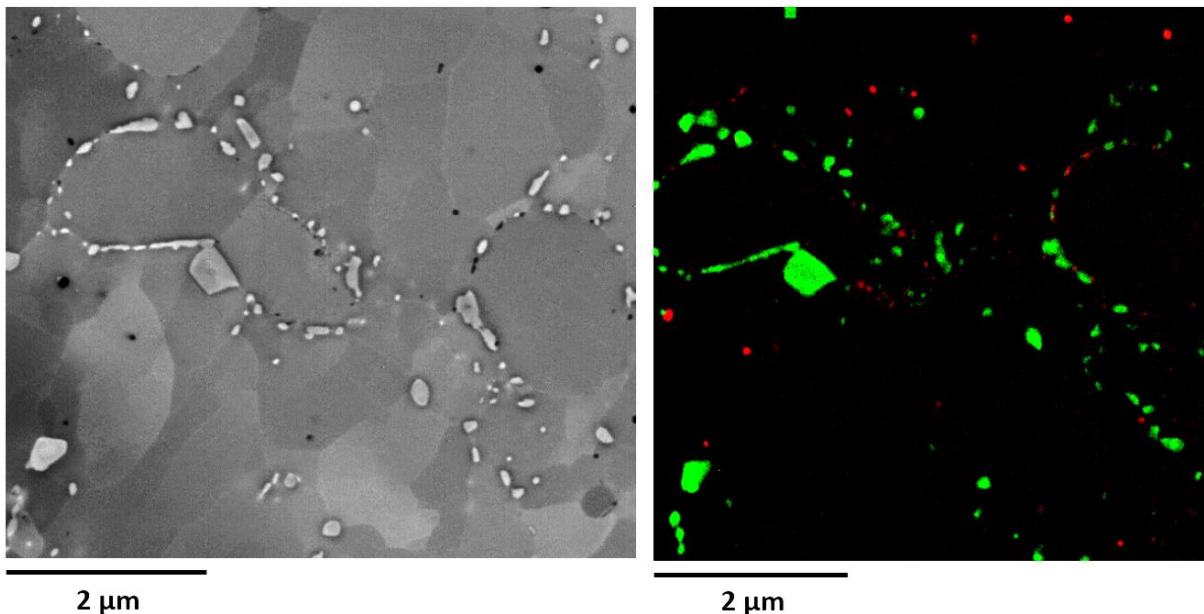


**Figure 4.56:** CBS image (left) and EFTEM RGB composite (right) of Cr (green) and V (red) elemental maps of the same area in creep aged 1 simulated FGHAZ twin-jet electropolished specimen.

Upon further analysis of the EFTEM RGB composite maps acquired from both the twin-jet electropolished and extraction replica specimens, precipitates were identified that are enriched with both Cr and V in the creep aged 2 parent material. These precipitates are shown in **Figure 4.57**(d) to (e), and **Figure 4.58**. Each of these precipitates is embedded in a Cr-enriched  $M_{23}C_6$  carbide(s). Even though the Z-phase nucleation process is not exactly known, previous studies have shown that the nucleation process is associated with Cr diffusion into V-enriched MX precipitates (Section 2.3.2). Thus, the observed precipitates are of the Z-phase (CrVN) type. V-enriched MX precipitates were also observed adjacent or in-between Cr-enriched  $M_{23}C_6$  carbides. Some of these precipitates are shown in **Figure 4.57**(b), (c), (e) and (f). These were the only type observed in the creep aged 1 parent material. Since there is no overlap, no diffusion has taken place, but it could be concluded that these regions are favoured to form Z-phase precipitates upon further creep aging.

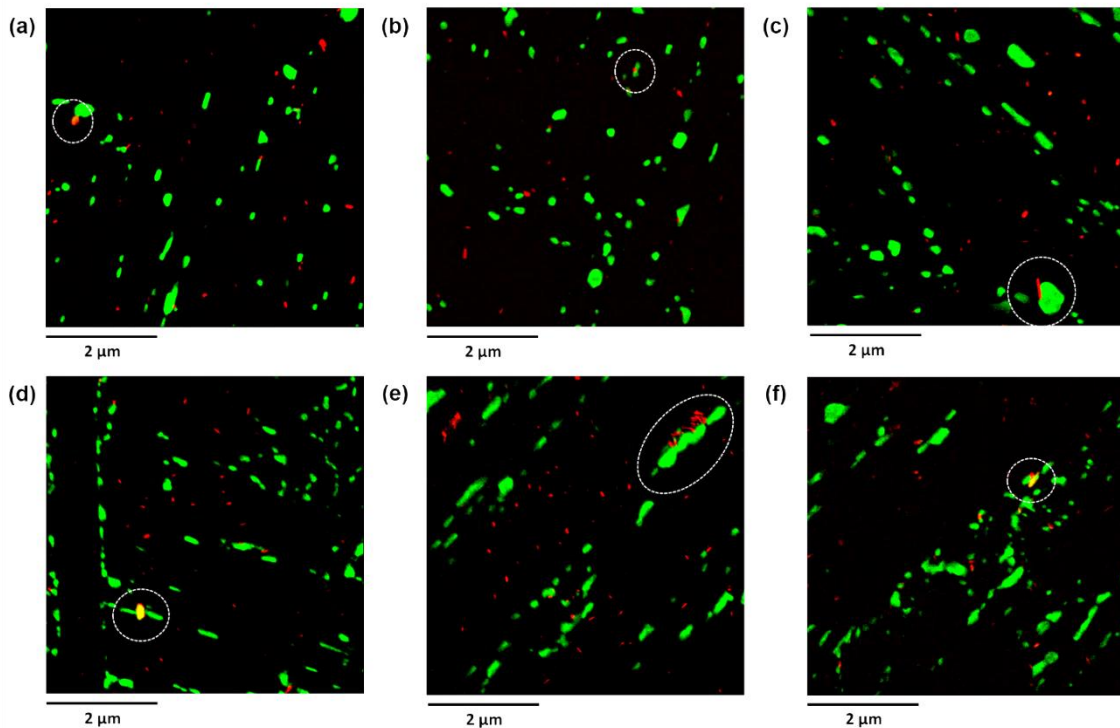


**Figure 4.57:**  $6 \times 6 \mu\text{m}^2$  EFTEM RGB composite of Cr (green) and V (red) maps of areas from the (a), (b), (c) creep aged 1 and (d), (e), (f) creep aged 2 parent twin-jet electropolished specimens. The white dotted outlines indicate possible Z-phase precipitates and/or regions favourable for Z-phase formation.

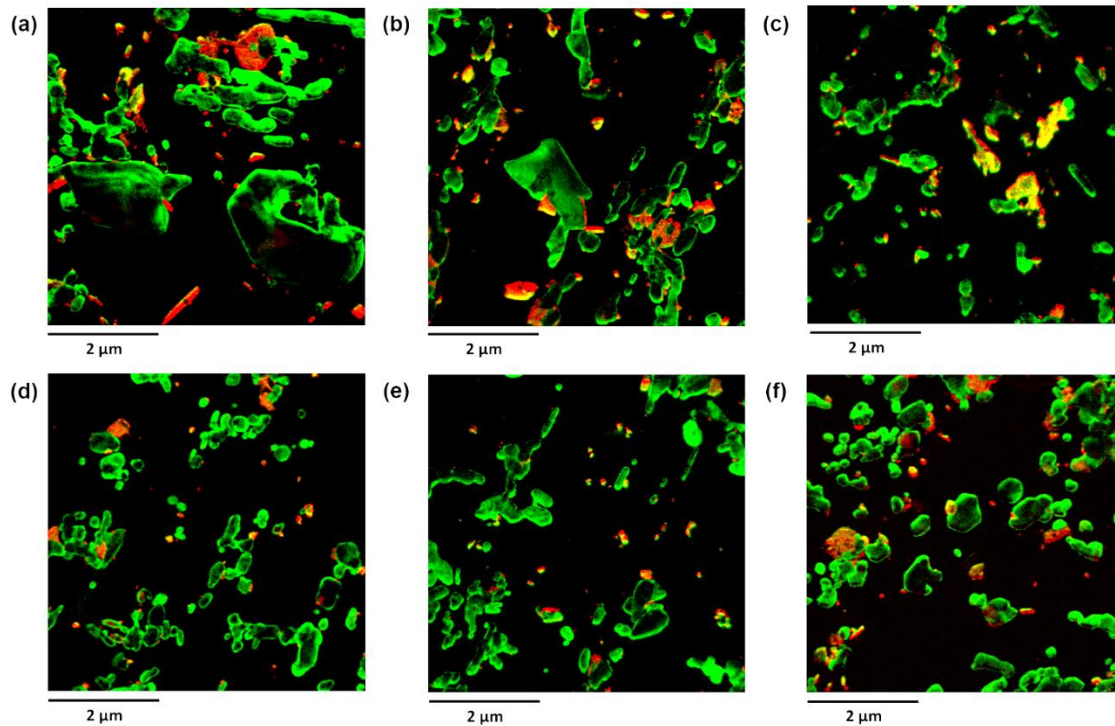
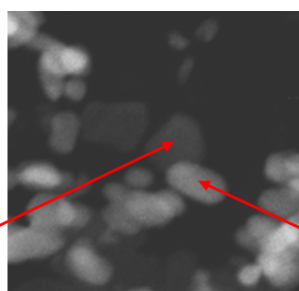


**Figure 4.58:**  $6 \times 6 \mu\text{m}^2$  EFTEM RGB composite of Cr (green) and V (red) maps of areas from the creep aged 2 parent extraction replica specimen. Areas of overlapping Cr and V signals indicate possible Z-phase precipitates.

During STEM-EDS point analysis of the creep aged 2 parent extraction replica specimen, a precipitate with a relative V and Cr content of 45% and 55%, respectively, was found adjacent to an  $\text{M}_{23}\text{C}_6$  carbide. This result is shown in **Figure 4.59**. Maile (2007) has reported that the V:Cr ratio in Z-phase precipitates of 9-12% Cr martensitic steels is approximately 0.7 to 1.0. Therefore, it can be concluded that this is a Z-phase precipitate. A total of 9 such Z-phase precipitates was identified in the creep aged 2 parent material and their mean V:Cr ratio was calculated as  $1.0 \pm 0.1$ . The extensive dissolution of VX precipitates and formation of many Z-phase precipitates in the creep aged 2 parent material is a cause for great concern since the premature failure of components has occurred due to rapid Z-phase formation (Section 2.3.2). In the case of the creep aged simulated FGHAZ materials, it is assumed that any nucleated Z-phase precipitates would dissolve during welding since the dissolution temperature of Z-phase precipitates in X20 is approximately 800 °C (Danielsen 2007). The fact that no Z-phase precipitates could be identified in the creep aged simulated FGHAZ materials substantiates this assumption.



0.5 μm

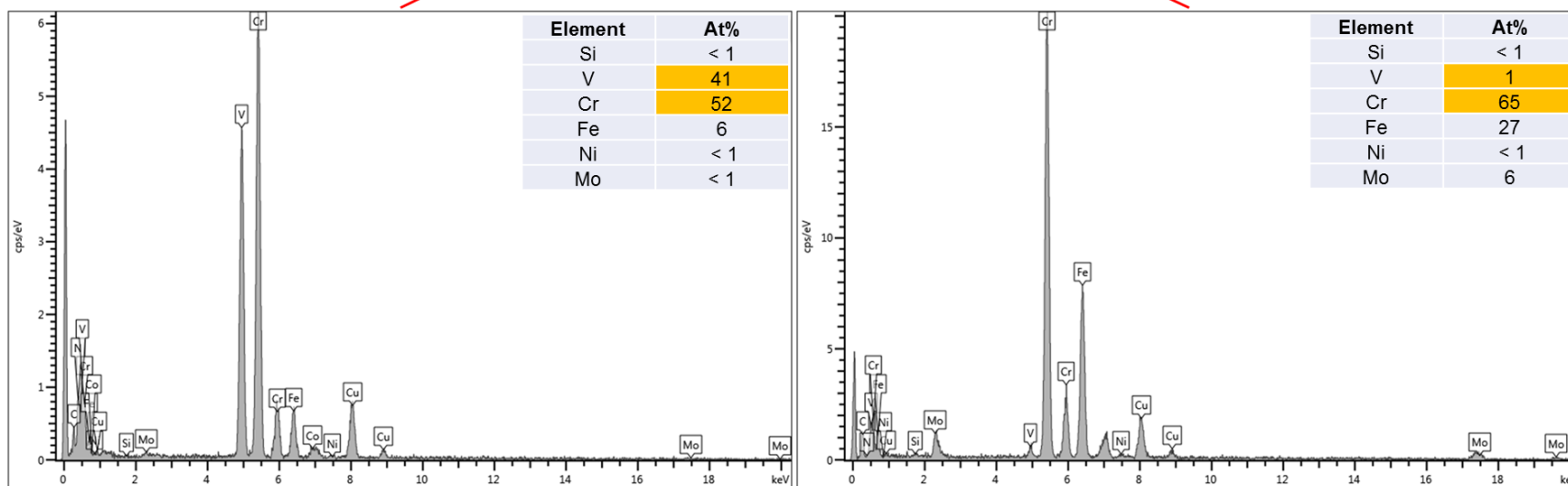


**Figure 4.59:** STEM-EDS image of adjacent precipitates in the creep aged 2 parent extraction replica specimen, and their corresponding spectrum and chemical composition. The % V and Cr are highlighted in yellow. The spectrum on the left corresponds to that of a Z-phase particle and on the right is the spectrum of the adjacent  $M_{23}C_6$  carbide.

## 4.9 MICRO-GRAIN AND SUBSTRUCTURE

### 4.9.1 Results

Areas of  $6 \times 6 \mu\text{m}^2$  in size were imaged from each twin-jet electropolished specimen with ADF-STEM. From the acquired images it is possible to analyse the dislocation substructure as described in Section 3.7.6. For cross-correlation, the same areas as with CBS imaging and TKD was analysed and a total of 16 images were acquired to cover the same sampling size as that of the TKD ( $576 \mu\text{m}^2$ ). Thus, it was possible to identify the different boundary types in the ADF-STEM images by comparing to the TKD GB map of the same area. This is illustrated in **Figure 4.60**. A micro-grain is indicated by label “x”. Here it is illustrated the importance of referring to “micro-grain” instead of “subgrain” with TKD data since MGB can be both LAGB and HAGB. Also, in the ADF-STEM image SGB are visible within the micro-grain, but not in the TKD GB map. Hence the limited angular resolution of the TKD data is proven.

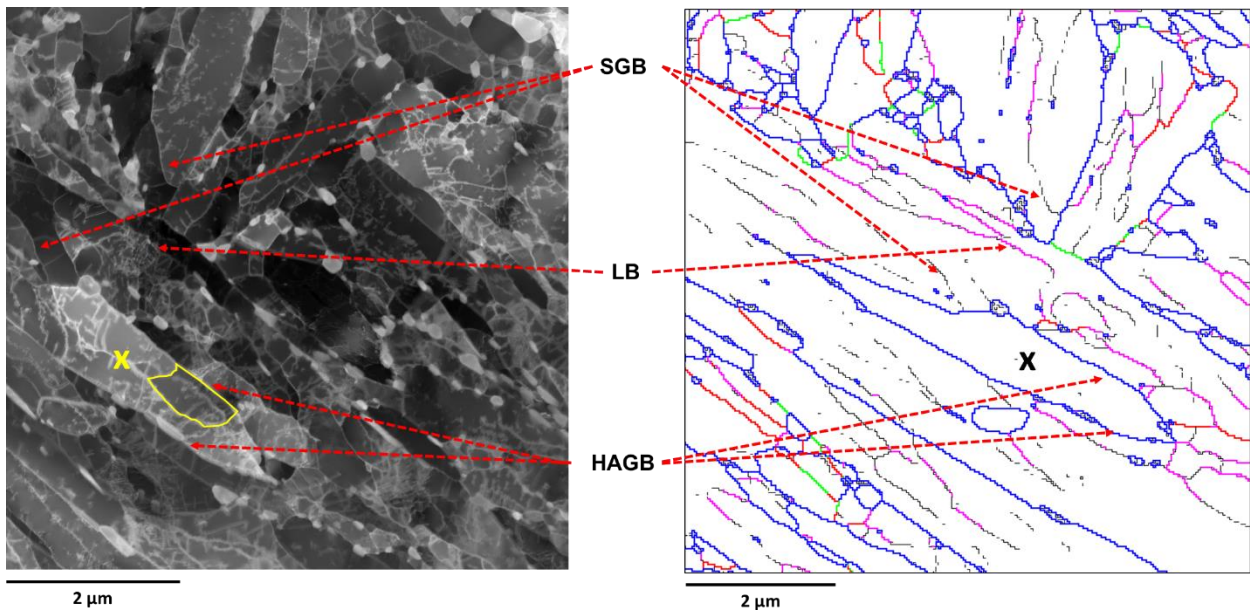


**Figure 4.60:**  $6 \times 6 \mu\text{m}^2$  ADF-STEM image (left) and TKD GB map (right) of the same area on new parent twin-jet electropolished specimen. Arrows indicate different boundary types identified from the TKD GB map, “x” labels a single micro-grain and a subgrain within in this micro-grain is outlined. The colour coding in the TKD GB map is the same as that used in Figure 4.26.



From **Figure 4.60** it can be concluded upon measuring the areas bounded by the boundaries in the ADF-STEM images, that the substructure is measured. **Figure 4.61** provides a montage of 4 ( $6 \times 6 \mu\text{m}^2$ ) ADF-STEM images for each of the parent and simulated FGHAZ materials. Distinct equiaxed micro-grains are observed in the creep aged 1 simulated FGHAZ material and to a lesser extent in the creep aged 2 simulated FGHAZ material. No such micro-grains were found in the imaged areas of the new simulated FGHAZ and any parent material. The observed equiaxed micro-grains in the ADF-STEM images are shown in **Figure 4.62**. Each of these micro-grains is surrounded by areas of high dislocation density (the different dislocations are illustrated in **Figure 4.68**).

Further qualitative analysis was performed on these micro-grains by comparing the ADF-STEM, EFTEM, TKD-EDS and CBS data acquired from these micro-grains. **Figure 4.63** provides the collection of such data for a equiaxed micro-grain in the creep aged 1 simulated FGHAZ material. This image illustrates the usefulness of the combination of these techniques for correlative microscopy. Upon comparison of the ADF-STEM (**Figure 4.63(a)**) and CBS image (**Figure 4.63(c)**) in this figure, it is confirmed that the boundaries in the CBS image outline micro-grains and not the substructure, similarly to the TKD map (**Figure 4.63(b)**).

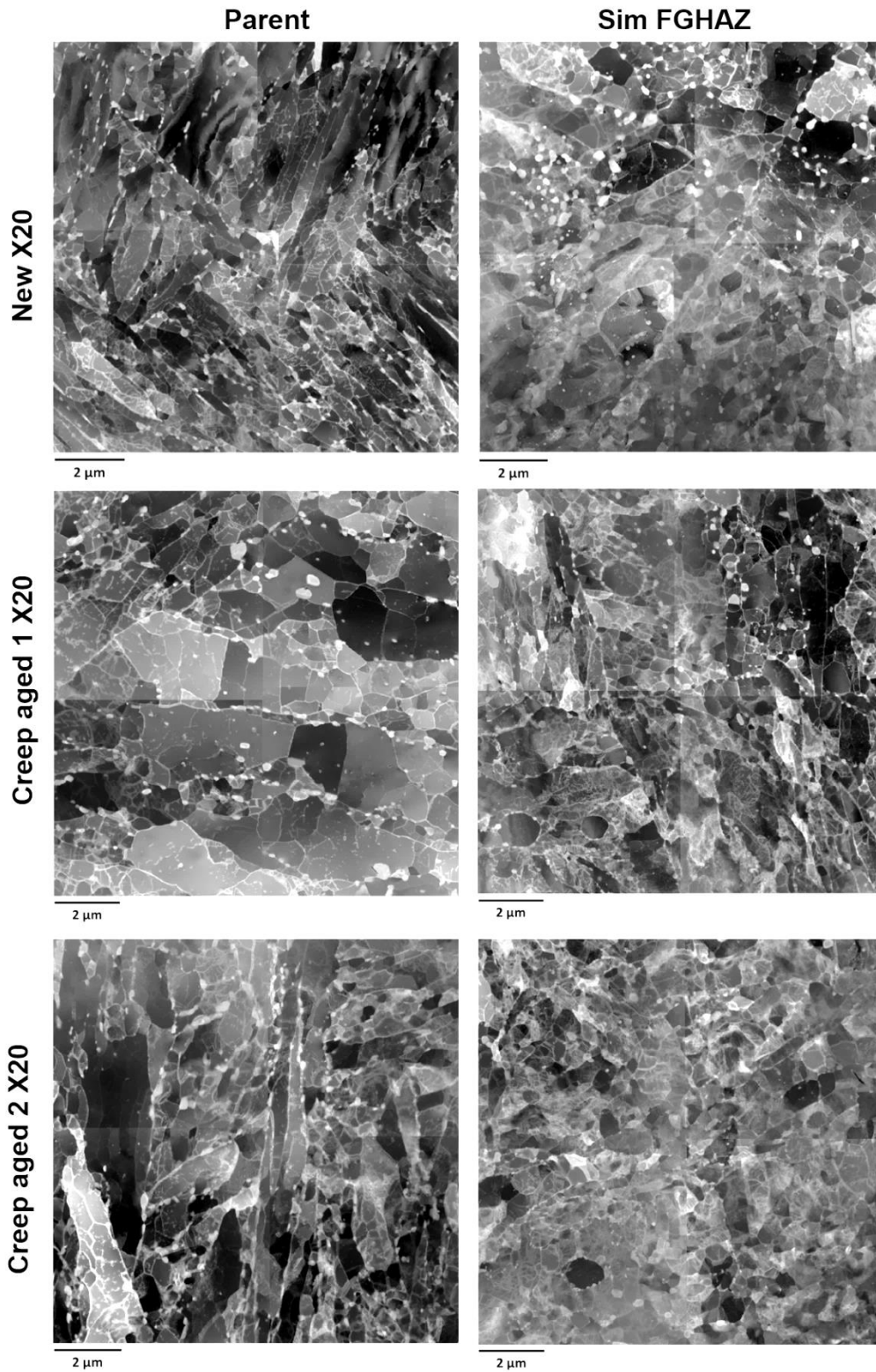


**Figure 4.61:** 576  $\mu\text{m}^2$  montage of ADF-STEM images acquired from parent and simulated FGHAZ twin-jet electropolished specimens.

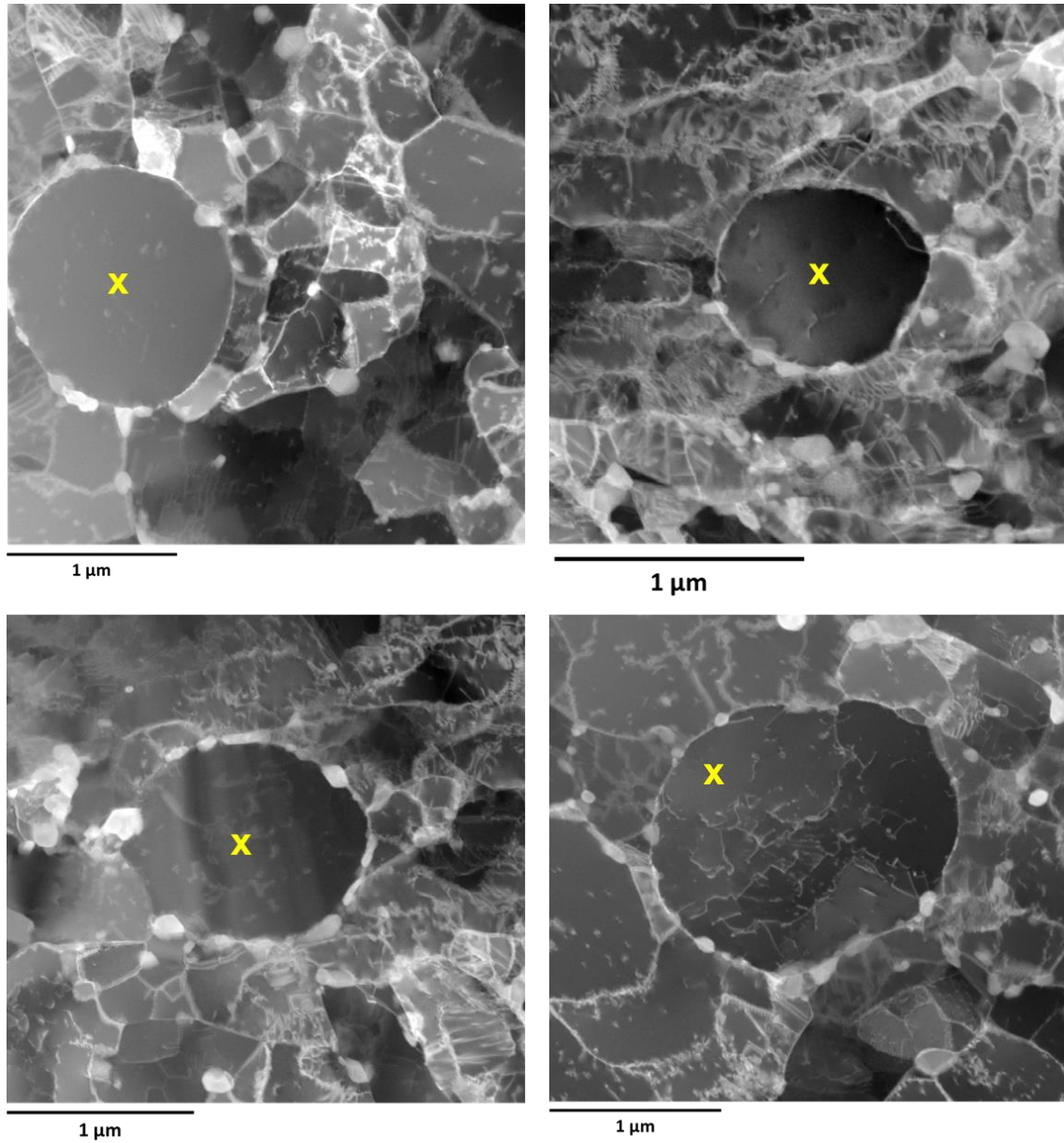


**Figure 4.62:** ADF-STEM images of equiaxed micro-grains (marked “x”) observed in the creep aged 1 simulated FGHAZ material.

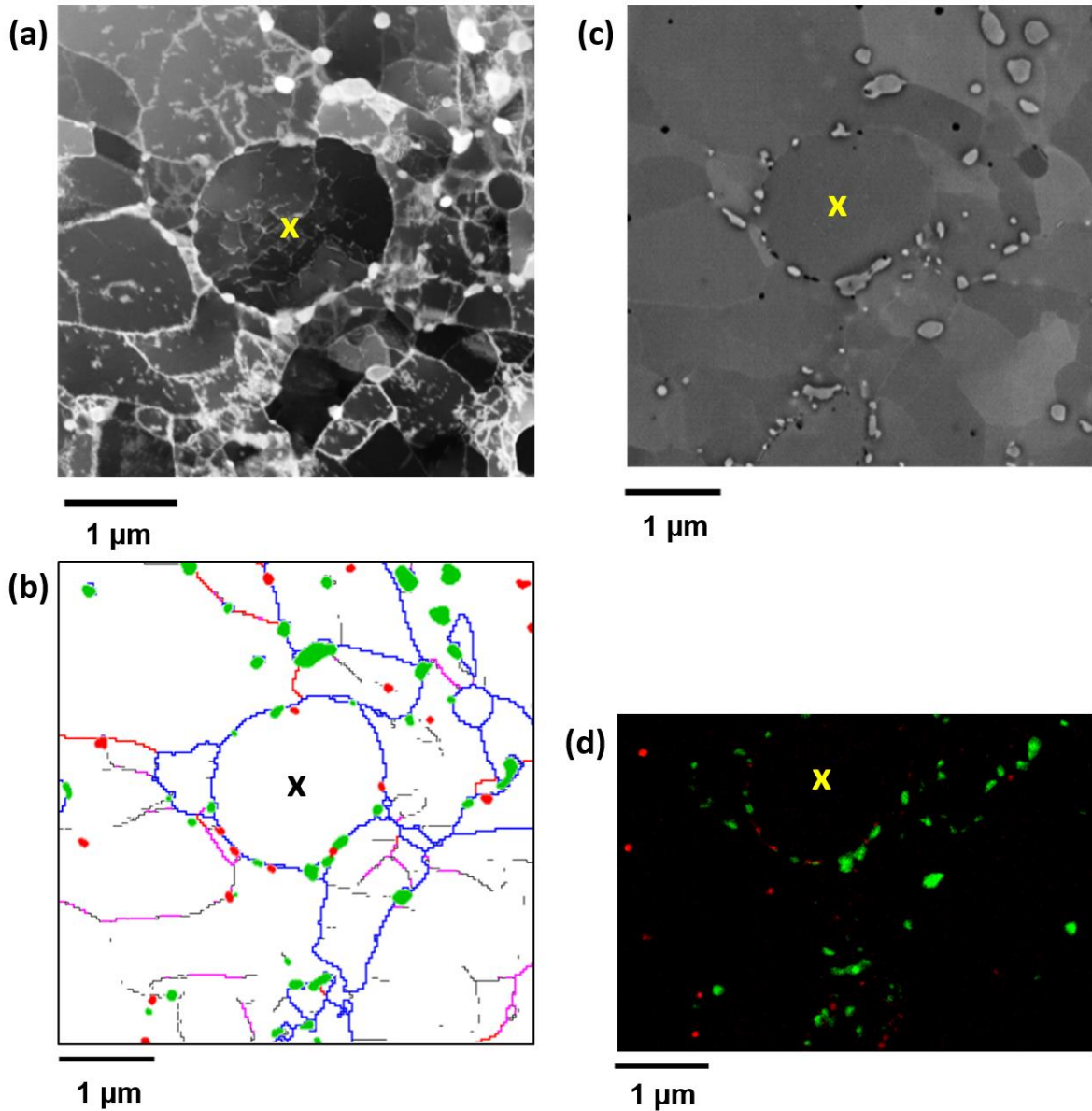


**Figure 4.63:** (a) ADF-STEM image, (b) TKD GB map overlaid onto thresholded TKD-EDS Cr (green) and V (red) elemental maps, (c) CBS image and (d) EFTEM RGB composite of Cr (green) and V (red) elemental maps of same micro-grain (marked by “x”) in creep aged 1 simulated FGHAZ twin-jet electropolished specimen.

As discussed in Section 3.7.6 and shown in **Figure 4.29** the MGB could be isolated from the CBS images and hence the micro-grains measured. Similarly, the substructure was measured by thresholding the boundaries in the ADF-STEM images (Section 3.7.6). For

comparison, the MGB was completed from the TKD GB maps (**Figure 4.26**) with  $MO > 2^\circ$  and  $MO > 5^\circ$  and the outlined micro-grains also measured (Section 3.7.6). Examples of the analysed images are given in **Figure 4.64** for each material type. Also described in Section 3.6.7 is the methodology of measuring the size of the micro-grains and substructure as the minor axis length of a fitted equivalent ellipse. The number of subgrains in the substructure and micro-grains measured is summarised in **Table 4.9**.

**Table 4.9:** Number of subgrains and micro-grains analysed.

	New		Creep aged 1		Creep aged 2	
	Parent	Sim FGHAZ	Parent	Sim FGHAZ	Parent	Sim FGHAZ
<b>DF-STEM</b> ( $576 \mu\text{m}^2$ )	6472	5780	1517	5305	2029	6742
<b>CBS</b> ( $916 \mu\text{m}^2$ )	903	906	580	944	756	1057
<b>TKD <math>MO &gt; 2^\circ</math></b> ( $576 \mu\text{m}^2$ )	856	668	374	819	714	795
<b>TKD <math>MO &gt; 5^\circ</math></b> ( $576 \mu\text{m}^2$ )	324	395	142	429	264	705

The substructure can also be quantified as the size of the coherently diffracting domains (crystallite size) measured from the XRD spectrum using TOPAS<sup>TM</sup> software (Section 3.7.6). **Figure 4.65** provides the XRD spectra acquired from the bulk specimens of the parent and simulated FGHAZ X20 materials. **Table 4.10** summarises the crystallite size and strain parameters measured from the broadened peaks in XRD spectra using TOPAS<sup>TM</sup>. The error, in this case, is given as a systematic error due to fitting determined in TOPAS<sup>TM</sup>.

**Table 4.10:** Crystallite size and strain parameters measured from XRD peak broadening using TOPAS™ (sampling area = 40-80 mm<sup>2</sup>).

	New		Creep aged 1		Creep aged 2	
	Parent	Sim FGHAZ	Parent	Sim FGHAZ	Parent	Sim FGHAZ
Crystallite size L (μm)	0.13 ± 0.01	0.19 ± 0.01	0.16 ± 0.01	0.17 ± 0.01	0.13 ± 0.01	0.15 ± 0.01
Lattice strain G (x10 <sup>-2</sup> )	8.97 ± 0.33	9.13 ± 0.37	7.82 ± 0.31	7.92 ± 0.23	9.79 ± 0.48	9.70 ± 0.28
ε <sub>0</sub> from strain (x10 <sup>-3</sup> )	22.42 ± 0.82	22.83 ± 0.93	19.54 ± 0.78	19.80 ± 0.57	24.50 ± 1.20	24.26 ± 0.71
*Refinement quality factor χ <sup>2</sup>	2.14	6.63	2.75	1.86	1.71	1.95

\*Refer to Toby (Toby 2006).

**Figure 4.66** summarises the measured micro-grain, substructure and crystallite sizes from CBS, TKD, ADF-STEM and XRD data, respectively. The mean micro-grain sizes and 95% CI for the CBS, TKD and ADF-STEM data was determined using Equations (3.16) and (3.17).

For better comparison, the distribution of the micro-grain sizes is plotted in **Figure 4.67** as the linear fit to the cumulative % (30 to 70%) as a function of the logarithm of the measured area of each micro-grain. Only the data from the TKD GB MO > 5° maps is given since the most distinct differences between the sizes is measured from these maps.

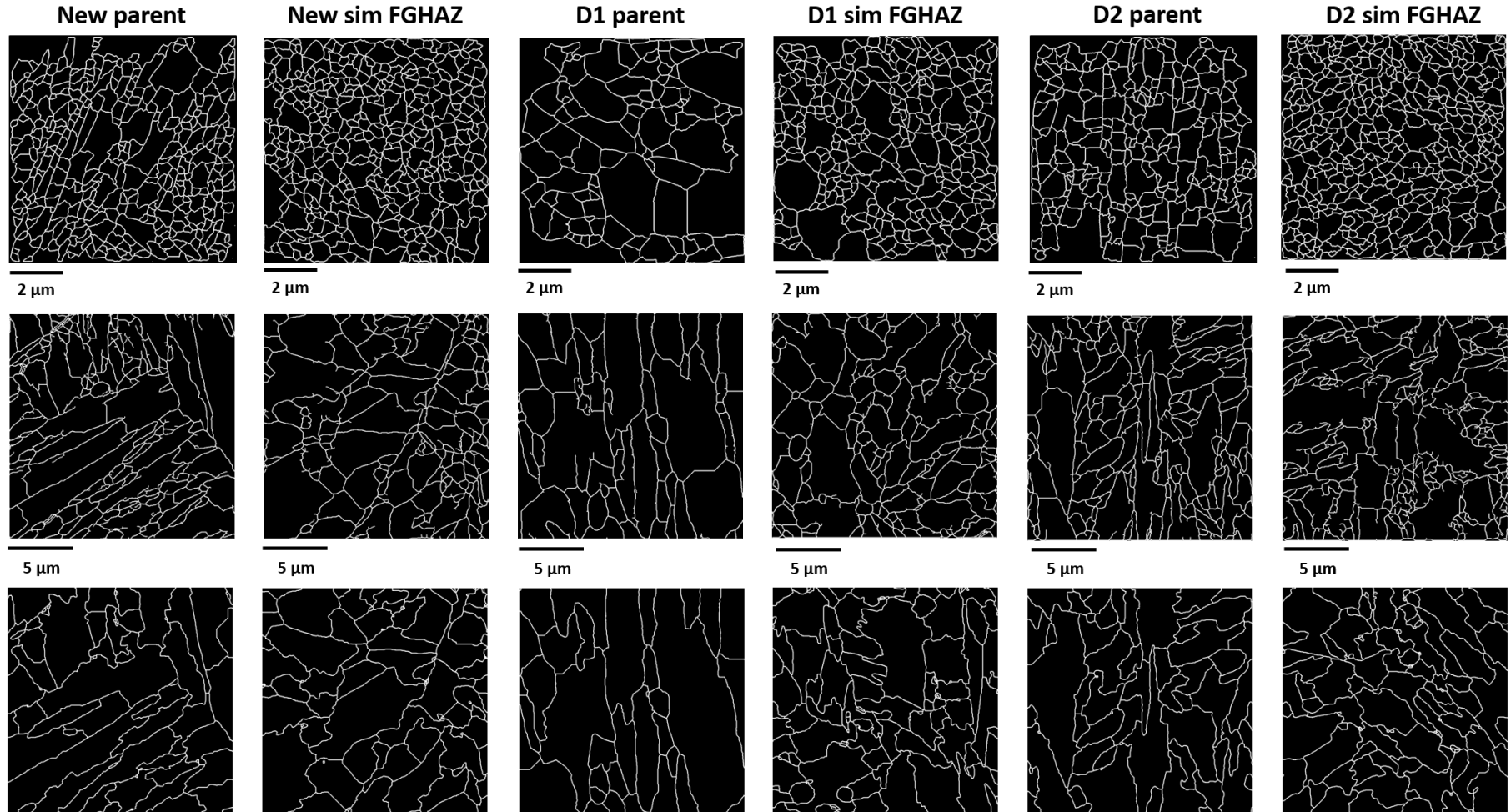
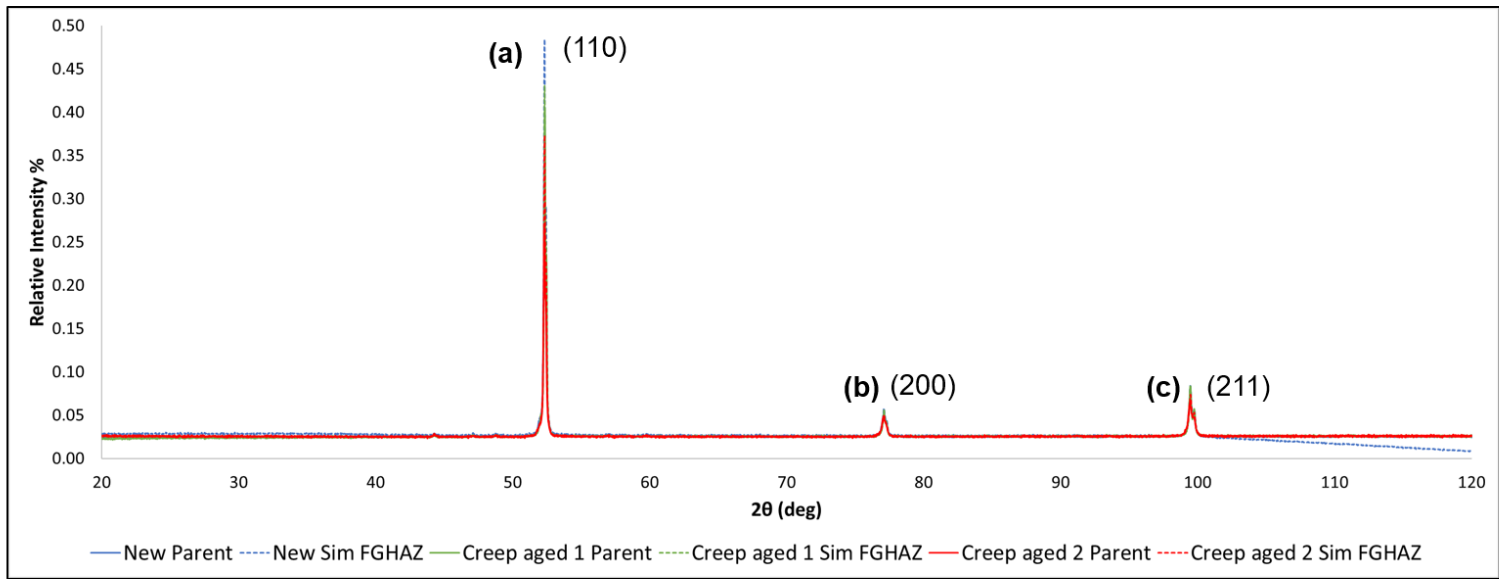


**Figure 4.64:** Thresholded substructure from  $6 \times 6 \mu\text{m}^2$  ADF-STEM image (top row), micro-grains drawn from  $12 \times 12 \mu\text{m}^2$  TKD GB MO  $> 2^\circ$  map (middle row) and  $12 \times 12 \mu\text{m}^2$  TKD GB MO  $> 5^\circ$  map (bottom row) for an area on the parent and simulated FGHAZ twin-jet electropolished specimens. The same area is illustrated for the TKD maps.



(a)

(b)

(c)

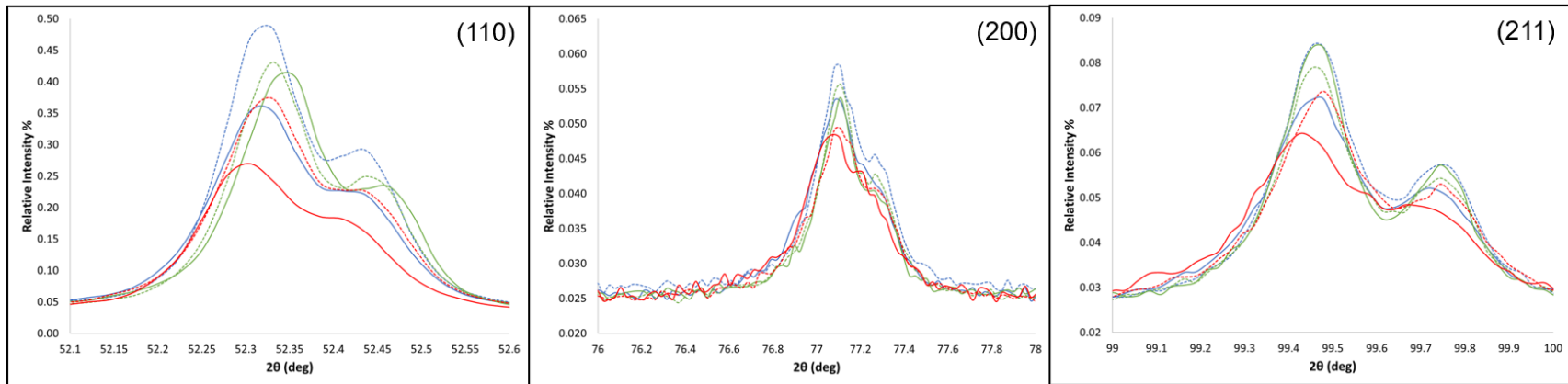


**Figure 4.65:** XRD spectra acquired from parent and simulated FGHAZ bulk specimens. The peaks labelled (a), (b) and (c) are enlarged.



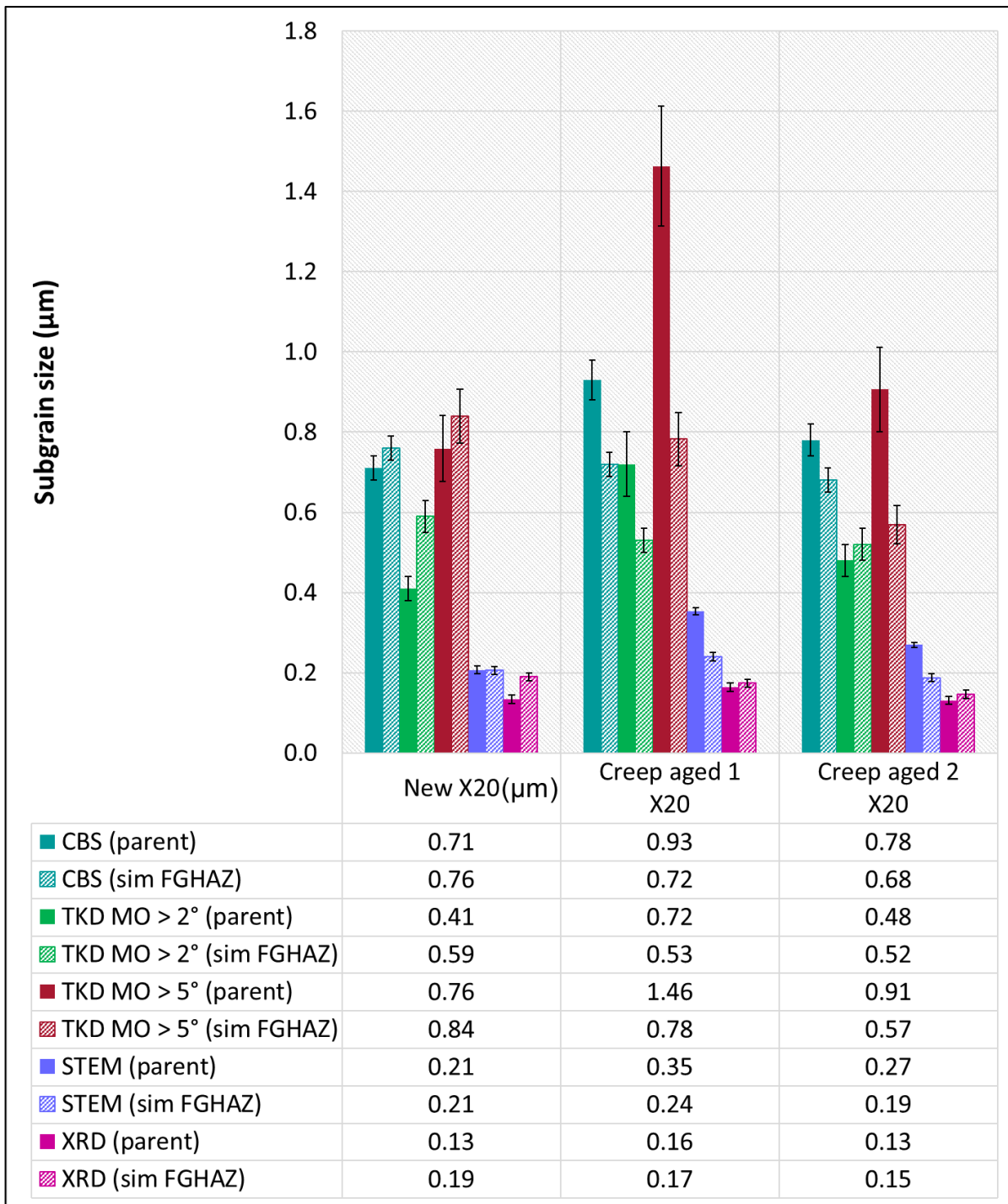


**Figure 4.66:** Summary of mean subgrain size measurements for parent and simulated FGHAZ X20 materials from CBS (916  $\mu\text{m}^2$ ), TKD (576  $\mu\text{m}^2$ ), DF-STEM (576  $\mu\text{m}^2$ ) and XRD (40-80  $\text{mm}^2$ ). Subgrain size is measured as minor axis length of micro-grains in CBS and TKD data, minor axis length of substructure in the DF-STEM images, and crystallite size from the XRD data. For visual purposes, all simulated FGHAZ data is pattern filled.

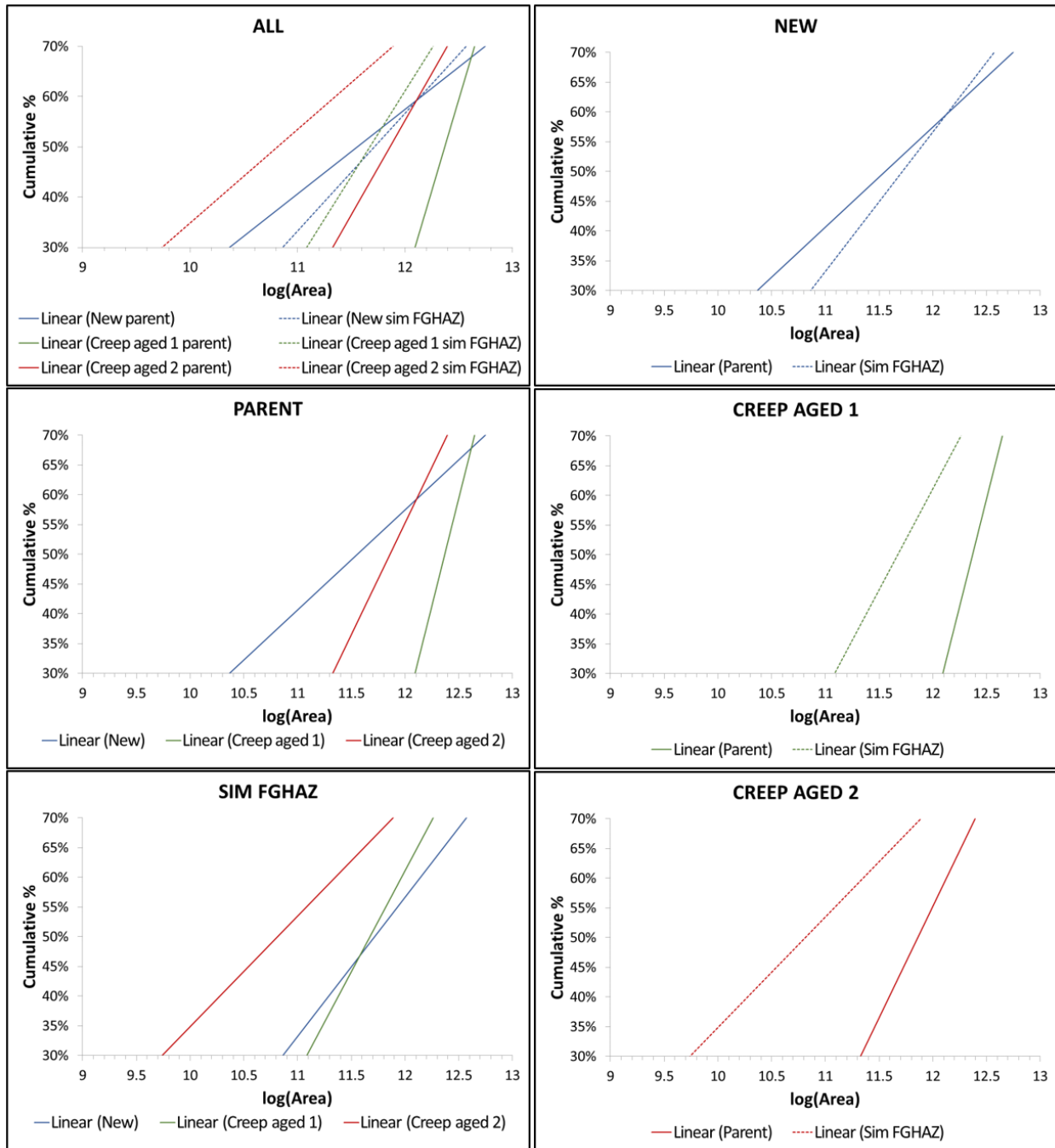


**Figure 4.67:** Linear fit plots of cumulative % (30 to 70%) vs log(area) for each measured micro-grain in TKD GB MO > 5° maps acquired from parent and simulated FGHAZ twin-jet electropolished specimens.

## 4.9.2 Discussion

### (i) Evolution of Substructure

A summary of the mean substructure (short width) sizes measured using ADF-STEM and crystallite (coherently diffracting domain) sizes using XRD is provided in **Table 4.11** for each material.

**Table 4.11:** Substructure and crystallite sizes measured from ADF-STEM and XRD results.

	New		Creep aged 1		Creep aged 2	
	Parent	Sim FGHAZ	Parent	Sim FGHAZ	Parent	Sim FGHAZ
<b>Substructure (<math>\mu\text{m}</math>)</b>	$0.21 \pm 0.01$	$0.21 \pm 0.01$	$0.35 \pm 0.01$	$0.24 \pm 0.01$	$0.27 \pm 0.01$	$0.19 \pm 0.01$
<b>Crystallite size (<math>\mu\text{m}</math>)</b>	$0.13 \pm 0.01$	$0.19 \pm 0.01$	$0.16 \pm 0.01$	$0.17 \pm 0.01$	$0.13 \pm 0.01$	$0.15 \pm 0.01$

From **Figure 4.61** and **Figure 4.64** coarsening of the substructure in the creep aged parent materials is observed as more visible SGB and larger subgrains, with creep aged 1 parent material having the greatest substructure development. After FGHAZ simulation, the substructure is more refined and equiaxed with an increase in the number of SGB. The substructure of the new and creep aged 2 simulated FGHAZ material is observed to be similar, but the substructure of the creep aged 2 simulated FGHAZ material is distinctly further developed with much rounder and larger subgrains. A strong bimodality of substructure size is visible.

Quantitatively the same trends are observed (**Figure 4.66**). The substructure is much smaller than the micro-grains. Even though there is a change in shape of the substructure, the new parent and simulated FGHAZ materials have the same mean substructure size of  $0.21 \pm 0.01 \mu\text{m}$ . The creep aged 1 parent material has the largest mean substructure size of  $0.35 \pm 0.01 \mu\text{m}$  and creep aged 2 parent material has a mean substructure size of  $0.27 \pm 0.01 \mu\text{m}$ .

The difference in the mean substructure size of the creep aged simulated FGHAZ materials compared to the new simulated FGHAZ material is statistically significant, but

the differences are not large. The creep aged 1 simulated FGHAZ material has the largest substructure ( $0.24 \pm 0.01 \mu\text{m}$ ), the substructure in the creep aged 2 simulated FGHAZ material is the smallest ( $0.19 \pm 0.01 \mu\text{m}$ ) and the substructure size of the new simulated FGHAZ material is in between ( $0.21 \pm 0.01 \mu\text{m}$ ). After FGHAZ simulation, the substructure significantly decreases in size for both creep aged simulated FGHAZ materials, while the substructure size is not altered for the new simulated FGHAZ material.

Considering the acquired XRD spectra in **Figure 4.65**, all the peaks show a broadening and differ from each other, indicating that there are crystallite size (coherently diffracting domain size) and strain differences in the materials. The most significant broadening is observed for the creep aged 2 parent material and the new simulated FGHAZ material has the narrowest peaks. From **Table 4.10** it follows that the first is due the creep aged 2 parent material having the largest strain and the new simulated FGHAZ material having the largest crystallite size.

In **Figure 4.66** the smallest sizes are measured from the XRD and ADF-STEM data. The crystallite sizes measured using XRD is slightly lower than the corresponding subgrain size (short width) measured using ADF-STEM. In general, XRD is affected by the size of the coherently diffracting domains, which can either be crystallites or domains within the crystallites (Girgsdies 2015). Subsequently, it follows that the crystallite sizes measured are the domain sizes within the crystallites. This could explain why the crystallite size does not follow the same trends as the substructure size.

The new and creep aged 2 parent materials have similar crystallite sizes of  $0.13 \pm 0.01 \mu\text{m}$  (**Table 4.11**). As with the substructure size, creep aged 2 parent material has the largest crystallite size of  $0.16 \pm 0.01 \mu\text{m}$ . Upon comparison of the simulated FGHAZ materials, the new material has the largest crystallite size of  $0.19 \pm 0.01 \mu\text{m}$ , the creep aged 1 material has a slightly smaller crystallite size of  $0.17 \pm 0.01 \mu\text{m}$ , and the smallest crystallite size of  $0.15 \pm 0.01 \mu\text{m}$  is measured for the creep aged 2 simulated FGHAZ.

After FGHAZ simulation, the crystallite sizes are larger in all the simulated FGHAZ materials with the most pronounced increase being in the new material. Yadav, Kalácska, Dománková *et al.* (2016) has measured the crystallite size of new X20 steel as  $0.12 \mu\text{m}$

using MAUD software. This value is slightly smaller than that measured in this study for the new parent material and the difference is most probably due to the different methods used for measuring the crystallite size.

## (ii) Evolution of Micro-grains

The mean subgrain (short width) sizes measured from the CBS images and TKD GB maps are summarised in **Table 4.12**.

**Table 4.12:** Summary of mean subgrain sizes measured using CBS imaging and TKD.

	New		Creep aged 1		Creep aged 2	
	Parent	Sim FGHAZ	Parent	Sim FGHAZ	Parent	Sim FGHAZ
<b>CBS (<math>\mu\text{m}</math>)</b>	$0.71 \pm 0.03$	$0.76 \pm 0.03$	$0.93 \pm 0.05$	$0.72 \pm 0.03$	$0.78 \pm 0.04$	$0.68 \pm 0.03$
<b>TKD MO &gt; 2° (<math>\mu\text{m}</math>)</b>	$0.41 \pm 0.03$	$0.59 \pm 0.04$	$0.72 \pm 0.08$	$0.53 \pm 0.03$	$0.48 \pm 0.04$	$0.52 \pm 0.04$
<b>TKD MO &gt; 5° (<math>\mu\text{m}</math>)</b>	$0.76 \pm 0.08$	$0.84 \pm 0.07$	$1.46 \pm 0.15$	$0.78 \pm 0.07$	$0.91 \pm 0.11$	$0.57 \pm 0.05$

The equiaxed micro-grains observed in the creep aged 1 and to a lesser extent creep aged 2 simulated FGHAZ materials was characterised by:

- diameters ranging from approximately 1 to 1.5  $\mu\text{m}$ ,
- surrounded by micro-grains with higher dislocation densities (**Figure 4.62**),
- had little to no SGB, only internal dislocations (**Figure 4.63(a)**),
- their boundaries have MO of more than 10° (**Figure 4.63(b)**),
- their boundaries are decorated by  $\text{M}_{23}\text{C}_6$  carbides and VX precipitates (**Figure 4.63(c)** and **(d)**),
- and no precipitates were observed within these micro-grains.

Consequently, it can be concluded that these are recovered micro-grains. Softening is enhanced by the growth of these recovered pre-existing equiaxed micro-grains upon

further creep exposure (Section 2.3.3). Consequently, since these micro-grains are not present in the new simulated FGHAZ material, they may contribute to the preferential Type IV failure of weldments on the creep aged rather than the new material side.

The strong dependence of the choice of MO to define the micro-grains in the TKD data is seen in **Figure 4.64**. Boundaries with MO more than  $2^\circ$  outline laths (ferrite subgrains), while those with MO more than  $5^\circ$  outline sub-blocks. This corresponds to the literature of the nature of the different boundaries in Section 2.3.3. Subsequently, smaller subgrain sizes are measured from the TKD MO  $> 2^\circ$  datasets (green) and larger subgrain sizes from the TKD MO  $> 5^\circ$  datasets (red) in **Figure 4.66**.

For most of the materials, the range of subgrain sizes measured from the CBS images (blue) and the TKD MO  $> 5^\circ$  (red) agree in **Figure 4.66**. The two datasets also follow the same trends, but the differences between the materials are more pronounced for the TKD MO  $> 5^\circ$  sizes. This indicates that the regions of varying contrast in the CBS images are mainly sub-blocks. The dissimilarities between the measured subgrain sizes for the two datasets can either be ascribed to the micro-grains in the CBS images being a mixture of laths and sub-blocks, or inaccuracies in thresholding of the boundaries in MIPAR™. To complete the boundaries a segmentation algorithm was used, and extra boundaries could have been included in the measurements, leading to smaller measured subgrain sizes.

The evolution of the sub-block size will be further discussed from the measured TKD MO  $> 5^\circ$  subgrain size data (**Figure 4.66** and **Figure 4.67**) since the most noticeable differences are observed from this data and evolution of lath size from the subgrain sizes measured from the TKD MO  $> 2^\circ$  data.

Similar to the substructure, from **Figure 4.29** and **Figure 4.64** coarsening of the micro-grains in the creep aged parent materials is observed, with creep aged 1 parent material having the furthest extent of development with widened and more equiaxed micro-grains. This corresponds to the results from previous studies summarised in Section 2.3.3. There is not much difference in the micro-grains in the new and creep aged 2 parent materials. After FGHAZ simulation, the micro-grains are more equiaxed with the most round micro-

grains observed in the creep aged 1 simulated FGHAZ material. Also, refined regions with very small laths are observed in the TKD MO > 2° data. These could have formed due to recovery during the cooling and subsequent PWHT. This indicates the heterogeneous nature of the recovery process. During thresholding of the TKD MO > 2° any Cr-enriched  $M_{23}C_6$  carbides boundaries were excluded by subtracting the corresponding Cr SEM-EDS map and therefore these tiny laths are not  $M_{23}C_6$  carbides falsely detected as micro-grains.

Considering the green dataset (TKD MO > 2°) in **Figure 4.66** for the lath size. The laths widen during creep aging from  $0.41 \pm 0.03 \mu\text{m}$  in the new parent material to the widest ( $0.72 \pm 0.08 \mu\text{m}$ ) in the creep aged 1 parent material and  $0.48 \pm 0.04 \mu\text{m}$  in the creep aged 2 parent material. The lath in the creep aged 1 ( $0.53 \pm 0.03 \mu\text{m}$ ) and creep aged 2 ( $0.52 \pm 0.04 \mu\text{m}$ ) simulated FGHAZ materials are statistically significantly smaller than the laths in the new simulated FGHAZ material ( $0.59 \pm 0.04 \mu\text{m}$ ). After FGHAZ simulation, the lath size significantly increases in the new simulated FGHAZ material and significantly decreases in the creep aged 1 simulated FGHAZ material. The decrease in lath size after FGHAZ simulation is insignificant for the creep aged 2 simulated FGHAZ material.

Considering the sub-block sizes as the red dataset (TKD MO > 5°) in **Figure 4.66** and the points at 50% cumulative % in **Figure 4.67**. It should be noted that the probability plots such as in **Figure 4.67** do not identify bimodal size distributions as easily (Harding 1949).

There is substantial growth of these micro-grains in the creep aged 1 parent material, where the size almost doubles from a mean value of  $0.76 \pm 0.08 \mu\text{m}$  in the new parent material to  $1.46 \pm 0.15 \mu\text{m}$ . Less pronounced widening of the sub-blocks is observed in the creep aged 2 parent material ( $0.91 \pm 0.11 \mu\text{m}$ ). Aghajani (2009) measured micro-grain sizes of  $0.70 \mu\text{m}$  in the as-received X20 steel and  $1.07 \mu\text{m}$  after 140 000 h long-term creep (rupture).

Section 2.3.2 explains that the significant micro-grain (laths and sub-blocks) coarsening in the creep aged 1 parent material can be attributed to the significant loss in pinning pressure of the  $M_{23}C_6$  boundary carbides in this material due to coarsening and low number density as measured in Section 4.6.5.

For the simulated FGHAZ materials, the sub-block sizes in the new ( $0.84 \pm 0.07 \mu\text{m}$ ) and creep aged 1 ( $0.78 \pm 0.07 \mu\text{m}$ ) materials does not significantly differ. The sub-blocks in the creep aged 2 material are the smallest of the simulated FGHAZ materials with a mean size of  $0.57 \pm 0.05 \mu\text{m}$ . After FGHAZ simulation, there is not a significant increase in the size of the sub-blocks in the new material, but significantly smaller sub-blocks form in the creep aged simulated FGHAZ materials. As discussed in Section 4.6.5, there are many small carbides within these materials that can pin the boundaries and inhibit the growth of the micro-grains upon cooling and subsequent PWHT. In the case of the new simulated FGHAZ materials, the carbides are larger and therefore do not pin the boundaries to the same extent, leading to the micro-grains to grow during cooling and subsequent PWHT. As the results suggest, this growth is not to a significant degree in the simulated FGHAZ materials.

## **4.10 DISLOCATION DENSITY**

### **4.10.1 Results**

Dislocation densities were investigated using ADF-STEM and XRD as described in Section 3.7.7. The different types of dislocations observable from the ADF-STEM images are distinguished in **Figure 4.68**. The term “internal” dislocations are used instead of “mobile” since it is not possible to distinguish between mobile and dipole dislocations in STEM images. Besides the substructure, the internal dislocations that are “free” were isolated in the STEM images (Section 3.7.7). **Figure 4.69** provides an example of the internal dislocations thresholded from a DF-STEM image of each material type.



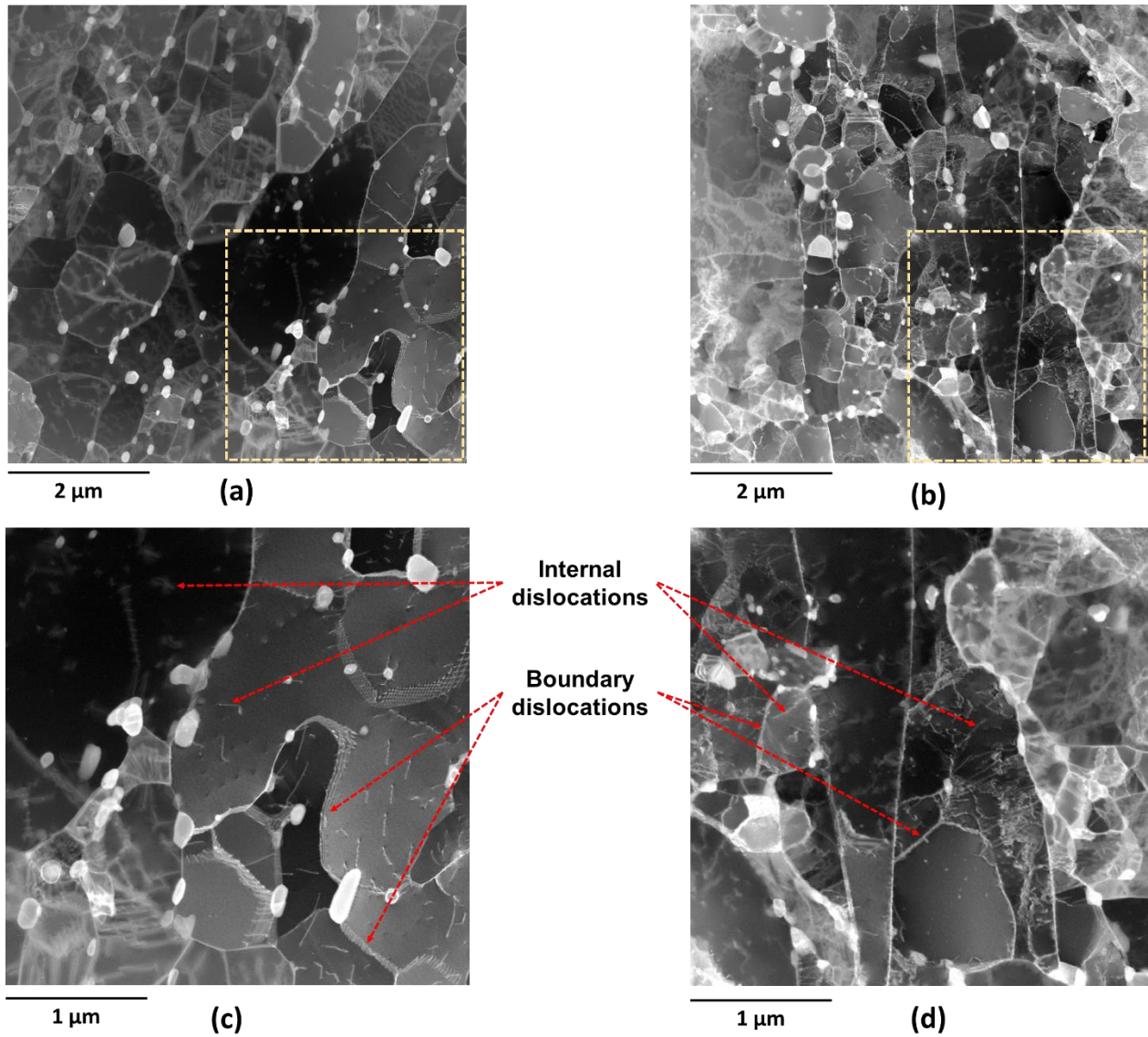


**Figure 4.68:** ADF-STEM images of the creep aged 1 (a) parent and (b) simulated FGHAZ X20 materials indicating the different dislocations visible. (c) and (d) are the enlarged areas outlined by the yellow squares in (a) and (b), respectively.

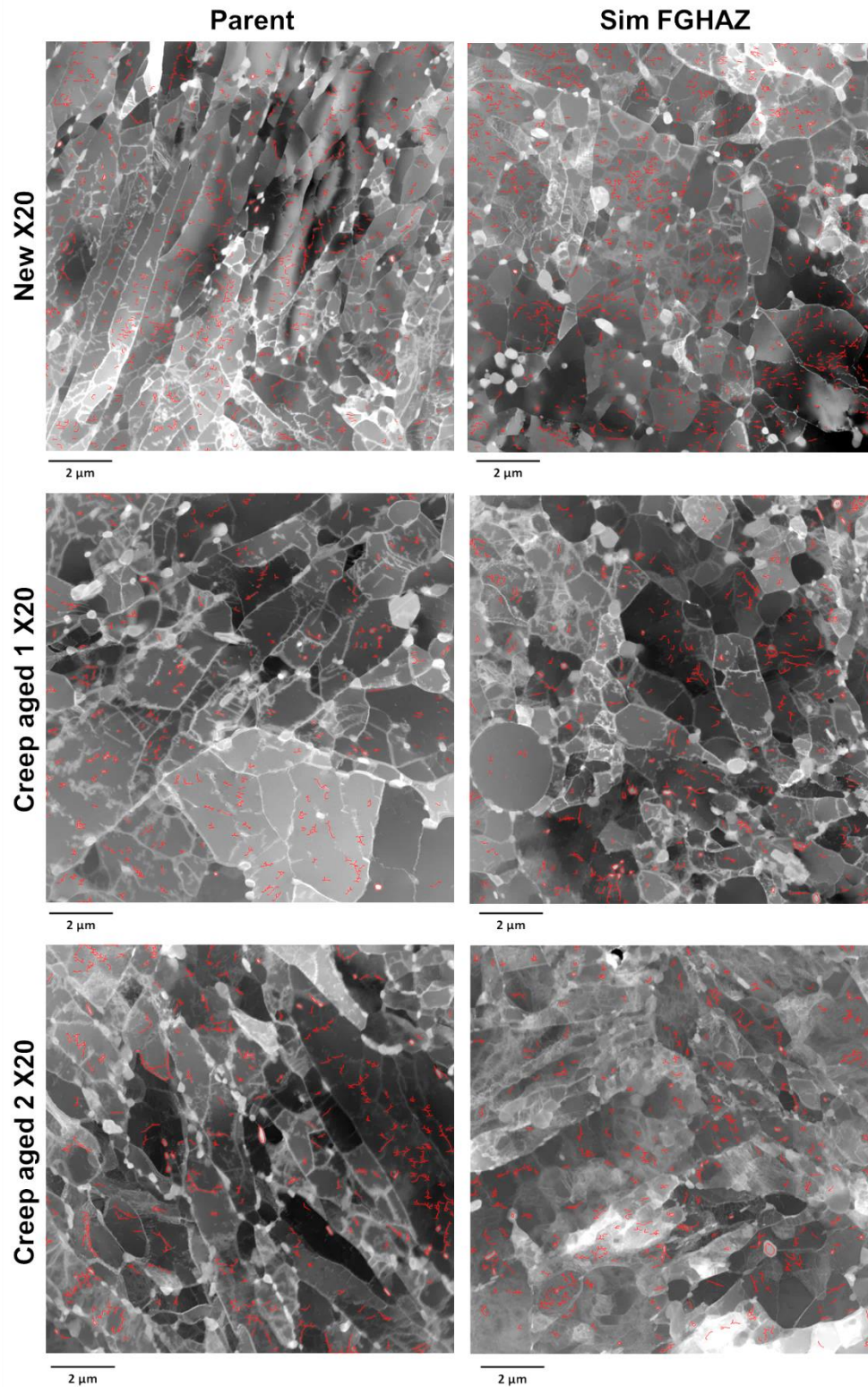


**Figure 4.69:** Internal dislocations (red) isolated from  $6 \times 6 \mu\text{m}^2$  ADF-STEM images acquired from the parent and simulated FGHAZ twin-jet electropolished specimens.

Subsequently, the internal dislocation density  $\rho_{int}$  was calculated using Equation (3.11). The most important dislocation density for creep strength is the mobile dislocation density  $\rho_m$  (Section 2.7.2). As explained in Section 3.7.7, this value was determined from the  $\varepsilon_0$  from strain value determined from XRD (**Table 4.10**) and Equations (3.12) and (3.13). The calculated internal, boundary and mobile dislocation densities are plotted in **Figure 4.70** and **Figure 4.71**, respectively.

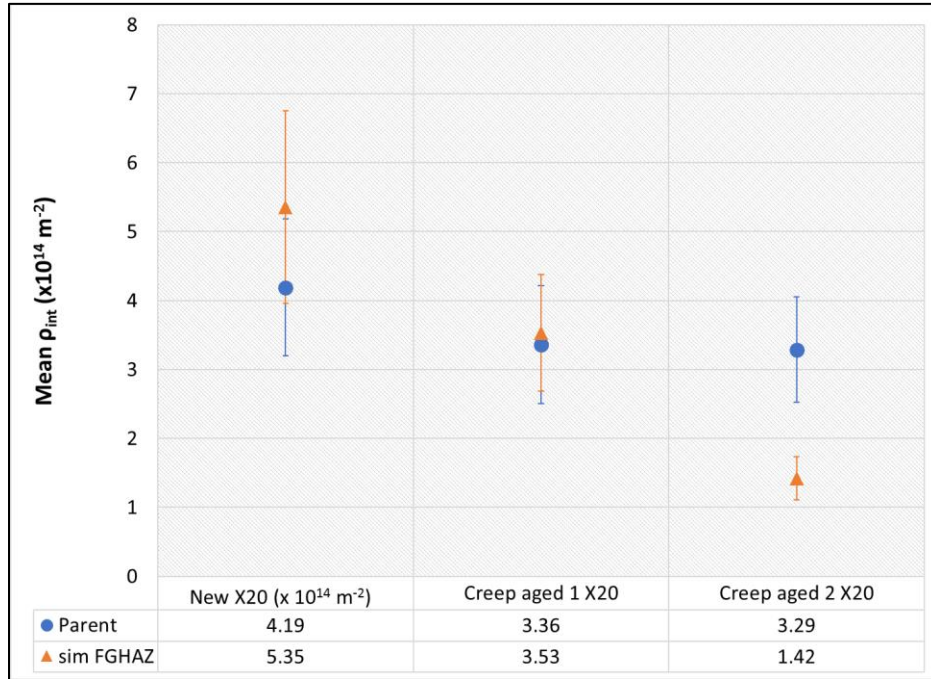


**Figure 4.70:** Internal dislocation densities  $\rho_{int}$  determined from ADF-STEM images of the parent and simulated FGHAZ twin-jet electropolished specimens (total area of  $576 \mu\text{m}^2$  analysed). The error is given by Equation (3.17).

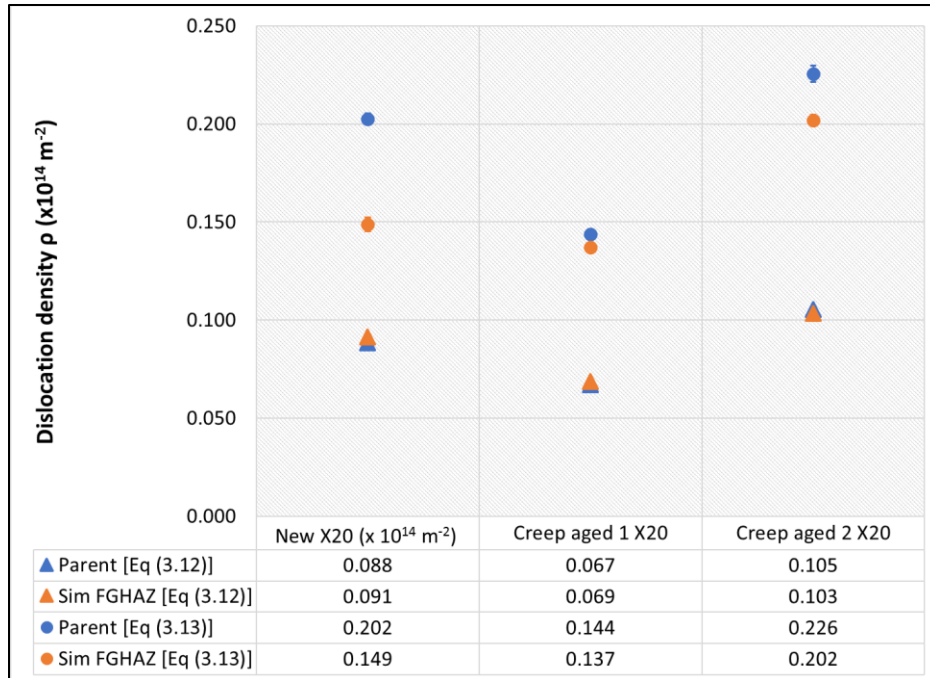


**Figure 4.71:** Dislocation densities  $\rho$  determined from peak broadening in XRD spectra (Equations (3.12) and (3.13)) acquired from the parent and simulated FGHAZ bulk specimens (total area of  $915 \mu\text{m}^2$  analysed). The error was calculated using systematic error calculated in TOPAS<sup>TM</sup> and standard error propagation.

#### 4.10.2 Discussion

**Table 4.13** provides a summary of the internal dislocation densities  $\rho_{\text{int}}$  measured from the ADF-STEM images and the mobile dislocations densities  $\rho_{\text{m}}$  determined using XRD.

**Table 4.13:** Mean dislocation densities determined using ADF-STEM and XRD.

	New		Creep aged 1		Creep aged 2	
	Parent	Sim FGHAZ	Parent	Sim FGHAZ	Parent	Sim FGHAZ
$\rho_{\text{int}}$ (x $10^{14} \text{ m}^{-2}$ )	$4.19 \pm 0.99$	$5.35 \pm 1.40$	$3.36 \pm 0.86$	$3.53 \pm 0.85$	$3.29 \pm 0.77$	$1.42 \pm 0.31$
* $\rho_{\text{m}}$ (x $10^{14} \text{ m}^{-2}$ )	$0.088 \pm 0.001$	$0.091 \pm 0.001$	$0.067 \pm 0.001$	$0.069 \pm 0.001$	$0.105 \pm 0.001$	$0.103 \pm 0.001$
+ $\rho_{\text{m}}$ (x $10^{14} \text{ m}^{-2}$ )	$0.202 \pm 0.003$	$0.149 \pm 0.003$	$0.144 \pm 0.002$	$0.137 \pm 0.002$	$0.226 \pm 0.004$	$0.202 \pm 0.003$

\* Calculated from Equation (3.12)

+ Calculated from Equation (3.13)

The differences in dislocation densities can be readily seen from **Figure 4.61** for the parent and simulated FGHAZ X20 materials. Good qualitative results are acquired from the ADF-STEM images. Much higher dislocation densities are observed in the simulated FGHAZ materials as expected (Section 2.4.1). As have been observed for parent X20 material (Section 2.3.4), the dislocation densities are heterogeneously distributed throughout the micro-grains with areas that are free from dislocations in both the creep aged and simulated FGHAZ materials, which is due to the inhomogeneity of recovery.

From the ADF-STEM images, more boundaries without any precipitates are observed in the simulated FGHAZ material than in the parent material (**Figure 4.68** and **Figure 4.69**). This follows from the fact that new boundaries form during FGHAZ simulation.

In **Figure 4.68(c)** the knitting reactions between the dislocations and SGB, and the interference of small carbides with these reactions are observed. The stabilisation of the MGB by the carbides are also observed. In addition to the equiaxed micro-grains observed in the creep aged 1 simulated FGHAZ material (**Figure 4.62**), a fully recovered subgrain with no precipitates on the boundaries is observed within a highly dislocated micro-grain (**Figure 4.68(d)**). Upon comparison to the corresponding TKD GB map, it is seen that the boundaries of this subgrain are LAGB with MO of 1 to 5°.

An internal dislocation density of  $4.19 \pm 0.99 \times 10^{14} \text{ m}^{-2}$  was measured inside the substructure of the new parent material (**Figure 4.70**). A decrease in internal dislocation density during creep aging is observed, with a measured mean value of  $3.36 \pm 0.86 \times 10^{14} \text{ m}^{-2}$  for the creep aged 1 parent material and  $3.29 \pm 0.77 \times 10^{14} \text{ m}^{-2}$  for the creep aged 2 parent material. Since the samples have had long-term creep exposure, it is expected that the decrease in internal dislocation density will be more pronounced as from literature (Section 2.3.4). For the simulated FGHAZ materials, the highest internal dislocation density was measured in the substructure of the new simulated FGHAZ material ( $5.35 \pm 1.40 \times 10^{14} \text{ m}^{-2}$ ) and the lowest in the creep aged 2 simulated FGHAZ material ( $1.42 \pm 0.31 \times 10^{14} \text{ m}^{-2}$ ). The creep aged 1 simulated FGHAZ material has a similar internal dislocation density as its parent material ( $3.53 \pm 0.85 \times 10^{14} \text{ m}^{-2}$ ). After FGHAZ simulation, the mean dislocation density increases for the new material, but due

to the heterogeneous distribution of the internal dislocation densities, the difference in the means is insignificant. The internal dislocation density distinctly decreases in the creep aged 2 material after FGHAZ simulation. It is expected that the dislocation densities will increase in the FGHAZ samples due to the martensitic transformation (Section 2.4.1).

Pešička, Aghajani, Somsen *et al.* (2010) measured  $1.01 \times 10^{14} \text{ m}^{-2}$  in the as-received parent X20 steel and  $0.68 \times 10^{13} \text{ m}^{-2}$  after 140 000h long-term creep aging (rupture). Yadav, Kalácska, Dománková *et al.* (2016) measured for new X20 steel an internal dislocation density of  $2.33 \pm 0.63 \times 10^{14} \text{ m}^{-2}$ . These densities were measured under two-beam conditions from TEM and HAADF-STEM images. The difference in using TEM and ADF-STEM for dislocation analyses is discussed in Section 3.6.7. It is not clear if they accounted for the fact that only half the dislocations are visible under two beam conditions for X20 steel (Baker 2001). In this study, the internal dislocation density was not measured under two beam conditions for reasons discussed in Section 3.6.7. Even though the ADF-STEM images were acquired from the un-tilted specimen, some of the micro-grains may be tilted such that the invisibility criterion is invoked. This uncertainty is the main limitation of the measured internal dislocation density data.

In addition, the measurements are specimen thickness dependent and as discussed in Section 3.7.7 some areas were thin due to the criterion of analysing the same areas as for TKD and EFTEM for cross-correlation. Also, the absolute thickness measurement conversion has an error of approximately 20% (Section 3.6.5). However, the creep aged 2 simulated twin-jet electropolished specimen has the thickest areas overall (**Table 3.13**), resulting in lower contrast and the less visible the internal dislocations (Section 3.6.7). The ADF-STEM image for the creep aged 2 simulated twin-jet electropolished specimen in **Figure 4.69** illustrates this point. For this specimen, the thickest areas were measured. Loss of dislocations due to surface relaxation effects in thin areas may also contribute to inaccuracies in the measured density values.

Consequently, the internal dislocation densities measured for this specimen has a high probability of being underestimated. For all the materials, it was difficult to distinguish internal dislocations from SGB in areas of high dislocation density. Therefore, the

measured internal dislocation densities should be interpreted with caution. To minimise the effect of the heterogeneous nature of the dislocation densities large enough sampling areas must be analysed, which is planned as future work.

Considering the dislocation densities calculated from the XRD results (**Figure 4.71**), all the values calculated from Equation (3.13) are of the same order of magnitude as the internal dislocation densities. The two datasets follow opposite trends for the new and creep aged 1 simulated FGHAZ materials, with the Equation (3.12) data following the same trends as the measured internal dislocation densities. The densities measured from Equation (3.12) is much lower than that measured from Equation (3.13). This is expected since Equation (3.12) determines the density from only the strain broadening, which is assumed to be from the mobile dislocations. Equation (3.13) considers the density from the crystallite size, which is the coherently diffracting domains, as well. Since the crystallite size was determined as smaller than the corresponding substructure sizes, the size of domains within the substructure (SGB) is measured with XRD. Therefore, the density from the crystallite size in Equation (3.13) can only correspond to the density of the mobile dislocations within the substructure.

Only the dislocation densities determined from Equation (3.13) will now be further considered since the difference between values calculated from Equation (3.12) is small. A dislocation density of  $0.202 \pm 0.003 \times 10^{14} \text{ m}^{-2}$  was determined for the new parent material. For new parent X20 material with no PWHT, the mobile dislocation density has been determined by Pešička, Kužel, Dronhofer and Eggeler (2003) as  $0.86 \times 10^{14} \text{ m}^{-2}$  from XRD. The much smaller measured value is most probably due to the annealing of the mobile dislocations during PWHT and different starting materials. Yadav, Kalácska, Dománková *et al.* (2016) measured for the new X20 steel a mobile dislocation density of  $1 \times 10^{14} \text{ m}^{-2}$  using Equation (3.12), which is much higher than the value of  $0.088 \times 10^{14} \text{ m}^{-2}$  calculated in this study from the same equation using the lattice strain value in **Table 4.10** instead of  $\varepsilon_0$  from strain. The difference in values is mainly due to Yadav, Kalácska, Dománková *et al.* (2016) not implementing the  $\varepsilon_0$  from strain value to determine this density (Section 3.7.7).

From the new parent material value, the mobile dislocation density drops by 1.5 times in the creep aged 1 parent material to a value of  $0.137 \pm 0.002 \times 10^{14} \text{ m}^{-2}$ , but the density increases to  $0.226 \pm 0.004 \times 10^{14} \text{ m}^{-2}$  in the creep aged 2 parent material. This anomalous trend corresponds to that observed for the hardness in **Figure 4.3**. Subsequently, the highest mobile dislocation density for the simulated FGHAZ materials is measured in the creep aged 2 material with a dislocation density of  $0.202 \pm 0.003 \times 10^{14} \text{ m}^{-2}$  which is the same density measured for the new parent material. Mobile densities of  $0.149 \pm 0.003 \times 10^{14} \text{ m}^{-2}$  and  $0.137 \pm 0.002 \times 10^{14} \text{ m}^{-2}$  was measured for the new and creep aged 1 simulated FGHAZ materials, respectively. After FGHAZ simulation, the mobile dislocation density decreases for each material type, with the most significant decrease in the new material and the smallest decrease in the creep aged 1 material.

The advantage of XRD is that the total volume of the specimen is considered, and the values measured are representative of the bulk of the material. However, XRD analysis suffers the following main limitations:

- The quality of the sample surface preparation affects the acquired spectra.
- The measured crystallite size and strain values are dependent on the input parameters used in TOPAS for the fitting of the peak profiles.
- Only the size of the coherent domains in the sample is measurable and not purely the micro-grain size, which is of importance for the creep strength.
- There are still many uncertainties in the formulae (Equations (3.12) and (3.13)) used to convert the micro-strain values into dislocation density values and further work is still required to determine the accuracy of these formulae to determine the mobile dislocation density. The accuracy of the constants of  $F$  and  $k$  in Equation (3.12) also need to be verified.

The reported error is a systematic error due to fitting determined in TOPAS™ and it is small. To determine the actual scatter in the XRD measurements, a reproducibility study of XRD analysis is included in the future work of this study.



# CHAPTER 5

## RECOMMENDATIONS FOR A MICROSTRUCTURE-BASED MODEL FOR REMAINING LIFE ASSESSMENT

---

### 5.1 INTRODUCTION

Chapter 4 provided the quantitative microstructural measurements performed to determine the microstructural state of each material. This chapter aims to demonstrate the use of the measured microstructural parameters as input into an existing microstructure-based creep model, such as the Back-Stress model, to predict the creep strength. Subsequently, recommendations are given for the use of a microstructure-based approach for remaining life assessment.

### 5.2 MICROSTRUCTURAL INPUT PARAMETERS

**Figure 5.1** summarises the main microstructural parameters for each parent and simulated FGHAZ X20 material. The subgrain size  $\lambda_{sg}$  is reported as the micro-grain size measured from the TKD MO > 5° data and the mobile dislocation density  $\rho_m$  as the values calculated from the XRD results with Equation (3.13). These values were chosen since they are the main microstructural contributions to creep strength. The values are plotted relative to the new material for comparison.

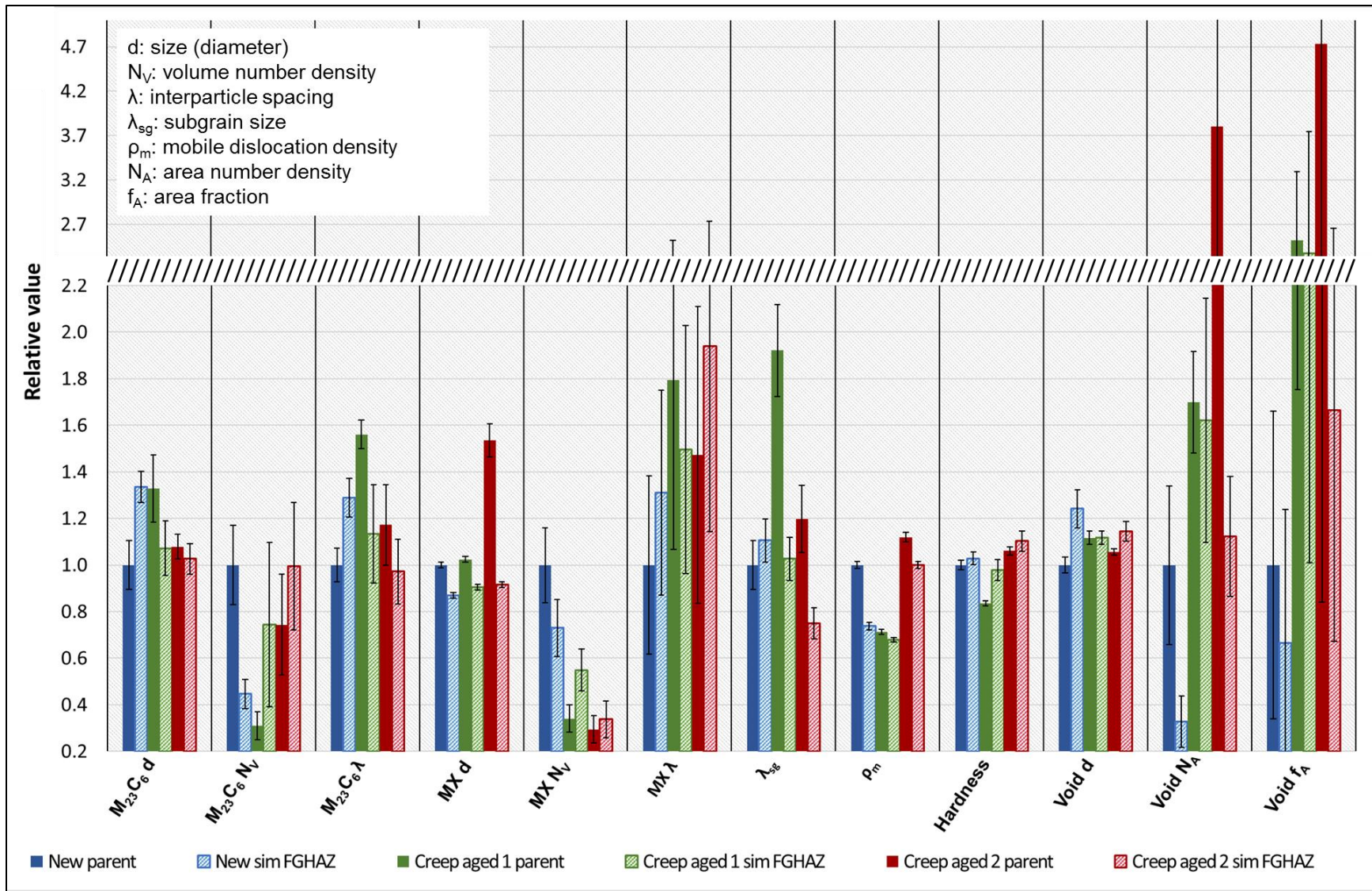


**Figure 5.1:** Summary of measured microstructural parameters for all materials. Values are plotted relative to the new parent material. Pattern filled columns correspond to simulated FGHAZ results.

### 5.3 BACK-STRESS MODEL APPLICATION

To quantify the creep strength of each material, the mean values of the microstructural parameters were used to calculate the strengthening from the precipitates (PH), dislocations (DH) and subgrains (SBH) using Equations (2.16), (2.19) and (2.21), respectively. The calculated values were linearly combined as in Equation (2.14) to give the back-stress. These values are summarised in **Figure 5.2**.

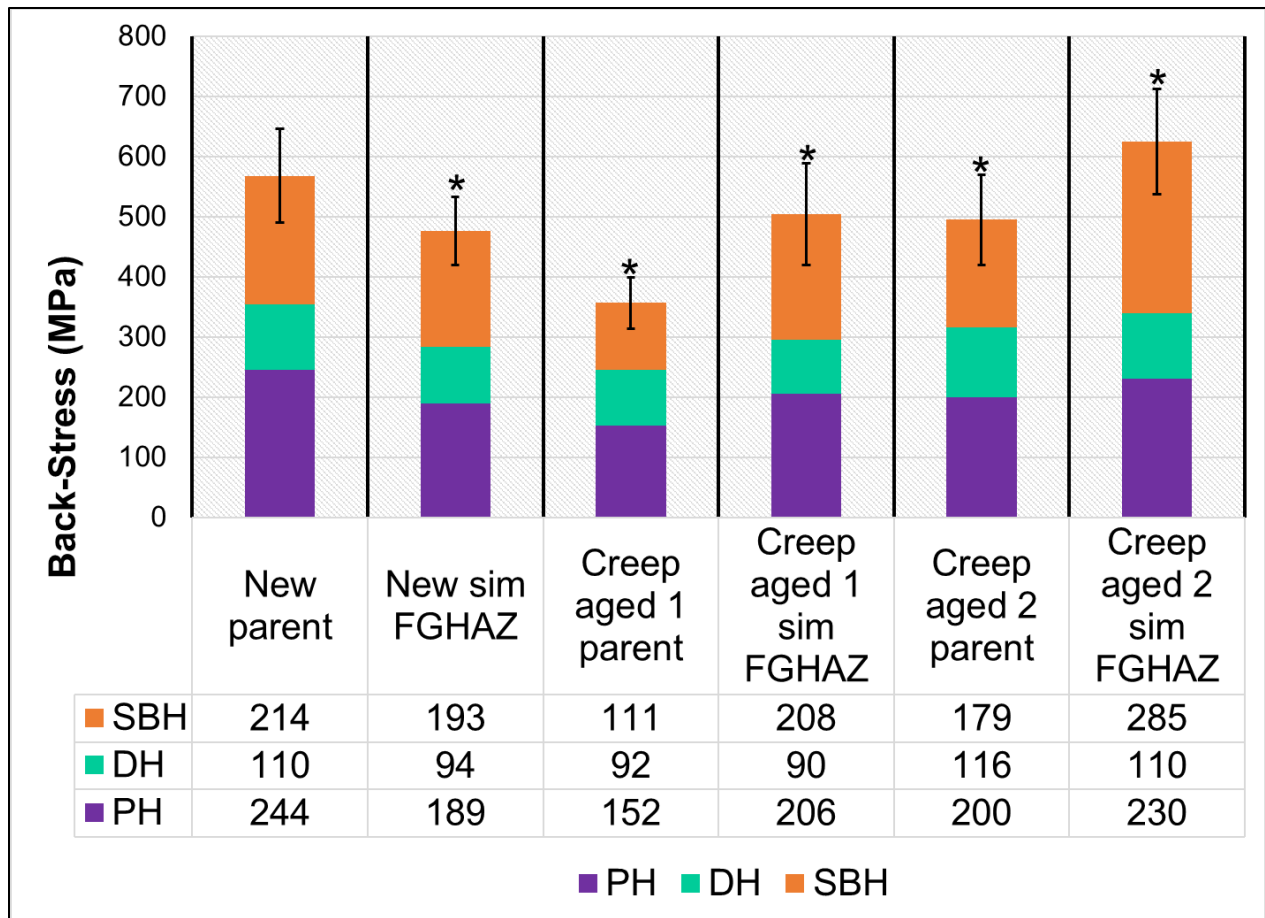


**Figure 5.2:** Back-stress as a linear combination of precipitate (PH), dislocation (DH) and sub-boundary (SBH) strengthening for each material determined using mean values and Equations (2.16), (2.19) and (2.21). The back-stress value in MPa is indicated in the data table. An asterisk indicates that the difference in back-stress value compared to the new parent material is statistically significant.

For each material, the mobile dislocations have the smallest strength contribution. The most substantial strength contribution for the parent materials was from the precipitates. Similar strength contributions from the precipitates and subgrains were calculated for the new and creep aged 1 simulated FGHAZ materials, while the subgrains have the most significant strength contribution in the creep aged 2 simulated FGHAZ material.

Instead of determining the creep strength from the back-stress that is only a linear combination of the creep strength contributions, the back-stress from a combined obstacle spacing value (Equation (2.25)) can instead be calculated using Equation (2.26). To compare the difference in predicted creep strength among the simulated FGHAZ materials, the combined back-stress, along with the other strength contributions such as PH, DH, SBH and approximate Zener pinning pressure of boundary  $M_{23}C_6$  carbides (Equation (2.5)) are plotted in **Figure 5.3** relative to the values calculated for the new simulated FGHAZ material.

The same trends are observed for the combined back-stress, which only considers the Orowan strengthening mechanism from the precipitates, and Zener pinning pressure. No significant difference in PH, which is the Orowan stress from the precipitates acting as obstacles to dislocation motion, is observed for the simulated FGHAZ materials. The creep aged 1 simulated material does not significantly differ in creep strength compared to the new simulated FGHAZ material, except for decreased DH. A consistent increase in DH, SBH, combined back-stress and Zener pinning pressure is observed for the creep aged 2 simulated FGHAZ material. Subsequently, from a microstructure-based approach using the back-stress concept and Zener pinning pressure, it is concluded that the creep aged simulated FGHAZ X20 material has a higher creep strength than the new simulated FGHAZ material. Upon further creep exposure, the new simulated FGHAZ material is expected to fail before the creep aged simulated FGHAZ material. This conclusion

contradicts the known phenomenon of weldments failing in the FGHAZ on the creep aged material side during creep exposure.

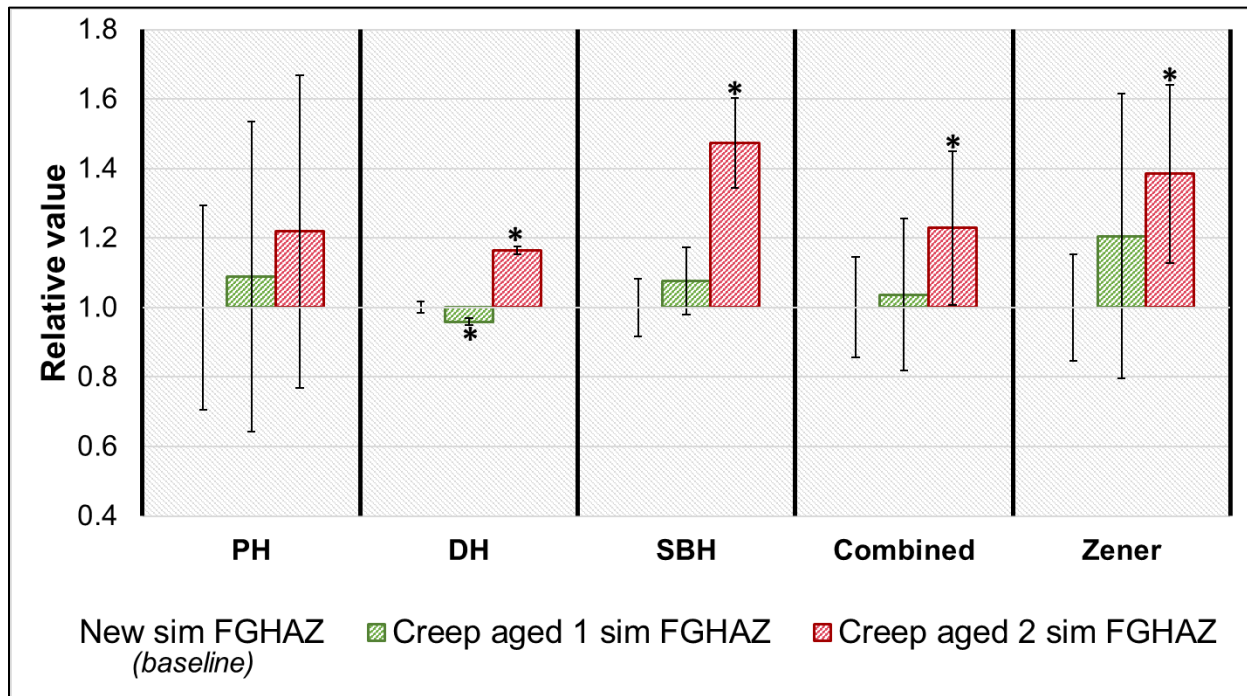


**Figure 5.3:** Difference in strengthening mechanisms (Equations (2.16), (2.19), (2.21), (2.26) and (2.27) of new and creep aged simulated FGHAZ X20 materials plotted relative to new simulated FGHAZ values. The asterisk indicates statistically significant differences in the mean values between the creep aged simulated FGHAZ material and the new simulated FGHAZ material.

#### 5.4 RECOMMENDATIONS FOR A MICROSTRUCTURE-BASED MODEL FOR REMAINING LIFE ASSESSMENT

The only microstructural parameter not considered in the microstructure-based model above is the creep voids. Smaller in size, but much higher densities and area fractions of creep voids were measured for both creep aged simulated FGHAZ materials compared to the new simulated FGHAZ material (Table 4.2). Therefore, the creep aged simulated FGHAZ materials have a higher degree of creep damage than the new simulated FGHAZ

material. This creep damage is inherited from the corresponding parent materials. Since it is known that upon further creep aging that the voids will grow, combine and eventually form Type IV cracks in the FGHAZ, it is concluded that the creep aged simulated FGHAZ material is expected to fail before the new simulated FGHAZ material. In the case of an actual weldment, this failure will occur slower due to mechanical constraint from the stronger surrounding material. Therefore, the creep void considerations correspond with weldments preferentially failing in the FGHAZ on the creep aged material side during creep exposure. This proves the validity of the explanation proposed by Rasiawan (2017) that the pre-existing creep voids in the creep aged material prior to welding that are the cause for failure in the FGHAZ of the creep aged side of the weldment.

It is known that creep cavitation originates from the decohesion between  $M_{23}C_6$  carbides and the matrix caused by stress concentrations resulting from GBS, inter-lath boundary deformation or dislocation pile-ups breaking through the boundary (Gooch 1982). The sites of decohesion then act as a preferred nucleation site for cavities. Therefore, it is not just the creep voids that must be considered in a microstructure-based approach for life assessment, but also the microstructural features that will enhance decohesion of the precipitate and matrix interface.

It can be concluded from the key findings of the study that the creep aged simulated FGHAZ materials have the following microstructural features in addition to the creep voids that distinguish them from the new simulated FGHAZ material:

- The corresponding long-term creep aged parent materials have much larger  $M_{23}C_6$  carbides than the new parent material and therefore the undissolved carbides upon heating during welding are much larger and enhanced coarsening of these carbides occur in the FGHAZ during cooling. Consequently, very large  $M_{23}C_6$  carbides are found in the creep aged simulated FGHAZ materials in addition to small newly formed carbides.
- These materials contain equiaxed micro-grains that have the characteristics of recovered subgrains.

Due to the higher boundary density in the FGHAZ, enhanced diffusion along GB occurs during further creep exposure. Subsequently, the large  $M_{23}C_6$  carbides will rapidly coarsen and substantial loss in the pinning pressure of the MGB by the carbides results. The rate of micro-grain growth and hence softening is increased. Therefore, inter-lath boundary deformation and GBS are caused, which in turn will result in the decohesion of the carbides and the matrix. Finally, new creep cavities will nucleate and combine with the pre-existing voids to eventually cause Type IV failure. Softening is further enhanced by the growth of the recovered pre-existing equiaxed micro-grains that is not present in the new simulated FGHAZ material.

Consequently, in conclusion, it is recommended that a microstructure-based model for remaining life assessment of welded components and setting of weldability limits need to include damage parameters for void nucleation and growth, and  $M_{23}C_6$  carbide evolution considering Zener pinning pressure. Therefore, the back-stress model and semi-physical creep models such as that developed by Oruganti, Karadge and Swaminathan (2013), which considers subgrain and MX precipitate evolution as the key parameters, are not applicable to 9-12% Cr martensitic steels. The semi-physical creep models developed by Yadav, Sonderegger, Muhammad and Poletti (2016), and Yin and Faulkner (2006) already take into account to some extent the suggested parameters. Therefore, it is proposed that these models are further developed for remaining life assessment and determination of weldability limits. These models need to be developed from the results acquired from samples that had been creep aged under controlled conditions such as was done in the study of Aghajani (2009).

# CHAPTER 6

## CONCLUSIONS

---

The results of this study have been provided and discussed in Chapter 4, and the final conclusions can now be drawn. This chapter serves as the penultimate chapter of this study and presents the final conclusions from this study. The main aim of the study was to investigate the microstructural evolution when welding on creep aged 9-12% Cr martensitic steels using advanced electron microscopy techniques. This aim was achieved by applying different techniques such as SE-SEM imaging, EBSD, TKD, EDS, ADF-STEM and CBS imaging on parent and simulated FGHAZ materials prepared from new and long-term creep aged 12% Cr (X20) steel. Qualitative and quantitative analysis was performed on the acquired results to determine the microstructural state of each material by considering the main creep strength contributions such as voids,  $M_{23}C_6$  carbides, MX, Laves phase and Z-phase precipitates, micro-grains, substructure and dislocations.

The present study presents a detailed investigation on the evolution of the microstructure during welding on new and service exposed (creep aged 1 = 535°C; 16.1 MPa; 156 kh and creep aged 2 = 555°C; 17.0 MPa; 130 kh) 12% Cr (X20) martensitic steel. This study was carried out in order to understand the impact of welding on prior creep exposed 9-12% Cr material and to explain the preferential failure of weldments in the FGHAZ of the creep aged material side instead of the new material side.

It is difficult to obtain reliable and representative results from the narrow FGHAZ caused by the microstructural gradient within the weldment region. To have a much larger sampling volume available to study, the FGHAZ was simulated in this study using a Gleeble™ weld thermal cycle simulator ( $T_p = 980^\circ\text{C}$ ; heating rate = 200 °C/s; holding time = 4 seconds). The successful verification of the simulation of the FGHAZ was achieved by observing that the hardness of the new FGHAZ simulated material was within the



range measured for the FGHAZ within an actual weldment performed on the same new X20 material. By reconstruction of the PAG from EBSD maps and observing fine PAG in each simulated FGHAZ material, the success of the simulation of the FGHAZ was further confirmed. Homogeneous simulation of the FGHAZ microstructure through the cross-section of the material, which was the plane of investigation for all analyses, was confirmed by analysing LM micrographs taken across the cross-section of each simulated FGHAZ material.

To summarise the microstructural difference between the new and creep aged simulated FGHAZ materials, the parameters of the creep aged materials are plotted relative to the parameters of the new material in **Figure 6.1**. The measured parameters of the simulated FGHAZ materials are plotted relative to the corresponding parent microstructural parameters in **Figure 6.2** to illustrate the effect of the FGHAZ simulation on the X20 material. The subgrain size  $\lambda_{sg}$  is reported as the micro-grain size measured from the TKD  $MO > 5^\circ$  data and the mobile dislocation density  $\rho_m$  as the values calculated from the XRD results with Equation (3.13). These values were chosen since they are the main microstructural contributions to creep strength. Unpaired t-testing was performed on the values to establish if the differences in the mean are statistically significant.

The main conclusions that can be drawn regarding the difference in microstructure between new and creep aged simulated FGHAZ materials are (**Figure 6.1**):

- There were no significant variations in the hardness among the simulated FGHAZ materials. The creep aged 2 simulated FGHAZ material had the highest hardness, which corresponds to its parent material having the highest hardness of the parent materials.
- Pre-existing voids (1 to 3  $\mu\text{m}$  ECD) were observed in the new parent material with both LM and SE-SEM imaging. The origin of these voids remains to be determined.
- The most significant difference between new and creep aged simulated FGHAZ materials is their void parameters. The creep aged simulated FGHAZ materials

have smaller voids with higher  $N_A$  and  $f_A$  compared to the new simulated FGHAZ material.

- Apart from the voids, the other most substantial difference between the new and creep aged simulated FGHAZ materials was observed in  $M_{23}C_6$  carbide parameters. The creep aged simulated FGHAZ materials have  $M_{23}C_6$  carbides with a smaller mean size  $d$ , higher mean number densities  $N_V$  and smaller mean interparticle spacings  $\lambda$  compared to the new simulated FGHAZ material. The differences in  $N_V$  and  $\lambda$  of the creep aged 1 simulated FGHAZ material was not significant. From the measured  $M_{23}C_6$  carbide ECD distributions and qualitative analysis of the CBS images, it was observed that a combination of large carbides ( $\varnothing > 300$  nm) with a higher fraction of small newly formed carbides exists in the creep aged simulated FGHAZ materials. In the case of the new simulated FGHAZ material, the carbides were equisized and no high fraction of small carbides is observed as for the creep aged simulated FGHAZ materials. Consequently, a larger mean size is measured. These observations are explained by the fact that the corresponding long-term creep aged parent materials have much larger  $M_{23}C_6$  carbides than the new parent material and therefore the undissolved carbides upon heating during welding are much larger and enhanced coarsening of these carbides occur in the FGHAZ during cooling. Consequently, very large  $M_{23}C_6$  carbides are found in the creep aged simulated FGHAZ materials in addition to small newly formed carbides. This higher fraction of smaller carbides resulted in the smaller mean size of the carbides in the creep aged simulated FGHAZ materials.
- The important difference is that no large carbides was observed in the new simulated FGHAZ material as in the creep aged simulated FGHAZ materials. Large carbides are known to have a decreased pinning pressure on boundaries and therefore the boundaries can easily move during creep (Kostka, Tak, Hellmig *et al.* 2007). Stress concentrations and subsequent decohesion between the carbides and matrix occurs, resulting in preferred void nucleation sites. Therefore, upon further creep exposure Type IV cracking is expected to be initiated sooner in

the creep aged simulated FGHAZ material compared to the new simulated FGHAZ material.

- Both creep aged simulated FGHAZ materials have slightly larger, more widely spaced and lower  $N_V$  of MX precipitates compared to the new simulated FGHAZ material.
- Smaller micro-grains were measured in the creep aged simulated FGHAZ material compared to the new simulated FGHAZ material, but only the micro-grains in the creep aged 2 simulated FGHAZ were significantly smaller.
- The substructure size was found to be much smaller than the micro-grain size. Among the simulated FGHAZ materials, the creep aged 1 material had the largest mean substructure size and the creep aged 2 material the smallest. However, overall the differences in substructure size of the simulated FGHAZ materials are not large.
- Distinct equiaxed micro-grains were observed only in the creep aged simulated FGHAZ materials. By analysing the TKD, ADF-STEM, EFTEM and CBS results of each micro-grain, it was possible to characterise these micro-grains. They were found to be bounded by boundaries with  $MO > 10^\circ$  and decorated by  $M_{23}C_6$  carbides and MX precipitates, their diameters ranged from approximately 1 to 1.5  $\mu\text{m}$ , they were surrounded by micro-grains with higher dislocation densities, and they had little to no SGB or dislocations in their interiors. This analysis demonstrated the powerful capability of cross-correlative microscopy to determine elemental, crystallographic, size and location information of microstructural features. It remains yet to be determined whether these characteristic round micro-grains are formed due to recrystallisation during the FGHAZ simulation and the extent of their effect on the creep strength. Since this, a distinct feature only observed in the creep aged simulated FGHAZ materials that are known to have the lowest creep properties during subsequent creep aging, these micro-grains may play some role in the degraded creep strength.

- Preferential texturing develops in the simulated FGHAZ materials since the number of variant intersections decreases after FGHAZ simulation of the parent materials. The extent of this texturing is increased for the creep aged simulated FGHAZ materials.
- A heterogeneous distribution of dislocations inside the substructure of the creep aged parent and simulated FGHAZ materials was observed. The differences in the  $\rho_m$  values of the simulated FGHAZ materials were found to be not large. Similar trends are observed among the  $\rho_m$  values of the simulated FGHAZ materials as for the hardness: the  $\rho_m$  is lower in the creep aged 1 simulated FGHAZ material and slightly higher in the creep aged 2 simulated FGHAZ material compared to the new simulated FGHAZ material.

The microstructure evolution after FGHAZ simulation on parent material can be summarised as follows (**Figure 6.2**):

- The hardness of creep aged materials has been shown by Sawada, Miyahara, Kushima *et al.* (2005) to increase with a decrease in dislocation spacing within the laths (increase in dislocation density), spacing between the precipitates and HAGB spacing. An increase in hardness was measured for all the simulated FGHAZ materials from the corresponding parent materials, with the most significant increase for the creep aged 1 material. No consistent increase in dislocation density and decrease in precipitate spacing across all the simulated FGHAZ materials is observed from the results. This leads to the conclusion that it may be the decrease in HAGB spacing that causes the increase in hardness, which is a reasonable conclusion since fine PAG form during FGHAZ simulation leading to an increase in the HAGB density.
- The void size increased and  $N_A$  decreased after FGHAZ simulation of the new and creep aged 2 parent materials. Lower  $f_A$  of the voids was measured for each simulated FGHAZ material compared to the parent material, but only the decrease in the creep aged 2 simulated FGHAZ material is significant. Consequently, a

disappearance of voids, whether entirely or to a smaller size of less than 1  $\mu\text{m}$ , is observed after FGHAZ simulation of the creep aged 2 parent material. This is possibly due to the volume changes associated with the phase transformations during welding. In addition, the larger void size and lower  $N_A$  indicate that growth and coalescence of voids occurred during FGHAZ simulation. This evolution of the voids in the simulated FGHAZ materials was confirmed by SE-SEM imaging.

- Even though the  $N_A$  does not increase after FGHAZ simulation, the SE-SEM results show that cavities with  $ECD < 1 \mu\text{m}$  is observed in the simulated FGHAZ materials. Therefore, it is not possible to conclude whether void nucleation has occurred during FGHAZ simulation. However, the SE-SEM also indicated stronger localisation of small cavities ( $ECD < 3 \mu\text{m}$ ) in the creep aged simulated FGHAZ material compared to the parent material. Therefore, upon further creep exposure, these closely spaced cavities will easily coalesce and promote Type IV cracking in the creep aged simulated FGHAZ materials. Eggeler, Earthman, Nilsvang and Ilschner (1989) has stated that cavity coalescence is not the main creep rupture criterion, but rather the formation and growth of microcracks from closely spaced cavitating grain boundary interfaces. Based on this criterion, it seems that cavitation damage has progressed the furthest in the creep aged 2 simulated FGHAZ material.
- The SE-SEM imaging results showed that larger cavities are mainly located on MGB and the smaller cavities also form inside the micro-grains for both the parent and simulated FGHAZ materials. Thus, intergranular and transgranular cavitation has occurred.
- No preferential cavitation damage was observed along the PAGB for any of the materials. Also, the cavities were found on both LAGB and HAGB. Thus, it can be concluded that there is no preferential creep cavitation perpendicular to the longitudinal direction of the steam pipe.
- The simulation of the FGHAZ had opposite effects on the  $M_{23}C_6$  carbide parameters in the new and creep aged parent materials. For the new X20 steel,

the carbides coarsened and decreased in  $N_V$ , as well as became further spaced from the parent to simulated FGHAZ material. On the other hand, the mean size and  $\lambda$  decreased, and the  $N_V$  increased significantly from the creep aged 1 parent to simulated FGHAZ materials. These effects are ascribed to the  $M_{23}C_6$  carbides in the parent material and Ostwald ripening during the FGHAZ simulation.

- A decrease in the mean MX size is observed after FGHAZ simulation. For both creep aged simulated FGHAZ materials the MX precipitate  $N_V$  is higher than the corresponding parent material, but for the new simulated FGHAZ the MX precipitate  $N_V$  is lower than the new parent material. The MX precipitates in the creep aged 1 simulated FGHAZ material became more closely spaced after FGHAZ simulation, while the spacing increased after FGHAZ simulation in the new and creep aged 2 simulated FGHAZ materials. By the Orowan stress (PH) the MX precipitates have been related to creep strength. The direct influence of the MX precipitates on Type IV cracking is not yet known. However, the trends in the MX precipitate parameters after FGHAZ simulation indicate an increase in creep strength after FGHAZ simulation of the creep aged materials.
- Mo-enriched Laves phase precipitates were observed in the CBS images of the creep aged parent and simulated FGHAZ materials. Due to the low numbers of these observed Mo-enriched Laves phase precipitates, no meaningful quantitative analysis was performed. Most of the Laves phase precipitates were located adjacent to  $M_{23}C_6$  boundary carbides, which confirmed the nucleation mechanism proposed by Isik, Kostka and Eggeler (2014).
- Precipitates were observed in the creep aged 2 parent materials that are enriched with both Cr and V. Each of these precipitates was embedded in a Cr-enriched  $M_{23}C_6$  carbide(s). These precipitates were identified as possibly being of the Z-phase (CrVN) type since previous studies have shown that its nucleation process is associated with Cr diffusion into V-enriched MX precipitates (Cipolla, Danielsen, Venditti *et al.* 2010, Yan, Wang, Shan and Yang 2013). Their mean V:Cr ratio was calculated as  $1.0 \pm 0.1$ .

- No Z-phase precipitates were observed in the corresponding creep aged simulated FGHAZ materials since the dissolution temperature of Z-phase precipitates in X20 are approximately 800 °C (Danielsen 2007) and upon cooling after welding MX precipitates are preferentially formed. This is further confirmed by the increase in  $N_V$  of the MX precipitates in the creep aged simulated FGHAZ materials after FGHAZ simulation.
- A high number of nucleated Z-phase precipitates in the creep aged 2 parent material is of great concern since the premature failure of 9-12% Cr martensitic steel components have occurred due to rapid Z-phase formation (Hald 2008). The creep aged 2 pipework had operated for a shorter time period than the creep aged 1 pipework but at high temperature and pressure. It also had higher Si and Nb content. Therefore, one of these differences or a combination of them may have promoted Z-phase formation.
- The micro-grains did not significantly coarsen during FGHAZ simulation of the new parent material. In the case of FGHAZ simulation of the creep aged parent materials, the micro-grain size decreased statistically significantly in the corresponding creep aged simulated FGHAZ materials. It was also observed qualitatively that the micro-grains became more equiaxed after FGHAZ simulation.
- The  $\rho_m$  decreases in each simulated FGHAZ material after FGHAZ simulation of the parent materials, which is contrary to the fact that dislocations increase during the martensitic transformation that occurs during welding. However, the decrease could be explained by the annealing of the mobile dislocations during PWHT. For the creep aged 1 simulated material, the decrease is not statistically significant. It remains to be determined if this dislocation density, which was obtained using XRD, is purely representative of the mobile dislocations.

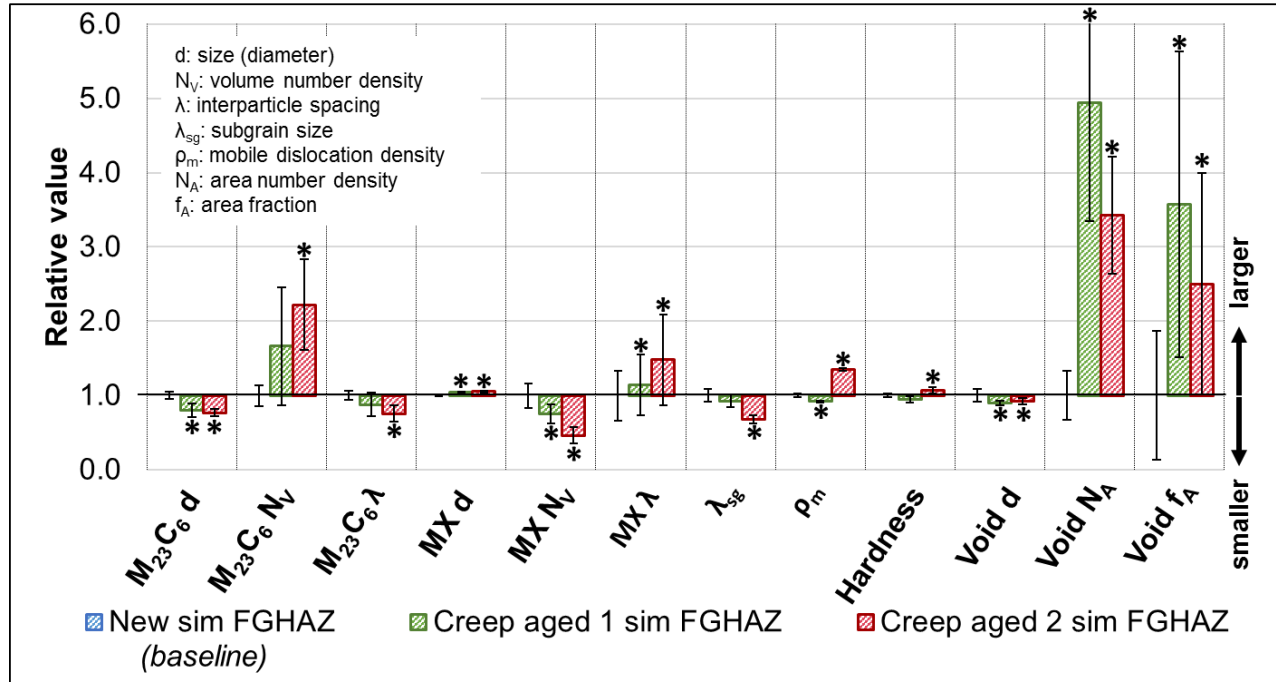
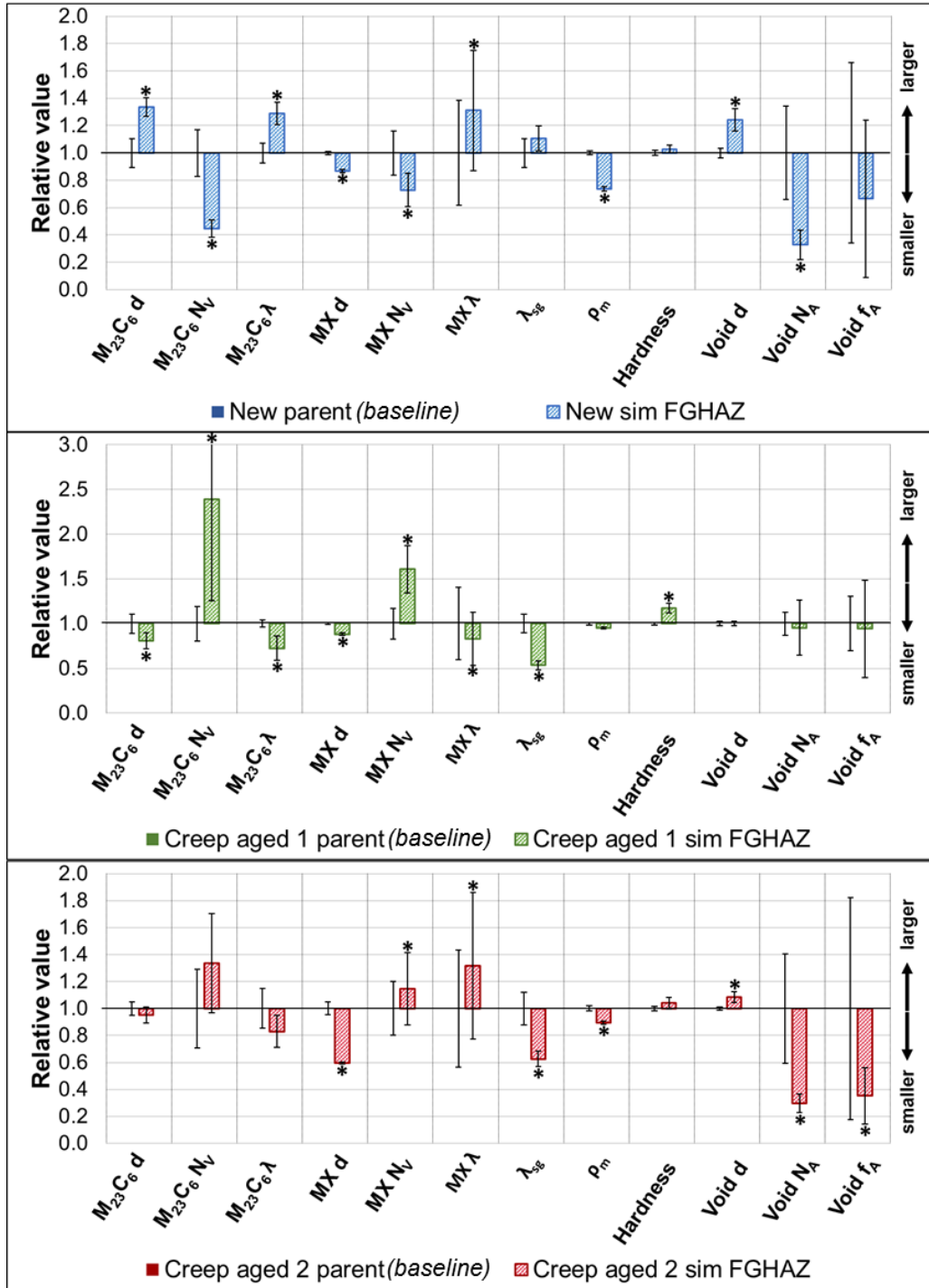


**Figure 6.1:** Difference in microstructural parameters of new and creep aged simulated FGHAZ X20 materials plotted relative to new simulated FGHAZ values. The asterisk indicates statistically significant differences in the mean values between the creep aged simulated FGHAZ material and the new simulated FGHAZ material.





d: size (diameter)  
 $N_V$ : volume number density  
 $\lambda$ : interparticle spacing  
 $\lambda_{sg}$ : subgrain size  
 $\rho_m$ : mobile dislocation density  
 $N_A$ : area number density  
 $f_A$ : area fraction

**Figure 6.2:** Difference in microstructural parameters of parent and corresponding simulated FGHAZ for new (blue), creep aged 1 (green) and creep aged 2 (red) X20 materials plotted relative to new simulated FGHAZ values. The asterisk indicates statistically significant differences in the mean values between the parent and corresponding simulated FGHAZ material.

The deliverables, based on the research objectives, that were achieved with this thesis include:

- (i) A literature review of Type IV cracking in 9-12% Cr martensitic steels to gain a better understanding of this mechanism.
- (ii) A literature review of existing microstructure-based creep-models.
- (iii) Developing microstructural measuring techniques to quantify the voids, precipitates, sub-grains and dislocation density.
- (iv) Determination of the microstructural state of creep aged parent and FGHAZ material by the quantitative measurement of the microstructure.
- (v) Recommendations made about the use of a microstructural-based assessment of 9-12%Cr steels for determining their weldability limits.

Hence, the research question “*How does the microstructure of a creep aged 9-12% Cr martensitic steel evolve when welded on in comparison to a virgin 9-12% Cr martensitic steel?*” and research objectives have been adequately addressed.

In conclusion, the pre-existing creep voids in the creep aged parent material and the large  $M_{23}C_6$  carbides ( $\varnothing > 300$  nm) in the FGHAZ after welding are identified as the main microstructural contributions that could accelerate Type IV failure in creep aged 9-12% Cr martensitic steel weldments. Techniques that quantify these two microstructural features, such as those developed in this study, provide the possibility to determine the weldability of these steels.

---

# CHAPTER 7

## **LIMITATIONS AND CALL FOR FUTURE RESEARCH**

---

Most of the limitations of the experimental techniques and methods have been discussed in Chapters 3 and 4. The main limitation of the microstructural measurements is the inaccuracies caused by the thresholding procedures using MIPAR™, especially when thresholding the boundaries from the TKD GB maps and CBS images. The procedures could only be developed to be semi-automatic since the parameters in the algorithms used needed to be manually re-adjusted for the different material types and in some instance's artefact features had to be removed manually. Even though the thresholding procedures employed isolated the desired features as accurately as possible, the microstructural measurements may have been over- or underestimated due to over-segmentation or exclusion of some features. Another limitation of the study that had to be kept in mind during analyses is that the initial X20 materials of the creep aged pipework may have undergone different processing during manufacturing, resulting in slightly different chemical compositions and sizes of the initial microstructural parameters.

The microstructural evaluation has been performed on simulated FGHAZ materials and not actual weldments. Nevertheless, the microstructure was verified to be that of the FGHAZ and the new simulated FGHAZ material measurements corresponded to that available for the FGHAZ of actual X20 weldments. Type IV cracking also occurred in the ICHAZ and future research will attempt to replicate this study on simulated ICHAZ samples.

Although the microstructural analyses have been performed on more than one sample of each material type, a representative sampling of the microstructure remains a limitation and future work will include the application of the microstructural measuring techniques on larger areas and different samples of the same material. Also, the void analyses will be repeated on the same specimens as for this study to observe the variation, if any, in

the void parameters of a single sample. From these results, it can be confirmed if there is a disappearance of voids in the FGHAZ during welding and if so, further research will include explaining this phenomenon. In addition, surface replica measurements from the same creep aged 2 pipework, but at a different location along the steam pipe have given lower void number densities. This illustrates the importance of sampling from the location on the steam pipes that will show the highest creep damage to ensure accurate life assessment. Future research would include a microstructural study of samples sectioned from the same pipe, but at different locations to determine the variation in results as a function of sampling location. Other future research will include:

- (i) High-Resolution EBSD/TKD to better resolve the SGB and accurately determine boundary dislocation density.
- (ii) Refining of the ARPGE software variables for more accurate reconstruction of the PAG and using the ARPGE software to better analyse the texture in the materials after the acquisition of more EBSD maps.
- (iii) Perform void analyses perpendicular to the circumferential stress of the pipe.
- (iv) Perform further creep void analysis using Laser Confocal Microscopy to map out the height variations in the samples to distinguish between the surface contamination and the voids.
- (v) Further analysis of the equiaxed micro-grains observed in the creep aged simulated FGHAZ materials using correlative microscopy.
- (vi) Perform a reproducibility study of XRD analyses.
- (vii) A strategy to exclude Z-phase particles from the EFTEM V elemental maps acquired from the extraction replica specimens and further analyse the Z-phase precipitates in the creep aged 2 parent material using selected area diffraction and high-resolution TEM.
- (viii) Perform uniaxial and small punch creep tests, as well as other mechanical tests on the simulated FGHAZ materials to determine if the creep aged simulated FGHAZ materials have lower creep and mechanical properties than the new simulated FGHAZ materials.
- (ix) Perform the creep tests in (vii) as interrupted tests until failure to evaluate the failure (creep void) development of Type IV cracking.

# REFERENCES

Abd El-Azim, M., El-Desoky, O., Ruoff, H., Kauffmann, F. and Roos, E. (2013). "Creep fracture mechanism in welded joints of P91 steel." Materials Science and Technology **29**(9): 1027-1033.

Abd El-Azim, M., Nasreldin, A., Zies, G. and Klenk, A. (2005). "Microstructural instability of a welded joint in P91 steel during creep at 600 C." Materials Science and Technology **21**(7): 779-790.

Abdallah, Z., Gray, V., Whittaker, M. and Perkins, K. (2014). "A critical analysis of the conventionally employed creep lifing methods." Materials **7**(5): 3371-3398.

Abdallah, Z., Perkins, K. and Arnold, C. (2018). Creep Lifing Models and Techniques. Creep, InTech.

Abe, F. (1999). Proceedings of 4th International Conference on Recrystallization and Related Phenomena, Sendai, JIM.

Abe, F. (2003). "Effect of quenching, tempering, and cold rolling on creep deformation behavior of a tempered martensitic 9Cr-1W steel." Metallurgical and materials transactions A **34**(4): 913-925.

Abe, F. (2004). "Coarsening behavior of lath and its effect on creep rates in tempered martensitic 9Cr-W steels." Materials Science and Engineering: A **387**: 565-569.

Abe, F. (2008). Strengthening mechanisms in steel for creep and creep rupture. Creep-Resistant Steels. F. Abe, T. U. Kern and R. Viswanathan. Cambridge, England, Woodhead Publishing Ltd.: 279-301.

Abe, F., Araki, H. and Noda, T. (1991). "The effect of tungsten on dislocation recovery and precipitation behavior of low-activation martensitic 9Cr steels." Metallurgical Transactions A **22**(10): 2225-2235.

Abe, F., Kern, T. U. and Viswanathan, R. (2008). Creep-resistant steels. Cambridge, England, Woodhead Publishing Ltd.

Abe, F. and Nakazawa, S. (1992). "The effect of tungsten on creep." Metallurgical Transactions A **23**(11): 3025-3034.

Abe, F. and Tabuchi, M. (2004). "Microstructure and creep strength of welds in advanced ferritic power plant steels." Science and technology of welding and joining **9**(1): 22-30.

Abe, F., Tabuchi, M., Tsukamoto, S. and Shirane, T. (2010). "Microstructure evolution in HAZ and suppression of Type IV fracture in advanced ferritic power plant steels." International Journal of Pressure Vessels and Piping **87**(11): 598-604.

Abson, D. and Rothwell, J. (2013). "Review of type IV cracking of weldments in 9–12% Cr creep strength enhanced ferritic steels." International Materials Reviews **58**(8): 437-473.

Aghajani, A., Richter, F., Somsen, C., Fries, S. G., Steinbach, I. and Eggeler, G. (2009). "On the formation and growth of Mo-rich Laves phase particles during long-term creep of a 12% chromium tempered martensite ferritic steel." Scripta Materialia **61**(11): 1068-1071.

Aghajani, A., Somsen, C. and Eggeler, G. (2009). "On the effect of long-term creep on the microstructure of a 12% chromium tempered martensite ferritic steel." Acta Materialia **57**(17): 5093-5106.

Aghajani, B. (2009). Evolution of Microstructure during Long-term Creep of a Tempered Martensite Ferritic Steel Dr.-Ing. Dissertation, University of Bochum.

Ahmadi, M. R., Povoden-Karadeniz, E., Öksüz, K. I., Falahati, A. and Kozeschnik, E. (2014). "A model for precipitation strengthening in multi-particle systems." Computational materials science **91**: 173-186.

Alang, N. A. and Nikbin, K. (2017). A Numerical Approach to a Multiaxial Ductility Constraint Based Model to Predict Uniaxial and Multiaxial Rupture in Engineering Alloys. 4th International ECCC Creep & Fracture Conference. Düsseldorf, Germany, ECCC: 147.

Aracil, R. S. (2014). Investigation of heavily deformed and dual phase materials by means of Transmission Kikuchi Diffraction. MEng Master Thesis, Ghent University.

Armaki, H. G., Chen, R., Maruyama, K. and Igarashi, M. (2011). "Creep Behavior and Degradation of Subgrain Structures Pinned by Nanoscale Precipitates in Strength-Enhanced 5 to 12% Cr Ferritic Steels." Metallurgical and Materials Transactions A **42**(10): 3084-3094.

Ashby, M. F. (1968). The theory of the critical shear stress and work hardening of dispersion-hardened crystals. Metallurgical Societ Conference, New York, USA.

Ashby, M. F. (1972). "A first report on deformation-mechanism maps." Acta Metallurgica **20**(7): 887-897.

ASTM (2010). Standard Practice for Determining Average Grain Size Using Electron Backscatter Diffraction (EBSD) in Fully Recrystallized Polycrystalline Materials, ASTM International. **E2627-10**.

ASTM (2011). Standard Test Method for Knoop and Vickers Hardness of Materials. ASTM E384-11. Pennsylvania, USA, ASTM International: 1-43.

ASTM (2014). Standard Test Methods, Practices and Terminology for Chemical Analysis of Steel Products, ASTM International. **ASTM A751-14a**.

Auerkari, P., Holmström, S., Veivo, J. and Salonen, J. (2007). "Creep damage and expected creep life for welded 9–11% Cr steels." International Journal of Pressure Vessels and Piping **84**(1-2): 69-74.

Auerkari, P., Salonen, J., Holmström, S., Laukkanen, A., Rantala, J. and Nikkarila, R. (2013). "Creep damage and long term life modelling of an X20 steam line component." Engineering Failure Analysis **35**: 508-515.

Ayache, J., Beaunier, L., Boumendil, J., Ehret, G. and Laub, D. (2010). Sample Preparation Handbook for Transmission Electron Microscopy: Techniques. New York, USA, Springer Science & Business Media.

Bain, E. C. and Dunkirk, N. (1924). "The nature of martensite." trans. AIME **70**(1): 25-47.

Baker, T. N. (2001). Quantitative Metallography using Transmission Electron Microscopy. Quantitative Microscopy of High Temperature Materials. A. Strang and J. Cawley. London, UK, IOM Communications Ltd. **5**: 161-190.

Balzar, D., Audebrand, N., Daymond, M. R., Fitch, A., Hewat, A., Langford, J. I., Bail, A. L., Loue, D., Masson, O., McCowan, C. N., Popa, N. C., Stephens, P. W. and Tobyk, B. H. (2004). "Size-strain line-broadening analysis of the ceria round-robin sample." Journal of Applied Crystallography **37**: 911-924.

Barkar, T. and Ågren, J. (2005). "Creep simulation of 9–12% Cr steels using the composite model with thermodynamically calculated input." Materials Science and Engineering: A **395**(1-2): 110-115.

Basirat, M., Shrestha, T., Potirniche, G. P., Charit, I. and Rink, K. (2012). "A study of the creep behavior of modified 9Cr–1Mo steel using continuum-damage modeling." International Journal of Plasticity **37**: 95-107.

Bhadeshia, H. K. D. H. (1999). "Neural networks in materials science." ISIJ international **39**(10): 966-979.

Bhadeshia, H. K. D. H. (2001). "Design of Ferritic Creep-Resistant Steels." ISIJ International **41**(6): 626–640



Bhadeshia, H. K. D. H. (2002). Martensite in Steels. Crystallography. P. T. C. P. R. Group, Department of Materials Science & Metallurgy, University of Cambridge. **2015**.

Bhadeshia, H. K. D. H. and Honeycombe, R. W. K. (2006). Steels: Microstructure and Properties. Oxford, UK, Elsevier Ltd.

Bhadeshia, H. K. D. H. and Wayman, C. M. (2014). Phase Transformations: Nondiffusive. Physical Metallurgy (Fifth Edition). D. E. Laughlin and K. Hono. Oxford, Elsevier: 1021-1072.

Białobrzęska, B., Konat, Ł. and Jasiński, R. (2017). "The influence of austenite grain size on the mechanical properties of low-alloy steel with boron." Metals **7**(1): 26.

Biglari, F. and Nikbin, K. (2015). "A diffusion driven carburisation combined with a multiaxial continuum creep model to predict random multiple cracking in engineering alloys." Engineering Fracture Mechanics **146**: 89-108.

Bilat, A.-S., Gourgues-Lorenzon, A.-F., Besson, J. and Pineau, A. (2006). Brittle fracture in heat-affected zones of girth welds of modern line pipe steel (X100). Fracture of Nano and Engineering Materials and Structures, Springer: 109-110.

Blum, W. (1993). Plastic deformation of materials. Materials science and technology. R. Cahn, P. Haasen and E. Kramer, Weinheim:VCH. **6**: 359.

Blum, W., Straub, S. and Vogler, S. (1991). "Creep of pure materials and alloys." in ICSMA-9, Haifa, Israel. Google Scholar.

Bolton, J. (2017). "Reliable analysis and extrapolation of creep rupture data." International Journal of Pressure Vessels and Piping **157**: 1-19.

Bolton, J. L. (1995). Design considerations for high temperature bolting. Conference on performance of bolting materials in high temperature applications, New York, USA.

Brear, J., Fairman, A., Middleton, C. and Polding, L. (2000). "Predicting the creep life and failure location of weldments." Key Engineering Materials **171-174**: 35-42.

Brett, S. (1994). Cracking experience in steam pipework welds in national power. Proc. of VGB Conf. on Materials and Welding Technology in Power Plants.

Brett, S. (2004). "Type IIIa cracking in ½ CrMoV steam pipework systems." Science and technology of welding and joining **9**(1): 41-45.

Brown, S., Evans, R. and Wilshire, B. (1986). "Creep strain and creep life prediction for the cast nickel-based superalloy IN-100." Materials Science and Engineering **84**: 147-156.

Brühl, F., Weber, H., Cerjak, H. and Schwaab, P. (1991). "Metallurgical investigation of the base material and weldments of the 9% chromium X 10 CrMoVNb 9 1." Steel Research **62**(2): 75-82.

Brust, A. F., Niezgoda, S. R., Yardley, V. A. and Payton, E. J. (2018). "Analysis of Misorientation Relationships between Austenite Parents and Twins." arXiv preprint arXiv:1804.02506.

Brydson, R. (2001). A Brief Review of Quantitative Aspects of Electron Energy Loss Spectroscopy and Imaging. Quantitative Microscopy of High Temperature Materials. A. Strang and J. Cawley. London, UK, IOM Communications Ltd. **5**: 277-306.

Buchmayr, B. (2005). "Characterisation of the creep behaviour of weldments by HAZ-simulation." ECCC Recommendations **3**(2): Appendix 2.

Caillard, D. and Martin, J.-L. (2003). Thermally Activated Mechanisms in Crystal Plasticity. Oxford, UK, Elsevier.

Carter, C. B. and Williams, D. B. (2016). Transmission Electron Microscopy; Diffraction, Imaging, and Spectrometry. Switzerland, Springer International Publishing.

Cayron, C. (2007). "ARPGE: a computer program to automatically reconstruct the parent grains from electron backscatter diffraction data." Journal of applied crystallography **40**(6): 1183-1188.

Cerjak, H., Hofer, P. and Schaffernak, B. (1999). "The influence of microstructural aspects on the service behaviour of advanced power plant steels." ISIJ International **39**(9): 874-888.

Cerjak, H. and Mayr, P. (2008). Creep strength of welded joints of ferritic steels. Creep-resistant steels. F. Abe, T. U. Kern and R. Viswanathan. Cambridge, England, Woodhead Publishing Ltd.: 472-503.

CFAMM. (2018). "Introduction to Energy Dispersive X-ray Spectrometry (EDS)." Concise introductory texts to the principles of electron microscopy and e-beam microanalysis Retrieved 2/12/2018, from <https://cfamm.ucr.edu/manuals.html>.

Chandrasekhar, S. (1943). "Stochastic problems in physics and astronomy." Reviews of modern physics **15**(1): 1.

Chilukuru, H. (2007). On the Microstructural Basis of Creep Strength and Creep-fatigue Interaction in 9-12% Cr Steels for Application in Power Plants. Doktor-Ingenieur Doctoral Dissertation, University of Erlangen-Nürnberg.

Christien, F., Telling, M. T. F. and Knight, K. S. (2013). "Neutron diffraction in situ monitoring of the dislocation density during martensitic transformation in a stainless steel." Scripta Materialia **68**(7): 506-509.

Christopher, J., Sainath, G., Srinivasan, V., Samuel, E. I., Choudhary, B., Mathew, M. and Jayakumar, T. (2013). "Continuum damage mechanics approach to predict creep behaviour of modified 9Cr-1Mo ferritic steel at 873 K." Procedia Engineering **55**: 798-804.

Cipolla, L., Danielsen, H. K., Venditti, D., Di Nunzio, P. E., Hald, J. and Somers, M. A. J. (2010). "Conversion of MX nitrides to Z-phase in a martensitic 12% Cr steel." Acta Materialia **58**(2): 669-679.

Cocks, A. and Ashby, M. (1980). "Intergranular fracture during power-law creep under multiaxial stresses." Metal science **14**(8-9): 395-402.

CompuTherm: For Materials Design. (2018). "PanPrecipitation." Retrieved 24/08/2018, from [http://www.computherm.com/index.php?route=product/product&product\\_id=27](http://www.computherm.com/index.php?route=product/product&product_id=27).

Crank, J. (1975). The Mathematics of Diffusion. London, UK, Oxford University Press.

Danielsen, H. K. (2007). Z-phase in 9-12% Cr Steels. Doctor in Engineering PhD thesis, Technical University of Denmark.

Danielsen, H. K. (2016). "Review of Z phase precipitation in 9–12 wt-% Cr steels." Materials Science and Technology **32**(2): 126-137.

Danielsen, H. K. and Hald, J. (2006). "Behaviour of Z phase in 9–12% Cr steels." Energy Materials **1**(1): 49-57.

Danielsen, H. K. and Hald, J. (2009). "Influence of Z-phase on long-term creep stability of martensitic 9 to 12% Cr steels." VGB powertech **5**: 68-73.

Di Gianfrancesco, A. (2017). The fossil fuel power plant technology. Materials for ultra-supercritical and advanced ultra-supercritical power plants. A. Di Gianfrancesco, Woodhead Publishing. **104**: 1-47.

Di Gianfrancesco, A. (2017). The fossil fuel power plants technology. Materials for Ultra-Supercritical and Advanced Ultra-Supercritical Power Plants. A. Di Gianfrancesco, Woodhead Publishing: 1-49.

Di Gianfrancesco, A., Vipraio, S. T. and Venditti, D. (2013). "Long term microstructural evolution of 9-12% Cr steel grades for steam power generation plants." Procedia Engineering **55**: 27-35.

Dimmler, G. (2003). Quantification of Creep Resistance and Creep Fracture Strength of 9-12%Cr Steels on Microstructural Basis PhD thesis, Graz University of Technology.

Dimmler, G., Weinert, P. and Cerjak, H. (2008). "Extrapolation of short-term creep rupture data—The potential risk of over-estimation." International journal of pressure vessels and piping **85**(1-2): 55-62.

Doane, D. P. (1976). "Aesthetic frequency classifications." The American Statistician **30**(4): 181-183.

Doherty, R., Hughes, D., Humphreys, F., Jonas, J., Jensen, D. J., Kassner, M., King, W., McNelley, T., McQueen, H. and Rollett, A. (1997). "Current issues in recrystallization: a review." Materials Science and Engineering: A **238**(2): 219-274.

Doherty, R. D. (1997). "Recrystallization and texture." Progress in Materials Science **42**(1-4): 39-58.

Doubell, P., Scheepers, R., Downes, A., Pottas, R., Stangroom, P. and Absenger, A. (2012). Weld Repair of Eskom High Pressure Turbine Rotor. IIW Regional Congress 2012 : 'Advancing Science and Technology of Welding in Sub-Saharan Africa'. Johannesburg, South Africa: 1-21.

Dronhofer, A., Pešicka, J., Dlouhý, A. and Eggeler, G. (2003). "On the nature of internal interfaces in tempered martensite ferritic steels." Zeitschrift für Metallkunde **94**(5): 511-520.

Ducati, C. (2013). T2: Electron Microscopy Department of Materials Science and Metallurgy, University of Cambridge.

Dyson, B. (2000). "Use of CDM in materials modeling and component creep life prediction." Journal of pressure vessel technology **122**(3): 281-296.

Dyson, B. (2009). "Microstructure based creep constitutive model for precipitation strengthened alloys: theory and application." Materials science and technology **25**(2): 213-220.

Dyson, B. and McLean, M. (1998). Microstructural evolution and its effects on the creep performance of high temperature alloys. Microstructural Stability of Creep Resistant Alloys for High Temperature Plant Applications. A. Strang, J. Cawley and J. W. Greenwood. London, UK, Institute of Materials: 371-393.

Easterling, K. (1992). Introduction to the Physical Metallurgy of Welding. London, England, Butterworth-Heinemann Ltd.

Edward, G. and Ashby, M. F. (1979). "Intergranular fracture during power-law creep." Acta Metallurgica **27**(9): 1505-1518.

Egerton, R. F. (1996). Electron Energy Loss Spectroscopy in the Electron Microscope. New York, USA, Plenum Press.

Eggeler, G. (1989). "The effect of long-term creep on particle coarsening in tempered martensite ferritic steels." Acta Metallurgica **37**(12): 3225-3234.

Eggeler, G., Earthman, J. C., Nilsvang, N. and Ilschner, B. (1989). "Microstructural study of creep rupture in a 12% chromium ferritic steel." Acta Metallurgica **37**(1): 49-60.

Eggeler, G., Nilsvang, N. and Ilschner, B. (1987). "Microstructural changes in a 12% chromium steel during creep." steel research **58**(2): 97-103.

Eggeler, G., Nilsvang, N. and Ilschner, B. (1991). Strength of metals and alloys. ICMA 9, London, Freud.

Ellis, F. V. and Viswanathan, R. (1998). Review of Type IV cracking in piping welds. 1st International Conference on Integrity of High Temperature Welds, London, UK, IOM.

Endo, T., Masuyama, F. and Park, K.-S. (2003). "Change in Vickers hardness and substructure during creep of a Mod. 9Cr-1Mo steel." Materials transactions **44**(2): 239-246.

Engler, O. and Randle, V. (2010). Introduction to texture analysis : macrotexture, microtexture, and orientation mapping. USA, CRC Press.

Ennis, P. (2002). "The mechanical properties and microstructures of 9% chromium steel P92 weldments." OMMI 1(2): 1-23.

Ennis, P. J., Zielinska-Lipiec, A. and Czyrska-Filemonowicz, A. (2001). The Influence of Heat Treatments on the Microstructural Parameters and Mechanical Properties of P92 Steel. Quantitative Microscopy of High Temperature Materials. A. Strang and J. Cawley. London, UK, IOM Communications Ltd. 5: 191-206.

EPRI (2006). X20 CrMoV12-1 Steel Handbook. Palo Alto, CA.

Eskom. (2016). "Coal In South Africa." CO 0007 Revision 14. Retrieved 3/7/2018, from <http://www.eskom.co.za/AboutElectricity/FactsFigures/Documents/CO0007CoalSARev14.pdf>.

Eskom (2017). 240-75109745 Standard for Metallographic Replication Applicable to High Temperature High Pressure Components in Eskom Plant. Revision 2, Eskom.

Eskom (2017). "Generation Plant Mix." GX 0001 Revision 19. Retrieved 3/7/2018, from <http://www.eskom.co.za/AboutElectricity/FactsFigures/Documents/GX0001GenPlantMixRev19.pdf>.

Esposito, L., Bonora, N. and Dichiario, S. (2013). Modeling of multiaxial stress effects on the creep resistance of high chromium steel. ASME 2013 Pressure Vessels and Piping Conference, ASME.

Faulkner, R. G. (2008). Grain boundaries in creep-resistant steels. Creep-Resistant Steels. F. Abe, T.-U. Kern and R. Viswanathan, Woodhead Publishing: 329-349.

FEI (2013). Information from Every Angle: Directional BSE Detector for Next-Level Imaging: 8.

Francis, J., Mazur, W. and Bhadeshia, H. (2006). "Review type IV cracking in ferritic power plant steels." Materials Science and Technology **22**(12): 1387-1395.

Frank, F. and Read Jr, W. (1950). "Multiplication processes for slow moving dislocations." Physical Review **79**(4): 722.

Friel, J. J. (2003). X-Ray and Image Analysis in Electron Microscopy, Princeton-Gamma Tech Inc.

Fujibayashi, S. and Endo, T. (2001). Creep behaviour of a low alloy ferritic steel weldment. 9th International Conference of Creep and Fracture of Engineering Materials and Structures. Cambridge, UK, Maney Publishing: 603-612.

Fujiyama, K., Mori, K., Matsunaga, T., Kimachi, H., Saito, T., Hino, T. and Ishii, R. (2009). "Creep-damage assessmen of high chromium heat resistant steels and weldments." Materials Science and Engineering: A **510-511**: 195-201.

Ghoniem, N. M., Matthews, J. R. and Amodeo, R. J. (1989). A dislocation model for creep in engineering materials, Institute of Plasma and Fusion Research, University of California, Los Angeles.

Ghosh, R. (2013). "Creep life predictions of engineering components: problems & prospects." Procedia engineering **55**: 599-606.

Girgsdies, F. (2015). "Peak Profile Analysis in X-ray Powder Diffraction." Retrieved 6/11/2018, from [http://www.fhi-berlin.mpg.de/acnew/department/pages/teaching/pages/teaching\\_\\_wintersemester\\_\\_2015\\_2016/frank\\_girgsdies\\_\\_peak\\_profile\\_fitting\\_in\\_xrd\\_\\_151106.pdf](http://www.fhi-berlin.mpg.de/acnew/department/pages/teaching/pages/teaching__wintersemester__2015_2016/frank_girgsdies__peak_profile_fitting_in_xrd__151106.pdf).

Gokhale, A. M. (2004). Quantitative Characterization and Representation of Global Microstructural Geometry. ASM Handbook Volume 9: Metallography and Microstructures. G. F. Vander Voort. Ohio, USA, ASM International. **9**: 428-447.



Goldstein, J. I., Newbury, D. E., Joy, D. C., Lyman, C. E., Echlin, P., Lifshin, E., Sawyer, L. and Michael, J. R. (2003). Scanning Electron Microscopy and X-Ray Microanalysis. New York, USA, Springer.

Gooch, D. (1982). "Creep fracture of 12Cr–Mo–V steel." Metal science **16**(2): 79-89.

Gooch, D. and Kimmins, S. (1987). Type IV Cracking in 1/2 Cr 1/2 Mo 1/4 V/21/4 Cr 1 Mo Weldments. 3rd International of Creep and Fracture of Engineering Materials and Structures. Swansea, UK, Maney Publishing: 689-703.

Graham, A. and Walles, K. (1955). "Relationships between long and short-time creep and tensile properties of a commercial alloy." Journal of the Iron and Steel Institute **179**: 104-121.

Grounes, M. (1969). "A reaction-rate treatment of the extrapolation methods in creep testing." Journal of Basic Engineering **91**(1): 59-62.

Gu, Y., West, G., Thomson, R. C. and Parker, J. D. (2014). "Investigation of creep damage and cavitation mechanisms in P92 steels."

Gupta, C., Toda, H., Mayr, P. and Sommitsch, C. (2015). "3D creep cavitation characteristics and residual life assessment in high temperature steels: a critical review." Materials science and technology **31**(5): 603-626.

Gustafson, Å. and Ågren, J. (2001). "Possible effect of Co on coarsening of M<sub>23</sub>C<sub>6</sub> carbide and Orowan stress in a 9% Cr steel." ISIJ international **41**(4): 356-360.

Gyhlesten Back, J. and Engberg, G. (2017). "Investigation of parent austenite grains from martensite structure using EBSD in a wear resistant steel." Materials **10**(5): 453.

Hald, J. (1996). "Metallurgy and creep properties of new 9-12% Cr steels." Steel research **67**(9): 369-374.

Hald, J. (2005). Creep resistant 9-12% Cr steels-long-term testing, microstructure stability and development potentials. Proceedings of Conference on Super-High Strength Steels.

Hald, J. (2008). "Microstructure and long-term creep properties of 9-12% Cr steels." International Journal of Pressure Vessels and Piping **85**: 30-37.

Hald, J. (2016). "Prospects for martensitic 12% Cr steels for advanced steam power plants." Transactions of the Indian Institute of Metals **69**(2): 183-188.

Hald, J. (2017). High-alloyed martensitic steel grades for boilers in ultra-supercritical power plants. Materials for Ultra-Supercritical and Advanced Ultra-Supercritical Power Plants. A. Di Gianfrancesco, Woodhead Publishing: 77-97.

Hammond, C. (2009). The Basics of Crystallography and Diffraction. Oxford, UK, Oxford University Press.

Hansen, N. and Barlow, C. Y. (2014). Plastic Deformation of Metals and Alloys. Physical Metallurgy (Fifth Edition). D. E. Laughlin and K. Hono. Oxford, Elsevier: 1681-1764.

Harding, J. (1949). "The use of probability paper for the graphical analysis of polymodal frequency distributions." Journal of the Marine Biological Association of the United Kingdom **28**(1): 141-153.

Hatem, T. and Zikry, M. (2009). "Modeling of Lath Martensitic Microstructures and Failure Evolution in Steel Alloys." Journal of Engineering Materials and Technology **131**(4): 041207-041201 - 041207-041210.

Hättestrand, M. and Andrén, H.-O. (1999). "Boron distribution in 9–12% chromium steels." Materials Science and Engineering: A **270**(1): 33-37.

Hayhurst, D. (2001). Computational Continuum Damaged Mechanics: Its use in the Prediction of Creep in Structures—Past, Present and Future. IUTAM Symposium on Creep in Structures, Springer.

Heinemann, C., Linn, S., Scwienheer, M., Kontermann, C. and Oechsner, M. (2017). Strain Based Methods and Approaches for the Extrapolation of Creep and Creep Rupture Data. 4th International ECCC Creep & Fracture Conference. Düsseldorf, Germany, ECCC: 131.

Hino, M., He, Y., Li, K., Chang, J. and Shin, K. (2013). "Microstructural Evolution of X20CrMoV12. 1 Steel upon Short-term Creep Rupture Test." Applied Microscopy **43**(4): 164-172.

Hofer, P. (1999). Microstructural Analysis as Basis for the Development of Novel Power Plant Materials on the Example of G-X12 CrMoWVNbN 10-1-1 PhD thesis, Graz University of Technology.

Holdsworth, S., Askins, M., Baker, A., Gariboldi, E., Holmström, S., Klenk, A., Ringel, M., Merckling, G., Sandstrom, R. and Schwienheer, M. (2008). "Factors influencing creep model equation selection." International Journal of Pressure Vessels and Piping **85**(1-2): 80-88.

Holmstrom, S. and Auerkari, P. (2004). Prediction of creep strain and creep strength of ferritic steels for power plant applications. Baltica conference on life management and maintenance for power plants, Espoo, Finland, VTT Symposium.

Holzer, I. (2010). Modelling and Simulation of Strengthening in Complex Martensitic 9-12% Cr Steel and a Binary Fe-Cu Alloy PhD thesis, Graz University of Technology.

Holzer, I. and Kozeschnik, E. (2010). "Computer simulation of the yield strength evolution in Cu-precipitation strengthened ferritic steel." Materials Science and Engineering: A **527**(15): 3546-3551.

Hoseiny, H., Caballero, F. G., San Martin, D. and Capdevila, C. (2012). The influence of austenitization temperature on the mechanical properties of a prehardened mould steel. Materials Science Forum, Trans Tech Publ.

Hosoi, Y., Wade, N., Kunimitsu, S. and Urita, T. (1986). "Precipitation behavior of laves phase and its effect on toughness of 9Cr-2Mo Ferritic-martensitic steel." Journal of Nuclear Materials **141-143**: 461-467.

Hu, P., Yan, W. and Sha, W. (2011). "Microstructure evolution of a 10Cr heat-resistant steel during high temperature creep." Journal of Materials Science and Technology **27**(4): 344-351.

Hu, Z., Yang, Z.-G., He, G.-Q. and Chen, C.-S. (2008). "Damage and Residual Life Assessment of Bends for X20CrMoV12.1 Main Steam Pipe after Long-Term Service." Journal of Failure Analysis and Prevention **8**: 41-47.

Hull, D. and Bacon, D. J. (2001). Introduction to Dislocations, Butterworth-Heinemann.

Hull, D. and Rimmer, D. (1959). "The growth of grain-boundary voids under stress." Philosophical Magazine **4**(42): 673-687.

Humphreys, F. J. (1998). "Quantitative metallography by electron backscattered diffraction." Journal of Microscopy **195**(3): 170-185.

Humphreys, F. J. (2001). "Grain and subgrain characterisation by electron backscatter diffraction." Journal of Materials Science **36**: 3833-3854.

Humphreys, F. J. (2001). Quantitative Metallography by High Resolution Electron Backscattered Diffraction. Quantitative Microscopy of High Temperature Materials. A. Strang and J. Cawley. London, UK, IOM Communications Ltd. **5**: 103-130.

Humphreys, F. J. (2004). "Characterisation of fine-scale microstructures by electron backscatter diffraction (EBSD)." Scripta Materialia **51**: 771-776.

Humphreys, F. J. (2004). "Reconstruction of grains and subgrains from electron backscatter diffraction maps." Journal of Microscopy **213**(3): 247-256.

Humphreys, F. J. and Hatherly, M. (2004). Recrystallization and Related Annealing Phenomena. Oxford, UK, Elsevier Ltd.

Humphreys, F. J., Huang, Y., Brough, I. and Harris, C. (1999). "Electron backscatter diffraction of grain and subgrain structures - resolution consideration." Journal of Microscopy **195**(3): 212-216.

Igarashi, M. (2008). 20 - Alloy design philosophy of creep-resistant steels. Creep-Resistant Steels. F. Abe, T.-U. Kern and R. Viswanathan, Woodhead Publishing: 539-572.

Isik, M. I., Kostka, A. and Eggeler, G. (2014). "On the nucleation of Laves phase particles during high-temperature exposure and creep of tempered martensite ferritic steels." Acta Materialia **81**: 230-240.

Isik, M. I., Kostka, A., Yardley, V. A., Pradeep, K. G., Duarte, M. J., Choi, P.-P., Raabe, D. and Eggeler, G. (2015). "The nucleation of Mo-rich Laves phase particles adjacent to M<sub>23</sub>C<sub>6</sub> micrograin boundary carbides in 12% Cr tempered martensite ferritic steels." Acta Materialia **90**: 94-104.

Ito, K., Yajima, H. and Arai, M. P., 2, 450 (2018). Creep Life Prediction Method by Using High-Temperature Indentation Creep Test. 18th International Conference on Experimental Mechanics (ICEM18), Brussels, Belgium, Proceedings.

Josefsson, F. (2012). Development of a quantitative method for grain size measurement using EBSD. Master of Science MSc. Thesis, Royal Institute of Technology.

Kalwa, G., Schnabel, E. and Schwaab, P. (1986). "Grain structure of bainitic and martensitic steels." Steel Research **57**(5): 207-215.

Kamm, J. and Vander Voort, G. (1997). "An Introduction to Microindentation Methods." Buchler Tech-Notes **1**(6).

Kassner, M. and Hayes, T. (2003). "Creep cavitation in metals." International Journal of Plasticity **19**(10): 1715-1748.

Keller, R., Geiss, R. and Rice, K. (2013). Transmission Kikuchi Diffraction in the Scanning Electron Microscope. Boulder, Colorado, USA, National Institute of Standards and Technology.

Kimmins, S. and Smith, D. (1998). "On the relaxation of interface stresses during creep of ferritic steel weldments." The Journal of Strain Analysis for Engineering Design **33**(3): 195-206.

Kimmins, S. T., Coleman, M. V. and Smith, D. J. (1993). An overview of creep failure associated with heat affected zones of ferritic weldments. 5th International Conference of Creep Fracture of Engineering Materials and Structures, 1993, London, UK, IOM.

Kimura, K., Kushima, H. and Booker, G. (2000). Heterogeneous changes in microstructure and degradation behaviour of 9Cr-1Mo-V-Nb steel during long term creep. Key Engineering Materials, Trans Tech Publ.

Kinoshita, Y., Yardley, V. A. and Tsurekawa, S. (2011). "Relation between microstructures of martensite and prior austenite in 12 wt% Cr ferritic steel." Journal of Materials Science **46**(12): 4261-4269.

Kipelova, A., Belyakov, A. and Kaibyshev, R. (2012). "Laves phase evolution in a modified P911 heat resistant steel during creep at 923K." Materials Science and Engineering: A **532**: 71-77.

Kitahara, H., Ueji, R., Tsuji, N. and Minamino, Y. (2006). "Crystallographic features of lath martensite in low-carbon steel." Acta Materialia **54**(5): 1279-1288.

Kocks, U. (1966). "A statistical theory of flow stress and work-hardening." Philosophical Magazine **13**(123): 541-566.

Kostka, A., Tak, K. G., Hellmig, R. J., Estrin, Y. and Eggeler, G. (2007). "On the contribution of carbides and micrograin boundaries to the creep strength of tempered martensite ferritic steels." Acta Materialia **2007**: 539-550.

Kou, S. (2003). Welding metallurgy. New Jersey, USA, John Wiley & Sons, Inc.

Kozeschnik, E. (2013). Modeling Solid-State Precipitation. New York, USA, Momentum Press.

Kozeschnik, E. and Holzer, I. (2008). 10 - Precipitation during heat treatment and service: characterization, simulation and strength contribution. Creep-Resistant Steels. F. Abe, T.-U. Kern and R. Viswanathan, Woodhead Publishing: 305-328.

Kozeschnik, E., Sonderegger, B., Holzer, I., Rajek, J. and Cerjak, H. (2007). Computer simulation of the precipitate evolution during industrial heat treatment of complex alloys. Materials science forum, Trans Tech Publ.

Krauss, G. (1999). "Martensite in steel: strength and structure." Materials Science and Engineering: A **273-275**: 40-57.

Krauss, G. (2015). Steels: Processing, Structure, and Performance. Ohio, USA, ASM International.

Krenmayr, B. and Sonderegger, B. (2016). Development of a creep strength estimation method based on microstructural simulation in mod. 9Cr-1Mo steels: Report Task 1 - Literature Review. Graz, Austria, Graz University of Technology.

Krenmayr, B. and Sonderegger, B. (2017). Physical Modeling of dislocation creep in high temperature steels. 4th International ECCO Creep & Fracture Conference. Düsseldorf, Germany, ECCO: 90.

Kroupa, F. (1966). "Dislocation dipoles and dislocation loops." Le Journal de Physique Colloques **27(C3)**: C3-154-C153-167.

Krumphals, F. (2014). Physical Based Modelling of Creep Fatigue in Hot Work Tool Steels. Doctor of Technology Doctoral Thesis, Graz University of Technology.

Krumphals, F., Reggiani, B., Donati, L., Wlanis, T. and Sommitsch, C. (2012). "Deformation behaviour of a ferritic hot-work tool steel with respect to the microstructure." Computational materials science **52**(1): 40-45.

Krumphals, F., Wlanis, T., Sommitsch, C., Holzer, I., Sonderegger, B. and Wieser, V. (2009). "Modelling of microstructure evolution in hot work tool steels during service." Computer Methods in Materials Science **9**(2): 228-233.

Kuchařová, K., Němec, J. and Dlouhý, A. (1996). Creep and fracture of engineering materials and structures. Warrendale (PA), TMS.

Kuhlmann-Wilsdorf, D. (1989). "Theory of plastic deformation:-properties of low energy dislocation structures." Materials Science and Engineering: A **113**: 1-41.

Kurdjumov, G. and Sachs, G. (1930). "Über den mechanismus der stahlhärtung." Zeitschrift für Physik **64**(5-6): 325-343.

Labossiere, P. E. (2007). Chapter 8- Time Dependant Behavior: Creep. ME 354: Mechanics of Materials Laboratory. P. E. Labossiere, University of Washington: 1-9.

Laha, K., Chandravathi, K., Parameswaran, P., Rao, K. B. S. and Mannan, S. (2007). "Characterization of microstructures across the heat-affected zone of the modified 9Cr-1Mo weld joint to understand its role in promoting type IV cracking." Metallurgical and Materials Transactions A **38**(1): 58-68.

Langdon, T. G. (2000). "Identifying creep mechanisms at low stresses." Materials Science and Engineering: A **283**(1-2): 266-273.

Larson, F. R. and Miller, J. (1952). "A Time-Temperature Relationship for Rupture and Creep Stresses." Trans. ASME **74**: 765-775.



Lee, J. S., Armaki, H. G., Maruyama, K., Muraki, T. and Asahi, H. (2006). "Causes of breakdown of creep strength in 9Cr–1.8 W–0.5 Mo–VNb steel." Materials Science and Engineering: A **428**(1-2): 270-275.

Lifshitz, I. M. and Slyozov, V. V. (1961). "The kinetics of precipitation from supersaturated solid solutions." Journal of physics and chemistry of solids **19**(1-2): 35-50.

Liu, F. and Andrén, H.-O. (2010). Initial study on Z-phase strengthened 9-12% Cr steels by atom probe tomography. 9th Liège Conference: Materials for Advanced Power Engineering. J. Lecomte-Beckers, Q. Contrepois, T. Beck and B. Kuhn. Liège, Belgium: 107-116.

Liu, F., Fors, D. H., Golpayegani, A., Andrén, H.-O. and Wahnström, G. (2012). "Effect of boron on carbide coarsening at 873 K (600 C) in 9 to 12 pct chromium steels." Metallurgical and Materials Transactions A **43**(11): 4053-4062.

Mackenzie, J. K. (1958). "Second paper on statistics associated with the random disorientation of cubes." Biometrika **45**(1-2): 229-240.

Magnusson, H. and Sandström, R. (2007). "Creep strain modeling of 9 to 12 Pct Cr steels based on microstructure evolution." Metallurgical and Materials Transactions A **38**(9): 2033-2039.

Maile, K. (2007). "Evaluation of microstructural parameters in 9–12% Cr-steels." International Journal of Pressure Vessels and Piping **84**(1): 62-68.

Maitland, T. and Sitzman, S. (2007). Electron Backscatter Diffraction (EBSD) Technique and Materials Characterization Examples. Scanning Microscopy for Nanotechnology: Techniques and Applications. W. Zhou and Z. L. Wang, Springer. **XIV**: 41-75.

Manson, S. S. and Haferd, A. M. (1953). A linear time-temperature relation for extrapolation of creep and stress-rupture data, NASA. **TN 2890**.

Marder, A. R. (1989). Replication Microscopy Techniques for NDE. ASM Handbook, Volume 17: Nondestructive Evaluation and Quality Control, ASM International. **17**: 52-56.

Maruyama, K., Nakamura, J., Sekido, N. and Yoshimi, K. (2017). "Causes of heat-to-heat variation of creep strength in grade 91 steel." Materials Science and Engineering: A **696**: 104-112.

Maruyama, K., Sawada, K. and Koike, J. (2001). "Strengthening Mechanisms of Creep Resistant Tempered Martensitic Steels." ISIJ International **41**(6): 641–653.

Marx, G. (2016). Quantitative microstructural evaluation of 12 Cr creep aged steels after welding. MSc Masters Dissertation, Nelson Mandela Metropolitan University.

Masuyama, F. (2001). "History of Power Plants and Progress in Heat Resistant Steels." ISIJ International **41**(6): 612–625.

MatCalc® Engineering. (2018). "General Information." Retrieved 24/8/2018, from <https://www.matcalc-engineering.com/index.php/matcalc-software/matcalc-software-sub>.

Mayer, K. H. and Masuyama, F. (2008). The development of creep-resistant steels. Creep-Resistant Steels. F. Abe, T.-U. Kern and R. Viswanathan, Woodhead Publishing: 15-77.

Mayr, P. (2007). Evolution of microstructure and mechanical properties of the heat affected zone in B-containing 9% chromium steels. Doctor of Technical Sciences Dissertation, Graz University of Technology.

Mayr, P. and Cerjak, H. (2010). "The impact of welding on the creep properties of advanced 9–12% Cr steels." Transactions of the Indian Institute of Metals **63**(2-3): 131-136.

Mayr, P., Holzer, I. and Cerjak, H. (2011). "Evolution Of Precipitate Structure in the heat-affected zone of a 9 wt.% Cr Martensitic Steel during welding and post-weld heat treatment." Welding in the World **55**(5-6): 70-77.

McHenry, D. (1943). A new aspect of creep in concrete and its application to design. ASTM Proceedings.

McLean, M. and Dyson, B. (2000). "Modeling the effects of damage and microstructural evolution on the creep behavior of engineering alloys." Journal of engineering Materials and Technology **122**(3): 273-278.

Middleton, C. and Metcalfe, E. (1990). A review of laboratory Type IV cracking data in high chromium ferritic steels. International Conference Steam Plants for the 1990's, London, UK, IMechE.

Middleton, C. J., Timmins, R. and Townsend, R. D. (1996). "The integrity of materials in high temperature components; Performance and life assessment." International Journal of Pressure Vessels and Piping **66**: 33-57.

Milović, L., Vuherer, T., Blačić, I., Vrhovac, M. and Stanković, M. (2013). "Microstructures and mechanical properties of creep resistant steel for application at elevated temperatures." Materials & Design **46**: 660-667.

Mitchell, D. R. G. and Sulaiman, S. (2006). "Advanced TEM specimen preparation methods for replication of P91 steel." Materials characterization **56**(1): 49-58.

Molokwane, T. J. (2014). Microstructural and Property Evaluation Of 12Cr Creep Aged Steels After Welding. MSc, University of Cape Town.

Monkman, F. and Grant, N. (1956). An Empirical Relationship Between Rupture Life and Minimum Creep Rate in Creep-Rupture Tests. ASTM Proceeding 1956 - Volume 56, ASTM International. **56**: 593 - 620.

Morito, S., Huang, X., Furuhashi, T., Maki, T. and Hansen, N. (2006). "The morphology and crystallography of lath martensite in alloy steels." Acta Materialia **54**(19): 5323-5331.

Morito, S., Nishikawa, J. and Maki, T. (2003). "Dislocation Density within Lath Martensite in Fe-C and Fe-Ni Alloys." ISIJ International **43**(9): 1475-1477.

Morito, S., Tanaka, H., Konishi, R., Furuhashi, T. and Maki, T. (2003). "The morphology and crystallography of lath martensite in Fe-C alloys." Acta Materialia **51**(6): 1789-1799.

Morito, S., Yoshida, H., Maki, T. and Huang, X. (2006). "Effect of block size on the strength of lath martensite in low carbon steels." Materials Science and Engineering: A **438-440**: 237-240.

Morris Jr, J. W., Kinney, C., Pytlewski, K. and Adachi, Y. (2013). "Microstructure and cleavage in lath martensitic steels." Science and technology of advanced materials **14**(1): 014208.

Morris, P. F. (2001). "Terms and Terminology for weld creep testing." ECCC Recommendations **2**: Appendix 2b.

Murchú, C. Ó., Leen, S. B., O'Donoghue, P. E. and Barrett, R. A. (2017). "A physically-based creep damage model for effects of different precipitate types." Materials Science and Engineering: A **682**: 714-722.

Muruganath, M. and Bhadeshia, H. K. D. H. (2002). Components of the Creep Strength of Welds. Mathematical modelling of weld phenomena **6**. H. Cerjak. London, UK, Maney Publishers. **6**: 243-260.

Nabarro, F. (2002). "Creep at very low rates." Metallurgical and Materials Transactions A **33**(2): 213-218.

Nabarro, F. R. N. and De Villiers, F. (1995). Physics Of Creep And Creep-Resistant Alloys. London, UK, Taylor & Francis.

Nandi, S., Vikrant, K., Ahv, P., Singh, K. and Ghosh, R. (2013). "Creep modelling of P91 steel for high temperature power plant applications." Procedia Engineering **55**: 751-755.

Nebhnani, M. C., Bhakta, U. C., Gowrisankar, I. and Biswas, D. (2002). "Failure of a martensitic stainless steel pipe weld in a fossil fuel power plant." Engineering Failure Analysis **9**: 227-286.

Nie, M., Zhang, J., Huang, F., Liu, J., Zhu, X., Chen, Z. and Ouyang, L. (2014). "Microstructure evolution and life assessment of T92 steel during long-term creep." Journal of Alloys and Compounds **588**: 348-356.

Norström, L. (1976). "On the yield strength of quenched low-C lath martensite." Scandinavian Journal of Metallurgy **5**(4): 159-165.

NPTEL (2013). "Module 2: Interfacial free energy." Part II: Interfaces Retrieved 27/10/2018, from <https://nptel.ac.in/courses/113101003/8>.

Ohtani, T. (2007). "Creep-induced microstructural evolution and acoustic characterization in tempered martensitic stainless steel." Metallurgical and Materials Transactions A **38**(7): 1587-1597.

Oikawa, H. and Iijima, Y. (2008). Diffusion behaviour of creep-resistant steels. Creep-Resistant Steels. F. Abe, T.-U. Kern and R. Viswanathan, Woodhead Publishing: 241-264.

Orowan, E. (1948). Discussion Symposium on Internal Stresses in Metals and Alloys Monograph and Rept. Series No. 5, London.

Oruganti, R., Karadge, M. and Swaminathan, S. (2013). "A comprehensive creep model for advanced 9-10% Cr ferritic steels." Procedia Engineering **55**: 727-734.

Panait, C., Gourgues-Lorenzon, A.-F., Besson, J., Fuchsmann, A., Bendick, W., Gabrel, J. and Piette, M. (2010). Long term aging effect on the creep strength of the T92 steel.

9th Liege conference: materials for advanced power engineering 2010, Julich forschungszentrum.

Panait, C. G., Bendick, W., Fuchsmann, A., Gourgues-Lorenzon, A. F. and Besson, J. (2010). "Study of the microstructure of the Grade 91 steel after more than 100,00 h of creep exposure at 600 °C." International Journal of Pressure Vessels and Piping **87**(6): 326-335.

Panait, C. G., Zielinska-Lipiec, A. and Koziel, T. (2010). "Evolution of dislocation density, size of subgrains and MX-type precipitation in a P91 steel during creep and during thermal aging at 600 °C for more than 100,000 h." Materials Science and Engineering: A **527**(16-17): 4062-4069.

Pandey, C., Giri, A. and Mahapatra, M. M. (2016). "Effect of normalizing temperature on microstructural stability and mechanical properties of creep strength enhanced ferritic P91 steel." Materials Science and Engineering: A **657**: 173-184.

Pandey, C., Giri, A. and Mahapatra, M. M. (2016). "Evolution of phases in P91 steel in various heat treatment conditions and their effect on microstructure stability and mechanical properties." Materials Science and Engineering: A **664**: 58-74.

Pandey, C., Mahapatra, M., Kumar, P. and Saini, N. (2017). "Characterization of cast and forged (C&F) Gr. 91 steel in different heat treatment condition." Transactions of the Indian Institute of Metals: 1-20.

Pandey, C., Mahapatra, M. M., Kumar, P. and Saini, N. (2018). "Some studies on P91 steel and their weldments." Journal of Alloys and Compounds **743**: 332-364.

Parker, J. and Stratford, G. (1996). "Strain localization in creep testing of samples with heterogeneous microstructures." International journal of pressure vessels and piping **68**(2): 135-143.

Payton, E. (2012). "Revisiting sphere unfolding relationships for the stereological analysis of segmented digital microstructure images." Journal of Minerals and Materials Characterization and Engineering **11**(03): 221.

Payton, E. J., Aghajani, A., Otto, F., Eggeler, G. and Yardley, V. A. (2012). "On the nature of internal interfaces in a tempered martensite ferritic steel and their evolution during long-term creep." Scripta Materialia **66**(12): 1045-1048.

PD 6525 (1990). Elevated temperature properties for steels for pressure purposes. Part 1. Stress Rupture Properties, BSI.

Perl, J., Shin, J., Schümann, J., Faddegon, B. and Paganetti, H. (2012). "TOPAS: An innovative proton Monte Carlo platform for research and clinical applications." Medical physics **39**(11): 6818-6837.

Perrin, I. and Hayhurst, D. (1999). "Continuum damage mechanics analyses of type IV creep failure in ferritic steel crossweld specimens." International journal of pressure vessels and piping **76**(9): 599-617.

Perry, A. (1974). "Cavitation in creep." Journal of Materials Science **9**(6): 1016-1039.

Pešička, J., Aghajani, A., Somsen, C., Hartmaier, A. and Eggeler, G. (2010). "How dislocation substructures evolve during long-term creep of a 12% Cr tempered martensitic ferritic steel." Scripta Materialia **62**: 353-356.

Pešička, J., Dronhofer, A. and Eggeler, G. (2004). "Free dislocations and boundary dislocations in tempered martensite ferritic steels." Materials Science and Engineering: A **387-389**: 176-180.

Pešička, J., Kužel, R., Dronhofer, A. and Eggeler, G. (2003). "The evolution of dislocation density during heat treatment and creep of tempered martensite ferritic steels." Acta Materialia **51**(16): 4847-4862.

Phillips, P. J., Brandes, M. C., M.J.Mills and M.DeGraef (2011). "Diffraction contrast STEM of dislocations: Imaging and simulations." Ultramicroscopy **111**: 1438-1487.

Porter, D. A., Easterling, K. E. and Sherif, M. (2009). Phase Transformations in Metals and Alloys, CRC press.

Powertech, V. (2018). Facts and Figures - Electricity Generation 2017/2018, VGB Powertech.

Prat, O., Garcia, J., Rojas, D., Carrasco, C. and Inden, G. (2010). "Investigations on the growth kinetics of Laves phase precipitates in 12% Cr creep-resistant steels: Experimental and DICTRA calculations." Acta Materialia **58**(18): 6142-6153.

Prat, O., Garcia, J., Rojas, D., Carrasco, C. and Kaysser-Pyzalla, A. (2010). "Investigations on coarsening of MX and M<sub>23</sub>C<sub>6</sub> precipitates in 12% Cr creep resistant steels assisted by computational thermodynamics." Materials Science and Engineering: A **527**(21-22): 5976-5983.

QuesTek Innovations LLC (2013). PrecipiCalc®: PRECIPitation CALCulation for Materials/Process Design and Optimization.

Raabe, D. (2014). Recovery and Recrystallization: Phenomena, Physics, Models, Simulation. Physical Metallurgy (Fifth Edition). D. E. Laughlin and K. Hono. Oxford, Elsevier: 2291-2397.

Ragab, A. (2002). "Creep rupture due to material damage by cavitation." Journal of engineering materials and technology **124**(2): 199-205.

Rashidi, M. (2017). Microstructure of Z-phase strengthened steels. Doctor of Engineering PhD thesis, Chalmers University of Technology.

Rasiawan, T. (2017). The influence of prior creep damage on the fracture localisation in X20 CrMoV12-1 cross-weld creep tests. MSc (Engineering) Masters Dissertation, University of Cape Town.



Rastogi, K. (2005). Mesosopic simulation of grain boundary diffusion creep in inhomogeneous microstructures. Master of Science in Mechanical Engineering (MSME) Master's Thesis, Louisiana State University and Agricultural and Mechanical College.

REOTEMP Inc. (2018). "Type K Thermocouple." Retrieved 13/12/2018, from <https://www.thermocoupleinfo.com/type-k-thermocouple.htm>.

Rice, J. R. and Tracey, D. M. (1969). "On the ductile enlargement of voids in triaxial stress fields\*." Journal of the Mechanics and Physics of Solids **17**(3): 201-217.

Rosenthal, D. (1941). "Mathematical theory of heat distribution during welding and cutting." Welding journal **20**: 220-234.

Roters, F., Raabe, D. and Gottstein, G. (2000). "Work hardening in heterogeneous alloys—a microstructural approach based on three internal state variables." Acta materialia **48**(17): 4181-4189.

Sakthivel, T., Laha, K., Vasudevan, M., Koteswara Rao, M. and Panneer Selvi, S. (2016). "Type IV cracking behaviour of modified 9Cr-1Mo steel weld joints." Materials at High Temperatures **33**(2): 137-153.

Salazar, J., Politano, O. and Walgraef, D. (1997). "On the dynamics of dislocation patterning." Materials Science and Engineering: A **234**: 397-400.

Sanchez-Hanton, J. and Thomson, R. (2007). "Characterization of isothermally aged Grade 91 (9Cr–1Mo–Nb–V) steel by electron backscatter diffraction." Materials Science and Engineering: A **460**: 261-267.

Sardela, M. (2008). Advanced Materials Characterization Workshop: X-Ray Analysis Methods, The Frederick Seitz Materials Research Laboratory, University of Illinois.

Sawada, K., Kubo, K. and Abe, F. (2001). "Creep behavior and stability of MX precipitates at high temperature in 9Cr–0.5 Mo–1.8 W–VNb steel." Materials Science and Engineering: A **319**: 784-787.

Sawada, K., Maruyama, K., Hasegawa, Y. and Muraki, T. (2000). "Creep and Fracture of Engineering Materials and Structures, ed. by T. Sakuma and K. Yagi." Trans. Tech Publications, Key Engineering Materials, vols **171**(174): 109-114.

Sawada, K., Miyahara, K., Kushima, H., Kimura, K. and Matsuoka, S. (2005). "Contribution of microstructural factors to hardness change during creep exposure in mod. 9Cr-1Mo steel." ISIJ international **45**(12): 1934-1939.

Sawada, K., Sekido, K., Kushima, H. and Kimura, K. (2017). Microstructural degradation during long-term creep in 9-12%Cr steels. 4th International ECCC Creep & Fracture Conference. Düsseldorf, Germany, ECCC: 96.

Sawada, K., Taneike, M. and Kimura, K. (2003). "*In situ* observation of recovery of lath structure in 9% chromium creep resistant steel." Journal of Materials Science and Technology **19**(6): 739-742.

Schaffernak, B. (2000). Characterization of 9-12% Cr Steels by Thermodynamic Model Calculations PhD thesis, Graz University of Technology.

Schindelin, J., Arganda-Carreras, I., Frise, E., Kaynig, V., Longair, M., Pietzsch, T., Preibisch, S., Rueden, C., Saalfeld, S. and Schmid, B. (2012). "Fiji: an open-source platform for biological-image analysis." Nature methods **9**(7): 676-682.

Schleyer, J., Speicher, M., Klenk, A. and Seidenfuß, M. (2017). Assessment of welds in components with similar martensitic welds using cross-weld data and numerical calculations. 4th International ECCC Creep & Fracture Conference. Düsseldorf, Germany, ECCC: 99.

Schnabel, E., Schwaab, P. and Weber, H. (1987). "Metallurgical Investigations on Creep Resistant Steels." Stahl Eisen **107**(14): 51-56.

Schüller, H. J., Hagn, L. and Woitscheck, A. (1974). "Risse im Schweißnahtbereich von Formstücken aus Heißdampfleitungen - Werkstoffuntersuchungen." Der Maschinenschaden **47**(1): 1-13.

Semba, H., Dyson, B. and McLean, M. (2008). "Microstructure-based creep modelling of a 9% Cr martensitic steel." Materials at High Temperatures **25**(3): 131-137.

Senior, B. A. (1989). "The precipitation of Laves' phase in 9Cr1Mo steels." Materials Science and Engineering: A **119**: L5-L8.

Shibli, A. (2017). "Aberrant P91 and its inspection, monitoring and life assessment." Materials at High Temperatures **34**(5-6): 442-447.

Shibli, I. and Le Mat Hamata, N. (2001). Creep and fatigue crack growth in P 91 weldments. 9 th International Conference on Creep & Fracture of Engineering Materials & Structures. Cambridge, UK, Maney Publishing: 777-787.

Shrestha, T., Alsagabi, S. F., Charit, I., Potirniche, G. P. and Glazoff, M. V. (2015). "Effect of heat treatment on microstructure and hardness of Grade 91 steel." Metals **5**(1): 131-149.

Sket, F., Dzieciol, K., Borbély, A., Kaysser-Pyzalla, A. R., Maile, K. and Scheck, R. (2010). "Microtomographic investigation of damage in E911 steel after long term creep." Materials Science and Engineering: A **528**(1): 103-111.

Sklenicka, V. (1996). "Development of intergranular damage under high temperature loading conditions." Mechanical Behaviour of Materials at High Temperature (edited by C. Moura Branco et al.): 43-58.

Sklenička, V., Kuchařová, K., Svoboda, M., Kloc, L., Buršík, J. and Kroupa, A. (2003). "Long-term creep behavior of 9–12% Cr power plant steels." Materials characterization **51**(1): 35-48.

Smith, C. S. (1948). "Grains, phases, and interfaces: An introduction of microstructure." Trans. Metall. Soc. AIME **175**: 15-51.

Smith, D. J., Walker, N. S. and Kimmins, S. T. (2003). "Type IV creep cavity accumulation and failure in steel welds." International Journal of Pressure Vessels and Piping **80**(9): 617-627.

Soleimanian, V. and Mojtahedi, M. (2015). "A comparison between different X-ray diffraction line broadening analysis methods for nanocrystalline ball-milled FCC powders." Applied Physics A **119**(3): 977-987.

Sonderegger, B. (2006). "Modifications of stereological correction methods for precipitate parameters using transmission microscopy." Ultramicroscopy **106**: 941-950.

Sonderegger, B. (2012). Aspects on measurement, modeling and impact of precipitates in alloys. Doctor of Technology, Graz University of Technology.

Sonderegger, B., Mitsche, S. and Cerjak, H. (2008). "Microstructural analysis on a creep resistant martensitic 9–12% Cr steel using the EBSD method." Materials Science and Engineering: A **481–482**(0): 466-470.

Sosa, J. M., Huber, D. E., Welk, B. and Fraser, H. L. (2014). "Development and application of MIPAR™: a novel software package for two-and three-dimensional microstructural characterization." Integrating Materials and Manufacturing Innovation **3**(1): 10.

Spencer, P. (2008). "A brief history of CALPHAD." Calphad **32**(1): 1-8.

Spindler, M. (2004). "The multiaxial creep ductility of austenitic stainless steels." Fatigue & fracture of engineering materials & structures **27**(4): 273-281.

Srinivas-Prasad, B. S., Rajkumar, V. B. and Hari Kumar, K. C. (2012). "Numerical simulation of precipitate evolution in ferritic–martensitic power plant steels." Calphad **36**: 1-7.

Storesund, J., Borggreen, K. and Zang, W. (2006). "Creep behaviour and lifetime of large welds in X 20 CrMOV 12 1—results based on simulation and inspection." International Journal of Pressure Vessels and Piping **83**(11): 875-883.

Stracey, M. G. (2016). Continuum Damage Mechanics (CDM) modelling of dislocation creep in 9-12% Cr creep resistant steels. Master of Science in Engineering Master's Dissertation, University of Cape Town.

Sulaiman, S., Li, H., Drew, M. and Dunne, D. (2009). Simulation of HAZ Microstructures in P91 Steel using Dilatometric and Gleeble Techniques. ECCC Creep Conference. Zurich, Switzerland, ECCC: 1046-1057.

Suryanarayana, C. and Norton, M. G. (1998). X-Ray Diffraction: A Practical Approach, Plenum Press

Szabó, P. J. (2004). "Microstructure development of creep resistant ferritic steel during creep." Materials Science and Engineering: A **387**: 710-715.

Tabuchi, M., Hongo, H., Watanabe, T., Sawada, K. and Takahashi, Y. (2009). Evaluation of Type-IV Creep Damages in Thick Welded Joint for High Cr Steels. 12th International Conference on Fracture 2009 (ICF-12), Ottawa, Canada, Curran Associates, Inc.

Tak, K. G., Schulz, U. and Eggeler, G. (2009). "On the effect of micrograin crystallography on creep of FeCr alloys." Materials Science and Engineering: A **510-511**: 121-129.

Takemasa, F., Nonaka, I., Ito, T., Saitou, K., Miyachi, Y. and Kagiya, Y. (2004). Type IV creep damage analysis for full size component test on welded P91 boiler hot reheat piping. International Conference on Elevated Temperature Design and Analysis, Nonlinear Analysis and Plastic Components, San Diego, USA, ASME.

Taneike, M., Sawada, K. and Abe, F. (2004). "Effect of carbon concentration on precipitation behavior of  $M_{23}C_6$  carbides and MX carbonitrides in martensitic 9Cr steel during heat treatment." Metallurgical and Materials Transactions A **35**(4): 1255-1262.

Tang, C. C., Lynch, P. A., Cheary, R. W. and Clark, S. M. (2006). "An In-Situ Method for the Study of Strain Broadening using Synchrotron X-ray Diffraction." Retrieved 22/10/2015, from <https://www.osti.gov/scitech/servlets/purl.pdf>.

Tezuka, H. and Sakurai, T. (2005). "A trigger of Type IV damage and a new heat treatment procedure to suppress it. Microstructural investigations of long-term ex-service Cr–Mo steel pipe elbows." International Journal of Pressure Vessels and Piping **82**(3): 165-174.

Thermo-Calc Software Inc. (2018). "Diffusion module (DICTRA)." Retrieved 24/08/2018, from [http://www.thermocalc.com/products-services/software/diffusion-module-\(dictra\)/](http://www.thermocalc.com/products-services/software/diffusion-module-(dictra)/).

Thermo-Calc Software Inc. (2018). "Precipitation module (TC-PRISMA)." Retrieved 24/08/2018, from [http://www.thermocalc.com/products-services/software/precipitation-module-\(tc-prisma\)/](http://www.thermocalc.com/products-services/software/precipitation-module-(tc-prisma)/).

Thomas, P. J. and Midgley, P. A. (2002). "An introduction to energy-filtered transmission electron microscopy." Topics in Catalysis **21**(4): 109-138.

Tiedt, L. R. (2002). An Introduction to Electron Microscopy and X-Ray Microanalysis. SA, North-West University.

Toby, B. H. (2006). "R factors in Rietveld analysis: How good is good enough?" Powder diffraction **21**(1): 67-70.

Trimby, P. (2013). Improving the spatial resolution of EBSD using transmission Kikuchi diffraction in the SEM, Oxford Instruments.

Tsuchida, Y., Okamoto, K. and Tokunaga, Y. (1995). "Improvement of Creep Rupture Strength of High Cr Ferritic Steel by Addition of W." ISIJ International **35**(3): 317-323.

Underwood, E. E. (1973). Quantitative stereology for microstructural analysis. Microstructural Analysis, Springer: 35-66.

Ungár, T. (2001). "Dislocation densities, arrangements and character from X-ray diffraction experiments." Materials Science and Engineering: A **309-310**: 14-22.

Van Rooyen, M. (2016). Thermal Power Plant Steel Creep Deformation Measurement Using Stereo Digital Image Correlation. Master of Engineering Masters Dissertation, Stellenbosch University.

Van Zyl, F., von dem Bongart, G., Bezuidenhout, M., Doubell, P., Havinga, F., Pegler, D. and Smit, W. (2005). Life Assessment and Creep Damage Monitoring of High Temperature Pressure Components in South Africa's Power Plant. ECCO Conference: Creep & Fracture in High Temperature Components—Design & Life Assessment Issues.

Vanaja, J., Laha, K., Mythili, R., Chandravathi, K. S., Saroja, S. and Mathew, M. D. (2012). "Creep deformation and rupture behaviour of 9Cr–1W–0.2V–0.06Ta Reduced Activation Ferritic–Martensitic steel." Materials Science and Engineering: A **533**: 17-25.

VanderPlas, J. (2016). Python Data Science Handbook: Essential Tools for Working with Data. California, Usa, O'Reilly Media, Inc.

Vanstone, R. W. (2001). Microstructure in Advanced 9-12%Cr Steam Turbine Steels. Quantitative microscopy of high temperature materials. A. Strang and J. Cawley. London, UK, 10M Communications Ltd: 355-372.

Vardeman, S. B. and Jobe, J. M. (2016). Statistical Methods for Quality Assurance. New York, USA, Springer-Verlag.

Viswanathan, R. (1989). Damage Mechanisms And Life Assessment of High Temperature Components. Metals Park, Ohio, USA, ASM International.

Voorhees, P. W. (1985). "The theory of Ostwald ripening." Journal of Statistical Physics **38**(1): 231-252.

Wagner, C. (1961). "Theorie der alterung von niederschlägen durch umlösen (Ostwald-reifung)." Zeitschrift für Elektrochemie, Berichte der Bunsengesellschaft für physikalische Chemie **65**(7-8): 581-591.

Walsh, D. W., Cieslak, M. J. and Savage, W. F. (1986). "Temperature measurements in resistance heated specimens: Longitudinal gradients." Welding Journal **65**(7).

Wang, C., Wang, M., Shi, J., Hui, W. and Dong, H. (2008). "Effect of microstructural refinement on the toughness of low carbon martensitic steel." Scripta Materialia **58**(6): 492-495.

Wang, Y., Kannan, R. and Li, L. (2016). "Characterization of as-welded microstructure of heat-affected zone in modified 9Cr–1Mo–V–Nb steel weldment." Materials Characterization **118**: 225-234.

Wang, Y., Kannan, R. and Li, L. (2016). "Identification and characterization of intercritical heat-affected zone in as-welded grade 91 weldment." Metallurgical and Materials Transactions A **47**(12): 5680-5684.

Wang, Y., Kannan, R., Zhang, L. and Li, L. (2017). "Microstructural Analysis of the As-Welded Heat-Affected Zone of a Grade 91 Steel Heavy Section Weldment." Weld. J **96**(6): 203-219.

Watanabe, M. (2011). X-Ray Energy-Dispersive Spectrometry in Scanning Transmission Electron Microscopes. Scanning Transmission Electron Microscopy: Imaging and Analysis. S. J. Pennycook and P. D. Nellist, Springer. **XII**: 291-352.

Wen, J.-F., Tu, S.-T., Xuan, F.-Z., Zhang, X.-W. and Gao, X.-L. (2016). "Effects of stress level and stress state on creep ductility: evaluation of different models." Journal of Materials Science & Technology **32**(8): 695-704.

Weyer, R. (2016). The Modelling of Damage due to Diffusional Creep in High Chromium Steels. Master of Science in Engineering Master's Dissertation, University of Cape Town.



Wiesner, C., Earthman, J., Eggeler, G. and Ilshner, B. (1989). "Creep crack growth and cavitation damage in a 12% CrMoV steel." Acta Metallurgica **37**(10): 2733-2741.

Williams, D. B. and Carter, C. B. (2009). Transmission Electron Microscopy: A Textbook for Material Science. New York, USA, Springer.

Williamson, G. and Smallman, R. (1956). "III. Dislocation densities in some annealed and cold-worked metals from measurements on the X-ray debye-scherrer spectrum." Philosophical Magazine **1**(1): 34-46.

Wilson, P. (1990). Remanent Creep Life Prediction in Low-Alloy Ferritic Steel Power Plant Components. Doctor of Philosophy Doctoral Dissertation, University of Cambridge.

World Coal Association (2017) "Basic coal facts." 1.

Wu, R. and Sandström, R. (1995). "Creep cavity nucleation and growth in 12Cr–Mo–V steel." Materials science and technology **11**(6): 579-588.

Xu, Y., Nie, Y., Wang, M., Li, W. and Jin, X. (2017). "The effect of microstructure evolution on the mechanical properties of martensite ferritic steel during long-term aging." Acta Materialia **131**: 110-122.

Xu, Y., Wang, M., Wang, Y., Gu, T., Chen, L., Zhou, X., Ma, Q., Liu, Y. and Huang, J. (2015). "Study on the nucleation and growth of Laves phase in a 10% Cr martensite ferritic steel after long-term aging." Journal of Alloys and Compounds **621**: 93-98.

Xu, Y., Zhang, X., Tian, Y., Chen, C., Nan, Y., He, H. and Wang, M. (2016). "Study on the nucleation and growth of M<sub>23</sub>C<sub>6</sub> carbides in a 10% Cr martensite ferritic steel after long-term aging." Materials Characterization **111**: 122-127.

Yadav, S. D., Kalácska, S., Dománková, M., Yubero, D. C., Resel, R., Groma, I., Beal, C., Sonderegger, B., Sommitsch, C. and Poletti, C. (2016). "Evolution of the substructure of a novel 12% Cr steel under creep conditions." Materials Characterization **115**: 23-31.

Yadav, S. D., Rosc, J., Sartory, B., Brunner, R., Sonderegger, B., Sommitsch, C. and Poletti, C. (2014). Investigation of pre-existing pores in creep loaded 9Cr steel. Proceedings of the 2nd International Congress on 3D Materials Science, Springer.

Yadav, S. D., Sonderegger, B., Muhammad, S. and Poletti, C. (2016). "Modeling the creep behaviour of tempered martensitic steel based on a hybrid approach." Materials Science & Engineering A **662**: 330-341.

Yadav, S. D., Sonderegger, B., Sartory, B., Sommitsch, C. and Poletti, C. (2015). "Characterisation and quantification of cavities in 9Cr martensitic steel for power plants." Materials science and technology **31**(5): 554-564.

Yadav, S. D., Sonderegger, B., Stracey, M. and Poletti, C. (2016). "Modelling the creep behaviour of tempered martensitic steel based on a hybrid approach." Materials Science and Engineering: A **662**: 330-341.

Yamakov, V., Wolf, D., Phillpot, S. and Gleiter, H. (2002). "Grain-boundary diffusion creep in nanocrystalline palladium by molecular-dynamics simulation." Acta Materialia **50**(1): 61-73.

Yamamoto, K., Kimura, Y. and Mishima, Y. (2003). "Effect of Matrix Substructures on Precipitation of the Laves Phase in Fe-Cr-Nb-Ni System." ISIJ International **43**(8): 1253-1259.

Yamasaki, S. (2004). Modelling precipitation of carbides in martensitic steels. Doctor of Philosophy Doctoral Dissertation, University of Cambridge.

Yan, B., Liu, Y., Wang, Z., Liu, C., Si, Y., Li, H. and Yu, J. (2017). "The Effect of Precipitate Evolution on Austenite Grain Growth in RAFM Steel." Materials **10**(9): 1017.

Yan, W., Wang, W., Shan, Y. and Yang, K. (2013). "Microstructural stability of 9-12Cr ferrite/martensite heat-resistant steels." Frontiers of Materials Science **7**(1): 1-27.

Yao, H.-T., Xuan, F.-Z., Wang, Z. and Tu, S.-T. (2007). "A review of creep analysis and design under multi-axial stress states." Nuclear Engineering and Design **237**(18): 1969-1986.

Yatomi, M. and Nikbin, K. (2014). "Numerical prediction of creep crack growth in different geometries using simplified multiaxial void growth model." Materials at High Temperatures **31**(2): 141-147.

Yin, Y. and Faulkner, R. (2006). "Continuum damage mechanics modelling based on simulations of microstructural evolution kinetics." Materials science and technology **22**(8): 929-936.

Yoshizawa, M. and Igarashi, M. (2007). "Long-term creep deformation characteristics of advanced ferritic steels for Usc power plants." International Journal of Pressure Vessels and Piping **84**(1-2): 37-43.

Yurioka, N. (2001). "Physical Metallurgy Of Steel Weldability." ISIJ International **41**(6): 566–570.

Zhang, C., Wang, Q., Ren, J., Li, R., Wang, M., Zhang, F. and Sun, K. (2012). "Effect of martensitic morphology on mechanical properties of an as-quenched and tempered 25CrMo48V steel." Materials Science and Engineering: A **534**: 339-346.

Zhang, C., Wang, Q., Ren, J., Li, R., Wang, M., Zhang, F. and Yan, Z. (2012). "Effect of microstructure on the strength of 25CrMo48V martensitic steel tempered at different temperature and time." Materials & Design (1980-2015) **36**: 220-226.

Zhang, X., Wu, X., Liu, R., Liu, J. and Yao, M. (2017). "Influence of Laves phase on creep strength of modified 9Cr-1Mo steel." Materials Science and Engineering: A **706**: 279-286.

Zhao, L., Jing, H., Xu, L., Han, Y. and Xiu, J. (2012). "Experimental study on creep damage evolution process of Type IV cracking in 9Cr–0.5 Mo–1.8 W–VNb steel welded joint." Engineering Failure Analysis **19**: 22-31.

# RESEARCH OUTPUTS

The following presentations were presented at both national and international conferences and workshops:

- Marx, G. (2016). Evaluation of 12Cr Creep Aged Steels after Welding. International Workshop on Advanced and In-situ Microscopies of Functional Nanomaterials and Devices, Boardwalk Convention Centre, Port Elizabeth.
- Marx, G. and Westraadt, J. E. (2016). Quantitative Microstructural Evaluation of a 12% Cr Creep Aged Power Plant Steel. Microscopy Society of Southern Africa 54th Annual Conference: 2016, Boardwalk Hotel and Convention Centre, Port Elizabeth.
- Marx, G. and Westraadt, J. E. (2017). Quantitative Evaluation of the Secondary Phase Particles in Welded 12% Cr Creep Aged Steel. Microscience Microscopy Congress 2017 (mmc2017) incorporating EMAG, Manchester, United Kingdom. Available from: Poster 4032 on <http://mmc-series.org.uk/conference/scientific-programme>
- Marx, G. and Westraadt, J. E. (2017). Quantitative microstructural evaluation of 12% Cr creep aged steel weldments. 4th International ECCC Conference (ECCC 2017), Düsseldorf, Germany. Available from: [https://eccc2017.com/files/eccc\\_preliminary\\_program.pdf](https://eccc2017.com/files/eccc_preliminary_program.pdf)
- Marx, G. (2018). Microstructural Evolution of Welded Creep Aged CSEF Steel. EPPEI (Eskom Power Plant Engineering Institute) 14th Technical Workshop Meeting (Materials Science), Cape Town, South Africa.